Silesian University of Technology
Faculty of Mechanical Engineering
Department of Fundamentals of Machinery Design

DOCTORAL DISSERTATION

Thermomechanical fatigue life assessment of polymer-matrix composites under temperature control and different loading regimes

in the form of a collection of thematically related published articles in scientific journals

Jafar Amraei, M.Sc., Eng.

Scientific discipline: Mechanical Engineering

Supervisor: Andrzej Katunin, Ph.D., D.Sc., Eng., prof. SUT
Auxiliary supervisor: Dominik Wachla, Ph.D., Eng.
Silesian University of Technology
Faculty of Mechanical Engineering
Department of Fundamentals of Machinery Design

Gliwice, 2025

Acknowledgements

The journey of my doctoral studies has been intellectually challenging and personally enriching. During this time, I had the opportunity to expand my knowledge, explore new research areas, and develop as a scholar. However, this transformative experience would not have been possible without the exceptional individuals who supported, encouraged, and inspired me.

I owe my deepest gratitude to my mother, whose constant encouragement and endless support have been my greatest source of strength, especially during the most challenging phases of my PhD journey.

I am so grateful to my supervisor, Prof. Andrzej Katunin, for his invaluable guidance, motivation, and continuous support throughout my PhD journey. I also extend my sincere appreciation to my auxiliary supervisor, Dr. Dominik Wachla, for his valuable assistance and advice. Furthermore, I sincerely thank to Dr. Tomasz Rogala, not only for his contributions to our collaborative research but also for his friendship and support.

I am also grateful to Prof. Anna Timofiejczuk and Prof. Marek Wyleżoł for their support and inspiration in starting my scientific career at the Silesian University of Technology.

I sincerely thank Prof. Chiara Colombo and Prof. Andrea Manes for hosting my internship at Politecnico di Milano, where I had the opportunity to work on thermography-based NDT techniques for PMCs. I also extend my appreciation to Prof. Paulo N. B. Reis from the University of Coimbra for his collaboration in the common research within the Structural Integrity Assessment Research group, led by Prof. Andrzej Katunin.

I sincerely appreciate the collaboration and contributions of my German co-authors: Prof. Dr.-Ing. Frank Balle, Dr. Aravind Premanand, Dr.-Ing. Bilal Khatri, and Mr. Michael Rienks, as well as my Polish co-authors: Dr. Magdalena Lipińska, Prof. Wacław Kuś, Prof. Grzegorz Kokot, Dr. Krzysztof Lis, Dr. Marcin Bilewicz, and Prof. Izabela Barszczewska-Rybarek, along with João M. Parente from Universidade da Beira Interior (Portugal). My sincere thanks also go to Mr. Daniel Pająk and Ms. Aneta Fryda for their technical and administrative support.

I am grateful to the Silesian University of Technology for providing the necessary resources and funding. Finally, I extend my heartfelt gratitude to my family and friends for their patience, encouragement, and support.

Preface

PMCs, including CFRPs and GFRPs, are increasingly used in the energy (e.g., wind turbines) and transportation (e.g., vehicles, aviation, rail, and marine) sectors for their superior strength-to-weight ratio, durability, environmental resilience, and design flexibility. However, the lack of knowledge of their fatigue responses necessitates conservative design approaches, often resulting in over-designed structures to mitigate the risk of significant damage accumulation under prolonged cyclic loading and to prevent premature failure. This imposes not only weight and cost penalties but also limits structural design optimization.

A fundamental challenge in the application of PMCs is understanding their fatigue responses under different loading regimes, from low- to very-high-cycle fatigue. Nevertheless, prolonged fatigue experiments at the conventional loading frequency range (i.e., 5 Hz or below) are unfeasible due to excessive time requirements and costs. For example, a single fatigue test reaching 10^9 cycles would take more than six years under a loading frequency of 5 Hz—equivalent to approximately one-fifth of the typical service lifetime of an aircraft. Therefore, it is of primary significance to reduce fatigue testing durations. Accelerating fatigue testing at higher frequencies is one pathway to address this limitation and enable fatigue testing within a feasible timeframe.

While high-frequency testing offers a feasible solution, it induces the self-heating phenomenon due to the viscoelastic nature of polymers, leading to complex thermal-mechanical synergy. Depending on the intensity of the self-heating effect, the integrity of the PMC can either be maintained without structural degradation or significantly altered, which can complicate the analysis of fatigue-induced damage. This, in turn, poses challenges in developing predictive life models essential for improving the longevity and reliability of PMCs.

This dissertation aims to bridge these gaps by developing a physics-based framework for understanding and modeling the self-heating phenomenon in fatigue-loaded PMCs. Furthermore, novel methodologies are introduced to assess the fatigue response of PMCs in the presence of self-heating, while strategies for mitigating the adverse effects of self-heating are also evaluated. Moreover, the potential use of self-heating phenomenon as a heat source, previously explored by our research group, is further developed for assessing the structural integrity of PMCs.

List of publications

This PhD thesis is presented as a collection of thematically related research articles published in scientific journals. It consists of eight research papers, which are categorized into seven chapters based on their thematic relevance. The full texts of these papers are included in the Appendices, and they are referenced below using Roman numerals.

Chapter I: Includes papers I and II.

I. **J. Amraei** and A. Katunin. "Recent advances in limiting fatigue damage accumulation induced by self-heating in polymer–matrix composites". *Polymers* 14.24 (Dec. 2022), p. 5384. ISSN: 2073-4360. DOI: 10.3390/polym14245384. (IF 2022: 5, MNiSW: 100).

II. P. N. B. Reis, A. Katunin, and **J. Amraei**. "Critical analysis of the systems used to reduce self-heating in polymer composites subjected to very high cycle fatigue regimes". *Fatigue & Fracture of Engineering Materials & Structures* 48 (Jan. 2025), p. 1371–1392. ISSN: 1460-2695. DOI: 10.1111/ffe.14561. (IF 2023: 3.1, MNiSW: 100).

Chapter II: Includes paper III.

III. **J. Amraei**, A. Katunin, and M. Lipińska. "Numerical simulation and experimental validation of self-heating of polymer-matrix composites during low-cycle fatigue loading". *International Journal of Fatigue* 188 (Nov. 2024), p. 108510. ISSN: 0142-1123. DOI: 10.1016/j.ijfatigue.2024.108510. (IF 2023: 5.7, MNiSW: 140).

Chapter III: Includes papers IV and V.

IV. **J. Amraei**, T. Rogala, A. Katunin, A. Premanand, G. Kokot, D. Wachla, W. Kuś, M. Bilewicz, B. Khatri, and F. Balle. "Thermomechanical fatigue behavior of CF/PEKK composite under low and ultrasonic frequencies". *Composites Part B: Engineering* 281 (July 2024), p. 111539. ISSN: 1359-8368. DOI: 10.1016/j.compositesb.2024.111539. (IF 2023: 12.7, MNiSW: 200).

V. A. Premanand, T. Rogala, D. Wachla, **J. Amraei**, A. Katunin, B. Khatri, M. Rienks, and F. Balle. "Fatigue strength estimation of a CF/PEKK composite through self-heating temperature analysis using cyclic bending tests at 20 kHz". *Composites Science and Technology* 243 (Oct. 2023), p. 110218. ISSN: 0266-3538. DOI: 10.1016/j.compscitech.2023.110218. (IF 2022: 9.1, MNiSW: 200).

Chapter IV: Includes paper VI.

VI. **J. Amraei** and A. Katunin. "Thermomechanical fatigue life assessment of polymer-matrix composites via entropy-based damage evolution and stiffness degradation under different frequencies". *Composites Part B: Engineering* 298 (Jun. 2025), p. 112353. ISSN: 1359-8368. DOI: 10.1016/j.compositesb.2025.112353. (IF 2023: 12.7, MNiSW: 200).

Chapter V: Includes paper VII.

VII. **J. Amraei**, T. Rogala, A. Katunin, I. Barszczewska-Rybarek, J. M. Parente, and P. N. B. Reis. "Synergistic effects of graphene nanoplatelets and carbon nanofibers on thermomechanical fatigue response of modified glass/epoxy composites". Submitted to *International Journal of Fatigue*, Under Review (Dec. 2024). (IF 2023: 5.7, MNiSW: 140).

Chapter VI: Includes paper VIII.

VIII. **J. Amraei**, A. Katunin, D. Wachla, and K. Lis. "Damage assessment in composite plates using extended non-destructive self-heating based vibrothermography technique". *Measurement* 241 (Feb. 2025), p. 115670.ISSN: 0263-2241.
DOI: 10.1016/j.measurement.2024.115670. (IF 2023: 5.2, MNiSW: 200).

Chapter VII: Includes the summary of papers I-VIII.

Author contribution statement

The contributions of each co-author, along with their respective percentages, are detailed in the appendices. Below is a summary of the author's key contributions to each paper:

Paper I: The author's contribution was equal to 70%.

CRediT: Writing – review & editing, Writing – original draft, Methodology, Investigation, Formal analysis, Data curation, Conceptualization. The author's key contributions include:

- Phenomenology of the self-heating effect,
- Fatigue fracture mechanisms in composites, accounting for the self-heating phenomenon,
- In-depth assessment of current surface cooling methods and feasible solutions for mitigating the self-heating effect during fatigue loading,
- Viable strategies for preventing the self-heating effect by selecting optimal materials,
- Recommendations for preventing the self-heating effect based on the optimal material design at the manufacturing stage, and the implementation of efficient, cost-effective cooling systems in the operational stage.

Paper II: The author's contribution was equal to 15%.

The author's key contributions include:

- Ideas related to feasible surface cooling techniques, and viable thermally conductive nanofillers for mitigating the self-heating effect,
- Critical review, and revisions throughout both pre-publication and post-publication stages.

Paper III: The author's contribution was equal to 65%.

CRediT: Writing – review & editing, Writing – original draft, Validation, Software, Methodology, Investigation, Funding acquisition, Formal analysis, Data curation, Conceptualization. The author's key contributions include:

- Design of experiments,
- Postprocessing oscillatory shear rheometry data,
- Constructing master curves and modeling the thermoviscoelastic response of PMCs using Prony series,
- Developing a numerical model to simulate the self-heating phenomenon,
- Validating the numerical model by comparing its results with experimental findings.

Paper IV: The author's contribution was equal to 25%.

CRediT: Writing – review & editing, Writing – original draft, Software, Methodology, Investigation, Formal analysis, Data curation, Conceptualization. The author's key contributions include:

- Design of experiments, and contribution to the low-frequency fatigue testing,
- Introducing a rapid procedure to explore the influence of mean stress using the thermographic approach (ΔT-σ), and subsequently constructing the stress-life (S-N) curves under different mean loads,
- Developing a model for combining low and ultrasonic fatigue testing results based on the heat dissipation rate concept.

Paper V: The author's contribution was equal to 10%.

CRediT: Conceptualization, Methodology, Data curation, Formal analysis, Software, Writing – original draft. The author's key contributions include:

- Estimation of critical self-heating temperature using the energy dissipation rate concept.

Paper VI: The author's contribution was equal to 80%.

CRediT: Writing – review & editing, Writing – original draft, Validation, Software, Methodology, Investigation, Funding acquisition, Formal analysis, Data curation, Conceptualization. The author's key contributions include:

- Design and performing of the experiments,
- Ideas, and formulation of overarching research goals and aims,

- Data processing and developing MATLAB routines,
- Developing a trilinear $\dot{q}$-σ model for reliable assessment of the fatigue response in PMCs,
- Developing and validating the proposed entropy-based damage evolution for fatigue life assessment of PMCs,
- Developing the stiffness degradation concept for constructing S-N curves, and correlating the AE-driven criticality with the stiffness degradation.

Paper VII: The author's contribution was equal to 35%.

CRediT: Writing-review & editing, Writing-original draft preparation, Validation, Software, Methodology, Investigation, Formal analysis, Data curation, Conceptualization. The author's key contributions include:

- Design and performing of the fatigue experiments,
- Ideas, and formulation of overarching research goals and aims,
- Preliminary investigation to select the appropriate loading frequency for the experiments,
- Adding the theory related to nano-reinforced PMCs,
- Estimation of fatigue strength using the heat dissipation rate concept ($\dot{q}$-σ) based on MCR and MPD procedures,
- Formal analysis for exploring the role of thermally conductive nanocarbon-based allotropes on the fatigue response of modified PMCs through the standard S-N curves, and thermal responses.

Paper VIII: The author's key contribution was equal to 50%.

CRediT: Writing – review & editing, Writing – original draft, Software, Project administration, Validation, Methodology, Investigation, Funding acquisition, Formal analysis, Data curation, Conceptualization. The author's key contributions include:

- Numerical simulations,
- Designing and performing the SHVT experiments,
- Image processing,
- Developing a procedure to identify the optimal raw thermograms.

Contents

List of Figures

List of important abbreviations

S-N curve	Stress-life curve
1D	One-dimensional
2D	Two-dimensional
3D	Three-dimensional
AE	Acoustic emission
ALIN	Peak amplitude
BC	Boundary condition
BET	Boundary of effective thermogram
CAT	Constant amplitude test
CCNT	Total counts of hit-cascade
CENY	Cumulative energy
CF/PEKK	Carbon fiber-reinforced poly-ether-ketone-ketone
CFRP	Carbon fiber-reinforced polymer
CNF	Carbon nanofiber
EDI	Entropy-based damage index
ETE	True energy
FBD	Flat bottom damage
FFE	Fracture fatigue entropy
GFRP	Glass fiber-reinforced polymer

GNP	Graphene nanoplatelet
GO	Graphene oxide
HCF	High-cycle fatigue
HDPE	High-density polyethylene
HNP	Hybrid nanoparticle
IAT	Increasing amplitude test
IC	Initial condition
IRT	Infrared thermography
LCF	Low-cycle fatigue
LF	Low frequency
LFFT	Low-frequency fatigue testing
LVID	Low-velocity impact damage
MCR	Minimum curvature radius
MPD	Maximum perpendicular distance
MWCNT	Multi-walled carbon nanotube
NDT	non-destructive testing
OF	Objective function
PMC	Polymer-matrix composite
ROI	Region of interest
RT	Room temperature
SHVT	Self-heating based vibrothermography
TTS	Time-temperature superposition
UF	Ultrasonic frequency
UFFT	Ultrasonic-frequency fatigue testing

VHCF	Very-high-cycle fatigue
VT	Vibrothermography
X-ray CT	X-ray computed tomography

Chapter 1

Introduction

Chapter 1 provides a comprehensive overview of the research, highlighting the significance of the self-heating phenomenon in fatigue analysis as well its applicability in the non-destructive evaluation of PMCs. Section 1.1 describes the phenomenology of self-heating in different phases. Section 1.2 reviews how the fatigue response of PMCs, in the presence of the self-heating effect, is affected by environmental factors, material types, and loading parameters. Recent advances in modeling the self-heating phenomenon in fatigue-loaded PMCs are presented in Section 1.3, highlighting several predictive approaches and their limitations. Considering the time-consuming nature of fatigue testing, Section 1.4 discusses the recent strategies implemented for the rapid fatigue analysis of PMCs through thermography-based approaches, which allow fatigue strength and life estimation in the presence of the self-heating effect. Section 1.5 provides a literature review on viable solutions, including surface cooling during loading and optimal material design, to mitigate structural degradation caused by the self-heating effect, thereby extending the fatigue life of PMCs. Section 1.6 highlights the potential of using self-heating as an alternative heat source for damage assessment of PMCs through thermography-based NDT techniques. In Section 1.7, the motivation, aim, and hypothesis of the research are established based on identified gaps in the existing literature. Finally, Section 1.8 defines the research scope and outlines the methodological framework for achieving the objectives.

1.1 Phenomenology of self-heating effect

When a PMC structure is subjected to cyclic loading, the cyclic response indicates a delay or phase lag between stress and strain magnitudes due to the viscoelastic nature of polymers, which is associated with hysteretic phenomena. Additionally, since the thermal conductivity of a typical polymeric composite is significantly lower than that of metallic components [1, 2, 3, 4, 5, 6], a substantial amount of heat is stored within the tested PMC specimen. This heat accumulation

manifests as a temperature rise in the structure, known as the self-heating phenomenon [6]. In addition to the laboratory fatigue testing, this phenomenon may also occur in industrial fatigue-loaded PMC structures such as wind turbine blade sections [7, 8], and CFRP composite gear shown in Figure 1.1 [9], see [6] for more details.

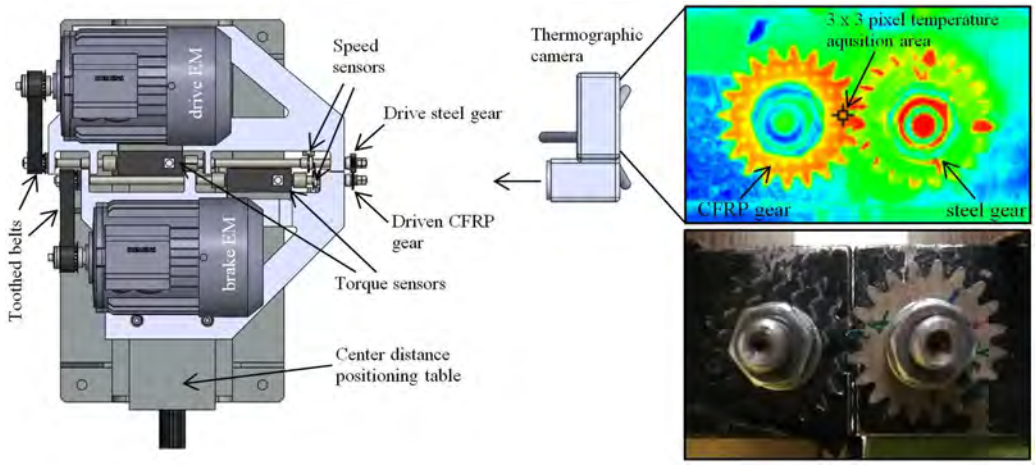

Figure 1.1: Illustration of the model and registered thermogram showing the self-heating effect during the operation of a CFRP composite gear [9].

The self-heating phenomenon is generally described by the following three phases as illustrated in Figure 1.2 [6]. Phase I involves rapid temperature growth in a relatively short period, which is primarily driven by friction. Phase II is characterized by a stabilized self-heating temperature over prolonged fatigue loading. This stabilization arises from the synergy between mechanical fatigue and viscoelastic-driven thermal energy, leading to a thermodynamic equilibrium where heat generation is nearly equal to heat dissipation through convection, conduction, and radiation. Phase III marks a sudden increase in self-heating temperature, resulting from mechanical softening and progressive damage accumulation. This leads to the dominance of heat storage, ultimately resulting in specimen failure or structural breakdown [6]. The boundary between phases II and III is related to the critical self-heating temperature, the parameter used in previous studies for evaluating the thermomechanical fatigue response of PMCs [10, 11, 12]. This parameter signifies a temperature value at which rapid damage propagation begins, accelerating fatigue damage accumulation and eventually resulting in premature failure [6]. If the self-heating temperature increase is maintained within the safe range (usually below 3°C [13]), it is feasible to implement this phenomenon for damage inspection using NDT techniques, without jeopardizing the structural integrity as schematically demonstrated in Figure 1.2 [13, 14, 15]. Otherwise, subjecting PMCs to high stress and/or frequency loading results in significant internal heat accumulation, and consequently high self-heating temperature [6]. This contributes to the stiffness degradation

of PMCs by accelerating the damage accumulation at different scales, ranging from micro- to macro-scale [6]. At the microscale, for example, the higher coefficient of thermal expansion of polymers compared to fibers leads to residual thermal stresses at the interface/interphase region between the reinforcement and bulk polymer [16]. The residual stress acts as a catalyst in increasing the self-heating temperature [17]. This results in chemical degradation and softening of crosslinked networks [18], reduction in intermolecular forces, and consequently debonding in the interphase zone, attributed to phase I [19, 20]. In the microscale linked to phase II, the fatigue-loaded PMC specimen may experience different damage types including matrix cracking, single fiber breakage, microdelamination, and microcrack [21, 22, 23]. The irreversible formation of microcracks and microdelaminations occurs continuously and generates entropy, aligning with the second law of thermodynamics (Clausius inequality statement) [24]. The evolution of macroscopic damage, triggered by the accumulation of microcracks and microdelaminations, forms macrocracks and macrodelaminations, which ultimately leads to sudden failure. A comprehensive understanding of the phenomenology of self-heating allows for reliably simulating the self-heating phenomenon.

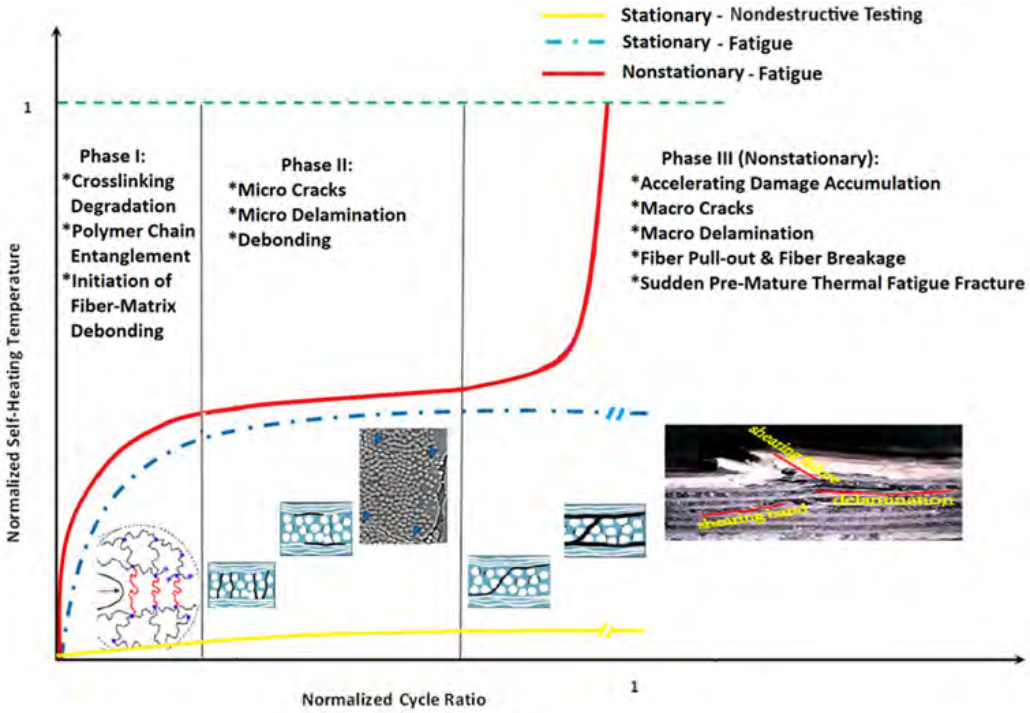

Figure 1.2: A schematic illustration of the self-heating evolution in different phases during cyclic loading [6].

1.2 Dependency of fatigue response on loading parameters

The fatigue response of PMCs is influenced by the self-heating effect, whose severity depends on (i) operational and environmental factors (e.g., ambient temperature) [25, 26, 27, 28], (ii) material types [12, 29, 30, 31, 32], and (iii) loading parameters (e.g., loading frequency, applied stress/strain ratio) [15, 33, 34, 35, 36, 37], see [6, 32] for additional information. For this purpose, Charalambous et al. [26] employed the four-point bending test to investigate the fatigue performance of CFRP composites under various ambient temperatures. Their findings revealed that the delamination rate increased with rising ambient temperature during fatigue testing. The crack propagation rate at 80 °C was observed to be twice as high as that at RT. In addition, several studies have investigated the fatigue behavior of GFRP specimens under axial loading at different stress ratios (R) and low frequencies (15 Hz or below) [38, 39, 40, 41]. The authors of the mentioned studies reported that increasing R at the same stress level led to longer fatigue life, while the slope of S-N curve dropped with more scattered responses. Additionally, different R values resulted in different damage distributions. Damage was uniformly distributed along the specimens for R=0.5, while damage zones were severe and localized at R=0.1 and caused continuous stiffness degradation. Moreover, despite extensive research highlighting the negative impact of loading frequency on the fatigue performance of PMCs, few studies have directly examined its specific role in the fatigue response, necessitating further investigation. The role of material types is discussed in Section 1.5, respectively, owing to their relevance. While high-frequency testing offers a feasible solution, it induces the self-heating phenomenon due to the viscoelastic nature of polymers, leading to complex thermal-mechanical synergy.

1.3 Advances in modeling the self-heating phenomenon

The self-heating effect can significantly alter the fatigue response of PMCs, complicating the accurate assessment of fatigue-induced damage. This, in turn, makes it difficult to develop reliable predictive life models, which are essential for enhancing the longevity and reliability of PMCs under real-world operating conditions. Therefore, understanding the physics and modeling the self-heating phenomenon within fatigue experiments is crucial. For this purpose, Ly et al. [42] developed a numerical viscoelastic constitutive model using the thermodynamic laws to study the self-heating effect that appeared in HDPE-carbon composite under cyclic loading with the low-frequency, i.e., 0.1 Hz and 1 Hz. Nonetheless, the model was not validated experimentally. Sevenois et al. [43] numerically investigated the influence of self-heating on the thermoviscoplastic behavior of representative volume element of a unidirectional carbon-polyamide 6 composite under monotonic loading. The influence of frequency was not

taken into consideration in their study. De Lima et al. [44] implemented a numerical-experimental concept based on a curve-fitting procedure for investigating the self-heating effect in viscoelastic dampers under cyclic loading. Furthermore, Sapozhnikov et al. [45]] developed an analytical self-heating model under three-point bending. In another study [46], they examined how loading frequency affected self-heating temperature. Despite their success in evaluating temperature distribution, the developed model has a limitation. The approach of substituting convection heat flux for all boundaries may not always be suitable in scenarios where at least one boundary remains unaffected by fluid interaction. Moreover, Lahuerta et al. [47] carried out an experimental–numerical investigation to predict the self-heating temperature of thick GFRP laminates (i.e., 10 mm, 20 mm, and 30 mm of thickness) under low frequencies, ranging from 0.25 Hz to 2.5 Hz. However, the assumption of uniform heat generation in their analysis may diminish the accuracy of the results, particularly in scenarios with high-stress levels. Therefore, developing a model that accounts for all the limitations outlined above is of primary importance for improving the predictability of the self-heating phenomenon.

1.4 Advances in rapid fatigue life assessment methods

To tackle the challenge of performing time-consuming fatigue experiments at conventional frequencies (e.g., 5 Hz or below), a viable strategy is to accelerate fatigue testing at higher frequencies within a feasible time duration, which induces the self-heating phenomenon. Advances in understanding the phenomenology of the self-heating effect have led to the development of thermographic approaches using non-contact infrared thermography to rapidly estimate fatigue strength or, in other studies, the fatigue limit. The concept of determining the fatigue strength/limit through IATs under sequential stress levels was first introduced by Luong [48], Rosa and Risitano [49], called temperature rise-stress (ΔT-σ). This approach evaluates the fatigue strength of the tested PMC by measuring the stabilized temperature increases corresponding to a wide range of stress levels without requiring extensive time or large datasets. According to this groundbreaking methodology, fatigue strength corresponds to the beginning of rapid thermal response, which marks the beginning of structural degradation. The classical method developed by Luong relies on bilinear regression to determine the fatigue strength at the intersection of two fitted lines. Numerous studies have demonstrated the utility of this method in predicting the fatigue strength of numerous PMCs, including CFRPs, GFRPs, and other PMCs [15, 23, 36, 49, 50, 51, 52, 53, 54, 55, 56]. Meanwhile, Huang et al. [52] proposed alternative curve-fitting methods, each potentially suitable for modeling the thermomechanical fatigue response of specific polymers and PMCs. In addition to ΔT-σ approach, the heat dissipation rate-stress (ΔT-σ) approach has shown its capability for determining the fatigue

strength of PMCs [57, 58]. In summary, both methods offer advantages depending on the material and application, with the ΔT-σ excelling in simplicity and speed, while the $\dot{q}$-σ approach, requiring further analysis, but may deliver a more in-depth assessment of fatigue behavior. This represents a key gap in the literature, highlighting the importance of selecting an appropriate thermographic approach for determining fatigue strength. In addition to the fatigue strength estimation [53, 59, 60], the fatigue life assessment of PMCs plays a key role in ensuring the PMC performance across different fatigue regimes, ranging from LCF to VHCF [11]. Unlike the widely used standard *S-N* curves, which rely on final failure and are constructed under conventional frequencies (5 Hz or below) without accounting for the self-heating effect, the entropy concept as a thermodynamic framework offers a more comprehensive analysis by incorporating results from the $\dot{q}$-σ approach [61]. Entropy-based models can advantageously capture the impact of self-heating at any arbitrary frequency, providing a more generalized assessment of fatigue behavior. Entropy generation, governed by the second law of thermodynamics [62], is a function of loading types [63], ambient temperature [64], stress level, and frequency [65, 66]. For fatigue-loaded PMCs, entropy generation may arise from different fracture mechanisms such as matrix cracking, fiber breakage, debonding, and delamination [67]. Several studies have implemented entropy-based models for fatigue life prediction in PMCs [53, 68, 69, 70]. By applying the first and second laws of thermodynamics, Naderi and Khonsari [67] developed a theoretical framework to assess the fracture fatigue entropy (FFE) as a material property. Their findings were further supported by Mohammadi and Mahmoudi [62], who proposed a micromechanical model for evaluating FFE. Huang et al. [53] assessed the FFE value for CFRP. For this reason, they implemented a quadratic function to separate the internal heat friction from the entire heat generation, and finally, determined the heat induced by damage as the key factor in the FFE determination. All previous works assumed constant heat capacity (C_p) when implementing the $\dot{q}$-σ approach for evaluating FFE, but incorporating temperature-dependent C_p is critical for accurately modeling and quantifying the heat dissipation rate.

1.5 Advances in limiting self-heating effect and prolonging fatigue life

The intensity of the self-heating effect is highly dependent on loading frequency – higher frequencies result in greater temperature rise and reduced fatigue lifetime. The severity of the self-heating effect in fatigue-loaded PMCs can be mitigated through two feasible strategies: (i) surface cooling of a tested PMC during fatigue loading [26, 27, 71, 72], and (ii) optimal materials design and selection [73].

The first strategy, as discussed in detail in [6, 32], involves the forced air or liquid cooling of a tested composite surface using various media and technologies. To limit the self-heating effect, researchers in [33, 11, 37] used a pulse-pause method alongside forced air cooling. Lee et al. [74] incorporated a Peltier ring-type cooling, while Wang et al. [30] utilized both cryogenic nitrogen cooling and pulse–pause method, see [6] for further details. In the second strategy for limiting self-heating, several studies have investigated the feasibility of PMC modifications using nanoparticles during the manufacturing process, see [6, 32] for more details. Among the diverse types of nanoparticles, carbon-based allotropes are distinguished owing to their exceptional mechanical, electrical, and thermal properties [75, 76, 77, 78, 79, 80]. In this context, the literature also highlights that incorporating hybrid nanoparticles into composites improves their performance by synergizing the unique benefits of each type of nanoparticle. These advantages can be obtained in multiple aspects, with notable gains in mechanical properties such as fatigue strength. For example, Böger et al. [81] hybridized silica nanoparticles with MWCNTs and obtained benefits of several orders of magnitude in fatigue life. Furthermore, Li et al. [82] hybridized CNFs with GO and found longer fatigue lives compared to those achieved with individual nanoparticle types. Using a semi-crystalline thermoplastic PEEK matrix, Papageorgiou et al. [83] achieved similar findings when hybridizing GNPs with short carbon fibers. Shokrieh et al. [84], for example, studied the fatigue response of composites reinforced with CNFs and GNPs. They reported that the fatigue life increased, respectively, 24 and 27.4 times compared to composites with a neat matrix. However, when they hybridized the two nanoparticles (CNF+GNP) in a 1:1 ratio, the improvements were around 37.2 times. According to the authors, while GNPs increased stiffness, CNFs increased strength. Therefore, hybridization with nanoparticles of different geometric shapes enables the CNFs to reduce the agglomeration of GNPs, providing better mechanical properties due to the resulting synergistic effect [75, 85, 86]. Nevertheless, the literature highlights the absence of studies exploring the potential benefits of the synergistic effect on heat dissipation and its subsequent impact on fatigue response.

1.6 Advances in using self-heating phenomenon for non-destructive damage evaluation

Ensuring the longevity of PMC structures necessitates periodic inspections using NDT techniques. Among the developed NDT techniques [87, 88, 89, 90], IRT stands out for its speed, and simplicity in PMC inspections, along with its high effectiveness in detecting various types of external and internal damage [36, 91, 92, 93]. There are several techniques within the

scope of IRT, with the VT distinguished by its ability to identify complex defects and cracks. VT has been successfully applied for inspecting the diverse categories of defects and cracks in PMCs, consisting of debonds [93], closed cracks [94], and vertical open cracks oriented orthogonally to the inspected surface [95], surface-breaking and fatigue-induced cracks [96, 97, 98, 99], delamination [100], impact damage [101], and corrosion [102]. In the cases, where the application of external excitation sources is unfeasible, e.g., single-sided access or limited accessibility to specific regions of the inspected specimen [103], the non-destructive SHVT technique can serve as an alternative [47]. The self-heating phenomenon was employed as a heat source in this method, eliminating the need for external sources like flash lamps, optical heaters, or lasers during damage inspection. The authors of [89, 98, 104, 105], excited the PMC specimens at their resonant frequencies for crack localization and crack propagation monitoring, which were likewise employed by the authors of [106]. SHVT technique was successfully implemented in the inspection of PMC elements with numerous defect types, consisting of simulated cracks, flat bottom holes [107], and LVID [14]. Previous studies primarily concentrated on one-dimensional composite beams when applying the SHVT technique. Furthermore, while some approaches exist in transient thermography for selecting the optimal thermograms, the literature highlights the challenges in selecting effective thermograms from large data sets captured during SHVT testing for further image processing, aimed at damage identification in PMC structures.

1.7 Motivations and objectives

The comprehensive literature reviews in [6, 32] highlighted several key research problems in understanding the phenomenology of self-heating and predicting the fatigue response of PMCs, as summarized below.

One research problem is the need to develop a robust physics-based framework to predict the self-heating effect under cyclic loading. This is of primary importance in the assessment of fatigue response of PMCs, and enabling non-destructive damage inspection using self-heating-based techniques.

To fully understand the fatigue performance of PMCs, it is essential to analyze their behavior across different loading regimes, ranging from LCF to VHCF. Typically, LFFT, operating below 100 Hz, is used for LCF and HCF studies, whereas UFFT, operating in the range of 20 kHz with forced air or liquid cooling, is implemented for VHCF experiments. Despite the availability of LFFT and UFFT systems, few studies have examined fatigue response across all regimes. A key challenge in this regard is the self-heating phenomenon, which arises at frequencies above 5 Hz and complicates fatigue behavior analysis. This highlights issues related to the transferability of LFFT and UFFT results and the need for further investigation to establish a feasible strategy to

bridge this gap.

Another critical limitation in the current fatigue assessment methods, like the *S-N* curve, is its reliance on extensive experimental campaigns, making it time-consuming and unfeasible for real-time predictive maintenance. Moreover, the current fatigue life prediction models often neglect or oversimplify the effects of self-heating, and primarily consider the final failure stages of fatigue-loaded PMC specimens. To enhance predictability and enable continuous damage evaluation, it is essential to develop a reliable model for thermomechanical fatigue life assessment of PMCs that incorporates self-heating effects throughout the entire fatigue process, from early-stage damage initiation to rapid damage accumulation leading to final failure.

Moreover, few studies have explored the strategies for mitigating the self-heating effect from the perspective of optimal materials design and selection at the stage of manufacturing of PMCs. According to the literature [6, 32], carbon-based allotropes are the prime candidates owing to their exceptional mechanical properties and excellent thermal conductivity. These nanofillers enhance the interconnected thermal conduction pathways for efficient heat transfer from the tested PMC to the environment. Therefore, exploring the effect of incorporating the thermally conductive nanofillers on the fatigue response of modified PMCs is essential as a cost-effective strategy.

In addition, the effectiveness of SHVT as a non-destructive technique for damage inspection in 1D composite beams has been successfully demonstrated. However, it is of primary importance to enhance its applicability to a broader range of structures, e.g., PMC plate-like structures, which are more commonly used in engineering applications than 1D composite elements. To bridge these gaps, this PhD research aims to achieve the following objectives:

(1) Development of a physics-based framework for reliably modeling the self-heating phenomenon in fatigue-loaded PMCs.

(2) Assessment of the feasibility of combining the low and ultrasonic fatigue testing results using the heat dissipation rate concept.

(3) Thermomechanical fatigue life assessment of PMCs by establishing an entropy-based model (index) and a stiffness degradation concept accounting for different stages of fatigue-induced damage evolution.

(4) Investigation of the potential synergistic effects of incorporating the nanocarbon-based allotropes (i.e., GNPs and CNFs) in mitigating self-heating, thereby improving the fatigue strength, and prolonging the fatigue lifetime of modified GFRP composite.

(5) Broadening the applicability of SHVT as an NDT technique for damage inspection in

composite plate-like structures by utilizing the self-heating phenomenon as an alternative heat source for thermal excitation.

Considering the identified research gaps and objectives, the dissertation hypothesis was formulated as follows:

It is possible to enhance the assessment of fatigue response and structural integrity of polymer-matrix composites by developing a thermomechanical framework that accounts for the self-heating phenomenon, while also improving the fatigue longevity of polymer-matrix composites by mitigating and controlling hysteretic heat accumulation.

These findings will contribute to more reliable fatigue assessments, enhanced non-destructive testing methods, and the development of advanced PMCs with improved performance in demanding engineering applications.

1.8 Research scope

As the primary objectives and hypothesis of this research are already defined in Section 1.7, the scope of this study focuses on achieving these objectives and validating the proposed hypothesis. The primary milestones defining the scope of this PhD research are highlighted below:

- **Modeling the self-heating phenomenon.** This milestone involves oscillatory shear rheometry testing to estimate the thermoviscoelastic response of PMCs using a mathematical temperature- and frequency-dependent Prony series representation. This aims to simulate the self-heating phenomenon induced during cyclic loading in the form of temperature distribution, see Chapter 2 and [108] for more details.

- **Transferability of fatigue testing results.** This milestone involves analyzing the transferability of fatigue results for the CF/PEKK composite derived from LFFT at 50 Hz under natural air cooling, and UFFT at 20.2 kHz under controlled temperature using a pulse-pause loading pattern with forced air cooling. A unitless heat dissipation rate factor is introduced to link the results from both testing conditions, with further details provided in Chapter 3 and [11, 37].

- **Fatigue life assessment using stiffness degradation and entropy-based damage analysis.** This milestone involves establishing a new trilinear $\dot{q}$-σ model by combining IAT and CAT results, considering the temperature-dependent heat capacity, enabling the determination of FFE values across different regimes. By implementing the developed trilinear $\dot{q}$-σ model, a novel EDI concept is then introduced, enabling the establishment

of the *S-N* curves based on different stages of fatigue-induced damage evolution. This milestone also includes establishing the *S-N* curve accounting for different levels of stiffness degradation, see Chapter 4 and [109] for more details.

- **Synergistic role of hybrid nanofillers in improving fatigue longevity.** This milestone introduces a new thermographic approach (i.e., MPD-based $\dot{q}$-σ), serving as an alternative to the commonly used bilinear ΔT-σ approach, offering a more efficient methodology for estimating the fatigue strength of modified PMCs, see Chapter 5 and [110] for more details. Additionally, this milestone assesses the synergistic effects of incorporating thermally conductive hybridization of GNPs and CNFs for mitigating the hysteretic heat accumulation and prolonging the fatigue lifespan of the modified GFRP composite, see Chapter 5 and [110] for more details.

- **Using self-heating effect for non-destructive testing of composites.** This milestone includes utilizing the scanning laser Doppler vibrometer to acquire the natural frequencies of the tested PMC plates, and exciting the plate-like structures at their natural frequencies to demonstrate the applicability of self-heating as a potential alternative heat source for damage inspection, see Chapter 6 and [111] for more details.

Chapter 2

Modeling the self-heating phenomenon

The necessity of understanding the self-heating phenomenology in accelerated fatigue testing and its potential impact on engineering applications have been highlighted in the benchmark review papers [6, 32]. Due to the importance of the self-heating effect, the first objective of this PhD research was to develop a model for simulating this phenomenon and address the limitations of existing models. To accomplish this, the GFRP composite was selected for the investigation, with further details provided in [108].

2.1 Theoretical background

Modeling the self-heating phenomenon and predicting the thermal response induced during fatigue loading requires solving the energy equation, expressed in the following form [112]:

$$\int \left(\rho C_p \frac{\partial T}{\partial t}\right) dV + \int \left(-K\nabla^2 T\right) dV + \int h\,(T - T_a)\; dA_{cv} + \int e\beta \left(T^4 - T_a^4\right) dA_{rd} = \int \dot{q}_{gen}\, dV, \tag{2.1}$$

where V is the control volume, T and t are the temperature and time, respectively. ρ is the density, A_{cv} and A_{rd} are the surface areas exposed to convection and radiation, respectively. e is the emissivity, and β is the Stefan Boltzmann constant. K denotes the thermal conductivity of the GFRP composite, which is assumed to be independent of temperature for GFRP as well as thermally isotropic (i.e., $K_x = K_y = K_z = K$), as specified in the manufacturer's datasheet [113]. Nevertheless, C_p exhibits temperature dependency and can be derived from Eq. 2.2 [114].

$$C_p = 828.7 + 2.71T. \tag{2.2}$$

$\dot{q}_{\text{gen}}$ denotes the volumetric heat generation rate, which is proportional to the thermomechanical strain amplitude (ε_0), frequency (f), and the dynamic shear loss modulus ($G''(f,T)$) [115].

$$\dot{q}_{\text{gen}} = 3\pi f \varepsilon_0^2 G''(f,T). \tag{2.3}$$

2.2 Thermoviscoelastic modeling

Solving the energy equation requires modeling the thermoviscoelastic response of the PMCs, particularly $G''(f,T)$, which is a key factor in quantifying heat generation during cyclic loading. Understanding this parameter is crucial for analyzing the conversion of mechanical energy into heat and its impact on the self-heating behavior of PMCs. Since thermoviscoelastic properties depend on both frequency and temperature, dynamic rheological measurements were conducted to determine $G''(f,T)$, along with storage shear modulus ($G'(f,T)$), which is required for the mathematical formulation of $G''(f,T)$ in the form of Prony series. These measurements were carried out using the ARES-G2 rheometer in torsional oscillation mode. Additional details are available in [108]. Measurements of storage and loss shear moduli were taken at temperatures ranging from 25 °C to 175 °C, covering 18 frequencies between 0.01 Hz and 99 Hz. The raw data extracted from ARES-G2 for all frequencies were first processed to obtain frequency-domain curves at various temperatures. Using the kinetic Arrhenius model, the reference temperature was then set at 140 °C, the lowest value among the 18 values for the glass transition temperature (T_g) acquired from experiments. Finally, the master curves for the storage and loss shear moduli, presented in Figures 2.1 and 2.2, respectively, were constructed based on the TTS principle in terms of reduced frequency (f_r), incorporating the combined effects of temperature and frequency.

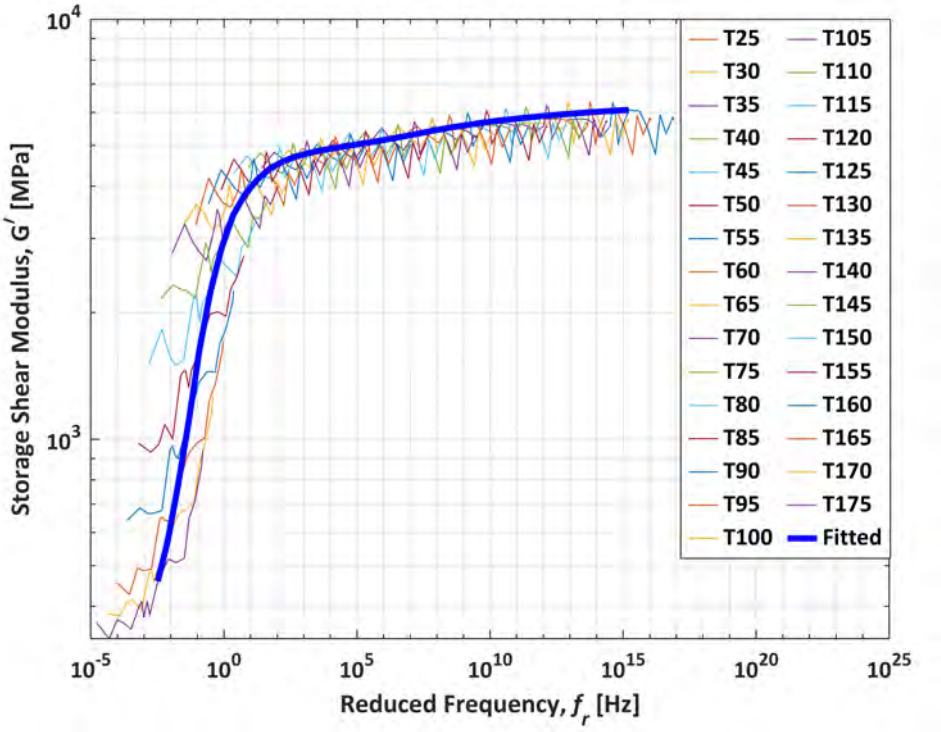

Figure 2.1: Master curve representing storage shear modulus versus reduced frequency [108].

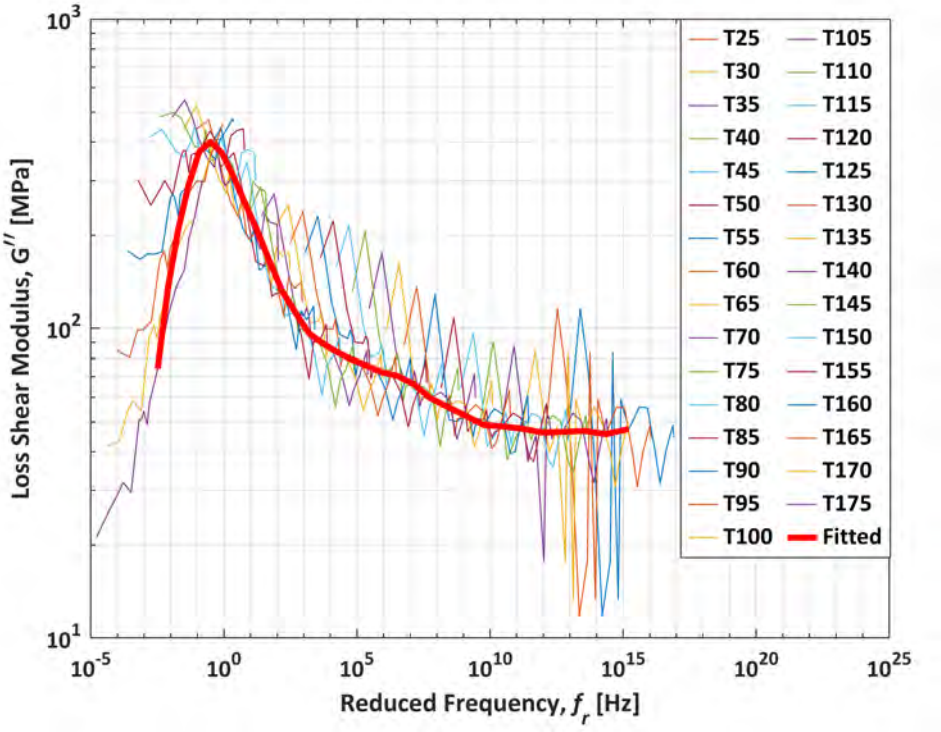

Figure 2.2: Master curve illustrating shear loss modulus versus reduced frequency [108].

The generalized Maxwell model, represented by Prony series, estimates the linear viscoelastic behavior of PMCs [116]. The frequency-dependent Prony series used in [45] can be mathematically rewritten as the frequency-temperature-dependent Prony series [46]:

$$G'(T,\omega) = G_\infty + G_0 \sum_{i=1}^{n} \frac{g_i \tau_i^2 a_T^2 \omega^2}{1 + \tau_i^2 a_T^2 \omega^2}, \tag{2.4}$$

$$G''(T,\omega) = G_0 \sum_{i=1}^{n} \frac{g_i \tau_i a_T \omega}{1 + \tau_i^2 a_T^2 \omega^2}, \tag{2.5}$$

where ω denotes the angular frequency, defined as $2\pi f$, and n denotes the number of required Prony parameters, i.e., g_i and τ_i. The parameter g_i represents the relaxation modulus at each relaxation time τ_i, indicating how much the material relaxes under an applied load over time. G_∞ is the long-term shear modulus obtained from a static test, while G_0 is the initial shear modulus at time $t = 0$ of a relaxation test. Such shear moduli can be converted to each other using the Prony parameter of g_i as follows:

$$G_\infty = G_0 \left(1 - \sum_{i=1}^{n} g_i\right), \tag{2.6}$$

$$G_0 = \frac{G_\infty}{1 - \sum_{i=1}^{n} g_i}. \tag{2.7}$$

Estimated parameter g_i should be positive and in a sum below one, i.e., $\sum_{i=1}^{n} g_i < 1, \quad g_i > 0$. For optimizing Prony parameters, n is an arbitrarily selected number, while g_i, τ_i, and G_0 were initially assumed. The storage and loss shear moduli (G' and G'') were then estimated using Eqs. 2.2 and 2.3 and compared with the extracted data from a torsional rheometer. The errors were finally minimized using the given objective function (OF) programmed in MATLAB software.

$$\frac{(G'_{ms} - G'_{es})^2}{\sigma_d(G'_{ms})} + \frac{(G''_{ms} - G''_{es})^2}{\sigma_d(G''_{ms})} + \frac{(\tan\delta_{ms} - \tan\delta_{es})^2}{\sigma_d(\tan\delta_{ms})} = (\mathrm{OF}), \tag{2.8}$$

where $\tan\delta_{es}$ denotes the dissipation factor estimated by Eq. 2.7, ms and es indices show the measured data from experiments and estimated data using the minimization algorithm, respectively, and σ_d indicates the standard deviations for each of these three measured values.

To represent the thermoviscoelastic behavior of the investigated PMCs with the required accuracy, up to 75 Prony series with corresponding coefficients were taken into account. Employing the minimization objective function (see Eq. 2.8), the optimal number of the Prony series was identified as 44, and coefficients are given in the Appendix in [108]. The loss shear modulus, crucial for determining the heat generation rate (see Eq. 2.3), was then mathematically

formulated and quantified using 44 Prony series. Figure 2.3 demonstrates a good agreement between the loss modulus obtained from the 44-term Prony series and the master curve.

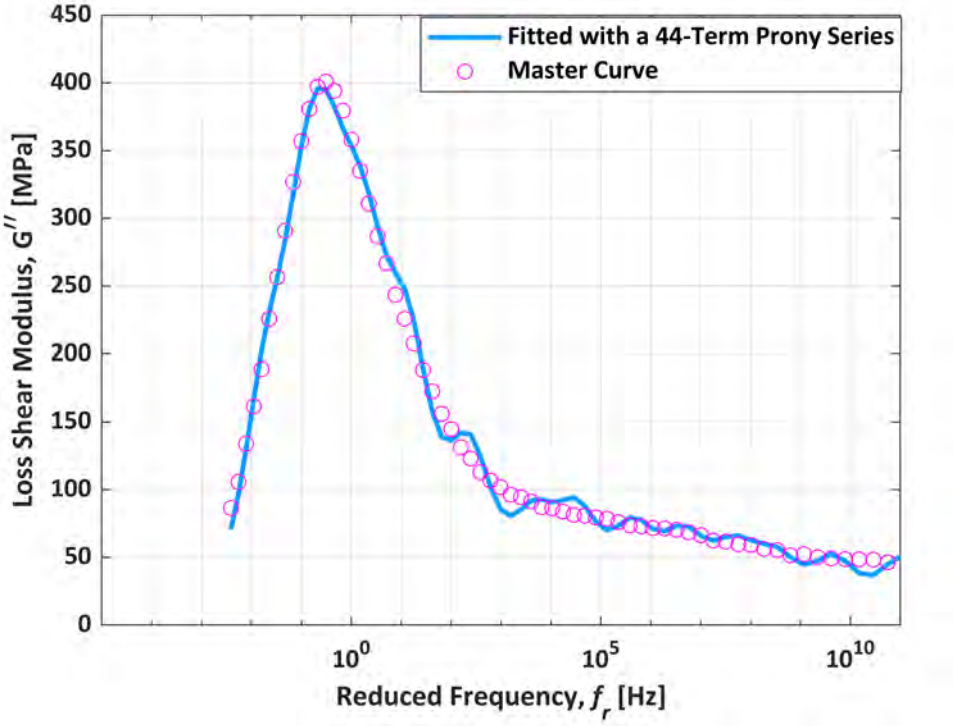

Figure 2.3: Evaluating the loss shear modulus via Prony series versus the master curve [108].

2.3 Simulation results and validation

IR cameras can only capture surface temperatures, making it impossible to directly measure the self-heating temperature variation through the PMC thickness. Therefore, the numerical simulation was essential to bridge this gap by estimating the internal temperature distribution.

To address this, the self-heating effect was numerically simulated by incorporating the heat generation rate, modeled with a 44-term Prony series, into the energy equation (Eq. 2.1) while accounting for the ICs and BCs. To solve the energy equation, a finite difference approach was applied, with a convergence criterion based on the unitless residual temperature, further details can be found in [108]. The results obtained from the self-heating model were validated through fatigue experiments on a cantilever PMC beam exposed to natural air cooling via a customized electrodynamic shaker-based setup in fully reversed displacement-controlled mode, see the details in [108].

Six ROIs were defined to numerically analyze temperature distributions across the cross-sectional (XZ-plane) and longitudinal (YZ-plane) dimensions (see [108]). Assuming

the symmetry of temperature response under fully reversed bending, ROIs were considered across half of the specimen's thickness. The temporal evolution of self-heating was examined in ROIs 1–3, located near the lower clamp where the maximum stress concentration occurs. Meanwhile, ROIs 4–6 captured the temperature distribution at the end of fatigue loading, as shown and discussed in [108]. Figure 2.4 shows the relationship between the heat generation rate and the temperature increase across ROIs 1-3. ROI 1 exhibited the highest heat generation due to the maximum bending stress, while ROI 3 showed negligible heat generation, as this ROI experienced only the shear stress (4.3 MPa), which was 66 times lower than the bending stress.

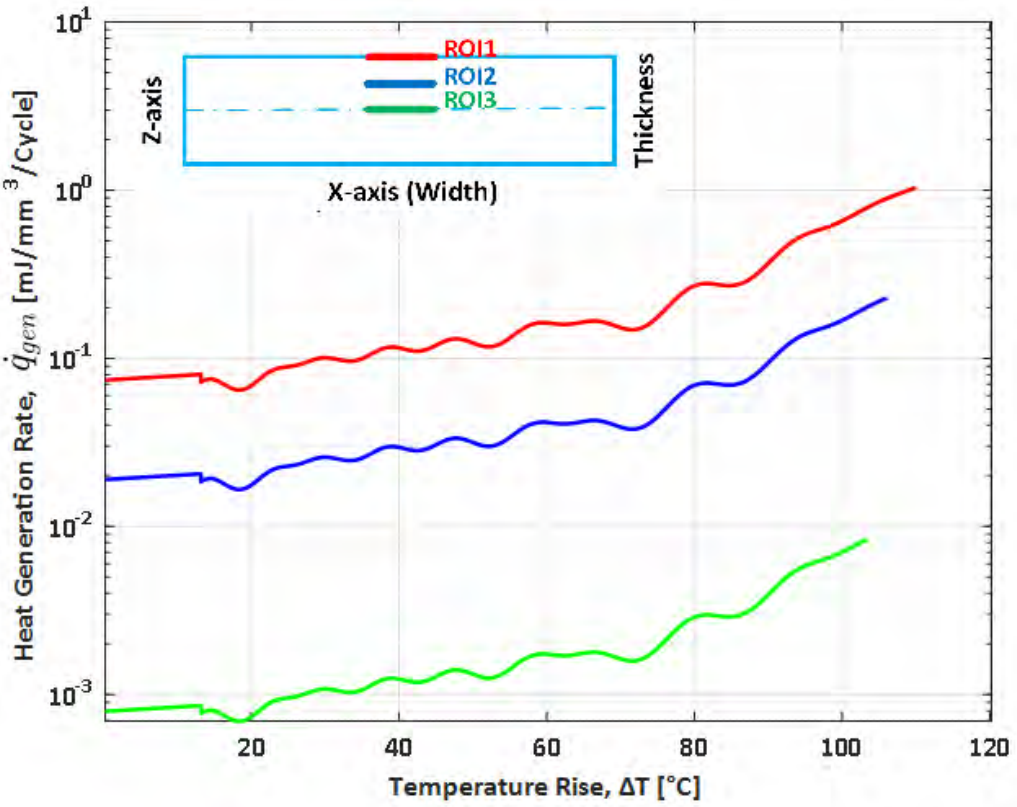

Figure 2.4: Heat generation rate versus temperature increase for ROIs 1 to 3 [108].

To evaluate the accuracy of the numerical model, only surface temperature results were compared with experiments, as IR cameras cannot capture through-thickness thermal variations. Furthermore, the impact of radiation was examined in the simulations. Figures 2.5(a) and 2.5(b) depict the numerical simulation results by excluding and including the influence of radiation, respectively, along with the experimental results shown in Figure 2.5(c). Figures 2.6(a) and 2.6(b) compare the cross-sectional temperature distributions with and without considering the radiative heat flux near the clamp.

Results obtained from the numerical simulations, as shown in Figures 2.5 and 2.6, provided a deeper understanding of the temperature distribution on the surface and through the thickness

of a fatigue-loaded PMC, respectively. In thin PMCs, such as the one tested with a thickness of 2.4 mm and a length-to-thickness ratio of 16, the surface temperature near the clamp on the surface (ROI 1) was consistently higher than that of the neutral axis (ROI 2), illustrated in Figure 2.5. The temperature variation between ROI 1 and ROI 2 remained below 4 °C when the radiation effect was considered and below 7 °C when the radiation effect was excluded (see Figure 2.6). This indicates that the surface temperature measurement suffices for thin PMC structures (see Figure 2.5). However, for thicker specimens, this temperature difference may be more pronounced and necessitates consideration in future investigations. The absence of radiative heat flux in the simulations led to increased temperature values across all ROIs due to the reduction of heat dissipation into the environment. However, the incorporation of radiation effects into numerical models significantly enhanced the accuracy of temperature predictions, highlighting its importance in capturing real-world thermomechanical fatigue behavior.

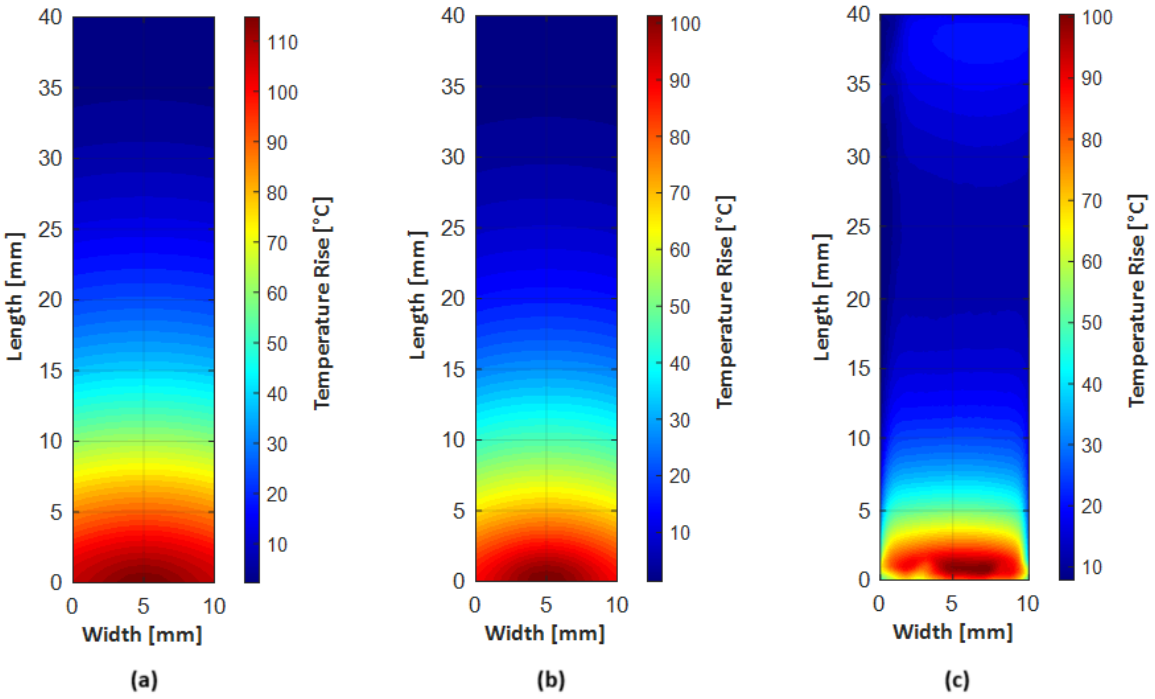

Figure 2.5: Relative temperature distributions on the specimen surface from (a) simulations excluding radiation, (b) simulations including radiation, and (c) experiment [108].

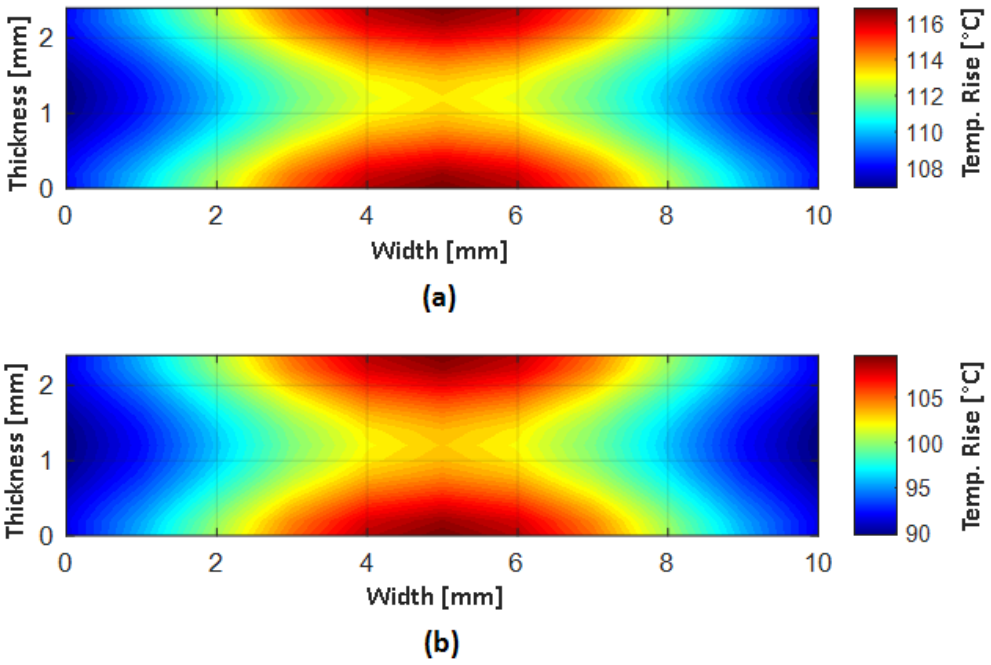

Figure 2.6: Relative temperature distributions near the clamp from numerical simulations: (a) excluding the radiation effect, and (b) including the radiation effect [108].

Incorporating the influence of radiation and considering the most critical region (i.e., ROI 1), further comparison between numerical simulations and experimental results was carried out under three stress levels, as depicted in Figure 2.7. Considering the computational constraints linked to the small time increment (i.e., 8.3 ms) and its consequential effect on simulation duration, the analyses were limited to a maximum of $3 \cdot 10^4$ cycles. It is evident that self-heating temperature exponentially increases from the beginning up to 10^4 cycles in both experiments and simulations. However, the discrepancies in temperature values are notable up to this range of loading cycles. Numerical results consistently indicated lower temperature values compared to experimental data. This inconsistency between numerical simulations and experimental measurements may be attributed to implementing the simplified model for the convective heat transfer coefficient. Notably, as the number of cycles increased, convergence became evident between numerical and experimental results, where the temperature stabilization occurred.

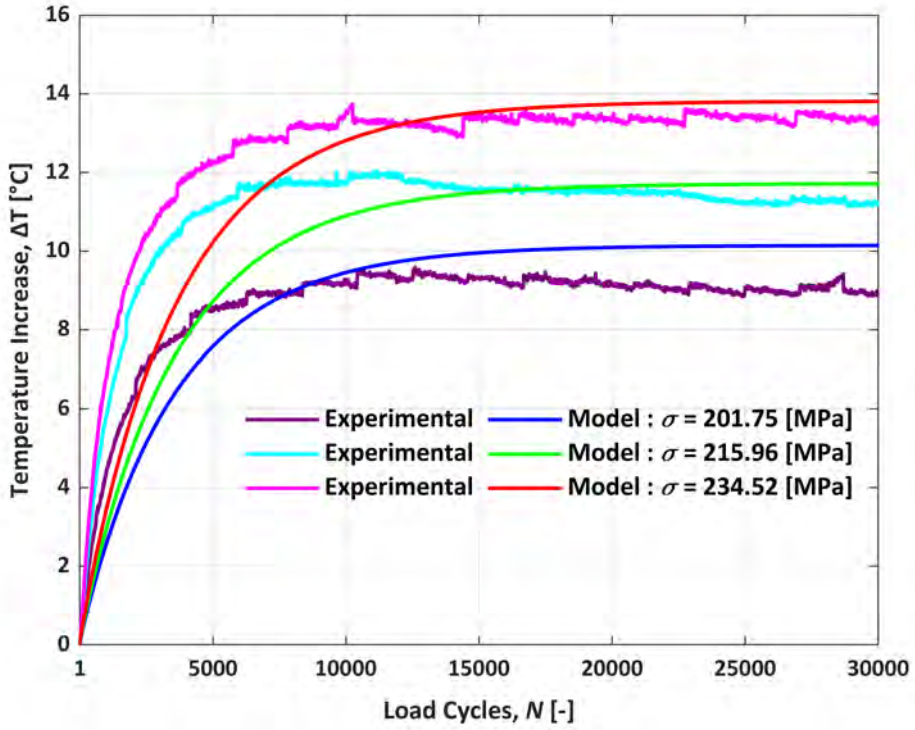

Figure 2.7: Comparing the numerical model and experiment results at three load levels [108].

2.4 Summary

As presented in this chapter, the first objective was successfully achieved by developing a robust physics-based framework that reliably modeled the self-heating phenomenon induced in the fatigue-loaded PMCs. This was accomplished by implementing a 44-term temperature- and frequency-dependent Prony series representation, enabling the mathematical formulation and reliable estimation of the thermoviscoelastic response, and finally the self-heating temperature distribution via the energy equation.

A key finding was that radiative heat flux significantly influences thermal response, necessitating its inclusion in self-heating models to ensure accurate predictions. In addition, for thin PMCs with a length-to-thickness ratio of 16, the through-thickness temperature variation was determined to be negligible (below 4 °C) compared to the substantial 100 °C increase observed on the surface of tested PMCs under high-stress conditions. This highlights the reliability of surface temperature measurements using IR thermography during the fatigue experiments.

Chapter 3

Thermomechanical fatigue analysis under different loading regimes

As highlighted in Section 1.7 and in [6, 32], understanding the fatigue behavior of high-performance PMCs, such as CF/PEKK, is crucial for advanced applications across all fatigue regimes, ranging from LCF to VHCF. Considering the inherent challenges and time-consuming nature of performing VHCF experiments at low frequencies, the second objective of this PhD research was to introduce a feasible strategy for combining the fatigue testing results within LFFT and UFFT (up to 10^6 and above 10^8 cycles, respectively). To achieve this, the fatigue behavior of the CF/PEKK composite was assessed under three-point bending, with LFFT performed under natural air cooling and UFFT conducted in a pulse-pause loading pattern with forced air cooling (see [11, 37] for more details). Furthermore, using UFFT results, the critical self-heating temperature was determined, corresponding to the transition between phases II and III, where rapid damage propagation occurs, as illustrated in Figure 1.2.

3.1 Combining low and ultrasonic fatigue results using the heat dissipation rate concept

Based on the recommendations in [6], the fatigue testing of GFRPs under natural air cooling should be conducted at frequencies below 10 Hz to minimize the self-heating effect resulting from loading frequency. However, this approach seems to be conservative for the CF/PEKK composite due to its higher thermal conductivity, which allows for more efficient heat transfer into the surroundings, and consequently limits the self-heating temperature. IATs were conducted over a 5–50 Hz frequency range to identify the maximum permissible loading frequency where self-heating is primarily driven by mechanical loading (i.e., phase lag between stress and

strain) rather than frequency. The preliminary results demonstrated that the induced self-heating temperature was unaffected by this frequency interval. This finding allowed for accelerating the fatigue experiments, enabling all LFFT tests to be performed at 50 Hz under the natural air cooling using a custom-designed three-point bending fixture, see [11] for further details. On the other hand, VHCF experiments were conducted at the frequency range of 20.2 ± 0.02 kHz using a pulse-pause loading pattern, with a temperature control achieved through forced air cooling to mitigate the thermal effects resulting from high loading frequency.

To combine LFFT and UFFT results, the CATs were conducted for both regimes at the same mean load of 283.5 MPa. The CAT results are illustrated in Figure 3.1. Analyzing the CAT results highlighted a transition zone between LFFT and UFFT regimes for CF/PEKK composite (see Figure 3.1). Constructing the transition zone only through LFFT requires extensive testing time, while UFFT is still limited by current technological constraints that prevent applying higher amplitudes to cause specimen failure at a lower number of cycles. For example, the maximum achievable load amplitude in UFFT is ±49.1 MPa with a corresponding displacement amplitude of ±54.2 μm [11].

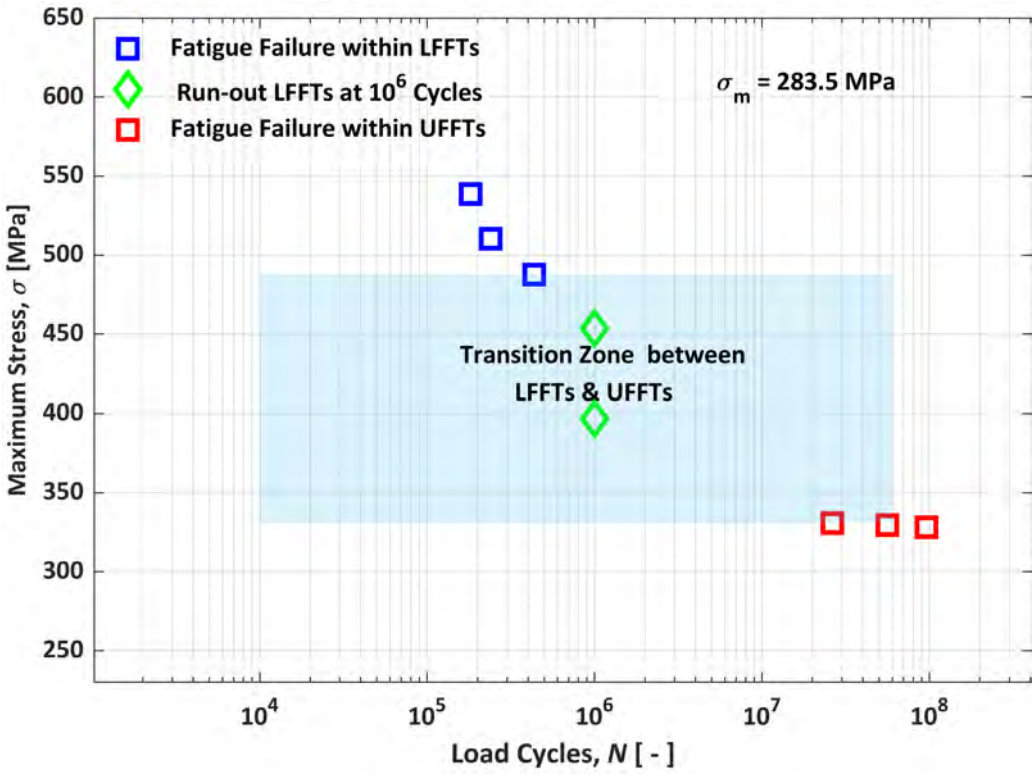

Figure 3.1: Combining the LFFT and UFFT results via the *S*-*N* curve driven from CATs [11].

Considering the time-consuming nature of LFFT and the technological constraints in UFFT for constructing the transition zone in the *S*-*N* curve, a novel approach was proposed to combine the thermomechanical fatigue responses of CF/PEKK composite derived from LFFTs and

UFFTs. This method is based on the heat dissipation rate concept by incorporating IATs under different mean loads using both testing scenarios.

In accordance with the first law of thermodynamics for a control volume in Eq. 2.1, when a PMC specimen reaches the stabilized self-heating temperature, the heat generation rate drops to zero at the moment of unloading (see Figure 3.2). At this stage, the rate of heat storage ($\dot{q}_s$) balances with the total heat dissipation rate ($\dot{q}$) through conduction, convection, and radiation, which is given by [117]:

$$\dot{q}_s = \dot{q} = -\rho C_p \frac{\partial T}{\partial t}\Big|_{t=t_u}, \tag{3.1}$$

where $\partial T/\partial t$ refers to the cooling rate at time t_u when the tested PMC is unloaded [11], see Figure 3.2 for more details.

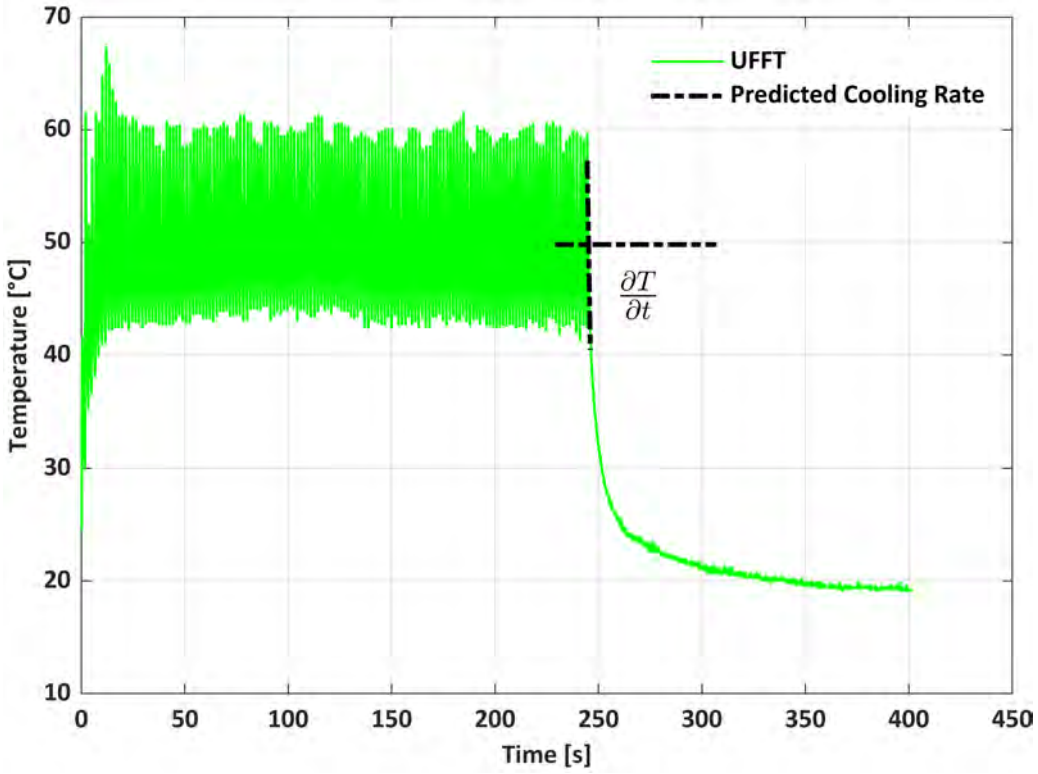

Figure 3.2: The exemplary thermal response under stress amplitude 44.6 MPa for evaluating the heat dissipation rate in the UFFT regime [11].

The heat dissipation rate ($\dot{q}$) is intrinsically influenced by several key variables, including loading frequency (f), oscillation displacement/force amplitude (δ_a/F_a), and the implemented cooling technique. Distinguishing the effects of these parameters on results obtained from LF and UF techniques poses a significant challenge. Among the mentioned factors, however, the mechanical loading from LF (force control) and UF (displacement control) has been linked using the correlation between force and displacement, as shown in Figure 3.3. By establishing a unitless

scalable factor that serves as an indicator of the cumulative effects of frequency and applied cooling technique, the results from LFFT and UFFT became transferable and comparable. This approach, indeed, simplified the interplay of such factors in the comparative analysis of LF and UF techniques. The proposed scalable energy ratio, represented as $\dot{q}_{\text{ratio}}$, facilitated the transferability of results from UFFT to LFFT regime under similar amplitude displacement conditions, which is given by:

$$\dot{q}_{\text{ratio}} = \frac{\dot{q}_{\text{UFFT}}}{\dot{q}_{\text{LFFT}}}, \tag{3.2}$$

where $\dot{q}_{\text{UFFT}}$ and $\dot{q}_{\text{LFFT}}$ denote the heat dissipation rates within the UFFT and LFFT scenarios, respectively. To quantify the dependency of $\dot{q}$ on the load amplitude, a series of IATs was performed with the same mean load of 283.5 MPa, as shown in Figure 3.3. The stress ratio for IATs within LFFTs ranged from 0.11 to 0.59, whereas for UFFTs, it varied between 0.67 and 0.88. Applying such a broad spectrum of load ratio was essential to comprehensively characterize the thermomechanical fatigue behavior of CF/PEKK composites, allowing for an in-depth understanding of their durability, potential failure modes, and fracture mechanisms.

The heat dissipation rate over the determined spectrum of displacement amplitudes (utilizing the relationship between displacement and force) is illustrated in Figure 3.3. It was assumed that the heat dissipation rate is negligible when the displacement amplitude is zero, denoted as $\delta_a = 0$, implying that $\dot{q} = 0$ under such a condition. This zero-displacement scenario was considered as the lower boundary condition, while data extracted from LFFTs performed at the higher displacement amplitudes were considered as the upper boundary condition. Considering these boundary conditions, a quadratic fit (4th-order polynomial) was applied to model $\dot{q}$ with satisfactory accuracy, illustrated in [11] with more details. Analysis of the extracted LFFT and UFFT results revealed an average energy ratio (i.e., $\dot{q}_{\text{ratio}}$) of 2107. In other words, this dimensionless energy ratio indicates that the interplay between frequency and the cooling system in UFFT enhanced the heat dissipation rate by a factor of 2107 compared to the LFFT under the same stress level. Accordingly, this scalable factor was implemented to account for the combined effects of loading frequency and cooling technique in further analyses of heat dissipation rates across LFFT and UFFT regimes.

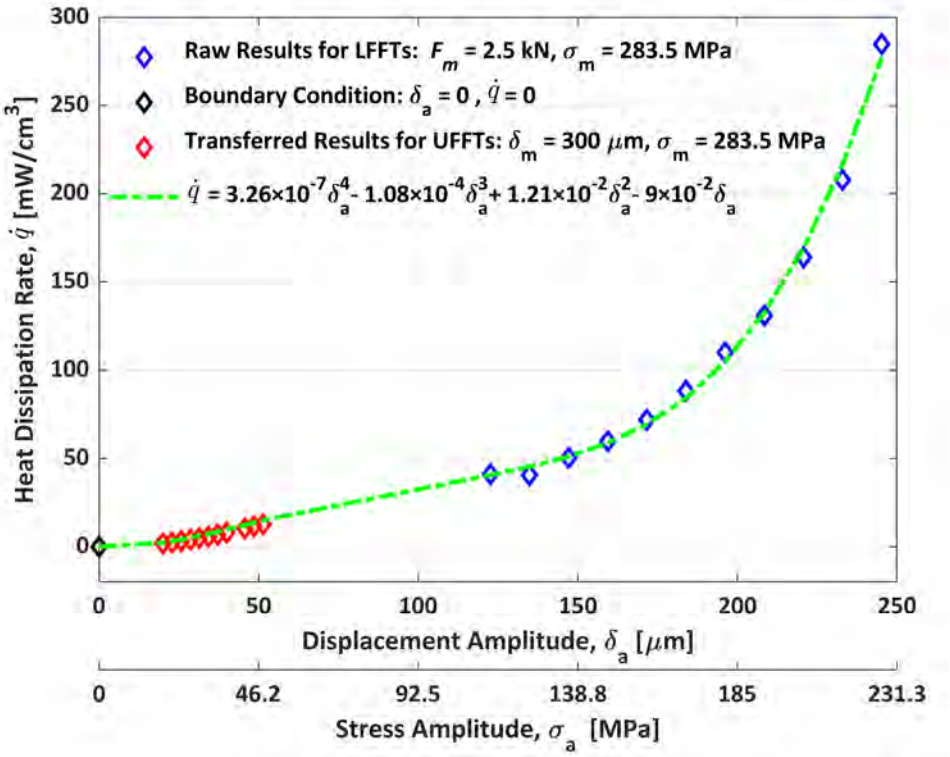

Figure 3.3: Dependency of heat dissipation rate on loading amplitude for LFFT and UFFT regimes [11].

Considering the aforementioned assumptions and applying $\dot{q}_{\text{ratio}}$, the heat dissipation rate for an equivalent mean load of 283.5 MPa was first evaluated based on the obtained results from IATs for both LFFT (2.5 kN) and UFFT (300 μm), illustrated by the blue and red squares in Figure 3.4, respectively, see [11] for the detailed testing conditions. It is important to note that the applied mean load of 283.5 MPa includes approximately one-third of the CF/PEKK ultimate strength (811 MPa [118]), which is insufficient for the comprehensive thermomechanical fatigue characterization of such a composite. For this purpose, the operational boundaries of performing three-point bending testing using both low and ultrasonic frequency techniques have been illustrated in Figure 3.4. As can be extracted from Figure 3.4, the UFFT technique allows for testing at lower mean loads, whereas the LFFT method enables testing at higher mean loads. By implementing these advantages, a range of mean loads was applied to the tested specimens. UFFTs were performed under the highest possible mean load of 283.5 MPa (300 μm, denoted by U300) and the lower mean load of 236 MPa (250 μm, denoted by U250). In both cases, the thermal responses were recorded using an IR camera. On the other hand, according to the preliminary LFFT results, the lowest load amplitude that resulted in a thermal response was 102 MPa (900 N). As the limitation of conducting three-point bending testing, the applied amplitude loading must not exceed the mean load value. Considering such limitations regarding

the testing technique and the necessity for thermal response registration, the tested specimens were additionally applied to higher mean loads (i.e., 340 MPa and 397 MPa, labeled as L3000 and L3500 in Figure 3.4, respectively) using the LFFT technique. Taking advantage of UFFTs, the thermomechanical fatigue responses were predicted for LFFTs for the lower mean load of 236 MPa (i.e., 250 μm or U250 in Figure 3.4). Using LFFTs, by contrast, the σ-$\dot{q}$ curves were predicted for higher mean loads of 340 MPa and 397 MPa (i.e., 368 μm and 429 μm, referred to as U368 and U429 in Figure 3.4, respectively), which exceed the capabilities of the current UFFT setup. These findings resulted in a foundation for a comprehensive understanding of thermomechanical fatigue behavior in CF/PEKK composites using LFFT and UFFT results.

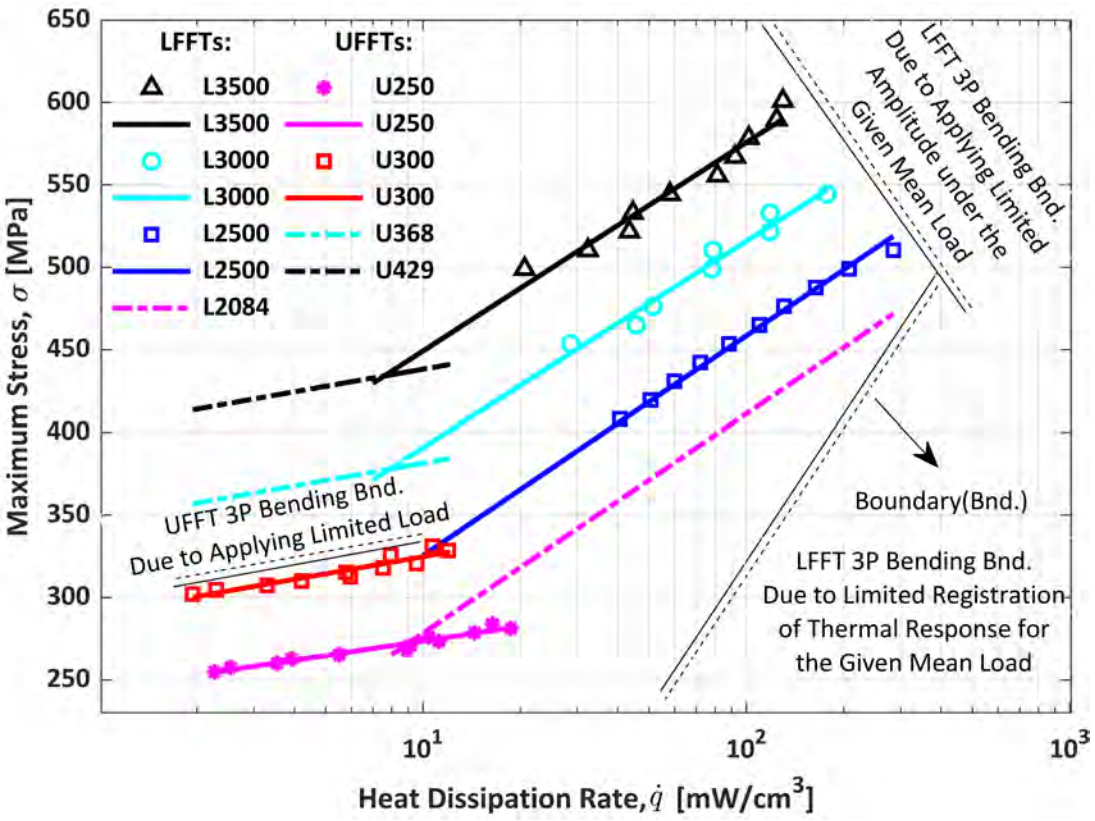

Figure 3.4: Combining the extracted fatigue responses under LFFT and UFFT conditions via stress-heat dissipation rate concept for CF/PEKK composite [11].

3.2 Determination of critical self-heating temperature using heat dissipation rate concept

Furthermore, the heat dissipation rate concept has been utilized to determine the critical self-heating temperature interval [37], which serves as an indicator for identifying the beginning of rapid damage accumulation in the fatigue-loaded CF/PEKK composite. To achieve this, heat

dissipation rate values were plotted versus the self-heating temperature, derived from a range of amplitude conditions in the UFFT scenario. These findings, shown in Figure 3.5, align with the three-phase self-heating behavior outlined in Figure 1.2. In phase I, rapid temperature growth driven by frictional heating corresponds to the initial increase in heat dissipation observed up to 54 °C. Phase II is characterized by temperature stabilization, with a steady heat dissipation rate of around 1.5 W/cm^3 between 54 °C and 65 °C, indicating a thermodynamic equilibrium between heat generation and dissipation. Finally, phase III marks a sharp temperature rise, correlating with a significant increase in heat dissipation beyond 65 °C, indicating severe damage accumulation, likely due to polymer softening, macrodelamination, macrocrack formation, and fiber breakage. The critical self-heating temperature interval (54-65 °C) identified in these phases potentially indicates the initiation of rapid damage accumulation in the CF/PEKK composite, highlighting the importance of temperature monitoring in evaluating the structural integrity of PMCs under fatigue loading.

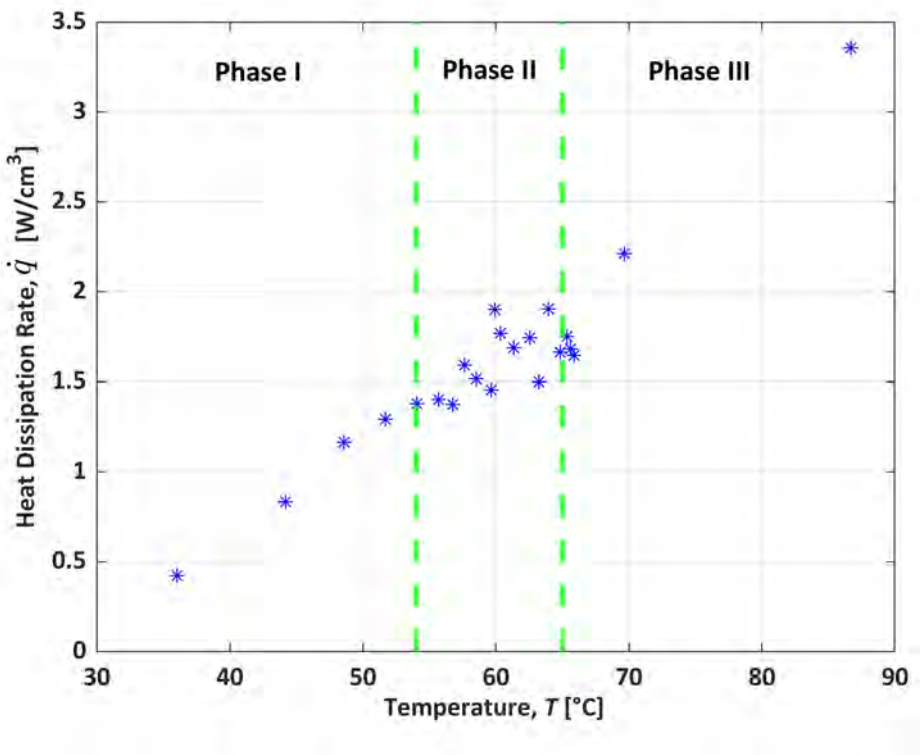

Figure 3.5: Heat dissipation rate versus the self-heating temperature, adopted from [37].

3.3 Summary

The findings presented in this chapter contributed to establishing a comprehensive framework for understanding the thermomechanical fatigue response of CF/PEKK composite under both LFFT and UFFT regimes. The second objective of this PhD dissertation was successfully accomplished by analyzing the transferability of fatigue results under controlled temperature conditions in aerospace-grade CF/PEKK composites.

A key finding was that implementing the standard *S-N* curve was unfeasible for capturing the fatigue response of CF/PEKK composite across all fatigue regimes, ranging from LCF to VHCF. Consequently, a transition zone between LFFT and UFFT regimes (i.e., from 10^6 to 10^8 cycles) was identified. Nevertheless, constructing this transition zone using the standard method (i.e., *S-N* curves) was challenging due to extensive testing time requirements and technological limitations. For this purpose, a novel heat dissipation rate factor was proposed to bridge the findings from both low and ultrasonic fatigue testing techniques. Furthermore, the critical temperature threshold (50-65 °C) was determined through the analysis of the heat dissipation rate within the UFFT scenario, which can be used as a failure criterion for future ultrasonic fatigue testing.

Chapter 4

Thermomechanical fatigue life assessment through different methods

As highlighted in Sections 1.4 and 1.7, the conventional fatigue life prediction models (e.g., the *S-N* curve) often overlook or oversimplify the self-heating effect, and primarily focus on the final failure stages of fatigue-loaded PMCs. Enhancing the accuracy of predictive models and enabling the continuous damage assessment requires a robust thermomechanical fatigue life model that incorporates the self-heating effect within the entire fatigue process, from early damage initiation to rapid accumulation leading to abrupt failure. Considering these limitations, the third objective of this research study was to assess the fatigue response of PMCs by establishing novel concepts of entropy-based damage evolution and stiffness degradation. These concepts account for the different stages of cumulative fatigue damage of PMCs, focusing on the GFRP composite in this study, with detailed information provided in [109].

4.1 Thermodynamic process of entropy generation for fatigue life assessment

When the applied stress level remains below the fatigue strength (σ_{FS}), the primary mechanism for heat dissipation is the internal friction (i.e., $\dot{q} = \dot{q}_f$), which is considered as a recoverable process [69]. However, when the applied stress exceeds the fatigue strength, the heat arises due to the internal friction and the fatigue-induced damage ($\dot{q}_d$), corresponding to the reversible and irreversible thermodynamic processes, respectively, which is given by [109]:

$$\dot{q} = \dot{q}_{f+d} = \dot{q}_f + \dot{q}_d. \tag{4.1}$$

For IAT scenarios, $\dot{q}$ is determined using Meneghetti's approach [117] based on the cooling

rate at the moment of unloading, see Figure 3.2 and [109] for further details. The heat dissipation rate led by damage ($\dot{q}_d$) can then be determined as a function of stress (σ) using:

$$\dot{q}_d = \dot{q}_{f+d}\,(\sigma \geq \sigma_{FS}) - \dot{q}_f\,(\sigma < \sigma_{FS}). \tag{4.2}$$

By implementing the second law of thermodynamics [62], the total volumetric entropy generation (γ) can then be quantified by [53]:

$$\gamma = \mathrm{FFE} = \int_{t_0}^{t_f} \dot{\gamma}\, dt = \int_{t_0}^{t_f} \frac{\dot{q}_d}{T}\, dt. \tag{4.3}$$

The cumulative entropy, termed as FFE, generated for multiple load levels within IATs can be expressed as follows [65]:

$$\mathrm{FFE} = \sum_{i=1}^{m} \frac{N_i \dot{q}_{d_i}}{f_i T_{si}}, \tag{4.4}$$

where m represents the number of load levels, and N_i is the number of cycles at the i-th step.T_{si} denotes the stabilized temperature in Kelvin, $\dot{q}_{d_i}$ indicates the damage-induced heat dissipation rate, and f_i is the loading frequency at the i-th step. Once the FFE value [67] is determined from fatigue testing results, it becomes possible to estimate the number of fatigue cycles to failure (N_f) for any arbitrary stress level above the fatigue strength ($\sigma \geq \sigma_{FS}$) using Eq. 4.5.

$$N_f(\sigma) = \mathrm{FFE} \frac{f T_s(\sigma)}{\dot{q}_d(\sigma)}. \tag{4.5}$$

For CAT scenarios, when $m = 1$ in Eq. 4.4, applying Meneghetti's approach [117] to measure the cooling rate for heat dissipation quantification becomes unfeasible at high-stress levels. This issue stems from the rapid temperature rise in the third phase of self-heating temperature evolution [11], associated with the fatigue damage accumulation in the tested PMC, making reliable cooling rate determination challenging at the end of testing [109]. A practical alternative is to use the initial temperature rise instead, as it provides an equivalent measure of heat dissipation [56, 65, 119]. Furthermore, the stabilized temperature in Eq. 4.4 can be substituted with the critical temperature for determining the FFE values within CAT scenarios. This substitution is justified because the stabilized temperature indicates the transition between phases II and III at lower stress levels, while the critical temperature serves the same role under higher stress levels [6, 12, 109].

4.2 Results and discussion

Figure 4.1 illustrates the sequential workflow of this chapter for achieving the third objective by defining four subgoals. The fatigue strength of PMCs was first assessed using IATs based on the bilinear thermographic approaches (i.e., $\Delta T - \sigma$ and $\dot{q} - \sigma$) in Section 4.2.1, followed by an analysis of their potential into the thermodynamic-based entropy generation for predicting the fatigue response of PMCs. CATs were then performed to construct the *S*-*N* curve by identifying the AE-based critical boundary, where the rapid damage accumulation begins, see Section 4.2.2. By combining IAT and CAT results, a novel trilinear $\dot{q} - \sigma$ model was then developed (see Section 4.2.3) to assess the FFE values across different loading regimes. This entropy-based methodology was further extended to introduce a novel EDI concept. This concept offers an alternative methodology for constructing the *S*-*N* curves based on progressive damage accumulation from the initiation to the final failure, as discussed in Sections 4.2.4 and 4.2.5. Furthermore, by using the measured force and displacement from twice-integrated acceleration data, the dynamic Young's modulus was calculated, allowing for the construction of *S*-*N* curves under different stiffness degradation levels (see Section 4.2.6), which addressed the final subgoal of the study.

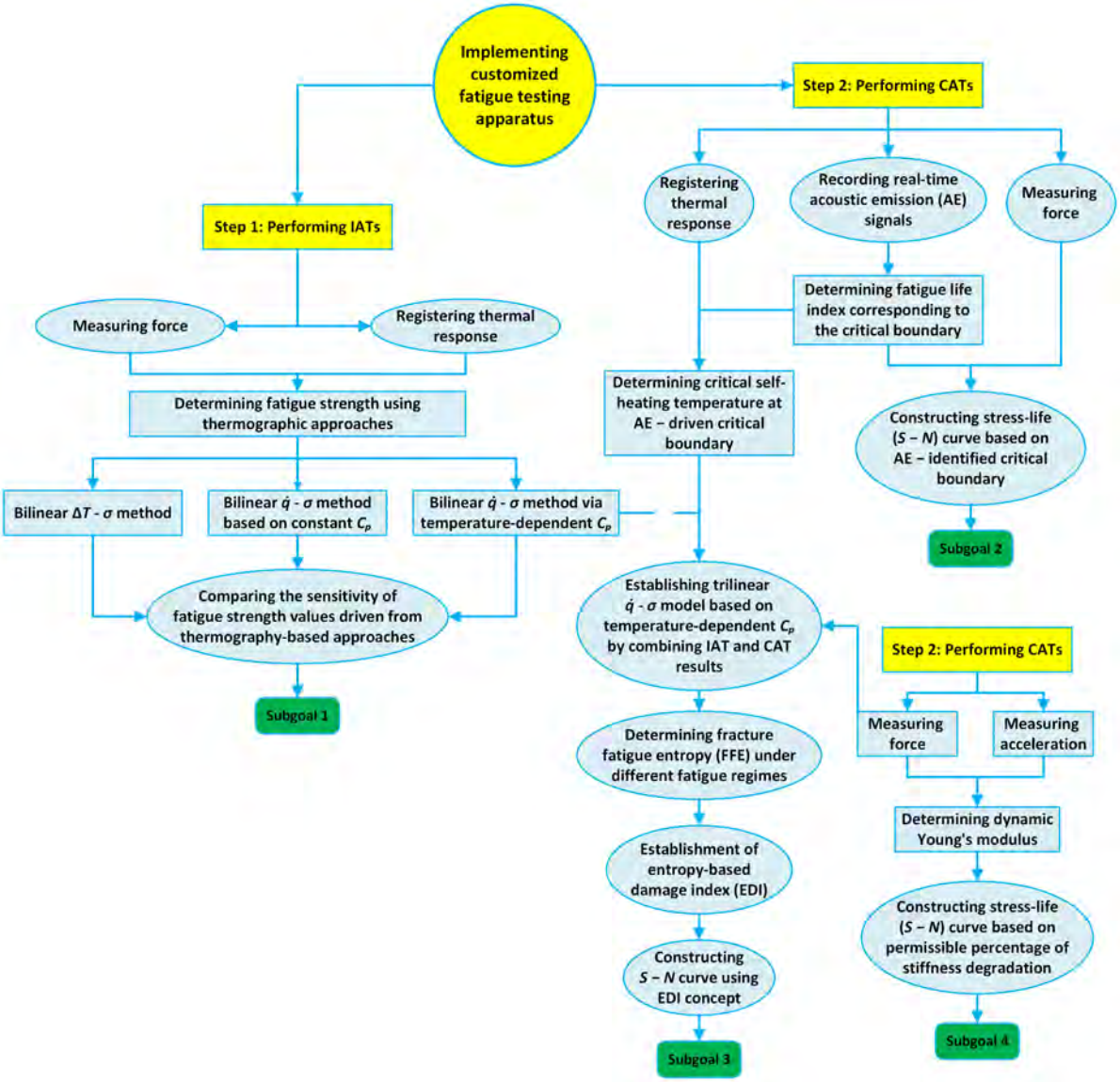

Figure 4.1: Schematic workflow of the thermomechanical fatigue assessment of tested PMCs [109].

4.2.1 Fatigue strength estimation via thermography-based approaches

The fatigue strength values were determined under four loading frequencies (20 Hz, 30 Hz, 40 Hz, and 50 Hz) using the bilinear ΔT-σ and $\dot{q}$-σ methods, represented by the value at the intersection of two characteristic lines in Figure 4.2. The role of constant and temperature-dependent C_p was investigated in the $\dot{q}$-σ approach, while only the results for temperature-dependent C_p are presented here; see [109] for further details.

The results obtained from both ΔT-σ and $\dot{q}$-σ approaches similarly demonstrated a decline in fatigue strength with rising frequency, e.g., see Figure 4.2 for the $\dot{q}$-σ results [109]. At lower frequencies, the viscoelastic nature of PMCs leads to dissipating the hysteretic energy into the

surroundings, which prevents the occurrence of a remarkable temperature rise of the surface of the tested PMC. This makes the fatigue-damage process more mechanically driven. In contrast, at higher frequencies, low thermal conductivity and larger phase lag between stress and strain during fatigue loading cause more heat storage at higher loading frequencies, leading to thermal hotspots and higher temperatures. These thermal effects, along with mechanical loading, accelerate the degradation mechanisms such as weakening of polymer chain interactions, matrix cracking, fiber-matrix debonding, and delamination, finally leading to a reduction in fatigue strength.

The $\dot{q}$-σ method consistently predicted higher fatigue strengths than the ΔT-σ method, especially at higher frequencies when incorporating temperature-dependent C_p, with the discrepancy becoming more pronounced at higher frequencies. Due to the relatively high discrepancy in the estimated fatigue strength values from ΔT-σ and $\dot{q}$-σ approaches at higher frequencies (40 Hz and 50 Hz), the standard S-N curves for these frequencies were constructed as a reference to assess the reliability of these thermographic approaches; see [109]. At both 40 Hz and 50 Hz, the $\dot{q}$-σ approach yielded more reliable fatigue strength results than the ΔT-σ method when compared to the standard S-N curve at 10^6 load cycles. This highlights the advantage of implementing the $\dot{q}$-σ approach, offering better accuracy in fatigue analysis of PMCs, particularly at higher frequencies where thermal effects become more pronounced.

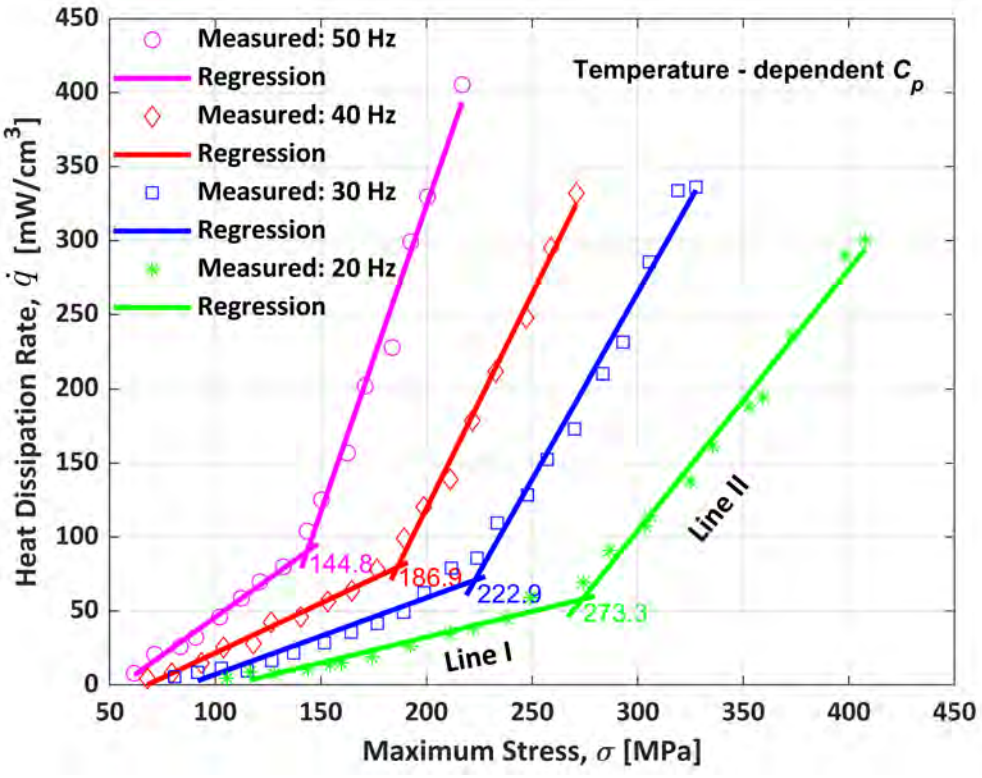

Figure 4.2: Fatigue strength estimation of PMCs under different loading frequencies using the $\dot{q}$-σ approach [109].

4.2.2 Fatigue life prediction via acoustic emission-based damage criticality

In addition to assessing the effect of frequency on fatigue strength, the AE responses of fatigue-loaded PMCs from CATs were examined to identify the critical damage accumulation boundaries. This analysis led to the establishment of a novel methodology for constructing the *S-N* curve using AE-based criticality. Unlike the standard *S-N* approach, accounting for the final stage of failure, the proposed criticality-based AE method relies on the boundaries where the damage is progressively accumulated throughout the remaining lifespan of the fatigue-loaded PMC specimen.

During the preliminary study, several AE features were evaluated, including CCNT, ETE, CENY, and ALIN. Among them, CCNT was identified as the most sensitive feature/indicator of early microstructural changes and microcrack growth, a finding that was also confirmed by previous studies (e.g., [12]). For example, some of the AE responses acquired from fatigue testing at the loading frequency of 40 Hz have been presented in Figure 4.3, see [109] for 50 Hz and further information. The results were categorized into three fatigue regimes: LCF with less than 10^5 cycles, ICF ranging from 10^5 to 10^6 cycles, and HCF beyond 10^6 cycles [120]. While these classifications may not be universally standardized, they allowed for establishing a regime-based framework to assess the fatigue behavior of PMCs within this research. For example, Figures 4.3 (a) and 4.3 (b) illustrate the AE data at 40 Hz for the LCF and HCF regimes, respectively, with further results available in [109]. In Figure 4.3, the abrupt/final fatigue failure events are marked by the peak values of the CCNT feature, alongside the critical boundary, denoted by black dashed lines, where significant damage accumulation begins.

Using the identified criticality boundary values derived from the CCNT feature for different stress levels, a new strategy, termed the AE-based *S-N* curve, was established. This approach allows for identifying the permissible number of cycles a tested PMC can endure at a given stress level before entering the accelerated fatigue damage phase. The *S-N* curves represented in Figure 4.4 derived from final failure events (e.g., denoted by diamonds in Figure 4.3 for 40 Hz) predict slightly higher fatigue strengths at 10^6 cycles for both frequencies of 40 Hz and 50 Hz compared to the criticality-based *S-N* curves. The fatigue strength under 40 Hz is estimated at 241.1 MPa based on the final failure, versus 222.9 MPa from the criticality-based *S-N* curve, showing a 7.5% discrepancy. This highlights that the criticality-based *S-N* method tends to predict a lower value, owing to identifying the fatigue damage at an earlier stage of degradation, thereby providing a more conservative estimation that is key to preventing sudden failures. Despite these findings, a key question arises regarding how the *S-N* curves extracted from the criticality of AE data correlate with the stiffness degradation of fatigue-loaded PMCs. Establishing such a relationship will enhance the predictive capabilities in fatigue assessments,

considering that the stiffness degradation serves as an indicator of structural integrity and residual service life of PMCs.

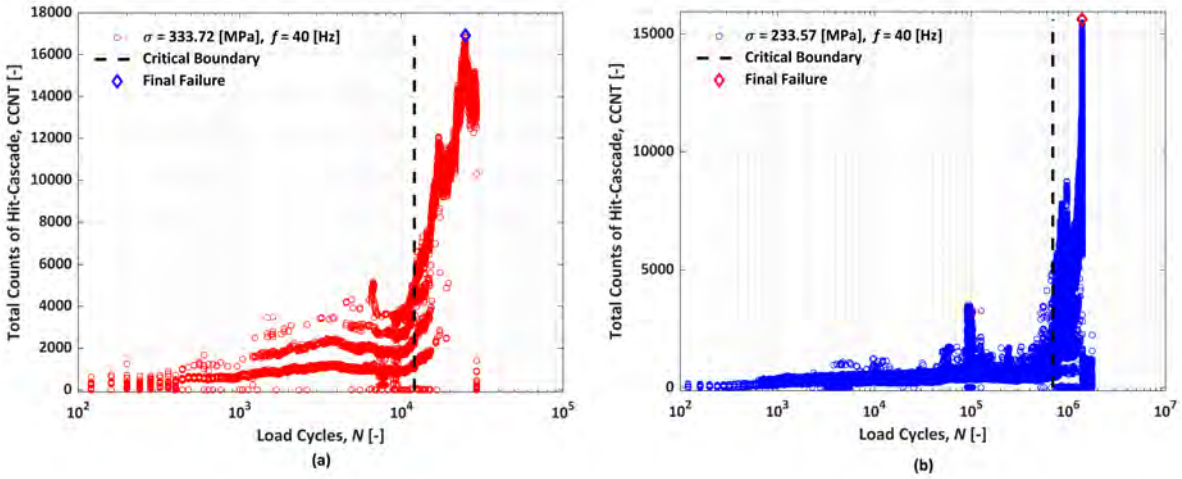

Figure 4.3: Exemplary AE results from fatigue testing of PMCs at 40 Hz for: (a) LCF, and (b) HCF regimes [109].

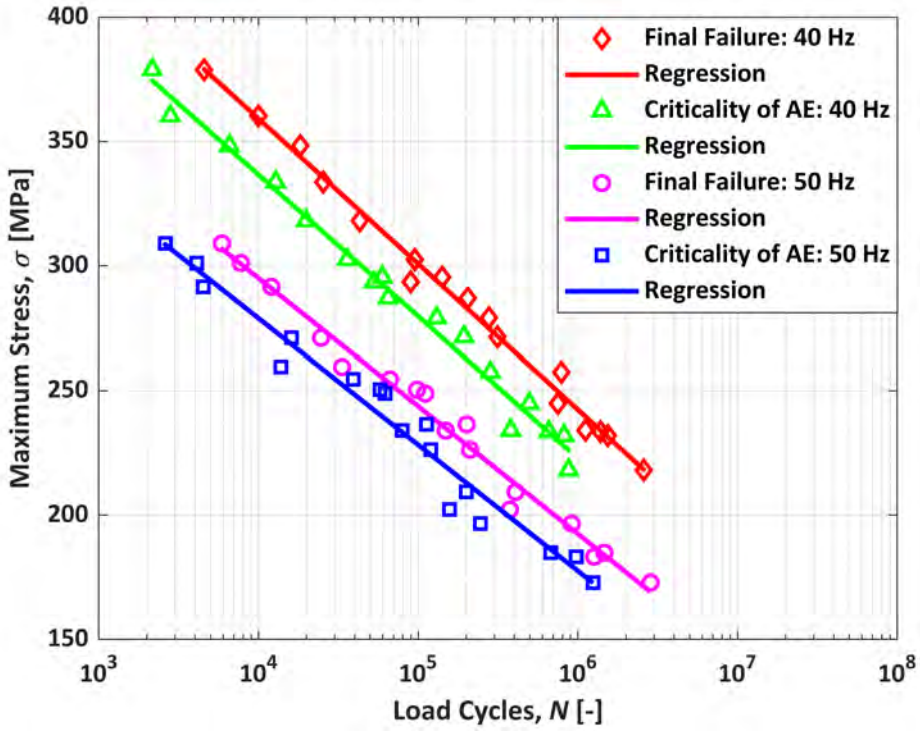

Figure 4.4: The *S-N* curves constructed using final failure and criticality of AE at 40 Hz and 50 Hz [109].

4.2.3 Analysis of fracture fatigue entropy across different loading regimes

Fatigue damage evolution depends on different loading parameters such as stress, frequency, and thermal response [65, 66]. The widely used standard S-N curves rely on final failure and are primarily constructed under low frequencies (5 Hz or below) without accounting for the self-heating effect. Nevertheless, by incorporating results from the $\dot{q}$-σ approach presented in Section 4.2.1, the entropy-based models can effectively capture the interplay between the mechanical loading and the thermal responses, providing a more reliable and generalized assessment of the fatigue damage evolution of PMCs at different stages of damage evolution.

For this purpose, the FFE values were first determined using Eq. 4.4 within IAT scenarios. However, preliminary results indicated that FFE values derived from the bilinear $\dot{q}$-σ model in Figure 4.2, consistent with prior studies within IATs [53, 69], were insufficient for fatigue life assessment across different regimes [109]. To address the unfeasibility of the bilinear model, the CAT results were also incorporated to cover a broader stress range at 40 Hz and 50 Hz.

For IAT scenarios, the stabilized temperature was used to evaluate FFE via Eq. 4.4, while for CAT scenarios, the critical temperature was used instead. The load cycle index corresponding to the AE-based critical boundary at each stress level (e.g., Figure 4.3 for 40 Hz) was used to determine the corresponding critical temperature value from the temperature history curves (e.g., see Figure 4.5 for 40 Hz). The AE event recording and thermal response registration were synchronized throughout the fatigue testing to ensure both datasets captured the same damage evolution stages.

Incorporating temperature-dependent C_P within the $\dot{q}$-σ approach was essential for accurately quantifying heat dissipation rates, thereby facilitating a better evaluation of entropy generation. This refined framework resulted in the trilinear $\dot{q}$-σ model by combining IAT and CAT results over a wide spectrum of stress levels under frequencies of 40 Hz and 50 Hz shown in Figure 4.6.

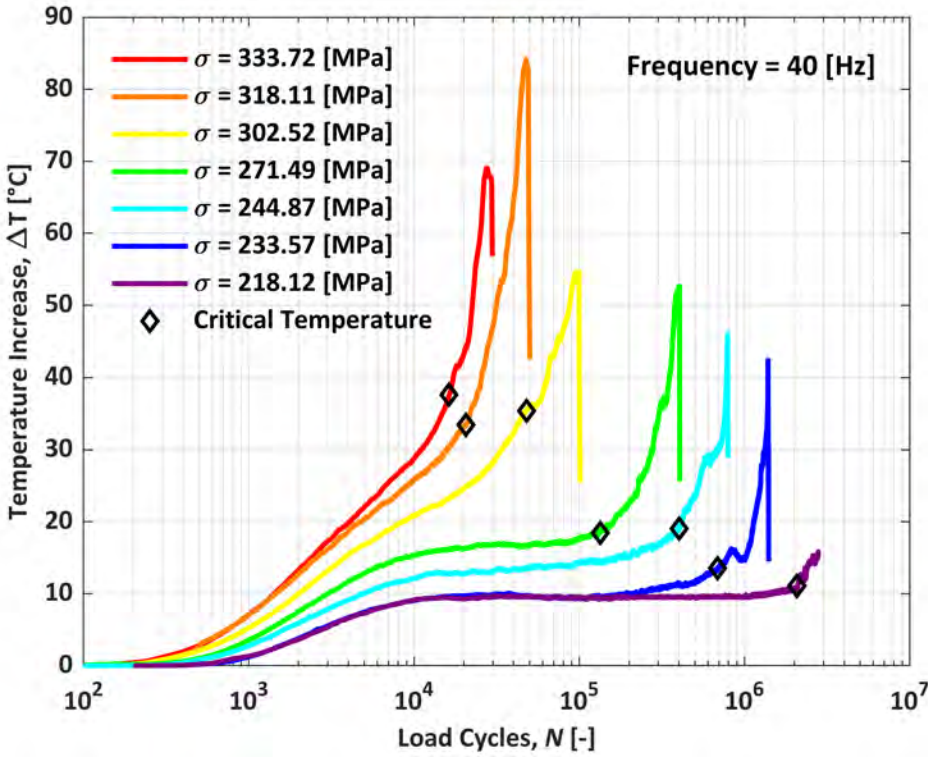

Figure 4.5: Thermal responses including critical temperature values for various stress levels at 40 Hz [109].

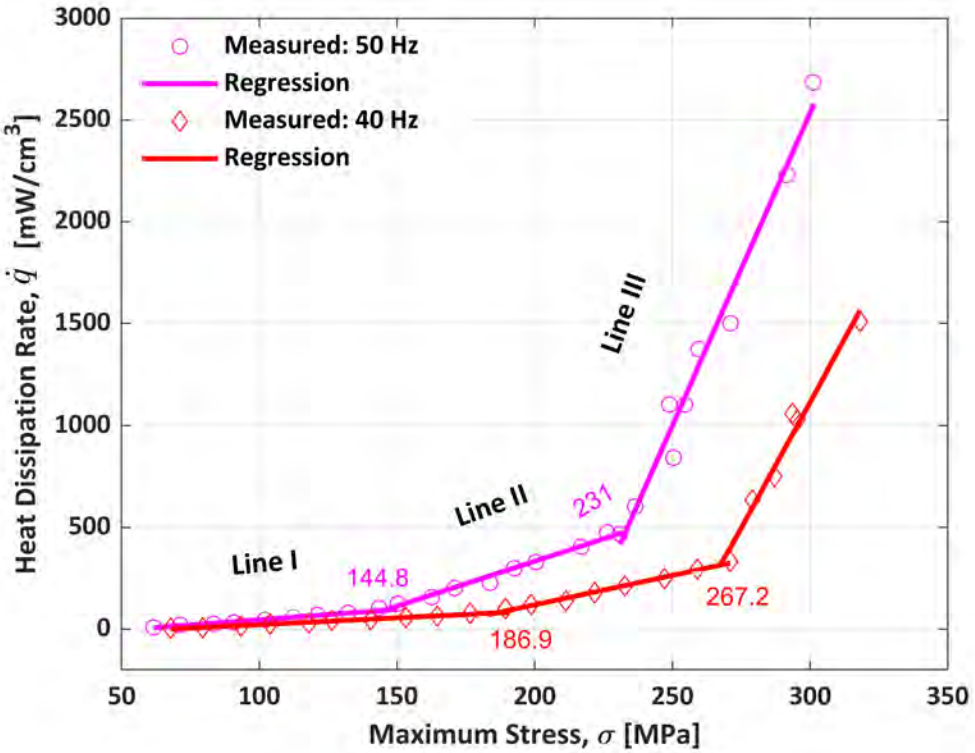

Figure 4.6: The constructed trilinear $\dot{q}$-σ models under 40 Hz and 50 Hz [109].

As shown in [109], the entropy evolved as a function of the load cycle, stress level, and frequency for different fatigue regimes until the final fracture, known as FFE [67]. Analysis of FFE values derived from the trilinear $\dot{q}$-σ results for 40 Hz and 50 Hz (Figure 4.6) illustrated three distinct trends corresponding to LCF (below 10^5 cycles), ICF (10^5 to 10^6 cycles), and HCF (above 10^6 cycles) regimes, see Figure 4.7. Consistent with other studies [53, 62, 70], FFE can still be treated as a material property with regime-based FFE values, making it a reliable metric for evaluating PMC fatigue behavior under different stress levels and frequencies. The mean FFE values for LCF, ICF, and HCF regimes were calculated as 1.8 ± 0.9 J/cm^3 K, 6.5 ± 1.2 J/cm^3 K, and 12.8 ± 2.1 J/cm^3 K, respectively.

As shown in [109], compared to the rapid entropy growth in the LCF regime per cycle, ICF showed a more gradual entropy increase. This behavior is linked to a moderate level of energy dissipation (see Figure 4.6), highlighting that more load cycles are necessary to reach the final fracture/failure. The FFE values within the ICF regime ranged between those of LCF and HCF values. The mean FFE value within the ICF regime is more than three times greater than those for LCF. Among all the fatigue regimes, the slowest entropy accumulation occurs in the HCF regime under relatively lower stress levels. Despite minimal energy dissipation per cycle, the large number of cycles until abrupt failure resulted in cumulative entropy exceeding that of LCF and ICF regimes. The determined mean FFE value for HCF regime was approximately double that of ICF and seven times higher than LCF.

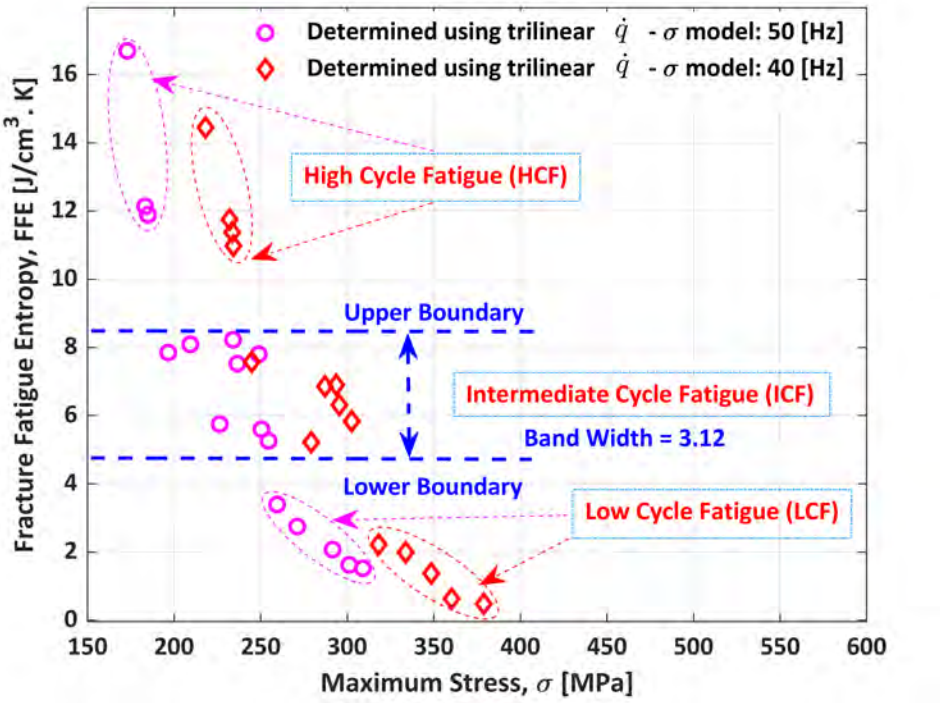

Figure 4.7: Determined FFE values for different loading regimes under 40 Hz and 50 Hz [109].

4.2.4 Evaluating the effectiveness of the entropy-based fatigue life model

Using three mean FFE values, determined for LCF, ICF, and HCF regimes derived from Figure 4.7, the FFE-based *S-N* curves were established for 40 Hz and 50 Hz, see Figure 4.8. These curves were then compared with the standard *S-N* curves to assess their effectiveness in predicting the fatigue life of PMC across different fatigue regimes. The comparative analysis demonstrates that the FFE-based *S-N* curves slightly underestimate the number of cycles in the LCF regime (below 10^5 cycles). This may be attributed to the sensitivity of considering the mean FFE value in the LCF regime, where the higher entropy accumulation rate per cycle leads to significant early-stage damage in the fatigue process due to the dominance of the self-heating effect. The FFE-based *S-N* curves illustrate a good agreement with the standard *S-N* curves in both ICF and HCF regimes. The primary reason for this better alignment may be rooted in a more balanced distribution of mechanical and thermal energy over the fatigue cycles compared to the LCF regime. This highlights that the FFE approach holds the potential as a reliable methodology for fatigue life assessment.

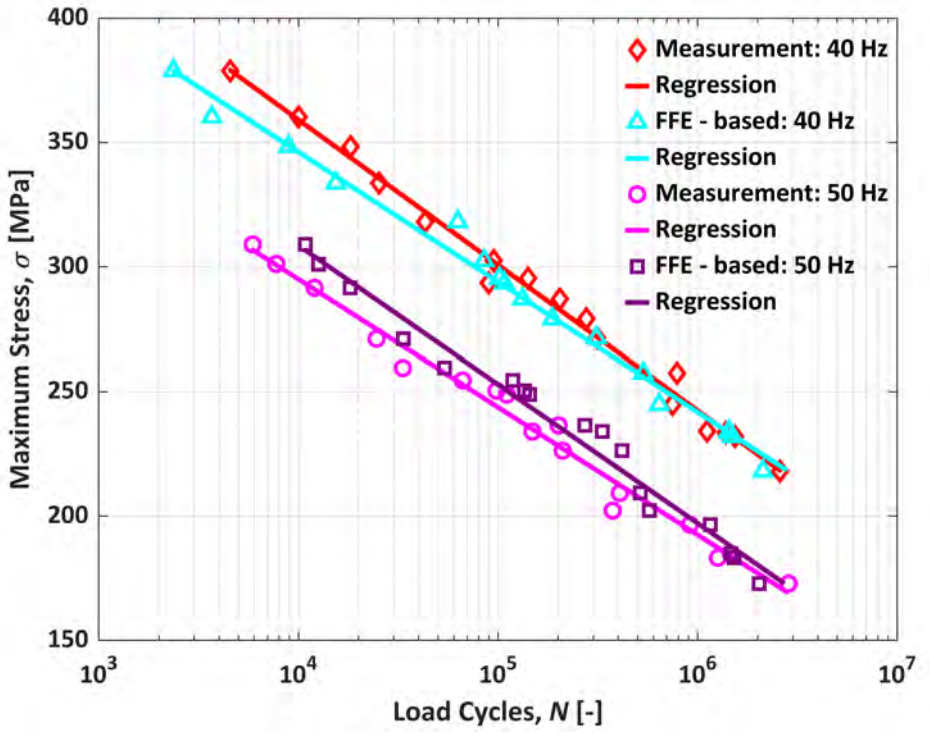

Figure 4.8: Comparison of the standard *S-N* curves and FFE-based *S-N* curves for 40 Hz and 50 Hz [109].

4.2.5 Fatigue life prediction using entropy-based damage index

The application of the FFE concept, which has shown its effectiveness in characterizing fatigue behavior across LCF, ICF, and HCF regimes, was further extended into the entropy-based damage index (EDI). This index was determined through dividing the cycle-dependent cumulative entropy (γ_N), see [109], by the FFE values (at the final fracture) presented in Figure 4.7 across various stress levels for 40 Hz and 50 Hz (i.e., EDI = γ_N/FFE). This index provides a normalized and dimensionless measure of damage accumulation throughout the lifespan of a fatigue-loaded PMC, where the EDI with the value of 100% represents the final fracture. In this study, the EDI concept was presented in the form of *S-N* curves to predict the fatigue life of PMCs [109]. The EDI-based *S-N* curves allow to identify the permissible number of cycles that a fatigue-loaded PMC can endure at a given stress level. For example, Figure 4.9 illustrates the EDI-based *S-N* curves based on various EDI levels ranging from 10% up to the final fracture, for the loading frequency of 40 Hz. The EDI concept can be considered as a failure criterion similar to the concept of damage tolerance in materials design.

A comparison between the EDI-based *S-N* curves and standard *S-N* curves highlights some key differences in the representation of fatigue life. As opposed to the standard *S-N* curves reflecting the fatigue cycles at the final fracture, i.e., EDI = 100%; the EDI-based *S-N* curves provide a continuous measure of the damage evolution at different stages. This is crucial for applications where identifying the early stages of fatigue damage is vital for their predictive maintenance and life extension strategies. In other words, the implementation of the FFE and EDI concepts provides a comprehensive framework for predicting fatigue life across different fatigue regimes and loading frequencies.

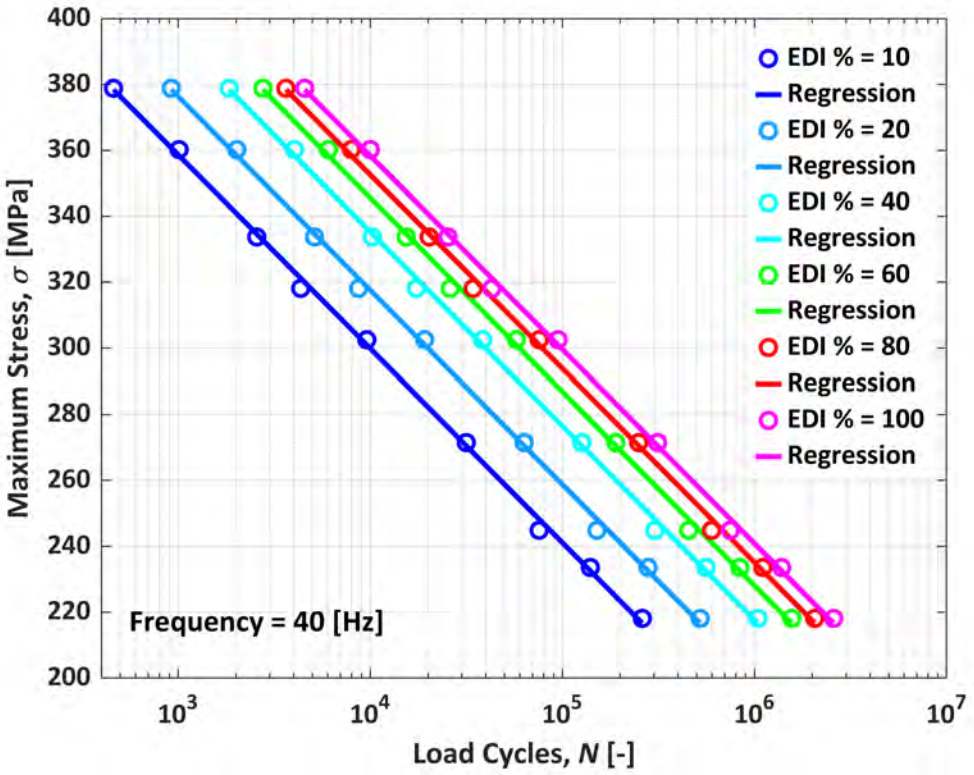

Figure 4.9: *S-N* curves corresponding to different EDI values for 40 Hz loading [109].

4.2.6 Fatigue life assessment based on stiffness degradation

The *S-N* curves were further established based on different levels of stiffness degradation (SD): 10%, 20%, 30%, 40%, and 50%, at frequencies of 40 Hz and 50 Hz, e.g., Figure 4.10 illustrates the results for 40 Hz. Similar to the EDI-based *S-N* curves, this Figure demonstrates the permissible fatigue life of a PMC under various SD levels at 40 Hz. Furthermore, the relationship between the AE-derived critical values (e.g., Figure 4.3 for 40 Hz) and the SD levels was analyzed for both 40 Hz and 50 Hz (see [109]). To establish this correlation, the SD-based *S-N* curves were constructed through the implementation of AE-based critical values, as exemplarily shown in Figure 4.10 for 40 Hz. Within the LCF, ICF, and HCF regimes at 40 Hz, the AE-based critical values correlate with the SD levels of approximately 11%, 12%, and 13%, respectively. This gradual increase in degradation (up to 2%) from the LCF to HCF regime can be attributed to the influence of creep during prolonged fatigue cycling [35]. Based on the analysis of results for 40 Hz and 50 Hz presented in [109], an SD threshold of 14–18% is recommended as a test termination criterion. Maintaining degradation within this range is vital to prevent catastrophic failure, especially in ultrasonic fatigue testing setups designed for the VHCF regime [11].

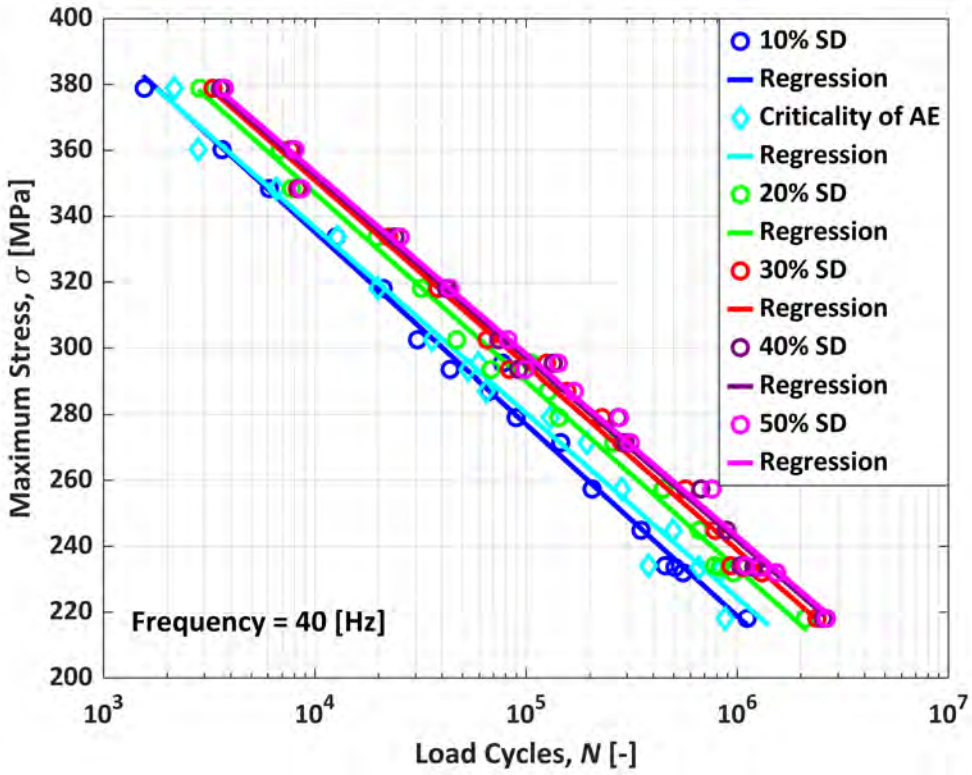

Figure 4.10: Constructed *S*-*N* curves using various SD levels for 40 Hz [109].

4.3 Summary

As presented in this chapter, the third objective was successfully achieved by systematically evaluating the effects of loading frequency (20–50 Hz) on fatigue strength, damage evolution, and lifespan of PMCs. The standard *S*-*N* curves and thermographic fatigue strength assessments (i.e., ΔT-σ, and $\dot{q}$-σ) consistently showed a significant decline in fatigue strength with increasing frequency. Incorporating temperature-dependent heat capacity within the $\dot{q}$-σ approach was essential for accurately quantifying heat dissipation rates, thereby facilitating a better evaluation of entropy generation. This refinement allowed for the development of a trilinear $\dot{q}$-σ model by combining IAT and CAT results, enabling a reliable determination of FFE values within different fatigue regimes (LCF, ICF, and HCF). The mean FFE values varied significantly across regimes, with HCF reaching 12.8 ± 2.1 J/(cm^3·K), approximately twice that of ICF (6.5 ± 1.2 J/(cm^3·K)), and seven times that of LCF (1.8 ± 0.9 J/(cm^3·K)).

The trilinear $\dot{q}$-σ model further allowed for the construction of *S*-*N* curves based on mean FFE values determined for different fatigue regimes. The FFE-based *S*-*N* curves were validated versus the standard *S*-*N* curves extracted from the real-time AE monitoring data at the point of abrupt failure. Unlike standard *S*-*N* curves, which represent fatigue cycles only at final failure,

the proposed EDI-based *S-N* concept as a normalized indicator for damage evolution allowed for a continuous assessment of damage progression. The constructed EDI-based *S-N* curves captured various stages of damage accumulation, ranging from 10% to 100% (i.e., final failure), providing a more comprehensive understanding of the fatigue response of PMCs. Furthermore, the SD-based *S-N* curves were developed for the SD levels ranging from 10% to 50%, indicating the permissible number of cycles that a fatigue-loaded PMC can endure under a given stress level depending on an arbitrary SD level. The correlation between the AE-based critical boundaries and the SD-based *S-N* curves indicated a stiffness degradation threshold of 11–13% under the loading frequency of 40 Hz. Such a threshold can serve as a criterion for fatigue testing termination, offering an alternative to the critical self-heating temperature interval concept discussed in Section 3.2. By implementing FFE-, EDI-, and SD-based *S-N* concepts, this chapter bridged the knowledge gap and established refined methodologies for the thermomechanical fatigue analysis of PMCs.

Chapter 5

Synergistic role of nanocarbon-based allotropes in improving fatigue longevity

The Sections 1.5 and 1.7 highlighted the importance of exploring the synergistic effects of nanocarbon-based allotropes on the fatigue response of PMCs, accounting for the self-heating effect. Considering the absence of research in this area, the fifth objective of this PhD thesis was to investigate how incorporating the thermally conductive nanocarbon-based fillers may mitigate the self-heating effect, and enhance the fatigue lifetime of modified GFRP composites. To achieve this, three composite materials were investigated including unmodified GFRP, GFRP modified with GNPs (0.75 wt.%), and GFRP modified with hybrid nano-reinforcements (0.375+0.375 wt.% GNPs and CNFs). Their fatigue responses were evaluated through the thermography-based approaches, and the standard *S-N* curves [110].

5.1 The role of nanofillers in improving the fatigue strength

The feasibility of implementing $\dot{q}$ as an alternative parameter to the ΔT for determining the fatigue strength was confirmed, demonstrating a more reliable estimation, as highlighted in Chapter 4 (see [109] for further details). Therefore, in addition to the ΔT-σ approach, $\dot{q}$-σ was also implemented to determine the fatigue strengths of the modified composites. The preliminary analysis of the results obtained from IATs illustrated that the bilinear models implemented within the thermography-based (i.e., ΔT-σ, and $\dot{q}$-σ) approaches in Chapter 4 [109], failed to provide a reliable fit to the experimental data for these composites. However, as demonstrated in [110], the exponential models presented in Eqs. 5.1 and 5.2 successfully captured the measured behavior of the three tested composite materials.

$$\Delta T = a_1 \exp(b_1 \sigma) + c_1, \tag{5.1}$$

$$\dot{q} = a_2 \exp(b_2 \sigma) + c_2, \tag{5.2}$$

where a_1, a_2, b_1, b_2, c_1, and c_2 indicate the coefficients derived from the exponential curve fitting. Once the parameters of the exponential models were adjusted, the fatigue strength for each type of composite was estimated using two different procedures for each thermographic method. These procedures included (i) the MCR, and (ii) the MPD of the chord linking the initial and final measured points to the exponential curve constructed for the measured data, see [110] for more details. The MPD procedure, previously employed in [121] only for the ΔT-σ approach, was not utilized for nano-reinforced composites. This research broadens its scope to bridge this gap [110].

Both MCR and MPD procedures were applied within the thermographic ΔT-σ and $\dot{q}$-σ approaches to determine the fatigue strengths of unmodified GFRP, GFRP-GNPs, and GFRP-HNPs composites. For example, Figure 5.1(a) and 5.1(b) illustrate the curves driven from the MCR- and MPD-based $\dot{q}$-σ approaches, respectively, see [110] for further details.

Table 5.1 summarizes the fatigue strength values obtained from the ΔT-σ and $\dot{q}$-σ approaches, along with the values derived from the standard S-N curves for three types of composites at 10^6 cycles. Both ΔT-σ and $\dot{q}$-σ approaches yielded comparable results, except for the unmodified GFRP, with the maximum discrepancy among all composites.

Table 5.1: Fatigue strength estimation for different composites using the ΔT-σ and $\dot{q}$-σ approaches, and S-N curve [110].

Type of Composite	ΔT-σ approach		$\dot{q}$-σ approach		S-N curve
	σ_{FS}^{MCR} [MPa]	σ_{FS}^{MPD} [MPa]	σ_{FS}^{MCR} [MPa]	σ_{FS}^{MPD} [MPa]	σ_{FS}^{SN} [MPa]
Unmodified GFRP	66.5	123.5	114.4	140.3	177.9
GFRP-GNPs	111.8	126.1	109.0	125.9	157.5
GFRP-HNPs	159.0	195.3	162.6	196.9	206.5

For unmodified GFRP, when the MCR and MPD procedures were incorporated into the ΔT-σ and $\dot{q}$-σ approaches, the maximum error found between MCR-based ΔT-σ and $\dot{q}$-σ approaches was roughly 46%. Nevertheless, incorporating the MPD procedure within $\dot{q}$-σ and ΔT-σ methods consistently yielded predictions closer to the S-N curve than the MCR procedure for all three types of PMCs. Notably, the results obtained from $\dot{q}$-σ approach demonstrated a closer alignment with the S-N curve predictions compared to the ΔT-σ method, especially for unmodified GFRP. Consistent with the results presented in Chapter 4 and [109], this highlights that incorporating heat dissipation rate enhances the accuracy of fatigue behavior assessment of PMCs. Therefore, implementing the $\dot{q}$-σ method and MPD-based analysis stand out as reliable tools for evaluating the fatigue strength of PMCs.

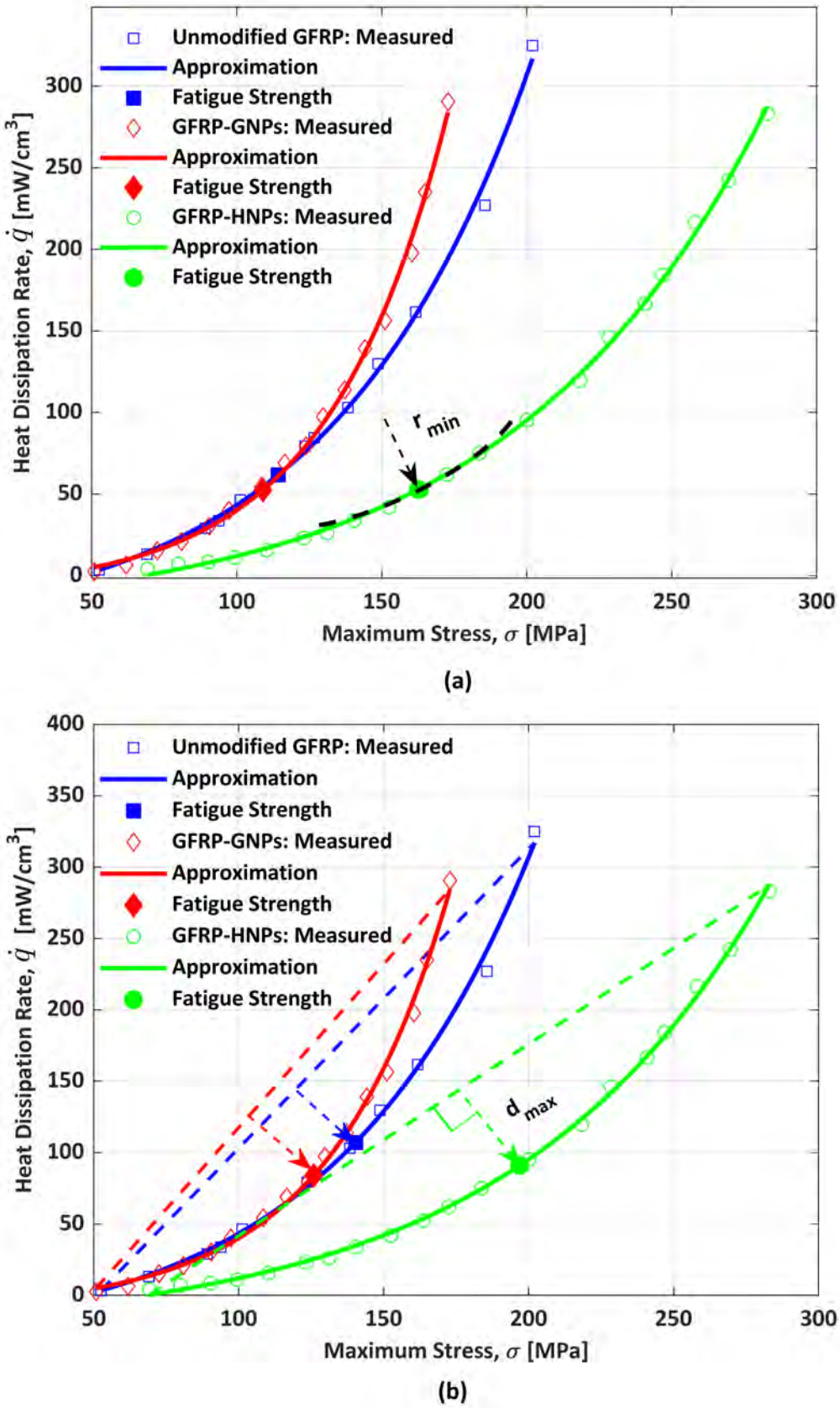

Figure 5.1: Estimated fatigue strength for GFRP composite marked in blue, GFRP-GNPs composite marked in red, and GFRP-HNPs marked in green [110].

5.2 Influence of nanofillers on mitigating the self-heating and extending the fatigue life

In addition to examining the influence of thermally conductive nanocarbon-based allotropes on the fatigue strength of modified PMCs in Section 5.1, their role in fatigue life is analyzed in Section 5.2. For detailed results, see [110].

Figure 5.2 illustrates the identified bilinear *S-N* curve for the unmodified GFRP, indicating the existence of two fatigue regimes, represented by line I and line II. The transition point between these two regimes, denoted as point A, occurs at a stress level of 193.4 MPa for around $2.1 \cdot 10^4$ cycles. The slope of the first line in the *S-N* curve is steeper, approximately five times higher than that of line II. This indicates that fatigue life rapidly decreases at higher stress levels due to the adverse effects of self-heating. Within line II, the influence of self-heating diminishes, which mitigates the fatigue degradation process in modified GFRP, illustrating the enhancement of fatigue life at lower stress levels.

Incorporating GNPs into the GFRP composite significantly altered the fatigue behavior, particularly within the LCF regime. The addition of GNPs extended the fatigue life of the composite, in the range of 10^3 cycles up to $1.8 \cdot 10^5$ cycles (up to Point B). This indicates that GNPs contribute to prolonged fatigue life by mitigating the self-heating effects during the early stages of fatigue. However, beyond $1.8 \cdot 10^5$ cycles, the benefits of GNPs declined with the increasing number of cycles, causing a considerable reduction in the fatigue performance of GFRP-GNPs. At point B, the *S-N* curves for GFRP and GFRP-GNPs converge, after which the fatigue life of GFRP-GNPs declines faster compared to unmodified GFRP. For example, under the stress level of 168.4 MPa, while unmodified GFRP maintained its endurance up to 10^7 cycles, GFRP-GNPs failed after only $5 \cdot 10^5$ cycles. This indicates that although GNPs enhance fatigue life in relatively low-cycle regimes, they may not be a viable candidate for improving the fatigue performance of GFRP in the high-cycle regime.

As shown in Figure 5.2, the fatigue performance of GFRP-GNPs outperformed the other composites up to point C ($5 \cdot 10^3$ cycles), while incorporating GNPs and CNFs into GFRP (GFRP-HNPs) led to a consistent improvement in prolonging fatigue life. This improvement was evident within all fatigue regimes, ranging from $5 \cdot 10^3$ cycles to $2.6 \cdot 10^6$ cycles, compared to unmodified GFRP and GFRP-GNPs. These findings on the improved thermomechanical fatigue response of GFRP-HNPs were supported by the heat dissipation analysis in Section 5.1 (see Figure 5.1), which illustrates that GFRP-HNPs maintain the lowest heat dissipation rate at similar applied stress levels. As a result, less heat is stored within the fatigue-loaded GFRP-HNPs specimen, leading to a reduction in the temperature rise and limiting the damage induced by thermal effects, thereby prolonging the fatigue life of the GFRP-HNPs compared to unmodified

GFRP and GFRP-GNPs.

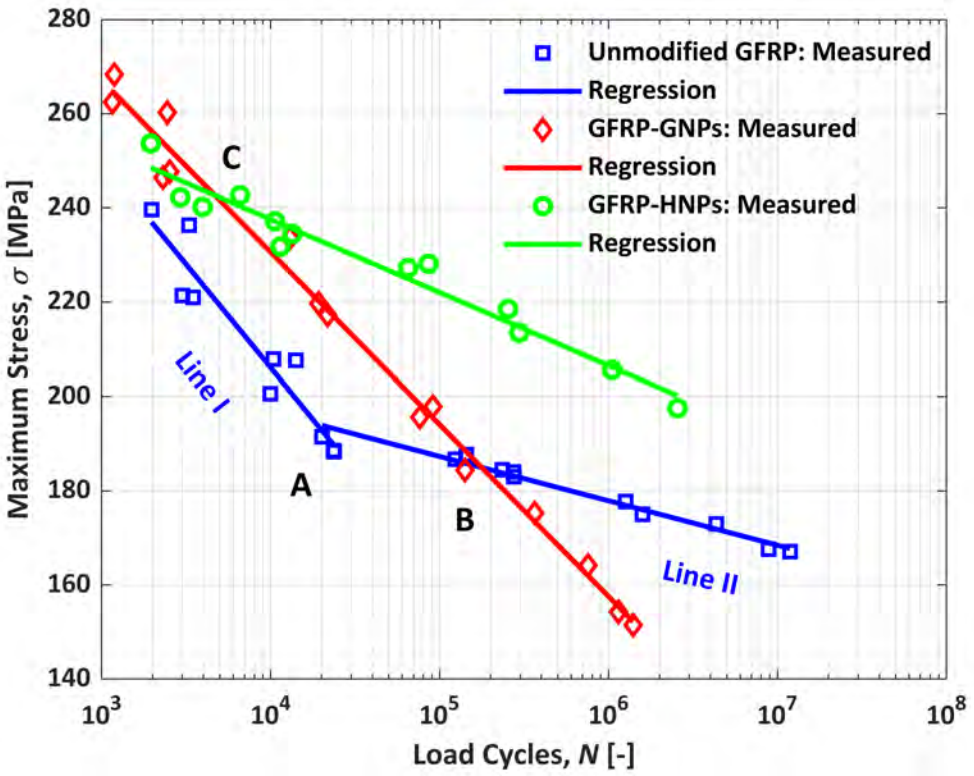

Figure 5.2: Constructed *S*-*N* curves for three different composite materials [110].

To further support the thermomechanical fatigue response of all composites presented in the *S*-*N* curves illustrated in Figure 5.2, the thermal responses of all types of fatigue-loaded PMCs were compared at two different stress levels at the end of loading, as shown in Figure 5.3. Figure 5.3(a-c) corresponds to the stress level of 198.7 ± 1.4 MPa, showing (a) unmodified GFRP, (b) GFRP-GNPs, and (c) GFRP-HNPs. Similarly, Figure 5.3(d-f) corresponds to the stress level of 219.7 ± 1.0 MPa, illustrating (d) unmodified GFRP, (e) GFRP-GNPs, and (f) GFRP-HNPs.

In Figure 5.3(b) and (e), the addition of GNPs vividly illustrated a significant reduction in the magnitude of temperature rise, particularly in the critical region (bottom) of the tested specimen. This effect is observed across the entire surface of the specimen for both stress levels, mitigating the thermal response effectively. From Figure 5.3(c) and (f), it is evident that incorporating HNPs further reduced the temperature rise magnitude and provided superior control over the thermal response for the entire specimen surface compared to GNPs, for both stress levels.

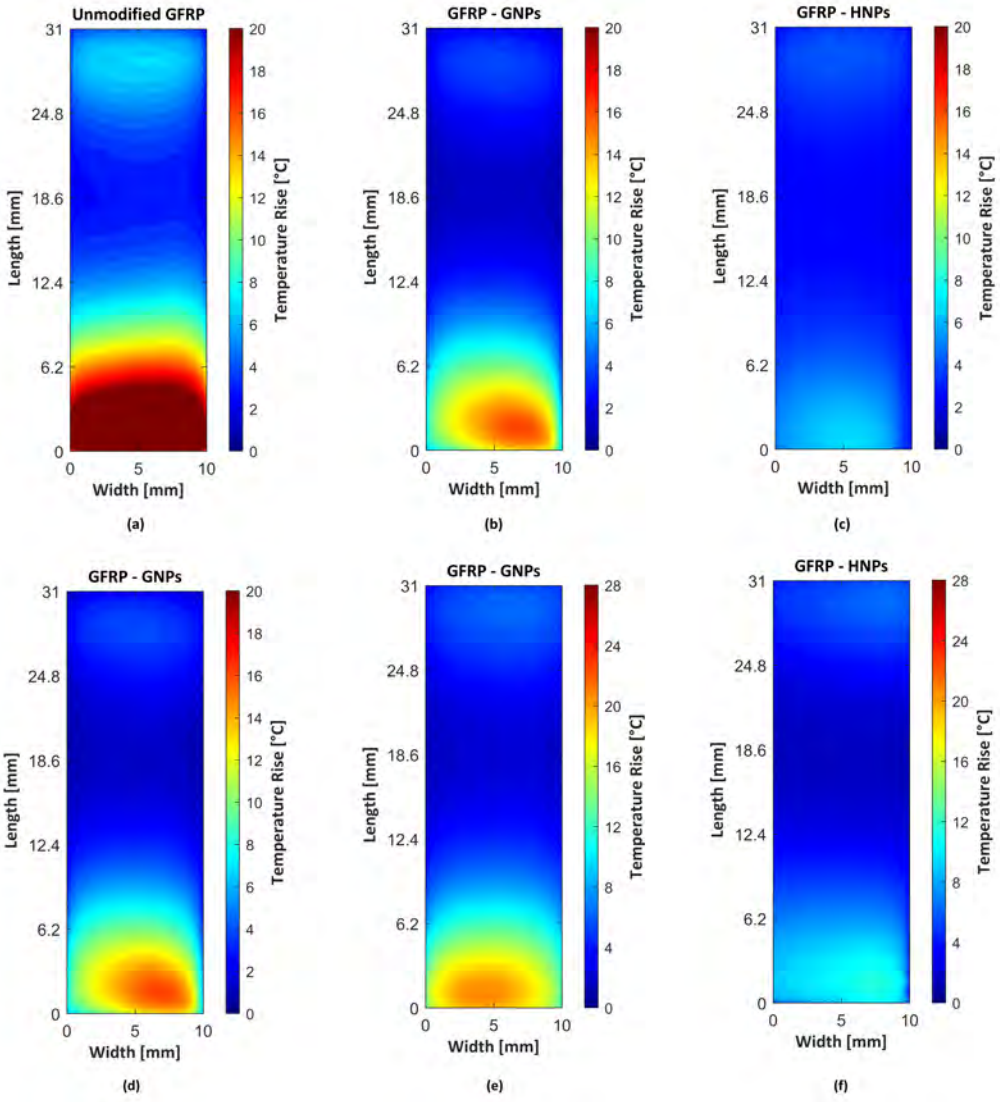

Figure 5.3: Recorded IR images corresponding to the stress level of 198.69 ± 1.36 MPa, for (a) unmodified GFRP, (b) GFRP-GNPs, and (c) GFRP-HNPs, and the stress level of 219.73 ± 1.00 MPa, for (d) unmodified GFRP, (e) GFRP-GNPs, and (f) GFRP-HNPs [110].

Controlling the temperature rise and reducing the heat dissipation rate by incorporating thermally conductive nanocarbon-based allotropes resulted in a substantial improvement in the fatigue lifetime of the tested PMCs, as illustrated in Figures 5.2 and 5.3. According to Figure 5.2, under the stress level of 198.7 ± 1.4 MPa, the fatigue life extended from 10^4 cycles (for unmodified GFRP) to $9.1 \cdot 10^3$ cycles with the addition of GNPs (approximately 9 times greater), and further to $2.6 \cdot 10^6$ cycles with HNPs (257 times higher). Similarly, under a stress level of 219.7 ± 1.0 MPa, the fatigue life increased from $3.5 \cdot 10^3$ cycles (for unmodified GFRP) to $1.9 \cdot 10^4$ cycles with GNPs, and to $2.5 \cdot 10^5$ cycles with HNPs. These findings highlight the beneficial role of adding nanocarbon-based allotropes, particularly the hybridization with GNPs and CNFs.

The hybridization of PMC composites with GNPs and CNFs improved the dispersion and bonds among the polymer chains and reinforcement, thereby reducing filler agglomeration and forming interconnected thermal pathways for efficient heat transfer. The hybridization with GNPs and CNFs mitigated localized heating by reducing mismatches in the coefficient of thermal expansion between the fibers and the surrounding polymer matrix [6]. This mitigated the induced self-heating effect, thereby decreasing the heat storage rate inside the fatigue-loaded GFRP-HNPs specimen, maintaining a mechanically driven fatigue process. In addition to the thermal benefits, the hybridization of GNPs and CNFs contributed to improving the stiffness and toughness of the modified PMCs, delaying crack initiation and propagation, and thereby prolonging the fatigue life of the modified GFRP composite.

5.3 Summary

As presented in this chapter, the fourth objective was successfully achieved by exploring the synergistic role of thermally conductive GNPs and CNFs on the thermomechanical fatigue response of modified GFRP composite. The results extracted from thermographic approaches highlighted the negative influence of GNPs on fatigue strength, while HNPs contributed to fatigue strength improvement. The *S*-*N* curves were then constructed as a reference to assess the reliability of fatigue strengths derived from thermographic approaches. Unlike the MCR, incorporating MPD analysis into ΔT-σ and $\dot{q}$-σ approaches demonstrated better alignment with fatigue strength values derived from the standard *S*-*N* curves. Nevertheless, the introduced MPD-based $\dot{q}$-σ approach provided a reliable strategy for assessing the fatigue strengths of these composites.

Analyzing the *S*-*N* curves and the thermal responses illustrated the capability of thermally conductive nanocarbon allotropes in mitigating the thermal responses induced by the self-heating phenomenon, leading to controlling temperature rise and prolonging the fatigue life of modified GFRP. However, the analysis also highlighted that while GNPs enhanced the low-cycle fatigue performance, incorporating HNPs notably improved the life of modified GFRP composite within both low- and high-cycle regimes. It is worth mentioning that controlling the self-heating temperature via the modifications of the material systems (e.g., hybridization of GNPs and CNFs) may be particularly advantageous for engineering applications where external cooling systems cannot be applied due to operational and technological limitations.

Chapter 6

Broadening the self-heating application in non-destructive damage analysis

In addition to assessing the fatigue response of PMCs, periodic NDT inspections play a vital role in ensuring their structural integrity and longevity. Among thermography-based NDT methods highlighted in Section 1.6, the SHVT technique, developed by the Structural Integrity Assessment Research Group, is a promising alternative for the inspection of composite structures, where the heat source has an internal character [13, 14, 122, 123].

Previous findings by the group highlighted the necessity to extend the application of the SHVT technique to a broader range of structures, e.g., 2D (i.e., plate-like) PMCs, which are more commonly used in engineering applications than 1D PMCs. Furthermore, studies have pointed to the necessity of developing a robust strategy for selecting effective thermograms from a large set of registered images during SHVT testing for damage inspection of PMCs. Considering these limitations, the fifth objective of this PhD thesis was to broaden the applicability of SHVT as an NDT technique for damage assessment in 2D PMCs and establish a robust methodology for selecting the optimal raw thermograms, see [111] for further details.

6.1 Specimens and testing procedure

A total of nine scenarios were examined, each incorporating a centrally located square FBD with a length of 50 mm. The FBDs were introduced in the GFRP plates with effective dimensions of 200 mm $\times$ 240 mm, with extrusion depths of 10%, 25%, and 50% relative to the total thicknesses of 0.5 mm, 0.75 mm, and 1 mm for each specimen; see [111] for further details. The own-designed SHVT testing configuration shown in Figure 6.1 was implemented for damage inspection in 2D PMCs, see [111] for further details.

According to the initially established procedure in the previous studies [122], the testing

procedure consisted of two steps. The modal analysis was first performed to acquire the natural frequencies of vibration of the tested specimens. Each PMC specimen was then excited under its fundamental natural frequency to induce the self-heating effect without unmounting from the fixing frame to preserve the BCs throughout the testing. An IR camera was used to capture the thermal response during the SHVT testing.

The modal analysis was performed on the PMC specimen using LDV with the grid of 9×11 measurement points, within a frequency range of 0 to 300 Hz, and a resolution of 0.25 Hz to accurately capture vibrational characteristics. Figure 6.2 presents the results, highlighting the first and fifth bending mode shapes as exemplary experimental findings in (a) and (b), respectively. The preliminary SHVT results, based on various natural frequencies obtained from the experimental modal analysis, indicated that only the fundamental natural frequency (i.e., the first mode shown in Figure 6.2) generated a sufficient excitation (displacement) amplitude to induce the self-heating effect. Notably, the vibrational loads applied within all nine scenarios resulted in a maximum deformation amplitude of 12 μm for the first mode, whereas higher modes exhibited a displacement amplitude of approximately 2 μm, as shown in Figure 6.2. Therefore, the first natural frequency was selected for all test campaigns. The fundamental natural frequencies determined for all scenarios have been presented in [111].

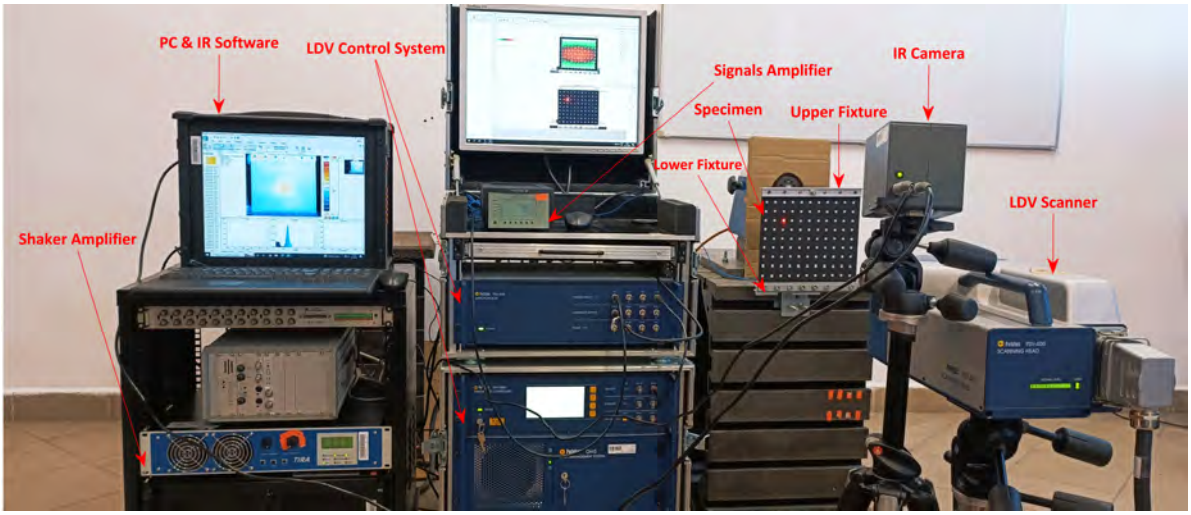

Figure 6.1: The experimental SHVT setup [111].

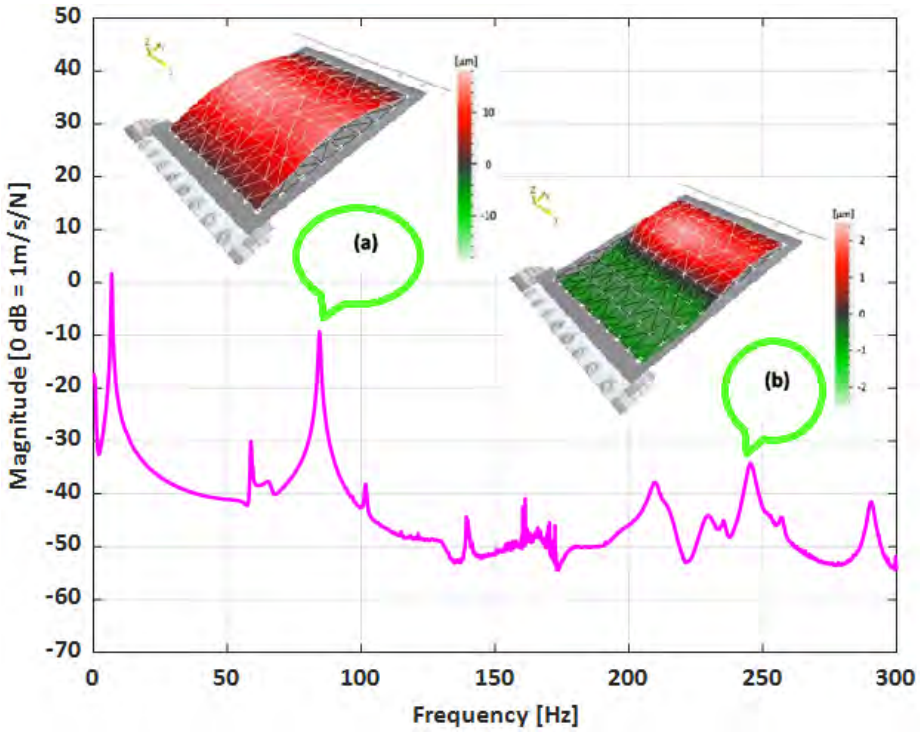

Figure 6.2: Mode shapes of the 1 mm thick PMC with 50% FBD depth: (a) first, and (b) fifth [111].

6.2 Procedure to identify the optimal raw thermograms

To identify the optimal raw thermograms among all the acquired raw thermograms during SHVT testing, the following two-step algorithm was developed. The first step involved determining the optimal period aligned with the boundary of effective thermograms (BETs), established as the maximum permissible number of recorded thermograms for further image processing. The BET for the tested laminated plate involving FBD was quantified based on two manners: (i) the number of thermograms required for the registered self-heating temperature to stabilize (T_s, see Eq. (6.1)), (ii) the number of thermograms needed for achieving the maximum self-heating temperature value ($T_{\max}$, see Eq. (6.2)), as follows:

$$\frac{T_s - T}{T_s - T_{\min}} \geq \frac{1}{e}, \tag{6.1}$$

$$\frac{T_{\max} - T}{T_{\max} - T_{\min}} \geq \frac{1}{e}, \tag{6.2}$$

where $T_{\min}$ denotes the minimum temperature registered during testing. Applying each criterion, which is consistent with the concept of thermal time constant [124, 125], yields a different result for BET. The value $1/e$, where e is the base of the natural logarithm, is known as one thermal time constant, and corresponds to approximately 63.2% of the maximum or stabilized self-heating

temperature. As an illustrative example for a 1 mm-thick laminated composite with the 50% FBD depth shown in Figure 6.3, the BET based on maximum self-heating temperature is 55, while employing the stabilized self-heating temperature sets BET at 116. The choice of criterion has a significant influence on the defined boundary on the interval of observation. As can be concluded, implementing BET based on $T_{\max}$, characterized by its conservative nature, offers a broader spectrum of thermograms, as opposed to using the stabilized self-heating temperature.

In the second step, the optimal raw thermogram for each scenario was selected based on the maximal value of the temperature ratio ($\overline{T}^{\max}_{\text{ratio}}$), within BET from the first step, using:

$$\overline{T}^{\max}_{\text{ratio}} = \max\left(\frac{\overline{T}_{\text{FBD}} - \overline{T}^{\min}_{\text{FBD}}}{\overline{T}_{\text{P-FBD}} - \overline{T}^{\min}_{\text{P-FBD}}}\right), \tag{6.3}$$

where $\overline{T}_{\text{FBD}}$ is the mean value of the temperature of the FBD for each recorded thermogram, i.e., one value per thermogram. $\overline{T}^{\min}_{\text{FBD}}$ denotes the minimal value of the mean temperature of the FBD, which typically occurs at the starting point of the test, i.e., close to the ambient temperature. This represents a constant value for each of the nine scenarios. $\overline{T}_{\text{P-FBD}}$ is the mean value of the temperature obtained by subtracting the values for the whole laminated plate from the values of FBD for every recorded thermogram in each scenario, and $\overline{T}^{\min}_{\text{P-FBD}}$ represents the minimal value of the mean temperature value extracted in the same manner and remaining constant across each of the nine scenarios. Like $\overline{T}^{\min}_{\text{FBD}}$, $\overline{T}^{\min}_{\text{P-FBD}}$ generally occurs at the beginning of the tests.

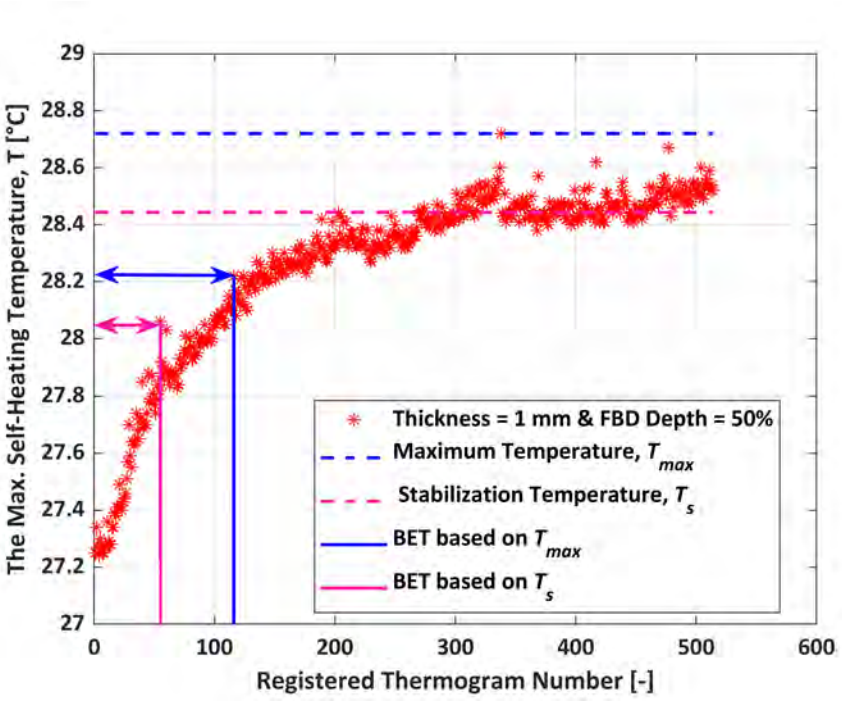

Figure 6.3: The boundary of effective thermograms determined using stabilized and maximum self-heating temperature evolution over registered thermograms [111].

6.3 Enhancement of damage identification and quantification

The enhancement procedure was based on the application of image processing algorithms to the selected thermograms in the first step of the proposed algorithm (i.e., BET). The sequence of thermograms was considered in image processing algorithms, where the identified optimal thermogram in each scenario in the previous step was considered as the upper boundary of the set of processed thermograms, and the lower boundary was always set as 1 [126]. The selection of such a set of thermograms is justified by the highest temperature gradient at the beginning of excitation (see Figure 6.3), allowing for better damage inspection.

To quantify damage in the considered plates, the contours of the identified damage signatures were manually circumscribed using polygons. The assumed boundaries between healthy and damaged regions were perceptually determined based on a sudden change of colors on the enhanced thermograms. The resulting images are presented in Figure 6.4, where the red line describes the identified boundary, while the black line describes the true contour of a damage. In every case, the determined area of damage in mm^2 was provided on the images. For the damage depth of 10%, notable inaccuracies were evident. The large inconsistencies in the quantitative results for flat damage at the 10% depth, as depicted in Figure 6.4 (a), (d), and (g) with damage depths of 0.05 mm, 0.075 mm, and 0.1 mm, respectively, can primarily be attributed to the insufficient thermal contrast. This consequently leads to a lower signal-to-noise ratio and reduced accuracy in damage quantification. Additionally, the flat morphology of the damage likely contributes to the weaker thermal signals, complicating the accurate detection. This limitation should be considered when applying this technique to materials with tiny damage depths, and additional procedure(s) may be necessary to complement the detection of such small damage depths. By contrast, for the damage at 25% and 50% depths, the quantification is significantly more accurate, indicating a more reliable identification of the true shape of damage and its location. This improved performance at greater depths can be attributed to the increased thermal contrast, which enhances the ability of the method to detect and accurately quantify the damage.

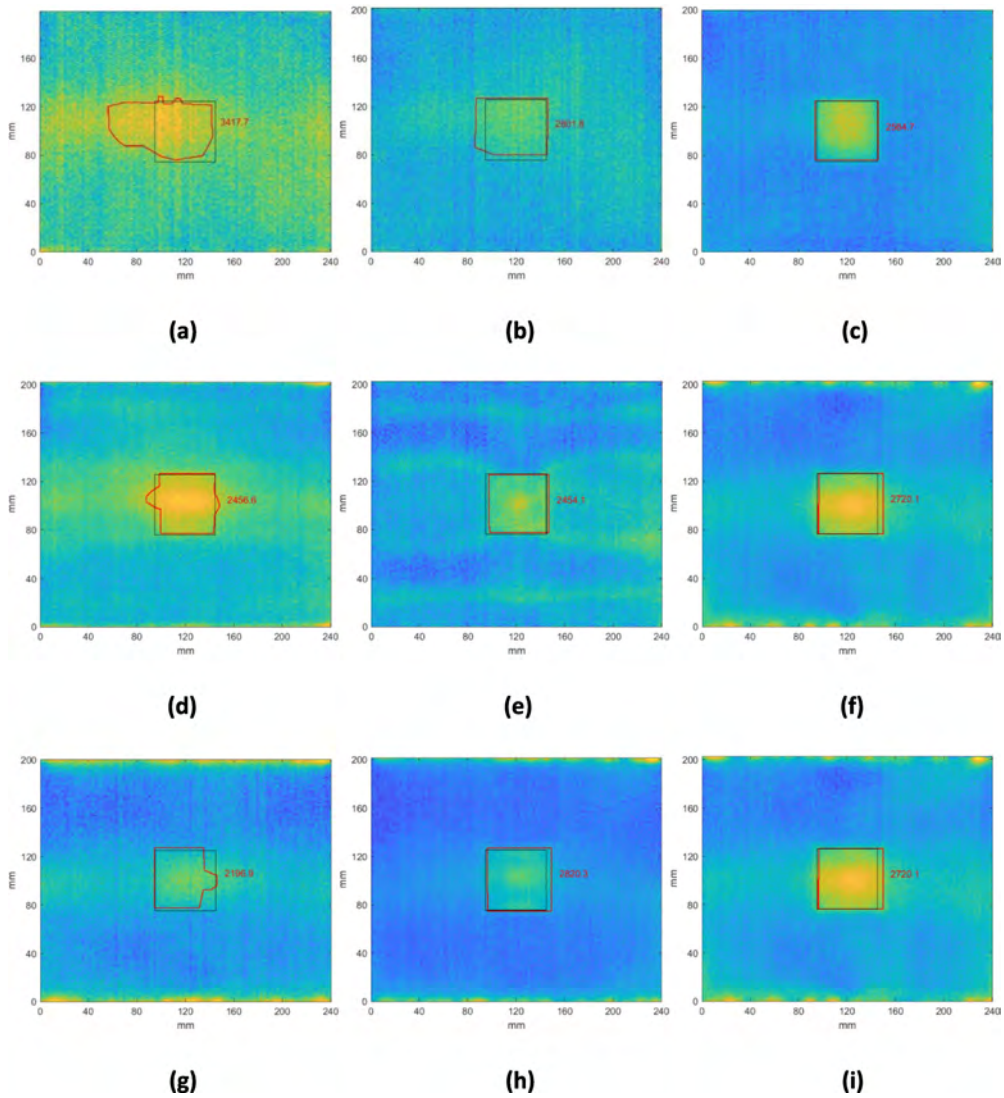

Figure 6.4: The results of enhancement of selected thermograms with the quantified damaged regions for the plates with a thickness of (a-c) 0.5 mm; (d-f) 0.75 mm; (g-i) 1 mm and the damage depth of 10%, 25%, and 50%, respectively, in each row from left to right [111].

6.4 Summary

The findings presented in this chapter illustrated that the recorded temperature rise on the tested PMCs remained below 2 °C without affecting the structural changes (see Figure 6.3), confirming the non-destructive nature of SHVT. The third objective was successfully achieved by establishing a new methodology for selecting the clearest thermograms to see structural damage from a large dataset (i.e., several hundred or even thousands of images) captured by an IR camera during SHVT testing. Additionally, the damage detectability was enhanced by implementing a novel image post-processing algorithm to identify the optimal raw thermogram. These advancements open up new possibilities for inspecting polymeric composite structures with a potential application in inspections of aircraft structures with single-sided access.

Chapter 7

Summary and conclusions

7.1 Conclusions

The findings presented in this PhD dissertation successfully addressed several key challenges in understanding the thermomechanical fatigue response, and the damage assessment of PMCs. These challenges include the phenomenology of self-heating, the transferability of LFFT and UFFT results, the fatigue strength estimation, the fatigue life assessment, and the synergistic effects of thermally conductive nanocarbon-based allotropes on the fatigue performance of modified PMCs. Furthermore, a robust methodology was proposed for identifying the most effective thermograms recorded during non-destructive SHVT testing, aiming to improve the damage detectability in PMCs. The novel physics-based frameworks and methodologies were introduced, significantly contributing to the field of fatigue characterization and the durability assessment of PMCs. The key conclusions drawn from this PhD thesis, in accordance with the five main objectives, are summarized below.

The first objective was successfully achieved through the development of a robust physics-based framework capable of reliably modeling the self-heating effect in PMCs under fatigue loading conditions (see Chapter 2). This framework was built upon experimental characterizations and numerical simulations, leading to the following conclusions:

- Radiative heat flux was identified as a critical environmental factor affecting the temperature evolution, necessitating its inclusion in the self-heating model for reliable predictions.

- In thin PMCs (length-to-thickness ratio of 16 in the tested cases), the through-thickness temperature variation was negligible (below 4 °C) compared to the 100 °C rise observed under high-stress levels. This finding confirmed the sufficiency of surface temperature measurements using an IR camera during fatigue testing.

- The developed numerical model provides valuable predictive capabilities for assessing self-heating behavior under different loading conditions.

The second objective was accomplished by evaluating the feasibility of combining LFFT and UFFT results to establish a unified framework for fatigue response prediction within both regimes (see Chapter 3). The key findings include:

- Constructing the standard S-N curve approach was found to be ineffective for evaluating fatigue response across the full spectrum of fatigue regimes, ranging from LCF to VHCF.
- Analysis of the fatigue results showed a transition zone between LFFT (up to 10^6 cycles) and UFFT (above 10^8 cycles), which is unfeasible to characterize using the standard approach due to testing time constraints and technological limitations.
- A unitless scalable factor was introduced to transfer the results from the UFFT to the LFFT regime. The findings illustrated a 2100-fold increase in the heat dissipation rate within the UFFT regime compared to the LFFT regime at the equivalent stress/displacement level, attributed to the frequency-dependent thermal effects.

The third objective was successfully accomplished by assessing the thermomechanical fatigue life of PMCs through the novel concepts of entropy-based damage evolution and stiffness degradation, allowing for capturing the continuous fatigue-induced damage progression (see Chapter 4). The key findings include:

- Increasing frequency led to a pronounced reduction in the fatigue strength, as shown by findings from the S-N curves and thermography-based approaches (i.e., ΔT-σ and $\dot{q}$-σ).
- As opposed to the ΔT-σ approach, which neglects the influence of heat capacity, the $\dot{q}$-σ resulted in more reliable fatigue strength predictions when compared with the results derived from the standard S-N curves.
- Incorporating temperature-dependent heat capacity into the $\dot{q}$-σ approach enabled accurate quantification of heat dissipation rates, thereby facilitating a better evaluation of entropy generation. This refined framework resulted in the trilinear $\dot{q}$-σ model over a wide range of stress.
- The established trilinear model allowed for a reliable determination of mean FFE values across different fatigue regimes (LCF, ICF, and HCF) by combining IAT and CAT results.
- Although the energy dissipation per cycle was minimal in the HCF regime, the large number of cycles to abrupt failure caused the cumulative entropy to exceed that of the LCF

and ICF regimes. Consequently, the mean FFE value for the HCF regime was the highest, approximately twice that of the ICF and seven times that of the LCF.

- Using the FFE values from LCF, ICF, and HCF regimes, the trilinear $\dot{q}$-σ model enabled the reliable life assessment of fatigue-loaded PMCs under different loading frequencies, with validation through the standard S-N curves obtained from real-time AE monitoring at the moment of abrupt failure.

- The novel EDI-based S-N curves were introduced, allowing for a continuous assessment of damage evolution from initiation to abrupt fracture, addressing the limitation of the standard S-N curves that capture only final failure.

- The S-N curves were additionally constructed for various SD levels (10% to 50%), illustrating the permissible number of cycles that a PMC specimen can endure under different stress and SD scenarios.

- AE-identified critical boundaries correlated with the SD-based S-N curves illustrated a stiffness degradation threshold of 14–18%, which can be considered as a potential test termination criterion to prevent catastrophic failure, especially in ultrasonic fatigue testing setups designed for VHCF regime.

The fourth objective was successfully accomplished by investigating the synergistic effects of GNPs and CNFs in mitigating and controlling the self-heating temperature, thereby improving the thermomechanical fatigue performance of modified GFRP (see Chapter 5). The main conclusions include:

- Implementing the $\dot{q}$-σ method and MPD-based analysis stand out as reliable tools for evaluating the fatigue strength of unmodified and modified PMCs.

- Analyzing the thermal responses confirmed that thermally conductive carbon-based nanofillers effectively controlled the self-heating temperature, reducing the detrimental effects of temperature rise on the lifetime of the fatigue-loaded PMCs.

- The analysis also highlighted that while the incorporation of GNPs (0.75 wt.%) enhanced the low-cycle fatigue performance, incorporating HNPs (0.375+0.375 wt.% GNPs and CNFs) remarkably improved the life of modified PMCs within both low- and high-cycle regimes.

- For example, incorporating GNPs enhanced fatigue life from 10^4 cycles to $9.1 \cdot 10^4$ cycles (9 times longer) under the stress level of 198.7±1.4 MPa, while adding HNPs provided a 250-fold improvement, extending fatigue life to $2.6 \cdot 10^6$ cycles under the same stress level.

- The improved fatigue performance from hybridizing GNPs and CNFs stems from their synergistic effects in reducing the filler agglomeration, enhancing the interconnected thermal pathways for efficient heat transfer, thereby delaying the crack initiation and mitigating the fatigue damage propagation.
- Controlling the self-heating temperature via the modifications of the material systems (e.g., hybridization of GNPs and CNFs) can be particularly advantageous for applications where the external cooling systems cannot be applied due to operational and technological limitations.

The final objective was achieved by broadening the application of the SHVT technique for damage inspection in 2D PMCs, utilizing the self-heating phenomenon as an alternative heat source (see Chapter 6). The key findings include:

- The surface temperature increase on 2D PMCs, remaining below 2 °C without inducing structural changes, confirmed the non-destructive characteristic of the SHVT technique.
- A two-step algorithm based on the concepts of the boundary of effective thermograms, and the maximal temperature ratio was proposed to methodically choose the optimal raw thermogram from a large set of registered thermograms for each damage scenario.

The findings of the accomplished research studies, as summarized in the conclusions drawn from the five defined objectives, provided a strong foundation for confirming and validating the hypothesis formulated in Section 1.7. These contributions offer valuable advancements in predicting and modeling the thermomechanical fatigue response, the optimal material design strategies, and the non-destructive evaluation techniques, paving the way for more reliable and high-performance PMCs in aerospace, automotive, and structural applications.

7.2 Future work

The analysis of the results highlighted several promising directions for future research, with the most important ones outlined below:

- Investigating the structural degradation mechanisms under complex fatigue loading conditions (e.g., random and multiaxial loading), while incorporating the self-heating effect.
- An in-depth study on the implementation of 3D damage reconstruction approaches, such as ultrasonic and X-ray CT data, is needed to bridge the gap in quantifying damage evolution induced by the self-heating effect during fatigue testing of PMCs.

- Investigating the synergistic effects of different GNP-to-CNF ratios on further mitigating the self-heating effect and improving the fatigue performance of modified PMCs under different loading regimes.
- Minimizing the self-heating effect, in addition to optimal material selection and design, requires an in-depth study of various cooling systems to identify the optimal cooling system based on thermal efficiency, viscosity, corrosion resistance, safety, and cost-effectiveness.
- Further development of the non-destructive SHVT technique is necessary to inspect more realistic damage types, such as fatigue damage, low-velocity impact damage, and delamination in PMCs.
- Investigating the applicability of SHVT for 3D composite structures, including thick laminate configurations and complex geometries, is essential for expanding its usage.

Bibliography

[1] N. Burger, A. Laachachi, M. Ferriol, M. Lutz, V. Toniazzo, and D. Ruch. "Review of thermal conductivity in composites: Mechanisms, parameters and theory". *Progress in Polymer Science* 61 (Oct. 2016), 1–28. ISSN: 0079-6700. DOI: 10.1016/j.progpolymsci.2016.05.001.

[2] Q. Zheng, M. Hao, R. Miao, J. Schaadt, and C. Dames. "Advances in thermal conductivity for energy applications: A review". *Progress in Energy* 3.1 (Jan. 2021), p. 012002. ISSN: 2516-1083. DOI: 10.1088/2516-1083/abd082.

[3] N. Wu, S. Che, H.-w. Li, C.-n. Wang, X.-j. Tian, and Y.-f. Li. "A review of three-dimensional graphene networks for use in thermally conductive polymer composites: Construction and applications". *New Carbon Materials* 36.5 (Oct. 2021), 911–926. ISSN: 1872-5805. DOI: 10.1016/s1872-5805(21)60089-6.

[4] Z. Wu, C. Xu, C. Ma, Z. Liu, H. Cheng, and W. Ren. "Synergistic effect of aligned graphene nanosheets in graphene foam for high-performance thermally conductive composites". *Advanced Materials* 31.19 (Mar. 2019). ISSN: 1521-4095. DOI: 10.1002/adma.201900199.

[5] H. Im and J. Kim. "Thermal conductivity of a graphene oxide–carbon nanotube hybrid/epoxy composite". *Carbon* 50.15 (Dec. 2012), 5429–5440. ISSN: 0008-6223. DOI: 10.1016/j.carbon.2012.07.029.

[6] J. Amraei and A. Katunin. "Recent advances in limiting fatigue damage accumulation induced by self-heating in polymer–matrix composites". *Polymers* 14.24 (Dec. 2022), p. 5384. ISSN: 2073-4360. DOI: 10.3390/polym14245384.

[7] Y. Ming, Y. Duan, S. Zhang, Y. Zhu, and B. Wang. "Self-heating 3D printed continuous carbon fiber/epoxy mesh and its application in wind turbine deicing". *Polymer Testing* 82 (Feb. 2020), p. 106309. ISSN: 0142-9418. DOI: 10.1016/j.polymertesting.2019.106309.

[8] C. Tongchitpakdee, S. Benjanirat, and L. N. Sankar. "Numerical simulation of the aerodynamics of horizontal axis wind turbines under yawed flow conditions". *Journal of Solar Energy Engineering* 127.4 (2005), pp. 464–474. ISSN: 1528-8986. DOI: 10.1115/1.2035705.

[9] D. Zorko, J. Tavčar, M. Bizjak, R. Šturm, and Z. Bergant. "High cycle fatigue behaviour of autoclave-cured woven carbon fibre-reinforced polymer composite gears". *Polymer Testing* 102 (Oct. 2021), p. 107339. ISSN: 0142-9418. DOI: 10.1016/j.polymertesting.2021.107339.

[10] A. Katunin, A. Wronkowicz, M. Bilewicz, and D. Wachla. "Criticality of self-heating in degradation processes of polymeric composites subjected to cyclic loading: A multiphysical approach". *Archives of Civil and Mechanical Engineering* 17.4 (Sept. 2017), 806–815. ISSN: 1644-9665. DOI: 10.1016/j.acme.2017.03.003.

[11] J. Amraei, T. Rogala, A. Katunin, A. Premanand, G. Kokot, D. Wachla, W. Kuś, M. Bilewicz, B. Khatri, and F. Balle. "Thermomechanical fatigue behavior of CF/PEKK composite under low and ultrasonic frequencies". *Composites Part B: Engineering* 281 (July 2024), p. 111539. ISSN: 1359-8368. DOI: 10.1016/j.compositesb.2024.111539.

[12] A. Katunin, D. Wachla, P. Santos, and P. N. Reis. "Fatigue life assessment of hybrid bio-composites based on self-heating temperature". *Composite Structures* 304 (Jan. 2023), p. 116456. ISSN: 0263-8223. DOI: 10.1016/j.compstruct.2022.116456.

[13] A. Katunin and D. Wachla. "Analysis of defect detectability in polymeric composites using self-heating based vibrothermography". *Composite Structures* 201 (Oct. 2018), 760–765. ISSN: 0263-8223. DOI: 10.1016/j.compstruct.2018.06.105.

[14] A. Katunin, A. Wronkowicz-Katunin, and D. Wachla. "Impact damage assessment in polymer matrix composites using self-heating based vibrothermography". *Composite Structures* 214 (Apr. 2019), 214–226. ISSN: 0263-8223. DOI: 10.1016/j.compstruct.2019.02.003.

[15] S. A. Grammatikos, E. Z. Kordatos, T. E. Matikas, and A. S. Paipetis. "On the fatigue response of a bonded repaired aerospace composite using thermography". *Composite Structures* 188 (Mar. 2018), 461–469. ISSN: 0263-8223. DOI: 10.1016/j.compstruct.2018.01.035.

[16] Z. Hashin. "Analysis of properties of fiber composites with anisotropic constituents". *Journal of Applied Mechanics* 46.3 (Sept. 1979), 543–550. ISSN: 1528-9036. DOI: 10.1115/1.3424603.

[17] M. Yekani Fard, B. Raji, and H. Pankretz. "Correlation of nanoscale interface debonding and multimode fracture in polymer carbon composites with long-term hygrothermal effects". *Mechanics of Materials* 150 (Nov. 2020), p. 103601. ISSN: 0167-6636. DOI: 10.1016/j.mechmat.2020.103601.

[18] A. Katunin, K Krukiewicz, and R Turczyn. "Ocena sieciowania resztkowego wywołanego efektem samorozgrzania we włóknistych kompozytach epoksydowych z wykorzystaniem spektroskopii Ramana". *Chemik* 68.11 (2014), pp. 957–966.

[19] J. Amraei, J. E. Jam, B. Arab, and R. D. Firouz-Abadi. "Effect of interphase zone on the overall elastic properties of nanoparticle-reinforced polymer nanocomposites". *Journal of Composite Materials* 53.9 (Sept. 2018), 1261–1274. ISSN: 1530-793X. DOI: 10.1177/0021998318798443.

[20] J. Amraei, J. E. Jam, B. Arab, and R. D. Firouz-Abadi. "Modeling the interphase region in carbon nanotube-reinforced polymer nanocomposites". *Polymer Composites* 40.S2 (Sept. 2018). ISSN: 1548-0569. DOI: 10.1002/pc.24950.

[21] M. Rose, S. Niverty, B. Schmidt, M. Kästner, M. Zimmermann, and N. Chawla. "X-ray computer tomography (XCT) of fatigue damage in laser-machined versus milled carbon fiber reinforced polymer matrix composites". *Engineering Fracture Mechanics* 252 (July 2021), p. 107820. ISSN: 0013-7944. DOI: 10.1016/j.engfracmech.2021.107820.

[22] C. Colombo and L. Vergani. "Influence of delamination on fatigue properties of a fibreglass composite". *Composite Structures* 107 (Jan. 2014), 325–333. ISSN: 0263-8223.

[23] C. Colombo, T. Bhujangrao, F. Libonati, and L. Vergani. "Effect of delamination on the fatigue life of GFRP: A thermographic and numerical study". *Composite Structures* 218 (June 2019), 152–161. ISSN: 0263-8223. DOI: 10.1016/j.compstruct.2019.03.023.

[24] Q. Guo, X. Guo, J. Fan, R. Syed, and C. Wu. "An energy method for rapid evaluation of high-cycle fatigue parameters based on intrinsic dissipation". *International Journal of Fatigue* 80 (Nov. 2015), 136–144. ISSN: 0142-1123. DOI: 10.1016/j.ijfatigue.2015.04.016.

[25] G. Voudouris, D. Di Maio, and I. A. Sever. "Experimental fatigue behaviour of CFRP composites under vibration and thermal loading". *International Journal of Fatigue* 140 (Nov. 2020), p. 105791. ISSN: 0142-1123. DOI: 10.1016/j.ijfatigue.2020.105791.

[26] G. Charalambous, G. Allegri, and S. R. Hallett. "Temperature effects on mixed mode I/II delamination under quasi-static and fatigue loading of a carbon/epoxy composite". *Composites Part A: Applied Science and Manufacturing* 77 (Oct. 2015), 75–86. ISSN: 1359-835X. DOI: 10.1016/j.compositesa.2015.05.016.

[27] A. Katunin and D. Wachla. “Minimizing self-heating based fatigue degradation in polymeric composites by air cooling”. *Procedia Structural Integrity* 18 (2019), 20–27. ISSN: 2452-3216. DOI: 10.1016/j.prostr.2019.08.136.

[28] A. I. Gagani, A. B. Monsås, A. E. Krauklis, and A. T. Echtermeyer. “The effect of temperature and water immersion on the interlaminar shear fatigue of glass fiber epoxy composites using the I-beam method”. *Composites Science and Technology* 181 (Sept. 2019), p. 107703. ISSN: 0266-3538. DOI: 10.1016/j.compscitech.2019.107703.

[29] J. B. Knoll, B. T. Riecken, N. Kosmann, S. Chandrasekaran, K. Schulte, and B. Fiedler. “The effect of carbon nanoparticles on the fatigue performance of carbon fibre reinforced epoxy”. *Composites Part A: Applied Science and Manufacturing* 67 (Dec. 2014), 233–240. ISSN: 1359-835X. DOI: 10.1016/j.compositesa.2014.08.022.

[30] C. Wang, X. Chen, L. Cheng, and J. Ding. “High-cycle and very-high-cycle fatigue properties of CFRP-aramid honeycomb sandwich structure in three-point bending”. *International Journal of Fatigue* 155 (Feb. 2022), p. 106576. ISSN: 0142-1123. DOI: 10.1016/j.ijfatigue.2021.106576.

[31] A. Katunin, M. Bilewicz, D. Wachla, J. Amraei, and J. Viana. “Investigation of fracture mechanisms of self-reinforced polypropylene/polycarbonate composites subjected to fatigue loading”. *Materials Science Forum* 1075 (Dec. 2022), 65–70. DOI: 10.4028/p-xvux5k.

[32] P. N. B. Reis, A. Katunin, and J. Amraei. “Critical Analysis of the Systems Used to Reduce Self-Heating in Polymer Composites Subjected to Very High Cycle Fatigue Regimes”. *Fatigue amp; Fracture of Engineering Materials amp; Structures* 48.4 (Jan. 2025), 1371–1392. ISSN: 1460-2695. DOI: 10.1111/ffe.14561. URL: http://dx.doi.org/10.1111/ffe.14561.

[33] D. Backe and F. Balle. “Ultrasonic fatigue and microstructural characterization of carbon fiber fabric reinforced polyphenylene sulfide in the very high cycle fatigue regime”. *Composites Science and Technology* 126 (Apr. 2016), 115–121. ISSN: 0266-3538. DOI: 10.1016/j.compscitech.2016.02.020.

[34] Y. Tao, C. A. Stevens, E. Bilotti, T. Peijs, and J. J. Busfield. “Fatigue of carbon cord-rubber composites: Effect of frequency, R ratio and life prediction using constant life models”. *International Journal of Fatigue* 135 (June 2020), p. 105558. ISSN: 0142-1123. DOI: 10.1016/j.ijfatigue.2020.105558. URL: http://dx.doi.org/10.1016/j.ijfatigue.2020.105558.

[35] A. P. Vassilopoulos. "The history of fiber-reinforced polymer composite laminate fatigue". *International Journal of Fatigue* 134 (May 2020), p. 105512. ISSN: 0142-1123. DOI: 10.1016/j.ijfatigue.2020.105512.

[36] A. Katunin, I. Pivdiablyk, L. Gornet, and P. Rozycki. "A hybrid method for determination of fatigue limit and non-destructive evaluation of composite structures after low-velocity impact loading". *Composites Part B: Engineering* 238 (June 2022), p. 109898. ISSN: 1359-8368. DOI: 10.1016/j.compositesb.2022.109898.

[37] A. Premanand, T. Rogala, D. Wachla, J. Amraei, A. Katunin, B. Khatri, M. Rienks, and F. Balle. "Fatigue strength estimation of a CF/PEKK composite through self-heating temperature analysis using cyclic bending tests at 20 kHz". *Composites Science and Technology* 243 (Oct. 2023), p. 110218. ISSN: 0266-3538. DOI: 10.1016/j.compscitech.2023.110218.

[38] A. Movahedi-Rad, T. Keller, and A. P. Vassilopoulos. "Stress ratio effect on tension-tension fatigue behavior of angle-ply GFRP laminates". *International Journal of Fatigue* 126 (Sept. 2019), 103–111. ISSN: 0142-1123. DOI: 10.1016/j.ijfatigue.2019.04.037.

[39] M. E. Deniz and F. Aydin. "Determination of fatigue life of the unidirectional GFRP/Al hybrid composite laminates". *Composites Part B: Engineering* 166 (June 2019), 580–587. ISSN: 1359-8368. DOI: 10.1016/j.compositesb.2019.02.060.

[40] C. Manjunatha, A. Taylor, A. Kinloch, and S. Sprenger. "The tensile fatigue behavior of a GFRP composite with rubber particle modified epoxy matrix". *Journal of Reinforced Plastics and Composites* 29.14 (Sept. 2009), 2170–2183. ISSN: 1530-7964. DOI: 10.1177/0731684409344652.

[41] P. Radhakrishnan and K. Ramajeyathilagam. "Effect of stress ratio on tension-tension fatigue behaviour of woven angle ply GFRP laminates". *International Journal of Fatigue* 172 (July 2023), p. 107633. ISSN: 0142-1123. DOI: 10.1016/j.ijfatigue.2023.107633.

[42] M. Ly, K. A. Khan, and A. Muliana. "Modeling self-heating under cyclic loading in fiber-reinforced polymer composites". *Journal of Materials Engineering and Performance* 29.2 (Feb. 2020), 1321–1335. ISSN: 1544-1024. DOI: 10.1007/s11665-020-04663-7.

[43] R. D. B. Sevenois, P. Hao, W. Van Paepegem, and F. A. Gilabert. "Numerical study on the effect of matrix self-heating on the thermo-visco-plastic response of continuous fiber-reinforced polymers under transverse tensile loading". *Polymers* 14.10 (May 2022), p. 1941. ISSN: 2073-4360. DOI: 10.3390/polym14101941.

[44] A. de Lima, D. Rade, H. Lacerda, and C. Araújo. "An investigation of the self-heating phenomenon in viscoelastic materials subjected to cyclic loadings accounting for prestress". *Mechanical Systems and Signal Processing* 58–59 (June 2015), 115–127. ISSN: 0888-3270. DOI: 10.1016/j.ymssp.2014.12.006.

[45] S. B. Sapozhnikov, A. A. Shabley, and A. V. Ignatova. "Predicting the kinetics of hysteretic self-heating of GFRPs under high-frequency cyclic loading". *Composite Structures* 226 (Oct. 2019), p. 111214. ISSN: 0263-8223. DOI: 10.1016/j.compstruct.2019.111214.

[46] A. V. Ignatova, A. V. Bezmelnitsyn, N. A. Olivenko, O. A. Kudryavtsev, S. B. Sapozhnikov, and A. D. Shavshina. "Prediction of GFRP self-heating kinetics under cyclic bending". *Mechanics of Composite Materials* 58.6 (Jan. 2023), 787–802. ISSN: 1573-8922. DOI: 10.1007/s11029-023-10068-z.

[47] F. Lahuerta, R. Nijssen, F. van der Meer, and L. Sluys. "Experimental–computational study towards heat generation in thick laminates under fatigue loading". *International Journal of Fatigue* 80 (Nov. 2015), 121–127. ISSN: 0142-1123. DOI: 10.1016/j.ijfatigue.2015.05.014.

[48] M. P. Luong. "Fatigue limit evaluation of metals using an infrared thermographic technique". *Mechanics of Materials* 28.1–4 (July 1998), 155–163. ISSN: 0167-6636. DOI: 10.1016/s0167-6636(97)00047-1.

[49] G. La Rosa and A. Risitano. "Thermographic methodology for rapid determination of the fatigue limit of materials and mechanical components". *International Journal of Fatigue* 22.1 (Jan. 2000), 65–73. ISSN: 0142-1123. DOI: 10.1016/s0142-1123(99)00088-2.

[50] J. Huang, M.-L. Pastor, C. Garnier, and X.-J. Gong. "A new model for fatigue life prediction based on infrared thermography and degradation process for CFRP composite laminates". *International Journal of Fatigue* 120 (Mar. 2019), 87–95. ISSN: 0142-1123. DOI: 10.1016/j.ijfatigue.2018.11.002.

[51] C. Colombo, F. Libonati, F. Pezzani, A. Salerno, and L. Vergani. "Fatigue behaviour of a GFRP laminate by thermographic measurements". *Procedia Engineering* 10 (2011), 3518–3527. ISSN: 1877-7058. DOI: 10.1016/j.proeng.2011.04.579.

[52] J. Huang, M.-L. Pastor, C. Garnier, and X. Gong. "Rapid evaluation of fatigue limit on thermographic data analysis". *International Journal of Fatigue* 104 (Nov. 2017), 293–301. ISSN: 0142-1123. DOI: 10.1016/j.ijfatigue.2017.07.029.

[53] J. Huang, C. Garnier, M.-L. Pastor, and X. Gong. "Investigation of self-heating and life prediction in CFRP laminates under cyclic shear loading condition based on the infrared thermographic data". *Engineering Fracture Mechanics* 229 (Apr. 2020), p. 106971. ISSN: 0013-7944. DOI: 10.1016/j.engfracmech.2020.106971.

[54] D. Palumbo, R. De Finis, P. G. Demelio, and U. Galietti. "A new rapid thermographic method to assess the fatigue limit in GFRP composites". *Composites Part B: Engineering* 103 (Oct. 2016), 60–67. ISSN: 1359-8368. DOI: 10.1016/j.compositesb.2016.08.007.

[55] R. De Finis, D. Palumbo, and U. Galietti. "Evaluation of damage in composites by using thermoelastic stress analysis: A promising technique to assess the stiffness degradation". *Fatigue Fracture of Engineering Materials Structures* 43.9 (July 2020), 2085–2100. ISSN: 1460-2695. DOI: 10.1111/ffe.13285.

[56] P. Pathak, S. Gururaja, V. Kumar, D. Nuttall, A. Mahmoudi, M. Khonsari, and U. Vaidya. "Examining infrared thermography based approaches to rapid fatigue characterization of additively manufactured compression molded short fiber thermoplastic composites". *Composite Structures* 351 (Jan. 2025), p. 118610. ISSN: 0263-8223. DOI: 10.1016/j.compstruct.2024.118610.

[57] M. Zaeimi, R. De Finis, D. Palumbo, and U. Galietti. "Fatigue limit estimation of metals based on the thermographic methods: A comprehensive review". *Fatigue Fracture of Engineering Materials Structures* 47.3 (Jan. 2024), 611–646. ISSN: 1460-2695. DOI: 10.1111/ffe.14206.

[58] F. Maquin and F. Pierron. "Heat dissipation measurements in low stress cyclic loading of metallic materials: From internal friction to micro-plasticity". *Mechanics of Materials* 41.8 (Aug. 2009), 928–942. ISSN: 0167-6636. DOI: 10.1016/j.mechmat.2009.03.003.

[59] K. Demilly, J. Cavoit, Y. Marco, G. Moreau, G. Dolo, and N. Carrere. "Estimating fatigue life of carbon/epoxy composites: A rapid method coupling thermo-mechanical analysis and residual strength". *Fatigue Fracture of Engineering Materials Structures* 47.6 (Feb. 2024), 1856–1867. ISSN: 1460-2695. DOI: 10.1111/ffe.14254.

[60] S. Mortazavian and A. Fatemi. "Fatigue of short fiber thermoplastic composites: A review of recent experimental results and analysis". *International Journal of Fatigue* 102 (Sept. 2017), 171–183. ISSN: 0142-1123. DOI: 10.1016/j.ijfatigue.2017.01.037.

[61] E. Ghane and B. Mohammadi. "Entropy-damage mechanics for the failure investigation of plain weave fabric composites". *Composite Structures* 250 (Oct. 2020), p. 112493. ISSN: 0263-8223. DOI: 10.1016/j.compstruct.2020.112493.

[62] B. Mohammadi and A. Mahmoudi. "Developing a new model to predict the fatigue life of cross-ply laminates using coupled CDM-entropy generation approach". *Theoretical and Applied Fracture Mechanics* 95 (June 2018), 18–27. ISSN: 0167-8442. DOI: 10.1016/j.tafmec.2018.02.012.

[63] M. Mehdizadeh and M. M. Khonsari. "On the application of fracture fatigue entropy to multiaxial loading". *International Journal of Fatigue* 150 (Sept. 2021), p. 106321. ISSN: 0142-1123. DOI: 10.1016/j.ijfatigue.2021.106321.

[64] M. A. Amooie and M. Khonsari. "On the effect of environmental temperature on fracture fatigue entropy". *International Journal of Fatigue* 168 (Mar. 2023), p. 107411. ISSN: 0142-1123. DOI: 10.1016/j.ijfatigue.2022.107411.

[65] M. Mehdizadeh and M. Khonsari. "On the application of fracture fatigue entropy to variable frequency and loading amplitude". *Theoretical and Applied Fracture Mechanics* 98 (Dec. 2018), 30–37. ISSN: 0167-8442. DOI: 10.1016/j.tafmec.2018.09.005.

[66] M. A. Amooie, K. P. Lijesh, A. Mahmoudi, E. Azizian-Farsani, and M. M. Khonsari. "On the characteristics of fatigue fracture with rapid frequency change". *Entropy* 25.6 (May 2023), p. 840. ISSN: 1099-4300. DOI: 10.3390/e25060840.

[67] M. Naderi and M. Khonsari. "On the role of damage energy in the fatigue degradation characterization of a composite laminate". *Composites Part B: Engineering* 45.1 (Feb. 2013), 528–537. ISSN: 1359-8368. DOI: 10.1016/j.compositesb.2012.07.028.

[68] A. Mahmoudi and B. Mohammadi. "On the evaluation of damage-entropy model in cross-ply laminated composites". *Engineering Fracture Mechanics* 219 (Oct. 2019), p. 106626. ISSN: 0013-7944. DOI: 10.1016/j.engfracmech.2019.106626.

[69] J. Huang, H. Yang, W. Liu, K. Zhang, and A. Huang. "Confidence level and reliability analysis of the fatigue life of CFRP laminates predicted based on fracture fatigue entropy". *International Journal of Fatigue* 156 (Mar. 2022), p. 106659. ISSN: 0142-1123. DOI: 10.1016/j.ijfatigue.2021.106659.

[70] A. Premanand, M. Rienks, and F. Balle. “Accelerated estimation of the very high cycle fatigue strength and life of polymer composites under ultrasonic cyclic three-point bending”. *Materials amp; Design* 240 (Apr. 2024), p. 112872. ISSN: 0264-1275. DOI: 10.1016/j.matdes.2024.112872.

[71] M. Bartkowiak, M. Kizak, W. Liebig, and K. Weidenmann. “Fatigue behavior of hybrid continuous-discontinuous fiber-reinforced sheet molding compound composites under application-related loading conditions”. *Composites Part C: Open Access* 8 (July 2022), p. 100265. ISSN: 2666-6820. DOI: 10.1016/j.jcomc.2022.100265.

[72] J. Ding and L. Cheng. “Ultra-high three-point bending fatigue performance of nano-silica-reinforced CFRP”. *International Journal of Fatigue* 145 (Apr. 2021), p. 106085. ISSN: 0142-1123. DOI: 10.1016/j.ijfatigue.2020.106085.

[73] S. N. Leung. “Thermally conductive polymer composites and nanocomposites: Processing-structure-property relationships”. *Composites Part B: Engineering* 150 (Oct. 2018), 78–92. ISSN: 1359-8368. DOI: 10.1016/j.compositesb.2018.05.056.

[74] C. S. Lee, H. J. Kim, A. Amanov, J. H. Choo, Y. K. Kim, and I. S. Cho. “Investigation on very high cycle fatigue of PA66-GF30 GFRP based on fiber orientation”. *Composites Science and Technology* 180 (Aug. 2019), 94–100. ISSN: 0266-3538. DOI: 10.1016/j.compscitech.2019.05.021.

[75] J. M. Parente, R. Simoes, A. P. Silva, and P. N. B. Reis. “Impact of the curing temperature on the manufacturing process of multi-nanoparticle-reinforced epoxy matrix composites”. *Materials* 17.8 (Apr. 2024), p. 1930. ISSN: 1996-1944. DOI: 10.3390/ma17081930.

[76] J. E. Jam and M. G. Ahangari. “Effect of carbon nanotubes on the rheological and electrical percolation of PP/EPDM blend”. *Polymer-Plastics Technology and Engineering* 51.14 (Oct. 2012), 1474–1482. ISSN: 1525-6111. DOI: 10.1080/03602559.2012.715360.

[77] P. Zamani, L. FM da Silva, R. Masoudi Nejad, D. Ghahremani Moghaddam, and B. Soltannia. “Experimental study on mixing ratio effect of hybrid graphene nanoplatelet/nano-silica reinforcement on the static and fatigue life of aluminum-to-GFRP bonded joints under four-point bending”. *Composite Structures* 300 (Nov. 2022), p. 116108. ISSN: 0263-8223. DOI: 10.1016/j.compstruct.2022.116108.

[78] P. Santos, A. P. Silva, and P. N. B. Reis. “The effect of carbon nanofibers on the mechanical performance of epoxy-based composites: A review”. *Polymers* 16.15 (July 2024), p. 2152. ISSN: 2073-4360. DOI: 10.3390/polym16152152.

[79] P. Santos, A. P. Silva, and P. N. B. Reis. “Effect of carbon nanofibers on the strain rate and interlaminar shear strength of carbon/epoxy composites”. *Materials* 16.12 (June 2023), p. 4332. ISSN: 1996-1944. DOI: 10.3390/ma16124332.

[80] A. Jafarpour, M. Safarabadi Farahani, and M. Haghighi-Yazdi. “Numerical investigation of oriented CNFs effects on thermo-mechanical properties and curing residual stresses field of polymeric nanocomposites”. *Mechanics of Materials* 138 (Nov. 2019), p. 103176. ISSN: 0167-6636. DOI: 10.1016/j.mechmat.2019.103176.

[81] L. Böger, J. Sumfleth, H. Hedemann, and K. Schulte. “Improvement of fatigue life by incorporation of nanoparticles in glass fibre reinforced epoxy”. *Composites Part A: Applied Science and Manufacturing* 41.10 (Oct. 2010), 1419–1424. ISSN: 1359-835X. DOI: 10.1016/j.compositesa.2010.06.002.

[82] F. Li, Y. Hua, C.-B. Qu, H.-M. Xiao, and S.-Y. Fu. “Greatly enhanced cryogenic mechanical properties of short carbon fiber/polyethersulfone composites by graphene oxide coating”. *Composites Part A: Applied Science and Manufacturing* 89 (Oct. 2016), 47–55. ISSN: 1359-835X. DOI: 10.1016/j.compositesa.2016.02.016.

[83] D. G. Papageorgiou, M. Liu, Z. Li, C. Vallés, R. J. Young, and I. A. Kinloch. “Hybrid poly(ether ether ketone) composites reinforced with a combination of carbon fibres and graphene nanoplatelets”. *Composites Science and Technology* 175 (May 2019), 60–68. ISSN: 0266-3538. DOI: 10.1016/j.compscitech.2019.03.006.

[84] M. M. Shokrieh, M. Esmkhani, A. Haghighatkhah, and Z. Zhao. “Flexural fatigue behavior of synthesized graphene/carbon-nanofiber/epoxy hybrid nanocomposites”. *Materials amp; Design (1980-2015)* 62 (Oct. 2014), 401–408. ISSN: 0261-3069. DOI: 10.1016/j.matdes.2014.05.040.

[85] L. Yue, G. Pircheraghi, S. A. Monemian, and I. Manas-Zloczower. “Epoxy composites with carbon nanotubes and graphene nanoplatelets – Dispersion and synergy effects”. *Carbon* 78 (Nov. 2014), 268–278. ISSN: 0008-6223. DOI: 10.1016/j.carbon.2014.07.003.

[86] S. Chatterjee, F. Nafezarefi, N. Tai, L. Schlagenhauf, F. Nüesch, and B. Chu. “Size and synergy effects of nanofiller hybrids including graphene nanoplatelets and carbon nanotubes in mechanical properties of epoxy composites”. *Carbon* 50.15 (Dec. 2012), 5380–5386. ISSN: 0008-6223. DOI: 10.1016/j.carbon.2012.07.021.

[87] O. Ahmed, X. Wang, M.-V. Tran, and M.-Z. Ismadi. "Advancements in fiber-reinforced polymer composite materials damage detection methods: Towards achieving energy-efficient SHM systems". *Composites Part B: Engineering* 223 (Oct. 2021), p. 109136. ISSN: 1359-8368. DOI: 10.1016/j.compositesb.2021.109136.

[88] G. F. Gomes, F. A. de Almeida, A. C. Ancelotti, and S. S. da Cunha. "Inverse structural damage identification problem in CFRP laminated plates using SFO algorithm based on strain fields". *Engineering with Computers* 37.4 (May 2020), 3771–3791. ISSN: 1435-5663. DOI: 10.1007/s00366-020-01027-6.

[89] G. F. Gomes, F. A. de Almeida, S. S. da Cunha, and A. C. Ancelotti. "An estimate of the location of multiple delaminations on aeronautical CFRP plates using modal data inverse problem". *The International Journal of Advanced Manufacturing Technology* 99.5–8 (Aug. 2018), 1155–1174. ISSN: 1433-3015. DOI: 10.1007/s00170-018-2502-z.

[90] L. A. de Oliveira, G. F. Gomes, J. L. J. Pereira, M. B. Francisco, A. Demarbaix, and S. S. Cunha. "New trends of damage detection and identification based on vibrothermography in composite materials". *Journal of Nondestructive Evaluation* 42.3 (June 2023). ISSN: 1573-4862. DOI: 10.1007/s10921-023-00963-9.

[91] J. Segers, S. Hedayatrasa, E. Verboven, G. Poelman, W. Van Paepegem, and M. Kersemans. "In-plane local defect resonances for efficient vibrothermography of impacted carbon fiber-reinforced polymers (CFRP)". *NDT amp; E International* 102 (Mar. 2019), 218–225. ISSN: 0963-8695. DOI: 10.1016/j.ndteint.2018.12.005.

[92] F. Jensen, J. F. Jerg, M. Sorg, and A. Fischer. "Active thermography for the interpretation and detection of rain erosion damage evolution on GFRP airfoils". *NDT amp; E International* 135 (Apr. 2023), p. 102778. ISSN: 0963-8695. DOI: 10.1016/j.ndteint.2022.102778.

[93] Q. Wei, J. Huang, J. Zhu, L. Zhuo, and C. Li. "Experimental investigation on detection of coating debonds in thermal barrier coatings using vibrothermography with a piezoceramic actuator". *NDT amp; E International* 137 (July 2023), p. 102859. ISSN: 0963-8695. DOI: 10.1016/j.ndteint.2023.102859.

[94] K. Truyaert, V. Aleshin, and K. Van Den Abeele. "Qualitative analysis of a 3D multiphysics model for nonlinear ultrasonics and vibration induced heating at closed defects". *Research in Nondestructive Evaluation* 33.1 (Jan. 2022), 17–32. ISSN: 1432-2110. DOI: 10.1080/09349847.2022.2049408.

[95] A. Mendioroz, K. Martínez, R. Celorrio, and A. Salazar. "Characterizing the shape and heat production of open vertical cracks in burst vibrothermography experiments". *NDT amp; E International* 102 (Mar. 2019), 234–243. ISSN: 0963-8695. DOI: 10.1016/j.ndteint.2018.12.006.

[96] C. Cavallone, M. Colom, A. Mendioroz, A. Salazar, D. Palumbo, and U. Galietti. "Sizing the length of surface breaking cracks using vibrothermography". *NDT amp; E International* 112 (June 2020), p. 102250. ISSN: 0963-8695. DOI: 10.1016/j.ndteint.2020.102250.

[97] L. Dong, B. Wang, H. Wang, M. Xiang, X. Chen, G. Ma, Y. Di, W. Guo, J. Kang, and X. Zhou. "Effects of crack surface roughness on crack heat generation characteristics of ultrasonic infrared thermography". *Infrared Physics amp; Technology* 106 (May 2020), p. 103262. ISSN: 1350-4495. DOI: 10.1016/j.infrared.2020.103262.

[98] D. Di Maio, G. Voudouris, and A. Sever. "Investigation of fatigue damage growth and self-heating behaviour of cross-ply laminates using simulation-driven dynamic test". *International Journal of Fatigue* 155 (Feb. 2022), p. 106617. ISSN: 0142-1123. DOI: 10.1016/j.ijfatigue.2021.106617.

[99] Q. Wei, M. Han, J. Zhu, L. Zhuo, J. Huang, W. Li, and W. Xie. "Experimental and numerical investigation on detection fatigue crack in metallic plate by vibro-thermography". *Infrared Physics amp; Technology* 126 (Nov. 2022), p. 104347. ISSN: 1350-4495. DOI: 10.1016/j.infrared.2022.104347.

[100] J. Zhu, Z. Mao, D. Wu, J. Zhou, D. Jiao, W. Shi, W. Zhu, and Z. Liu. "Progress and trends in non-destructive testing for thermal barrier coatings based on infrared thermography: A review". *Journal of Nondestructive Evaluation* 41.3 (June 2022). ISSN: 1573-4862. DOI: 10.1007/s10921-022-00880-3.

[101] G. Zhou, Z. C. Ong, Z. Zhang, W. Yin, H. Chen, H. Ma, and Y. Fu. "Defect detection of carbon fiber deflectors based on laser infrared thermography and experimental modal analysis". *Mechanical Systems and Signal Processing* 221 (Dec. 2024), p. 111763. ISSN: 0888-3270. DOI: 10.1016/j.ymssp.2024.111763.

[102] P. Liu, C. Xu, Y. Zhang, L. Chen, Y. Han, R. Liu, and Y. Qin. "Detection and quantification of corrosion defects in CFRP-strengthened steel structures based on low-power vibrothermography". *Nondestructive Testing and Evaluation* 40.2 (Mar. 2024), 585–609. ISSN: 1477-2671. DOI: 10.1080/10589759.2024.2326603.

[103] A. Wronkowicz, A. Katunin, and D. Wachla. "Enhancement of damage identification in composite structures with self-heating based vibrothermography". *Optik* 181 (Mar. 2019), 545–554. ISSN: 0030-4026. DOI: 10.1016/j.ijleo.2018.12.132.

[104] F. Magi, D. Di Maio, and I. Sever. "Damage initiation and structural degradation through resonance vibration: Application to composite laminates in fatigue". *Composites Science and Technology* 132 (Aug. 2016), 47–56. ISSN: 0266-3538. DOI: 10.1016/j.compscitech.2016.06.013.

[105] D. Di Maio, F. Magi, and I. A. Sever. "Damage monitoring of composite components under vibration fatigue using scanning laser doppler vibrometer". *Experimental Mechanics* 58.3 (Jan. 2018), 499–514. ISSN: 1741-2765. DOI: 10.1007/s11340-017-0367-y.

[106] J. S. Vaddi, S. D. Holland, and M. R. Kessler. "Absorptive viscoelastic coatings for full field vibration coverage measurement in vibrothermography". *NDT E International* 82 (Sept. 2016), 56–61. ISSN: 0963-8695. DOI: 10.1016/j.ndteint.2016.04.004.

[107] F. Ciampa, P. Mahmoodi, F. Pinto, and M. Meo. "Recent advances in active infrared thermography for non-destructive testing of aerospace components". *Sensors* 18.2 (Feb. 2018), p. 609. ISSN: 1424-8220. DOI: 10.3390/s18020609.

[108] J. Amraei, A. Katunin, and M. Lipińska. "Numerical simulation and experimental validation of self-heating of polymer-matrix composites during low-cycle fatigue loading". *International Journal of Fatigue* 188 (Nov. 2024), p. 108510. ISSN: 0142-1123. DOI: 10.1016/j.ijfatigue.2024.108510.

[109] J. Amraei and A. Katunin. "Thermomechanical fatigue life assessment of polymer-matrix composites via entropy-based damage evolution and stiffness degradation under different frequencies". *Composites Part B: Engineering* 298 (June 2025), p. 112353. ISSN: 1359-8368. DOI: 10.1016/j.compositesb.2025.112353. URL: http://dx.doi.org/10.1016/j.compositesb.2025.112353.

[110] J. Amraei, T. Rogala, A. Katunin, I. Barszczewska-Rybarek, J. M. Parente, and P. N. Reis. "Synergistic effects of graphene nanoplatelets and carbon nanofibers on thermomechanical fatigue response of modified glass/epoxy composites". *Submitted to International Journal of Fatigue, Under Review* (Dec. 2024).

[111] J. Amraei, A. Katunin, D. Wachla, and K. Lis. "Damage assessment in composite plates using extended non-destructive self-heating based vibrothermography technique". *Measurement* 241 (Feb. 2025), p. 115670. ISSN: 0263-2241. DOI: 10.1016/j.measurement.2024.115670.

[112] B. Hajshirmohammadi and M. M. Khonsari. “An approach for fatigue life prediction based on external heating”. *International Journal of Mechanical Sciences* 204 (Aug. 2021), p. 106510. ISSN: 0020-7403. DOI: 10.1016/j.ijmecsci.2021.106510.

[113] A. Katunin. “Evaluation of criticality of self-heating of polymer composites by estimating the heat dissipation rate”. *Mechanics of Composite Materials* 54.1 (Mar. 2018), 53–60. ISSN: 1573-8922. DOI: 10.1007/s11029-018-9717-9.

[114] G. Kalogiannakis, D. Van Hemelrijck, and G. Van Assche. “Measurements of thermal properties of carbon/epoxy and glass/epoxy using modulated temperature differential scanning calorimetry”. *Journal of Composite Materials* 38.2 (Jan. 2004), 163–175. ISSN: 1530-793X. DOI: 10.1177/0021998304038647.

[115] F. Dinzart, A. Molinari, and R. Herbach. “Thermomechanical response of a viscoelastic beam under cyclic bending; self-heating and thermal failure”. *Archives of Mechanics* 60.1 (2008), 59–85. ISSN: 03732029.

[116] A. Katunin and M. Fidali. “Self-heating of polymeric laminated composite plates under the resonant vibrations: Theoretical and experimental study”. *Polymer Composites* 33.1 (Dec. 2011), 138–146. ISSN: 1548-0569. DOI: 10.1002/pc.22134.

[117] G. Meneghetti and M. Quaresimin. “Fatigue strength assessment of a short fiber composite based on the specific heat dissipation”. *Composites Part B: Engineering* 42.2 (Mar. 2011), 217–225. ISSN: 1359-8368. DOI: 10.1016/j.compositesb.2010.12.002.

[118] A. Premanand and F. Balle. “Influence of pulse–pause sequences on the self-heating behavior in continuous carbon fiber-reinforced composites under ultrasonic cyclic three-point bending loads”. *Materials* 15.10 (May 2022), p. 3527. ISSN: 1996-1944. DOI: 10.3390/ma15103527.

[119] M. A. Amooie, P. J. Wilson, A. Mahmoudi, E. Azizian-Farsani, and M. M. Khonsari. “On the measurement of total entropy generation for determining fatigue fracture”. *International Journal of Fatigue* 189 (Dec. 2024), p. 108578. ISSN: 0142-1123. DOI: 10.1016/j.ijfatigue.2024.108578.

[120] F. Cao and K. Ravi Chandran. “The role of crack origin size and early stage crack growth on high cycle fatigue of powder metallurgy Ti-6Al-4V alloy”. *International Journal of Fatigue* 102 (Sept. 2017), 48–58. ISSN: 0142-1123. DOI: 10.1016/j.ijfatigue.2017.05.004.

[121] L. Dolbachian, W. Harizi, I. Gnaba, and Z. Aboura. “Rapid fatigue limit estimation of smart polymer-matrix composite under self-heating bending tests using an innovative automatic approach: Knee method”. *International Journal of Fatigue* 192 (Mar. 2025), p. 108684. ISSN: 0142-1123. DOI: 10.1016/j.ijfatigue.2024.108684.

[122] A. Katunin. “A concept of thermographic method for non-destructive testing of polymeric composite structures using self-heating effect”. *Sensors* 18.1 (Dec. 2017), p. 74. ISSN: 1424-8220. DOI: 10.3390/s18010074.

[123] A. Katunin. “Method for non-destructive testing of polymer materials, preferably the polymer composite materials (in Polish)”. Pat. No. PL234169. Polish Patent Office. Issued 20 Sep 2019.

[124] M. Ye, K. Nagano, A. A. Serageldin, and H. Sato. “Field studies on the energy consumption and thermal comfort of a nZEB using radiant ceiling panel and open-loop groundwater heat pump system in a cold region”. *Journal of Building Engineering* 67 (May 2023), p. 105999. ISSN: 2352-7102. DOI: 10.1016/j.jobe.2023.105999.

[125] T. Yuan, J. Fu, Y. Chen, Y. Lu, Y. Hou, G. Sun, and D. Chen. “Pulse-voltage-based method of thermal parameter extraction for thermopile infrared sensors”. *IEEE Sensors Journal* 23.6 (Mar. 2023), 5593–5600. ISSN: 2379-9153. DOI: 10.1109/jsen.2023.3239643.

[126] A. Katunin, J. Amraei, K. Lis, and D. Wachla. “Improvement of damage identification in GFRP plates using self-heating based vibrothermography and image processing”. *Journal of Physics: Conference Series* 2784.1 (June 2024), p. 012030. ISSN: 1742-6596. DOI: 10.1088/1742-6596/2784/1/012030.

Abstract

This PhD dissertation investigated the challenges associated with the thermomechanical fatigue response and structural integrity of PMCs by incorporating the self-heating phenomenon into the analysis through a series of in-depth studies, resulting in five main contributions.

The first key contribution of this dissertation was the development of a physics-based framework for modeling the self-heating effects in the fatigue-loaded PMCs. This framework enabled the simulation of temperature distribution through the thickness of PMCs, which cannot be directly measured using an IR camera. The second key contribution of this research was the establishment of a novel unitless and scalable factor based on the heat dissipation rate concept. This factor served as a bridge for transferring fatigue results from UFFT (20.2 kHz) under controlled temperature using a pulse-pause loading pattern with forced air cooling to LFFT (50 Hz) under natural air cooling. Furthermore, the scope of the heat dissipation rate concept was broadened and utilized for determining the critical self-heating temperature interval within the UFFT scenario, which can serve as a failure criterion for future ultrasonic fatigue testing. The third key contribution of this research was the determination of FFE values within different fatigue regimes (LCF, ICF, and HCF) by combining IAT and CAT results. The FFE-based *S*-*N* curves were then established and validated against the standard *S*-*N* curves at the final failure of PMCs. The EDI-, and SD-based *S*-*N* curves were further established for assessing the fatigue damage evolution. These approaches allowed for monitoring the continuous fatigue-induced degradation process, from the early stage of damage initiation to the final failure, overcoming the limitations of standard *S*-*N* curve-based assessments.

The fourth key contribution of this research was the assessment of the capability of thermally conductive nanocarbon-based allotropes in mitigating the thermal responses induced by the self-heating phenomenon. This allowed for controlling the self-heating temperature effectively, thereby prolonging the life of modified PMCs within different fatigue regimes.

The final key contribution was extending the use of SHVT for non-destructive evaluation of 2D PMCs and developing a two-step algorithm based on the concepts of the boundary of effective thermograms, and the maximal temperature ratio. This algorithm allowed for methodically selecting the optimal raw thermogram from a large set for each damage scenario.

Streszczenie

Niniejsza rozprawa doktorska podejmuje problematykę odpowiedzi zmęczeniowej termomechanicznej oraz integralności strukturalnej kompozytów z osnową polimerową (PMCs), uwzględniając w analizie zjawisko samorozgrzania. W wyniku przeprowadzonych badań sformułowano pięć kluczowych osiągnięć naukowych.

Pierwszym istotnym osiągnięciem tej pracy było opracowanie fizykalnego modelu uwzględniającego wpływ samorozgrzania na kompozyty PMCs poddane obciążeniom zmęczeniowym. Model ten umożliwia symulację rozkładu temperatury na całej grubości materiału, co nie jest możliwe przy bezpośrednim pomiarze za pomocą kamery termowizyjnej. Drugim kluczowym wkładem było wprowadzenie nowego, bezwymiarowego i skalowalnego współczynnika opartego na koncepcji szybkości rozpraszania ciepła. Współczynnik ten pozwala na przenoszenie wyników testów zmęczeniowych z UFFT (20,2 kHz), przeprowadzanych w kontrolowanej temperaturze przy wykorzystaniu impulsowego schematu obciążenia z wymuszonym chłodzeniem powietrznym, do warunków LFFT (50 Hz) z naturalnym chłodzeniem powietrzem. Ponadto rozszerzono zakres zastosowania koncepcji szybkości rozpraszania ciepła do określania krytycznych przedziałów temperatury samorozgrzania w warunkach UFFT, co może stanowić kryterium uszkodzenia w przyszłych badaniach zmęczeniowych metodą ultradźwiękową.

Trzecim kluczowym osiągnięciem było wyznaczenie wartości FFE w różnych warunkach zmęczeniowych (LCF, ICF i HCF) poprzez połączenie wyników testów IAT i CAT. Na tej podstawie opracowano i zweryfikowano krzywe *S-N* oparte na FFE w odniesieniu do standardowych krzywych S-N odpowiadających finalnemu zniszczeniu PMCs. Dodatkowo skonstruowano krzywe *S-N* bazujące na wskaźnikach EDI i SD, co umożliwiło ocenę procesu degradacji zmęczeniowej. Takie podejście pozwoliło na ciągłe monitorowanie procesu degradacji zmęczeniowej – od początkowej inicjacji uszkodzeń aż do całkowitego zniszczenia – przezwyciężając ograniczenia klasycznych ocen bazujących na krzywych *S-N*.

Czwartym kluczowym wkładem było określenie zdolności nanostruktur węglowych o wysokiej przewodności cieplnej do redukcji efektów cieplnych wywołanych samorozgrzaniem. Pozwoliło to na skuteczną kontrolę temperatury samorozgrzania, a tym samym na wydłużenie

trwałości zmodyfikowanych PMCs w różnych reżimach zmęczeniowych.

Ostatnim istotnym osiągnięciem było rozszerzenie zastosowania SHVT do nieniszczącej oceny 2D PMCs oraz opracowanie dwuetapowego algorytmu bazującego na koncepcjach granicy efektywnego termogramu i maksymalnego stosunku temperatur. Algorytm ten umożliwia systematyczny dobór optymalnego termogramu spośród dużego zbioru dla każdego scenariusza uszkodzenia.

Appendices

Paper I

Recent advances in limiting fatigue damage accumulation induced by self-heating in polymer–matrix composites

polymers

MDPI

Review

Recent Advances in Limiting Fatigue Damage Accumulation Induced by Self-Heating in Polymer–Matrix Composites

Jafar Amraei and Andrzej Katunin *

Department of Fundamentals of Machinery Design, Faculty of Mechanical Engineering, Silesian University of Technology, Konarskiego 18A, 44-100 Gliwice, Poland
* Correspondence: andrzej.katunin@polsl.pl; Tel.: +48-32-237-10-69

Abstract: The self-heating effect can be considered as a catastrophic phenomenon that occurs in polymers and polymer–matrix composites (PMCs) subjected to fatigue loading or vibrations. This phenomenon appears in the form of temperature growth in such structures due to their relatively low thermal conductivities. The appearance of thermal stress resulting from temperature growth and the coefficient of thermal expansion (CTE) mismatch between fibers and neighboring polymer matrix initiates and/or accelerates structural degradation and consequently provokes sudden fatigue failure in the structures. Therefore, it is of primary significance for a number of practical applications to first characterize the degradation mechanism at the nano-, micro- and macroscales caused by the self-heating phenomenon and then minimize it through the implementation of numerous approaches. One viable solution is to cool the surfaces of considered structures using various cooling scenarios, such as environmental and operational factors, linked with convection, contributing to enhancing heat removal through convection. Furthermore, if materials are appropriately selected regarding their thermomechanical properties involving thermal conductivity, structural degradation may be prevented or at least minimized. This article presents a benchmarking survey of the conducted research studies associated with the fatigue performance of cyclically loaded PMC structures and an analysis of possible solutions to avoid structural degradation caused by the self-heating effect.

Keywords: self-heating effect; polymer–matrix composites (PMCs); viscoelasticity; structural degradation of PMCs; scale-based fatigue damage mechanism; cooling techniques; materials design; thermal conductivity

Citation: Amraei, J.; Katunin, A. Recent Advances in Limiting Fatigue Damage Accumulation Induced by Self-Heating in Polymer–Matrix Composites. *Polymers* **2022**, *14*, 5384. https://doi.org/10.3390/polym14245384

Academic Editor: Maria Bercea

Received: 19 October 2022
Accepted: 25 November 2022
Published: 9 December 2022

1. Introduction

The self-heating phenomenon appears in engineering structures made of polymers and polymer–matrix composites (PMCs) and usually has a negative influence on structural performance and residual life, especially when it dominates a fatigue process. To prevent the intensive degradation of such structures, it is essential to investigate the degradation mechanisms introduced by self-heating and its influence on the thermomechanical response of a structure. Based on this knowledge, it is possible to define preventing approaches for minimizing this degradation, which is of key importance in numerous applications, especially during intensive cyclic loading, e.g., nominal loading or fatigue testing of PMCs. In this section, the consideration of the self-heating effect as a catastrophic phenomenon in civil, mechanical and aerospace engineering applications is rationally justified. Furthermore, the primary motivations for conducting the current research are discussed. Many researchers have investigated this catastrophic phenomenon, which has been reviewed, e.g., in [1].

1.1. The Self-Heating Effect

The self-heating effect is an unfavorable phenomenon that occurs in both polymers and PMC structures subjected to vibrations or fatigue loading. The intensity of the self-heating

phenomenon in such structures can be a function of material properties, geometry and loading conditions [2,3]. When a PMC specimen is subjected to a cyclic mechanical loading, such a composite due to its viscoelastic nature tends to dissipate a portion of mechanical energy in the form of thermal energy. The rest of the energy is dissipated due to elastoplastic behavior and fracture mechanisms, which occur from the very beginning of the operation. Due to the generally low thermal conductivity (*K*) of polymers, this thermal energy is stored in a structure. Since the stored thermal energy is accumulated, it provokes the heating of a structure and consequently the decrease in its mechanical performance causing irreversible changes in a material at the final stages of degradation [4]. The structural changes in a material influenced by the self-heating are caused by the increase in the activity of polymer chains with the increase in temperature, which, in consequence, results in material softening and, in ultimate cases, in the breaking of polymer chains. This can be considered a source of irreversible structural changes at the macroscopic level. This phenomenon is manifested by mechanical hysteresis when a structure is under cyclic loading. Figure 1 schematically illustrates how hysteresis loops or self-heating intensity of a cyclically loaded PMC can be influenced by changing the number of applied cycles [5]. As can be concluded, if we assume that the temperature of such a structure remains constant at the ambient temperature during its entire life, the total area of a loop, which represents dissipated energy, experiences a significant reduction as the number of applied cycles increases. In other words, it may be rational to expect that the area of a loop represents the dissipated mechanical energy in such a material for relatively low frequency and amplitude of loading to remain unchangeable as the number of cycles increases [6]. The primary reason behind this expectation may be explained by how the damage mechanisms in cyclically loaded PMC structures after some initial fatigue cycles depend on the material properties, load conditions and component geometry [5]. On the other hand, when the amplitude of cyclic loading or frequency is high, the area of dissipated energy will tremendously increase (see Figure 2) [7], as a direct consequence of which the magnitude of temperature will increase. This suggests the higher temperature that such a PMC experiences, the amount of thermal energy dissipated increases. Figure 3 depicts how the area of hysteresis loops for DuPont™ Delrin® (Wilmington, DE, USA) acetal homopolymer resin, as an example, increases as the temperature increases [8].

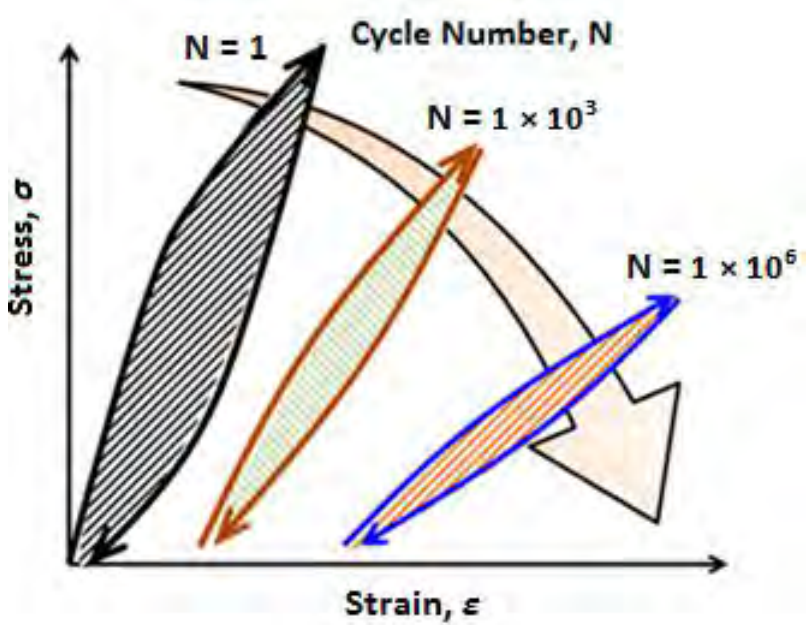

Figure 1. A schematic illustration of dissipated hysteresis thermal energy variations of a cyclically loaded PMC structure, adapted with permission from Ref. [5]. Copyright © 2017 Elsevier Ltd.

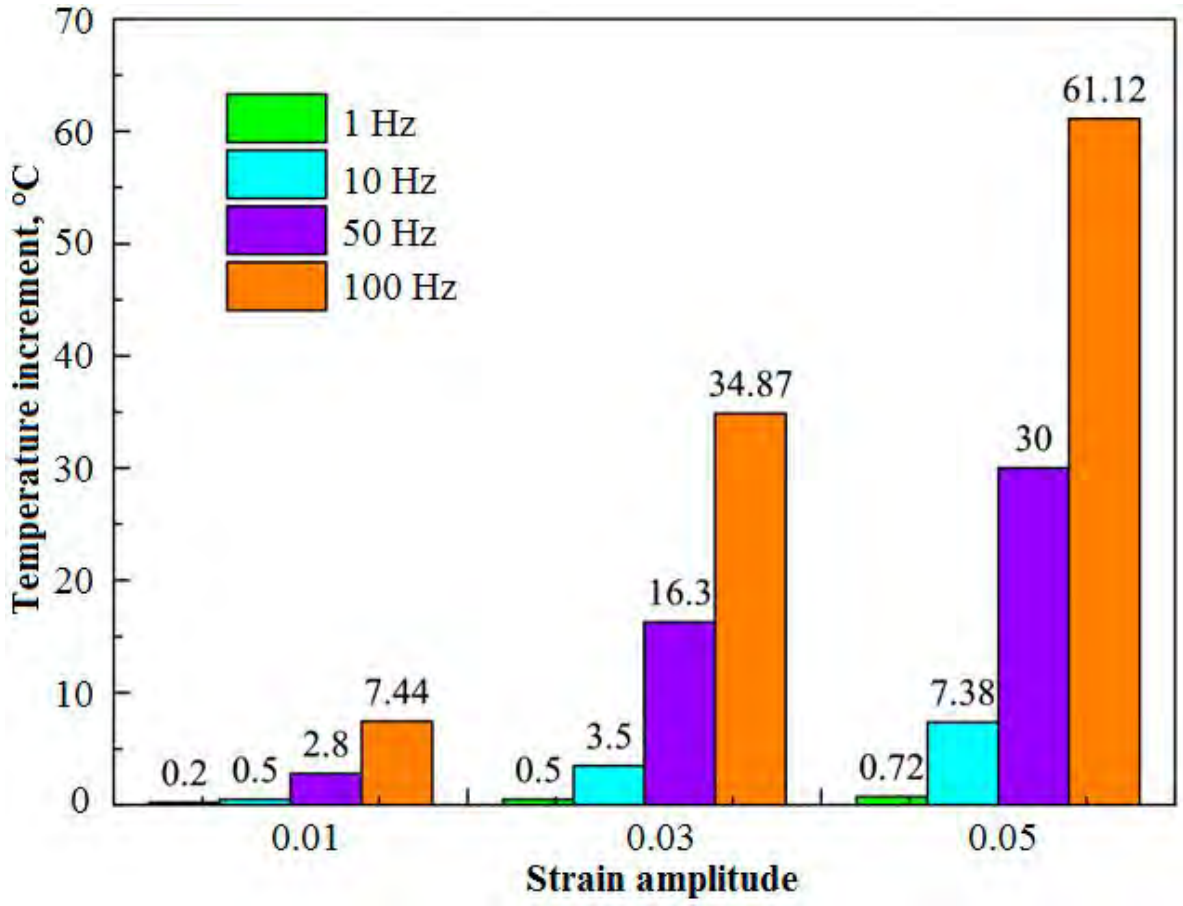

Figure 2. The influence of frequency and strain amplitude on the temperature of hydroxyl-terminated polybutadiene (HTPB) propellant under cyclic fatigue test, adapted with permission from Ref. [7]. Copyright © 2020 Elsevier Ltd.

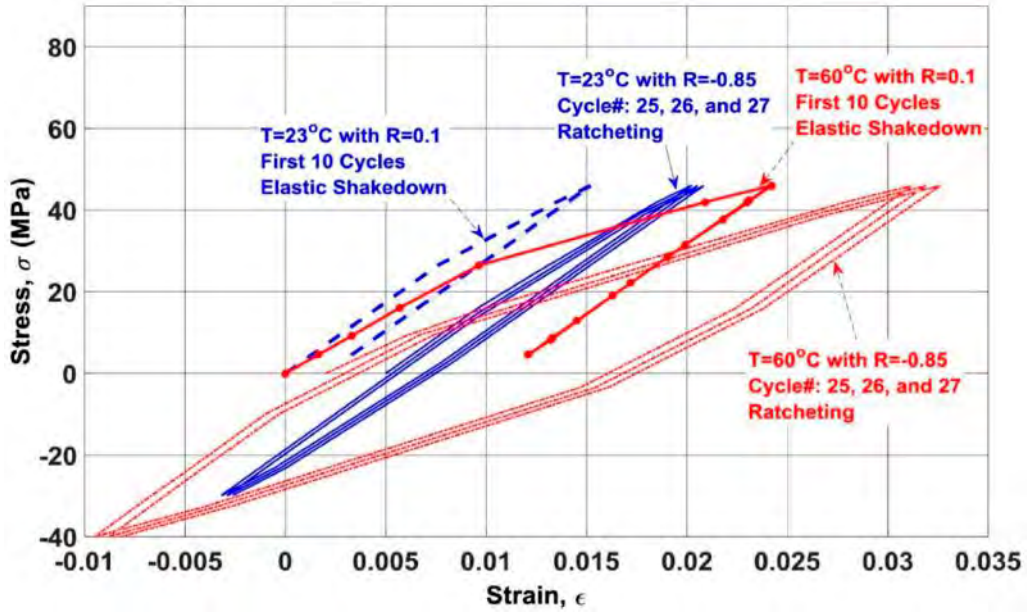

Figure 3. Hysteresis thermal energy loops for highly crystalline thermoplastic DuPont™ Delrin® 100 polymer under fatigue loading at two different temperatures, 23 °C and 60 °C, adapted with permission from Ref. [8]. Copyright © 2017 Elsevier Ltd.

The loading conditions have a significant influence on the development of the self-heating effect and the structural degradation as a consequence. In this case, one can observe the following relation: with the increase in the amplitude and/or frequency loading a structure is subjected to, the level of degradation caused by the self-heating effect occurring in a PMC structure will increase. It should be mentioned that the extracted thermal energy is irreversible according to the second law of thermodynamics (Clausius–Duhem inequality) [9], which justifies the danger behind the development of the self-heating phenomenon. From the microstructural point of view, the prime roots of the self-heating phenomenon in the polymer-based structures under high fatigue loading can be explained by the high amplitude and/or frequency of fatigue loading, which accelerates mechanical energy dissipation owing to the viscoelastic nature of polymers. This may consequently act as a catalyst in intensifying the structural degradation, provoking the premature destruction of such a structure [3,10].

1.2. Self-Heating Phenomenon as a Problem in Industrial Applications

In order to characterize the fatigue behavior of polymer-based structures dominated by the self-heating effect, a variety of stress amplitudes with constant frequency (see Figure 4a) or manifold frequencies with unchangeable stress during the fatigue test can be applied to such a structure, regardless of whether the test is carried out in low- or high-cycle fatigue regimes (see Figure 4b) [11]. An example of a thermal response of a structure under elevated stress levels is presented in Figure 5. Such a response is used in the determination of a fatigue limit in polymers and composites, which is broadly discussed further in Section 2.3.

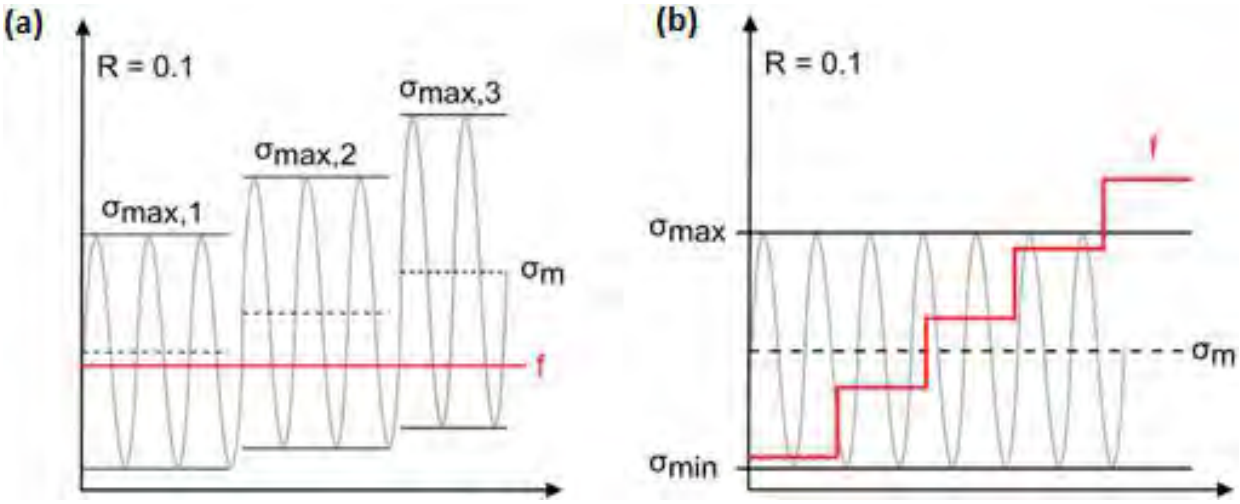

Figure 4. The schematic demonstration of (**a**) applying multiple-amplitude cyclic loads and (**b**) multiple-amplitude frequencies, adapted with permission from Ref. [11]. Copyright © 2020 Elsevier Ltd.

According to [12], fatigue regimes can be generally classified as follows: very-low-cycle fatigue ($1 \leq N_{VLCF} \leq 20$), low-cycle fatigue ($10^2 \leq N_{VLCF} \leq 10^5$), high-cycle fatigue ($10^6 \leq N_{HCF} \leq 10^7$) and very-high-cycle or gigacycle fatigue ($10^8 \leq N_{VHCF} \leq 10^{11}$). Numerous differences occur for various fatigue regimes, both in loading type and mechanical response, which affect the development of the self-heating effect and subsequently the development of fracture mechanisms, which are analyzed below.

Generally, low-cycle fatigue (LCF) failure is described as a condition wherein a PMC specimen can tolerate a relatively low number of cycles until irrecoverable mechanical/thermal failure. The LCF regime is associated with the loading conditions where the applied stress in a PMC structure may be sufficient to provoke irrecoverable thermal or/and mechanical fatigue failure. To be more precise, LCF loads vary typically between 50% and 95% of the ultimate strength of such a composite, leading to high mechanical strains or thermal failure due to the occurrence of the self-heating effect, which may induce

macrocracking and premature failure. In addition, LCF tests are typically conducted at a sufficiently low frequency (i.e., 10 Hz or below [13–19]); otherwise, premature thermal failure will occur before mechanical fatigue failure. From the other perspective, if such a PMC specimen is subjected to a relatively lower level of stress or strain loading, it may experience a higher number of fatigue cycles before its failure, as opposed to low-cycle fatigue failure wherein the specimen's lifetime may be relatively short. The LCF failures in the presence of the self-heating effect have been reported in many engineering and military applications [20] involving turbojet engine elements subjected to short-time overloads [21] and solid rocket propulsion elements [22].

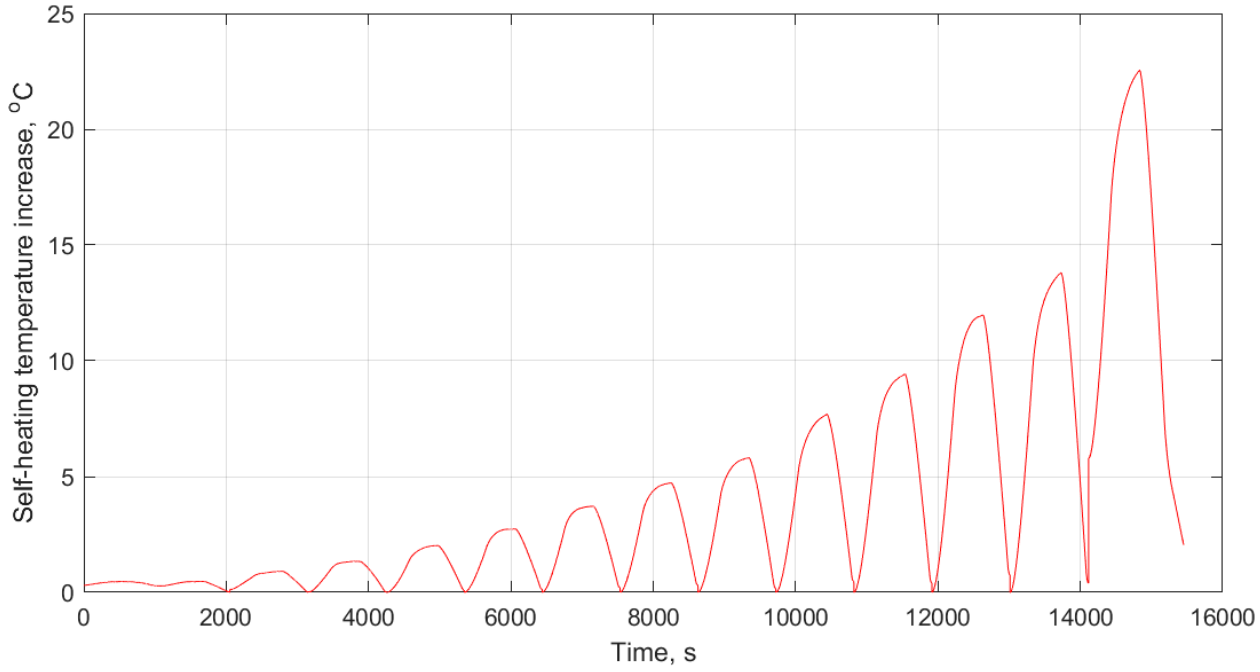

Figure 5. An exemplary illustration of self-generated heating temperature response for elevated loading.

In advanced applications, such as cyclically loaded wind turbine blades (WTBs), carbon fiber-reinforced polymer (CFRP) and glass fiber-reinforced polymer (GFRP) composite sections are primarily designed and manufactured to experience high-cycle fatigue (HCF) and very-high-cycle fatigue (VHCF) regimes during their lifetime [23,24]. The primary causative factor contributing to this preference may be explained by how different the damage mechanisms in VHCF and LCF can be. The HCF regime is connected with the loading conditions where the subjected stress is below 30% of the ultimate strength of a composite material [25]; as a result of these conditions, the material remains within its elastic limit [26]. As opposed to LCF tests, wherein the loading frequency is typically lower than 10 Hz, HCF and VHCF tests are mainly conducted using accelerated fatigue testing techniques using comparatively high loading frequencies (i.e., ranging from approximately 10 Hz to 20.5 kHz [10,27–31]). Such testing modes are gaining a high level of interest, as they allow fatigue tests to be relatively affordable, and testing speed will be accelerated due to high loading frequency, which will result in a tremendous shortening of testing time. Implementing VHCF for up to 10^9 cycles offers the opportunity to effectively characterize the fatigue damage mechanisms during the real lifetime, which may be unable to be determined by LCF testing. Nonetheless, fatigue testing of FRP composites under 10^9 cycles with a conventional system at a frequency of 5 Hz will take just above 6 years [31]. In other words, it seems impractical, meaning that testing in the VHCF regime is extensively time-consuming and costly [32] unless the experiments are carried out at a higher level of frequencies so as to rationally reduce the time of fatigue experiments of PMCs [31]. From the other perspective, cyclic testing at high frequency (e.g., frequency in the ultrasonic

range) will lead to a comparatively higher amount of dissipated energy, as a consequence of which a higher temperature is observed in a structure during testing, which is undesirable. This is especially important to be taken into consideration for many situations where the self-heating effect significantly influences the operation lifetime of a structure or element. The self-heating phenomenon has been reported in a variety of engineering applications including viscoelastic dampers [33,34], drive shafts [35–37], helicopter elements (e.g., helicopter tail rotor drivelines) [38–41], composite reservoirs for storing liquid fuels and methanol for the purpose of preventing self-ignition and explosion [42,43], composite sandwich panel structures in aviation industry [44], thick laminate sections (e.g., roots) of WTBs [45,46], and teeth of CFRP composite gears exposed to fatigue loading and rolling friction [47].

Sandwich structures (e.g., CFRP-aramid honeycomb), which are often used in the aviation industry due to their superior flexural resistance to HCF and VHCF, may also experience accelerated degradation due to self-heating, e.g., when subjected to ultrasonic frequency loading; see, for instance, Figure 6 [44].

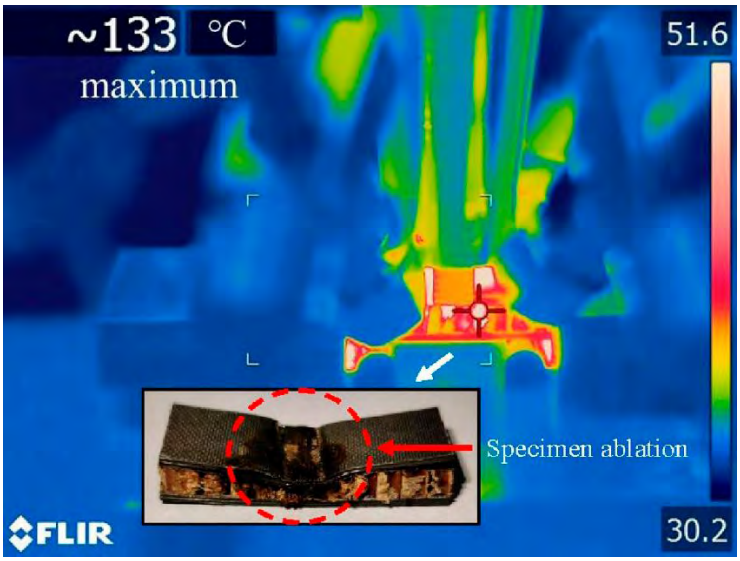

Figure 6. An exemplary thermal fatigue failure induced by self-heating effect in CFRP-aramid honeycomb sandwich structure under three-point cyclic bending in ultrasonic HCF regime, adapted with permission from Ref. [44]. Copyright © 2022 Elsevier Ltd.

CFRP composite driveshafts are primarily implemented due to their outstanding specific stiffness and strength against torsion/bending loading. Nonetheless, the overall mechanical performance of such load-bearing driveshafts is highly temperature-dependent. This means that as the amount of heat generated on the surface of CFRP driveshafts increases, the level of strength degradation reached increases [47]. A thermogram that illustrates the occurrence of the self-heating effect in a CFRP-epoxy gear with a carbon volume fraction of 48% is presented in Figure 7.

Another example presented in Figure 8 reveals the top surface of a composite blade under fatigue loading, wherein the thermal failure occurred because of the self-heating effect (e.g., the friction between delaminated plies) [28].

In conclusion, the self-heating effect can appear in all the above-mentioned fatigue regimes. However, depending on specific loading parameters, the evolution of the self-heating effect may significantly vary and accelerate the structural degradation and, in consequence, may lead to a sudden failure. Therefore, the characterization of the self-heating phenomenon in PMCs induced by cyclic fatigue (both stress- and strain-driven) loading is of utmost importance. In the following parts of this paper, the possibilities of limiting or preventing the self-heating effect during fatigue loading are discussed.

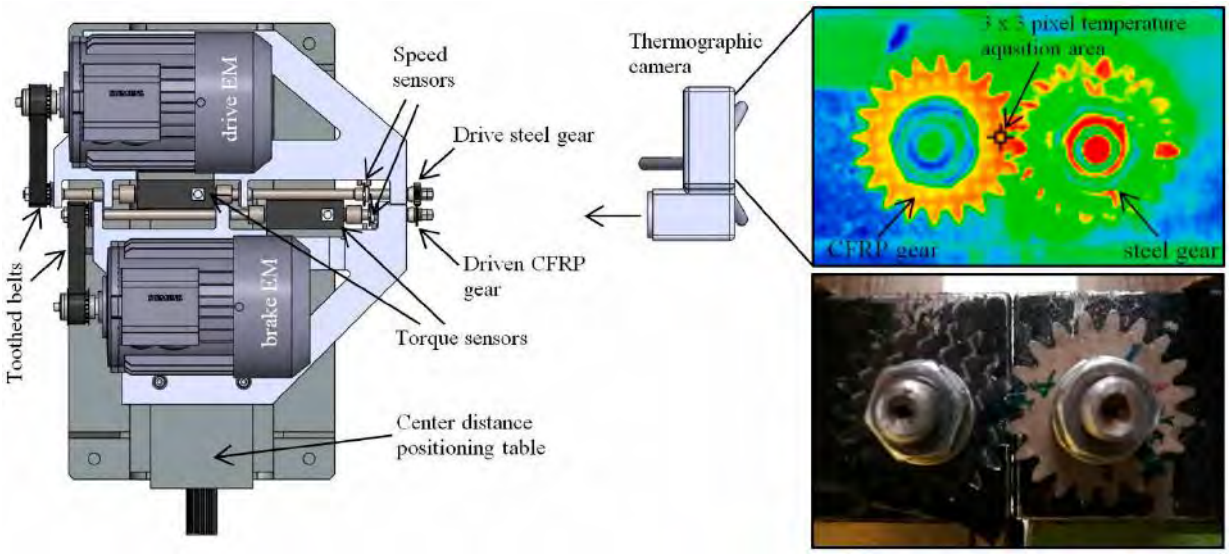

Figure 7. Model, illustration and thermogram illustrating the occurrence of the self-heating effect during the operation of a CFRP composite gear [47].

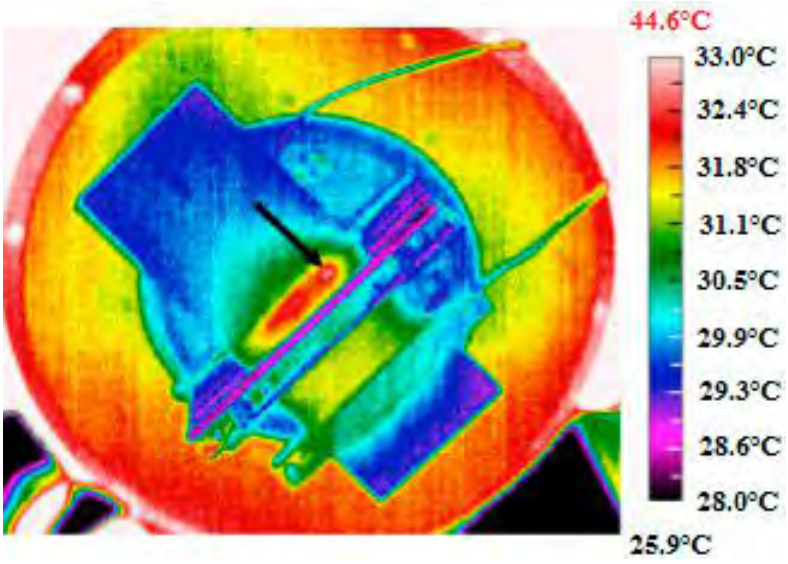

Figure 8. Thermal failure in a composite blade due to the self-heating effect shown by the arrow, adapted with permission from Ref. [28]. Copyright © 2016 Elsevier Ltd.

1.3. Motivation

The performed survey demonstrates that polymer and PMC structures subjected to fatigue loading may reach a critical condition in which the self-heating effect will dominate the fatigue process and significantly accelerate it and consequently lead to structural failure. In such a case, the main factor influencing fatigue acceleration is the self-heating temperature growth, which induces mechanical degradation, resulting in a special type of failure known as thermal failure [1]. This is especially important in the case of previously mentioned accelerated fatigue tests [29,31,48] when temperature growth has a rapid character due to generally high loading frequency. The occurrence of such problematic issues in the above-described engineering applications of PMC structures and, on the other hand, testing such structures under extreme loading conditions motivated the authors to carry out the current overview of the viable solutions for tackling the self-heating phenomenon with accompanying fracture mechanisms as well as analyzing reliable possibilities for reducing its influence on structures under fatigue loading. For this objective,

the fatigue damage mechanisms with the presence of the self-heating effect at different scales are analyzed. The solutions are then introduced and categorized into two different aspects. Firstly, implementing different cooling scenarios may be the prime direction of studies for the purpose of effectively addressing the self-heating effect. Having provided an effective coolant system, such structures can even operate in extreme loading conditions; in particular, they were tested in a VHCF regime and resulted in a significant reduction in the time required for testing as well as expenditure. Secondly, optimal materials design and selection can be favorably considered as the viable solution to effectively avoid micro- and macroscopic structural degradation. This can be explained and achieved by the implementation of high thermally conductive and stable materials. The primary cores of the current study are focused on the comprehensive understanding of the scale-based fatigue damage mechanism and the possible viable solutions through cooling scenarios and optimal materials selection and design proposed by the authors to prevent or at least minimize the self-heating effect in such structures.

2. State-of-the-Art Review on the Self-Heating Effect

2.1. Phenomenological Analysis of the Self-Heating Effect

The generated thermal energy in polymeric and/or PMC structures due to their viscoelastic behavior caused by the self-heating phenomenon can be mathematically formulated regardless of whether the polymer matrix is thermoset or thermoplastic. For example, when a cyclic strain-driven loading is applied to a PMC specimen, the resultant stress would be similar, but with a phase lag (δ) (see Equation (1) and Figure 9) [49]. By δ, materials can be generally categorized into purely elastic ($\delta = 0$), purely viscous $\left(\delta = \frac{\pi}{2}\right)$ and viscoelastic $\left(0 < \delta < \frac{\pi}{2}\right)$ (see Figure 9). The stress–strain relation for these classes of materials is as follows:

$$\varepsilon = \varepsilon_0 \sin(\omega t) \rightarrow \sigma = \sigma_0 \sin(\omega t + \delta), \tag{1}$$

where ε and ε_0 denote the instantaneous strain and the amplitude of applied strain, respectively; σ and σ_0 indicate the instantaneous stress and stress amplitude of the loaded material, respectively; ω and t denote frequency and time, respectively. By implementation of the angle addition and subtraction theorem, the relation of stress can be expanded and then rewritten as follows:

$$\begin{gathered} \sigma = E^* \varepsilon_0 = \sigma_0 \sin(\omega t + \delta) \sin(\omega t) \rightarrow \\ \underbrace{\sigma_0 \cos\delta}_{Elastic\ \ Responce} \sin(\omega t) + \underbrace{\sigma_0 \sin\delta}_{Viscous\ \ Responce} \sin\left(\omega t + \tfrac{\pi}{2}\right), \end{gathered} \tag{2}$$

The mechanical response of viscoelastic materials can be alternatively represented by a complex modulus as follows:

$$E^* = E' + iE'', \tag{3}$$

where E^* is the complex modulus; E' is the storage modulus and E'' is the loss modulus which are proportional to elastic response and viscous response, respectively. From (2) and (3), the following relation is extracted for such a PMC material:

$$\sigma_0 \cos\delta = E'\varepsilon_0; \quad \sigma_0 \sin\delta = E''\varepsilon_0 \rightarrow \delta = \tan^{-1}\frac{E''}{E'}, \tag{4}$$

It should be mentioned that the storage and loss moduli, which are the real and imaginary parts of the complex modulus, respectively, are dependent on numerous factors, particularly temperature, frequency and strain intensity [50–54].

Over the entire applied cyclic strain loading, the elastic and inelastic energy of polymeric materials can be extracted after integration and implementation (4) as follows:

$$\int_0^{\varepsilon_0}\sigma d\varepsilon = \int_0^{\pi/2\omega}\sigma\frac{d\varepsilon}{dt} = \omega\varepsilon_0\sigma_0\int_0^{\pi/2\omega}\left(\cos\omega t\sin\omega t\cos\delta + \sin^2\omega t\sin\delta\right)dt$$
$$= \underbrace{\varepsilon_0\sigma_0\frac{\cos\delta}{2}}_{\text{Elastic Dissipated Energy}} + \underbrace{\varepsilon_0\sigma_0\frac{\pi\sin\delta}{4}}_{\text{Inelastic Dissipated Thermal Energy}} \quad ; \quad 0 < \delta < \tfrac{\pi}{2}, \tag{5}$$

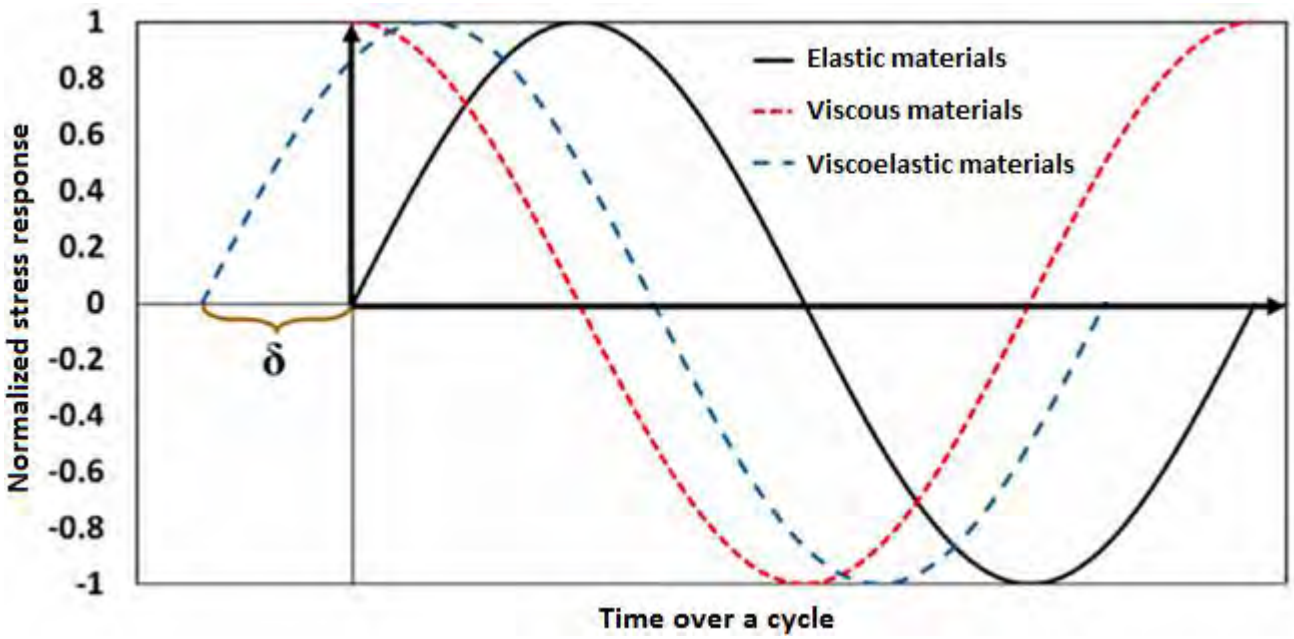

Figure 9. Schematic diagram of resulting stress under applied cyclic strain-driven loading for elastic, viscous and viscoelastic materials, adapted with permission from Ref. [49]. Copyright © 2021 Elsevier Ltd.

The dynamic mechanical analysis (DMA) test is primarily used in order to determine the value of phase lag, δ. As the temperature increases, δ of a polymeric material exponentially increases to reach its glass transition (Tg) or melting (Tm) temperature, and then it exhibits a rubbery or glassy condition depending on the polymer behavior (i.e., storage and loss moduli) (see Figure 10 for example).

From the microstructural point of view, polymers may reveal amorphous, crystalline or semi-crystalline behavior. The glass transition region mainly appears in an amorphous polymer exposed to heat wherein a viscous, liquid or rubbery state may occur (see Figure 11). This can be explained by how such polymers possess random molecular structures. As a result of an increase in temperature, such amorphous polymers soften gently (e.g., polymethyl methacrylate (PMMM)). Crystalline polymers have a highly ordered molecular morphology, as a result of which the softening may not occur as the temperature increases. The melting point (T_m) is mainly defined for crystalline polymers, which may be significantly higher than the glass transition temperature, i.e., $T_m > T_g$. Furthermore, for semi-crystalline polymers, both T_m and T_g are defined since they also have amorphous chains in their structures (e.g., polyetheretherketone (PEEK) and polyphenylene sulfide (PPS)). It is worth mentioning that the ratio of T_g/T_m for semi-crystalline polymers varies from 0.5 up to 0.75 depending on the degree of crystallinity, so a polymer with a higher level of crystallinity reveals a lower value [55].

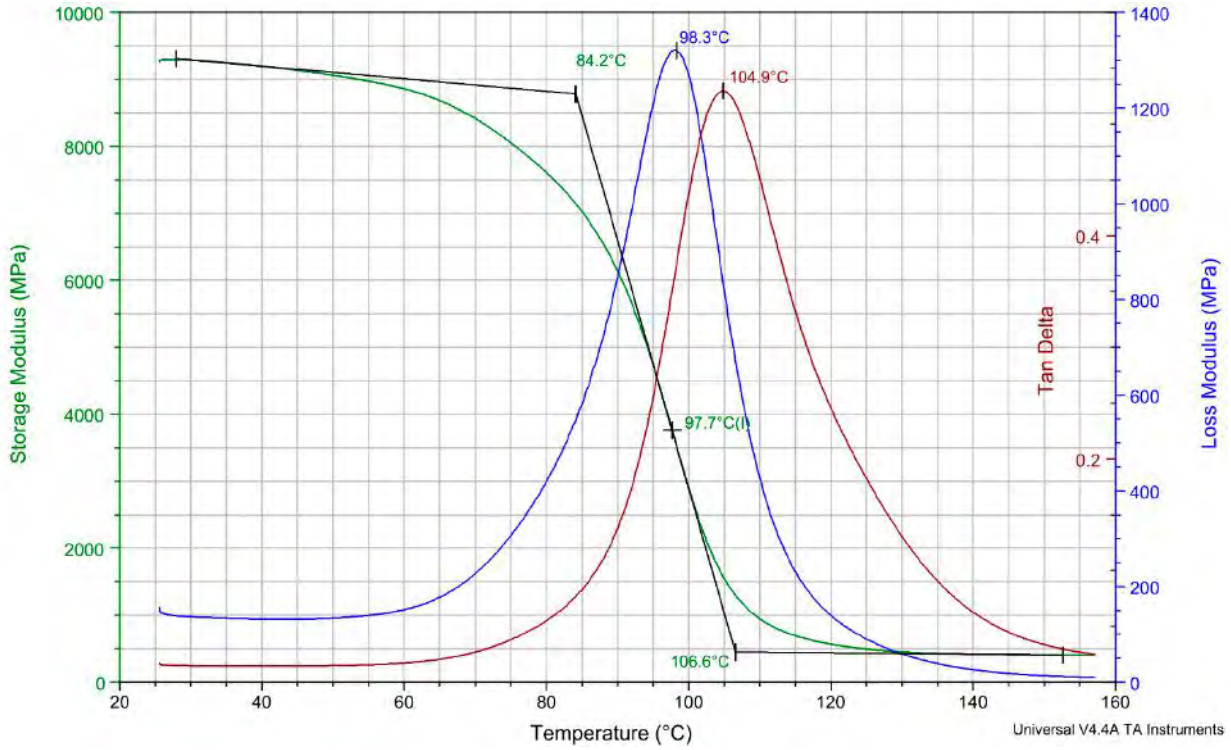

Figure 10. The exemplary DMA test results for the GFRP specimen.

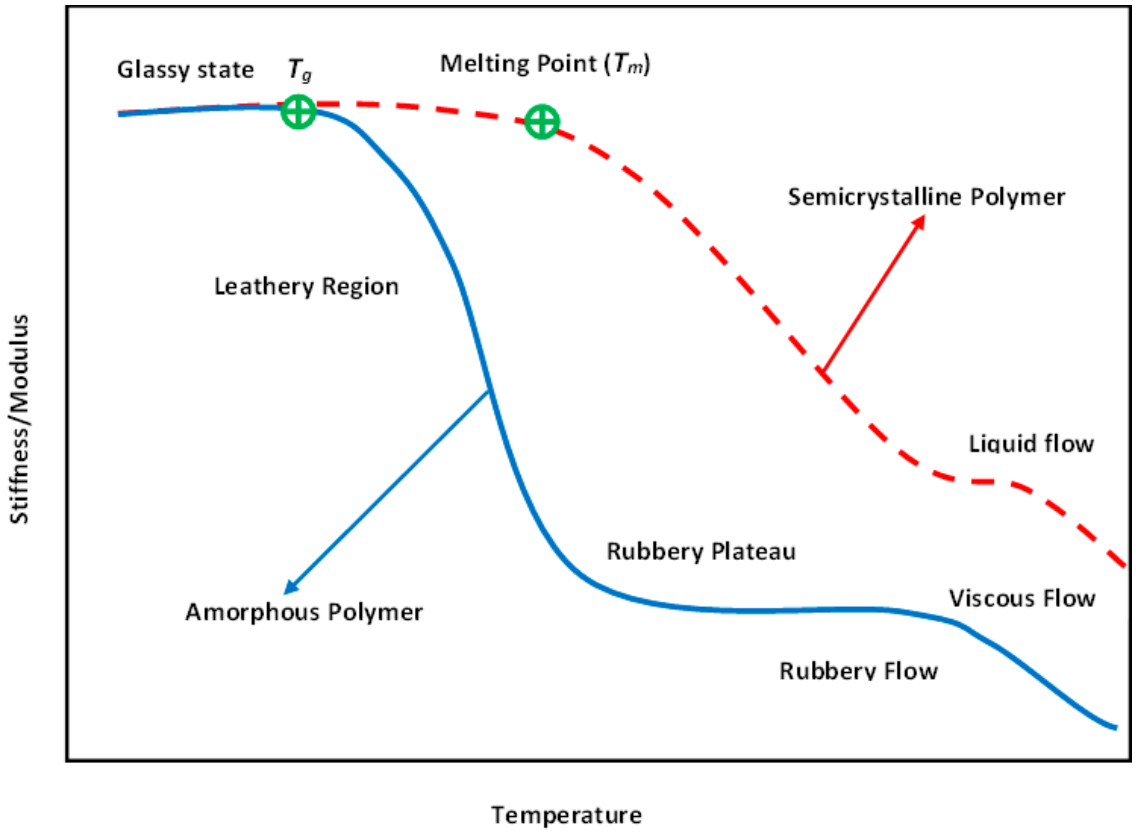

Figure 11. Melting and softening behavior of semi-crystalline and amorphous polymers.

Figure 12 schematically depicts the level of energy generation versus time for a polymer-based structure due to phase lag between stress and strain over an entire cy-

cle [49]. This corresponds to a hysteresis resulting from the viscoelastic response of a structure, which is schematically presented in Figure 13 with an indication of energy-based parameters [11]. As can be vividly extracted from the diagram, the energy-based parameters can be categorized into storage and loss properties. The storage energy, which is proportional to storage modulus, can be explained when the cyclically loaded polymeric material is indeed unloaded, illustrated as the hatched area in Figure 13. From the other perspective, the elliptical area in Figure 13 (which has been obtained as the result of both loading and unloading over a cycle) is known as the loss energy, represented by a hysteresis loop, which is proportional to the loss modulus. To put it differently, if we connect the two vertices of the ellipse which form the major axis, the dynamic/complex modulus (overall viscoelastic performance) can be then defined and computed as the differences between the maximum and minimum response stresses divided by the differences between the maximum and minimum applied strains over a cycle. This parameter consists of both storage and loss moduli. Thus, the lower boundary of the hysteresis loop can locally illustrate the storage modulus during the relaxation time over an entire cycle, while the upper boundary of the hysteresis loop can locally demonstrate the level of loss modulus. It should be mentioned that since a PMC may experience more than 1 million cycles during its life, the estimation of the dissipated thermal energy over the entire life is of key importance.

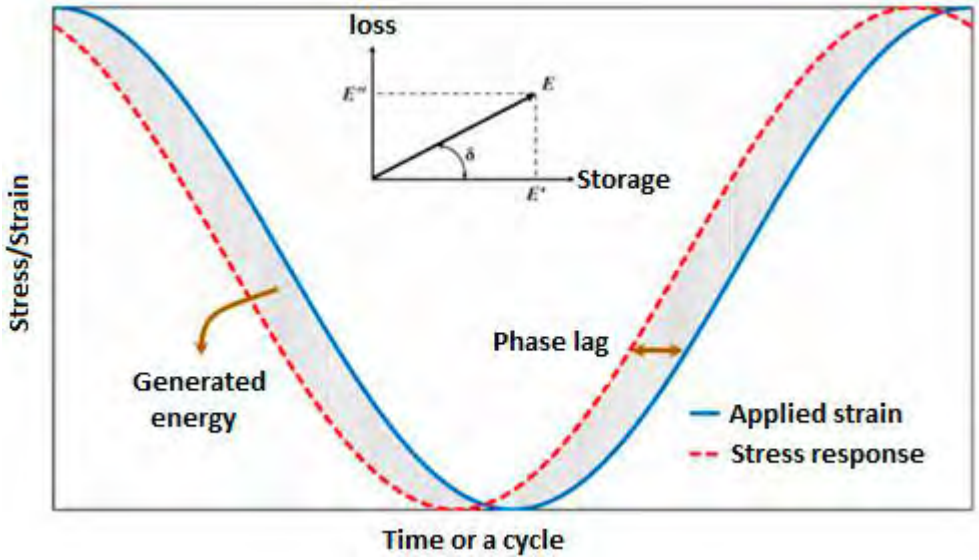

Figure 12. Schematic demonstration of the generated thermal energy for a polymer-based structure due to phase lag between stress and strain over an entire cycle, adapted with permission from Ref. [49]. Copyright © 2021 Elsevier Ltd.

From the thermodynamics point of view, by taking into account the self-heating effect in PMC structures, the generated energy (q_{gen}) over a fatigue cycle can be calculated by the summation of mechanical energy dissipation (q_{dissip}) and the rate of internal energy change per unit volume ($\Delta\dot{u}$) at loading frequency f as follows [56]:

$$q_{gen} = q_{dissip} + \Delta\dot{u}, \tag{6}$$

The amount of heat generation (q_{gen}) over a fatigue cycle per unit volume can be computed by multiplying the loading frequency by the total area of the hysteresis loop corresponding to such a frequency, as follows [56,57]:

$$q_{gen} = f\left(\int_0^{2\pi/\omega} \sigma \frac{\partial \varepsilon}{\partial t} dt\right) = f A_{hystersis}, \tag{7}$$

where f is the loading frequency applied to the specimen, ω is the angular frequency (i.e., $\omega = 2\pi f$), σ is the stress, ε is the strain, t is time and $A_{hystersis}$ is the area of hysteresis loop

(stress–strain curve) over a cycle. Furthermore, the heat generation over a cycle per unit volume can also be determined using the loss modulus (E'') and the amplitude of applied strain (ε_0) in the following form [58,59]:

$$q_{gen} = \pi f {\varepsilon_0}^2 E'', \tag{8}$$

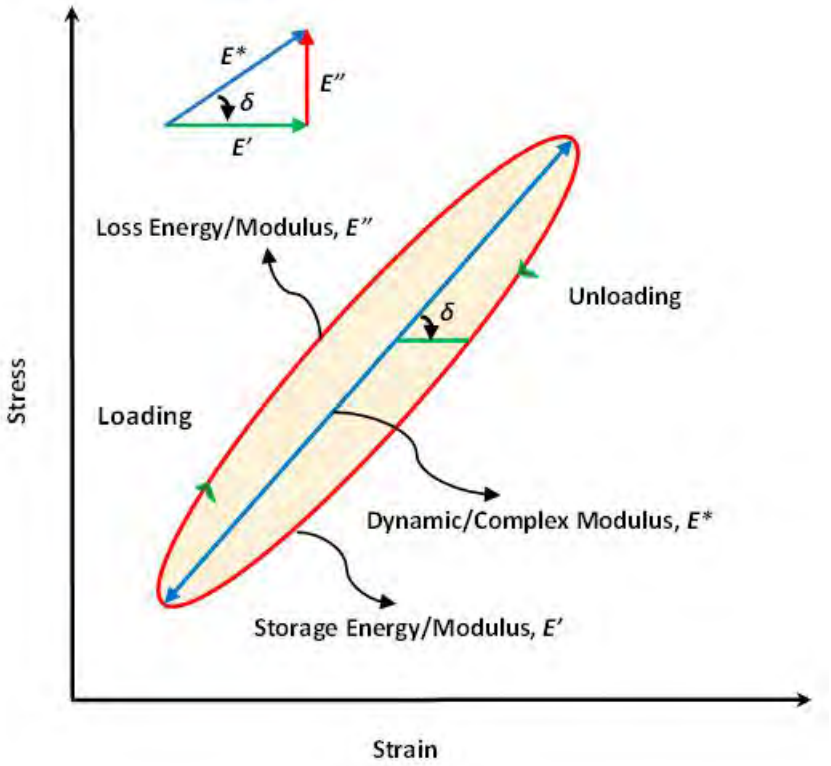

Figure 13. Schematic representation of the generated hysteresis loop and energy-based parameters.

The energy dissipated over a fatigue cycle per unit volume (V) can be determined by summing the heat transfer via conduction (Q_{cond}), convection (Q_{conv}) and radiation (Q_{rad}), as follows:

$$q_{dissip} = \frac{1}{V}(Q_{cond} + Q_{conv} + Q_{rad}), \tag{9}$$

where Q_{cond}, Q_{conv}, Q_{conv} and $\Delta\dot{u}$ are described in the following forms:

$$Q_{cond} = -KA_c \nabla T, \tag{10}$$

$$Q_{conv} = \overline{h}A_l(T - T_\infty), \tag{11}$$

$$Q_{rad} = \sigma e A_l\left(T^4 - T_\infty^4\right), \tag{12}$$

$$\Delta u = \rho c_p(T - T_\infty) \rightarrow \Delta\dot{u} = \rho c_p \frac{\partial T}{\partial t}, \tag{13}$$

where K is the thermal conductivity over the cross-section area of the specimen (A_c) and $\overline{h}$ denotes the average convective heat transfer coefficient over the lateral surfaces of the specimen (A_l); T and T_∞ indicate the maximum surface temperature of such a composite specimen and the ambient temperature, respectively; σ and e denote the Stefan–Boltzmann constant ($5.67 \times 10^{-8}\,\mathrm{W/m^2K^4}$) and emissivity, respectively; u is internal energy, ρ is the density, c_p is the specific heat capacity of a material and t is time. Therefore, the temperature growth as the result of fatigue cycling can be determined as follows:

$$\frac{\partial T}{\partial t} = \frac{\Delta \dot{u}}{\rho c_p} = \frac{q_{gen} - q_{dissp}}{\rho c_p} = \frac{f A_{hystersis} - q_{dissp}}{\rho c_p}, \quad (14)$$

Noticeably, the heat flux via conduction during tension–tension fatigue loading can be negligible [60]. This can be explained by constant stresses across the cross-section of the composite specimen and the unchanged power of internal heat sources. In other words, the temperature gradient through the specimen thickness during tension fatigue loading is approximately zero. On the other hand, heat dissipation via radiation can be eliminated. Therefore, Equation (14) can be simplified for a composite specimen under merely tension–tension fatigue loading as follows:

$$\frac{\partial T}{\partial t} = \frac{f A_{hystersis} - q_{conv}/V}{\rho c_p}, \quad (15)$$

In order to logically formulate the caused self-heating effect under stationary or non-stationary conditions in a cyclically loaded polymeric structure [61], a couple of scenarios can be taken into consideration, which are broadly discussed in Section 4.

Generally, low-cycle fatigue failure, described as the state wherein a tested structure can tolerate a relatively low cycle until failure, occurs due to the application of high-frequency loading and/or a high amplitude of stress/strain during experiments. When the loading frequency is sufficiently low (e.g., below 5 Hz), low-cycle fatigue failure normally occurs as the result of applying a high level of cyclic stress/strain, which should be lower than the ultimate strength/strain. In such a case, the self-heating effect does not occur and fatigue has a purely mechanical character. By contrast, if such a structure is subjected to a relatively lower level of stress- or strain-driven loading, it may experience higher fatigue cycles before its failure, as opposed to low-cycle fatigue failure during which a structural lifetime may be relatively short. Since PMC structures are mostly designed and implemented for the long term, testing in HCF and VHCF regimes may be more favorable. The primary causative factor contributing to this preference may be explained by how different the damage mechanisms in VHCF and LCF can be. Characterization of failure mechanisms in the LCF regime may possess some complexities involving insufficient damage visibility. Testing specimens in the VHCF regime, however, may unfavorably be quite time-consuming and costly, unless the experiments are carried out at a higher frequency level, so as to rationally reduce the time of fatigue experiments of PMCs [31]. This loading frequency may vary from just below 1 Hz up to 20 kHz [16,29,62,63]. Lower frequency levels (normally less than 5 Hz) are primarily implemented for obtaining stress–life (S-N) curves to avoid the hysteresis effect [64], while the accelerated fatigue limit techniques using comparatively high loading frequency [58] as potential candidates have gained a high level of interest. Implementing the accelerated fatigue tests will result in comparatively high testing speed, low testing time [65] and consequently lower cost for testing.

2.2. Prevention of Self-Heating by Controlling Loading Parameters

The primary factors contributing to the lifetime of a polymeric component can be sought in (a) materials (e.g., type of polymer and reinforcement, volume fraction of fiber, stacking sequence of layers, hybridization of fibers and/or polymers, crosslinking of polymers), (b) processing parameters (e.g., void content, manufacturing defects) and (c) loading parameters (e.g., temperature, strain rate, frequency, stress ratio). Although all mentioned aspects take center stage simultaneously in the life assessment of such a composite under fatigue loading, the influence of loading parameters is deeply investigated in this section due to the scope of the current paper.

The classical approach to the evaluation of fatigue in structures is based on the determination of S-N curves, representing a decrease in residual stress as a function of a number of loading cycles. The S-N curve approach can be regarded as a cycle-dependent

but time-independent technique for estimating the fatigue life of materials, including PMCs, which can be characterized according to ASTM and ISO standards. Such standards have been developed for cyclic axial loading (tension and compression) consisting of standards D3479 [66], D3039/D3039M-14 [13] and D3410 [67]. Similarly, the recommended ISO standards for fatigue testing include ISO 13003:2003 [68] and ISO EN 527-4:1997 [69]. Since the S-N method is conventional, it requires comparatively less advanced equipment for evaluating the fatigue performance of FRP composites. Considering that S-N data are mostly determined for low frequency loading (mainly 5 Hz or below), characterizing the fatigue behavior of PMC structures using this technique would be a time-consuming process.

For many decades, the following question has been asked: How are the data obtained during fatigue testing influenced by loading frequency?

Although countless studies have been carried out in order to explore a trend to categorize and standardize the dependency of fatigue lifetime of a component on frequency, no reliable approach has been reported for this objective yet. Interestingly, the vast majority of studies advocate that at a low frequency regime, the fatigue performance of polymeric components is approximately frequency-independent. Some researchers have reported that roughly 5 Hz is the upper limit of frequency in which fatigue tests can be carried out without dependency on frequency [64]. For this reason, Zhou and Mallick [70,71] investigated the influence of load frequency on the fatigue behavior of 40 wt.% talc-filled polypropylene (PP) and 33 wt.% short glass fiber-reinforced polyamide-6.6 (SGFR-PA6.6) with stress ratio R of 0.1. They showed that increasing frequency up to 2 Hz will directly lead to an improvement in the fatigue performance of the talc-filled PP composite at maximum stress levels of 80% and 85% of ultimate strength at the ambient temperature. They also revealed an opposite trend for the fatigue life of such a composite when the frequency is in the range of $2 < f < 5$ Hz, remaining unchanged for the rest of frequency ranges (up to 20 Hz). Tao et al., however, investigated the effect of frequency and stress ratio R on tensile fatigue of carbon cord-reinforced hydrogenated nitrile butadiene rubber (CC-HNBR) composites [72]. They tested the composite specimens with different frequencies ranging up to 20 Hz. According to their results, this frequency regime had an unimportant influence on the fatigue performance of such polymeric specimens because of the generation of an insignificant amount of thermal heat during the entire fatigue test [72]. However, many studies reported the upper limit of frequency at which the mechanical properties will be unimportantly affected is 5 Hz. This means that if the loading frequency is increased (normally more than 5 Hz), this may intensively increase the total area of hysteresis loops generated in this high frequency regime, as a result of which the temperature on the surface of such a structure may increase sharply [72]. This may provoke thermal failure or even jeopardize the structural integrity of a cyclically loaded composite if a temperature overtakes T_g [3,49] or T_m of polymers. However, the results of previous research studies by the authors [1] clearly showed that a critical self-heating temperature was understood as a temperature at which a significant intensification of degradation mechanisms occurs and also leads to a thermal failure. As reported previously, this temperature is usually much lower than T_g. The concept of critical self-heating temperature is discussed in detail in Section 3.2.

It can be concluded that the hysteretic effects can be negligible when such a composite is implemented at a very low frequency regime. In other words, during testing, the total area of hysteresis loops of such a composite caused by a very low loading frequency would be comparatively insignificant. In order to obtain the S-N curve for such a PMC specimen, the frequency of fatigue loading is assumed to be roughly 5 Hz or even less because of preventing the unfavorable influence caused by the self-heating phenomenon. The intensity of loading using the concept of strain rate ($\dot{\varepsilon}$), regardless of the types of polymers and fibers, as one of the fatigue loading parameters can be classified into different types. As can be seen in Figure 14 based on recommendations [13,66–69] (ASTM and ISO standards mentioned earlier), static tests of such composites can be carried out in a quasi-static regime, while cyclic tests, involving fatigue tests, are mainly performed in an intermediate

regime [73]. However, as the strain rate (or strain intensity) applied to a structure during cyclic testing increases, the amount of mechanical energy dissipated in the form of thermal energy increases, resulting in an increase in surface specimen temperature. This elevated temperature primarily acts as a catalyst in the degradation of mechanical properties (i.e., strength, storage modulus and residual life) of such a structure. This leads to the following conclusion: as the temperature that a PMC experiences increases, the level of structural degradation or stiffness degradation that takes place increases regardless of whether that temperature has been applied externally [74] or internally caused by the self-heating effect.

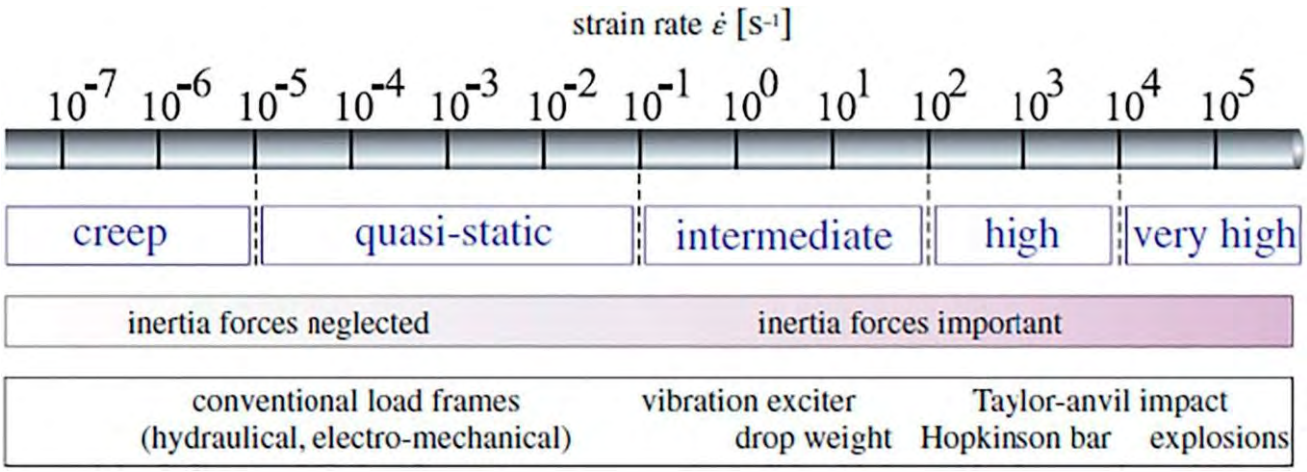

Figure 14. Classifying the strain rate regimes, adapted with permission from Ref. [73]. Copyright © 2021 Elsevier Ltd.

From the point of view of the fatigue loading ratio, Figure 15a schematically illustrates the cyclic loading ratios [75], wherein R denotes the fatigue stress/strain ratio ($R = \sigma_{\min}/\sigma_{\max}$), and σ_{uT} and σ_{uC} indicate the ultimate tensile and compression strengths of the specimen, respectively. It should be mentioned that $\sigma_{\max}$ indicates either σ_{uT} or σ_{uC}, depending on the type of loading. The stress ratio ($R = \sigma_{\min}/\sigma_{\max}$) takes a center stage in obtaining the S-N curve during fatigue testing. The fatigue loads can be classified by the stress ratio parameter. Noticeably, (+) and (−) are algebraic representations for tension and compression loading, respectively. $R = 1$ demonstrates the static loading, while $R = -1$ is an indication for symmetric (known also as alternating fully reversed) strain/stress loading, which may be taken into consideration as the most catastrophic type of fatigue loading. In other words, when $R = -1$, the fatigue life of the PMC specimen would be at the minimum level compared with other forms of loading. $R = 0$ depicts the repeated (zero-tension) cyclic loading, while $R = -\infty$ reveals repeated (zero-compression) stress/strain loading, which may be described as the same as $R = 0$. In addition,$0 < R < 1$ demonstrates tension–tension cyclic loading (the most common type of fatigue testing), while $1 < R < \infty$ shows compression–compression cyclic loading. However, $-\infty < R < 0$ indicates compression–tension loading, which has not yet been standardized due to its complexity. Figure 15b demonstrates the fatigue life for hybrid carbon/Kevlar-49/epoxy laminate with various mean stress (σ_m) effects with constant life (Goodman) diagrams shifting from left to right [64,76]. The main causative factor contributing to this left-to-right shifting in Goodman diagrams can be rooted in how PMC structures normally reveal a greater magnitude of strength during cyclic tension loading, as opposed to compression fatigue loading [64].

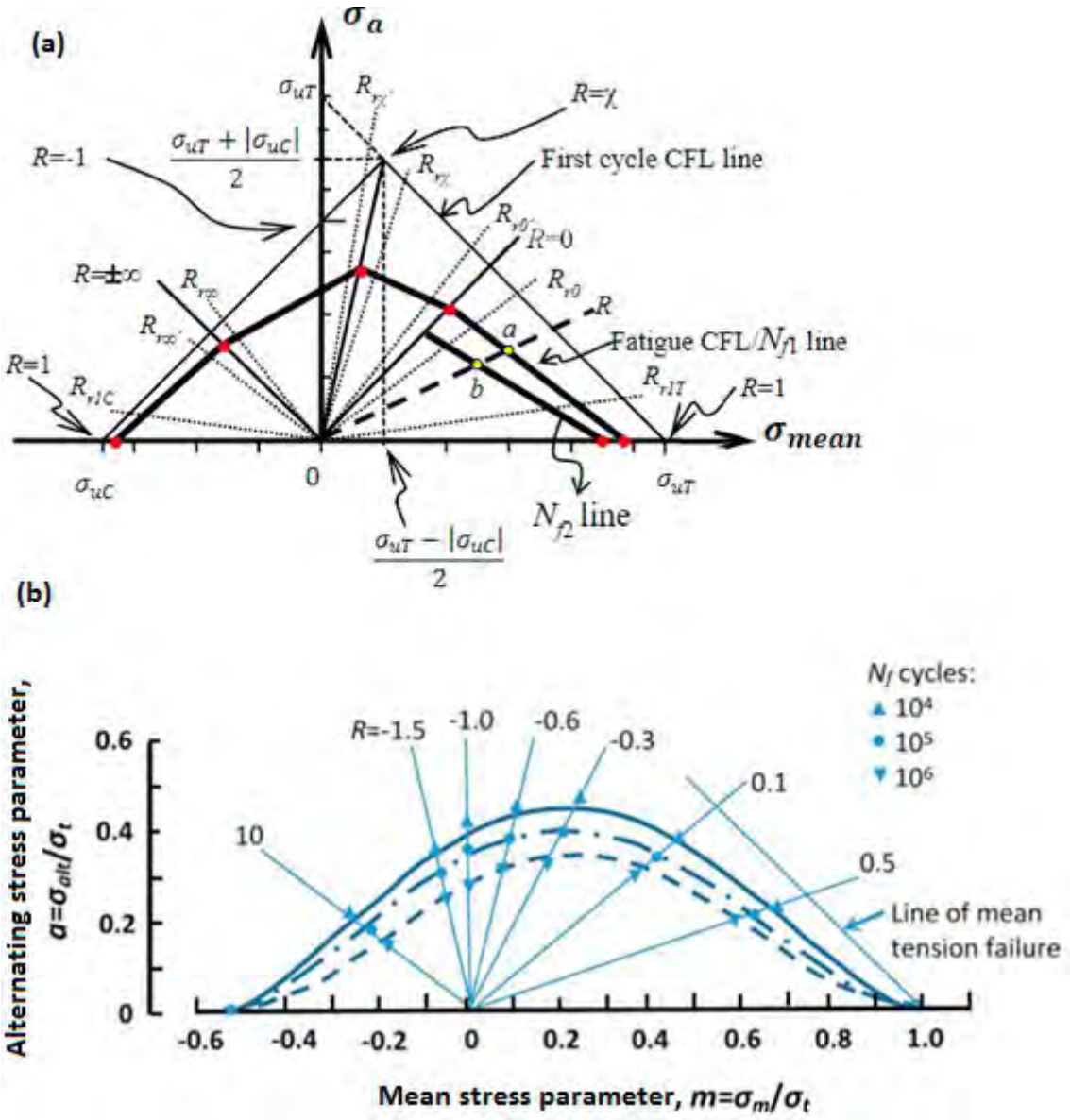

Figure 15. (**a**) A schematical illustration of cyclic loading ratios (adapted with permission from Ref. [75]. Copyright © 2019 Elsevier Ltd.) and (**b**) an exemplary illustration of fatigue life based on the Goodman diagram for carbon/Kevlar-49/epoxy laminate (adapted with permission from Ref. [64]. Copyright © 2020 Elsevier Ltd.).

Figure 16 vividly depicts how the stiffness of a specific FRP laminated composite is undesirably degraded as the cyclic load ratio increases [74]. Movahedi-Rad et al. [77] investigated how the energy dissipation of angle-ply glass/epoxy composite laminates with stacking sequence of $(\pm 45)_{2s}$ was influenced by different stress levels with an unchanged ratio of 0.1 so as to cover many fatigue lives, ranging from 500 cycles up to 10^6 cycles. They showed that as the number of cycles and/or stress ratio increased, a relatively larger amount of mechanical energy was dissipated, and consequently a greater amount of thermal energy was stored, which was explained by much more friction in the area of unbounded zones as a consequence of damage growth. As shown in Figure 17, the specimens experienced the maximum temperature values of 30 °C and 45 °C when they were subjected to low/intermediate stress levels and higher stress levels, respectively.

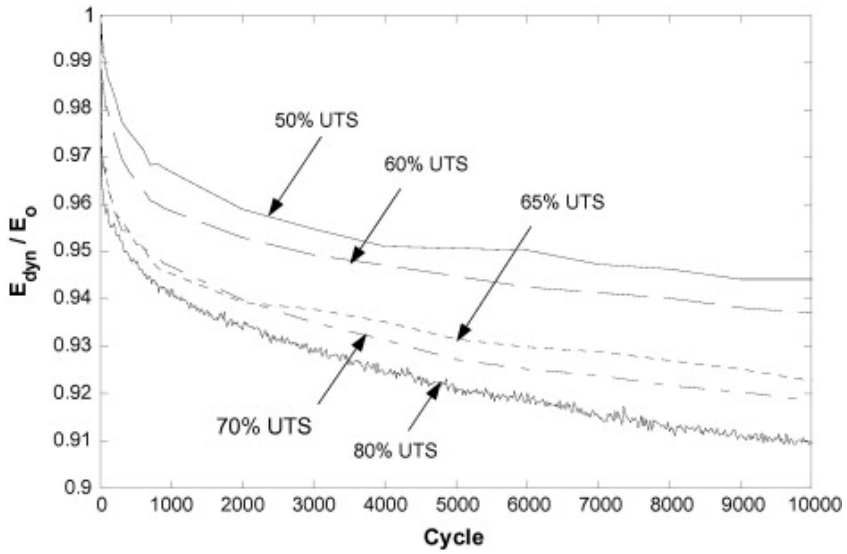

Figure 16. An exemplary demonstration of normalized stiffness reduction under stress ratios of one-half or above ($0.5 \leq R \leq 0.8$), adapted with permission from Ref. [74]. Copyright © 2013 Elsevier Ltd.

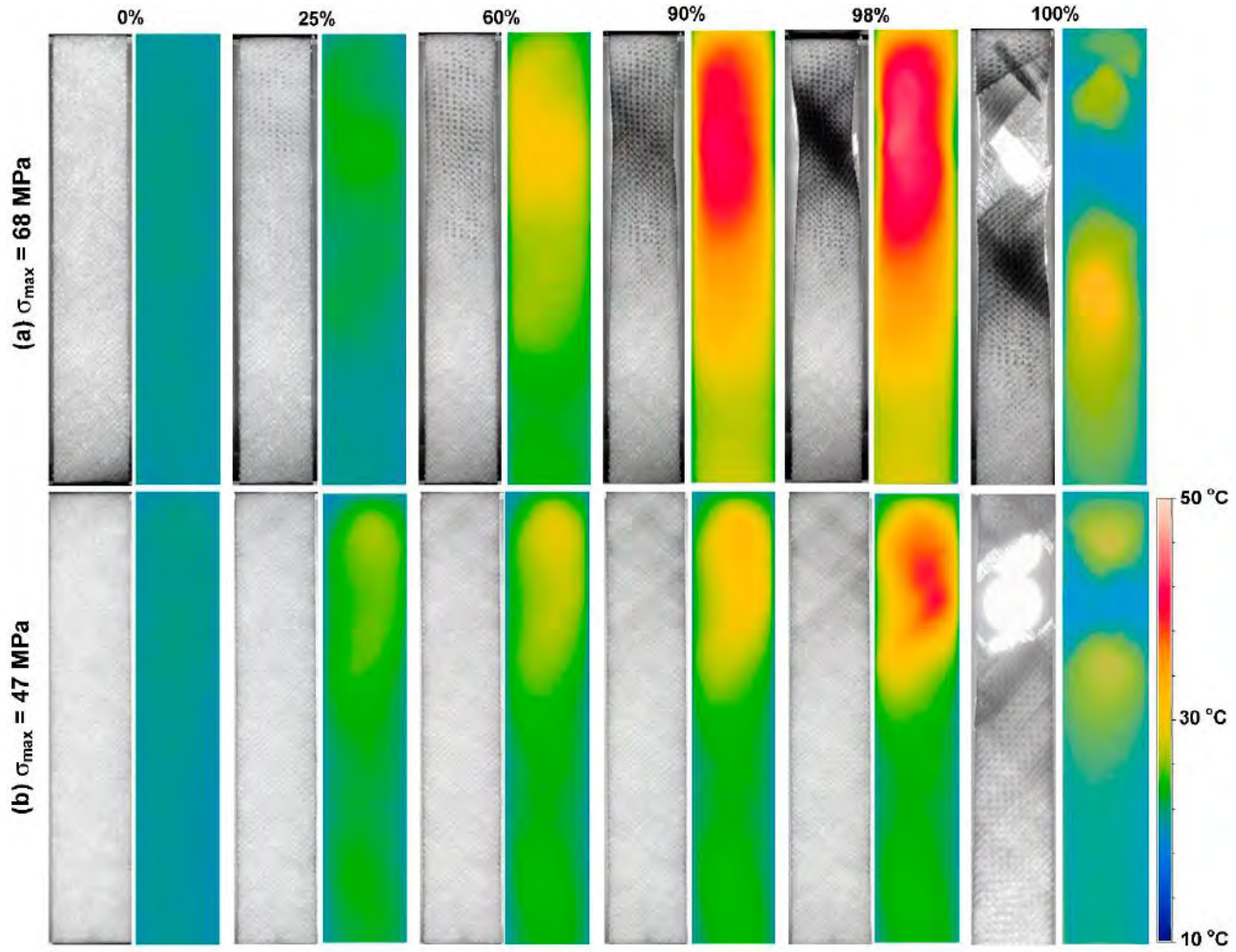

Figure 17. An experimental demonstration recorded using an infrared thermal camera for the self-heating effect at various percentages of fatigue life of $(\theta = \pm 45)_{2s}$ GFR/epoxy composite, adapted with permission from Ref. [77]. Copyright © 2018 Elsevier Ltd.

2.3. Fatigue Limit and Role of Self-Heating

The FRP laminated specimens at different stress regimes should be tested before being implemented in potential engineering applications to obtain an acceptable safety factor. Since the FRP composites due to their extraordinary mechanical properties are normally subjected to HCF and VHCF regimes, implementing the conventional S-N curve method technique at very low frequency may be extensively time-consuming and consequently expensive. The number of cycles is the key factor when it comes to fatigue life assessment so that the residual life of such a polymeric structure can be computed. Figure 18 reveals how the hysteresis effect is influenced by variation of the applied stress and the number of fatigue cycles, which can be indicated by the slope of the major axis of elliptical-like hysteresis loops [77]. As can be concluded, an increase in the number of cycles resulted in a decrease in the slope of the major axis of the elliptical hysteresis loop, which is directly connected with the stiffness of the specimen. This means that the residual stiffness of a PMC specimen decreased as the number of cycles increased, which is a result of the viscoelastic nature of a polymeric matrix of a PMC. More importantly, it had been demonstrated that as the stress and number of cycles experienced by the typical PMC structure increased, the amount of thermal energy that could be generated increased (see Figure 19a). The same trend was reported for the self-heating temperature. As can be seen, the effect of self-heating had been accelerated as the number of fatigue cycles and the stress levels increased (see Figure 19b).

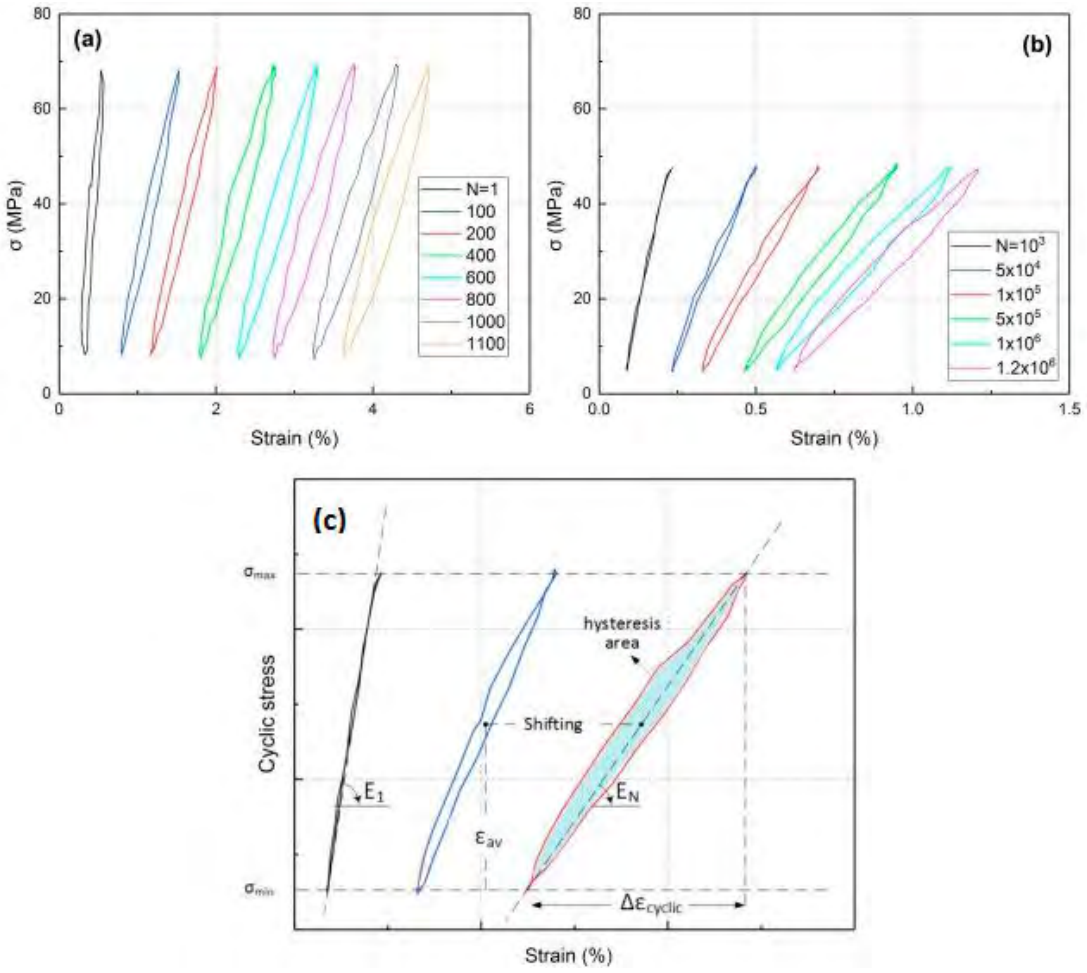

Figure 18. Hysteresis area alteration (**a**) applied to σ_{max} = 68 MPa and (**b**) σ_{max} = 47 MPa and (**c**) slope variation as the result of an increase in the number of cycles, adapted with permission from Ref. [77]. Copyright © 2018 Elsevier Ltd.

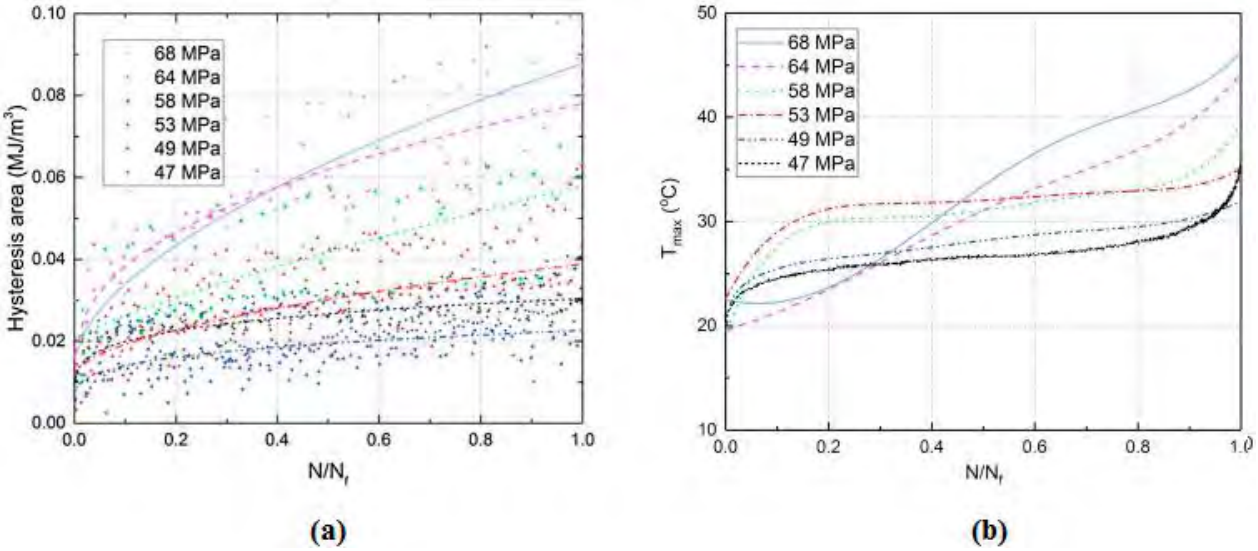

Figure 19. (**a**) Alteration of hysteresis area and (**b**) variation of maximum self-heating temperature as the function of applied stress level and cycle ratio (N/N_f), adapted with permission from Ref. [77]. Copyright © 2018 Elsevier Ltd.

To effectively address this problematic issue and accelerate the speed of cyclic loading tests, researchers have considered the development of rapid fatigue limit techniques for the characterization of the fatigue damage evolution, which is considered an irreversible process through which energy is dissipated. For this objective, many intrinsic thermodynamic-based techniques (e.g., purely experimental or combined theoretical/numerical/experimental methodologies) have been developed and implemented involving acoustic emission (AE), digital image correlation (DIC), X-ray industrial computed tomography (ICT), infrared thermography (IR), self-heating-based thermography (SHT) and surface crack density, which have been reviewed in [1,78–80]. Among them, the SHT methods have been recently gaining great attention due to their comparative simplicity and acceptable accuracy. The SHT methods were first proposed for metals; however, they were then developed for PMCs.

Unlike conventional S-N curves for FRP composites which are both time-demanding and costly due to requiring numerous specimens for testing at various levels of R [81,82], the developed fatigue limit methods require much less time for testing compared to the conventional S-N curve method [29,31]. This can be explained by how the fatigue limit of such a composite can be determined using merely a single specimen, as opposed to constructing an S-N curve for which numerous specimens should be tested, and the approximation technique should then be implemented.

The fatigue limit in a PMC structure can be described as the highest level of stress at which the temperature gradient on the specimen surface is approximately zero. As a direct consequence of implementing energy-based fatigue limit techniques, temperature–cycle (T–N) and temperature–strength ($T-\sigma$) curves can be normally achieved.

Risitano's model [83,84] and Luong's approach [85,86] have been well known as thermodynamic-based techniques for characterizing the fatigue limit during cyclic loading based on a temperature–strength ($T-\sigma$) curve. Figure 20 schematically shows how the fatigue limit can be characterized by implementing the energy-based Risitano's and Luong's models, which are known as the one curve model (OCM) and two curve model (TCM), respectively [81]. According to Risitano's model, the fatigue limit can be calculated with the aim of a crossover between the horizontal axis and the second or enhanced temperature line induced by dominated thermoplastic (friction and microstructural evolution) under comparatively high stress loading amplitudes [83,84]. This approach may be quite conservative. On the other hand, two lines are implemented in Luong's model, which is

comparatively less conservative [85,86]. In addition to OCM and TCM, the temperature integral technique has received great interest from researchers. Unlike OCM and TCM which are completely intrinsic, the temperature integral technique implements the internal FRP composite thermal conduction properties and the external heat transfer (mainly in the form of convection) with the surrounding environment [87,88]. For this purpose, Huang et al. [89] determined the fatigue limit of angle-ply CFRP laminates with the stacking sequence of $[\pm 45^{\circ}]_8$ subjected to cyclic shear loading with the presence of a self-heating phenomenon. The exemplary results for the determination of the fatigue limit are presented in Figure 21. This figure reveals the relationship between maximum loading amplitude and stabilized temperature rising. As can be seen from the provided graph, the heat generation rate increased gradually at comparatively lower stress values and increased significantly at greater stress levels. The maximum changing point between those two different stabilized temperature increases was assumed as the fatigue limit, which was just above 100 MPa.

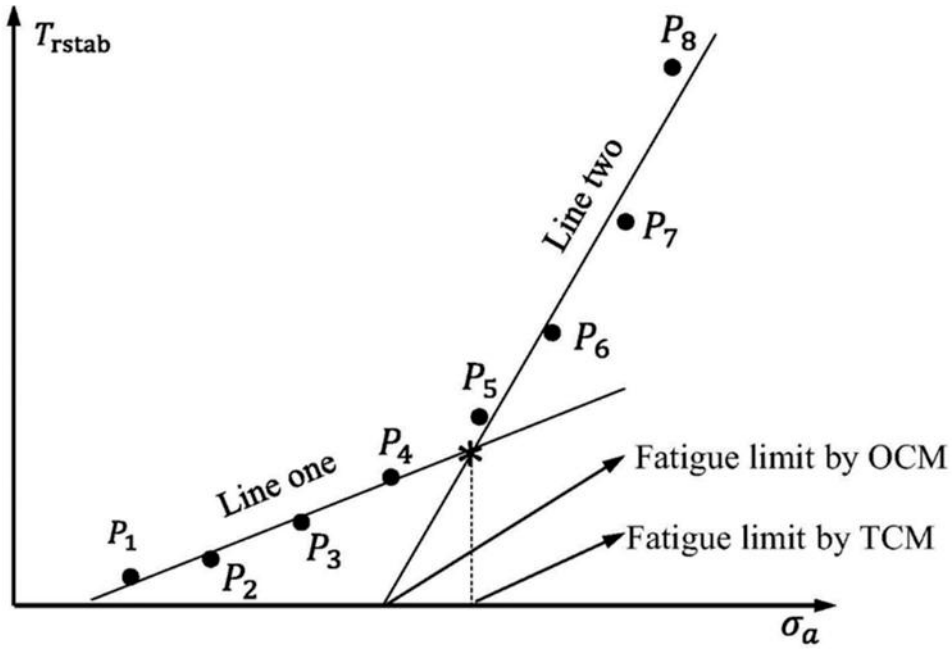

Figure 20. A schematic illustration of fatigue limit prediction using energy-based Risitano's and Luong's models, adapted with permission from Ref. [81]. Copyright © 2017 Elsevier Ltd.

In addition to the $T-\sigma$ curve, the temperature–cycle ($T-N$) curves can be used for the sake of characterizing the fatigue behavior of composites. Figure 22 illustrates a schematic representation of temperature–cycle ($T-N$) curves for different applied stress levels [90]. In order to extract $T-N$ curves, the assumption of three different phases existing is implemented (see Figure 22). Firstly, a rapid temperature change on the specimen surface occurs, whose rate is dependent on the applied stress level. After the initial increment, the temperature value will approximately remain unchanged for a comparatively high number of fatigue cycles, called temperature stabilization (ΔT_{st}) or stationary condition. In the final phase, the temperature significantly increases until mechanical/thermal fatigue failure occurs, which is called a nonstationary situation. Additionally, as the level of stress amplitude applied to a tested structure increases, there will be an increase in the value stable temperature appearing on the specimen surface, which can be described by the energy parameter (Φ). It is assumed to be independent of applied stress, the stress ratio (R) and the loading frequency (f). By knowing Φ and the stabilized temperature associated with a subjected stress level, it is possible to determine the number of cycles at which the specimen fails (i.e., $N = \Phi/\Delta T$).

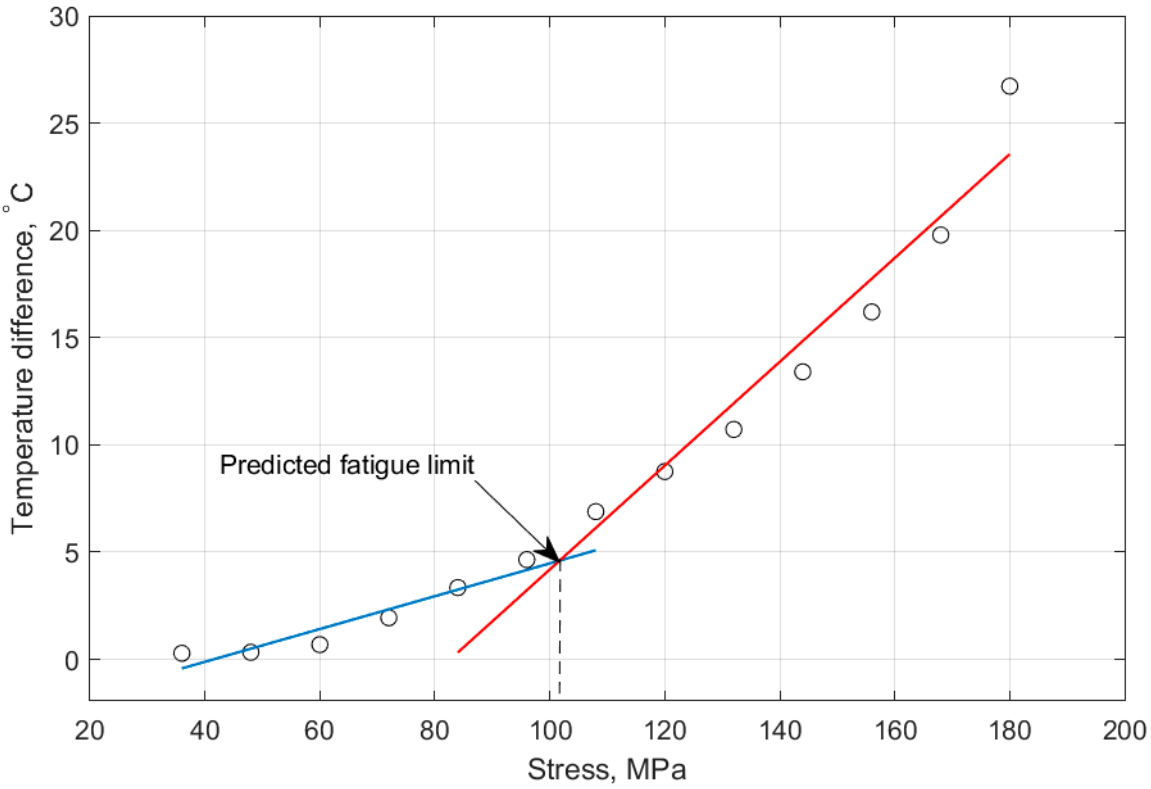

Figure 21. An exemplary fatigue limit determination of CFRP composite.

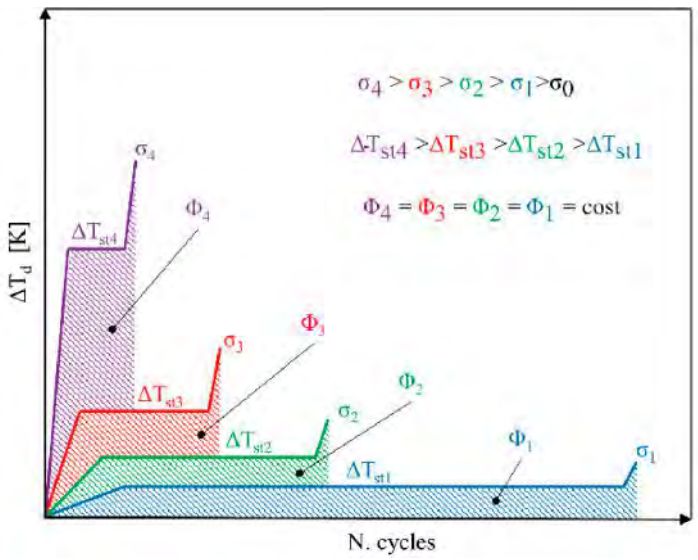

Figure 22. A schematic representation of temperature–cycle ($T - N$) curves under different applied stress levels, adapted with permission from Ref. [90]. Copyright © 2020 Elsevier Ltd.

For this purpose, Mandegarian et al. [91] investigated the in-plane shear fatigue behavior of $[\pm 45]_{2s}$ angle-ply CFRP composite under fully reversed loading ($R = -1$). A number of staircase-like stress amplitudes were applied to such a composite specimen so as to obtain the same number of cycles wherein the fatigue failure occurs in such a laminated CFRP composite. Figure 23 illustrates how the number of cycles until failure can vary as a function of applied stress levels (e.g., ranging from R of 0.4 to 0.8) [91].

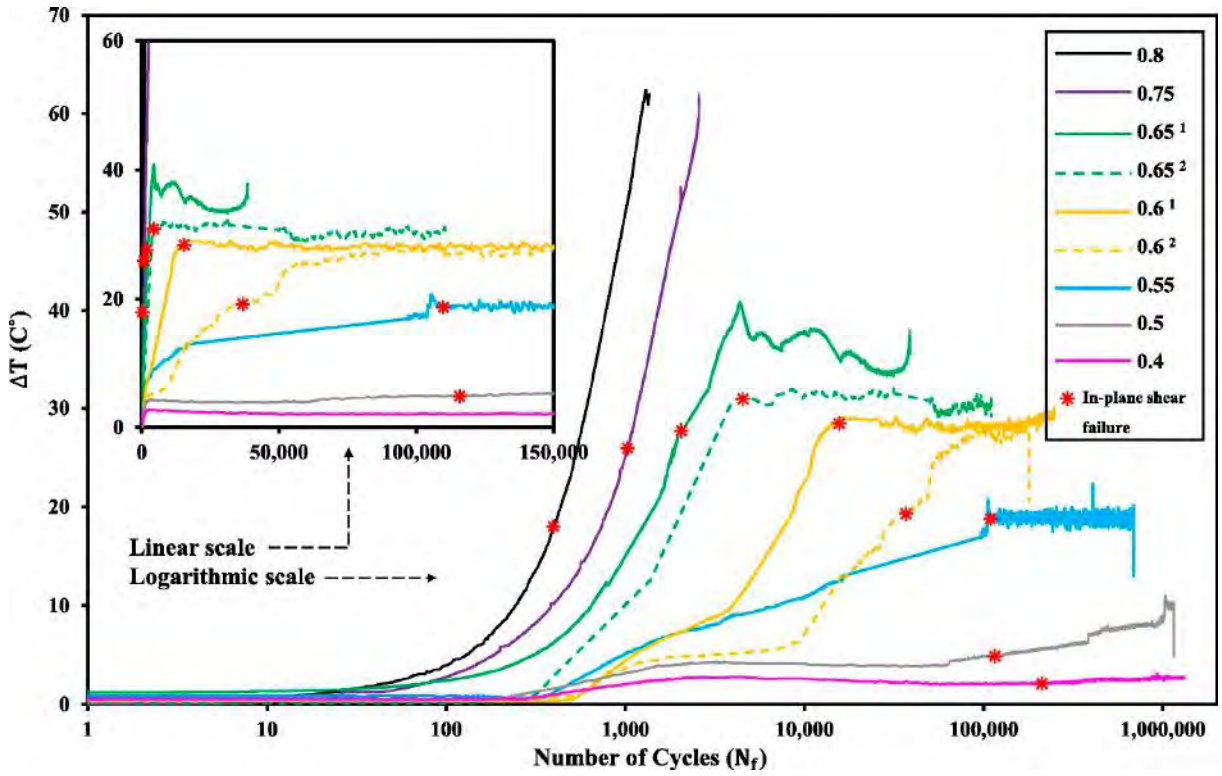

Figure 23. An exemplary plot of temperature evolution vs. stress alteration for the angle-ply $[\pm 45]_{2s}$ CFRP composite, adapted with permission from Ref. [91]. Copyright © 2022 Elsevier Ltd.

From the other perspective, a PMC structure, depending on the type of applied mechanical fatigue loading (i.e., bending, tension, shear tension–compression or multiaxial loading) and the magnitude of applied loading (i.e., frequency and stress/strain amplitude), may indeed experience both mechanical and thermal loading, as the result of which various fracture mechanisms may occur [92–94], which are deeply discussed in Section 3. Due to the entropy generation in the irreversible thermodynamic process caused by the self-heating effect [19,54,95], a structure may face mechanical failure or thermal failure. According to this, a mechanical fracture may occur when the influence of mechanical loading is comparatively more dominant than thermal loading, while thermal failure will occur if the self-heating effect is more dominant [64,89]. Thus, mechanical and thermal failures are associated with stationary and nonstationary scenarios, respectively.

As can be extracted from both stationary and nonstationary self-heating conditions illustrated in Figure 24 [87], the incremental temperature gradients begin steeply and decline slightly as the number of cycles increases in the first phase for both scenarios, which can be characterized and quantified by the implementation of equilibrium thermodynamics. During this stage, crosslinking degradation of polymer chains occurs and fiber–matrix debonding begins. During the next stage of the stationary self-heating scenario, a steady-state evolution called the stabilized self-heating temperature takes place over a prolonged period of time or a multitude of fatigue cycles. This trend can be explained by a thermal equilibrium point between the generated thermal energy on the polymer-based specimen surface and the heat removal through convective and conductive heat transfers as well as radiation into the surrounding environment [87]. Notably, the magnitude of heat transfer via radiation is comparatively lower than other forms, which can be negligible [87].

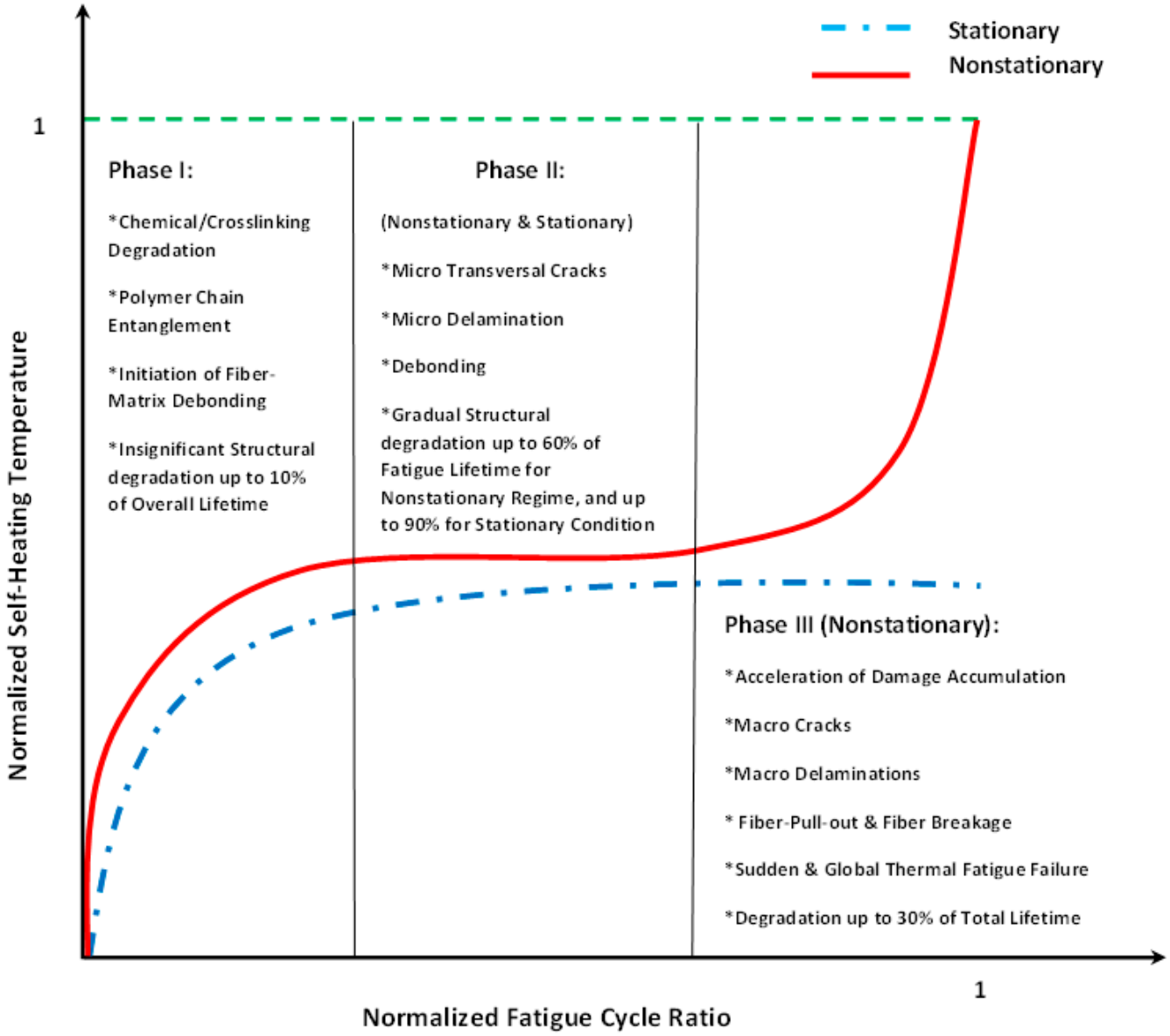

Figure 24. A schematic process of fatigue damage propagation in both stationary and nonstationary self-heating regimes.

On the other hand, during the second phase of the nonstationary self-heating regime, the temperature profile experiences an upward trend linearly as the number of fatigue cycles increases (see Figure 24). The primary causative factors contributing to this trend can be sought in the synergy between mechanical fatigue and entropy generation (irreversible morphological and chemical variations [3]) because of the viscoelastic nature of polymers. Therefore, due to the high level of entropy generation caused by accumulated microcracking and delamination [3], structural performance may begin to remarkably degrade, which will be more catastrophic as the applied frequency and stress/strain amplitude of fatigue increase. The third phase of the nonstationary self-heating scenario begins when the macrocracks and macrodelaminations appear initially and their numbers increase with the increase in cycle number. The main causative parameters contributing to the continuous macrocrack formation process in FRP composites can be rooted in the high frequency and stress/strain ratio during testing, which indeed act as catalysts for propagating and interacting among the transverse and interlaminar microcracks and delamination in the vicinity of macrocracks, leading to releasing a large amount of energy in the structure. The

released heat energy will undesirably provoke mechanical softening among polymer chains and consequently result in a sharp exponential temperature growth on the PMC surface, leading to structural degradation and sudden thermal failure.

Unlike the stationary condition induced by mechanical fatigue loading wherein a gradual linear temperature growth occurs [61], the nonstationary scenario is a complex phenomenon wherein a large amount of heat generation appears in the form of internal energy (see Equations (6) and (13), extracted from the first principle of conservation of energy thermodynamics [96]), which is highly dependent on environmental factors (e.g., ambient temperature, convective heat transfer coefficient), material properties (e.g., thermal conductivity), geometry (particularly thickness) and loading parameters (e.g., the magnitude of applied frequency and stress/strain ratio). This can be additionally explained by entropy inequality (i.e., second law of thermodynamics) [5]. In a stationary self-heating scenario, two different phases may occur, while three separate stages will take place during a nonstationary scenario in a cyclically loaded polymeric structure [3]. These two or three different phases can be extracted from the beginning of cyclic fatigue testing until the final breakage/failure in a loaded structure by using some devices, such as an infrared (IR) thermographic camera [97] (see Figure 24). Figure 25 illustrates the exemplary measured temperature responses during stationary and nonstationary self-heating regimes [97]; in addition, an exemplary IR image of the polymeric specimen surface temperature in different phases in the presence of the self-heating effect is shown in Figure 26.

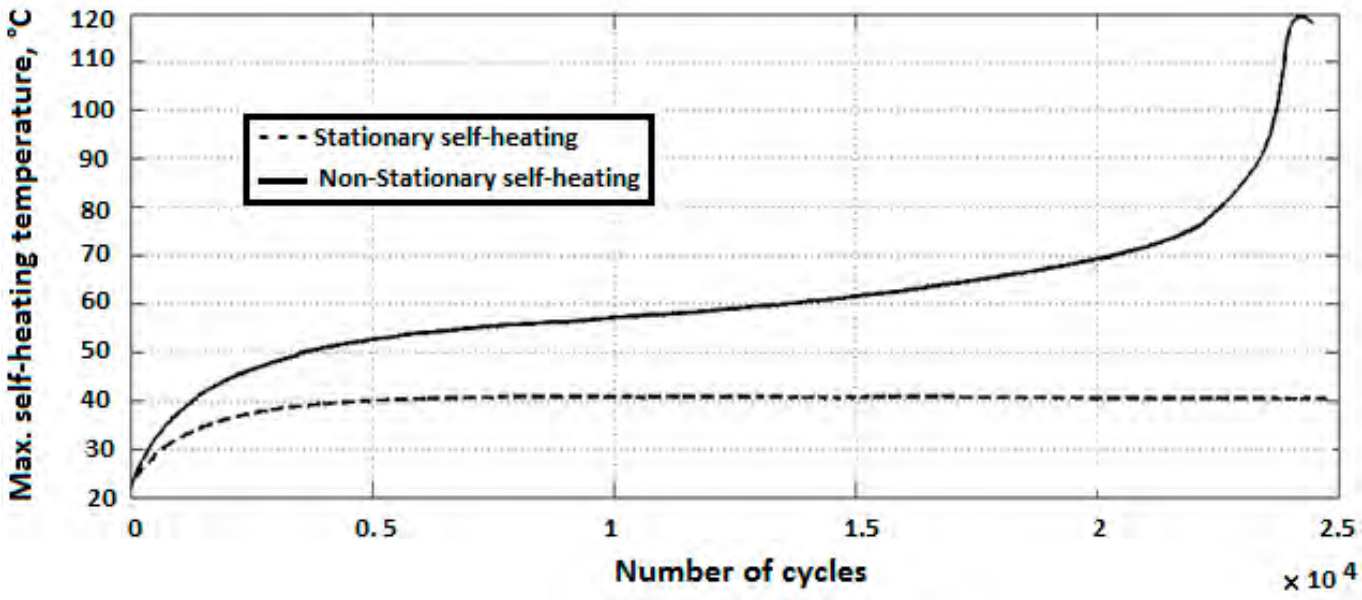

Figure 25. Exemplary self-heating temperature history curves for stationary and nonstationary self-heating scenarios, adapted with permission from Ref. [97]. Copyright © 2017 Elsevier Ltd.

A scheme of failure modes resulting from frequency alteration is presented in Figure 27 [64]. For example, regardless of the effect of the load ratio, the critical condition occurs at the frequency transition. This means that if the applied frequency is greater than the frequency transition, the thermal fatigue failure mode would be dominant in such a structure. Otherwise, at a constant level of stress when the frequency is sufficiently low, the decrease in fatigue life is due to the creep influences.

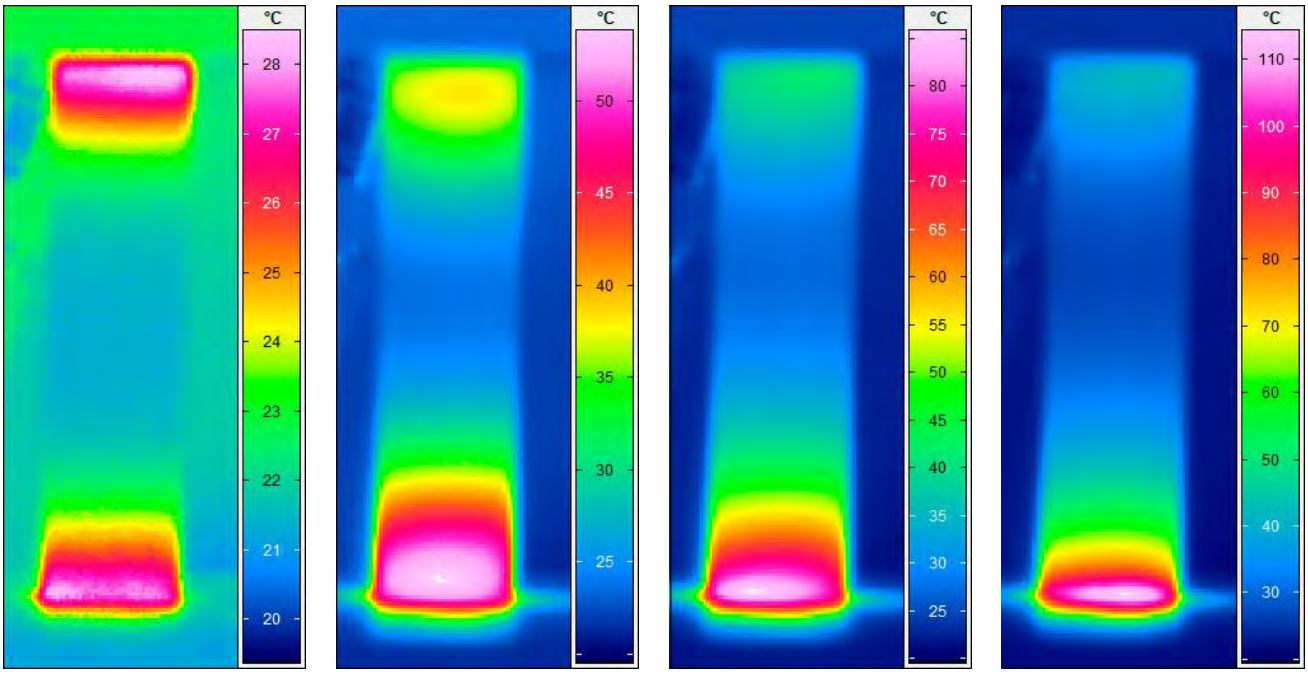

Figure 26. Infrared images of the cyclically loaded GFRP specimen with self-heating effect at (**a**) the beginning of loading (phase I), (**b**) near the end of phase II, (**c**) in the middle of phase III and (**d**) at failure.

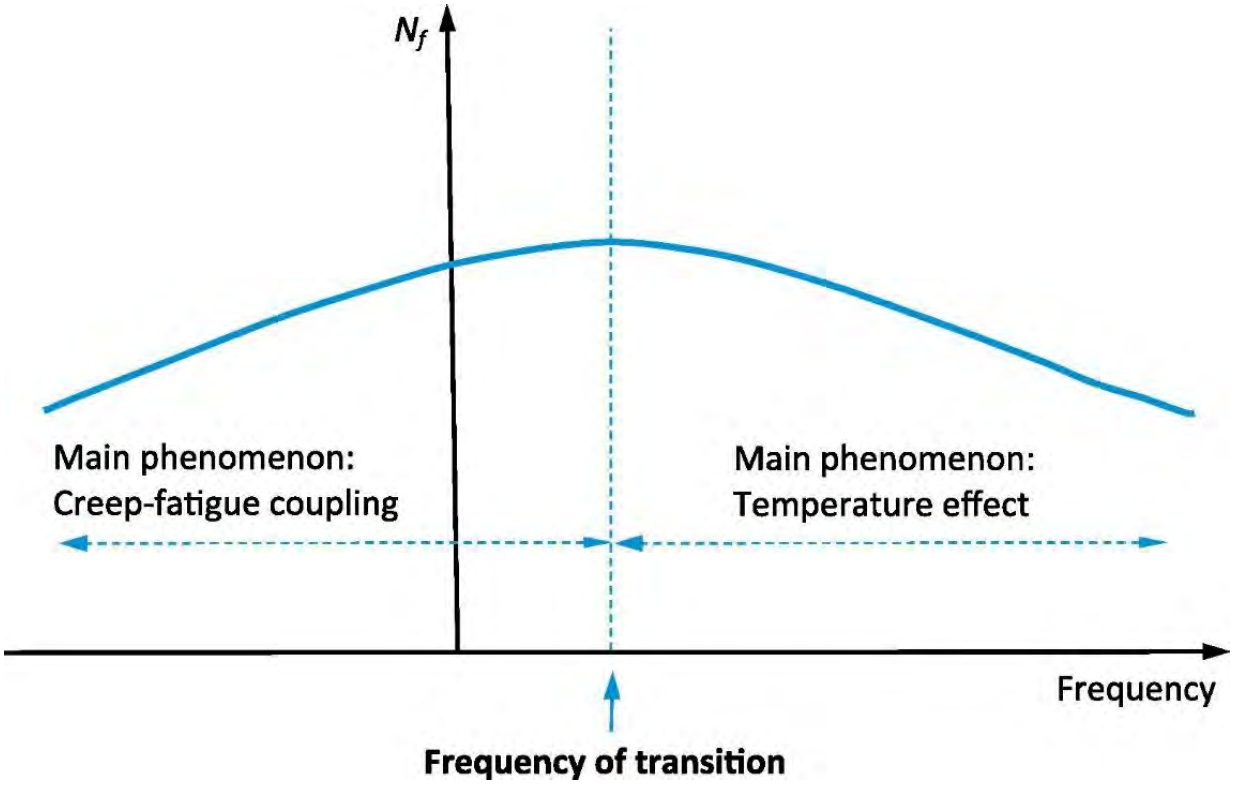

Figure 27. The schematic representation of the frequency transition effect on of critical self-heating temperature induced by failure modes, adapted with permission from Ref. [64]. Copyright © 2020 Elsevier Ltd.

3. Fatigue Behavior of Polymers and PMCs Dominated by Self-Heating Effect

The fatigue damage mechanisms of the PMC structures may be thoroughly different compared with metallic ones (see Figure 28). Unlike metals wherein crack propagation appears in a predictable way until final failure, damage propagation in the cyclically loaded PMC structures may be unpredictable due to the heterogeneity and anisotropic properties of such materials, as well as the viscoelastic nature of polymers. Noticeably, the critical size of damage in a typical PMC structure (e.g., fiber breakage, delamination, debonding, matrix cracking and voids) is comparatively greater, as opposed to the sizes of metal damage (mainly cracks) [64].

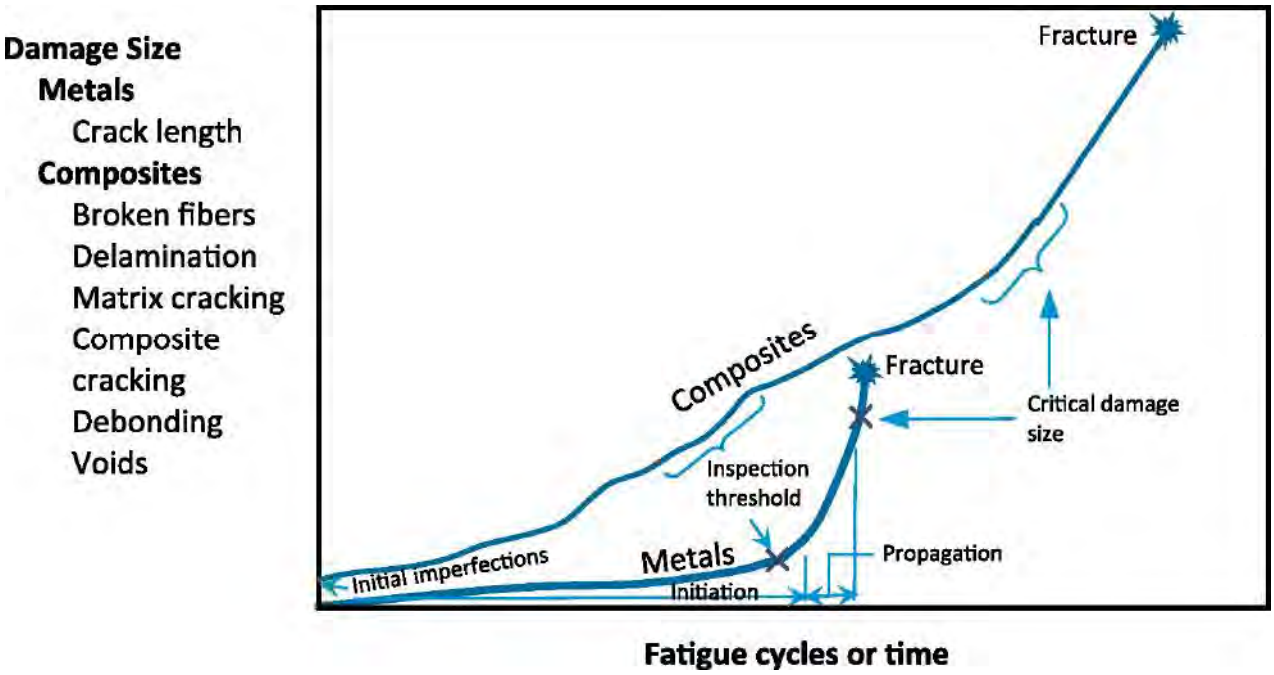

Figure 28. The schematic illustration of the difference between fatigue damage mechanisms between PMCs and metals, adapted with permission from Ref. [64]. Copyright © 2020 Elsevier Ltd.

One of the primary open questions associated with evaluating the fatigue performance of FRP composites experiencing the self-heating effect has been as follows for many years:

What exactly occurs in a cyclically loaded PMC structure with the presence of the self-heating phenomenon at different scales?

To answer this question, it may be more rational to define the level of structural degradation induced by the self-heating effect in PMC structures at different scales.

3.1. Definition of Degradation in Nano-, Micro- and Macroscales

In general, a fabricated FRP composite structure before experiencing fatigue loading may possess various types of damage (see Figure 29a,b) which can be classified based on the effects of air entrapment and fiber volume fraction as follows:

- Porosity, blisters and voids caused by air entrapment;
- Resin-rich and -poor zones caused by inhomogeneous distribution of a reinforcement in composites.

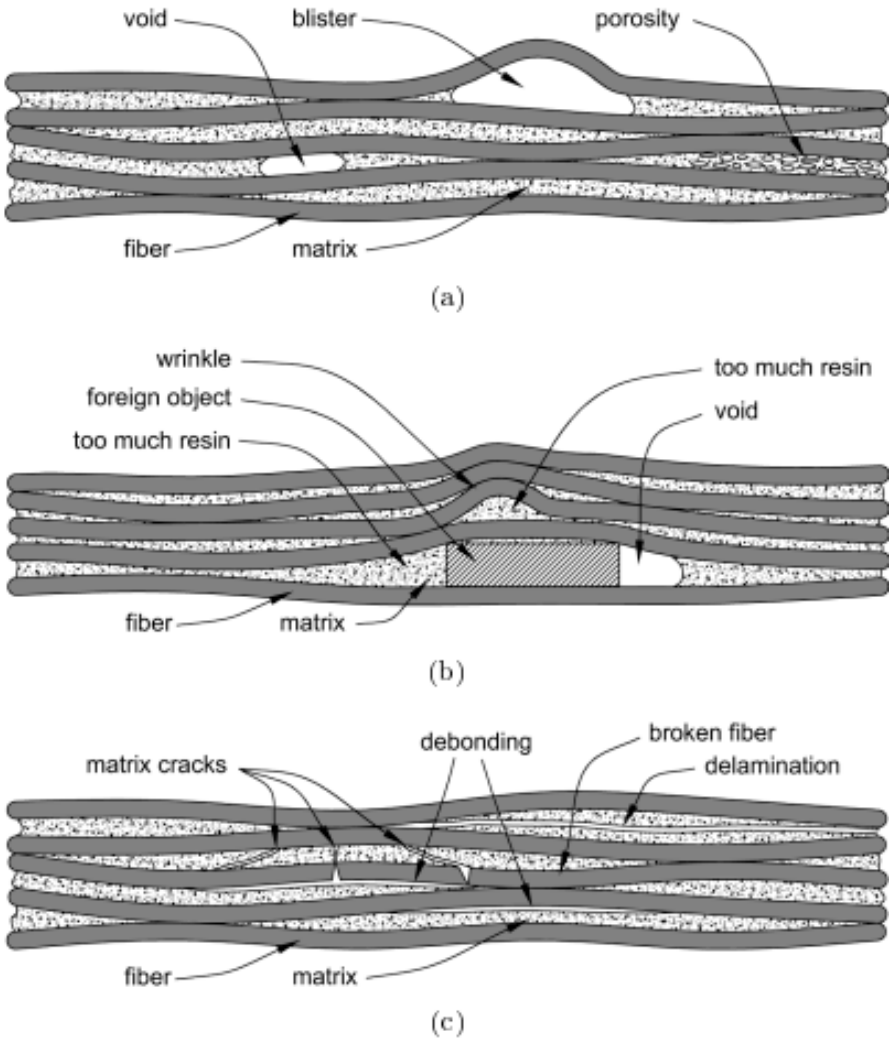

Figure 29. Typical damage in PMCs induced during the manufacturing process due to (**a**) improper curing processing, (**b**) incorrect fiber volume distribution and foreign bodies, and (**c**) insufficient wetting of fibers and lack of adhering between fibers and polymer matrix [98].

Although it is assumed that the PMC specimens are devoid of any pre-existing damage before conducting the fatigue tests, such PMC structures may even face a mixed damage types (combination of interface/fiber/matrix damage) during manufacturing process (see Figure 29c):

- Reinforcement and polymer–matrix damage: fiber breakage and matrix microcracks;
- Interface damage: fiber bridging/pull-out, delamination/interlaminar cracking, debonding;

The above-mentioned damage types (see Figure 29c) can appear in a cyclically loaded PMC structure. Regardless of the effect of loading frequency, a typical PMC structure may experience different modes of failure depending on the type of applied loading, stress ratio (R), fiber volume fraction (V_f) and stacking sequence (known also as the test angle). For this reason, Zaghloul et al. [99] investigated the influence of fiber volume fraction on the fatigue performance of glass fiber-reinforced polyester at five different stress levels (i.e., 75%, 65%, 50%, 40% and 25%) during tension–tension fatigue testing. They reported that the fatigue strength increased by 100.4% as the result of an increase in the fiber volume fraction from 20% up to 50% subjected to a high stress level. Nevertheless, the fatigue strength increased by only 38.2% when subjected to low stress level as the fiber volume fraction increased from 20% to 50%. In another study, Zaghloul et al. [100] experimentally showed that adding 4% cellulose nanocrystals to a polyester polymer matrix resulted in optimum

fatigue performance. They reported that the low fiber volume fraction caused interfacial debonding and matrix cracking, while the high fiber volume fraction resulted in fiber pull-out [99]. Brunbauer and Pinter [101] conducted a comparative study on laminated CFRP composite in order to investigate the effect of the above-mentioned parameters. Samples with fiber volume fractions of 30 and 55% were prepared to be tested at two different levels of R (i.e., $R = 0.1$ and $R = -1$) under three separate test angles (i.e., 0°, 45°, and 90°). They reported that both R and V_f play a key role in the type of damage mechanisms (see Figure 30). For example, for a test angle of 0° (i.e., loading is parallel with the fiber direction), the main damage mechanism is fiber breakage for fully reversed fatigue loading ($R = -1$), while both fiber pull-out and fiber breakage were observed under tensile loading ($R = 0.1$). Moreover, fiber crushing was observed under tensile–compressive load ($R = -1$).

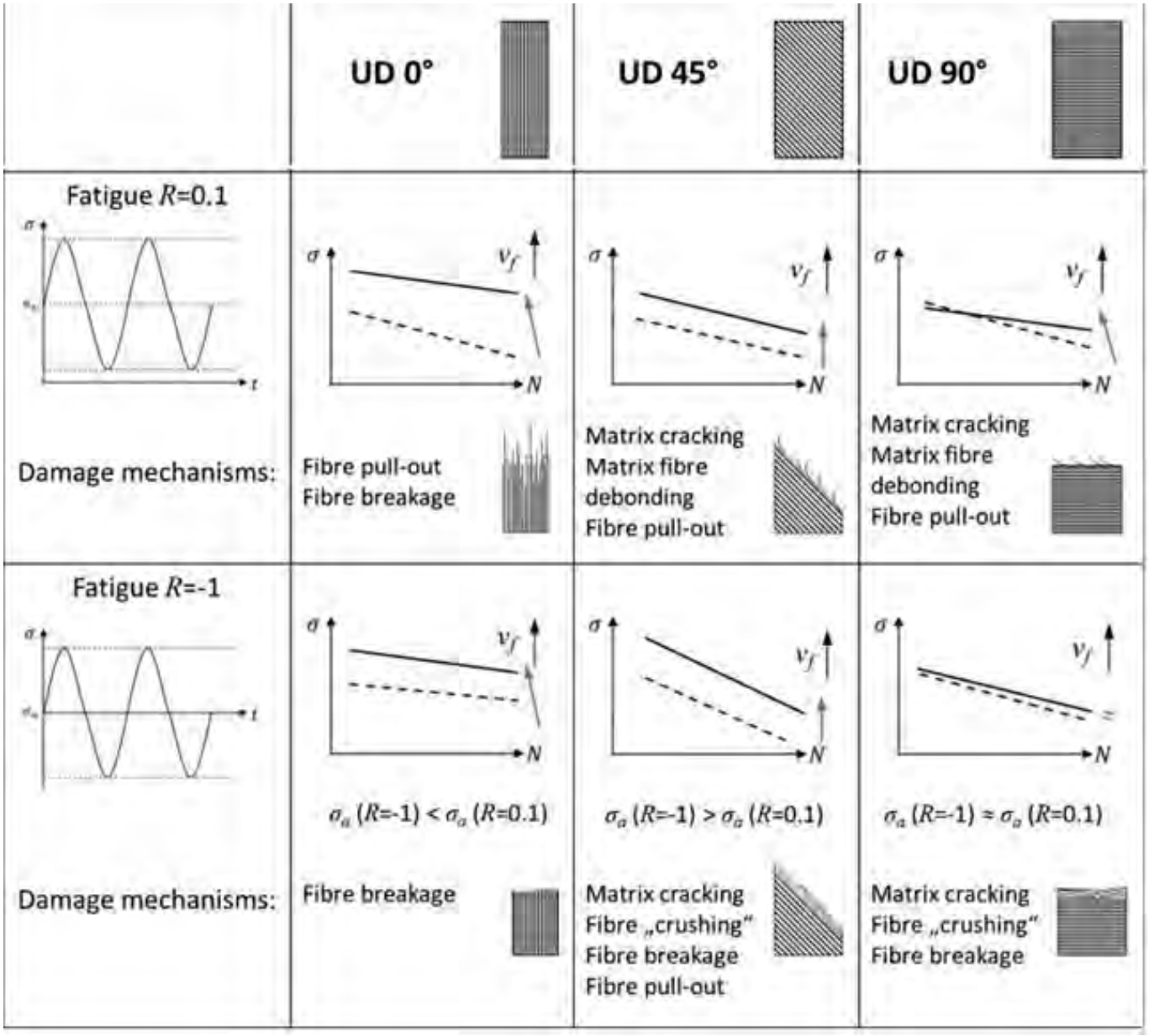

Figure 30. Schematic fatigue damage mechanisms for laminated CFRP composites depending on stress ratio, fiber volume fraction and test angle, adapted with permission from Ref. [101]. Copyright © 2015 Elsevier Ltd.

The induced damage types during fatigue loading of PMC structures can be classified from nano-, micro- and/or macroscopic points of view as follows.

3.1.1. Nanoscale

The concept of degradation in cyclically loaded FRP composites at the nanoscale can be mainly associated with the dynamic behavior of polymer chains and the interface/interphase between fibers and polymer chains [102] during both stationary (phases I and II) and nonstationary (phase III) self-heating regimes. According to this, the overall performance of a polymer matrix is highly dependent on the macromolecular crosslinking chains, intermolecular forces and dynamic behavior of polymer chains (e.g., chemical degradation of polymer–matrix performance at elevated temperatures) [103].

Most engineering polymeric materials have randomly crosslinked networks or imperfection structures (e.g., epoxy [104], polyacrylamide hydrogels [105] and elastomers [106]). Structural imperfections involve non-uniform chain length (i.e., the total number of monomers of a chain connected through neighboring crosslinks), non-uniform functionality (i.e., the number of chains connected to a crosslink), chain entanglements and/or uncontrolled topological defects (e.g., dangling chains, cyclic loops) [107]. In this context, Lin et al. [107] investigated the fracture and fatigue threshold, defined as the intrinsic energy needed for fracture of a layer of polymer chains, behavior of ideal polymer networks (i.e., possessing uniform chain length and uniform functionality, without chain entanglement) with controlled dangling chain defect densities (see Figure 31a). Figure 31b demonstrates a schematic representation of the key concept for the defect-network fracture model: a crack propagates by fracturing unaffected polymer chains as well as affected chains due to defects that they used [108]. According to their experimental measurements (Figure 31c), no significant difference was observed between the fracture toughness ($\Gamma_{fracture}$) and fatigue threshold ($\Gamma_{fatigue}$) of an ideal polymer network with low-density dangling-chain defects (i.e., $\Gamma_{fracture} = \Gamma_{fatigue}$). In addition, both fracture toughness and fatigue threshold were independent of the cyclic loading ratio for the ideal polymer networks without chain entanglements.

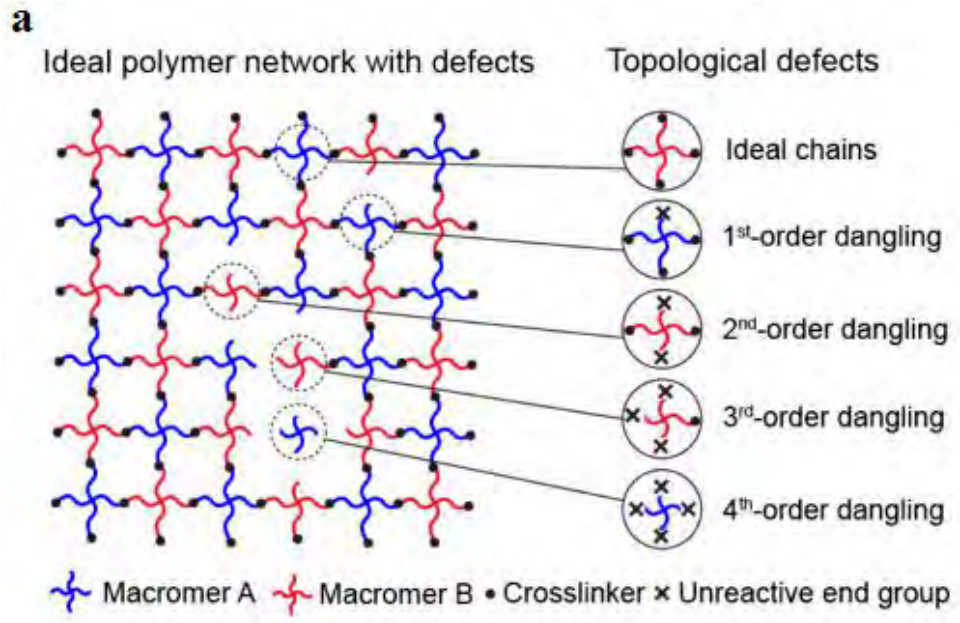

Figure 31. *Cont.*

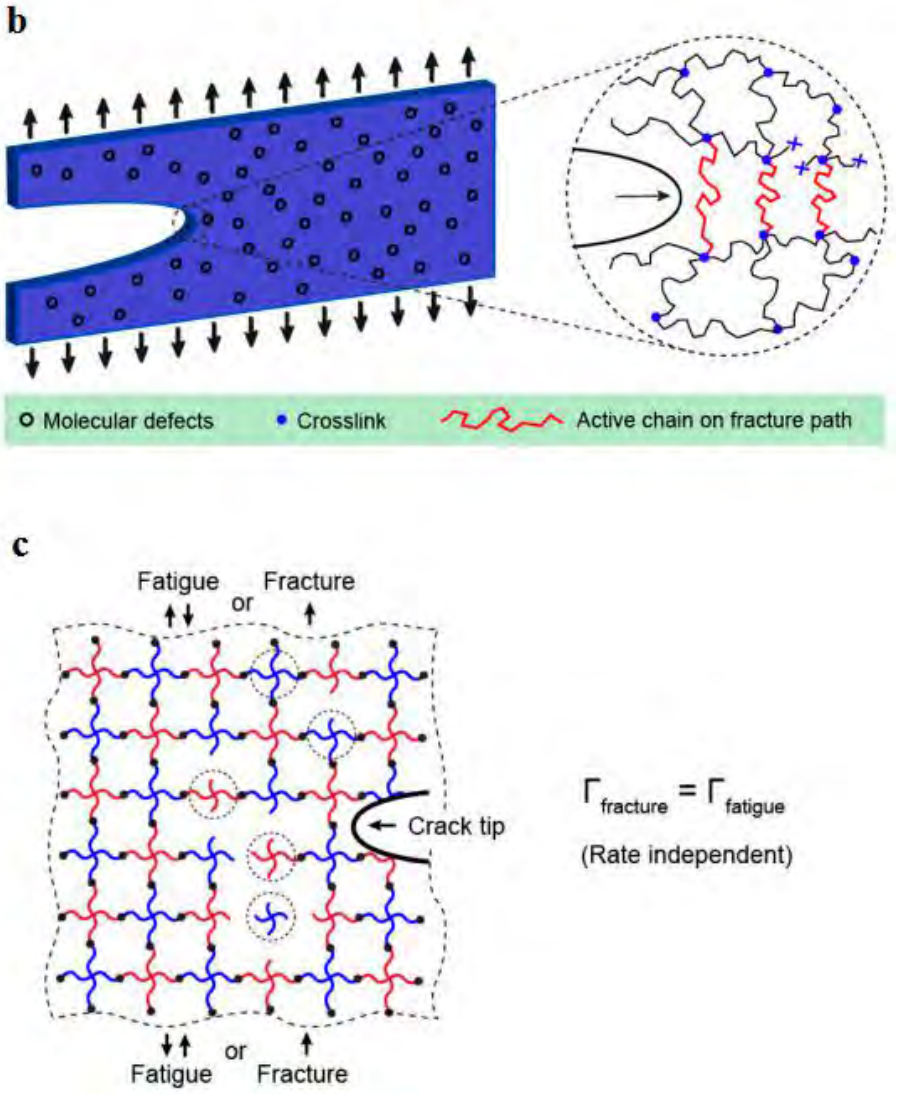

Figure 31. (**a**) Schematic representation of ideal polymer networks involving the imperfection of dangling chains (adapted with permission from Ref. [107]. Copyright © 2021 Elsevier Ltd.). (**b**) Illustration of defect-network fracture model (adapted with permission from Ref. [108]. Copyright © 2020 American Physical Society). (**c**) Schematic illustration of the equality of fracture toughness and fatigue threshold of the ideal polymer networks (adapted with permission from Ref. [107]. Copyright © 2021 Elsevier Ltd.).

In another study, Zhang et al. [109] implemented polyacrylamide (PAAm) hydrogels to investigate the influence of chain entanglement on fracture and fatigue of polymer networks under fatigue loading. Although the nearly unentangled polymer networks involve structural heterogeneity (i.e., non-uniform chain lengths and non-uniform functionalities) and topological defects (i.e., dangling chains and cyclic loops), they showed that the equality of fracture toughness and fatigue threshold is valid even in the presence of such structural imperfections (see Figure 32a [110]). Additionally, although the maximum stress–stretch hysteresis ratio of the entangled polymer network (i.e., the ratio of the dissipated mechanical energy to the total mechanical work done to the material) due to bulk dissipation of polymer networks was below 10%, the measured fracture toughness of an entangled polymer network was 16 times greater than its fatigue threshold (Figure 32b [110]). This discrepancy was because of the near-crack energy dissipation.

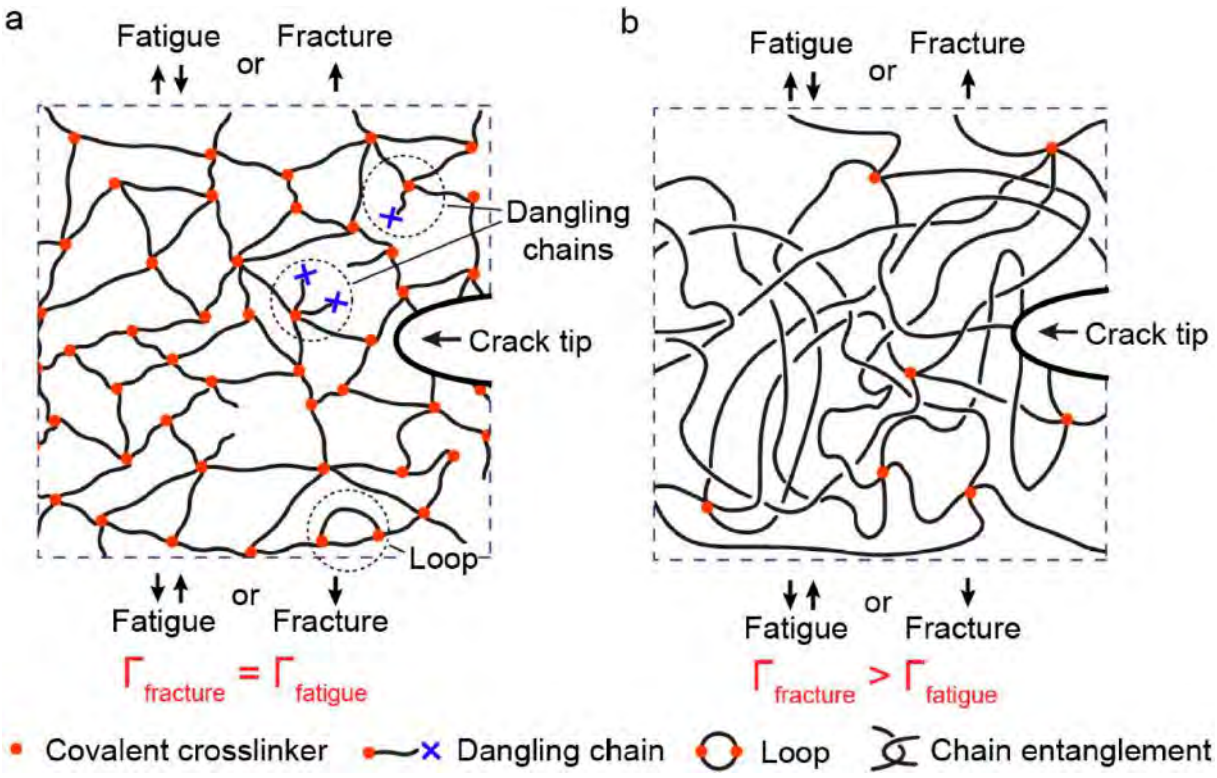

Figure 32. Fracture and fatigue of (**a**) entangled and (**b**) unentangled polymer networks under cyclic loading, adapted with permission from Ref. [110]. Copyright © 2022 Elsevier Ltd.

The fracture mechanism in an entangled polymer network under cyclic loading–unloading tests can be characterized using the bulk dissipation model [111] and near-crack dissipation. The former model refers to the toughening mechanism by the implementation of the large stress–stretch hysteresis of a bulk material, consisting of two physical processes (see Figure 33a). Firstly, the scission of a layer of polymer chains in the crack path causes the intrinsic fracture energy of the material Γ_0 equal to the fatigue threshold (i.e., $\Gamma_D = \Gamma_{fatigue}$). In the second step, material elements in a process zone around the crack experience cyclic loading as the crack propagates, as a consequence of which a significant portion of mechanical energy is dissipated in the form of a hysteresis effect. Thus, the total fracture toughness of a soft material can be described as the sum of bulk hysteretic mechanical dissipation (Γ_D^{bulk}) and intrinsic fracture energy ($\Gamma_{fatigue}$), i.e., $\Gamma_{fracture} = \Gamma_{fatigue} + \Gamma_D^{bulk}$. According to the latter model (i.e., near-crack dissipation), two physical mechanisms occur during the fatigue loading of soft materials (see Figure 33b). The first process is similar to the former one. During the second physical process, highly entangled polymer chains across the crack plane are pulled out during crack propagation, dissipating substantial mechanical energy because of numerous intermolecular interactions among neighboring chains. Moreover, scissions of chains can be delocalized to multiple adjacent layers around the crack plane as the result of remarkably stretched entangled polymer chains, leading to the dissipation of more energy than fracturing a single layer of chains. However, the pull-out and/or delocalized damage of chains in the bulk entangled polymer network under stretches might be negligible due to the comparatively lower stretch applied on the bulk entangled polymer network before failure rather than the stretch of the crack tip, resulting in relatively small stress–stretch hysteresis of the polymer chains. In the near-crack dissipation model, the overall fracture energy can be defined as the sum of the fatigue threshold and the dissipative fracture energy due to pull-out and/or delocalized damage of chains near the crack tip (Γ_D^{tip}), i.e., $\Gamma_{fracture} = \Gamma_0 + \Gamma_D^{tip}$.

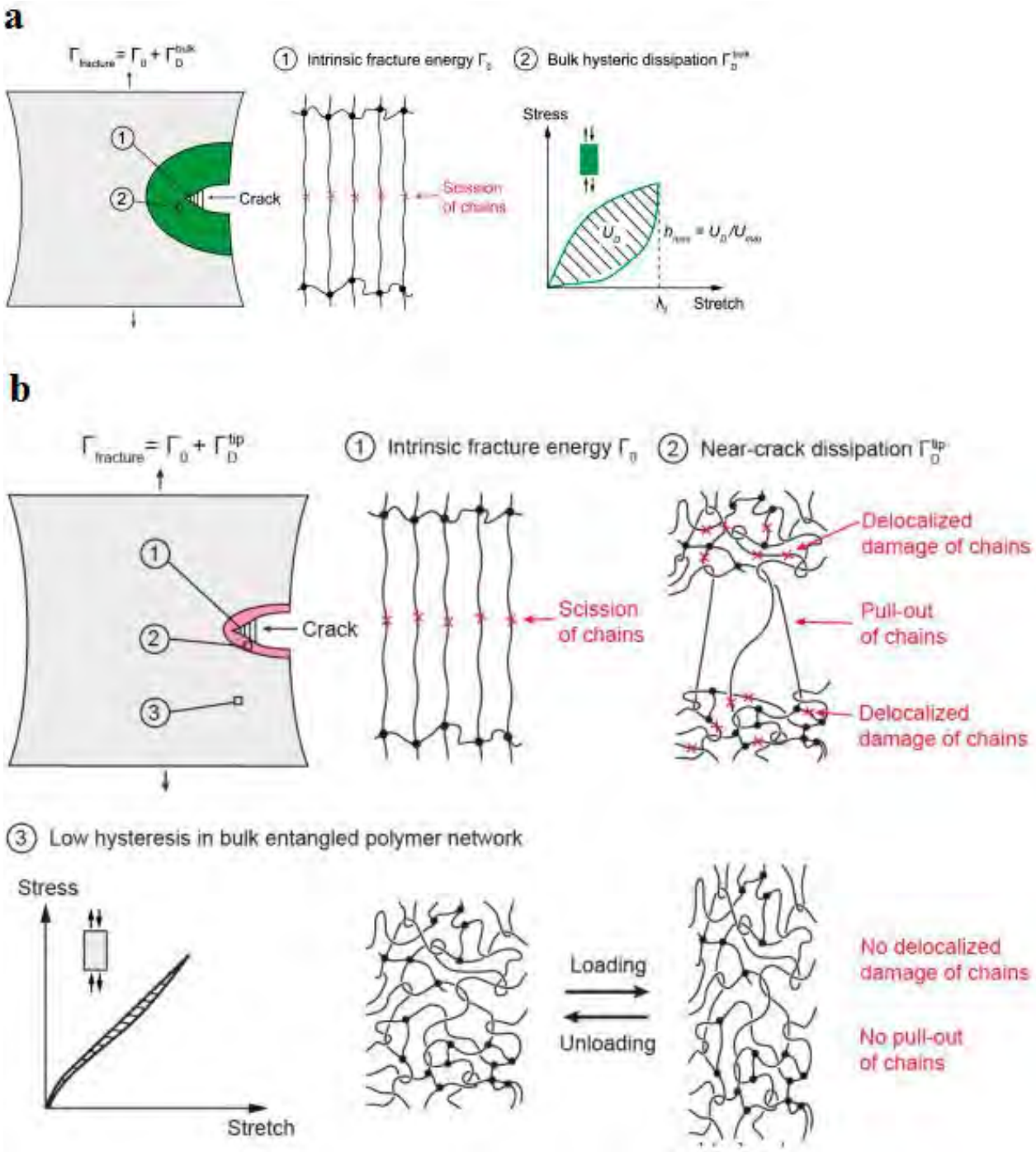

Figure 33. Schematic demonstrations of (**a**) bulk dissipation model and (**b**) the near-crack energy dissipation mechanism for entangled polymer networks, adapted with permission from Ref. [110]. Copyright © 2022 Elsevier Ltd.

Since the induced self-heating effect during fatigue loading may accelerate the dynamic behavior of polymer chains, it is worth discussing the effect of self-heating temperature. In soft materials, particularly amorphous and semi-crystalline PMCs, the rate of temperature growth caused by the self-heating effect during fatigue loading is relatively low when the ratio of maximum measured temperature through the thickness (T) to the glass transition temperature (T_g) is approximately lower than 0.8 (i.e., $T < 0.8T_g$) [112]. It should be mentioned that the maximum temperature during cyclic loading normally occurs in the

midplane of such a composite specimen, and thus determining it experimentally is very difficult due to the need to insert sensors in the midplane during the specimen manufacturing process. This may even have negative influence on the fracture mechanisms of such structures. To address this issue, it may be rational to link T_g with the specimen surface temperature (T_s), which can be experimentally measured with less complexity using IR thermography, and its value is relatively lower than the maximum temperature in midplane due to exposure to a coolant agent (e.g., air). It can be assumed that when $T_s < 0.5T_g$ (i.e., stationary self-heating mode and lower than critical self-heating temperature [1]), the dynamic modulus of polymer is primarily controlled by bond stretching and bending. This directly reflects the stiffness of van der Waals bonds binding one molecular chain to another [112]. On the other hand, when the temperature induced by the self-heating effect sees a sudden rise (phase III), thermal expansion increases the molecular separation and lowers the van der Waals forces, and consequently bonds begin to be weaker. The polymer chains slide relative to each other, and the crosslinking degree of chains changes, so van der Waals bonds may be melted thoroughly. This can lead to chemical degradation, which is directly connected with structural degradation. For this purpose, Katunin et al. [113] conducted studies for the purpose of analyzing the chemical degradation of glass–epoxy composite specimens under fatigue loading in the presence of the self-heating effect. They measured the residual cross-linking of epoxy using Raman spectra with band of 1256 cm^{-1} at the location of highest mechanical stress concentration for a set of specimens with variable degradation degrees. As can be concluded from the extracted results illustrated in Figure 34, a sudden drop appeared at the maximal self-heating temperature of 45 °C, associated with the residual cross-linking of epoxy in GFRP composite. In another study, Turczyn et al. [114] investigated how the structural and chemical degradation of PMCs are affected by self-heating phenomenon using Raman and FTIR spectroscopy. They reported that no significant structural integrity degradation was observed below the self-heating temperature of 80 °C because of residual cross-linking reactions. By contrast, intensity ratios of peaks degraded by 30% when the temperature rose to 95 °C, which was due to the reduction in the degree of cross-linking chains [115]. This confirms that the domination of thermal effects rather than mechanical effects beyond the temperature of 80 °C influences the structural integrity at lower temperatures; the self-heating temperatures below 80 °C have a negligible effect on the intensities assigned to epoxy groups. Starting from 80 °C, the relative intensity decreases, reaching its minimum at 95 °C. At this temperature, the peak intensity dropped by 30%, probably due to the occurrence of a residual cross-linking reaction.

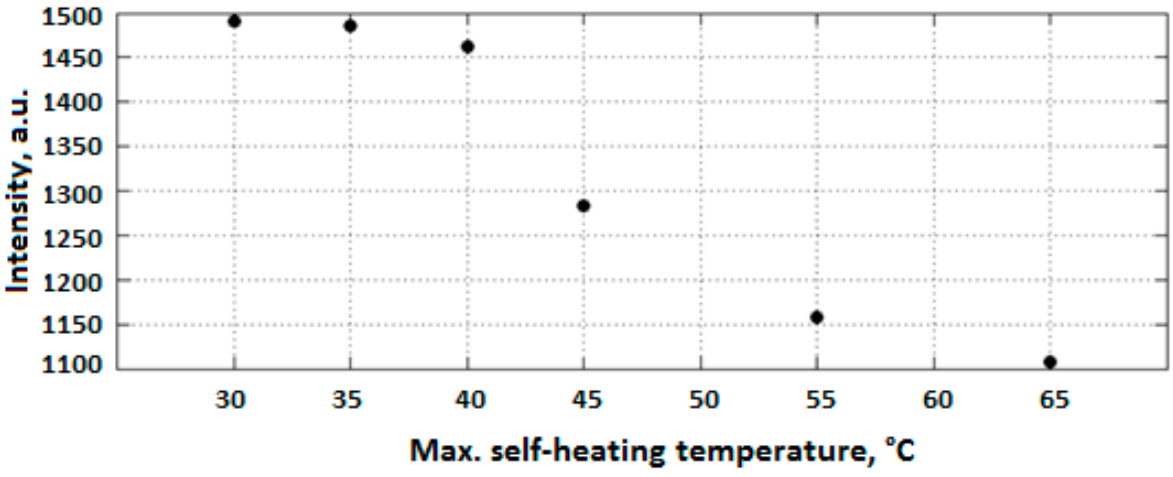

Figure 34. Intensity of Raman band versus self-heating temperature induced during fatigue loading for epoxy [1,113].

Furthermore, since the coefficient of thermal expansion (CTE) of polymers is greater than that of fibers, the residual thermal stresses may exist at the interface/interphase region between the fiber and polymer [102]. This may provoke intermittent debonding and cracking in the interphase zone at the submicron scale, and the order of the interphase zone in nanocomposites is mainly in the nanoscale [116,117]. One of the most viable solutions for the interfacial bond between the fiber and polymer matrix is to utilize chemical functionalization [118]. Therefore, measuring the level of remaining crosslinking of the polymer matrix as well as the fiber/matrix interface behavior during fatigue loading with the presence of the self-heating effect will provide comprehensive information for understanding the degree of structural degradation. Since there is no specific study quantifying the influence of the interface/interphase zone on the overall fatigue performance of FRP composites, this can be considered in further studies.

3.1.2. Microscale

The failure mechanism of PMC structures under fatigue loading at the microscale consists of crack nucleation, microcracks and open cracks. A good illustration of the different fatigue damage types in the microscale appearing in a CFRP composite, as an example, subjected to cyclic bending loading is presented in Figure 35 [78].

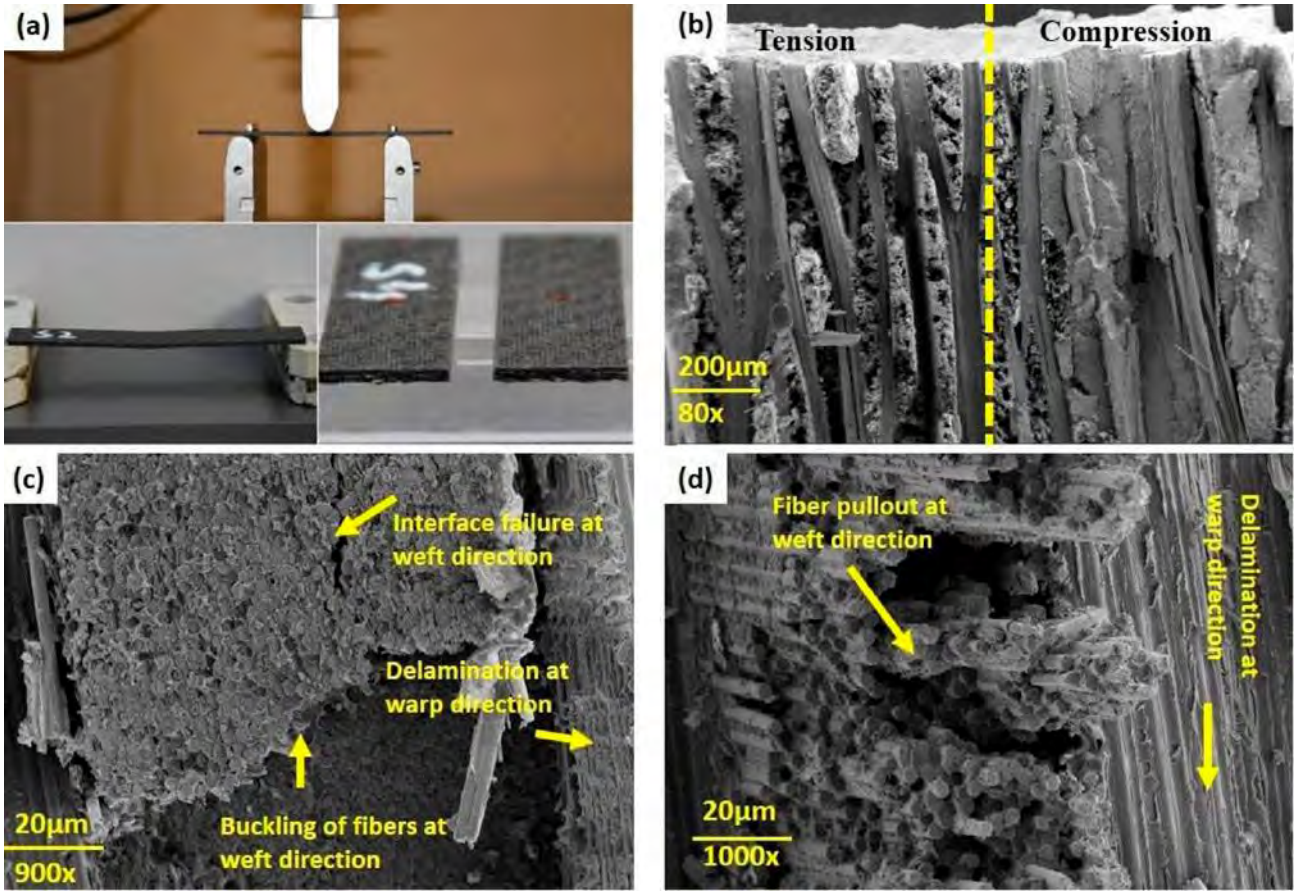

Figure 35. (**a**) Fractured/damaged composite specimen; (**b**–**d**) an illustration of different failure modes induced by three-point cyclic bending loading, adapted with permission from Ref. [119]. Copyright © 2019 Elsevier Ltd.

Regardless of the effect of voids and defects during the fabrication process, the level of crack nucleation is highly dependent on the stress intensity factor (K_I), which is a function of the topography of surfaces or interfaces [26]. For this reason, Kishi et al. [120] studied the fatigue threshold and fatigue crack propagation (FCP) of toughened epoxy blends with polyamide 12 (PA12) and core–shell rubber (CSR) polymer particles. They reported that

unlike fatigue thresholds of toughened epoxies with PA12 particles which were induced by the greater stress intensity factor (ΔK) values, fatigue thresholds of epoxies modified with CSR polymer particles were influenced by molecular weight between crosslinks (*Mc*) (see Figure 36). The gently (*Mc* of 2360 g/mol) and highly (*Mc* of 1110 g/mol) crosslinked CSR-toughened epoxy blends were extracted from comparatively lower and higher ΔK ranges, respectively, as opposed to pure epoxy blends. Crack bridging appeared in toughened epoxy blends with PA12 due to particle dominance, while crack propagation took place in toughened epoxy blends with CSR particles because of matrix dominance.

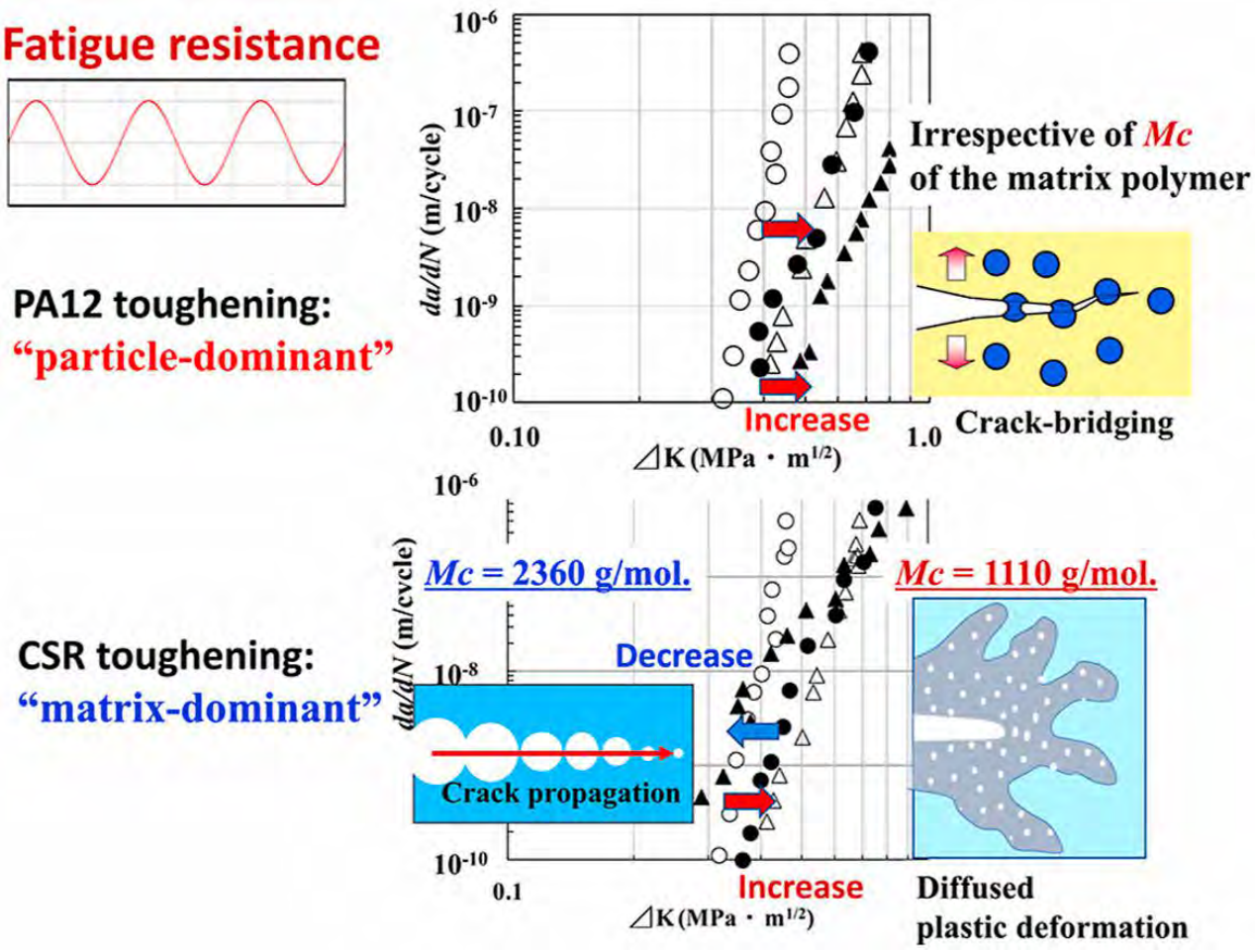

Figure 36. An exemplary illustration of the fatigue crack propagation (FCP) and fatigue threshold of moderately and highly toughened epoxy blends with PA12 and CSR polymer particles, adapted with permission from Ref. [120]. Copyright © 2021 Elsevier Ltd.

Furthermore, Rose et al. [121] studied the damage mechanisms of the milled CFRP and the laser-cut specimens under fatigue loading. In their investigation, they revealed that although the milled CFRP specimens showed some common failure modes with laser-cut samples, such specimens experienced some different failure modes as well. Figure 37a–c demonstrate the 2D virtual cross-sections in which single-fiber breakage (red circles), delamination (yellow arrows) and 0° ply cracks (green arrows) are visible. Although the 0° ply cracks were closely similar to those demonstrated in the remote laser-cut specimens, such cracks showed relatively smaller crack opening displacement and comparatively lower fiber breakage and reorientation within the ply. This specimen was also investigated in the transverse direction (90° ply cracks). Figure 37d–f illustrate these cracks on the three orthogonal planes. It was matrix cracking that took place in areas of the ply consisting of a higher density of fibers in the ZY plane, and Figure 37g–i reveal volume renderings in

different planes. The ZX plane demonstrates a zone with minimal fiber damage on the cut surface (top) and all the mechanisms at play.

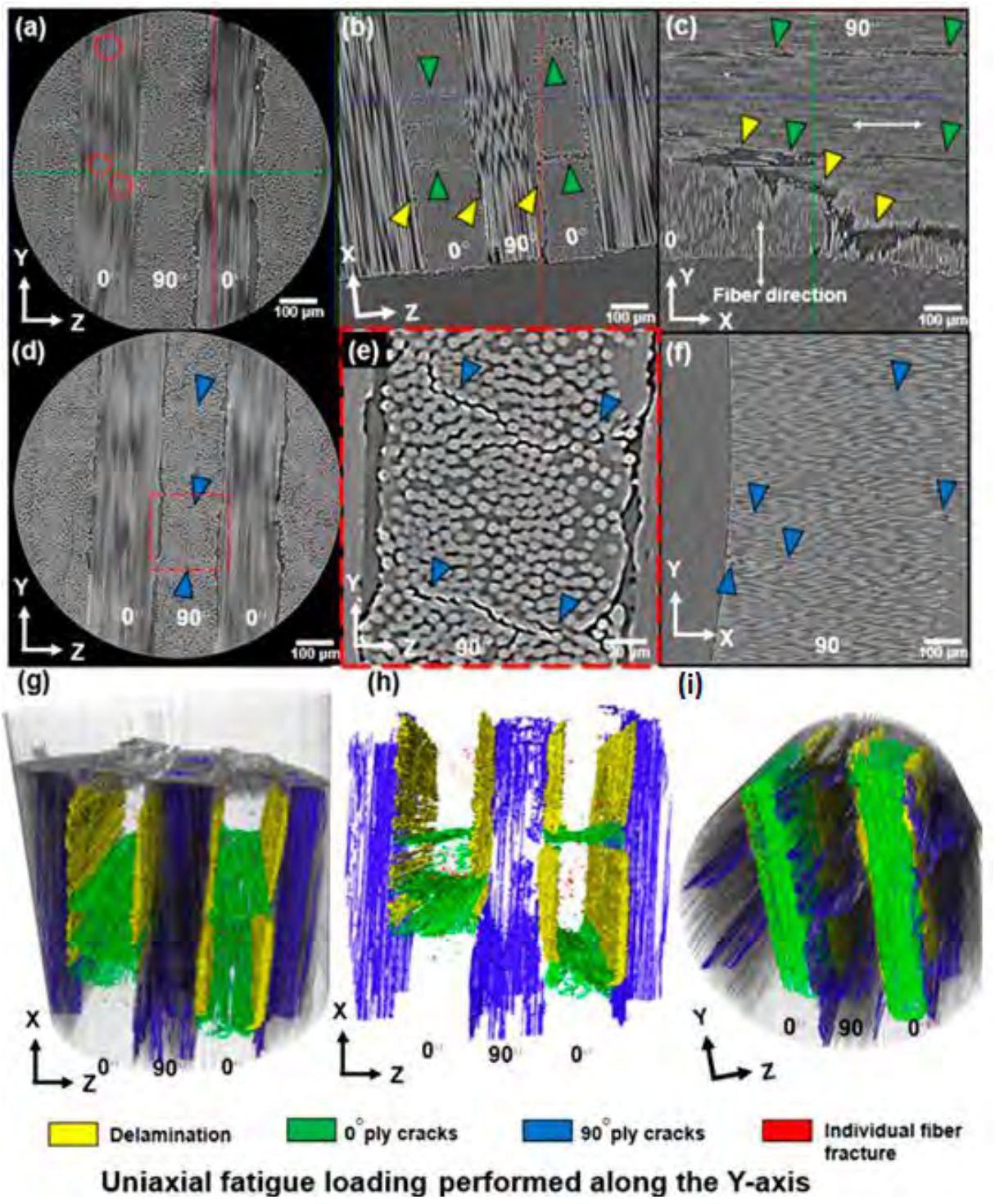

Figure 37. The 3D imaging and segmentation of the milled CFRP sample after fatigue loading process (**a**) fiber breakage in ZY plane, (**b**) combination of 0° ply cracks and delamination in ZX plane, (**c**) delamination at the interface between two orthogonal adjacent plies in XY plane, (**d**) ZY plane showing another location on 90° ply with interfiber cracking magnified in (**e**), (**f**) 90° ply cracking running horizontally in XY plane, (**g**–**i**) segmented volume renderings showing the ZX plane region of interest with minimal fiber damage on cut surface (top) and all the mechanisms in play, adapted with permission from Ref. [121]. Copyright © 2021 Elsevier Ltd.

The formation of microcracks and microdelaminations, and consequently macrocracks, in PMC structures can be taken into account as a continuous process, which can be intensified by loading conditions. To put it differently, according to the Clausius inequality statement (second law of thermodynamics), the gradient of generated entropy and intrinsic dissipation in an irreversible thermodynamic process would be constantly positive. As the result of produced entropy induced by the self-heating effect, a cyclically loaded PMC structure may experience an irreversible microstructure evolution or degradation regardless of whether a high magnitude of frequency or stress is applied. These irreversible alternations in the microscale will collectively result in entropy generation, so the entropy generation rate can remarkably change based on the amplitude of frequency or stress. In other words, as such a PMC structure is subjected to a higher frequency regime or stress/strain ratio, a greater level of entropy and consequently greater temperature value will be generated. High structural degradation in the microscale or stiffness reduction can be directly explained by an increase in the entropy generation rate [122]. For the purpose of characterizing the structural degradation of PMC structures, Balle and Backe [123] investigated the fatigue fracture mechanisms of carbon fiber-reinforced polyphenylene sulfide (CF-PPS) laminated composites by computing stiffness degradation under the VHCF regime wherein the loading frequency, maximum shear stress and load ratio were considered to be 20 kHz, 8 MPa and 0.51, respectively. During the fatigue fracture process of such a PMC specimen, they reported five separate phases, which are schematically illustrated in Figure 38. The first stage of the process was explained by the initialization and consequent accumulation of fiber–polymer interface debonding induced by the comparatively high shear stress value in the transverse direction of carbon fibers, followed by second phase, wherein the rate of fiber–matrix debonding increased, as the result of which the first cracks in transverse direction of carbon fibers appeared. CF-PPS specimen life was reduced by just below one-third (30%) due to being occupied with such damage. During the third phase, the appearance of microdelaminations between the longitudinal and transverse directions of reinforcement was reported, approximately after 35% of the entire CF-PPS specimen's lifetime, meaning less than 5% of degradation occurred in this stage involving crack lengths of 9 μm or below. This comparatively slow damage propagation and consequent stiffness degradation trend can be explained by the appearance of crack density saturation and delaminations in the interface of fiber and polymer chains [124]. The fourth stage took place when the metadelaminations propagated, occurring after approximately the two-thirds (70%) of the entire specimen fatigue life, containing maximum crack lengths of about 25 μm or less. It should be mentioned that the crack length which provokes the failure is highly dependent on the dimension of the specimen. For example, when the dimension of the structure is high, the crack length of 25 μm may not cause failure.

As a guideline, it should be mentioned that when the size of the crack is microscale, using nanoparticles such as CNTs can extend the fatigue life of the PMC structure. Figure 39 schematically reveals how the fatigue life of a CFRP composite can be extended as the result of adding CNT to a polymer [125]. The black line depicts the degradation process of an unmodified polymer matrix, while the dotted red lines illustrate the degradation mechanisms of a matrix modified with CNTs. It is noteworthy to conduct comprehensive studies in this area due to its practical importance. For example, depending on the loading conditions and geometry, the influence of adding different nanoparticles can be investigated.

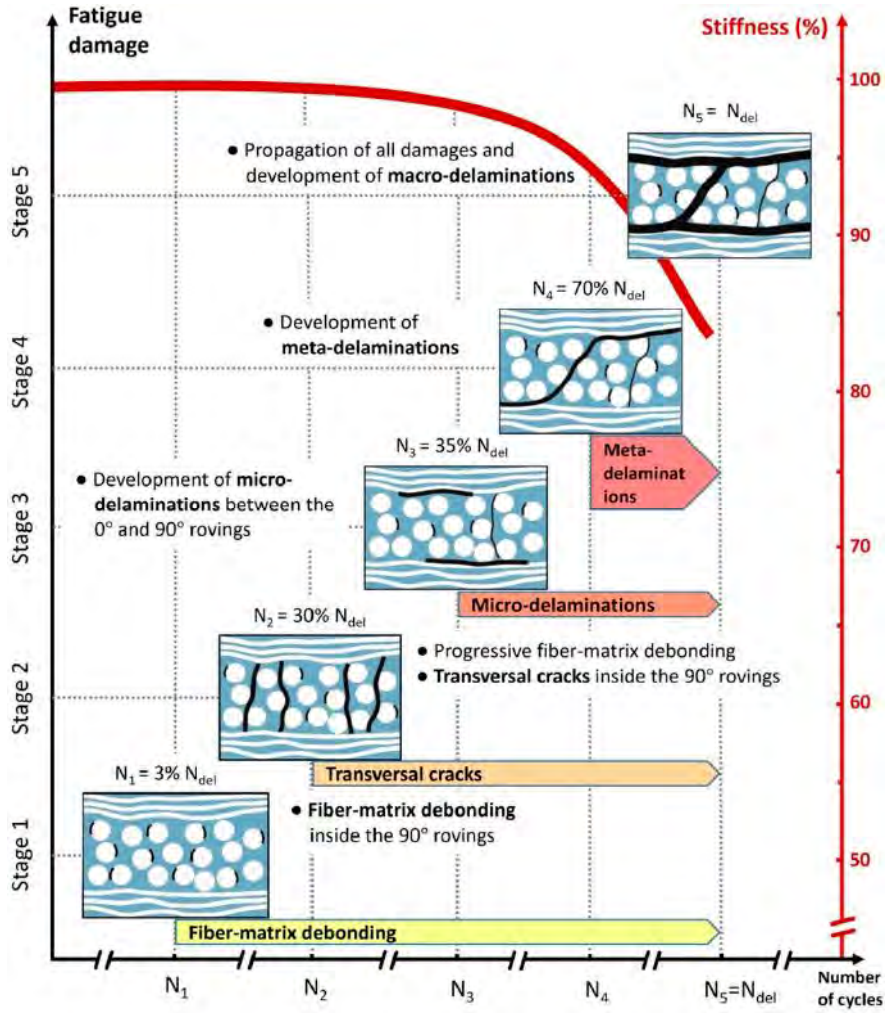

Figure 38. Characterizing fatigue damage propagation of CF-PPS within different stages, adapted with permission from Ref. [58]. Copyright © 2021 Elsevier Ltd. [123].

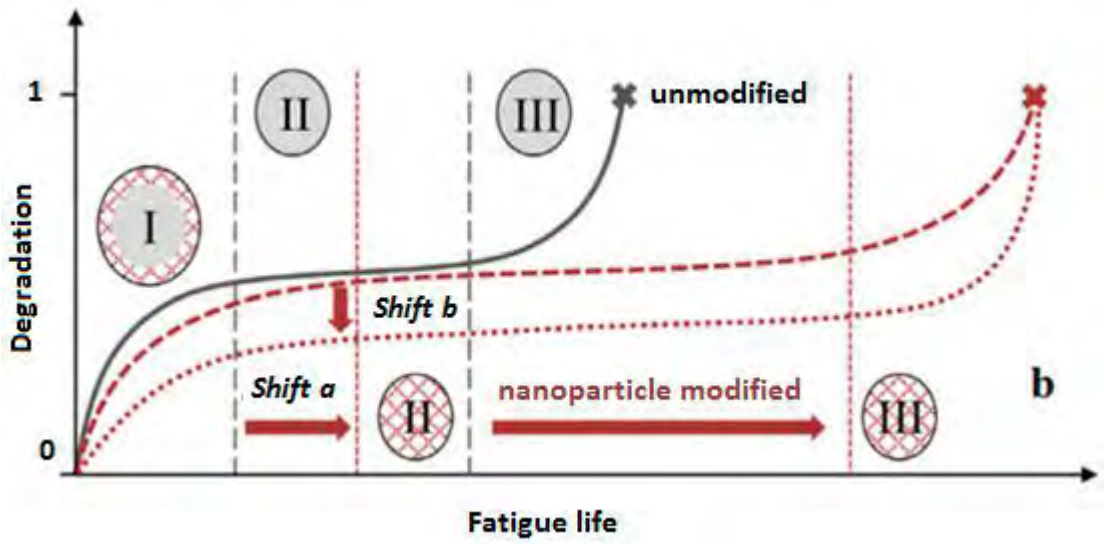

Figure 39. A schematic representation of extending fatigue life of CFRP composite led by adding through an extension of phase I and II (shift a) and a less pronounced degradation increase (shift b), adapted with permission from Ref. [125]. Copyright © 2014 Elsevier Ltd.

3.1.3. Macroscale

The accumulation of the above-mentioned micro damage types (stages I to IV in Figure 38) in the PMC structure can continually develop macrocracks and delaminations [126], resulting in the ultimate failure of the material (stage V in Figure 38). Within the final stage, a high level of stiffness degradation is observed, which can be justified by the formation of macrodelaminations. Since the growth rate of fatigue damage accumulation was very high in this stage, structural failure occurred, which is also named sudden death. In general, the occurrence of ultimate failure is the direct consequence of the contributions of mechanical fatigue loading, thermal gradients, chemical ingress and environmental conditions [26]. Nevertheless, in such a problem, stages IV and V (i.e., the main stages contributing to the failure) may be justified by the generated high self-heating temperature values induced during fatigue loading on the surface of the composite specimen ($\Delta T > 20\ ^{\circ}C$).

Using a 3D microscope for the purpose of monitoring failure propagation and morphologies, Fan et al. [127] investigated the fatigue behavior of a 3D orthogonal carbon/glass fiber hybrid composite under three-point bending fatigue. Figure 40 depicts the front and back cross-sections of the used 3D hybrid composite from the weft yarn direction views.

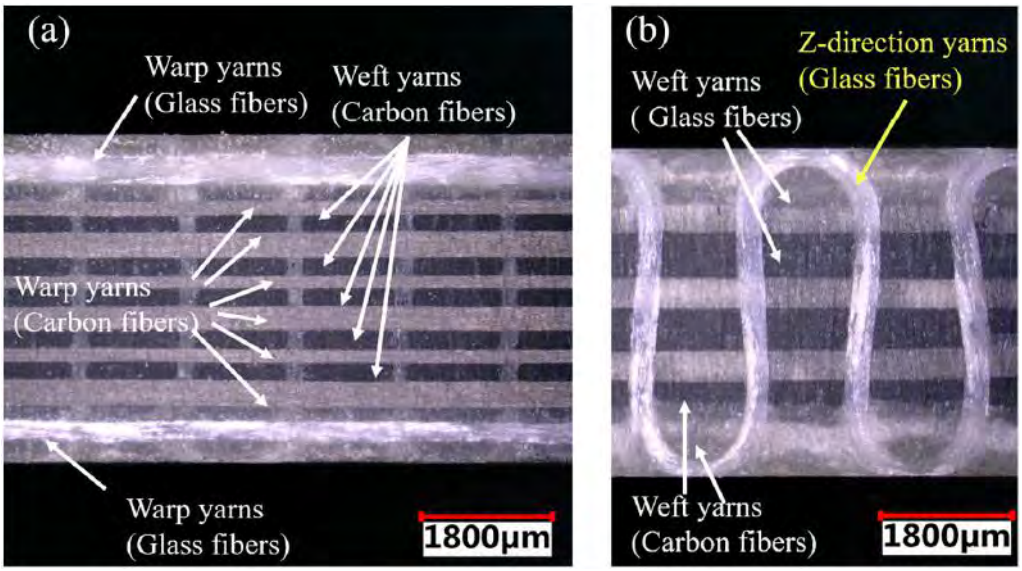

Figure 40. The front (**a**) and back (**b**) cross-sections of the 3D hybrid composite from the weft yarn direction views, adapted with permission from Ref. [127]. Copyright © 2019 Elsevier Ltd.

The exemplary ultimate fatigue failure morphologies of the laminated hybrid composite along with warp yarn directions on a macroscopic scale at three different stress levels, namely (a) and (a') 60%, (b) and (b') 55%, (c) and (c') 50%, are presented in Figure 41. According to the results extracted for the laminated hybrid composite, a shear damage band was observed in the specimen subjected to the stress level of 60%, while both shear damage and local delamination were captured in such a specimen when subjected to 55% of the maximum stress. When the stress levels decreased to 50%, the damage of the composite slowly propagated to the entire region area of such a specimen in the form of delamination. This means that the relatively lower stress was unable to cut the fibers at one time, leading to propagation of the crack parallel to the longitudinal direction of the fibers.

Similarly, lateral fracture morphologies of the 3D hybrid composite in the macroscopic scale at three different stress levels, namely (a) and (a') 60%, (b) and (b') 55%, (c) and (c') 50%, are presented in Figure 42. Figure 42a–c illustrate the failure of the surface without the Z-direction yarns, while Figure 42a'–c' denote the surface damage involving the Z-binder yarns. The results showed that the stress level of 50% was reported to be comparatively the most critical condition for both laminated and 3D hybrid composites. This can be explained

by how the greater stress level provoked the failure without damage evolution. Due to the Z-direction yarn-controlled propagation of the crack in the longitudinal direction of fibers, no delamination damage was monitored.

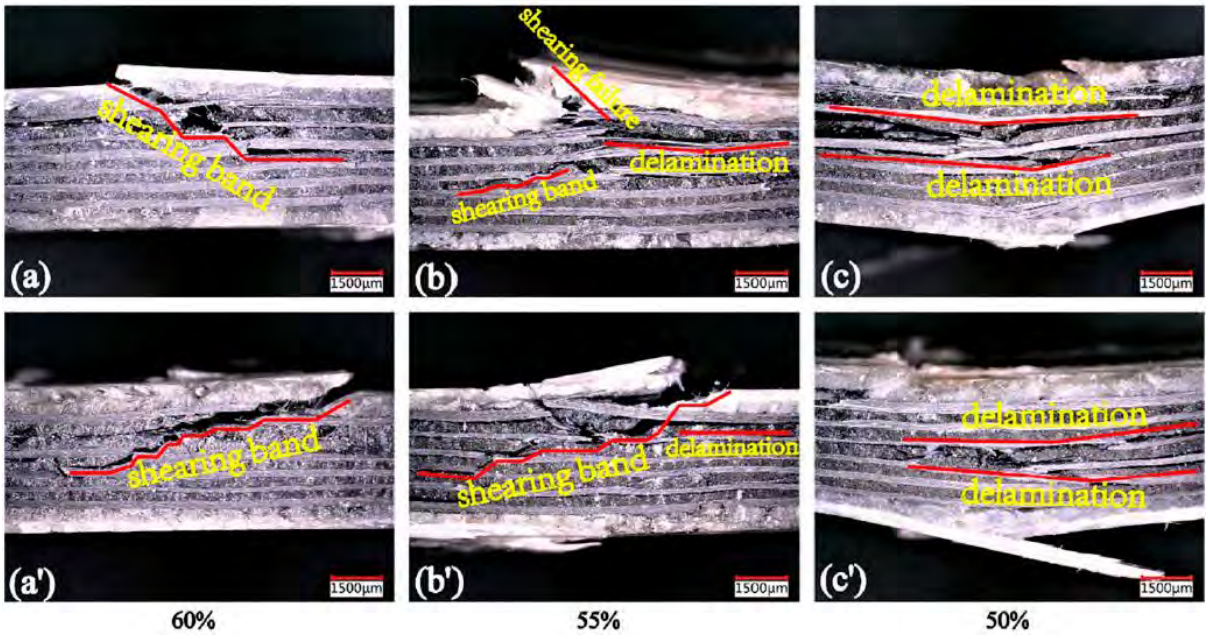

Figure 41. Exemplary fatigue failure mechanism of a laminated hybrid PMC structure under different stress levels: (**a**,**a′**) 60%; (**b**,**b′**) 55%; (**c**,**c′**) 50%, adapted with permission from Ref. [127]. Copyright © 2019 Elsevier Ltd.

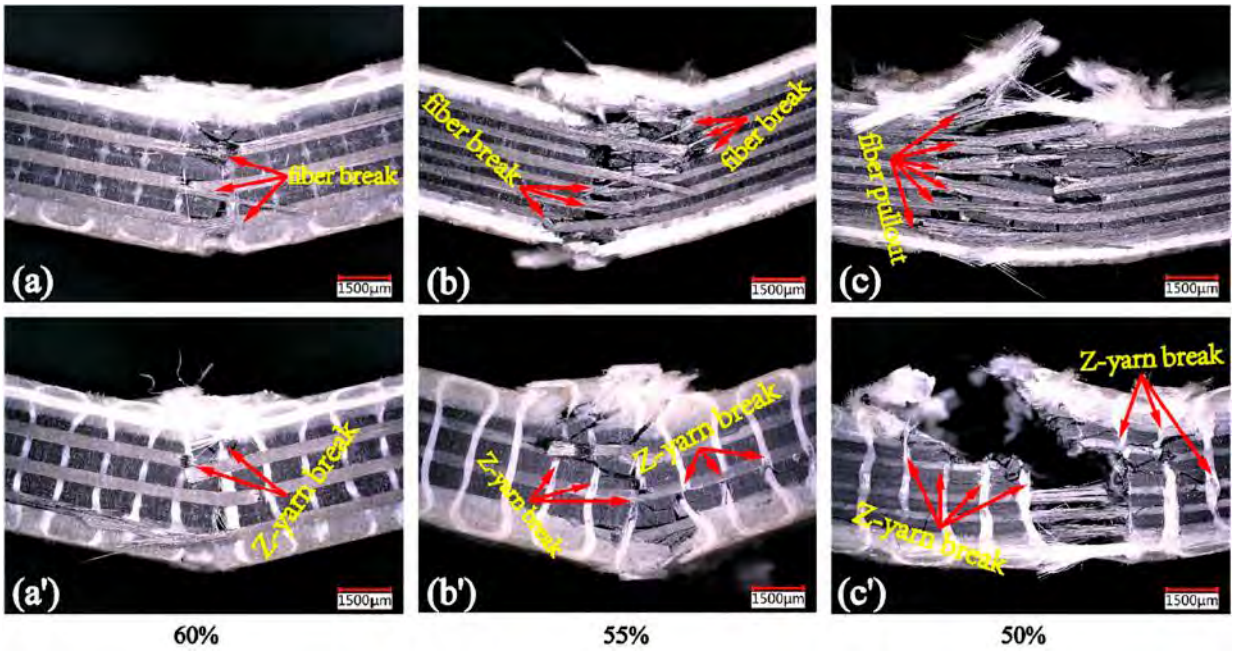

Figure 42. Exemplary fatigue failure process of a 3D hybrid PMC structure under different stress levels: (**a**,**a′**) 60%; (**b**,**b′**) 55%; (**c**,**c′**) 50%, adapted with permission from Ref. [127]. Copyright © 2019 Elsevier Ltd.

On the other hand, drilled holes are macrodefects, leading to reduction in the ultimate strength of a PMC structure by 50, depending on the stacking sequence [128]. Due to the stress concentration near the areas of holes, the self-heating effect may be comparatively

more critical in such regions. An exemplary thermographic image for a cyclically loaded CFRP specimen involving open holes with stress concentrations dominated by self-heating temperature is presented in Figure 43 [121]. Since PMC structures may consist of holes in their real lifetimes, it is noteworthy to conduct further studies in this field.

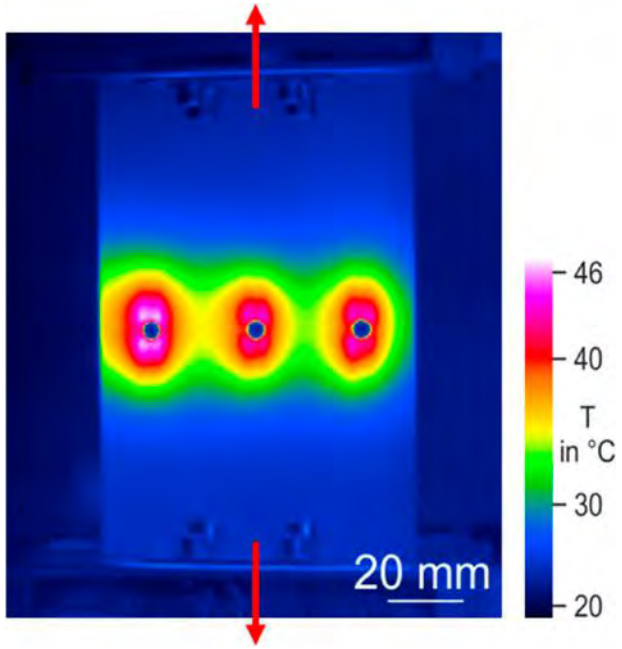

Figure 43. Self-heating temperature profile induced by the cyclic fatigue test extracted from thermography, adapted with permission from Ref. [121]. Copyright © 2021 Elsevier Ltd.

3.2. Criticality of the Self-Heating Effect in Polymers and PMCs

The concept of the critical self-heating effect was initially introduced by Ratner et al. [129], who described it as a critical stress at thermal fracture or a critical temperature value appearing under this critical stress. Moreover, Gumenyuk et al. [130] explained the criticality of the self-heating effect by a remarkable temperature growth beyond which the self-heating temperature history profile becomes unstable, provoking softening in viscoelastic materials. Katunin [131] described the self-heating effect as a measure of degradation degree of a PMC structure subjected to cyclic loading (e.g., bending fatigue). Later, Kahirdeh and Khonsari [132] developed a similar criterion based on thermal and AE responses for characterizing the structural degradation criticality of PMCs under fully reversed bending fatigue loading. In general, the critical self-heating in PMCs can be defined as the temperature at which damage initiates, and accordingly below which such PMC specimens can be safely maintained [1]. The critical self-heating temperature value can be determined using a variety of techniques, reviewed in [1]. As tested for GFRP composites by the authors, the most effective of these techniques are X-ray ICT, morphological analysis (SEM), approximation of self-heating temperature history curves and variability of self-heating temperature distributions. Katunin and Wronkowicz [3] performed fatigue tests for GFRP specimens until obtaining the critical self-heating temperature value on the tested specimens' surfaces using X-ray CT scans. They proposed a general phenomenology for characterizing the structural degradation of PMC structures dominated by the self-heating effect. They reported that a higher temperature obtained on the specimen's surfaces induced by the self-heating effect resulted in higher crack density, volume of cracks and volume of delaminations (see Figure 44). Thus, critical self-heating temperature can act as a catalyst in terms of accelerating the volume of cracks and delaminations in a PMC specimen under fatigue. This increase in crack and delamination densities will provoke the formation of macrocracks or structural degradation at the macroscale. This can also be presented in the form of residual stiffness, which can be implemented as input for FEM software packages for further mechanical analysis [133]. To the best of the authors' knowledge, cracks and

delaminations exist below this temperature, but they do not have influence on the mechanical properties of a considered structure and can be negligible.

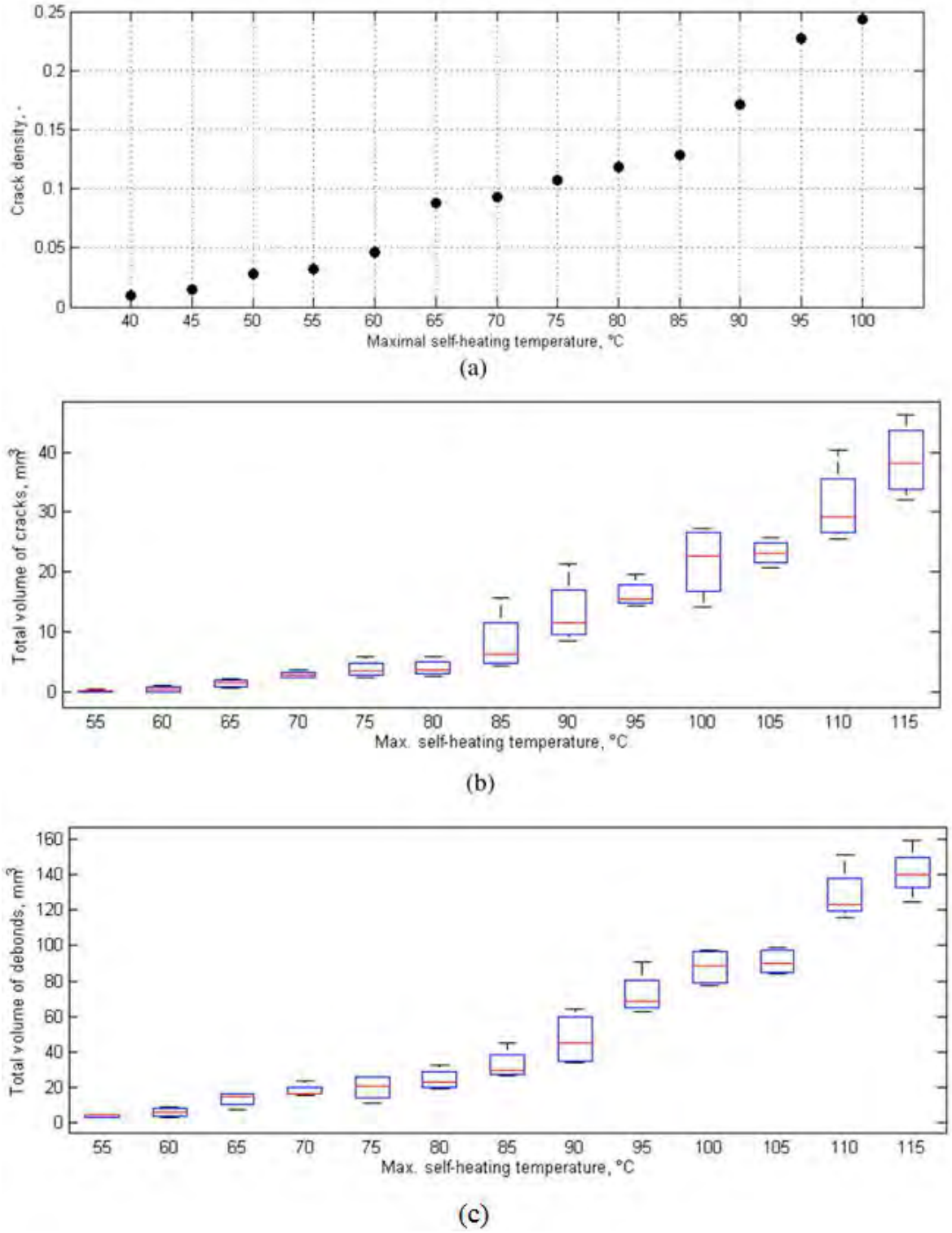

Figure 44. (**a**) Crack density [1], (**b**) total volume of cracks and (**c**) total volume of debonds induced by fatigue loading dominated by self-heating temperature, adapted with permission from Ref. [3]. Copyright © 2017 Elsevier Ltd.

Furthermore, Magi et al. [28] proposed a model for monitoring the structural degradation of a laminated composite blade under fatigue loading, working based on critical

self-heating temperature. In other words, the rate of structural degradation at a given excitation level suddenly changed as the critical self-heating temperature appeared on the specimen surface (see Figure 45). As the recommendation, the specimen surface temperature should be monitored and controlled to experience a safe range of temperature (below the critical self-heating temperature). Otherwise, thermal fatigue failure may occur before mechanical failure, which is undesirable. For this objective, the viable solutions are deeply reviewed and elaborated in Section 4.

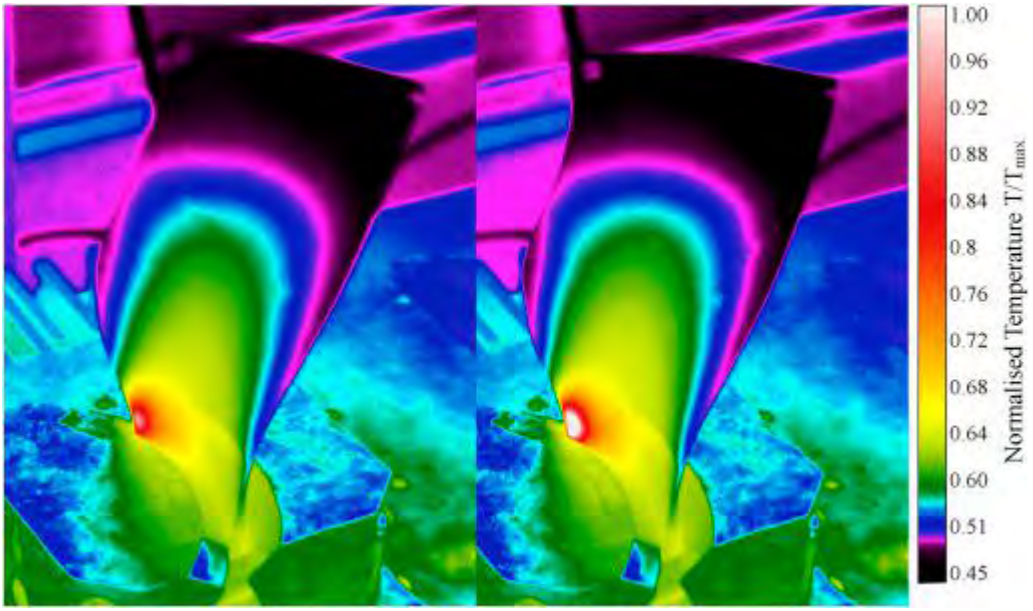

Figure 45. An exemplary illustration of dominating self-heating process in a composite blade: (**left**) before and (**right**) after the occurrence of the critical self-heating temperature, adapted with permission from Ref. [28]. Copyright © 2016 Elsevier Ltd.

3.3. Application of the Self-Heating Effect in Nondestructive Testing (NDT)

Although the self-heating effect may negatively provoke structural degradation, this concept has been interestingly employed for a variety of engineering applications involving NDT damage characterization in CFRP composites [28,134]. This concept was coupled with classical vibrothermography as an NDT technique for detecting debonding-like defects in a hybrid plate (aluminum alloy glued with a cork plate) [135] and damage detection in polymer-based structures [136,137]. Additionally, Katunin and Wachla [138] developed in-house self-heating-based vibrothermography (SHVT) as an accelerated NDT technique based on the excitation of a structure at multiple resonant frequencies [139] for monitoring fatigue cracks and damage in such structures. As a result of the cyclic mechanical excitation of such a structure, a noticeable amount of mechanical energy is dissipated, which highly depends on the magnitude of resonant frequencies. In this way, the higher magnitudes of resonant frequencies of such a structure are excited, the higher amount of thermal energy will be stored due to the viscoelastic behavior of the polymer. The extracted thermal energy is the primary source of the self-heating phenomenon (as was elaborated earlier). Vaddi et al. [140] also implemented SHVT for detecting fatigue damages in viscoelastic polymer coatings. It should be mentioned that SHVT can be implemented in a wide range of frequencies. For example, Katunin and Wachla [138] implemented SHVT in a comparatively low frequency regime (varying from 0 to 1.25 kHz), while Vaddi et al. [140] employed it for high frequency loading (ranging from 19 kHz to 38 kHz). Figure 46 depicts the exemplary results of damage detectability enhancement using the SHVT technique for notch-type damage with different depths (D), ranging from 0.25 mm to 1.5 mm. As can be seen, the thermal signatures of the introduced defects were completely detectable when the depth of defects was 1 mm or more, which can reveal the effectiveness of the developed

approach [138]. It should be mentioned the temperature appearing on the specimen surface during the application of the SHVT technique is significantly lower than the critical self-heating temperature, avoiding premature thermal failure. Furthermore, Maio et al. [141] implemented the SHVT technique for the purpose of monitoring the dynamic properties of laminated CFRP composites during the crack propagation caused by fatigue.

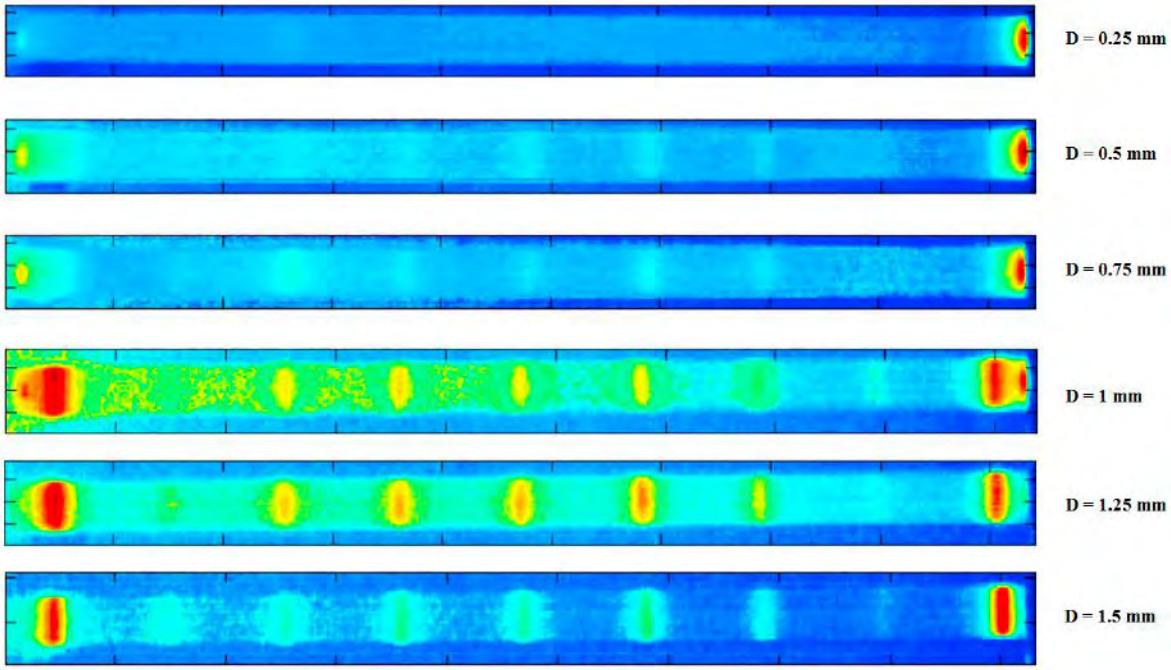

Figure 46. The exemplary results of defect detectability for notch-type damage with different depths using the SHVT method, adapted with permission from Ref. [138]. Copyright © 2018 Elsevier Ltd.

4. Concepts of Preventing Structural Degradation in Cyclically Loaded PMCs

As shown in previous sections, the appearance of the self-heating effect can significantly shorten the structural lifetime, which is especially important during fatigue testing of polymers and PMCs. Therefore, a limitation of the influence of the self-heating effect on a structure subjected to fatigue loading is of primary interest in numerous applications. In this section, two different concepts consisting of cooling scenarios and optimal materials selection and design are analyzed for the purpose of preventing or limiting the intensive structural degradation induced by the self-heating effect in both polymers and FRP composite structures under high-magnitude vibrations or fatigue loading.

4.1. Cooling Scenarios and Techniques Considering Thermodynamics

Investigating the effect of different cooling scenarios in cyclically loaded polymer–matrix structures is of key interest and practical importance since this topic has not been studied deeply yet. When the value of the surrounding temperature during the fatigue testing of a polymeric or composite specimen is greater than room temperature (RT), it plays the role of a heating system, which intensifies the self-heating effect due to thermal energy generation caused by such a high temperature. This will consequently provoke a noticeable level of structural degradation in PMCs. Therefore, the initial assumption when implementing a cooling scenario is to conduct such high-magnitude vibration excitations or fatigue tests at RT or below. In addition, to control surrounding temperature, it is also of paramount importance to monitor and limit the polymeric specimen surface temperature during such cyclic tests in order to prevent the structural degradation induced by the self-heating effect. For this objective, the influence of cooling scenarios in terms of environmental and operational aspects in cyclically loaded PMC structures is discussed, allowing us to define efficient coolant systems for such tests.

4.1.1. Environmental Factors

Regarding the conditions in which such structures are planned to be implemented, the structures may experience different humidity levels and operating temperatures even before being subjected to any mechanical fatigue loading. The moisture content [142] and ambient temperature can be assumed to be the environmental factors that may have an influence on the degradation of polymeric structures under such cyclic tests. A good illustration of this can be found in marine applications involving static off-shore structures and sea-going vessels [143,144]. This may call into question whether moisture content has a negative influence on the mechanical performance of such structures. For this purpose, Chen et al. [145] experimentally investigated how the cyclic softening/hardening and mechanical energy dissipation of polyamide-6 (PA6) under different applied strain amplitudes at room temperature (RT) are affected by the relative humidity (RH) levels. They showed that the lower RH level relatively resulted in a noticeable temperature increase on the specimen surface. In addition, as the level of RH increased, the level of recoverable viscoelastic deformation increased. Moreover, they illustrated that the average stress relaxation of PA6, regardless of the level of RH, took place in a symmetric cyclic loading with mean tensile strain so that its magnitude saw a reduction as RH increased, while it increased as the result of increasing mean strain. By contrast, the mean temperature and cyclic softening/hardening of PA6 were affected insignificantly by the applied mean strain. In another study, Gholami et al. [146] developed a micromechanical finite element method (FEM)-based degradation model in order to investigate how the elastic properties of FRP composites are influenced by the hygrothermal conditions. They revealed that increasing both temperature and humidity simultaneously provoked a significant reduction in the transverse Young's modulus and shear modulus of such polymeric specimens. In other words, when an FRP composite was tested under the RH of 95% and the operating temperature ranging from 23 °C to 150 °C, for merely a period of one hour, the transverse Young's modulus and shear modulus of such a composite were degraded by 90% and 80%, respectively. By contrast, during the desorption stage, although such mechanical properties were also initially degraded because of the extreme temperature value, the stiffness (Young's moduli) of such a composite increased as the direct consequence of the acceleration of the moisture desorption mechanism. Nonetheless, when such structures are subjected to the high cyclic fatigue regimes or extremely high-magnitude vibration excitations, they may experience relatively high temperature values on their surfaces due to presence of the catastrophic self-heating phenomenon (e.g., rocket propellant composites [22] or a driver shaft [35,36]). In such applications unlike marine ones, moisture may even have an advantageously positive influence, playing the role of a coolant agent for such structures (with the assumption of limiting the presence of moisture content merely on the polymeric specimen surface, but not inside a structure); as a result, the level of structural degradation of such structures may favorably illustrate a downward trend. This leads to the following observation: as the area of a cyclically loaded PMC structure exposed to the humidity of surrounding directly (the area between two grips) and indirectly (the regions located in holding grips) increases, the temperature growth occurring on the specimen surface may decrease [145]. As the direct consequence of this, a relatively lower structural degradation may occur. Further research is required to effectively quantify how the structural degradation of cyclically loaded PMC structures dominated by the self-heating effect are influenced by the moisture content.

In [87], Katunin and Wachla discussed how the ambient temperature can take a center stage as a causative factor contributing to the structural degradation of PMC structures under cyclic loading, which may have a significant influence on the overall mechanical and fatigue performance of operating structures. In general, variation in ambient temperature can play the role of a coolant system or a heater. For this purpose, Charalambous et al. [147] employed the four-point bending test in order to investigate the fatigue performance of CFRP composites under various ambient temperatures (−50 °C, 20 °C, 50 °C and 80 °C). The authors demonstrated that the ambient temperature may act as a catalyst in

accelerating or postponing the influence of delamination growth in PMCs, which may be highly dependent on whether the loading belongs to a quasi-static or fatigue loading regime. They reported that the delamination rate of such a composite under fatigue test saw an upward trend as the direct consequence of an increase in ambient temperature. Additionally, the rate of crack propagation at 80 °C was twice greater than the same figure at RT for an unchanged normalized energy release rate value. Voudouris et al. [27] experimentally studied how the failure time of cyclically loaded CFRP composites dominated by the self-heating effect is influenced by different elevated ambient temperatures (25 °C, 50 °C, 65 °C and 75 °C). As they reported, the propagation of delamination was comparatively faster as the result of greater ambient temperature under the fixed excitation frequency and strain values.

If the ambient temperature is lower than RT, this can function as a cooling phenomenon to prevent intensive structural degradation in cyclically loaded PMC structures. Thus, industries and researchers can come forward with viable solutions by providing a cooler ambient temperature in order to address the catastrophic self-heating phenomenon resulting from either fatigue loading or high-magnitude vibration excitations. Regarding providing the system with a relatively low temperature for such experiments, one of the viable solutions is to carry out fatigue tests on samples exposed to different gases, e.g., CO_2. For this purpose, Charalambous et al. [147] implemented a carbon dioxide (CO_2) skid comprising 15 cylinders of liquid CO_2 gas attached to the environmental chamber through a decanting hose to provide the temperature of −50 °C for fatigue testing up to 10^6 cycles with a frequency of 5 Hz, that is, approximately 57 h for a fatigue test. To effectively address the tendency of formation of an ice layer on the grooved roller surface, anti-icing liquid was used on the rollers and the end-tab area. An unimportant difference regarding the mean bending moment was needed for propagating delamination to observe the results induced at room temperature and at −50 °C. During the fatigue experiments, the gas injection took place in regular intervals in order to keep the temperature at the constant value of −50 °C, they exploited the large bending moment drops following delamination onset. The main causative factor contributing to this can be explained by more a brittle polymer matrix induced by low temperature, leading to increased stick–slip behavior [148]. In another study, Bartkowiak et al. [17] investigated how the three-point bending fatigue properties of hybrid sheet molding compound (SMC) composite-reinforced with discontinuous glass fibers (DGF) in the core and unidirectional continuous carbon fibers (UCCFs) in the face layers up to 2.6×10^6 cycles are influenced by different ambient temperatures (−20 °C, 21 °C and 80 °C). They implemented liquid nitrogen (N_2) as the coolant agent for the purpose of providing a temperature of −20 °C for experiments. They exploited that increasing the ambient temperature from 21 °C to 80 °C for DGF-reinforced SMC and hybrid [UCCF/DGF/UCCF] SMC samples provoked a remarkable reduction in flexural strength by 24% and 7% at a quasi-static strain rate (2 mm/min) and 14% and 12% at a fatigue strain rate (90 mm/min), respectively. Nevertheless, decreasing the ambient temperature to −20 °C resulted in increases in flexural strength by 2% and 3% for quasi-static strain and fatigue strain rates, respectively. They also revealed that when the temperature of the specimen was reduced from 21 °C to −20 °C using liquid nitrogen, the flexural strength of the hybrid SMC composite experienced a downward trend, which was increased by 25% and 14% in quasi-static and fatigue strain regimes. The S-N results obtained for DGF-reinforced SMC composite specimens and hybrid [UCCF/DGF/UCCF] SMC specimens under three-point bending fatigue load (R = 0.1 and f = 5 Hz) exposed to three separate temperatures with failure probabilities of PS = 10% and PS = 90% are illustrated in Figure 47 [17]. As can be seen from Figure 47a, the fatigue life expectancy of DGF-reinforced SMC specimens exposed to a lower temperature (−20 °C) was comparatively longer than that of specimens subjected to higher temperature values. When such composites were subjected to temperature values of 21 °C and 80 °C, they revealed roughly similar fatigue behavior. According to Figure 47b, the residual fatigue life of hybrid [UCCF/DGF/UCCF] composites was highly dependent on ambient temperature; i.e., with the decrease in the

temperature such a hybrid composite was exposed to, there was an increase in the fatigue life obtained. For example, the fatigue limit of such composites subjected to the liquid nitrogen at −20 °C was roughly 100 MPa higher than such data obtained at RT. Therefore, implementation of liquid nitrogen as a coolant agent has the capability to extend the fatigue life of cyclically loaded discontinuous and/or continuous FRP composites.

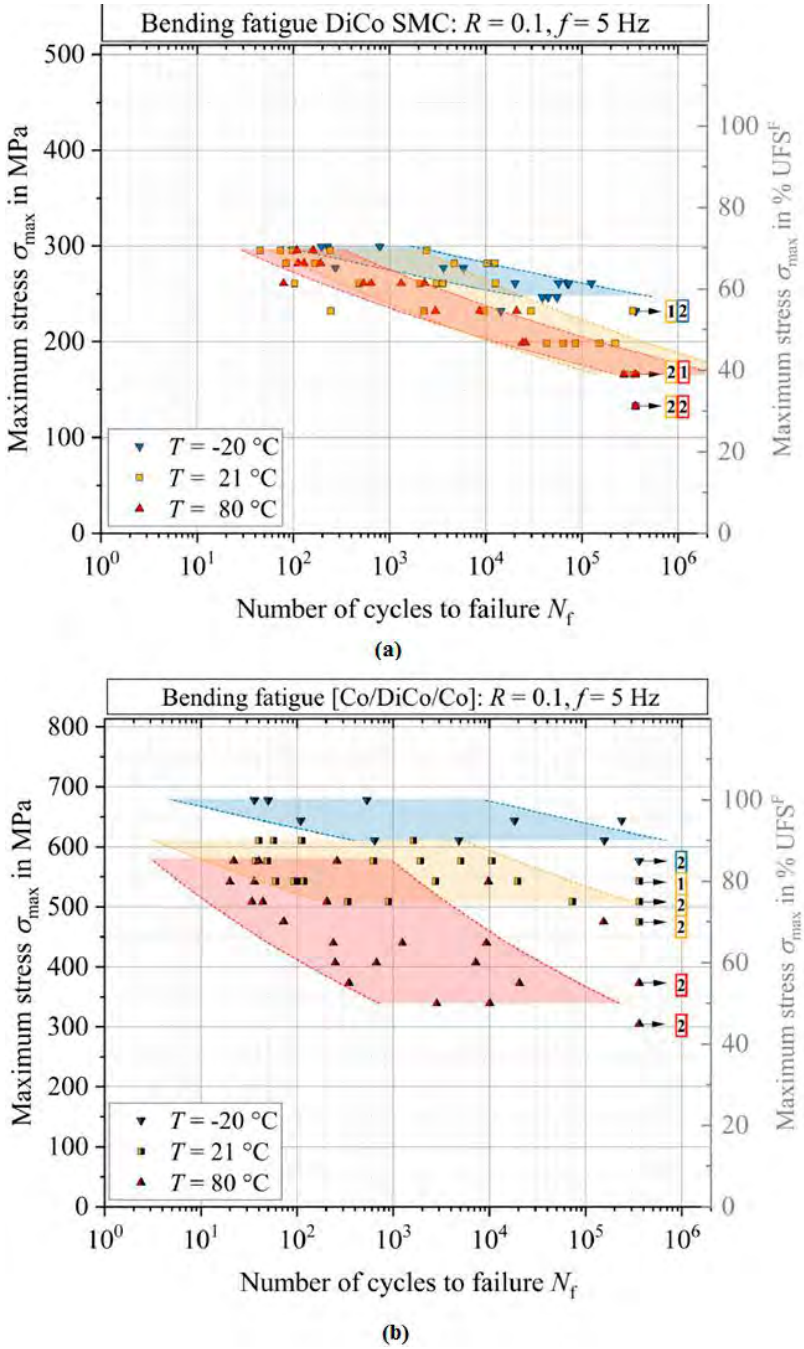

Figure 47. S-N data for (**a**) DGF-reinforced SMC composite specimens and (**b**) hybrid [UCCF/DGF/UCCF] SMC specimens under 3-point bending fatigue load at different temperatures for failure probabilities of *PS* = 10% and *PS* = 90% [17].

4.1.2. Operational Factors

There are a number of operational parameters associated with the coolant systems which might actively function as a catalyst for avoiding or at least minimizing the structural degradation in polymers and PMC structures, which are associated with the average

convective heat transfer coefficient ($\bar{h}$) of the fluid around a composite structure. In 1883, Osborne Reynolds illustrated two different fluid flow regimes, namely laminar and turbulent [149]. However, the laminar flow mainly experiences a transition state to be converted into a turbulent stream (see Figure 48). In laminar flow, the fluid layers slide smoothly over each other, taking place normally in low-velocity regimes, while turbulent flow is defined as a complex process in which erratic motion and eddies in different sizes are superimposed onto the streamlines [150]. Additionally, the behavior of a transient stream may be quite similar to that of a turbulent stream.

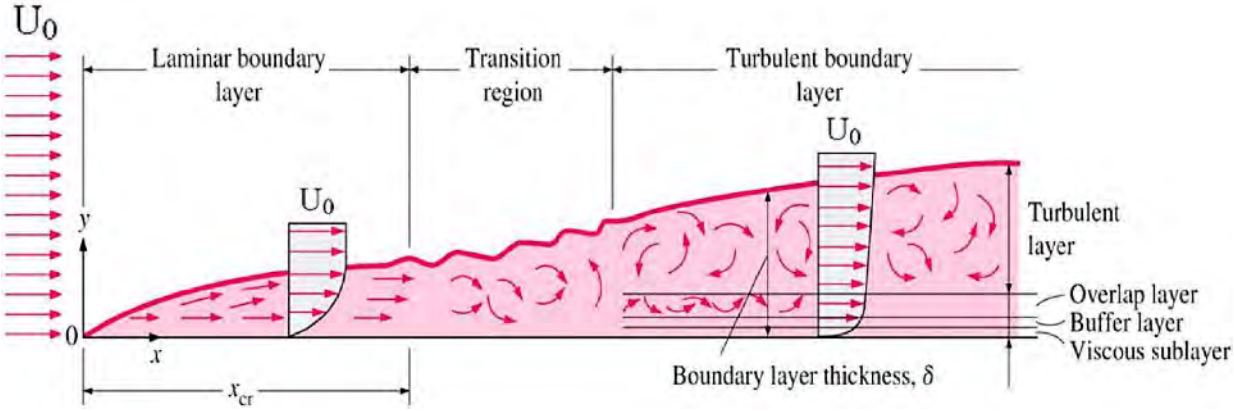

Figure 48. Different types of flows, adapted with permission from Ref. [150]. Copyright © 2017 Elsevier Ltd.

The Reynolds number, associated with this behavior, can be defined as the ratio of inertial to viscous forces of the fluid [151], depending on four parameters, namely viscosity (μ), speed (U_0), density (ρ) and characteristic dimension (D) (see Equation (16)).

$$\mathrm{Re} = \frac{Inertia\ Forces}{Viscous\ Forces} = \frac{\rho U_0 D}{\mu} \tag{16}$$

Increasing viscosity will lead to a reduction in the Reynolds number, while increasing the value of each three other parameters will lead to an increase in this number. It should be mentioned that for pipes, D is the diameter of a cylinder, while for plates, D is the length or width of a plate which is parallel to the direction of the fluid. In the case of a pipe or cylinder, if the Reynolds number is below 2300, the fluid particles tend to behave as a laminar flow extracted from smooth and constant fluid motion due to adequate viscous force. Otherwise, the propagating rate of eddies, vortices and other flow instabilities may be intensified, leading to a turbulent flow. However, the critical Reynolds number for a flat plate geometry, which is implemented primarily for cyclic fatigue tests, is 5×10^5 [152]. Otherwise, a transient and/or turbulent flow may take place.

The following is still an open question: how can the generated thermal energy level induced by the self-heating effect in cyclically loaded FRP composite structures be reliably quantified and then be thoroughly removed by the implementation of coolant systems?

Every type of flow may come with its complexities. Among all three types of flows, it is merely the laminar flow that allows us not only to reliably analyze the fluid flow using computational fluid dynamics (CFD) software, but also to mathematically model and predict the location of the fluid particles with the passage of time. As the promising potential of this, the fatigue performance of a cyclically loaded PMC structure dominated by the self-heating phenomenon exposed to a laminar flow cooling system may be more reliably characterized, as opposed to transient or turbulent fluid [153].

Katunin and Wachla [87] reported that the lifetime of a cyclically loaded epoxy-based GFRP composite can be significantly extended by implementing airflow as forced air cooling. According to the authors' experience, it should be noticed that although it might

theoretically seem easy to have a laminar flow, providing such a flow and controlling such conditions for a prolonged period experimentally may not be as easy as expected. On the other hand, it may be difficult and complex to rationally predict the influence of both other cooling scenarios (transient and turbulent flows) on the value of transferred heat from the cyclically loaded FRP composite structures caused by the self-heating phenomenon. The most compelling reason justifying this can be explained by the vortices and eddies in flow, which are normally formed during both transient and turbulent fluid regimes, making the reliable predictability of fluid flow influence as a coolant system on fatigue performance of such a composite almost impossible. In order to logically formulate the caused self-heating effect under stationary or nonstationary condition in a cyclically loaded polymeric structure [61], a couple of scenarios can be taken into consideration.

The first scenario is to assume the generated heat (q_{gen}) induced by the self-heating effect in a cyclically loaded polymeric structure is equal to the dissipated energy through convection, conduction and radiation in a loaded structure. One can obtain the ideal scenario due to the appearance of the thermodynamic equilibrium, wherein the effect of internal energy ($\Delta \dot{u}$) can be negligible (see Equation (6)). Therefore, the heat transfer equilibrium in Equation (6) for such a condition can be written in the following form [154]:

$$q_{gen} = q_{dissip} \rightarrow \quad q_{gen} = \frac{1}{V}(Q_{cond} + Q_{conv} + Q_{rad}), \tag{17}$$

It should be mentioned that since the heat transfer via radiation has an insignificant influence in such a condition, its effect can be eliminated due to the simplicity of equation systems [87]. Thus, Equation (17) can be rewritten as follows:

$$q_{gen} \approx \frac{1}{V}(Q_{cond} + Q_{conv}), \tag{18}$$

This scenario may ideally provide us with the opportunity to completely remove the generated heat caused by the self-heating effect. Therefore, the structural degradation will be desirably prevented and merely limited to the influence of mechanical fatigue loading. To understand whether the overall generated heat has been removed via convection and conduction during fatigue testing, the surface temperature variations of a typical composite should be frequently monitored using the available techniques, including the use of IR thermographic cameras [74,87,89,155]. If there is no significant difference between the surface temperature before testing and the history temperature measurements extracted from IR thermographic data during fatigue testing, the stationary self-heating regime will appear for a long period until mechanical fatigue failure. Otherwise, the catastrophic nonstationary regime will appear.

In the second scenario, nonequilibrium conditions will occur between the amount of heat generation and the amount of heat dissipated via convection and conduction if there is a noticeable deviation between the specimen surface temperature during fatigue testing and the initial specimen surface temperature before testing. This is the appearance of a nonstationary regime due to the storage of a relatively high level of internal energy in the specimen. It would be, however, of utmost significance to estimate the difference between the resultant generated heat caused by the self-heating phenomenon and the heat removal via convection and conduction. In the case of heat transfer via conduction, the most influential parameter is thermal conductivity, which is discussed in the optimal materials design and selection section (see Section 4.2). Regarding the total heat removal via convection, what would be more significant is to compute the average convective heat transfer coefficient ($\overline{h}$) in the cyclically loaded PMC structure, which seems to be a time-demanding task. Although proposing empirical or semiempirical formulas for computing $\overline{h}$ on the entire surfaces of PMC structures seems to be a time-consuming task due to a number of uncertainties associated with the surface behavior (which can be rooted in the manufacturing techniques and the types of fibers, woven fibers and polymers used during the manufacturing process), a general technique may be implemented in order to

acceptably estimate $\overline{h}$ on the entire surfaces of FRP composite structures regardless of the types of flow and fluid as follows [156]:

(1) The geometry of the fluid stream should be specified in advance (e.g., whether the fluid flows over a thin-walled FRP composite cylinder or a plate with a different thickness (i.e., ranging from FRP laminates to sandwich panel structures)).
(2) Since the Reynolds number is highly dependent on the boundary layer conditions, it should be correctly computed as a function of the characteristic length of the FRP composite structure and the kinematic viscosity and velocity of the flow.
(3) An appropriate reference temperature should be specified for the purpose of calculating the properties of the flow.
(4) In some cases, if a typical FRP composite structure has a complex geometry, it may be of utmost importance to understand whether a local convection coefficient or an average convection coefficient over the surface is needed for simulation.

In general, the average convection coefficient of such a PMC structure exposed to any external fluid flow can be predicted using the Nusselt number [156], expressed as follows:

$$Nu = \frac{\overline{h}\,L}{K} = C\,\mathrm{Re}^{m}\mathrm{Pr}^{n}, \tag{19}$$

where C, m and n are constants, varying based on how the fluid behaves, acting as laminar, transient or turbulent flow. Re and Pr are respectively called the Reynolds and Prandtl numbers.

The average Nusselt number based on the type of fluid flow over the entire isothermal FRP composite specimen can be denoted as follows:

For laminar flow:

$$Nu = \frac{\overline{h}\,L}{K} = 0.664\mathrm{Re}^{1/2}\mathrm{Pr}^{1/3}; \quad \mathrm{Pr} \geq 0.6, \tag{20}$$

For turbulent flow:

$$Nu = \frac{\overline{h}\,L}{K} = 0.680\mathrm{Re}^{1/2}\mathrm{Pr}^{1/3} \tag{21}$$

and the average convection coefficient for both laminar and turbulent regimes can then be determined as follows:

$$\overline{h} = \frac{NuK}{L} \tag{22}$$

where K is the thermal conductivity of the fluid around the specimen and L indicates the characteristic length of cyclically loaded flat FRP composite structure.

On the other hand, the Nusselt number for the thin-walled PMC structures, regardless of the type of cross-section and the type of flow around the thin-walled FRP composite structures, may be described as follows:

$$Nu = \frac{\overline{h}\,D}{K} = 0.3 + \frac{0.62\mathrm{Re}^{1/2}\mathrm{Pr}^{1/3}}{\left[1+(0.4/\mathrm{Pr})^{2/3}\right]^{1/4}}\left[1+\left(\frac{\mathrm{Re}}{282,000}\right)^{5/8}\right]^{4/5}; \quad \mathrm{RePr} \geq 0.2, \tag{23}$$

The average convective heat transfer coefficient for a thin-walled composite structure may then be computed as follows:

$$\overline{h} = \frac{NuK}{D} \tag{24}$$

where D is the characteristic diameter of a typical cyclically loaded FRP composite structure. Thus, interestingly, having computed the average convection heat transfer coefficient, one could acceptably evaluate the value of heat removal by the forced flow on the entire surface of a cyclically loaded FRP composite structure (see Equation (11)).

As can be concluded from Equation (11), associated with the criticality of $\overline{h}$, as the average convection coefficient increases, the amount of generated heat caused by the self-heating phenomenon in such a structure that can be desirably removed increases. To put it differently, computing the average convective heat transfer coefficient allows us to search for some viable solutions in order to tremendously remove the generated heat caused by such a cyclic loading. Knowing this could be also important to estimate the difference between the generated heat induced by the self-heating phenomenon and the heat removed via convection and conduction.

In general, numerous cooling methods based on enhancing $\overline{h}$ have been developed, namely airflow, passive, liquid and phase change cooling (see Figures 49 and 50). Figure 50 generally categorizes numerous cooling methods of the heat-flux-removal capabilities per surface area via convection for the specific type of fluids with their heat transfer coefficients. It should be mentioned that although no report has been published to quantitively depict how such cooling techniques may positively increase $\overline{h}$, a number of reports have shown the noticeable overall heat flux removed via convection as the result of implementing the coolant systems [44], which is linearly proportional to $\overline{h}$ (see Equation (11)).

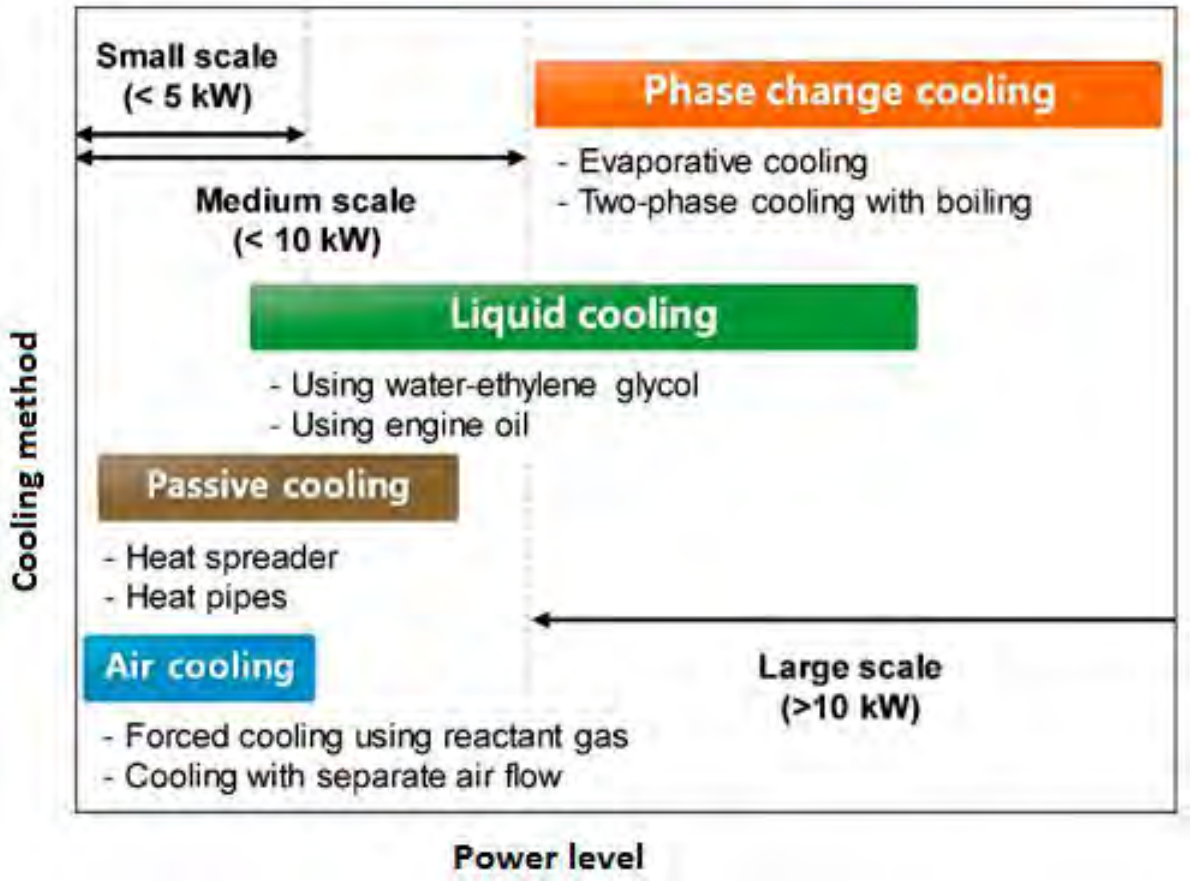

Figure 49. Different cooling techniques, adapted with permission from Ref. [157]. Copyright © 2019 Elsevier Ltd.

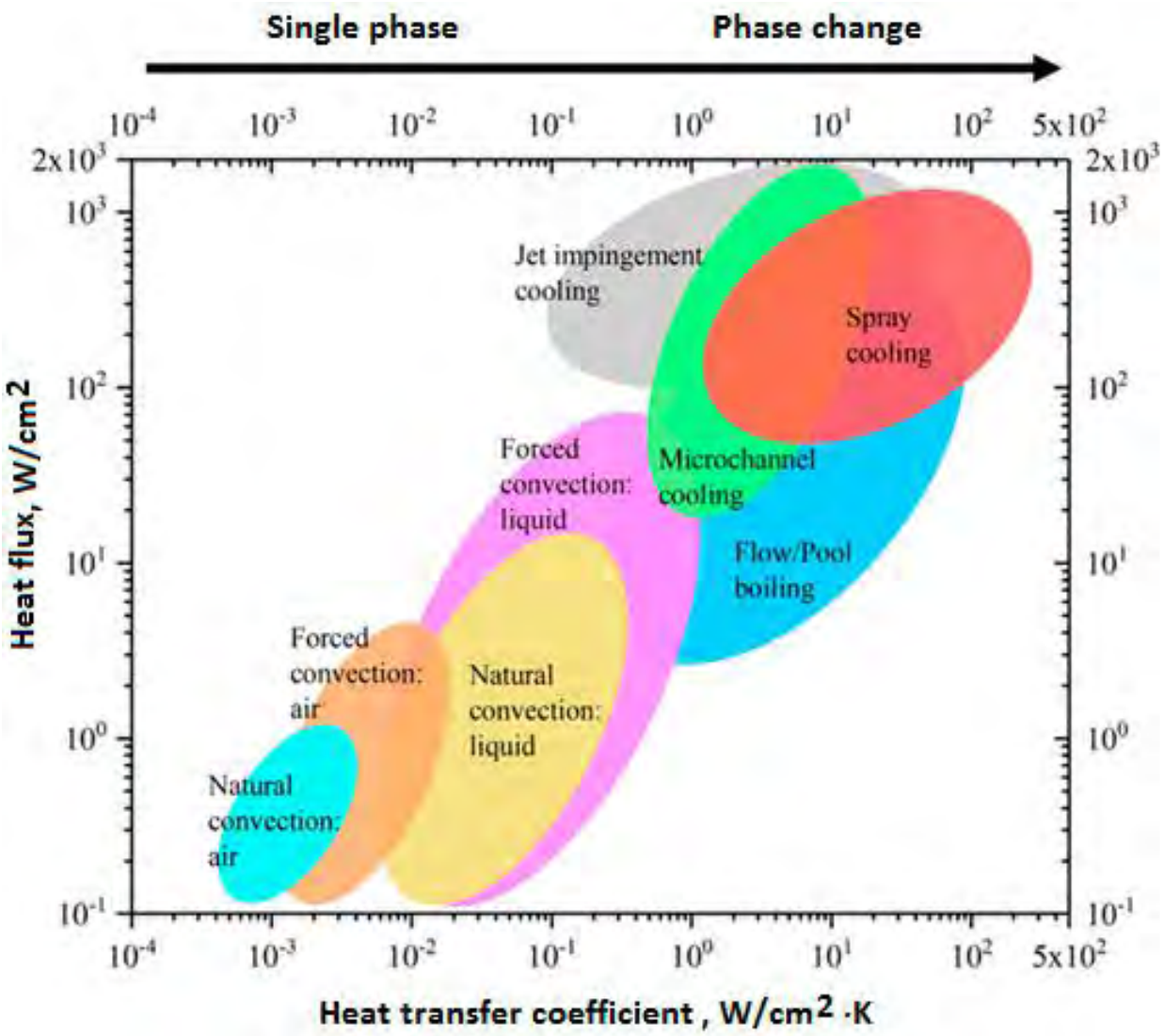

Figure 50. Classifying various cooling techniques according to the heat flux and heat transfer coefficient (adapted with permission from Ref. [158]. Copyright © 2022 Elsevier Ltd.) [159].

Airflow cooling, for which either a fan or blower is mainly implemented, is the simplest cooling approach. Although this may be the most affordable cooling technique, due to the comparatively lower specific heat of air than water, this technique can be used when the rate of generated thermal heat on the surface of a PMC specimen is roughly small (normally less than 5 kW). For this purpose, Müller et al. [160] implemented air cooling (vortex tube) so as to avoid excessive warming of both angle-ply and cross-ply CFRP specimens in a damaged condition during the HCF regime. Additionally, Apinis [161] implemented forced air cooling when the specimen temperature was greater than 50 °C so as to prevent the self-heating effect resulting from the accelerated fatigue testing of carbon–carbon composites using high loading frequency. Katunin and Wachla [87] reported that the lifetime of a GFRP composite could be extended twice using airflow. Furthermore, Movahedi-Rad et al. [77] employed a couple of fans as the coolant system to circulate the air inside the chamber to remain at the constant temperature of 20 °C and cool down the angle-ply glass/epoxy composite laminates (see Figure 51). According to the obtained data, the values of 30 °C and 45 °C appeared as the maximum specimen surface temperatures at low/intermediate stress levels and higher stress levels before failure, respectively.

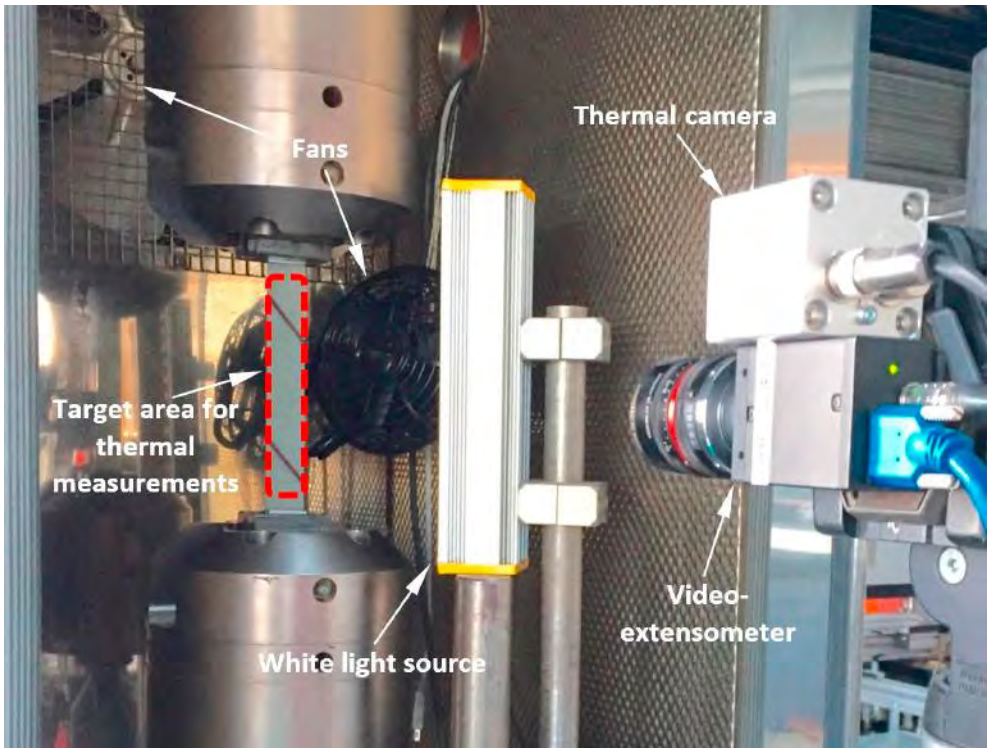

Figure 51. The experimental setup including coolant system for fatigue testing of angle-ply glass/epoxy structures, adapted with permission from Ref. [77]. Copyright © 2018 Elsevier Ltd.

In addition, the pulse–pause air cooling technique has been mainly implemented for ultrasonic fatigue experiments [29,65,123,162]. Premanand and Balle [29] developed an ultrasonic fatigue test setup using the reverse piezoelectric effect to obtain a cyclic mechanical oscillation of 20 kHz. A schematic representation of the developed facility and online-monitoring devices along with their model names is shown in Figure 52. This system involves an ultrasonic generator, a piezoelectric convertor and two boosters. The control unit had been implemented to handle the ultrasonic oscillation parameters from the generator inside the LABVIEW environment. For the purpose of preventing the appearance of the self-heating effect, the entire fatigue experiments were conducted in an unchanged pulse–pause ratio with 200 ms of ultrasonic pulse and 2000 ms of pause. While this constant pulse–pause ratio was applied, dry compressed air was employed as the coolant agent to limit the surface temperature of the specimen to 30 °C. Additionally, Flore et al. [30] used an unchanged pulse–pause ratio including 100 ms of pulse and 2000 ms of pause during fully reversed ultrasonic cyclic tension testing of a GFRP composite for the purpose of limiting temperature to 25 °C on the specimen surface. In another study, Premanand and Balle [65], as opposed to their previous study in which pause time was assumed to be constant with the value of 2000 ms [29], investigated CFRP specimens at three different cyclic amplitudes (40 µm, 45 µm and 50 µm) and three pause time durations (1000 ms, 2000 ms and 4000 ms) using the similar ultrasonic testing setup for three-point fatigue bending of CFRPs developed by Backe et al. [48] (see Figure 52c) to prevent premature thermal failure of specimens induced by the self-heating effect (see Figure 53). As can be seen in Figure 53, the surface temperature of the CFRP specimen was significantly affected by the value of pause time and cyclic amplitude loading. The longer pause duration advantageously resulted in lower temperature growth. For example, the temperature growth of almost 5 °C at the end of the shown time period was measured as the result of applying a cyclic oscillation of 50 µm and a pause time of 4 s, which was approximately one-fifth of the value obtained when 1 s pause was used. In addition, with the increase in the loading amplitude applied to the specimen, the temperature growth measured increased.

Lee et al. [163] implemented a Peltier ring-type cooler, also known as a thermoelectric-based air cooler [164], in order to positively generate a high cooling effect for polyamide 66/glass fiber composite structures (see Figure 54). They used a constant pulse–pause ratio with a pulse time of 300 ms and a pause time of 3000 ms to avoid specimen heating.

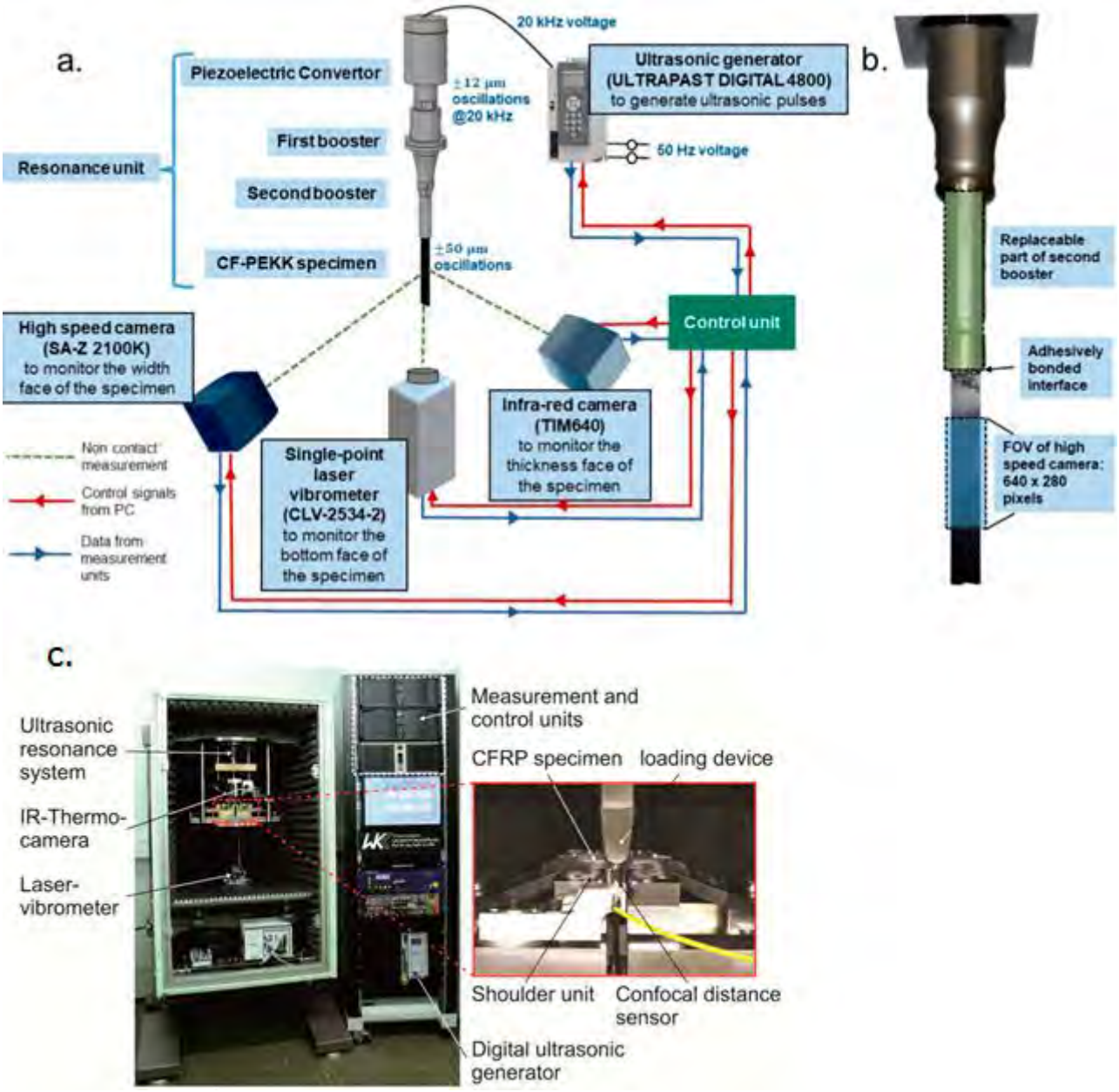

Figure 52. (**a**) Schematic experimental setup of the developed ultrasonic testing facility for axial cyclic loading of PMCs at a frequency of 20 kHz; (**b**) connecting the specimen to the system using the high-speed camera [29]; (**c**) ultrasonic testing setup for 3-point fatigue bending of CFRP (adapted with permission from Ref. [31]. Copyright © 2016 Elsevier Ltd.) [48].

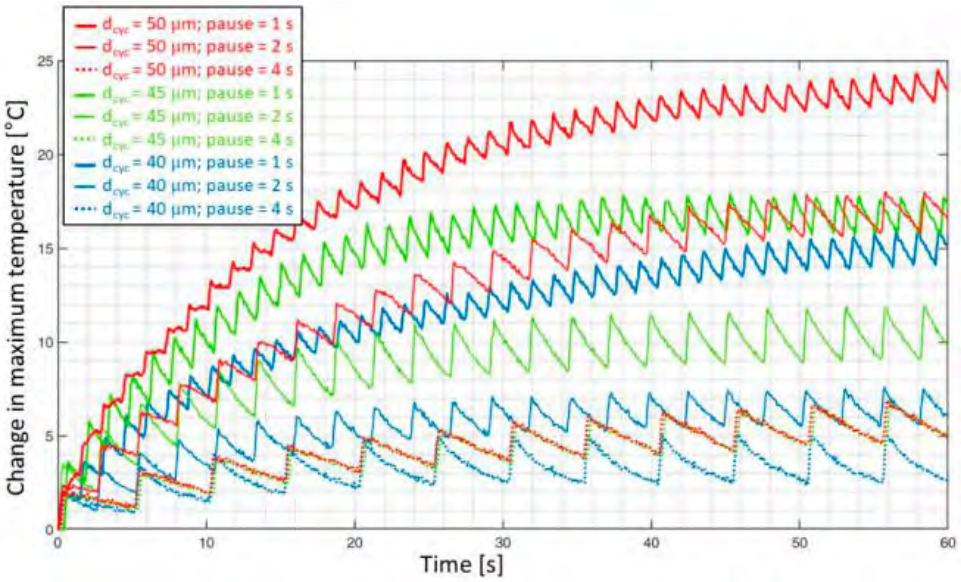

Figure 53. The influence of various load amplitudes and pause times on the surface temperature of a CFRP specimen during cyclic loading at the frequency of 20 kHz during the first minute [65].

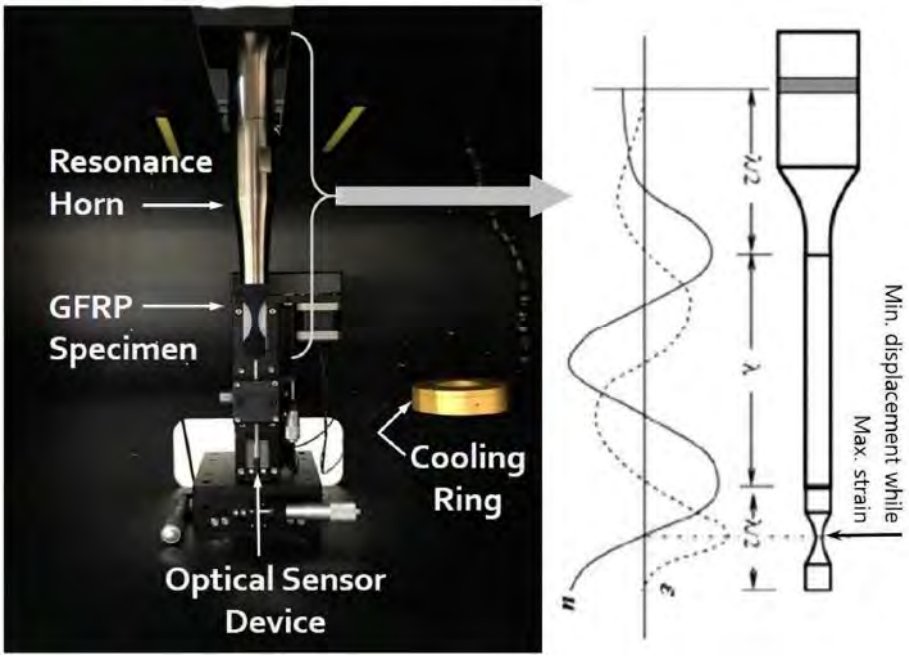

Figure 54. The experimental setup for ultrasonic fatigue testing of GFRP specimens and schematic illustration of resonance test, adapted with permission from Ref. [163]. Copyright © 2019 Elsevier Ltd.

The generated heat caused by the self-heating effect can be also removed via liquid cooling technique. As can be seen in Figures 49 and 50, the level of heat removal resulting from the use of this cooling method can be comparatively higher than that resulting from the use of air cooling. The main causative root justifying this is the relatively greater convective heat transfer coefficient of liquids ($\overline{h}$) as opposed to air. Implementing liquids as the coolant systems may relatively result in more uniform temperature distribution on the specimen surface as compared to air due to their higher $\overline{h}$ [165]. According to the recommendations, the implementation of liquid-based coolant systems may be taken into consideration when the rate of generated thermal energy is higher than 5 kW since the developed air cooling systems may probably be unable to remove such a large amount of heat flux via convention [166]. As a general rule, high thermal capacity, low viscosity, chemical

inertness, anticorrosion properties, nontoxicity and affordable price are the main factors in the selection of an appropriate coolant system [167]. Water has been the primary candidate among all liquids due to its high thermal capacity and low price. For this purpose, Just et al. [168] used a water-cooled base plate attached underneath the VHCF-tested cross-ply CFRP specimen so as to limit the generated heat flux induced by shaker. Additionally, Trauth et al. [169] implemented a water cooling system (see Figure 55) to study the effect of temperature on cyclically loaded continuous–discontinuous sheet molding composites (SMCs) by providing an integrated temperature chamber ranging from −100 °C to 350 °C for dynamic mechanical thermal analysis (DMTA). In another study, Cui et al. [170] developed a liquid nitrogen coolant system (see Figure 56) to limit the surface temperature of a CFRP specimen to lower than 40 °C during three-point bending fatigue testing in the VHCF regime. As shown in Figure 56, during the test, they inserted a metal tube into a liquid nitrogen tank; the liquid nitrogen absorbed heat, and the value of fluid temperature dropped remarkably with the passage of time, cooling the fluid to −39 °C. They justified the implementation of liquid nitrogen due to observing a remarkable temperature rise up to 106 °C in only 7 s on the surface of a CFRP specimen subjected to high loading frequency. This means that implementing compressed air cooling during ultrasonic loading of CFRP could not guarantee the normal conditions of a test (i.e., preventing the self-heating effect). As mentioned above (see the Section 4.1.1), Bartkowiak et al. [82] implemented liquid nitrogen (N_2) as the coolant system for the purpose of providing a temperature of −20 °C for fatigue testing. In another study, Charalambous et al. [79] used liquid carbon dioxide as a coolant agent in order to limit the negative influence of the self-heating effect during cyclic fatigue testing of CFRP specimens by obtaining temperatures up to −50 °C.

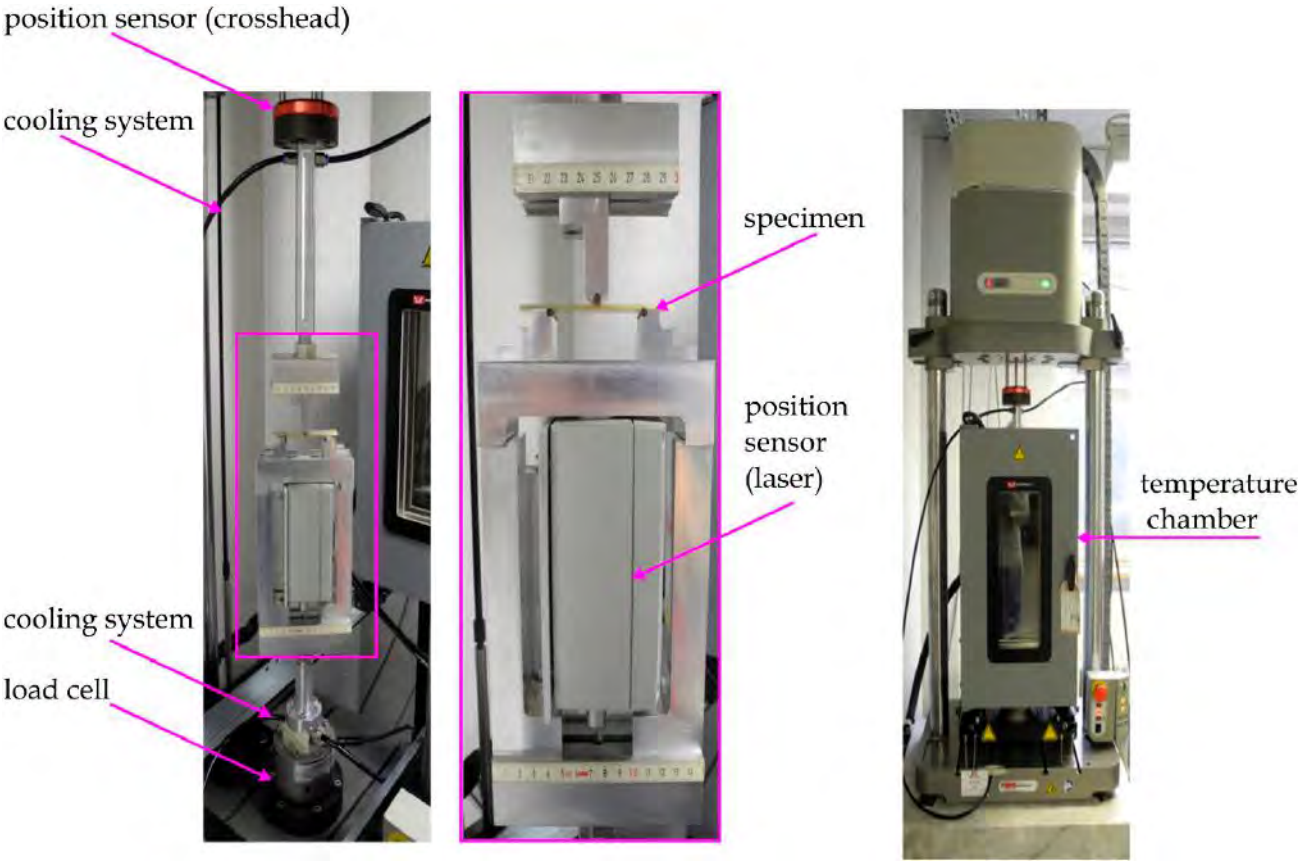

Figure 55. The experimental setup for characterizing DMTA using a water-based coolant system [169].

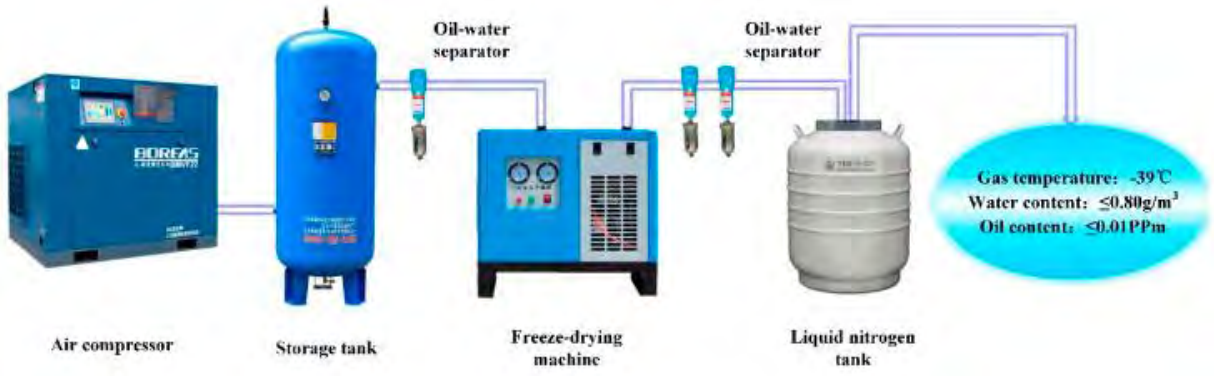

Figure 56. An exemplary illustration of a liquid nitrogen cooling system [170].

The use of liquids with relatively high thermal conductivity (K) which may, similar to $\overline{h}$, act as a catalyst in removing heat generation on the surface of a PMC structure under cyclic loading experiments has been suggested. Nowadays, nanofluids, which are defined as the colloidal suspensions of nanoscale particles in a base fluid such as silicon dioxide (SiO_2), carbon nanotube (CNT), graphene (GN) and alumina (Al_2O_3) nanoparticles in water, have been gaining great attention due to possessing a capability for enhancing the K of such a fluid [171–173]. This has advantageously resulted in the need for a relatively smaller coolant system, compared to traditional liquid cooling systems due to lower K. Although such techniques have been developed, they have not been implemented during fatigue testing of PMC structures. Therefore, implementing such nanoparticles in water or other liquid fluids can be taken into consideration as a coolant system during accelerated fatigue tests with high loading frequency in future trials.

In another study, Wang et al. [44] investigated the HCF and VHCF properties of a CFRP-aramid honeycomb sandwich structure under three-point bending ultrasonic loading with the applied loading frequency ranging from 18.5 to 20.5 kHz. They implemented cryogenic nitrogen and intermittent loading (i.e., pulse–pause technique) simultaneously to cool down the specimen for the purpose of limiting the self-heating temperature to below 40 °C (see Figure 57). The schematic diagram of the supporting device and cryogenic nitrogen as a coolant agent is shown in Figure 58. It should be mentioned that none of the authors of the previous studies reported the exact information about the rate of heat removal by the applied coolant systems during fatigue testing of PMC specimens, which is of key interest in conducting comprehensive studies in order to characterize the pros and cons of the available cooling techniques in terms of their simplicity, cost, etc.

Another cooling technique is passive cooling or edge cooling, which mainly implements heat spreaders with microchannel-based heat sinks [174,175]. High heat spreaders involving copper, aluminum, silver and silica, due to their high thermal conductivities, can be the prime candidates for implementation as thermal management for PMC specimens subjected to fatigue testing, which are also analyzed in the section on materials design and selection. For this purpose, Bahiraei et al. [174] implemented hybrid graphene–silver nanoparticles in a nanofluid base via a microchannel heat sink in a laminar flow with a Reynolds number of 100. They reported that adding 0.1% graphene nanoplatelets to the base fluid increased the average heat coefficient by 17%, which is proportional to heat removal by convection.

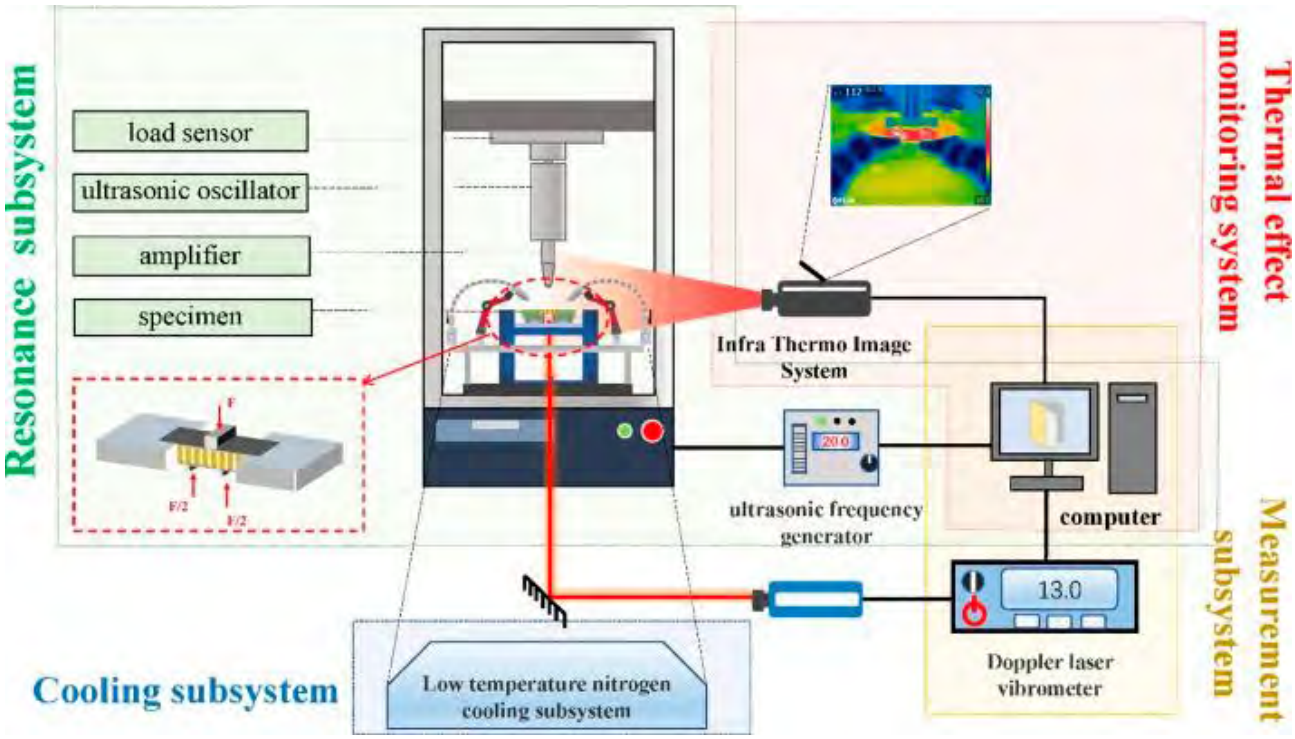

Figure 57. Schematic illustration of ultrasonic fatigue testing system, adapted with permission from Ref. [44]. Copyright © 2022 Elsevier Ltd.

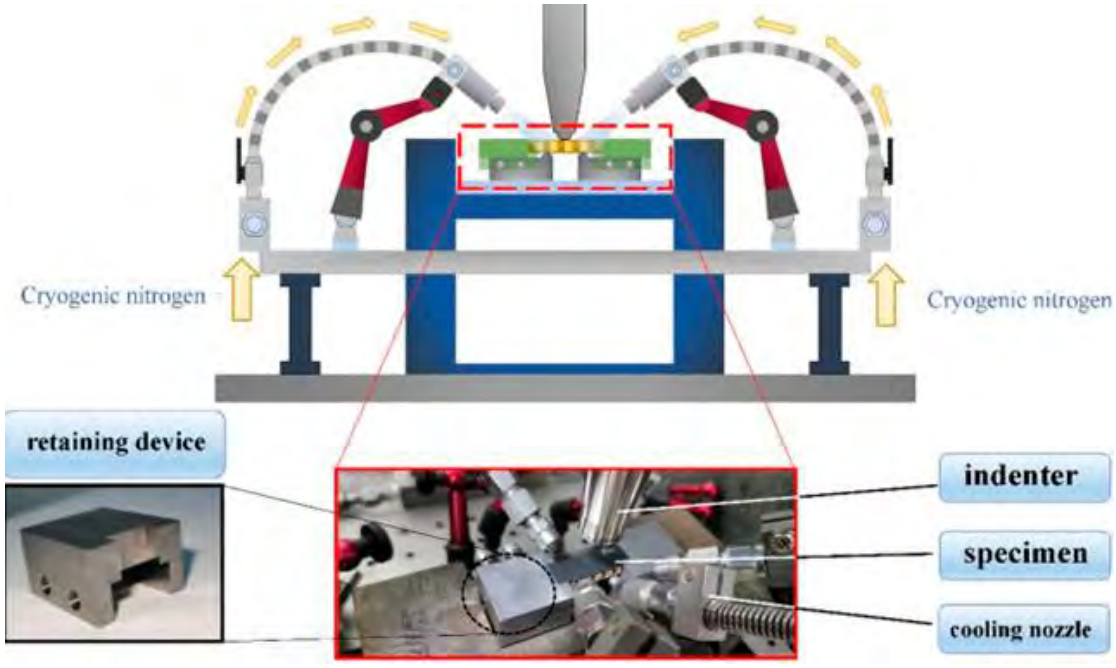

Figure 58. Schematic illustration of supporting device and cryogenic nitrogen as a coolant agent, adapted with permission from Ref. [44]. Copyright © 2022 Elsevier Ltd.

Another viable cooling technique is phase change cooling, for which coolant pumps are advantageously not required [176]. It may be interesting to know that the phase change technique implements significantly greater latent heat during the two-phase heat removal mechanism, as opposed to air and water cooling. For instance, the latent heat of water is 2250 kJ/kg, which is more than 500 times greater in comparison to the sensible heat

absorbed by liquid water with a temperature increase of 1 °C, meaning a comparatively lower coolant flow rate is required [166]. Among phase change cooling techniques, including microchannel flow boiling, heat pipe cooling and spray cooling, it is spray cooling that has been receiving great attention due to its excellent cooling capacity, uniformity, fluid utilization efficiency and system flexibility [159]. As can be seen from Figure 59, a spray of droplets generated by pressure/gas atomized nozzles is forced to impinge onto the targeted heating surface (i.e., the surface of the composite specimen), cooling it efficiently with a phase change of the coolant. Spray cooling can be implemented for both steady-state and transient cooling conditions. Steady-state cooling is employed when the specimen surface temperature is kept below the critical heat flux limit, while transient spray cooling is associated with the quenching of a target with a high initial temperature where the target is gradually cooled down. Since the initial specimen temperature during the fatigue test is often equal to RT, steady-state spray cooling can be efficiently implemented. For example, Putnam et al. [177] implemented steady-state spray cooling based on water microdroplet evaporation. They reported that when the heat flux reaches the critical heat flux in the heating-up direction, the continuous liquid film may degrade to isolated microdroplets, resulting in a high heat flux (1000 W/cm^2) and convective heat transfer coefficient (60 W/cm^2K).

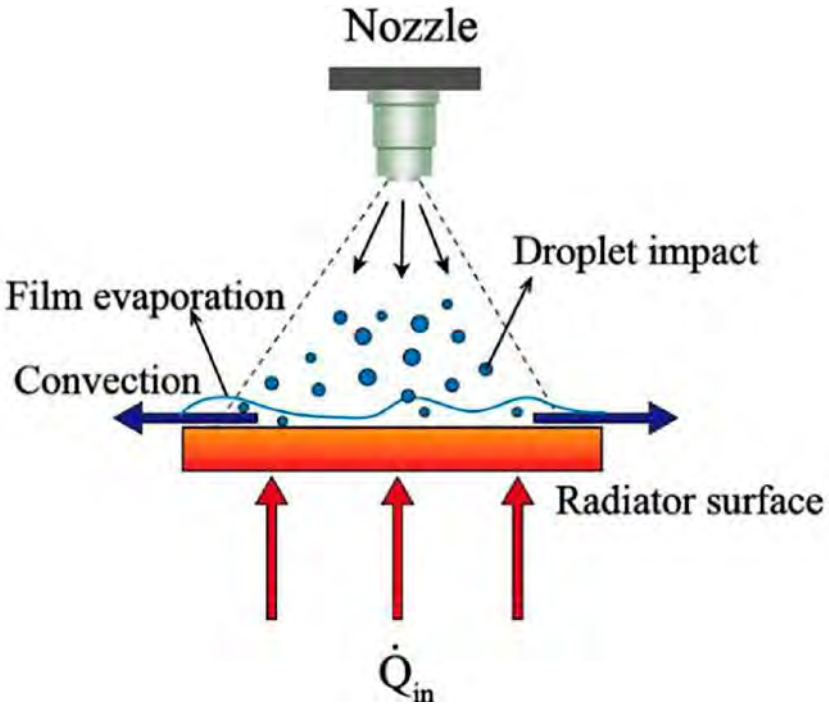

Figure 59. A schematic demonstration of spray cooling process, adapted with permission from Ref. [158]. Copyright © 2022 Elsevier Ltd.

As a recommendation, it may be more practical if the researchers quantify and report the heat flux during fatigue testing to rationally justify the reason behind selecting a specific cooling technique in future studies. As a result of having information about the generated heat flux rate induced by the self-heating effect under cyclic tests, reliable classification and standardization according to the material selection, the type of fatigue loading and the specimen geometry can be desirably carried out. This will provide us with the opportunity to select the most appropriate (optimal) coolant system for a specific cyclically loaded PMC structure. For this purpose, Huang et al. [89] numerically quantified the heat generation per unit volume during fatigue testing for CFRP laminates. They illustrated how the rate of generated heat in a PMC may significantly vary as the direct consequence of the viscoelastic behavior of the polymer, and damage propagation simultaneously, during

fatigue testing [89] (see Figure 60). As they reported, the heat generation rates under different stress levels can be explained by internal friction and damage mechanisms (e.g., delamination and crack propagation). The heat generation rate resulting from internal friction and delamination/crack propagation is separately shown in Figure 60, wherein the blue region depicts the heat generated caused by internal friction (i.e., the self-heating effect) and the red area reveals the generated heat caused by damage. Those two factors are proportional to the applied stress magnitude. As the stress level applied to such a PMC specimen increased, the measured heat generation increased. As they reported, the heat generation rate caused by damage noticeably increased when the stress levels exceeded the fatigue limit. The primary reason behind the heat generation associated with internal friction can be sought in recoverable microstructure motion (e.g., the interface between fiber and polymer matrix and the interlaminar interfaces between two adjacent layers).

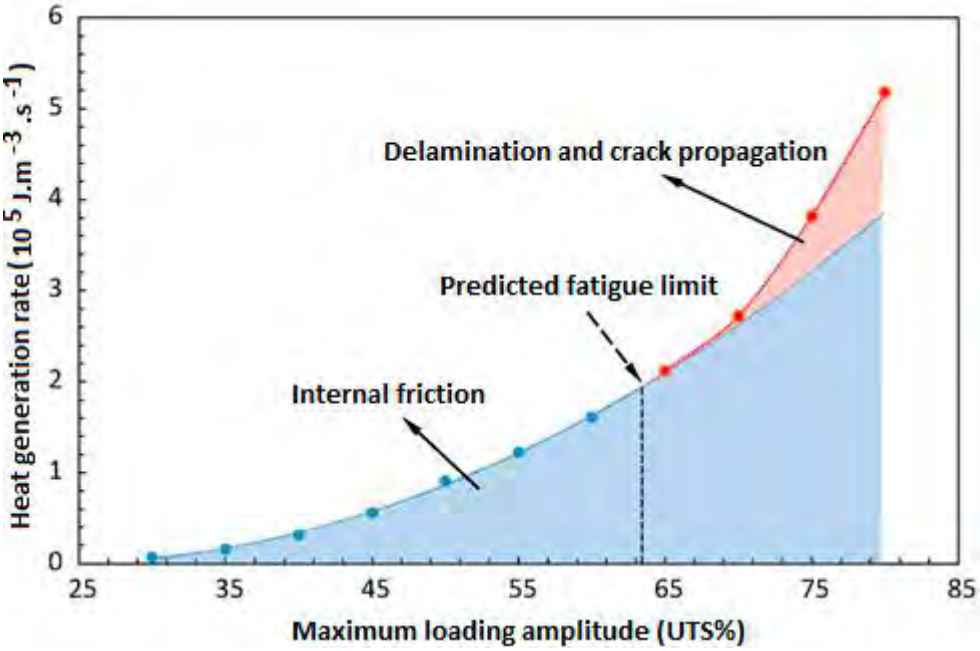

Figure 60. The exemplary illustration of heat generation rates depending on loading amplitude, adapted with permission from Ref. [89]. Copyright © 2020 Elsevier Ltd.

Figure 61 reveals the total heat generation per unit volume for a CFRP laminated composite caused by damage during fatigue life under different stress levels based on numerical data. As can be concluded, the average value of heat generation after the fatigue limit is exceeded is dominated by other heat sources and seems to be less dependent on applied stress levels. This means that for quantifying the total heat generation by damage, a fatigue test at one specific stress level would be sufficient.

In order to appropriately implement a cooling method, the entire mechanical energy dissipation associated with both internal friction and damage should be reported and quantified, not merely the heat generation caused by damage, which can be taken into consideration for the future studies.

4.2. Limiting Structural Degradation Caused by Self-Heating via Optimal Materials Design and Selection

The effects of loading conditions on the level of heat generation induced by fatigue loading were discussed for LCF, HCF and VHCF regimes. As discussed, depending on the loading conditions, a high level of temperature may appear on the surface of a composite structure during fatigue testing in all mentioned fatigue regimes, which may accelerate structural degradation in such a structure. Materials design and selection, as well as implementing cooling scenarios, can effectively limit the structural degradation of PMC

structures resulting from the self-heating effect. Thus, if materials are appropriately implemented (e.g., using materials with high thermal conductivity (*K*)) during the manufacturing process of PMC structures, structural degradation might be avoided or at least minimized. Otherwise, when the manufacturing processes of PMC structures have been thoroughly completed, it may be indeed unjustifiable due to being a time-consuming and costly process or even impossible to change and replace the used materials with other ones in order to enhance the *K* of such PMC structures. Thus, in such conditions when the composite structures have been produced, using different cooling scenarios (which were broadly discussed in the previous section) may be the only option for preventing intensive structural degradation with the presence of the self-heating phenomenon under fatigue loading.

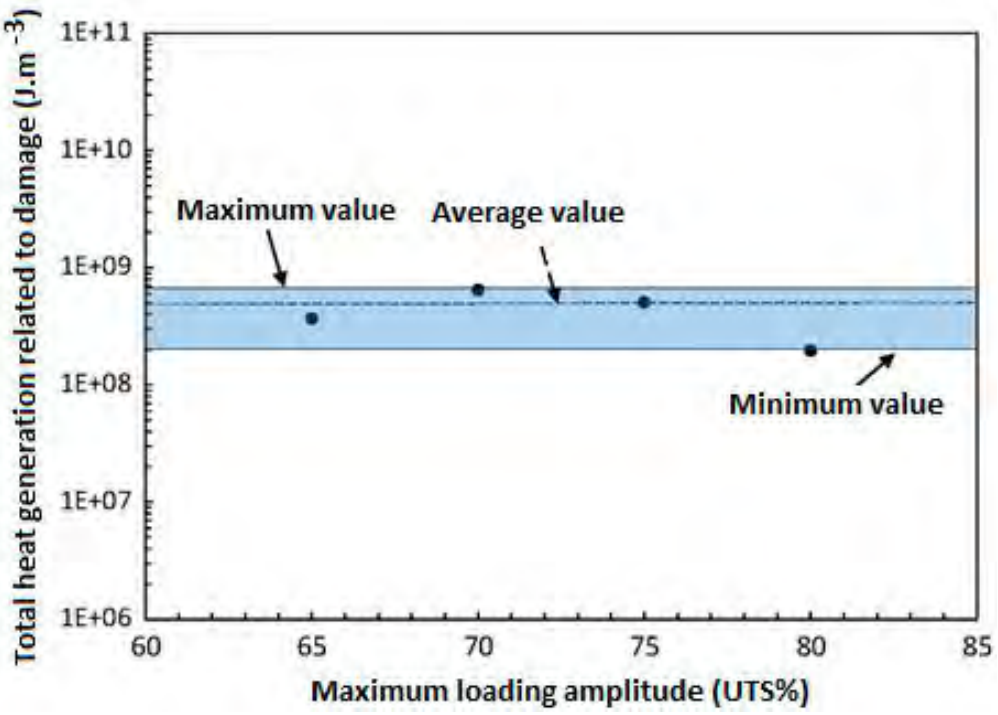

Figure 61. The exemplary heat generation plot for CFRP composite induced by damage over the entire fatigue life, adapted with permission from Ref. [89]. Copyright © 2020 Elsevier Ltd.

K can favorably play a key role in limiting the intensive structural degradation of PMC structures. Enhancing *K* of PMCs will lead to increasing heat dissipation via conduction. This can minimize the stored internal energy, resulting in a relatively low temperature on a composite surface. This prevents the occurrence of premature thermal fatigue failure in such a structure, extending residual fatigue lifetime or reducing the structural degradation of the PMC structures. The most rational justification behind this can be rooted in how increasing the value of *K* functions, transferring the heat caused by the self-heating phenomenon with a higher rate from the surface of the PMC structure into the surrounding environment via convection and consequently cooling down a PMC specimen surface temperature. Therefore, implementation of PMC materials with higher *K* values is of key interest to tackle the issue of the self-heating effect resulting from high-amplitude vibrations or fatigue loading. In general, to characterize how the self-heating phenomenon of a PMC can be advantageously minimized through utilization of thermally conductive materials, the influence of numerous parameters which are analyzed in detail in the subsequent subsections, should be taken into consideration.

4.2.1. Role of PMC Specimen Thickness

In the case of optimal materials design and selection, there may be a number of causative factors contributing to improving the *K* values of PMC structures to avoid the

intensive structural degradation of such PMCs, one of which may be the specimen thickness. For this purpose, Ueki [178] provided analytical relations for the determination of the temperature growth during a fatigue test and the temperature distribution through the laminated specimen thicknesses with values of 3 mm and 6 mm. As a result of increasing the specimen thickness, the temperature rose significantly by almost 100%, ranging from 20 °C to 40 °C in bending mode, and varying from just below 60 °C to 120 °C in uniaxial tension/compression mode with loading conditions of f = 200 Hz, σ = 100 MPa and $R = -1$ (see Figure 62). In the case of axial loading, when the thickness was 6 mm, the temperature value dropped by about 15 °C, and the midplane of the specimen experienced the highest value of temperature. To put it differently, in the case of one-dimensional heat transfer under unchanged loading conditions, the thinner a PMC specimen is, the more uniform the temperature distribution in the cross-sectional direction and the lower the temperature value can be. For this reason, Mandell et al. [179] used a thin laminated composite with a thickness of 1.5 mm for fatigue testing. Furthermore, Hosoi et al. [180–182] implemented thin laminated specimens with a thickness of about 1 mm for fatigue testing in order to limit the self-heating effect through the thickness direction. According to the ASTM D3039 standard [13], unidirectional laminated composites with a thickness of 1 mm can be tested under axial fatigue loading.

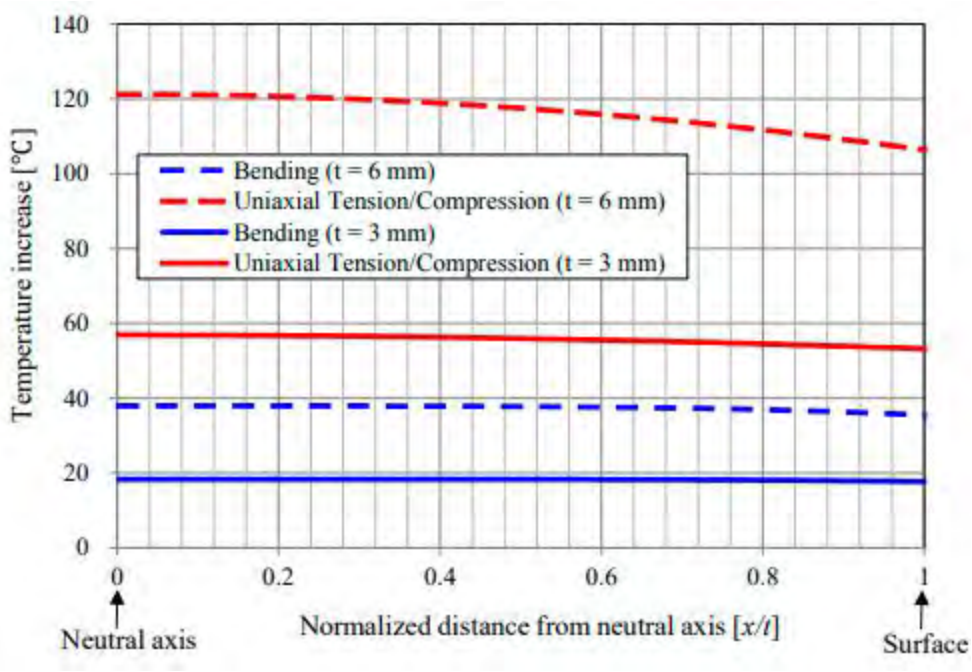

Figure 62. The cross-sectional temperature distribution in laminated GFRP composite specimens with thicknesses of 3 and 6 mm estimated under the assumption of one-dimensional heat transfer [178,183].

4.2.2. Role of Polymer Matrix

It has been suggested that the self-heating effect can be controlled using appropriate polymers. Table 1 summarizes the K values for the most common thermoset and thermoplastic polymers. Although polymers may have manifold merits, their K values are relatively low, ranging from just below 0.15 up to roughly 0.5 for commonly used polymers [184–191]. This means that polymers may not be considered the prime candidates for improving the K values of PMC structures. It is worth mentioning that the primary causative factor contributing to the difference between the K values of such polymers can be explained by the polymer structures (i.e., level of crystallinity). A higher degree of crystallinity may lead to a greater K value. According to Table 1, a good illustration of this can be high-density polyethylene (HDPE), which offers a greater K value due to possessing a higher degree of crystallinity, as opposed to low-density polyethylene (LDPE). Figures 31 and 63 depict both amorphous and crystalline polymer structures, wherein

amorphous polymers consist of chain entanglements, chain ends, crystal–amorphous interfaces and voids [192], as the direct consequence of which the heat transfer mechanism along chains may be frequently interrupted. As an example, Figure 64 schematically reveals the influence of the self-heating phenomenon on the structural variation of a PA 66 gear during fatigue operation [193]. Additionally, the heat transfer mechanism in polymers with crystalline and amorphous zones is schematically shown in Figure 65a [189].

Table 1. Thermal conductivity (*K*) of commonly used polymers.

Polymer Matrix	*K* (W/m K)	Refs.
Elium	0.18	[184]
Epoxy resin (EP)	0.148, 0.22	[185,186]
Polyimide (PI)	0.2, 0.27	[187,189]
Polycarbonate (PC)	0.19	[188]
Polyetheretherketone (PEEK)	0.25	[190]
Polyphenylene sulfide (PPS)	0.22–0.25	[190,194]
Polysulfone (PSU)	0.28	[190]
Polytetrafluoroethylene (PTFE)	0.25	[190]
Nylon-6 (PA6)	0.29	[190]
Nylon-6.6 (PA66)	0.23	[190]
Poly (ethylene terephthalate) (PET)	0.24	[190]
Polymethylmethacrylate (PMMA)	0.18	[190]
Polypropylene (PP)	0.17–0.22	[190]
Low-density polyethylene (LDPE)	0.32–0.40	[190]
High-density polyethylene (HDPE)	0.38–0.51	[190]
Polyester	0.091	[191]
Polystyrene (PS)	0.14	[192]

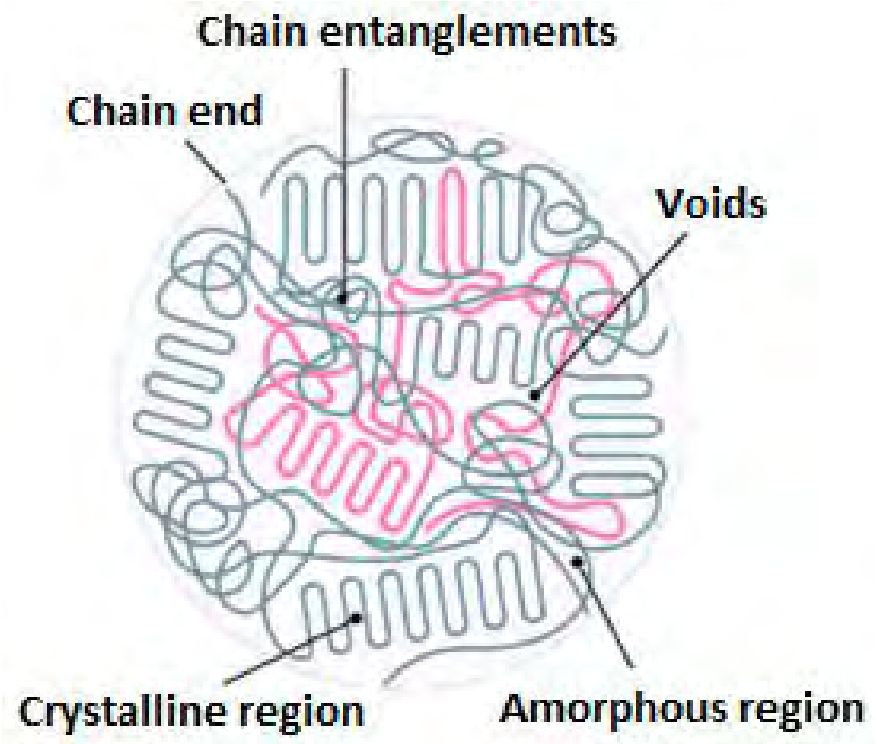

Figure 63. Demonstration of amorphous and crystalline polymer–matrix structures, adapted with permission from Ref. [192]. Copyright © 2021 Elsevier Ltd.

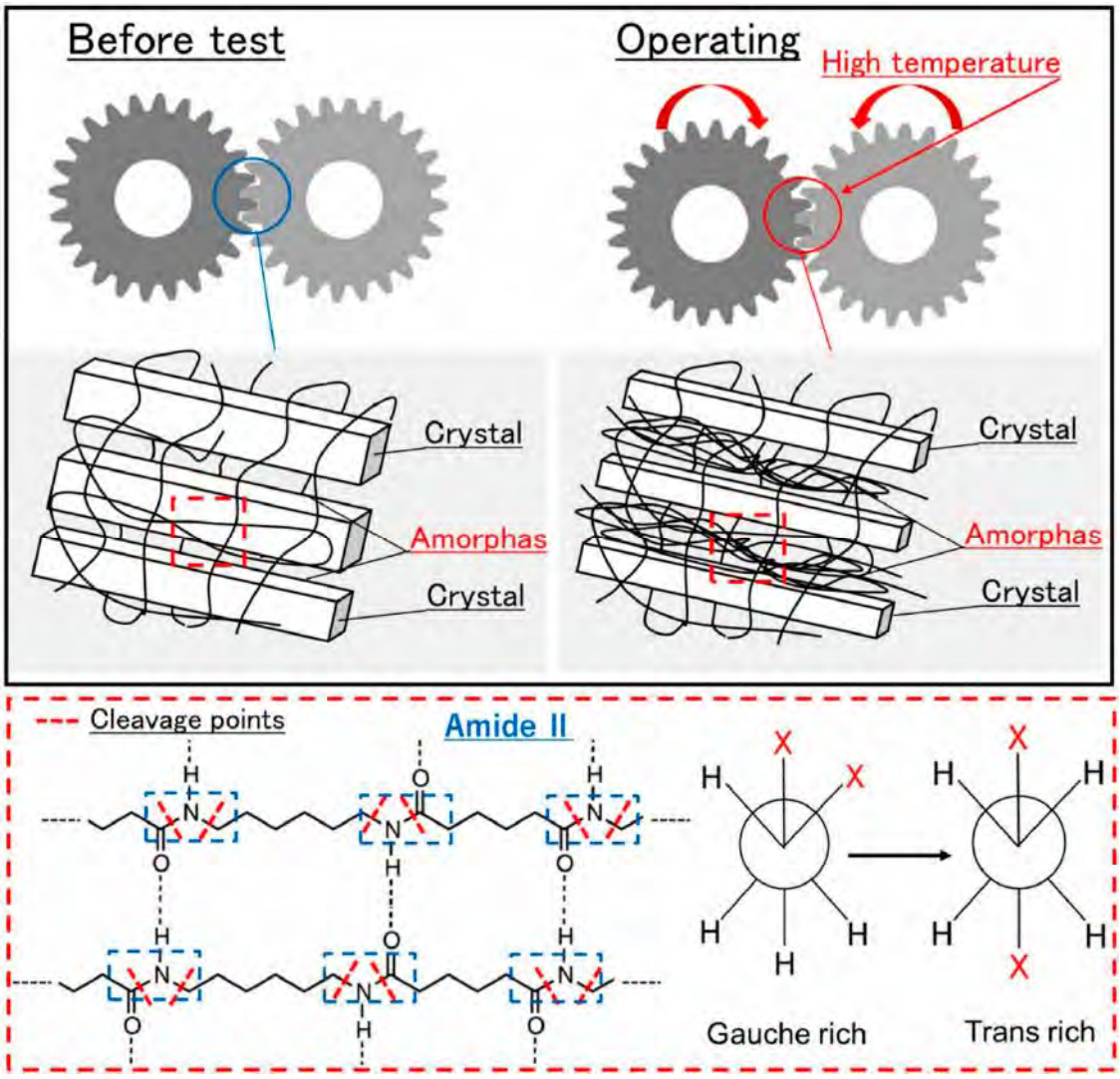

Figure 64. Schematic representation of the structural change of a PA 66 gear induced by self-heating effect during fatigue loading [193].

4.2.3. Type of Fillers

As opposed to polymers which possess relatively low range of *K*, fillers offer a comparatively wider range of *K* values. Such materials can be categorized by their family groups (e.g., carbon allotropes, ceramics, metals and polymeric fibers). Table 2 reveals the *K* values of fillers which are commonly implemented in a variety of engineering applications. According to provided data in Table 2, among all thermally conductive filler candidates, leading the pack would be the carbon-based allotropes consisting of carbon nanotubes (CNTs), graphene, graphite and carbon fibers, offering ultrahigh *K* values of up to 6000 W/m K. The potential carbon-based fillers offer *K* values approximately 14 times greater than those of common metals and roughly 6000 times higher than that of glass fiber. These are followed by commonly used ceramics and metals, which also offer relatively high *K* values, ranging from 50 W/m K for steel to greater than 1000 W/m K for diamond. Polymer-based fibers such as Kevlar (aramid) as well as basalt fiber trail the pack, possessing comparatively unimportant *K* values of 0.04 W/m K or below, which are even lower than the *K* values of common engineering polymers. This means that such fibers do not have the capability to be implemented for improving the overall *K* of a PMC structure. Figure 65b–d schematically classify different materials in terms of their *K* values [189].

Therefore, carbon-based fillers can be selected as the prime candidates for enhancing the *K* of PMC structures, as discussed in the next section.

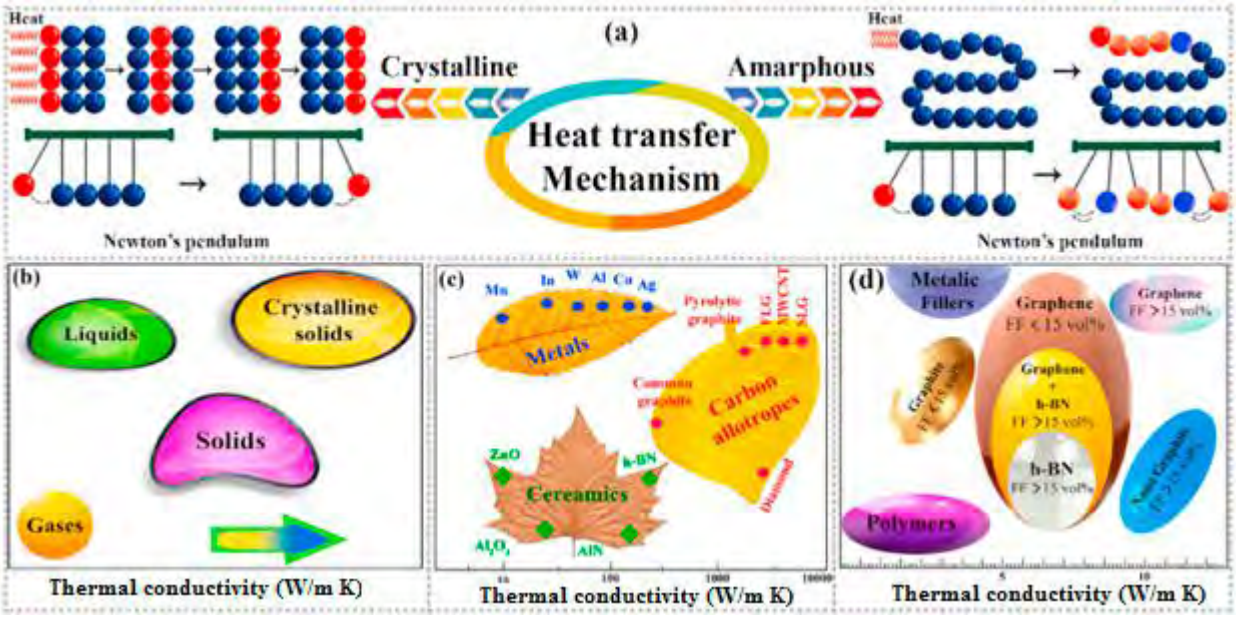

Figure 65. Schematic demonstration of (**a**) heat transfer mechanism in crystalline and amorphous polymers, (**b**) *K* levels in different phases of materials, (**c**) classifying common thermally conductive solid materials for various filler materials and (**d**) categorizing various filler-reinforced PMCs regarding their thermal conductivities, adapted with permission from Ref. [189]. Copyright © 2022 Elsevier Ltd.

Table 2. Thermal conductivity of commonly used fibers.

Filler	*K* (W/m K)	Ref.
Graphene (GNP)	2000–6000	[194,195]
Carbon nanotube (CNT)	2000–6000	[194,196,197]
Diamond	2000	[196,198]
Pitch-based carbon fiber	400–1100 (along the axis)	[194,196]
PAN-based carbon fiber	8–70 (along the axis)	[196]
Carbon black	6–174	[196]
Graphite	100–800	[196,199]
Boron nitride (BN)	250–1300	[196,200]
Silver (Ag)	427	[198]
Copper (Cu)	398	[198]
Gold (Au)	315	[198]
Aluminum (Al)	247	[198]
Tungsten (W)	155	[198]
Nickel	158	[196]
Zink (Zn)	115	[189]
Steel	50	[189]
Silicon carbide (SiC)	270	[198]
Glass	1–1.03	[191,201]
Kevlar (aramid)	0.04	[191]
Basalt	0.031–0.038	[202]

4.2.4. Role of Fillers in Overall *K* of PMC Structures

One of the viable strategies for the purpose of enhancing the *K* values of PMCs is to implement ultrahigh-thermal-conductivity micro- or nanocarbon allotropes involving carbon nanotubes (CNTs) [203], graphene [204,205] and carbon fibers [206,207], as well as boron nitride (BN) platelets/nanosheets [188,208–213], silicon carbide (SiC) [214–216], silicon nitride (Si_3N_4) [217], gold (Au) [218], copper (Cu) [219–222], silver (Ag) [223–225], aluminum

nitride (AlN) [226], aluminum oxide (Al_2O_3) [227] and hybrid fillers [188,228–230] during the fabrication of PMC structures. To predict how the overall *K* value of a typical PMC is influenced by adding fillers into the polymer matrix, the implementation of the rule of mixture equations is indeed impractical due to providing a huge mismatch, as opposed to experimental results [189,192]. The primary causative factors contributing to this mismatch between extracting *K* values using the rule of mixture and experiments can be sought in the (i) geometry of the filler, (ii) thickness of the surface coating and film, (iii) orientation of the filler, (iv) interface between the polymer matrix and filler and (v) loading fraction of the filler.

In the case of filler geometry, the size and shape of fillers play a key role in the *K* of PMCs. This can be explained by the aspect ratio of a filler, which is defined as the ratio of length to diameter for cylindrical fillers (e.g., CNTs) and the ratio of length to thickness for platelet fillers (e.g., graphene nanoplatelets (GNPs)). A greater aspect ratio may result in a relatively lower mismatch [231–234]. Additionally, the diameter plays a key role in determining the *K* of composites reinforced with spherical particles. PMCs filled with spherical fillers normally offer comparatively lower *K* due to a lack of perfect connection with each other, limiting the movement of phonons. In the case of fiber orientation, fillers mainly possess anisotropy of properties and heterogeneity, influencing the heat flow efficiency. Therefore, implementing fillers with controlled orientation using hot pressing [235], magnetic alignment [236] or electrospinning [237] can offer relatively high *K* values. For example, Pan et al. [235] reported a 350% increase in the *K* of epoxy/Al_2O_3 composite using the hot pressing orientation technique.

The loading fraction of fillers is another key factor in increasing or decreasing the *K* value of PMCs. From the experimental point of view for low and moderate filler fractions, Chudek et al. [238] mixed graphene nanoplatelets (GNPs) with polylactic acid (PLA) randomly using the hot pressing technique. They reported the *K* value of 1.72 W/m K for a GNP/PLA composite as the result of adding 15 wt.% GNPs, increasing the *K* of the host PLA polymer matrix by 406%. In addition, Raza et al. [239,240] reported the *K* values of 1.909 W/m K and 2.2 W/m K for GNP/silicone composites with a filler fraction of 20 wt.% fabricated by mechanical mixing and three-roll milling, respectively. Moreover, Wang et al. [241] illustrated the in-plane *K* value of 15.8 W/m K for GNP-nylon composites fabricated using vacuum-assisted filtration (VAF) and compression molding (CM) by adding 11.8 wt.% graphene, which was 62.2 times greater than that of the pure polymer. In another study, Wang et al. [203] fabricated polyoxymethylene (POM)/multiwalled carbon nanotube (MWCNT) and POM/GNP composites (PMCNT and PMGNP, respectively). They exhibited the through-plane *K* values of 1.95 W/m K and 4.24 W/m K for the PMCNT40 (with 40 wt.% MWCNT) and PMGNP48 (with 48 wt.% GNP), respectively, which were approximately 4.6 and 11.1 times greater than those of neat POM in the through-plane direction, respectively. Nevertheless, the in-plane *K* values of the PMCNT40 and PMGNP48 composites were 4.17 W/m K and 36.35 W/m K, respectively. The in-plane *K* of PMGNP48 composite was ca. 13 times greater than that of pure POM. In addition, Wang et al. [242] implemented single crystalline copper nanowires with large aspect ratios as fillers in an acrylate polymer matrix. They measured the *K* of 2.46 W/m K at an ultralow loading fraction, roughly 0.9 vol.%, increasing it by 13.5 times compared with the host polymer matrix. In another study, Balachander et al. [218] developed a highly conductive polydimethylsiloxane nanocomposite filled with a low volume fraction of gold nanowires. They reported the *K* value of 5 W/m K using just below 3 vol.% gold nanowire fillers, leading to a 30-fold increase in the *K* of polydimethylsiloxane (PDMS).

It should be mentioned that the upper limit of graphene loading fraction in PMCs is normally 20 vol.% to avoid electrical percolation [243], obtaining a moderate *K* value of 20 W/m K or below. However, there may be some exceptions. On the other hand, BNNS and fluorinated graphene (F-graphene) fillers as the prime candidates can be even implemented for manufacturing composites with high loading filler fractions. For this purpose, Wang and Wu [244] used F-graphene filler, exfoliated from commercial fluorinated graphite, with loading fraction of 93 wt.%. They reported the in-plane *K* value of 61.3 W/m K. In

another study, Wu et al. [245] implemented BNNS with loading fraction 90 wt.% in a poly diallyl dimethyl ammonium chloride (PDDA) matrix. They showed a high in-plane K with the value just above 200 W/m K and a relatively low out-of-plane K of 1.0 W/m K.

According to the obtained data for K ranges of isotropic and anisotropic (in-plane direction) PMCs and K enhancement (K_c/K_m) reviewed in [243], the vast majority of PMCs possess K values higher than 1 W/m K. Nonetheless, a minority of them have values greater than 20 W/m K (see Figure 6 in [243]), which mainly happen at moderate and high filler loading fractions (more than 40 vol%). Additionally, K was reported to be increased compared to pure polymer matrix (K_c/K_m) by 10 times for most composites, 100 times for a minority of composites and by roughly 4200 times for nanofibrillated cellulose (NFC)/BNNS.

Furthermore, the mathematical models developed for quantifying the K of PMCs filled with particles have been reviewed in [192,246]. The proposed models are briefly presented in Table 3, wherein K_{eff}, K_f and K_m denote the effective thermal conductivity of the filler-embedded polymer matrix, the thermal conductivity of the filler and the thermal conductivity of the host polymer matrix, respectively; φ, d and R_k indicate the filler volume fraction, the filler diameter and the thermal interface resistance between the particle and the host polymer matrix, respectively; and K_{CNT}, L and t represent the K of a carbon nanotube, the length of a CNT and the thickness of the laminated composite, respectively. As can be concluded, the K of PMC is considerably lower than that of fillers (see Table 2). This significant difference can be explained by the high thermal resistance (R_k) at the filler–host interfaces and other factors, which are discussed later. As a recommendation, the results obtained from experiments can be compared with such data extracted from the proposed mathematical models in Table 3 in further studies by researchers. For this purpose, Wang et al. [247] illustrated that both the Maxwell and Nielsen models can accurately predict the K of PMCs when the filler volume fraction is lower than 10 vol.%, while the Nielsen model is in good agreement with experiments when the filler volume fraction is above 10%.

Table 3. Typical models for determining K of filler-embedded PMCs.

Authors	Filler Shape	Model	Remarks
Hasselman et al. [248]	Sphere	$\frac{K_{eff}}{K_m} = \frac{K_f(1+2\alpha)+2K_m+2\phi[K_f(1-\alpha)-K_m]}{K_f(1+2\alpha)+2K_m-\phi[K_f(1-\alpha)-K_m]}$ *where* $\alpha = 2R_kK_m/d$	Appropriate for moderate volume fraction, $\phi < 0.4$
Maxwell [249]	Sphere	$\frac{K_{eff}}{K_m} = \frac{K_f+2K_m+2f[K_f-K_m]}{K_f+2K_m-f[K_f-K_m]}$	Assuming perfect thermal contacts in polymer–filler interface (i.e., $R_k = \alpha = 0$), and $\phi < 0.4$
Eucken [250]	Sphere	$\frac{K_{eff}}{K_m} = \frac{1-\phi}{1+\phi/2}$	Assuming nanoparticles act like nanopores (i.e., $\alpha \to \infty$), and $\phi < 0.4$
Hasselman et al. [248]	Sphere	$\frac{K_{eff}}{K_m} = \frac{1+2\alpha+2\phi(1-\alpha)}{1+2\alpha-\phi(1-\alpha)}$	Suitable when $K_f \gg K_m$, e.g., using CNTs and GNPs
Ma and Na [251]	Sphere	$(1-\phi)\frac{K_m-K_{eff}}{K_m+2K_{eff}} + \phi\frac{K_f-K_{eff}(1+\alpha K_f/K_m)}{K_f+2K_{eff}(1+\alpha K_f/K_m)} = 0$	Appropriate for high volume fraction, and $\phi > 0.4$
Every et al. [252]	Sphere	$(1-\phi)^3 = \left(\frac{K_m}{K_{eff}}\right)^{(1+2\alpha)/(1-\alpha)}\left[\frac{K_{eff}-K_f(1-\alpha)}{K_m-K_f(1-\alpha)}\right]^{3/(1-\alpha)}$	Assuming $\alpha = 0$ or $K_f \gg K_m$, and $\phi > 0.4$
Bryning et al. [253]	Cylinder	$\frac{K_{eff}}{K_m} = \frac{\left(3+\phi\left(\beta_\perp+\beta_\parallel\right)\right)}{(3-\phi\beta_\perp)}$ *where* $\beta_\perp = \frac{2(d(K_{CNT}-K_m)-2R_kK_{CNT}K_m)}{d(K_{CNT}+K_m)+2R_kK_{CNT}K_m}$ $\beta_\parallel = \frac{L(K_{CNT}-K_m)-2R_kK_{CNT}K_m}{LK_m+2R_kK_{CNT}K_m}$	Appropriate for CNT-embedded composites, e.g., for N-N-Dimethylformamide (DMF)-processed composites $R_k = (2.4 \pm 1.3) \times 10^{-9}$ m^{2}K/W, and for surfactant-processed composites $R_k = (2.6 \pm 0.9) \times 10^{-8}$ m^{2}K/W

Table 3. *Cont.*

Authors	Filler Shape	Model	Remarks
Hasselman et al. [248]	Cylinder	$\frac{K_{eff}}{K_m} = \frac{\left[\phi\left(K_f/K_m - 1 - 2K_f/(dR_k)\right) + \left(1 + K_f/K_m + 2K_f/(dR_k)\right)\right]}{\left[\phi\left(1 - K_f/K_m + 2K_f/(dR_k)\right) + \left(1 + K_f/K_m + 2K_f/(dR_k)\right)\right]}$	Developed for a continuous matrix phase with dilute concentrations of dispersions with cylindrical geometry
Hasselman et al. [248]	Flat plate	$K_{eff} = \frac{K_f}{\phi\left(1 - K_f/K_m + 2K_f/(tR_k)\right) + K_f/K_m}$	Used for flat plate dispersions oriented perpendicular to the heat flow with thickness of t
Nielsen [254]	Various particle shapes	$K_{eff} = \frac{1 + AB\varphi}{1 - B\psi\varphi}$ where $B = \left(\frac{K_f/K_m - 1}{K_f/K_m + A}\right);\ \psi = 1 + \left(\frac{1 - \varphi_m}{\varphi_m{}^2}\right)\varphi$	Appropriate for moderate volume fraction, $\phi < 0.4$. A is the shape coefficient for the filler particles; φ_m is the maximum filler volume fraction

According to the previous studies reviewed in [243], as the amount of filler utilized increases, up to a specific limit depending on the type and geometry of fillers and polymers, the *K* value that can be achieved increases. This limitation for adding filler up to a certain level can be explained by agglomeration and/or saturation of fillers in the polymer matrix [255], the formation of voids and poor dispersion [256,257], etc.

4.2.5. Influence of Hybrid Fillers in Overall *K* of PMC Structures

One of the viable solutions in order to achieve higher *K* values is to fabricate and implement hybrid fillers in polymeric materials; for targeting highly conductive hybrid composites, such hybrid fillers must possess adequate functionalities so as to make an interconnected structure with each other using chemical vapor deposition (CVD) (see for example [258]). For this objective, Bozlar et al. [259] illustrated a 1.3 times increase in *K* value of a host Al_2O_3-epoxy composite as the result of adding a low MWCNT mass fraction of 0.15 wt.%, obtaining the *K* value of 0.39 W/m K. In addition, Yu et al. [229] implemented hybrid fillers of single-walled carbon nanotubes (SWNTs) and graphite nanoplatelets (GNPs), with the hybrid loading mass fraction of 10%, consisting of 2.5 wt.% SWNTs and 7.5 wt.% GNPs. They reported a *K* value of 1.75 W/m K, which was roughly 5 times greater than that of pure epoxy. Teng et al. [260] studied the synergistic influence of combining MWCNTs and boron nitride (BN) flakes on the *K* of epoxy-based composites. In order to form the covalent bonds between the epoxy and fillers, the surfaces of such fillers were functionalized, leading to a reduction in the thermal interfacial resistance (R_k). They illustrated a *K* value of 1.913 W/m K as the result of adding 30 vol.% modified BN and 1 vol.% functionalized MWCNTs, obtaining a 7.43-fold increase in such a figure for pure epoxy (0.2267 W/m K). Im et al. [261] investigated the *K* behavior of a graphene oxide (GO)–MWCNT hybrid/epoxy composite. As they showed, adding merely 0.36 wt.% of MWCNT into 50 GO-epoxy composites resulted in the highest enhancement ratio (about 140%) relative to the GO/epoxy composite, which was explained by the formation of 3D heat conduction paths due to the addition of MWCNTs. Yu et al. [262] investigated how the *K* of an Al_2O_3-silicon composite is positively influenced by graphene. They demonstrated that adding 1 wt.% of graphene increased the *K* of Al_2O_3-silicon from 2.70 W/m K to 3.45 W/m K for a graphene-Al_2O_3-silicon composite. Sharma et al. [263] investigated how the *K* of SWCNT-metallic glass (MG) composites is influenced by the variation in the SWCNT volume fraction. They reported the values of 1.52 W/m K, 4.07 W/m K and 4.60 W/m K for the addition of 0%, 5% and 12% SWCNT. Additionally, Wu et al. [264] investigated the *K* of a continuous network of graphene foam (GF) filled with aligned graphene nanosheets (GNs). A relatively high in-plane *K* of 10.64 W/m K at the filler loading of 6.2 vol% was measured, which can be explained by the synergistic influence between 3D GF and graphene nanosheets.

4.2.6. Improving Out-of-Plane Thermal Conductivity Value Using 3D Fillers

The self-heating phenomenon appearing in a PMC specimen during fatigue testing is often quantified by measuring the specimen's surface temperature. If we assume the PMC specimen as a rectangular plate for simplicity, the total area of four lateral faces of a rectangular laminated PMC specimen ($2W \times t + 2L \times t$, where L is length, W is width and t is thickness) is, in general, lower than the area of the two bases ($2L \times W$) during standard fatigue testing. This means that using thermally conductive fillers through the thickness (out-of-plane) direction can act as a catalyst for transferring heat generation induced by the self-heating effect. According to the provided data for out-of-plane K values of PMCs (see Figure 7 in [243]), the out-of-plane K values of PMCs are relatively low. Numerous composites possess a K value of 4 W/m K or below, whereas a minority of them have a value higher than 10 W/m K when using a noncovalently functionalized boron nitride nanosheet (BNNS). Additionally, when a PMC has anisotropic and heterogeneous properties (e.g., transversely isotropic and orthotropic), the range of K values in the out-of-plane direction is significantly lower than that of other directions in general. Therefore, it is of primary significance to enhance the out-of-plane K of such composites.

For the purpose of enhancing the K value in out-of-plane direction by constructing a 3D thermally conductive pathway, Yu et al. [265] prepared z-filler CFRP laminated composites filled with spherical copper particles and coated with aluminum foil in order to investigate the influence of z-filler volume fraction on the out-of-plane K value. Figure 66 reveals a schematic representation of the developed z-filler CFRP laminated composites shown by them. With the decrease in the distance between z-copper fillers (i.e., higher volume fraction), the measured K value increased. They reported a maximum increase of roughly 12 times in the out-of-plane K of z-filler laminated composites (7.6 W/m K) for a 2 mm distance between every two z-fillers, compared with unmodified CFRP composites (0.6 W/m K).

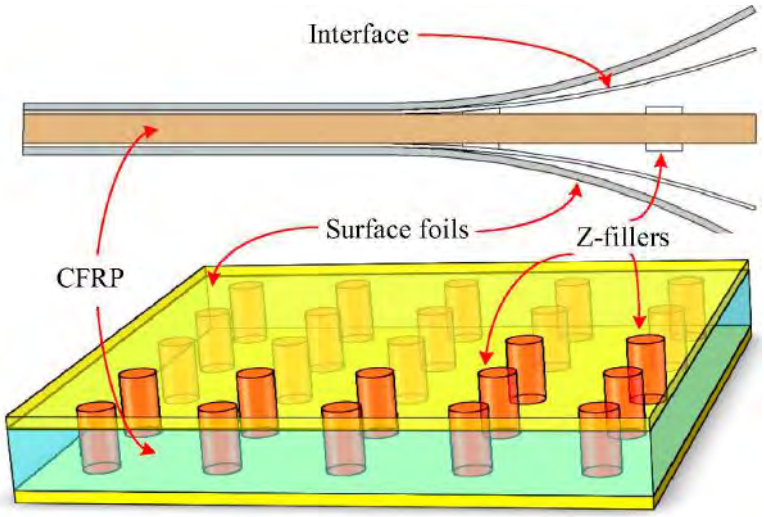

Figure 66. Schematic demonstration of z-filler CFRP laminated composites, adapted with permission from Ref. [265]. Copyright © 2016 Elsevier Ltd.

The implementation of 3D fillers and the construction of interconnected three-dimensional (3D) graphene networks can be also a solution. As opposed to PMCs reinforced with dispersed graphene nanoplates (GNPs), implementing 3D GNPs in PMC structures can result in comparatively higher K values. This can be explained by adequate phonon transmission channels and a reduction in the thermal resistance in the continuously interconnected 3D GNPs [266]. Nevertheless, the high cost and unfavorable mechanical properties limit the application of 3D graphene-based polymer composites in many engineering fields involving thermoregulation applications [266]. Compared to the traditional polymer composites filled with randomly

dispersed graphene nanosheets, constructing 3D GNs in polymer composites emerges as a more effective strategy to achieve high *K* values at relatively low filler loadings due to sufficient phonon transmission channels and reduced thermal resistance in the continuous interconnected 3D GNs. In another study, Hu et al. [230] constructed 3D hybrid networks in poly(vinylidene fluoride) composites via positively charged hexagonal boron nitride- and silica-coated carbon nanotubes (m-hBN/MWCNT-SiO_2/PVDF). Three-dimensional networks could decrease the interfacial thermal resistance (R_k), leading to a higher level of phonon transmission (or decreasing phonon scattering at the filler–matrix interface) (see Figure 67). They measured a *K* value of 1.51 Wm·K for a 3D network of m-hBN/MWCNT-SiO2/PVDF with filler loading of 25 wt.%, and this *K* value was just below 6 times higher than that of pure PVDF.

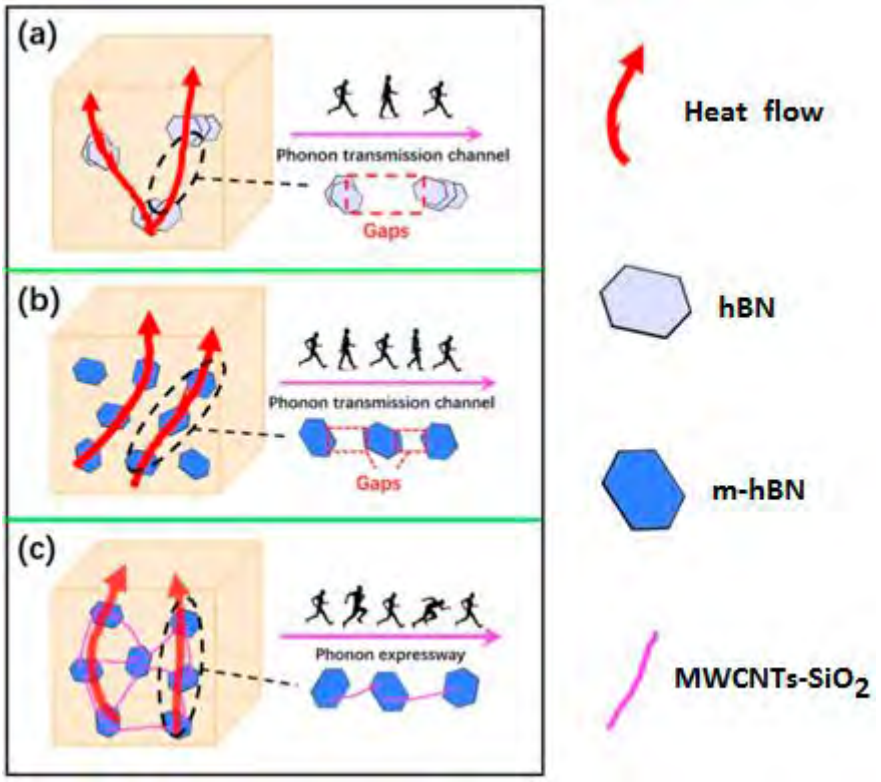

Figure 67. The schematic representation of thermally conductive pathways of (**a**) hBN/PVDF, (**b**) m-hBN/PVDF and (**c**) m-hBN/MWCNT-SiO2/PVDF composites, adapted with permission from Ref. [230]. Copyright © 2020 Elsevier Ltd.

4.2.7. The Role of Interface Treatment, Coating and Core in Enhancing Out-of-Plane Thermal Conductivity

One of the other possible solutions to enhance the out-of-plane *K* value of the MC structures is to implement surface treatment (e.g., coating and films). Although films and coated layers are thermally conductive, their thicknesses may act as a driving factor in obtaining high *K* values; the thickness should be sufficient, neither very thick nor very thin, depending on the type of materials. A greater thickness may disadvantageously provoke a low in-plane *K* value. For this reason, Chen et al. [237] studied the influence of thickness on the in-plane *K* value of boron nitride nanosheet (BNNS)-poly vinylidene difluoride (PVDF) nanocomposite films. They reported a significant *K* reduction in BNNS- PVDF nanocomposite film, varying from 16.3 W/m K to 5 W/m K as the result of increasing thickness from 18 μm to 170 μm. Therefore, the thickness of a thermally conductive coating layer or film takes center stage in prompting phonon transmission for achieving high *K* values. This parameter is highly dependent on the material types, which should be taken into consideration before the manufacturing process of composite structures. On the other

hand, controlling the fiber–matrix interface is of primary significance and is not an easy task due to the scattering of phonons at the interface. A sizable portion of phonon scattering is due to poor nonbonded van der Waals interactions in the interface of the polymer matrix and filler. The insufficient vibrations among atoms at the interface resulting from weak nonbonded interactions lead to a significant thermal resistance at the interphase region, and consequently a low *K* value [189,267]. To address this issue, a non-covalent filler surface modification (coating) can be implemented, which decreases the thermal resistance between fibers and the bulk polymer matrix [268]. The main approaches for preparing coating structures include silica deposition [269] and the self-polymerization of dopamine [270] and tannic acid [271] via bio-inspired polyphenols. The *K* value of such coated polymeric materials may vary and drop compared to that of uncoated composite, unless the coating layer thickness is below 10 nm [229]; i.e., the coated layer acts as a thermal resistance barrier if its thickness exceeds the mentioned value. In general, the interface between the filler and polymer and the interface between composite layers subjected to thermal fatigue play a key role in the service life of the composite structures, so a weak interface can provoke thermal fatigue delamination and structural degradation [272]. Nevertheless, there is still a lack of knowledge about how such surface treatments and the use of thermally conductive films can extend the fatigue life of PMC structures. As a recommendation, a comprehensive investigation of the effects of surface treatment on the overall fatigue performance of the PMC structures by taking into account the loading parameters (e.g., loading frequency, stress level and strain rate) is meaningful and necessary in future studies.

From another perspective, in addition to FRPs, composite sandwich panel structures have gained great interest, particularly in WTB, aerospace and marine industries, due to their superior specific flexural properties and cost-effectiveness [273,274]. Such structures may be subjected to cyclic loading and experience self-heating effects (e.g., WTB). Therefore, for such applications, the idea is to select an appropriate core with relatively high thermomechanical performance (i.e., high *K* value). Such structures involve laminated facesheets and cores. It has been suggested that the core can be appropriately selected to obtain thermally conductive sandwich structures. Typical cores with engineering applications can be primarily categorized into corrugated, truss, foam and honeycomb cores [275]. Among them, foam cores offer more uniform heat transfer distribution due to forming comparatively lower empty volumes in the core region (e.g., carbon foam) [276]. When it comes to finding or proposing an alternative solution for minimizing the catastrophic effect of the self-heating phenomenon, polymeric foams involving low-density polyethylene (LDPE) and polypropylene may not be good options due to exhibiting very low thermal conductivities and poor thermal instability under high temperature regimes; additionally, metallic foams including aluminum might be an ineffective solution despite possessing good thermal stability and *K*. The applications of metallic foams in polymeric sandwich structures have been limited due to the inherently weak bonding between the metallic core and the FRP facesheets and significant mismatch in their thermal expansion properties leading to facesheet/core delamination. Carbon foam, however, can be a prime candidate in terms of enhancing heat transfer through the thickness of lightweight sandwich panel structures [276–278]. Among available carbon foams, graphitic foam provides an outstanding *K* value with a low thermal expansion coefficient and density. For this reason, Sihn and Rice [279] conducted four-point bending fatigue tests for FRP facesheet/carbon foam core sandwich beams. In another study, Sihn et al. [276] measured the *K* of a sandwich structure composed of unidirectional graphite/epoxy facesheets and a carbon foam core. They reported the out-of-plane *K* values of 19.21 W/m K for the co-cured foam–facesheet sandwich with 5.99 mm thickness and 6.44 W/m K for the adhesively bonded sandwich specimens with 5.69 mm thickness. The main root of this comparatively high difference can be explained by interface thermal resistance (R_k), which was reported to be 0.0251 mm^2K/W for co-cured and 0.312 mm^2K/W for the co-cured and adhesively bonded sandwich specimens. Furthermore, Quintana and Mower [280] determined the *K* of sandwich panels. They reported *K* values of 60 W/m K and 10 W/m K, respectively, for an adhesively bonded Al

facesheet–graphitic foam core, which was approximately 10 times greater than that of a CFRP facesheet–graphitic foam core sandwich panel.

On the other hand, honeycomb cores have received significant attention in advanced industries because they offer superior specific stiffness and strength [281], not because of their thermomechanical properties. Nonetheless, there are insufficient data to characterize whether honeycombs can effectively tackle the problematic issue of structural degradation induced by self-heating during fatigue loading. To correctly answer this, the K value of a typical honeycomb should be quantified first. For this reason, Bezazi et al. [282] developed an analytical in-plane model for determining the K of honeycombs, allowing us to understand whether the honeycomb acts as a heat sink or an insulator. It should be mentioned that, regarding minimizing the self-heating effect in sandwich panel structures, the through-thickness K may be more important and should be taken into consideration in further studies.

On the one hand, the amount of energy dissipation via conduction in honeycomb sandwich structures may be relatively lower compared to that in laminated FRP composites due to honeycomb sandwich structures possessing higher empty volume in the core region, which consequently leads to a low-density material/structure. A good illustration of this is a Nomex honeycomb with a density of 48 kg/m^3 [283], which is more than 20 times lighter than engineering polymers such as epoxy at a constant volume. It should be mentioned that what primarily provokes thermal fatigue failure in a composite structure is a high level of stored internal energy. Assuming that the temperature is time-independent, one can conclude that the rate of stored internal energy ($\Delta\dot{u}$) in a sandwich panel with such a core remains constant and may be more than 20 times lower than the same figure for a composite without a core according to $\Delta\dot{u} = \rho c_p \frac{\partial T}{\partial t}$ (see Equation (13)). However, this assumption can be rational if and only if the steady-state heat transfer (i.e., stationary regime) occurs. Otherwise, the appearance of greater temperature accelerates the rate of internal energy storage and consequently maximizes the effect of self-heating. In general, it is difficult to exactly characterize the relation between the density of the core and the amount of internal energy because the density of the core may influence the heat capacity (c_p).

For this reason, Rajaneesh et al. [284] investigated the performance of CFRP/Nomex-honeycomb sandwich beams under four-point bending fatigue using the time–temperature superposition (TTS) principle by ignoring the influence of temperature on the honeycomb core behavior. However, it has not been proved yet whether the classical TTS principle can be used for high loading frequency (e.g., in the ultrasonic range).

One of the most challenging issues related to the honeycomb core sandwich panels may be developing accurate and nonlinear models for the purpose of predicting the residual life or structural degradation of such structures reliably. The primary reason behind this can be sought in the complexity of modeling the interfaces between facesheets. For this reason, Hu and Wang [285] developed a theoretical model in order to study the thermal fatigue delamination damage of auxetic and non-auxetic honeycomb layer/substrate structures under thermal cycling.

5. Conclusions

This paper systematically reviewed and discussed the appearance of the self-heating effect in polymers and PMCs under fatigue loading, including the theoretical and physical aspects. For this purpose, the fatigue fracture mechanisms in a PMC structure induced by the self-heating phenomenon were analyzed at three different scales (i.e., nano, micro, and macro). The practical solutions implemented by various teams for addressing the issue of a nonstationary self-heating regime induced during fatigue loading were then broadly reviewed. The viable solutions were classified based on optimal materials design and selection and cooling scenarios, considered the main core of the current paper. In the case of the former, selecting thermally conductive materials was proposed. Improving the K values of PMC structures was proposed. To increase the in-plane and out-of-plane K values of PMC structures, the influences of filler type (e.g., BN and carbon allotropes), the

size (i.e., nano-, micro- or macroscale) and shape (e.g., 2D or 3D) of thermally conductive fillers, the filler volume fraction, the type of polymer in terms of the level of polymer crystallinity, the implementation of thermally conductive foams (e.g., carbon and graphite foams) and the use of coatings and interfacial films were analyzed, and these factors are taken into account during the manufacturing process of PMCs. From the other perspective, to limit the effect of internal energy, the influence of environmental factors (i.e., relative humidity and coolant agent temperature) and operational factors (i.e., mainly average convective heat transfer coefficient ($\bar{h}$)) was analyzed. In the case of operational factors, the influence of different cooling techniques, including air cooling, liquid cooling (e.g., water, liquid N_2 and CO_2 as the coolant agents), multiphase cooling (e.g., spray cooling) and the newly developed pulse–pause techniques, was investigated. In addition, the vital role of measuring heat flux via convection as well as quantifying $\bar{h}$ and improving the value of this parameter was broadly discussed as a guideline for future studies. Using cooling scenarios will decrease the amount of internal energy and consequently cool down the PMC specimen temperature. The diagram below represents the summary of the paper and provides a practical guideline for limiting the self-heating effect in PMC structures (see Figure 68). The diagram involves the characterization of (i) fatigue damage accumulations as well as searching for viable solutions to (ii) limit the self-heating effect and consequently limit the structural degradation in PMCs. The maximum temperature on the specimen surface is determined from the former using numerical simulations or experiments. If the maximum temperature is below the critical self-heating temperature, the specimen remains safe and without any requirement for implementing a cooling system or changing the ambient temperature. Otherwise, an appropriate cooling system and/or coolant agent should be selected according to the level of internal heat generation. The fatigue damage mechanisms and aspects connected with preventing structural degradation are briefly summarized in Sections 5.1–5.3.

5.1. Scale-Based Fatigue Damage Mechanisms

Due to the self-heating effect, the larger shrinkage of the polymer matrix compared to thermally conductive fibers may provoke chemical stress. However, to the best of the authors' knowledge, the level of chemical shrinkage is sufficiently low below the critical self-heating temperature (i.e., before the beginning of phase III in the nonstationary regime—see Figure 24), which can be negligible. Furthermore, the self-heating phenomenon can cause thermal stress concentration in addition to the applied mechanical stress during fatigue. This can be explained by the CTE mismatch between fibers and the neighboring polymer matrix. The covalent bonds among polymer chains and the nonbonded electrostatic and van der Waals interactions begin to be weaker as the result of thermal stress. On the other hand, laminated PMC structures show different CTE values in different directions (e.g., for CTE, values are different in longitudinal and transverse directions of a transversely isotropic PMC structure such as CFRP). This difference can be explained by using layers with different staking sequences and the anisotropy behavior of layers. These factors can initiate and/or accelerate the degradation process of cyclically loaded PMC structures, which leads to quite complex fracture mechanisms and consequently the sudden fatigue failure in the structure. The main conclusions associated with the scale-based fatigue damage mechanisms with the presence of the self-heating effect are summarized as follows:

1. Polymer degradation due to the self-heating effect, which is associated with residual crosslinking, can initiate the crack nucleation process and propagate the damage.
2. To avoid structural degradation in PMCs, it is necessary to measure and quantify the size of cracks and delaminations in both the micro- and macroscale.
3. Delamination and interfacial debonding damage can be the critical forms of fatigue damage mechanisms. To characterize this in continuum mechanics, it is assumed that both fibers and polymer matrix are perfectly bonded. This means that there is a continuity in the displacement field, and consequently a continuity in the strain field, as opposed to the stress field wherein there may be discontinuity due to the

dependency of stress on viscoelastic moduli. Therefore, measuring the strain field can be an indicator of damage caused by the self-heating effect in a PMC structure.

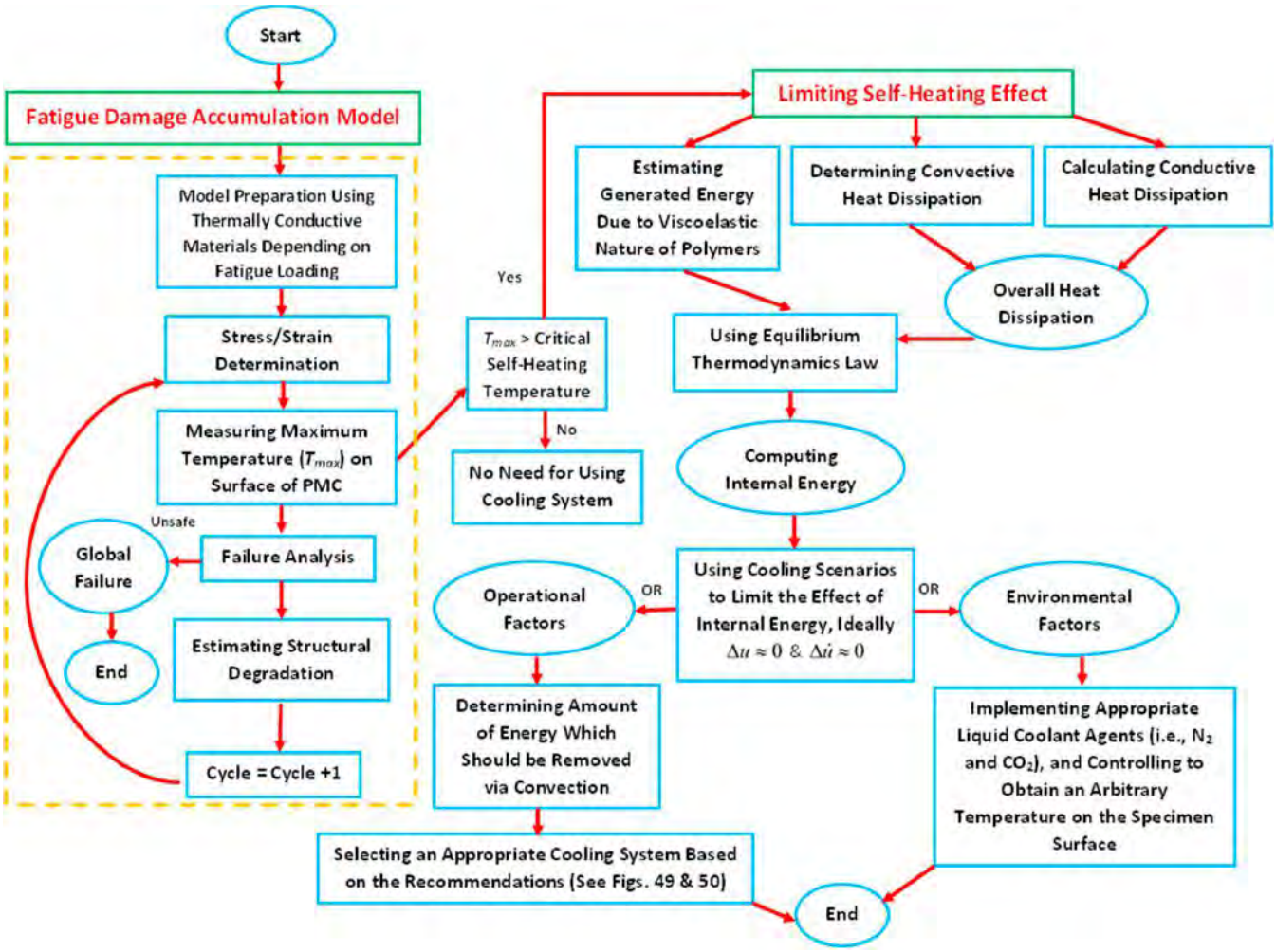

Figure 68. Schematic model for estimating structural degradation and preventing the appearance of self-heating phenomenon using cooling scenarios.

5.2. Cooling Scenarios and Techniques

As a practical guideline, before implementation of any cooling scenario, it is of primary significance to monitor whether the cyclically loaded PMC structure operates in a stationary or nonstationary regime. This can be understood by measuring the critical self-heating temperature. If. the specimen's surface temperature is below the critical temperature, there is no need to implement any cooling technique. Otherwise, implementing an appropriate cooling technique is vital to provide uniform temperature distribution as well as limit the PMC specimen surface temperature growth induced by the self-heating effect. For this reason, two possible scenarios were discussed, involving environmental factors (i.e., relative humidity and ambient temperature of coolant agent) and operational parameters (i.e., Nusselt number, thermal conductivity of fluid around the specimen and characteristic length of the specimen). The operational parameters were explained by the average convective heat transfer coefficient ($\bar{h}$). The main points related to cooling techniques and scenarios are as follows:

1. Conducting fatigue testing exposed to an environment with high moisture content can degrade the mechanical properties of a PMC specimen unless the moisture does not penetrate through the specimen's thickness. This means that the time of fatigue testing should be sufficiently low, which may be achieved in ultrasonic frequency.

2. Reduction in ambient temperature using liquid coolant agents such as water, liquid nitrogen and liquid carbon dioxide is a viable solution. An appropriate coolant system can be selected by making an optimization based on high thermal capacity, low viscosity, anticorrosion properties, nontoxicity and affordable price.
3. The operational factors, which have a direct influence on the fatigue life of PMCs, are directly connected with $\overline{h}$. A greater $\overline{h}$ offers a larger amount of heat removal through convection. Therefore, fatigue life extension can be obtained by enhancing this parameter.
4. The discussed cooling techniques, including air cooling, liquid cooling, passive cooling, pulse–pause air cooling, ring-type Peltier cooling and spray cooling, can be implemented for removing the heat induced by the self-heating effect. This will consequently extend the fatigue life of a typical PMC structure.
5. Air cooling, as the simplest cooling method, is applicable for removing relatively low heat flux (i.e., 5 kW or below according to recommendations, see Figures 49 and 50 for more details). However, for removing higher amounts of heat up to 80 kW, liquid-based cooling techniques are the prime candidates. For amounts higher than 80 kW, phase change techniques (e.g., spray cooling using the latent heat of vaporization of water) can be implemented.
6. The pulse–pause air cooling technique and the use of cryogenic nitrogen and pulse–pause simultaneously as a cooling technique have only been implemented for the VHCF regime in an ultrasonic frequency range.
7. Quantifying the heat flux during fatigue testing leads to a reliable classification and standardization according to the type of fatigue loading, the type of materials used in the PMC structure and the specimen geometry.
8. The temperature distributions might not be uniform in in-plane directions and through the thickness, which, in connection with the heterogeneity of PMCs, results in quite complex fracture mechanisms.

5.3. Optimal Material Design and Selection

In the real life, a typical PMC structure may undergo a low number and/or very high number of cycles by experiencing different mechanical loading conditions, as well as various hygrothermal effects (i.e., moisture content and ambient temperature). Such a PMC structure should be designed and fabricated by considering all the below-mentioned material aspects, which are directly connected with improving thermal conductivity. It is then crucial to carry out comprehensive studies for a wide range of fatigue tests (i.e., LCF, HCF and VHCF regimes) to quantify the effect of material aspects on the K value and limit the structural degradation. The primary conclusions relevant to material aspects are as follows:

1. Implementing a thermally conductive filler with a sufficient volume fraction increases the K value of PMCs. Otherwise, it may be difficult to obtain relatively high K values because of phonon scattering accelerated by defects and imperfections involving chain dangling ends, entanglement and irregular orientation. Moreover, the addition of such a filler should be appropriately balanced from the mechanical point of view.
2. Using polymers with a high level of chain crystallinity is recommended since it can enhance the K values of polymers.
3. Thermally conductive carbon allotropes (e.g., carbon fiber, CNT, GN), ceramics (e.g., BN) and metals (Cu, Ag, Au) can be the prime candidates for improving the thermal conductivity of a typical pure polymer matrix.
4. Although implementing 3D fillers offers greater K values, using 2D fillers with greater aspect ratios (i.e., length to diameter for cylindrical fillers and the ratio of length to thickness for platelet fillers) may also offer quite good K values. In addition, 2D fillers can be easily implemented during the fabrication process of composites. Therefore, using 2D fillers with a high aspect ratio is preferable.

5. Implementing thermally conductive nanoparticles (e.g., BN, CNT and GN) is preferable to implementing micro- or macrofillers because thermally conductive nanoparticles have a significantly larger surface area to volume ratio.
6. Since the CTE of a typical polymer is generally higher than that of thermally conductive fillers, the residual thermal stresses during fatigue loading may appear at the interface/interphase region between the reinforcement and polymer, accelerating the molecular separation and lowering nonbonded van der Waals forces at the interphase zone between the filler surface and polymer chains. This will cause interfacial debonding and consequently high interfacial thermal resistance (R_k) between fillers and polymer chains, leading to relatively low K values. Therefore, it is promising to use fillers with low CTE values (e.g., carbon allotropes that have almost zero or even negative CTE values).
7. Using carbon/graphite foam can increase the K value, consequently limiting the self-heating effect.
8. Using films and surface coating has been proposed as a technique to achieve strong phonon transmission, consequently improving the K value.
9. Since thermal conductivity is temperature-dependent, it is noteworthy to measure and quantify the influence of self-heating temperature induced during fatigue loading on this parameter for an investigated PMC. This will help to evaluate the amount of heat flux via conduction in a more precise way.

6. Gap Analysis and Future Directions

As discussed in the previous sections, various studies have been conducted for characterizing the fatigue damage accumulation induced by self-heating at different scales during fatigue loading. To limit the self-heating effect, some cooling scenarios and thermally conductive materials were implemented by researchers, which were broadly discussed. Nevertheless, the challenging issues connected with understanding fatigue damage mechanisms, cooling techniques and material selections, which should be taken into consideration in future studies, are as follows:

1. It is worth conducting further studies to quantify the residual crosslinking in different engineering PMCs at various fatigue loading levels with the presence of the self-heating effect.
2. There are no studies in the open literature about how the self-heating phenomenon can be quantitively influenced by changing the level of chain crystallinity of the polymer matrix. Therefore, the effect of polymer chain crystallinity alongside the self-heating phenomenon on the overall fatigue performance of PMC structures should be studied under different loading conditions in the future.
3. Although using image-based techniques such as X-ray CT scanning offers the opportunity to measure the volume of microcracks and delaminations, there is still a lack of knowledge and understanding to quantify the size of delaminations and cracks caused by the self-heating effect in PMC structures.
4. It is of key interest to experimentally and numerically characterize the strain distribution at the fiber–matrix interface and measure the strain between every two layers as an indicator of fatigue damage accumulation.
5. Although a PMC structure is subjected to a complex type of loading during its real lifetime, the vast majority of studies have focused on merely one-directional loading to characterize the structural degradation mechanism of PMC coupons. Therefore, it is noteworthy to investigate the structural degradation mechanisms under more complex fatigue loading (e.g., random and multiaxial loading) considering numerous practical problems, where self-heating may appear in such loading conditions.
6. To limit the fatigue damage propagation in PMC structures, it is useful to conduct further studies to investigate the effect of different stacking sequences, as well as various types of nanoparticles in polymers as modified FRP composites.

7. To limit the self-heating effect, it is of primary significance to conduct a comprehensive investigation of different liquids for the purpose of selecting an appropriate coolant system by making an optimization based on high thermal capacity, low viscosity, anticorrosion properties, nontoxicity and affordable price.
8. Although the mentioned techniques indeed operate based on increasing $\overline{h}$, there are no data about this parameter from the previous studies wherein cooling techniques had been implemented to minimize the influence of the self-heating effect. Thus, it would be a practical guideline if this parameter is also reported when using a cooling method for cyclically loaded PMC structures in further studies.
9. There are insufficient data to understand how liquid-based cooling techniques can effectively address the heat generation caused by the self-heating effect in PMCs.
10. In the pulse–pause cooling technique, the investigation of the optimal pulse–pause ratio at a specific applied stress/displacement loading is still ongoing. In addition, no results have been reported about the capability of pulse–pause technique in terms of removing the amount of heat energy. Another challenging issue associated with this technique is the characterization of whether it is possible to use this technique for a relatively low range of frequency (e.g., 1000 Hz or below). Moreover, since the common fatigue tests are mainly conducted at a continuous strain rate, using the pulse–pause technique leads to discontinuity of applied loading. It should be investigated whether this discontinuity has an influence on fatigue performance. Therefore, it is noteworthy to conduct research in this area to comprehensively quantify and generalize the effect of pulse–pause ratio and find the optimal pulse–pause ratio as a function of material configuration, loading conditions and geometry of the PMC specimens.
11. It is recommended to quantify and report the heat flux during fatigue testing to justify the reason behind selecting a specific cooling technique in future studies.
12. It is of high importance to compare the fatigue fracture mechanisms of PMCs using cooling techniques versus natural air convection as this will allow the effectiveness of such cooling techniques to be understood.
13. Although implementing thermally conductive fillers is preferable, the thermomechanical performance of such materials should be characterized in further studies.
14. Quantification of the influence of thermally conductive fillers on limiting the self-heating effect and consequently extending the fatigue life of PMC structures in the presence of the self-heating effect is of key interest.
15. It is useful to conduct various comparative studies to characterize the influence of 2D and 3D fillers under different levels of fatigue loading on limiting/accelerating the self-heating effect in PMCs.
16. The effect of scale-based fillers on the fatigue performance of PMC structures with the presence of the self-heating effect can be taken into consideration for the future studies.
17. Quantifying the admissible thermally conductive film thickness is of key importance, resulting in limiting the self-heating effect
18. Since PMCs have anisotropic properties, it is useful to study how the self-heating can be limited in the in-plane and the out-of-plane directions by measuring K values.
19. Whether the use of cores accelerates the rate of thermal fatigue failure is still an open question. Additionally, it is unknown how the maximum temperature values on the specimen surfaces under fatigue loading are influenced by variations in core thickness. As a recommendation, it would be useful to conduct comprehensive studies to quantify the fatigue behavior of sandwich structures with a wide range of core types with different thicknesses in the presence of the self-heating effect by controlling loading conditions (e.g., mainly loading frequency, stress levels, stress ratios for both LCF and VHCF regimes) and compare the obtained data with such data for composites without cores.

Author Contributions: Conceptualization, J.A. and A.K.; methodology, J.A. and A.K.; data curation, J.A. and A.K.; formal analysis, J.A. and A.K.; investigation, J.A; writing—original draft, J.A. and A.K.; writing—review and editing, J.A. and A.K. All authors have read and agreed to the published version of the manuscript.

Funding: This research received no external funding.

Data Availability Statement: Not applicable.

Conflicts of Interest: The authors declare no conflict of interest.

References

1. Katunin, A. Criticality of the self-heating effect in polymers and polymer matrix composites during fatigue, and their application in non-destructive testing. *Polymers* **2018**, *11*, 19. [CrossRef] [PubMed]
2. Lu, Z.; Li, Z.; Liu, H.; Wei, P.; Xia, B.; Ye, M. An accelerated fatigue test method of polymer gears based on thermostress conversion relation. *Eng. Fract. Mech.* **2022**, *266*, 108388. [CrossRef]
3. Katunin, A.; Wronkowicz, A. Characterization of failure mechanisms of composite structures subjected to fatigue dominated by the self-heating effect. *Compos. Struct.* **2017**, *180*, 1–8. [CrossRef]
4. Song, R.; Berer, M.; Muliana, A. Mechanical responses of semi-crystalline thermoplastic polymers at various temperatures. *Int. J. Solids Struct.* **2022**, *238*, 111398. [CrossRef]
5. Shojaei, A.K.; Volgers, P. Fatigue damage assessment of unfilled polymers including self-heating effects. *Int. J. Fatigue* **2017**, *100*, 367. [CrossRef]
6. Zhang, C.; Gou, X.; Xiao, R. Hysteresis in glass microsphere filled elastomers under cyclic loading. *Polym. Test.* **2021**, *95*, 107081. [CrossRef]
7. Tong, X.; Xu, J.; Doghri, I.; El Ghezal, M.I.; Krairi, A.; Chen, X. A nonlinear viscoelastic constitutive model for cyclically loaded solid composite propellant. *Int. J. Solids Struct.* **2020**, *198*, 126. [CrossRef]
8. Shojaei, A.K.; Wedgewood, A.R. An anisotropic cyclic plasticity, creep and fatigue predictive tool for unfilled polymers. *Mech. Mater.* **2017**, *106*, 20. [CrossRef]
9. Hao, P.; Laheri, V.; Dai, Z.; Gilabert, F. A rate-dependent constitutive model predicting the double yield phenomenon, self-heating and thermal softening in semi-crystalline polymers. *Int. J. Plast.* **2022**, *153*, 103233. [CrossRef]
10. Katunin, A.; Pivdiablyk, I.; Gornet, L.; Rozycki, P. A hybrid method for determination of fatigue limit and non-destructive evaluation of composite structures after low-velocity impact loading. *Compos. Part B Eng.* **2022**, *238*, 109898. [CrossRef]
11. Hülsbusch, D.; Kohl, A.; Striemann, P.; Niedermeier, M.; Strauch, J.; Walther, F. Development of an energy-based approach for optimized frequency selection for fatigue testing on polymers–Exemplified on polyamide 6. *Polym. Test.* **2020**, *81*, 106260. [CrossRef]
12. Mughrabi, H. On 'multi-stage'fatigue life diagrams and the relevant life-controlling mechanisms in ultrahigh-cycle fatigue. *Fatigue Fract. Eng. Mater. Struct.* **2002**, *25*, 755. [CrossRef]
13. *ASTM ASTM-D3039*; Standard Test Method for Tensile Properties of Polymer Matrix Composite Materials. ASTM International: West Conshohocken, PA, USA, 2017.
14. Couillard, R.A.A.; Schwartz, P. Bending fatigue of carbon-fiber-reinforced epoxy composite strands. *Compos. Sci. Technol.* **1997**, *57*, 229. [CrossRef]
15. Ogin, S.; Smith, P.; Beaumont, P. Matrix cracking and stiffness reduction during the fatigue of a (0/90) s GFRP laminate. *Compos. Sci. Technol.* **1985**, *22*, 23. [CrossRef]
16. Khatri, B.; Rehra, J.; Schmeer, S.; Breuer, U.; Balle, F. Metal/Carbon-Fiber Hybrid Composites—Damage Evolution and Monitoring of Isothermal Fatigue at Low and Elevated Temperatures. *J. Compos. Sci.* **2022**, *6*, 67. [CrossRef]
17. Bartkowiak, M.; Kizak, M.; Liebig, W.; Weidenmann, K. Fatigue behavior of hybrid continuous-discontinuous fiber-reinforced sheet molding compound composites under application-related loading conditions. *Compos. Part C Open Access* **2022**, *8*, 100265. [CrossRef]
18. Staab, F.; Balle, F. Fatigue and fracture of ultrasonically welded aluminum alloys to carbon fiber reinforced thermoplastics. *Fatigue Fract. Eng. Mater. Struct.* **2022**, *45*, 607. [CrossRef]
19. Kahirdeh, A.; Khonsari, M. Energy dissipation in the course of the fatigue degradation: Mathematical derivation and experimental quantification. *Int. J. Solids Struct.* **2015**, *77*, 74. [CrossRef]
20. Harik, V.M.; Fink, B.K.; Bogetti, T.A.; Klinger, J.R.; Gillespie, J.W., Jr. *Low Cycle Fatigue of Composite Materials in Army Structural Applications: A Review of Literature and Recommendations for Research*; Army Research Lab: Aberdeen Proving Ground, MD, USA, 2000.
21. Senchenkov, I.; Karnaukhov, V. Thermomechanical behavior of nonlinearly viscoelastic materials under harmonic loading. *Int. Appl. Mech.* **2001**, *37*, 1400. [CrossRef]
22. Tormey, J.; Britton, S. Effect of cyclic loading on solid propellant grain structures. *AIAA J.* **1963**, *1*, 1763. [CrossRef]
23. Mishnaevsky, L.; Branner, K.; Petersen, H.N.; Beauson, J.; McGugan, M.; Sørensen, B.F. Materials for wind turbine blades: An overview. *Materials* **2017**, *10*, 1285. [CrossRef]

24. Bathias, C.; Paris, P.C. *Gigacycle Fatigue in Mechanical Practice*; CRC Press: New York, NY, USA, 2004.
25. Harik, V.; Klinger, J.; Bogetti, T. Low-cycle fatigue of unidirectional composites: Bi-linear S–N curves. *Int. J. Fatigue* **2002**, *24*, 455. [CrossRef]
26. Alam, P.; Mamalis, D.; Robert, C.; Floreani, C.; Brádaigh, C.M.Ó. The fatigue of carbon fibre reinforced plastics—A review. *Compos. Part B Eng.* **2019**, *166*, 555. [CrossRef]
27. Voudouris, G.; Di Maio, D.; Sever, I.A. Experimental fatigue behaviour of CFRP composites under vibration and thermal loading. *Int. J. Fatigue* **2020**, *140*, 105791. [CrossRef]
28. Magi, F.; Di Maio, D.; Sever, I. Damage initiation and structural degradation through resonance vibration: Application to composite laminates in fatigue. *Compos. Sci. Technol.* **2016**, *132*, 47. [CrossRef]
29. Premanand, A.; Balle, F. Development of an axial loading system for fatigue testing of textile-composites at ultrasonic frequencies. *Mater. Lett. X* **2022**, *13*, 100131. [CrossRef]
30. Flore, D.; Wegener, K.; Mayer, H.; Karr, U.; Oetting, C.C. Investigation of the high and very high cycle fatigue behaviour of continuous fibre reinforced plastics by conventional and ultrasonic fatigue testing. *Compos. Sci. Technol.* **2017**, *141*, 130. [CrossRef]
31. Backe, D.; Balle, F. Ultrasonic fatigue and microstructural characterization of carbon fiber fabric reinforced polyphenylene sulfide in the very high cycle fatigue regime. *Compos. Sci. Technol.* **2016**, *126*, 115. [CrossRef]
32. Adam, T.; Horst, P. Fatigue damage and fatigue limits of a GFRP angle-ply laminate tested under very high cycle fatigue loading. *Int. J. Fatigue* **2017**, *99*, 202. [CrossRef]
33. Xu, Y.; Xu, Z.; Guo, Y.; Huang, X.; Dong, Y.; Li, Q. Dynamic Properties and Energy Dissipation Study of Sandwich Viscoelastic Damper Considering Temperature Influence. *Buildings* **2021**, *11*, 470. [CrossRef]
34. De Cazenove, J.; Rade, D.; De Lima, A.; Araújo, C. A numerical and experimental investigation on self-heating effects in viscoelastic dampers. *Mech. Syst. Signal Process.* **2012**, *27*, 433. [CrossRef]
35. Badie, M.A.; Mahdi, E.; Hamouda, A. An investigation into hybrid carbon/glass fiber reinforced epoxy composite automotive drive shaft. *Mater. Des.* **2011**, *32*, 1485. [CrossRef]
36. Henry, T.C.; Bakis, C.E.; Smith, E.C. Viscoelastic characterization and self-heating behavior of laminated fiber composite driveshafts. *Materials Design* **2015**, *66*, 346. [CrossRef]
37. Henry, T.C.; Bakis, C.E.; Miller, S.W.; Smith, E.C. Multi-objective optimal design of composite rotorcraft driveshaft including strain rate and temperature effects. *Compos. Struct.* **2015**, *128*, 42. [CrossRef]
38. Shan, Y.; Bakis, C. Viscoelastic characterization and self-heating behavior of a flexible matrix composite driveshaft. *J. Compos. Mater.* **2009**, *43*, 1335. [CrossRef]
39. Shin, E.; Wang, K.; Smith, E. *Annual Forum Proceedings-American Helicopter Society*; American Helicopter Society: Fairfax, VA, USA, 2003; p. 1961.
40. Mayrides, B.; Smith, E.; Wang, K. December. Analysis and synthesis of highly flexible helicopter drivelines with flexible matrix composite shafting. In Proceedings of the 61st American Helicopter Society International Annual Forum, Grapevine, TX, USA, 1–3 June 2005; p. 1675.
41. Bakis, C.E.; Smith, E.; Sollenberger, S. Development and validation of a self-heating model for thick, mixed angle ply composite shafts under rotating bending load. In Proceedings of the 26th Annual Technical Conference of the American Society for Composites 2011 and the 2nd Joint US-Canada Conference on Composites, DEStech, Lancaster, PA, USA, 26–29 September 2011; p. 843.
42. Boyarov, A. Mechanism of Formation and Protection from Spontaneous Ignition of the Pyrophoric Sedimentations in Vertical Reservoirs. Ph.D. Thesis, University of Potsdam, Potsdam, Germany, 2010.
43. Faghri, A.; Guo, Z. Challenges and opportunities of thermal management issues related to fuel cell technology and modeling. *Int. J. Heat Mass Transf.* **2005**, *48*, 3891. [CrossRef]
44. Wang, C.; Chen, X.; Cheng, L.; Ding, J. High-cycle and very-high-cycle fatigue properties of CFRP-aramid honeycomb sandwich structure in three-point bending. *Int. J. Fatigue* **2022**, *155*, 106576. [CrossRef]
45. Ming, Y.; Duan, Y.; Zhang, S.; Zhu, Y.; Wang, B. Self-heating 3D printed continuous carbon fiber/epoxy mesh and its application in wind turbine deicing. *Polym. Test.* **2020**, *82*, 106309. [CrossRef]
46. Tongchitpakdee, C.; Benjanirat, S.; Sankar, L.N. Numerical simulation of the aerodynamics of horizontal axis wind turbines under yawed flow conditions. *J. Sol. Energy Eng.* **2005**, *127*, 464–474. [CrossRef]
47. Zorko, D.; Tavčar, J.; Bizjak, M.; Šturm, R.; Bergant, Z. High cycle fatigue behaviour of autoclave-cured woven carbon fibre-reinforced polymer composite gears. *Polym. Test.* **2021**, *102*, 107339. [CrossRef]
48. Backe, D.; Balle, F.; Eifler, D. *Three Point Bending Fatigue of Carbon Fiber Fabric Reinforced Polyphenylensulfide in the Very High Cycle Fatigue Regime. Key Engineering Materials*; Trans Tech Publications Ltd.: Wollerau, Switzerland, 2016; p. 47.
49. Mirzaei, A.; Shokrieh, M. Simulation and measurement of the self-heating phenomenon of carbon/epoxy laminated composites under fatigue loading. *Compos. Part B Eng.* **2021**, *223*, 109097. [CrossRef]
50. Hashemi, M.; Amraei, J. The effect of physical nonlinearity of the interfacial layer between carbon nanotube and polymer matrix on viscoelastic response of nanocomposite materials under harmonic loading. *J. Compos. Mater.* **2018**, *52*, 3731. [CrossRef]
51. Soltannia, B.; Haji Gholami, I.; Masajedian, S.; Mertiny, P.; Sameoto, D.; Taheri, F. Parametric study of strain rate effects on nanoparticle-reinforced polymer composites. *J. Nanomater.* **2016**, *2016*, 9841972. [CrossRef]

52. Soltannia, B.; Duke, K.; Taheri, F.; Mertiny, P. Quantification of the effects of strain rate and nano-reinforcement on the performance of adhesively bonded single-lap joints. *Rev. Adhes. Adhes.* **2020**, *8*, S1. [CrossRef]
53. Sevenois, R.D.; Hao, P.; Van Paepegem, W.; Gilabert, F.A. Numerical Study on the Effect of Matrix Self-Heating on the Thermo-Visco-Plastic Response of Continuous Fiber-Reinforced Polymers under Transverse Tensile Loading. *Polymers* **2022**, *14*, 1941. [CrossRef] [PubMed]
54. Ly, M.; Khan, K.A.; Muliana, A. Modeling self-heating under cyclic loading in fiber-reinforced polymer composites. *J. Mater. Eng. Perform.* **2020**, *29*, 1321. [CrossRef]
55. Boyer, R.F. Mechanical motions in amorphous and semi-crystalline polymers. *Polymer* **1976**, *17*, 996. [CrossRef]
56. Lahuerta, F.; Nijssen, R.; Van Der Meer, F.; Sluys, L. Experimental–computational study towards heat generation in thick laminates under fatigue loading. *Int. J. Fatigue* **2015**, *80*, 121. [CrossRef]
57. Katunin, A. Self-heating effect in laminate plates during harmonic forced loading. *Sci. Probl. Mach. Oper. Maint.* **2009**, *44*, 73.
58. Shabani, P.; Taheri-Behrooz, F.; Samareh-Mousavi, S.S.; Shokrieh, M.M. Very high cycle and gigacycle fatigue of fiber-reinforced composites: A review on experimental approaches and fatigue damage mechanisms. *Prog. Mater. Sci.* **2021**, *118*, 100762. [CrossRef]
59. Hajshirmohammadi, B.; Khonsari, M. An approach for fatigue life prediction based on external heating. *Int. J. Mech. Sci.* **2021**, *204*, 106510. [CrossRef]
60. Sapozhnikov, S.; Shabley, A.; Ignatova, A. Predicting the kinetics of hysteretic self-heating of GFRPs under high-frequency cyclic loading. *Compos. Struct.* **2019**, *226*, 111214. [CrossRef]
61. Katunin, A. Fatigue of polymeric composites during stationary and non-stationary self-heating. *Compos. Theor. Pract.* **2018**, *18*, 19.
62. Katunin, A.; Wachla, D. Determination of fatigue limit of polymeric composites in fully reversed bending loading mode using self-heating effect. *J. Compos. Mater.* **2019**, *53*, 83. [CrossRef]
63. Panin, S.V.; Bogdanov, A.A.; Eremin, A.V.; Buslovich, D.G.; Alexenko, V.O. Estimating Low- and High-Cyclic Fatigue of Polyimide-CF-PTFE Composite through Variation of Mechanical Hysteresis Loops. *Materials* **2022**, *15*, 4656. [CrossRef]
64. Vassilopoulos, A.P. The history of fiber-reinforced polymer composite laminate fatigue. *Int. J. Fatigue* **2020**, *134*, 105512. [CrossRef]
65. Premanand, A.; Balle, F. Influence of Pulse–Pause Sequences on the Self-Heating Behavior in Continuous Carbon Fiber-Reinforced Composites under Ultrasonic Cyclic Three-Point Bending Loads. *Materials* **2022**, *15*, 3527. [CrossRef]
66. *ASTM D3479/D3479M-19*; Standard Test Method for Tension-Tension Fatigue of Polymer Matrix Composite Materials. ASTM International: West Conshohocken, PA, USA, 2019.
67. *ASTM D3410/D3410M*; Standard Test Method for Compressive Properties of Polymer Matrix Composite Materials with Unsupported Gage Section by Shear Loading. Available online: https://www.astm.org/Standards/D3410 (accessed on 23 May 2022).
68. *ISO 13003*; Fibre-Reinforced Plastics: Determination of Fatigue Properties Under Cyclic Loading Conditions. International Organization for Standardization: Geneva, Switzerland, 2003.
69. *ISO 527-4:1997*; Determination of Tensile Properties—Part 4: Test Conditions for Isotropic and Orthotropic Fibre-Reinforced Plastic Composites. International Organization for Standardization: Geneva, Switzerland, 1997.
70. Zhou, Y.; Mallick, P. Fatigue performance of an injection-molded short E-glass fiber-reinforced polyamide 6, 6. I. Effects of orientation, holes, and weld line. *Polym. Compos.* **2006**, *27*, 230. [CrossRef]
71. Zhou, Y.; Mallick, P. Fatigue performance of an injection molded talc-filled polypropylene. *Polym. Eng. Sci.* **2005**, *45*, 510. [CrossRef]
72. Tao, Y.; Stevens, C.A.; Bilotti, E.; Peijs, T.; Busfield, J.J. Fatigue of carbon cord-rubber composites: Effect of frequency, R ratio and life prediction using constant life models. *Int. J. Fatigue* **2020**, *135*, 105558. [CrossRef]
73. Ahmed, A.; Rahman, M.Z.; Ou, Y.; Liu, S.; Mobasher, B.; Guo, S.; Zhu, D. A review on the tensile behavior of fiber-reinforced polymer composites under varying strain rates and temperatures. *Constr. Build. Mater.* **2021**, *294*, 123565. [CrossRef]
74. Montesano, J.; Fawaz, Z.; Bougherara, H. Use of infrared thermography to investigate the fatigue behavior of a carbon fiber reinforced polymer composite. *Compos. Struct.* **2013**, *97*, 76. [CrossRef]
75. Kim, H.S. Prediction of SN curves at various stress ratios for structural materials. *Procedia Struct. Integr.* **2019**, *19*, 472. [CrossRef]
76. Dickson, R.; Fernando, G.; Adam, T.; Reiter, H.; Harris, B. Fatigue behaviour of hybrid composites. *J. Mater. Sci.* **1989**, *24*, 227. [CrossRef]
77. Movahedi-Rad, A.V.; Keller, T.; Vassilopoulos, A.P. Fatigue damage in angle-ply GFRP laminates under tension-tension fatigue. *Int. J. Fatigue* **2018**, *109*, 60. [CrossRef]
78. Xiong, J.-j.; Zhu, Y.-t.; Luo, C.-y.; Li, Y.-s. Fatigue-driven failure criterion for progressive damage modelling and fatigue life prediction of composite structures. *Int. J. Fatigue* **2021**, *145*, 106110. [CrossRef]
79. Naderi, M.; Maligno, A. Fatigue life prediction of carbon/epoxy laminates by stochastic numerical simulation. *Compos. Struct.* **2012**, *94*, 1052. [CrossRef]
80. Sørensen, B.F.; Goutianos, S. Micromechanical model for prediction of the fatigue limit for unidirectional fibre composites. *Mech. Mater.* **2019**, *131*, 169. [CrossRef]
81. Huang, J.; Pastor, M.-L.; Garnier, C.; Gong, X. Rapid evaluation of fatigue limit on thermographic data analysis. *Int. J. Fatigue* **2017**, *104*, 293. [CrossRef]
82. Feng, Y.; Gao, C.; He, Y.; An, T.; Fan, C.; Zhang, H. Investigation on tension–tension fatigue performances and reliability fatigue life of T700/MTM46 composite laminates. *Compos. Struct.* **2016**, *136*, 64. [CrossRef]

83. La Rosa, G.; Risitano, A. Thermographic methodology for rapid determination of the fatigue limit of materials and mechanical components. *Int. J. Fatigue* **2000**, *22*, 65. [CrossRef]
84. Fargione, G.; Geraci, A.; La Rosa, G.; Risitano, A. Rapid determination of the fatigue curve by the thermographic method. *Int. J. Fatigue* **2002**, *24*, 11. [CrossRef]
85. Luong, M.; Van, K.D. Metal fatigue limit evaluation using infrared thermography. *Proc. AITA Capri* **1994**, 245–253. (In Italian)
86. Luong, M.P. Fatigue limit evaluation of metals using an infrared thermographic technique. *Mech. Mater.* **1998**, *28*, 155. [CrossRef]
87. Katunin, A.; Wachla, D. Minimizing self-heating based fatigue degradation in polymeric composites by air cooling. *Procedia Struct. Integr.* **2019**, *18*, 20. [CrossRef]
88. Katunin, A.; Wachla, D. Influence of Air Cooling on the Fatigue of a Polymer Composite Under Self-Heating. *Mech. Compos. Mater.* **2020**, *56*, 93. [CrossRef]
89. Huang, J.; Garnier, C.; Pastor, M.-L.; Gong, X. Investigation of self-heating and life prediction in CFRP laminates under cyclic shear loading condition based on the infrared thermographic data. *Eng. Fract. Mech.* **2020**, *229*, 106971. [CrossRef]
90. Foti, P.; Santonocito, D.; Ferro, P.; Risitano, G.; Berto, F. Determination of fatigue limit by static thermographic method and classic thermographic method on notched specimens. *Procedia Struct. Integr.* **2020**, *26*, 166. [CrossRef]
91. Mandegarian, S.; Samareh-Mousavi, S.S.; Taheri-Behrooz, F. Experimental investigation on in-plane shear fatigue failure criteria of $\pm 45^{\circ}$ angle-ply carbon epoxy composite. *Int. J. Fatigue* **2022**, *160*, 106873. [CrossRef]
92. Mohammadi, B.; Shokrieh, M.; Jamali, M.; Mahmoudi, A.; Fazlali, B. Damage-entropy model for fatigue life evaluation of off-axis unidirectional composites. *Compos. Struct.* **2021**, *270*, 114100. [CrossRef]
93. Wu, X.; Li, L. An Overview of Self-Heating Phenomena and Theory Related to Damping and Fatigue of Metals. *Appl. Sci.* **2022**, *12*, 3054. [CrossRef]
94. Naderi, M.; Khonsari, M. An experimental approach to low-cycle fatigue damage based on thermodynamic entropy. *Int. J. Solids Struct.* **2010**, *47*, 875. [CrossRef]
95. Kahirdeh, A.; Khonsari, M.M. Acoustic entropy of the materials in the course of degradation. *Entropy* **2016**, *18*, 280. [CrossRef]
96. Mohammadi, B.; Mahmoudi, A. Developing a new model to predict the fatigue life of cross-ply laminates using coupled CDM-entropy generation approach. *Theor. Appl. Fract. Mech.* **2018**, *95*, 18. [CrossRef]
97. Katunin, A. Domination of self-heating effect during fatigue of polymeric composites. *Procedia Struct. Integr.* **2017**, *5*, 93. [CrossRef]
98. Wronkowicz, A. Non-Destructive Evaluation of Composite Aircraft Elements Based on Ultrasonic Testing and Image Analysis. Ph.D. Thesis, Silesian University of Technology, Gliwice, Poland, 2018.
99. Zaghloul, M.Y.; Zaghloul, M.M.Y.; Zaghloul, M.M.Y. Influence of stress level and fibre volume fraction on fatigue performance of glass fibre-reinforced polyester composites. *Polymers* **2022**, *14*, 2662. [CrossRef]
100. Zaghloul, M.M.Y.; Mohamed, Y.S.; El-Gamal, H. Fatigue and tensile behaviors of fiber-reinforced thermosetting composites embedded with nanoparticles. *J. Compos. Mater.* **2019**, *53*, 709–718. [CrossRef]
101. Brunbauer, J.; Pinter, G. Effects of mean stress and fibre volume content on the fatigue-induced damage mechanisms in CFRP. *Int. J. Fatigue* **2015**, *75*, 28. [CrossRef]
102. Fard, M.Y.; Raji, B.; Pankretz, H. Correlation of nanoscale interface debonding and multimode fracture in polymer carbon composites with long-term hygrothermal effects. *Mech. Mater.* **2020**, *150*, 103601. [CrossRef]
103. Pei, X.; Han, W.; Ding, G.; Wang, M.; Tang, Y. Temperature effects on structural integrity of fiber-reinforced polymer matrix composites: A review. *J. Appl. Polym. Sci.* **2019**, *136*, 48206. [CrossRef]
104. Alian, A.; Kundalwal, S.; Meguid, S. Multiscale modeling of carbon nanotube epoxy composites. *Polymer* **2015**, *70*, 149. [CrossRef]
105. Yang, C.; Yin, T.; Suo, Z. Polyacrylamide hydrogels. I. Network imperfection. *J. Mech. Phys. Solids* **2019**, *131*, 43. [CrossRef]
106. Slootman, J.; Waltz, V.; Yeh, C.J.; Baumann, C.; Göstl, R.; Comtet, J.; Creton, C. Quantifying rate-and temperature-dependent molecular damage in elastomer fracture. *Phys. Rev. X* **2020**, *10*, 041045. [CrossRef]
107. Lin, S.; Ni, J.; Zheng, D.; Zhao, X. Fracture and fatigue of ideal polymer networks. *Extrem. Mech. Lett.* **2021**, *48*, 101399. [CrossRef]
108. Lin, S.; Zhao, X. Fracture of polymer networks with diverse topological defects. *Phys. Rev. E* **2020**, *102*, 052503. [CrossRef] [PubMed]
109. Zhang, W.; Hu, J.; Tang, J.; Wang, Z.; Wang, J.; Lu, T.; Suo, Z. Fracture toughness and fatigue threshold of tough hydrogels. *ACS Macro Lett.* **2018**, *8*, 17. [CrossRef]
110. Zheng, D.; Lin, S.; Ni, J.; Zhao, X. Fracture and fatigue of entangled and unentangled polymer networks. *Extrem. Mech. Lett.* **2022**, *51*, 101608. [CrossRef]
111. Zhang, T.; Lin, S.; Yuk, H.; Zhao, X. Predicting fracture energies and crack-tip fields of soft tough materials. *Extrem. Mech. Lett.* **2015**, *4*, 1. [CrossRef]
112. Cebon, D.; Cheung, C. *Advances in Asphalt Materials*; Elsevier: Amsterdam, The Netherlands, 2015.
113. Katunin, A.; Krukiewicz, K.; Turczyn, R. Evaluation of residual cross-linking caused by self-heating effect in epoxy-based fibrous composites using Raman spectroscopy. *Chemik* **2014**, *68*, 957.
114. Turczyn, R.; Krukiewicz, K.; Katunin, A. Spectroscopic evaluation of structural changes in composite materials subjected to self-heating effect. *Compos. Struct.* **2018**, *204*, 192. [CrossRef]
115. Katunin, A.; Krukiewicz, K. Physicochemical analysis of self-heating of glass-epoxy composites cured by novolac. *Chemik* **2012**, *66*, 1326.

116. Amraei, J.; Jam, J.E.; Arab, B.; Firouz-Abadi, R.D. Effect of interphase zone on the overall elastic properties of nanoparticle-reinforced polymer nanocomposites. *J. Compos. Mater.* **2019**, *53*, 1261. [CrossRef]
117. Amraei, J.; Jam, J.E.; Arab, B.; Firouz-Abadi, R.D. Modeling the interphase region in carbon nanotube-reinforced polymer nanocomposites. *Polym. Compos.* **2019**, *40*, E1219. [CrossRef]
118. Najafi, F.; Wang, G.; Mukherjee, S.; Cui, T.; Filleter, T.; Singh, C.V. Toughening of graphene-based polymer nanocomposites via tuning chemical functionalization. *Compos. Sci. Technol.* **2020**, *194*, 108140. [CrossRef]
119. Ali, H.Q.; Tabrizi, I.E.; Khan, R.M.A.; Tufani, A.; Yildiz, M. Microscopic analysis of failure in woven carbon fabric laminates coupled with digital image correlation and acoustic emission. *Compos. Struct.* **2019**, *230*, 111515. [CrossRef]
120. Kishi, H.; Matsuda, S.; Imade, J.; Shimoda, Y.; Nakagawa, T.; Furukawa, Y. The effects of the toughening mechanism and the molecular weights between cross-links on the fatigue resistance of epoxy polymer blends. *Polymer* **2021**, *223*, 123712. [CrossRef]
121. Rose, M.; Niverty, S.; Schmidt, B.; Kästner, M.; Zimmermann, M.; Chawla, N. X-ray computer tomography (XCT) of fatigue damage in laser-machined versus milled carbon fiber reinforced polymer matrix composites. *Eng. Fract. Mech.* **2021**, *252*, 107820. [CrossRef]
122. Guo, Q.; Guo, X.; Fan, J.; Syed, R.; Wu, C. An energy method for rapid evaluation of high-cycle fatigue parameters based on intrinsic dissipation. *Int. J. Fatigue* **2015**, *80*, 136. [CrossRef]
123. Balle, F.; Backe, D. Very high cycle fatigue of carbon fiber reinforced polyphenylene sulfide at ultrasonic frequencies. In *Fatigue of Materials at Very High Numbers of Loading Cycles*; Springer: Berlin/Heidelberg, Germany, 2018; pp. 441–461.
124. Gao, J.; Yuan, Y. Probabilistic modeling of stiffness degradation for fiber reinforced polymer under fatigue loading. *Eng. Fail. Anal.* **2020**, *116*, 104733. [CrossRef]
125. Knoll, J.; Riecken, B.T.; Kosmann, N.; Chandrasekaran, S.; Schulte, K.; Fiedler, B. The effect of carbon nanoparticles on the fatigue performance of carbon fibre reinforced epoxy. *Compos. Part A Appl. Sci. Manuf.* **2014**, *67*, 233. [CrossRef]
126. Gerlach, R.; Siviour, C.R.; Wiegand, J.; Petrinic, N. In-plane and through-thickness properties, failure modes, damage and delamination in 3D woven carbon fibre composites subjected to impact loading. *Compos. Sci. Technol.* **2012**, *72*, 397. [CrossRef]
127. Fan, W.; Dang, W.; Liu, T.; Li, J.; Xue, L.; Yuan, L.; Dong, J. Fatigue behavior of the 3D orthogonal carbon/glass fibers hybrid composite under three-point bending load. *Mater. Des.* **2019**, *183*, 108112. [CrossRef]
128. Dai, S.; Cunningham, P.; Marshall, S.; Silva, C. Open hole quasi-static and fatigue characterisation of 3D woven composites. *Compos. Struct.* **2015**, *131*, 765. [CrossRef]
129. Ratner, S.; Korobov, V.; Agamalyan, S. Mechanical and thermal fracture of plastics under cyclic strains. Soviet materials science: A transl. of Fiziko-khimicheskaya mekhanika materialov. *Acad. Sci. Ukr. SSR* **1972**, *5*, 66.
130. Gumenyuk, B.; Karnaukhov, V. Dynamic behavior of viscoelastic bodies during harmonic excitation. *Sov. Appl. Mech.* **1980**, *16*, 623. [CrossRef]
131. Katunin, A. Critical self-heating temperature during fatigue of polymeric composites under cyclic loading. *Compos. Theory Pract.* **2012**, *12*, 72.
132. Kahirdeh, A.; Khonsari, M. Criticality of degradation in composite materials subjected to cyclic loading. *Compos. Part B Eng.* **2014**, *61*, 375. [CrossRef]
133. Hajikazemi, M.; Sadr, M.H. Stiffness reduction of cracked general symmetric laminates using a variational approach. *Int. J. Solids Struct.* **2014**, *51*, 1483. [CrossRef]
134. Steinberger, R.; Leitão, T.V.; Ladstätter, E.; Pinter, G.; Billinger, W.; Lang, R. Infrared thermographic techniques for non-destructive damage characterization of carbon fibre reinforced polymers during tensile fatigue testing. *Int. J. Fatigue* **2006**, *28*, 1340. [CrossRef]
135. Guo, X.; Zhu, L. Vibro-thermography of calibrated defects in hybrid plates focusing on viscoelastic heat generation. *Quant. InfraRed Thermogr. J.* **2021**, *18*, 314. [CrossRef]
136. Renshaw, J.; Chen, J.C.; Holland, S.D.; Thompson, R.B. The sources of heat generation in vibrothermography. *NDT E Int.* **2011**, *44*, 736. [CrossRef]
137. Montanini, R.; Freni, F. Correlation between vibrational mode shapes and viscoelastic heat generation in vibrothermography. *NDT E Int.* **2013**, *58*, 43. [CrossRef]
138. Katunin, A.; Wachla, D. Analysis of defect detectability in polymeric composites using self-heating based vibrothermography. *Compos. Struct.* **2018**, *201*, 760. [CrossRef]
139. Katunin, A.; Fidali, M. Self-heating of polymeric laminated composite plates under the resonant vibrations: Theoretical and experimental study. *Polym. Compos.* **2012**, *33*, 138. [CrossRef]
140. Vaddi, J.S.; Holland, S.D.; Kessler, M.R. Absorptive viscoelastic coatings for full field vibration coverage measurement in vibrothermography. *NDT E Int.* **2016**, *82*, 56. [CrossRef]
141. Di Maio, D.; Magi, F.; Sever, I. Damage monitoring of composite components under vibration fatigue using scanning laser Doppler vibrometer. *Exp. Mech.* **2018**, *58*, 499. [CrossRef]
142. Dzul-Cervantes, M.; Pacheco-Salazar, O.; Can-Herrera, L.; Moreno-Chulim, M.; Cauich-Cupul, J.; Herrera-Franco, P.; Valadez-González, A. Effect of moisture content and carbon fiber surface treatments on the interfacial shear strength of a thermoplastic-modified epoxy resin composites. *J. Mater. Res. Technol.* **2020**, *9*, 15739. [CrossRef]
143. Harussani, M.; Sapuan, S.; Nadeem, G.; Rafin, T.; Kirubaanand, W. Recent applications of carbon-based composites in defence industry: A review. *Def. Technol.* **2022**, *18*, 1281. [CrossRef]

144. Chakraborty, B.C. FRP for Marine Application. In *Fiber-Reinforced Plastics*; Masuelli, M.A., Ed.; IntechOpen: London, UK, 2021; pp. 135–166.
145. Chen, K.; Kang, G.; Lu, F.; Chen, J.; Jiang, H. Effect of relative humidity on uniaxial cyclic softening/hardening and intrinsic heat generation of polyamide-6 polymer. *Polym. Test.* **2016**, *56*, 19. [CrossRef]
146. Gholami, M.; Afrasiab, H.; Baghestani, A.M.; Fathi, A. Hygrothermal degradation of elastic properties of fiber reinforced composites: A micro-scale finite element analysis. *Compos. Struct.* **2021**, *266*, 113819. [CrossRef]
147. Charalambous, G.; Allegri, G.; Hallett, S.R. Temperature effects on mixed mode I/II delamination under quasi-static and fatigue loading of a carbon/epoxy composite. *Compos. Part A Appl. Sci. Manuf.* **2015**, *77*, 75. [CrossRef]
148. Nettles, A.T.; Biss, E.J. *Low Temperature Mechanical Testing of Carbon-Fiber/Epoxy-Resin Composite Materials*; NASA Technical paper 3663; NASA, Marshall Space Flight Center: Huntsville, AL, USA, 1996.
149. Green, J. Laminar Flow Control—Back to the Future? In Proceedings of the 38th Fluid Dynamics Conference and Exhibit, Seattle, WA, USA, 23–26 June 2008. AIAA 2008–3738.
150. Krishnan, K.; Bertram, O.; Seibel, O. Review of hybrid laminar flow control systems. *Prog. Aerosp. Sci.* **2017**, *93*, 24. [CrossRef]
151. Takeuchi, Y.; Takeuchi, J.; Fujihara, M. Numerical investigation of inertial, viscous, and capillary effects on the drainage process in porous media. *Comput. Fluids* **2022**, *237*, 105324. [CrossRef]
152. Incropera, F.P.; DeWitt, D.P. *Fundamentals of Heat Transfer*; John Wiley & Sons: Hoboken, NJ, USA, 1981.
153. Kirchner, M.E. *Laminar Flow: Challenge and Potential*; NASA Technical Report; NASA, Langley Research Center: Hampton, VA, USA, 1987; pp. 25–44.
154. Incropera, F.P.; DeWitt, D.P.; Bergman, T.L.; Lavine, A.S. *Fundamentals of Heat and Mass Transfer*; Wiley: New York, NY, USA, 1996.
155. Guo, Q.; Zaïri, F.; Yang, W. Evaluation of intrinsic dissipation based on self-heating effect in high-cycle metal fatigue. *Int. J. Fatigue* **2020**, *139*, 105653. [CrossRef]
156. Bergman, T.L.; Lavine, A.S.; Incropera, F.P.; DeWitt, D.P. *Introduction to Heat Transfer*; John Wiley & Sons: Hoboken, NJ, USA, 2011.
157. Choi, E.J.; Park, J.Y.; Kim, M.S. Two-phase cooling using HFE-7100 for polymer electrolyte membrane fuel cell application. *Appl. Therm. Eng.* **2019**, *148*, 868. [CrossRef]
158. Huang, Y.; Xiao, X.; Kang, H.; Lv, J.; Zeng, R.; Shen, J. Thermal management of polymer electrolyte membrane fuel cells: A critical review of heat transfer mechanisms, cooling approaches, and advanced cooling techniques analysis. *Energy Convers. Manag.* **2022**, *254*, 115221. [CrossRef]
159. Xu, R.; Wang, G.; Jiang, P. Spray cooling on enhanced surfaces: A review of the progress and mechanisms. *J. Electron. Packag.* **2022**, *144*, 010802. [CrossRef]
160. Müller, A.; Trappe, V.; Hickmann, S.; Ortwein, H.P. Investigation of the infinite life of fibre-reinforced plastics using X-ray refraction topography for the in-situ, non-destructive evaluation of micro-structural degradation processes during cyclic fatigue loading. In *Fatigue of Materials at Very High Numbers of Loading Cycles*; Springer: Berlin/Heidelberg, Germany, 2018; pp. 417–439.
161. Apinis, R. Accceleration of fatigue tests of polymer composite materials by using high-frequency loadings. *Mech. Compos. Mater.* **2004**, *40*, 107. [CrossRef]
162. Heinz, S.; Balle, F.; Wagner, G.; Eifler, D. Innovative ultrasonic testing facility for fatigue experiments in the VHCF regime. *Mater. Test.* **2012**, *54*, 750. [CrossRef]
163. Lee, C.S.; Kim, H.J.; Amanov, A.; Choo, J.H.; Kim, Y.K.; Cho, I.S. Investigation on very high cycle fatigue of PA66-GF30 GFRP based on fiber orientation. *Compos. Sci. Technol.* **2019**, *180*, 94. [CrossRef]
164. Moria, H.; Pourhedayat, S.; Dizaji, H.S.; Abusorrah, A.M.; Abu-Hamdeh, N.H.; Wae-hayee, M. Exergoeconomic analysis of a Peltier effect air cooler using experimental data. *Appl. Therm. Eng.* **2021**, *186*, 116513. [CrossRef]
165. Ramezanizadeh, M.; Nazari, M.A.; Ahmadi, M.H.; Chen, L. A review on the approaches applied for cooling fuel cells. *Int. J. Heat Mass Transf.* **2019**, *139*, 517. [CrossRef]
166. Zhang, G.; Kandlikar, S.G. A critical review of cooling techniques in proton exchange membrane fuel cell stacks. *Int. J. Hydrogen Energy* **2012**, *37*, 2412. [CrossRef]
167. Bargal, M.; Abdelkareem, M.; Tao, Q.; Li, J.; Shi, J.; Wang, Y. Liquid cooling techniques in proton exchange membrane fuel cell stacks: A detailed survey. *Alexandria Eng. J.* **2020**, *59*, 635. [CrossRef]
168. Just, G.; Koch, I.; Thieme, M.; Gude, M. Inter fibre cracking behaviour of CFRP under very high cycle fatigue loading: Experimental and analytical multi-scale approach. In Proceedings of the 20th International Conferences on Composite Materials, Copenhagen, Denmark, 19–24 July 2015; pp. 19–24.
169. Trauth, A.; Kirchenbauer, K.; Weidenmann, K. Dynamic-mechanical-thermal analysis of hybrid continuous–discontinuous sheet molding compounds. *Compos. Part C Open Access* **2021**, *5*, 100148. [CrossRef]
170. Cui, W.; Chen, X.; Chen, C.; Cheng, L.; Ding, J.; Zhang, H. Very high cycle fatigue (VHCF) characteristics of carbon fiber reinforced plastics (CFRP) under ultrasonic loading. *Materials* **2020**, *13*, 908. [CrossRef]
171. Islam, M.R.; Shabani, B.; Rosengarten, G. Nanofluids to improve the performance of PEM fuel cell cooling systems: A theoretical approach. *Appl. Energy* **2016**, *178*, 660. [CrossRef]
172. Taylor, R.; Coulombe, S.; Otanicar, T.; Phelan, P.; Gunawan, A.; Lv, W.; Rosengarten, G.; Prasher, R.; Tyagi, H. Small particles, big impacts: A review of the diverse applications of nanofluids. *J. Appl. Phys.* **2013**, *113*, 1. [CrossRef]
173. Zakaria, I.; Mohamed, W.; Zailan, M.; Azmi, W. Experimental analysis of SiO2-Distilled water nanofluids in a Polymer Electrolyte Membrane fuel cell parallel channel cooling plate. *Int. J. Hydrogen Energy* **2019**, *44*, 25850. [CrossRef]

174. Bahiraei, M.; Jamshidmofid, M.; Goodarzi, M. Efficacy of a hybrid nanofluid in a new microchannel heat sink equipped with both secondary channels and ribs. *J. Mol. Liq.* **2019**, *273*, 88. [CrossRef]
175. Japar, W.M.A.A.; Sidik, N.A.C.; Saidur, R.; Asako, Y.; Yusof, S.N.A. A review of passive methods in microchannel heat sink application through advanced geometric structure and nanofluids: Current advancements and challenges. *Nanotechnol. Rev.* **2020**, *9*, 1192. [CrossRef]
176. Song, T.-W.; Choi, K.-H.; Kim, J.-R.; Jung, S.Y. Pumpless thermal management of water-cooled high-temperature proton exchange membrane fuel cells. *J. Power Sources* **2011**, *196*, 4671. [CrossRef]
177. Putnam, S.A.; Briones, A.M.; Byrd, L.W.; Ervin, J.S.; Hanchak, M.S.; White, A.; Jones, J.G. Microdroplet evaporation on superheated surfaces. *Int. J. Heat Mass Transf.* **2012**, *55*, 5793. [CrossRef]
178. Ueki, Y. High-speed bending-fatigue testing of composite materials. In *IOP Conference Series: Materials Science and Engineering*; IOP Publishing Ltd.: Risø near Roskilde, Denmark, 2018; p. 012008. [CrossRef]
179. Mandell, J.F.; Samborsky, D.D.; Wang, L.; Wahl, N.K. New fatigue data for wind turbine blade materials. *J. Sol. Energy Eng.* **2003**, *125*, 506. [CrossRef]
180. Hosoi, A.; Sato, N.; Kusumoto, Y.; Fujiwara, K.; Kawada, H. High-cycle fatigue characteristics of quasi-isotropic CFRP laminates over 108 cycles (Initiation and propagation of delamination considering interaction with transverse cracks). *Int. J. Fatigue* **2010**, *32*, 29. [CrossRef]
181. Hosoi, A.; Arao, Y.; Karasawa, H.; Kawada, H. High-cycle fatigue characteristics of quasi-isotropic CFRP laminates. *Adv. Compos. Mater.* **2007**, *16*, 151. [CrossRef]
182. Hosoi, A.; Takamura, K.; Sato, N.; Kawada, H. Quantitative evaluation of fatigue damage growth in CFRP laminates that changes due to applied stress level. *Int. J. Fatigue* **2011**, *33*, 781. [CrossRef]
183. Ueki, Y. A high-speed bending fatigue testing method for resin materials (An attempt of application to a glass fiber-reinforced plastic). *Trans. JSME* **2015**, *81*, 821.
184. Han, N.; Baran, I.; Zanjani, J.S.M.; Yuksel, O.; An, L.; Akkerman, R. Experimental and computational analysis of the polymerization overheating in thick glass/Elium® acrylic thermoplastic resin composites. *Compos. Part B Eng.* **2020**, *202*, 108430. [CrossRef]
185. Bian, W.; Yao, T.; Chen, M.; Zhang, C.; Shao, T.; Yang, Y. The synergistic effects of the micro-BN and nano-Al2O3 in micro-nano composites on enhancing the thermal conductivity for insulating epoxy resin. *Compos. Sci. Technol.* **2018**, *168*, 420. [CrossRef]
186. Wang, L.; Qiu, H.; Liang, C.; Song, P.; Han, Y.; Han, Y.; Gu, J.; Kong, J.; Pan, D.; Guo, Z. Electromagnetic interference shielding MWCNT-Fe3O4@ Ag/epoxy nanocomposites with satisfactory thermal conductivity and high thermal stability. *Carbon* **2019**, *141*, 506. [CrossRef]
187. Wang, Y.; Zhang, X.; Ding, X.; Li, Y.; Zhang, P.; Shu, M.; Zhang, Q.; Gong, Y.; Zheng, K.; Wu, B. Enhanced thermal conductivity of carbon nitride-doped graphene/polyimide composite film via a "deciduous-like" strategy. *Compos. Sci. Technol.* **2021**, *205*, 108693. [CrossRef]
188. Jin, X.; Wang, J.; Dai, L.; Wang, W.; Wu, H. Largely enhanced thermal conductive, dielectric, mechanical and anti-dripping performance in polycarbonate/boron nitride composites with graphene nanoplatelet and carbon nanotube. *Compos. Sci. Technol.* **2019**, *184*, 107862. [CrossRef]
189. Maqbool, M.; Aftab, W.; Bashir, A.; Usman, A.; Guo, H.; Bai, S. Engineering of polymer-based materials for thermal management solutions. *Compos. Commun.* **2022**, *29*, 101048. [CrossRef]
190. Leung, S.N. Thermally conductive polymer composites and nanocomposites: Processing-structure-property relationships. *Compos. Part B Eng.* **2018**, *150*, 78. [CrossRef]
191. Cecen, V.; Tavman, I.H.; Kok, M.; Aydogdu, Y. Epoxy-and polyester-based composites reinforced with glass, carbon and aramid fabrics: Measurement of heat capacity and thermal conductivity of composites by differential scanning calorimetry. *Polym. Compos.* **2009**, *30*, 1299. [CrossRef]
192. Xu, Y.; Wang, X.; Hao, Q. A mini review on thermally conductive polymers and polymer-based composites. *Compos. Commun.* **2021**, *24*, 100617. [CrossRef]
193. Okubo, H.; Kobayashi, K.; Iba, D.; Moriwaki, I.; Yao, S.; Sasaki, S. Time-resolved ex situ Raman/FT-IR spectroscopic study of structural changes in polymeric gears during operation: Towards the development of operando spectroscopic systems for polymer gears. *Polym. Test.* **2022**, *113*, 107675. [CrossRef]
194. Khan, M.O.; Leung, S.N.; Chan, E.; Naguib, H.E.; Dawson, F.; Adinkrah, V. Effects of microsized and nanosized carbon fillers on the thermal and electrical properties of polyphenylene sulfide based composites. *Polym. Eng. Sci.* **2013**, *53*, 2398. [CrossRef]
195. Stankovich, S.; Dikin, D.A.; Dommett, G.H.; Kohlhaas, K.M.; Zimney, E.J.; Stach, E.A.; Piner, R.D.; Nguyen, S.T.; Ruoff, R.S. Graphene-based composite materials. *Nature* **2006**, *442*, 282. [CrossRef]
196. Han, Z.; Fina, A. Thermal conductivity of carbon nanotubes and their polymer nanocomposites: A review. *Prog. Polym. Sci.* **2011**, *36*, 914.
197. Kim, H.S.; Jang, J.-u.; Yu, J.; Kim, S.Y. Thermal conductivity of polymer composites based on the length of multi-walled carbon nanotubes. *Compos. Part B Eng.* **2015**, *79*, 505. [CrossRef]
198. Chung, D.D. Materials for thermal conduction. *Appl. Therm. Eng.* **2001**, *21*, 1593. [CrossRef]
199. Ha, S.M.; Lee, H.L.; Lee, S.-G.; Kim, B.G.; Kim, Y.S.; Won, J.C.; Choi, W.J.; Lee, D.C.; Kim, J.; Yoo, Y. Thermal conductivity of graphite filled liquid crystal polymer composites and theoretical predictions. *Compos. Sci. Technol.* **2013**, *88*, 113. [CrossRef]

200. Jeong, S.-H.; Song, J.-B.; Kim, K.L.; Choi, Y.H.; Lee, H. Enhanced thermal properties of epoxy composite containing cubic and hexagonal boron nitride fillers for superconducting magnet applications. *Compos. Part B Eng.* **2016**, *107*, 22. [CrossRef]
201. Liu, M.; Chen, B.; Zhang, D.; Wang, Y.; Kan, P. Numerical studies on effective thermal conductivities of the glass/polyimide composite materials under the conditions of conduction & radiation. *Int. J. Heat Mass Transf.* **2021**, *180*, 121764.
202. Grzesiak, S.; Pahn, M.; Klingler, A.; Akpan, E.I.; Schultz-Cornelius, M.; Wetzel, B. Mechanical and Thermal Properties of Basalt Fibre Reinforced Polymer Lamellas for Renovation of Concrete Structures. *Polymers* **2022**, *14*, 790. [CrossRef]
203. Li, J.; Wang, Y.; Yue, T.-N.; Gao, Y.-N.; Shi, Y.-D.; Shen, J.-B.; Wu, H.; Wang, M. Robust electromagnetic interference shielding, joule heating, thermal conductivity, and anti-dripping performances of polyoxymethylene with uniform distribution and high content of carbon-based nanofillers. *Compos. Sci. Technol.* **2021**, *206*, 108681. [CrossRef]
204. Cai, X.; Dong, X.; Lv, W.; Ji, C.; Jiang, Z.; Zhang, X.; Gao, T.; Yue, K.; Zhang, X. Synergistic enhancement of thermal conductivity for low dielectric constant boron nitride–polytetrafluoroethylene composites by adding small content of graphene nanosheets. *Compos. Commun.* **2020**, *17*, 163. [CrossRef]
205. Soltannia, B.; Mertiny, P.; Taheri, F. Vibration characteristics of thermally cycled graphene nanoplatelet (GNP) reinforced 3D-fiber metal laminates (3D-FML). In Proceedings of the 37th Annual Technical Conference of the Canadian Machinery Vibration Association (CMVA2019), Canadian Machinery Vibration Association (CMVA), Halifax, NS, Canada, 28–29 October 2019; pp. 1–11.
206. Wu, X.; Zhao, J.; Rao, X.; Chung, D. Carbon fiber epoxy-matrix composites with hydrothermal-carbon-coated halloysite nanotube filler exhibiting enhanced strength and thermal conductivity. *Polym. Compos.* **2020**, *41*, 2687. [CrossRef]
207. Choi, B.-K.; Lee, H.-J.; Choi, W.-K.; Lee, M.-K.; Park, J.-H.; Hwang, J.-Y.; Seo, M.-K. Effect of carbon fiber content on thermal and electrical conductivity, EMI shielding efficiency, and radiation energy of CMC/PVA composite papers with carbon fibers. *Synth. Met.* **2021**, *273*, 116708. [CrossRef]
208. Wang, H.; Ding, D.; Liu, Q.; Chen, Y.; Zhang, Q. Highly anisotropic thermally conductive polyimide composites via the alignment of boron nitride platelets. *Compos. Part B Eng.* **2019**, *158*, 311. [CrossRef]
209. Mosanenzadeh, S.G.; Naguib, H.E. Effect of filler arrangement and networking of hexagonal boron nitride on the conductivity of new thermal management polymeric composites. *Compos. Part B Eng.* **2016**, *85*, 24. [CrossRef]
210. Yang, S.-Y.; Huang, Y.-F.; Lei, J.; Zhu, L.; Li, Z.-M. Enhanced thermal conductivity of polyethylene/boron nitride multilayer sheets through annealing. *Compos. Part A Appl. Sci. Manuf.* **2018**, *107*, 135. [CrossRef]
211. Haruki, M.; Tada, J.; Tanaka, K.; Onishi, H.; Tada, Y. Enhancing the effective thermal conductivity of Kapton-type polyimide sheets via the use of hexagonal boron nitride. *Thermochim. Acta* **2018**, *662*, 1–7. [CrossRef]
212. Liu, X.; Ji, T.; Li, N.; Liu, Y.; Yin, J.; Su, B.; Zhao, J.; Li, Y.; Mo, G.; Wu, Z. Preparation of polyimide composites reinforced with oxygen doped boron nitride nano-sheet as multifunctional materials. *Mater. Des.* **2019**, *180*, 107963. [CrossRef]
213. Jiang, Y.; Shi, X.; Feng, Y.; Li, S.; Zhou, X.; Xie, X. Enhanced thermal conductivity and ideal dielectric properties of epoxy composites containing polymer modified hexagonal boron nitride. *Compos. Part A Appl. Sci. Manuf.* **2018**, *107*, 657. [CrossRef]
214. Song, J.; Zhang, Y. Vertically aligned silicon carbide nanowires/reduced graphene oxide networks for enhancing the thermal conductivity of silicone rubber composites. *Compos. Part A Appl. Sci. Manuf.* **2020**, *133*, 105873. [CrossRef]
215. Gu, J.; Lv, Z.; Wu, Y.; Zhao, R.; Tian, L.; Zhang, Q. Enhanced thermal conductivity of SiCp/PS composites by electrospinning–hot press technique. *Compos. Part A Appl. Sci. Manuf.* **2015**, *79*, 8. [CrossRef]
216. Gu, J.; Guo, Y.; Lv, Z.; Geng, W.; Zhang, Q. Highly thermally conductive POSS-g-SiCp/UHMWPE composites with excellent dielectric properties and thermal stabilities. *Compos. Part A Appl. Sci. Manuf.* **2015**, *78*, 95. [CrossRef]
217. Zhou, W.; Wang, C.; Ai, T.; Wu, K.; Zhao, F.; Gu, H. A novel fiber-reinforced polyethylene composite with added silicon nitride particles for enhanced thermal conductivity. *Compos. Part A Appl. Sci. Manuf.* **2009**, *40*, 830. [CrossRef]
218. Balachander, N.; Seshadri, I.; Mehta, R.J.; Schadler, L.S.; Borca-Tasciuc, T.; Keblinski, P.; Ramanath, G. Nanowire-filled polymer composites with ultrahigh thermal conductivity. *Appl. Phys. Lett.* **2013**, *102*, 093117. [CrossRef]
219. Yang, X.; Fan, S.; Li, Y.; Guo, Y.; Li, Y.; Ruan, K.; Zhang, S.; Zhang, J.; Kong, J.; Gu, J. Synchronously improved electromagnetic interference shielding and thermal conductivity for epoxy nanocomposites by constructing 3D copper nanowires/thermally annealed graphene aerogel framework. *Compos. Part A Appl. Sci. Manuf.* **2020**, *128*, 105670. [CrossRef]
220. Wang, Z.; Mao, B.; Wang, Q.; Yu, J.; Dai, J.; Song, R.; Pu, Z.; He, D.; Wu, Z.; Mu, S. Ultrahigh conductive copper/large flake size graphene heterostructure thin-film with remarkable electromagnetic interference shielding effectiveness. *Small* **2018**, *14*, 1704332. [CrossRef] [PubMed]
221. Rai, A.; Moore, A.L. Enhanced thermal conduction and influence of interfacial resistance within flexible high aspect ratio copper nanowire/polymer composites. *Compos. Sci. Technol.* **2017**, *144*, 70. [CrossRef]
222. Yin, C.-G.; Liu, Z.-J.; Mo, R.; Fan, J.-C.; Shi, P.-H.; Xu, Q.-J.; Min, Y.-L. Copper nanowires embedded in boron nitride nanosheet-polymer composites with enhanced thermal conductivities for thermal management. *Polymer* **2020**, *195*, 122455. [CrossRef]
223. Suh, D.; Moon, C.M.; Kim, D.; Baik, S. Ultrahigh thermal conductivity of interface materials by silver-functionalized carbon nanotube phonon conduits. *Adv. Mater.* **2016**, *28*, 7220. [CrossRef] [PubMed]
224. Wang, F.; Zeng, X.; Yao, Y.; Sun, R.; Xu, J.; Wong, C.-P. Silver nanoparticle-deposited boron nitride nanosheets as fillers for polymeric composites with high thermal conductivity. *Sci. Rep.* **2016**, *6*, 19394. [CrossRef]

225. Guo, Y.; Yang, X.; Ruan, K.; Kong, J.; Dong, M.; Zhang, J.; Gu, J.; Guo, Z. Reduced graphene oxide heterostructured silver nanoparticles significantly enhanced thermal conductivities in hot-pressed electrospun polyimide nanocomposites. *ACS Appl. Mater. Interfaces* **2019**, *11*, 25465. [CrossRef]
226. Luo, H.; Liu, J.; Yang, Z.; Zhang, Q.; Ao, H.; Wan, Y. Manipulating thermal conductivity of polyimide composites by hybridizing micro-and nano-sized aluminum nitride for potential aerospace usage. *J. Thermoplast. Compos. Mater.* **2020**, *33*, 1017. [CrossRef]
227. Ren, L.; Li, Q.; Lu, J.; Zeng, X.; Sun, R.; Wu, J.; Xu, J.-B.; Wong, C.-P. Enhanced thermal conductivity for Ag-deposited alumina sphere/epoxy resin composites through manipulating interfacial thermal resistance. *Compos. Part A Appl. Sci. Manuf.* **2018**, *107*, 561. [CrossRef]
228. Zhang, W.-b.; Zhang, Z.-x.; Yang, J.-h.; Huang, T.; Zhang, N.; Zheng, X.-t.; Wang, Y.; Zhou, Z.-w. Largely enhanced thermal conductivity of poly (vinylidene fluoride)/carbon nanotube composites achieved by adding graphene oxide. *Carbon* **2015**, *90*, 242. [CrossRef]
229. Yu, A.; Ramesh, P.; Sun, X.; Bekyarova, E.; Itkis, M.E.; Haddon, R.C. Enhanced thermal conductivity in a hybrid graphite nanoplatelet–carbon nanotube filler for epoxy composites. *Adv. Mater.* **2008**, *20*, 4740. [CrossRef]
230. Hu, B.; Guo, H.; Wang, Q.; Zhang, W.; Song, S.; Li, X.; Li, Y.; Li, B. Enhanced thermal conductivity by constructing 3D-networks in poly (vinylidene fluoride) composites via positively charged hexagonal boron nitride and silica coated carbon nanotubes. *Compos. Part A Appl. Sci. Manuf.* **2020**, *137*, 106038. [CrossRef]
231. Li, J.; Ma, P.C.; Chow, W.S.; To, C.K.; Tang, B.Z.; Kim, J.K. Correlations between percolation threshold, dispersion state, and aspect ratio of carbon nanotubes. *Adv. Funct. Mater.* **2007**, *17*, 3207. [CrossRef]
232. Park, J.G.; Cheng, Q.; Lu, J.; Bao, J.; Li, S.; Tian, Y.; Liang, Z.; Zhang, C.; Wang, B. Thermal conductivity of MWCNT/epoxy composites: The effects of length, alignment and functionalization. *Carbon* **2012**, *50*, 2083. [CrossRef]
233. Isarn, I.; Ramis, X.; Ferrando, F.; Serra, A. Thermoconductive thermosetting composites based on boron nitride fillers and thiol-epoxy matrices. *Polymers* **2018**, *10*, 277. [CrossRef]
234. Hu, J.; Huang, Y.; Zeng, X.; Li, Q.; Ren, L.; Sun, R.; Xu, J.-B.; Wong, C.-P. Polymer composite with enhanced thermal conductivity and mechanical strength through orientation manipulating of BN. *Compos. Sci. Technol.* **2018**, *160*, 127. [CrossRef]
235. Pan, G.; Yao, Y.; Zeng, X.; Sun, J.; Hu, J.; Sun, R.; Xu, J.-B.; Wong, C.-P. Learning from natural nacre: Constructing layered polymer composites with high thermal conductivity. *ACS Appl. Mater. Interfaces* **2017**, *9*, 33001. [CrossRef]
236. Lim, H.S.; Oh, J.W.; Kim, S.Y.; Yoo, M.-J.; Park, S.-D.; Lee, W.S. Anisotropically alignable magnetic boron nitride platelets decorated with iron oxide nanoparticles. *Chem. Mater.* **2013**, *25*, 3315. [CrossRef]
237. Chen, J.; Huang, X.; Sun, B.; Jiang, P. Highly thermally conductive yet electrically insulating polymer/boron nitride nanosheets nanocomposite films for improved thermal management capability. *ACS Nano* **2018**, *13*, 337. [CrossRef] [PubMed]
238. Zeranska-Chudek, K.; Wróblewska, A.; Kowalczyk, S.; Plichta, A.; Zdrojek, M. Graphene infused ecological polymer composites for electromagnetic interference shielding and heat management applications. *Materials* **2021**, *14*, 2856. [CrossRef] [PubMed]
239. Raza, M.A.; Westwood, A.; Brown, A.; Hondow, N.; Stirling, C. Characterisation of graphite nanoplatelets and the physical properties of graphite nanoplatelet/silicone composites for thermal interface applications. *Carbon* **2011**, *49*, 4269. [CrossRef]
240. Raza, M.; Westwood, A.; Brown, A.; Stirling, C. Texture, transport and mechanical properties of graphite nanoplatelet/silicone composites produced by three roll mill. *Compos. Sci. Technol.* **2012**, *72*, 467. [CrossRef]
241. Wang, W.-Y.; Ma, X.; Shao, Y.-W.; Qi, X.-D.; Yang, J.-H.; Wang, Y. Flexible, multifunctional, and thermally conductive nylon/graphene nanoplatelet composite papers with excellent EMI shielding performance, improved hydrophobicity and flame resistance. *J. Mater. Chem. A* **2021**, *9*, 5033. [CrossRef]
242. Wang, S.; Cheng, Y.; Wang, R.; Sun, J.; Gao, L. Highly thermal conductive copper nanowire composites with ultralow loading: Toward applications as thermal interface materials. *ACS Appl. Mater. Interfaces* **2014**, *6*, 6481. [CrossRef]
243. Lokanathan, M.; Acharya, P.V.; Ouroua, A.; Strank, S.M.; Hebner, R.E.; Bahadur, V. Review of nanocomposite dielectric materials with high thermal conductivity. *Proc. IEEE* **2021**, *109*, 1364–1397. [CrossRef]
244. Wang, X.; Wu, P. Highly thermally conductive fluorinated graphene films with superior electrical insulation and mechanical flexibility. *ACS Appl. Mater. Interfaces* **2019**, *11*, 21946. [CrossRef] [PubMed]
245. Wu, Y.; Xue, Y.; Qin, S.; Liu, D.; Wang, X.; Hu, X.; Li, J.; Wang, X.; Bando, Y.; Golberg, D. BN nanosheet/polymer films with highly anisotropic thermal conductivity for thermal management applications. *ACS Appl. Mater. Interfaces* **2017**, *9*, 43163. [CrossRef] [PubMed]
246. Pietrak, K.; Wiśniewski, T.S. A review of models for effective thermal conductivity of composite materials. *J. Power Technol.* **2015**, *95*, 14–24.
247. Wang, X.; Gu, W.; Lu, H. A new thermal conductivity relational expression for polymer composites with constructal design fillers. *Int. Commun. Heat Mass Transf.* **2022**, *136*, 106198. [CrossRef]
248. Hasselman, D.; Johnson, L.F. Effective thermal conductivity of composites with interfacial thermal barrier resistance. *J. Compos. Mater.* **1987**, *21*, 508. [CrossRef]
249. Maxwell, J.C. *A Treatise on Electricity and Magnetism: Pt. III. Mkagnetism. Pt. IV. Electromagnetism*; Clarendon Press: Oxford, UK, 1881.
250. Eucken, A. Thermal conductivity of ceramic refractory materials; calculation from thermal conductivity of constituents. *Ceram. Abstr.* **1932**, *11*, 353–360.

251. Ma, J.; Nan, C. Effective-medium approach to thermal conductivity of heterogeneous materials. *Annu. Rev. Heat Transf.* **2014**, *17*, 303–331. [CrossRef]
252. Every, A.; Tzou, Y.; Hasselman, D.; Raj, R. The effect of particle size on the thermal conductivity of ZnS/diamond composites. *Acta Metall. Mater.* **1992**, *40*, 123. [CrossRef]
253. Bryning, M.; Milkie, D.; Islam, M.; Kikkawa, J.; Yodh, A. Thermal conductivity and interfacial resistance in single-wall carbon nanotube epoxy composites. *Appl. Phys. Lett.* **2005**, *87*, 161909. [CrossRef]
254. Nielsen, L.E. Thermal conductivity of particulate-filled polymers. *J. Appl. Polym. Sci.* **1973**, *17*, 3819. [CrossRef]
255. Cho, E.-C.; Huang, J.-H.; Li, C.-P.; Chang-Jian, C.-W.; Lee, K.-C.; Hsiao, Y.-S.; Huang, J.-H. Graphene-based thermoplastic composites and their application for LED thermal management. *Carbon* **2016**, *102*, 66. [CrossRef]
256. Zhu, Z.; Li, C.; Songfeng, E.; Xie, L.; Geng, R.; Lin, C.-T.; Li, L.; Yao, Y. Enhanced thermal conductivity of polyurethane composites via engineering small/large sizes interconnected boron nitride nanosheets. *Compos. Sci. Technol.* **2019**, *170*, 93. [CrossRef]
257. Zhang, J.; Wang, X.; Yu, C.; Li, Q.; Li, Z.; Li, C.; Lu, H.; Zhang, Q.; Zhao, J.; Hu, M. A facile method to prepare flexible boron nitride/poly (vinyl alcohol) composites with enhanced thermal conductivity. *Compos. Sci. Technol.* **2017**, *149*, 41. [CrossRef]
258. Wang, P.; Chong, H.; Zhang, J.; Lu, H. Constructing 3D graphene networks in polymer composites for significantly improved electrical and mechanical properties. *ACS Appl. Mater. Interfaces* **2017**, *9*, 22006. [CrossRef] [PubMed]
259. Bozlar, M.; He, D.; Bai, J.; Chalopin, Y.; Mingo, N.; Volz, S. Carbon nanotube microarchitectures for enhanced thermal conduction at ultralow mass fraction in polymer composites. *Adv. Mater.* **2010**, *22*, 1654. [CrossRef] [PubMed]
260. Teng, C.-C.; Ma, C.-C.M.; Chiou, K.-C.; Lee, T.-M.; Shih, Y.-F. Synergetic effect of hybrid boron nitride and multi-walled carbon nanotubes on the thermal conductivity of epoxy composites. *Mater. Chem. Phys.* **2011**, *126*, 722. [CrossRef]
261. Im, H.; Kim, J. Thermal conductivity of a graphene oxide–carbon nanotube hybrid/epoxy composite. *Carbon* **2012**, *50*, 5429. [CrossRef]
262. Yu, W.; Xie, H.; Yin, L.; Zhao, J.; Xia, L.; Chen, L. Exceptionally high thermal conductivity of thermal grease: Synergistic effects of graphene and alumina. *Int. J. Therm. Sci.* **2015**, *91*, 76. [CrossRef]
263. Sharma, S.; Tiwari, S.; Shakya, S. Mechanical properties and thermal conductivity of pristine and functionalized carbon nanotube reinforced metallic glass composites: A molecular dynamics approach. *Def. Technol.* **2021**, *17*, 234. [CrossRef]
264. Wu, Z.; Xu, C.; Ma, C.; Liu, Z.; Cheng, H.M.; Ren, W. Synergistic effect of aligned graphene nanosheets in graphene foam for high-performance thermally conductive composites. *Adv. Mater.* **2019**, *31*, 1900199. [CrossRef]
265. Yu, G.-C.; Wu, L.-Z.; Feng, L.-J.; Yang, W. Thermal and mechanical properties of carbon fiber polymer-matrix composites with a 3D thermal conductive pathway. *Compos. Struct.* **2016**, *149*, 213. [CrossRef]
266. Wu, N.; Che, S.; Li, H.-w.; Wang, C.-n.; Tian, X.-j.; Li, Y.-f. A review of three-dimensional graphene networks for use in thermally conductive polymer composites: Construction and applications. *New Carbon Mater.* **2021**, *36*, 911. [CrossRef]
267. Nan, C.-W.; Liu, G.; Lin, Y.; Li, M. Interface effect on thermal conductivity of carbon nanotube composites. *Appl. Phys. Lett.* **2004**, *85*, 3549. [CrossRef]
268. Li, R.; Yang, X.; Li, J.; Shen, Y.; Zhang, L.; Lu, R.; Wang, C.; Zheng, X.; Chen, H.; Zhang, T. Review on polymer composites with high thermal conductivity and low dielectric properties for electronic packaging. *Mater. Today Phys.* **2021**, *22*, 100594. [CrossRef]
269. Kim, Y.; Kim, M.; Seong, H.-G.; Jung, J.Y.; Baeck, S.-H.; Shim, S.E. Roles of silica-coated layer on graphite for thermal conductivity, heat dissipation, thermal stability, and electrical resistivity of polymer composites. *Polymer* **2018**, *148*, 295. [CrossRef]
270. Ball, V.; Del Frari, D.; Toniazzo, V.; Ruch, D. Kinetics of polydopamine film deposition as a function of pH and dopamine concentration: Insights in the polydopamine deposition mechanism. *J. Colloid Interface Sci.* **2012**, *386*, 366. [CrossRef] [PubMed]
271. Sileika, T.S.; Barrett, D.G.; Zhang, R.; Lau, K.H.A.; Messersmith, P.B. Colorless multifunctional coatings inspired by polyphenols found in tea, chocolate, and wine. *Angew. Chem.* **2013**, *125*, 10966. [CrossRef]
272. Zhou, Y.; Hashida, T. Thermal fatigue failure induced by delamination in thermal barrier coating. *Int. J. Fatigue* **2002**, *24*, 407. [CrossRef]
273. Ramnath, B.V.; Alagarraja, K.; Elanchezhian, C. Review on sandwich composite and their applications. *Mater. Today Proc.* **2019**, *16*, 859. [CrossRef]
274. Birman, V.; Kardomateas, G.A. Review of current trends in research and applications of sandwich structures. *Compos. Part B Eng.* **2018**, *142*, 221. [CrossRef]
275. Feng, Y.; Qiu, H.; Gao, Y.; Zheng, H.; Tan, J. Creative design for sandwich structures: A review. *Int. J. Adv. Robot. Syst.* **2020**, *17*, 1729881420921327. [CrossRef]
276. Sihn, S.; Ganguli, S.; Anderson, D.P.; Roy, A.K. Enhancement of through-thickness thermal conductivity of sandwich construction using carbon foam. *Compos. Sci. Technol.* **2012**, *72*, 767. [CrossRef]
277. Kwon, Y.; Yoon, S.; Sistare, P. Compressive failure of carbon-foam sandwich composites with holes and/or partial delamination. *Compos. Struct.* **1997**, *38*, 573. [CrossRef]
278. Liu, H.; Li, T.; Shi, Y.; Zhao, X. Thermal insulation composite prepared from carbon foam and silica aerogel under ambient pressure. *J. Mater. Eng. Perform.* **2015**, *24*, 4054. [CrossRef]
279. Sihn, S.; Rice, B.P. Sandwich construction with carbon foam core materials. *J. Compos. Mater.* **2003**, *37*, 1319. [CrossRef]
280. Quintana, J.M.; Mower, T.M. Thermomechanical behavior of sandwich panels with graphitic-foam cores. *Mater. Des.* **2017**, *135*, 411. [CrossRef]

281. Yu, G.-C.; Feng, L.-J.; Wu, L.-Z. Thermal and mechanical properties of a multifunctional composite square honeycomb sandwich structure. *Mater. Des.* **2016**, *102*, 238. [CrossRef]
282. Bezazi, A.; Remillat, C.; Innocenti, P.; Scarpa, F. In-plane mechanical and thermal conductivity properties of a rectangular–hexagonal honeycomb structure. *Compos. Struct.* **2008**, *84*, 248. [CrossRef]
283. Xie, S.; Jing, K.; Zhou, H.; Liu, X. Mechanical properties of Nomex honeycomb sandwich panels under dynamic impact. *Compos. Struct.* **2020**, *235*, 111814. [CrossRef]
284. Rajaneesh, A.; Zhao, Y.; Chai, G.; Sridhar, I. Flexural fatigue life prediction of CFRP-Nomex honeycomb sandwich beams. *Compos. Struct.* **2018**, *192*, 225. [CrossRef]
285. Hu, J.; Wang, B. Enhanced fatigue performance of auxetic honeycomb/substrate structures under thermal cycling. *Int. J. Mech. Sci.* **2021**, *199*, 106432. [CrossRef]

Paper II

Critical analysis of the systems used to reduce self-heating in polymer composites subjected to very high cycle fatigue regimes

Fatigue & Fracture of Engineering Materials & Structures

WILEY

FFEMS Fatigue & Fracture of Engineering Materials & Structures

INVITED REVIEW

Critical Analysis of the Systems Used to Reduce Self-Heating in Polymer Composites Subjected to Very High Cycle Fatigue Regimes

P. N. B. Reis[1] | A. Katunin[2] | J. Amraei[2]

[1]University of Coimbra, CEMMPRE, ARISE, Department of Mechanical Engineering, Coimbra, Portugal | [2]Department of Fundamentals of Machinery Design, Faculty of Mechanical Engineering, Silesian University of Technology, Gliwice, Poland

Correspondence: P. N. B. Reis (paulo.reis@dem.uc.pt)

Received: 7 October 2024 | **Revised:** 1 December 2024 | **Accepted:** 19 December 2024

Funding: The first author would like to acknowledge the grant BPN/ULM/2023/1/00119/U/00001 awarded to him by NAWA - Narodowa Agencja Wymiany Akademickiej. This research was also sponsored by national funds through FCT – Fundação para a Ciência e a Tecnologia, under the project UIDB/00285/2020 and LA/P/0112/2020.

Keywords: composites | cooling systems | nanofillers | self-heating | very high-cycle fatigue (VHCF)

ABSTRACT

The self-heating effect occurring during fatigue loading of polymer-matrix composites remains to be a significant problem due to its role in accelerating structural lifespan degradation. This is especially challenging when accelerated tests are applied at very high-frequency regimes since without cooling the tested structure is dominated by this phenomenon and rapidly reaching critical temperature value, and finally fails prematurely. This study reviews the approaches to reduce self-heating effect through the modification of materials systems to increase heat transfer and by applying specific load sequences or external cooling systems. The authors describe the possibility of hybridizing the reinforcement to obtain multifunctionality and an overall improvement in mechanical and thermal performance of the composites, as well as applying surface cooling techniques with the physical limitations of their applications. The results of this review demonstrate the practical possibilities of applying cooling approaches to reduce the negative impact of self-heating on structural residual life.

1 | Introduction

Fiber-reinforced composite (FRC) materials are the ideal choices for many industrial applications due to their high specific strength and stiffness properties, good fatigue strength, and, depending on the fiber used, low friction coefficient and wear rate, as well as good thermal and electrical properties [1, 2]. Examples of these applications are related to the automotive sector, high-speed rail systems, shipbuilding, aerospace/aircraft (helicopter rotor blades, aircraft propellers, etc.), and wind turbine blades, among others, whose structures/components have to withstand vibratory, cyclical, highly dynamic or, at least, quasi-static loads, with fatigue standing out in this context as a very relevant phenomenon to take into consideration [2, 3]. Furthermore, in many of these applications, the operating time is more than 20 years, causing loadings to be repeated in more than 10^8 cycles [4, 5].

The first studies related to the fatigue behavior of composite materials began in the 1960s and it is possible to verify that there is a vast knowledge about the low cycle fatigue (LCF) regime, ranging between 10^2 and 10^4 cycles, and the high cycle fatigue (HCF) regime, ranging from 10^4 up to 10^6 cycles [6]. However, for longer lives, these data become too conservative to adopt reliable design criteria, and the literature is also very scarce for the very high-cycle fatigue (VHCF) regime, ranging from 10^6 up to 10^8 cycles, and for the giga-cycle (GC) regime, longer than 10^8 cycles [7, 8]. This lack of studies is because the test periods are very long. For example, using conventional

Summary

- Without adequate cooling, VHCF tests lead to a significant increase in temperature.
- Modifying the materials' architecture improves their thermal conductivity and self-heating.
- Cooling techniques benefit the fatigue response of PMCs in the VHCF regime.
- A critical analysis of these methodologies is necessary for the VHCF regime.

servo-hydraulic machines, fatigue lives of up to 10^9 cycles at frequencies of around 5 Hz would take at least 6 years, and for 10^8 cycles at 10 Hz, it would take approximately 4 months, in addition to testing becoming very expensive [5, 8]. Therefore, the solution to overcome this problem is to perform fatigue testing under higher frequencies, but, in this context, the self-heating phenomenon responsible for thermal fatigue proves to be a huge challenge due to the viscoelastic properties of the polymer matrix at high temperatures [9, 10].

Given these considerations, it is necessary to minimize the self-heating effect, especially for values below the T_g (glass transition temperature) of the composite material, to prevent thermally induced fatigue [11–13]. Based on the literature, the appropriate selection of the polymer is one of several recommended strategies [14], because the self-heating effect can be controlled based on the thermal conductivity (K) of the matrices. Amraei and Katunin [14] and Leung [15], for example, present a summary of the thermal conductivity (K) values for different polymers, which depend not only on the specificity of the polymer but also on their degree of crystallinity (a higher crystallinity degree promotes higher K values). From this analysis, it is possible to conclude that, in fact, the thermal conductivity values of the polymers most commonly used in composite materials, whether thermoplastic or thermosetting, are characterized by very low values ranging from 0.091 W/(m × K) for polyester to 0.88 W/(m × K) for the epoxy resin [14, 15]. In terms of the most popular reinforcements, the values are 0.04 W/(m × K) for aramid fibers, 1.03 W/(m × K) for glass fibers, and 15 W/(m × K) for carbon fibers [16].

However, due to very specific design requirements, it is not possible to select materials based on singular specificities. In this case, it is suggested to add fillers/nanofillers to the matrix in order to increase its thermal conductivity. Furthermore, polymers are generally brittle and with poor fatigue strength, which is why the literature also suggests the use of nanofillers to improve their mechanical properties [3]. Inherently, this goal aims to combine the interest of two distinct areas of research available in the literature: electrical, whose goal is to maximize thermal conductivity (beyond electrical conductivity), and mechanical from the perspective of structural integrity. However, due to the reinforcement/nano-reinforcement content used, they can become incompatible, because maximizing one can drastically affect the other. It is in this context that this document is inserted and makes a critical analysis based on the adoption of this methodology to improve the fatigue performance of polymer-based composites in terms of VHCF. Finally, this scenario will be confronted with another one related to the external cooling systems used to reduce the surface temperature of the specimens.

2 | Fillers' Effect on the Self-Heating Process

A very efficient way to avoid excessive self-heating in structures/components, and the consequent faster degradation due to thermal fatigue, is to implement materials with higher thermal conductivity. However, some constraints imposed right at the design stage immediately limit the freedom to select materials. In the particular case of composite materials, the possibility arises of using reinforcements at different scales, ranging from nano to macro, that can allow considerable improvements in their mechanical properties and, at the same time, increase their thermal conductivity. Therefore, it is advisable to use particles/nanoparticles with high thermal conductivity (*TC*) to promote greater heat dissipation by conduction and, consequently, minimize the stored internal energy. The elements that are most frequently used in the field of engineering applications are summarized in Figure 1, along with their corresponding *TC* values, which are grouped into three classes (metallic, ceramic, and carbon-based).

Considering ceramics, for example, heat transfer occurs exclusively through vibration waves in the lattice, which explains the wide range of thermal conductivity. For example, silicon dioxide (SiO_2) and Zirconia (ZrO_2) have the lowest values with 1.3 W/(m × K) and 2 W/(m × K), respectively, while the highest one is obtained for cubic boron nitride (cBN) with 1000 W/(m × K). Cubic boron nitride has the same structure as diamond and its properties mirror those of diamond. The thermal conductivities of aluminum nitride (AlN), boron nitride (BN), and silicon carbide (SiC) are between 100 and 300 W/(m × K), while that of beryllium oxide (BeO) is between 230 and 330 W/(m × K) and that of hexagonal boron nitride (hBN) is around 300 W/(m × K). On the other hand, metal and carbon-based fillers are both electrically and thermally conductive, in contrast to ceramics. Furthermore, it should be noted that the dispersion of metallic fillers in polymeric

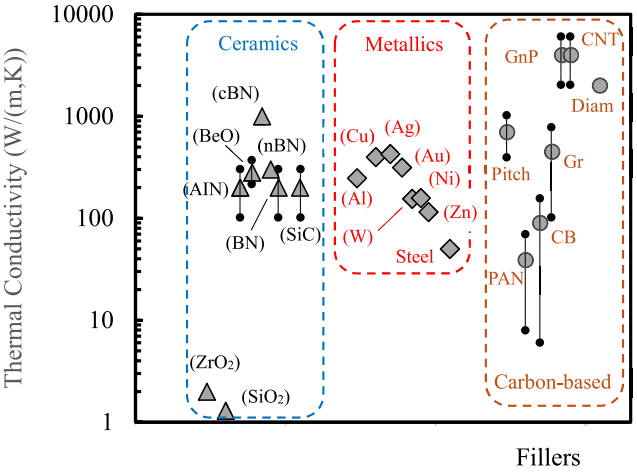

FIGURE 1 | Thermal conductivity values for fillers that are most frequently used in engineering. [Colour figure can be viewed at wileyonlinelibrary.com]

matrices significantly compromises their electrical insulation properties and dielectric breakdown threshold. In this case, the highest thermal conductivities are obtained for silver (Ag), copper (Cu), and gold (Au) with 427 W/(m × K), 398 W/(m × K), and 315 W/(m × K), respectively, and the lowest for steel with 50 W/(m × K). For zinc (Zn), tungsten (W), nickel (Ni), and aluminum (Al), the thermal conductivity values vary between 115 W/(m × K) and 247 W/(m × K). Finally, regarding carbon-based fillers, the thermal conductivity of carbon fibers depends on their organic precursors, which explains the different values obtained for pitch-based carbon fibers (Pitch), between 400 and 1000 W/(m × K), and for PAN-based carbon fibers (PAN), between 8 and 70 W/(m × K). Graphite (Gr), with its sp^2 configuration, is characterized by values between 100 and 800 W/(m × K), the latter being very high in-plane. The highest values are between 2000 and 6000 W/(m × K) and can be found for Carbon nanotube (CNT) and Graphene nanoplatelets (GNPs), but GNPs are preferable because their 2-D geometry forms thermally conductive paths along the in-plane directions to the detriment of CNT (with 1-D geometry), which is highly efficient along the tube direction. For the other ones, carbon black (CB) has values between 6 and 174 W/(m × K), while diamond is around 2000 W/(m × K) [14, 15].

In addition to the intrinsic properties of the fillers, the thermal conductivity of a polymer matrix composite material also depends on other factors, such as the geometry and orientation of the filler, the alteration of the interface promoted by the surface treatments of the fillers, and the filler content in the matrix. In terms of fillers' geometry, both shape and size are very important parameters because they significantly affect their aspect ratio [15]. However, the literature is not unanimous regarding the size of the fillers. While some studies report that using smaller fillers reduces thermal conductivity, because interfacial thermal barriers prevent phonon transport, other authors concluded that the use of nano-fillers leads to values comparable to or even higher than those of micro-scale counterparts [17–20]. According to Leung [15], nanoparticles are preferable to micro-particles for forming thermally conductive pathways, but to achieve maximum effectiveness of thermally conductive networks, thermal contact resistance at polymer-filler and filler-filler interfaces must be minimized. On the other hand, the literature is unanimous regarding the aspect ratio of the fillers and how their increase leads to higher thermal conductivity values. In terms of 1-D fillers, for example, the benefits are achieved when they are highly dispersed in the mat and lead to a thermally conductive network [21–23]. Concerning 2-D fillers, when processed correctly, they tend to align, essentially in directions parallel to the material flow direction, and promote a network along in-plane directions [21, 24, 25]. Finally, 3-D fillers will be ideal when thermal conductivity is desired in the various planes of the polymer composite [25, 26]. These advantages obtained with high aspect ratio fillers also highlight that they must have a preferred orientation to maximize thermal conductivity, where electrospinning technique stands out for this purpose [15].

It is also common practice to use surface treatments on fillers (silane-based coupling agents or surface functionalization) to reduce their thermal contact resistance, which simultaneously helps to improve their dispersion in the matrix. However, Leung [15] suggests that there is an ideal amount of coupling agent and any deviation from it can be detrimental.

Another very important parameter that influences thermal conductivity is the filler fraction. It may even be the most dominant of all those considered. In this case, increasing the filler content increases the thermal conductivity of the composite until it reaches a limit value resulting from the agglomeration of the fillers [27] or their saturation in the matrix [28, 29]. According to some authors, this increase is linear up to load fractions close to 95 wt.% [30–34], although an abrupt drop in thermal conductivity is also reported after its maximum value due to the presence of voids and/or poor dispersion [35–38]. Lokanathan et al. [39], for example, developed a very interesting review study on nanocomposites with high thermal conductivity in which they summarize all the studies carried out for this purpose. This analysis evaluated both in-plane and out-of-plane thermal conductivity, and the results are summarized in Figure 2. In their representations, the authors adopted TC_c and TC_m as the thermal conductivity of the composite and polymer matrix, respectively, and the results were analyzed according to intervals that group together the papers published for different fillers contents (vol.%).

In terms of in-plane thermal conductivity, Figure 2a evidence that values of thermal conductivity (*TC*) higher than 20 W/(m × K) are obtained essentially for a filler fraction of 80 vol.%, while for fractions equal to or less than 20 vol.% the reinforced composites that have reached these values (20 W/(m × K)) are very scarce. According to the authors, reinforced composites with a *TC* of more than 10 W/(m × K) and filler fractions of less than 10 vol.% can only be obtained with graphene and/or BN (boron nitride) fillers [39]. However, some studies provide different results. For example, in the study carried out by Wang et al. [40], a *TC* about 13.5 times higher was obtained when the matrix was reinforced with 0.9 vol.% single-crystalline copper nano-wires with a high aspect ratio. Balachander et al. [41] reinforced a polydimethylsiloxane (PDMS) matrix with around 3 vol.% of gold nanowires and obtained a 30-fold increase compared to the neat polymer. Figure 2a also shows that, compared to the neat matrix, the fillers mostly lead to an increase in *TC* of around 10 times more, and not many provide increases of around 100 times more (the highest value observed was 4200 times more). On the other hand, regarding out-of-plane thermal conductivity, Figure 2b shows that, compared to in-plane thermal conductivity, there are much fewer studies available in the literature. In this case, the values are an order of magnitude lower than those obtained for in-plane thermal conductivity and, although most of them are less than 4 W/(m × K), the highest *TC* values found in the literature are around 11.1 W/(m × K). In terms of composite laminates, Yu et al. [42] produced CFRP composites with spherical copper particles coated by aluminum foil to create a 3D thermally conductive patch and, consequently, increase the *TC* value in the out-of-plane direction. They achieved an increase of almost 12 times over the unmodified CFRP composites (0.6 W/(m × K)). Moreover, Hu et al. [43] developed 3D hybrid networks involving carbon nanotubes coated with silica and hexagonal boron nitride, obtaining improvements of around six times with this strategy. In fact, three-dimensional networks reduce interfacial thermal resistance and promote a higher degree of phonon transmission [43, 44].

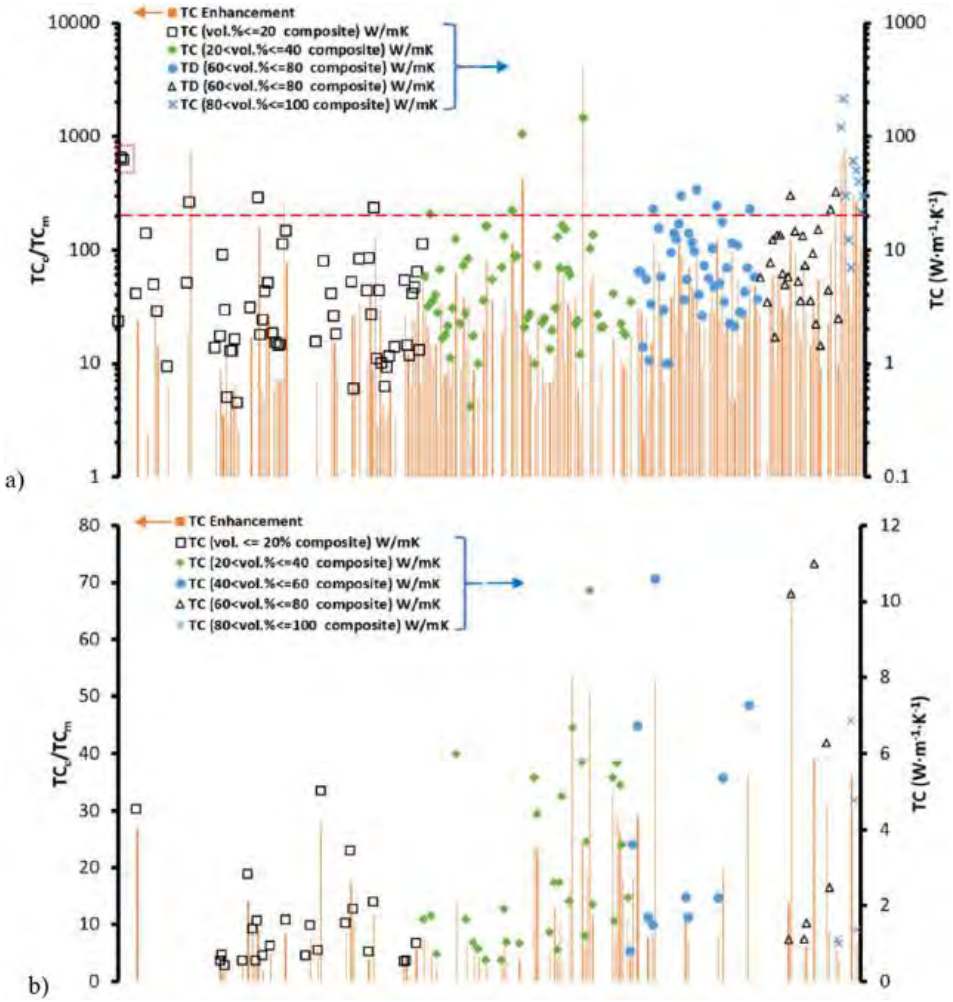

FIGURE 2 | Thermal conductivity and thermal conductivity improvement for: (a) In-plane of the composite; (b) Out out-of-plane of the composite [39]. [Colour figure can be viewed at wileyonlinelibrary.com]

Alternatively, filler hybridization is also proving to be a very effective strategy for increasing thermal conductivity, especially when low filler fractions are imposed. In this case, it is possible to create a thermally conductive network in polymer matrices involving fillers of various types, sizes, and/or shapes.

According to the literature [45–48], 1-D fillers are flexible and can act as bridges between dispersed 2-D or 3-D fillers to form thermally conductive networks. For example, Bozlar et al. [49], by adding 0.15 wt.% of MWCNTs (multi-walled carbon nanotubes) to an Al_2O_3-epoxy nanocomposite, obtained thermal conductivity values around 1.3 times higher. Yu et al. [50] reinforced an epoxy resin with 2.5% SWCNTs (single-walled carbon nanotubes) and 7.5% GNPs and the increase was five times higher than that of the neat resin. Using epoxy resins, Teng et al. [51] obtained a 7.43-fold increase when they added 30 vol.% of modified BN flakes and 1 vol.% of functionalized MWCNTs, while Im et al. [52] obtained an increase of around 140% when they added 0.36 wt.% of MWCNTs to a GO-epoxy nanocomposite. TabkhPaz et al. [53] using 3.1 vol% CNT and hBN together obtained an increase of 290%, a much higher value than that obtained with a single filler. On the other hand, when Yu et al. [54] added GNPs and MWCNTs together, they obtained better thermal conductivity results than if they used only GNPs.

3 | Cooling Methodologies Used in the VHCF

To overcome the problems related to long fatigue tests and the costs associated with conventional methodologies, test systems have emerged that operate in the ultrasonic frequency range and with time reductions of a factor of 20 to 100 [55]. Nonetheless, self-heating can lead to thermal fatigue, which, beyond affecting the viscoelastic properties of the polymer matrix, accelerates the damage mechanisms and promotes the collapse faster [9, 10]. Therefore, in addition to material selection, literature also proposes the use of various methods to cool the specimens and delay or even prevent the problems related to self-heating.

According to the literature, the first consideration is the environmental temperature, because it can act as both a cooling and heating system. For example, Charalambous et al. [56] studied the fatigue delamination growth rate of a carbon-fiber/epoxy material subject to different environmental temperatures (−50 °C, 20 °C, 50 °C, and 80 °C), and concluded that the delamination crack propagated two orders of magnitude faster at 80 °C than at room temperature. Furthermore, the effect of temperature was most noticeable close to the threshold regime, which was a very important finding for the design criteria based on “no growth”. Voudouris et al. [57] obtained similar results and observed that, in

the high-cycle fatigue regime, mechanical and thermal behaviors compete with each other. Figure 3 summarizes the authors' main conclusions, which confirm the influence of the environmental temperature on the fatigue response. Therefore, the lower environmental temperatures are favorable because they act as cooling systems and prevent structural degradation when the structures/components are subjected to cyclic loads. In this context, the self-heating phenomenon is retarded by the environmental temperature. For these purposes, the literature provides several studies in which the authors carried out their tests with specimens exposed continuously to different gases (such as CO_2 and N_2) or which are injected at regular time intervals [14, 56, 58].

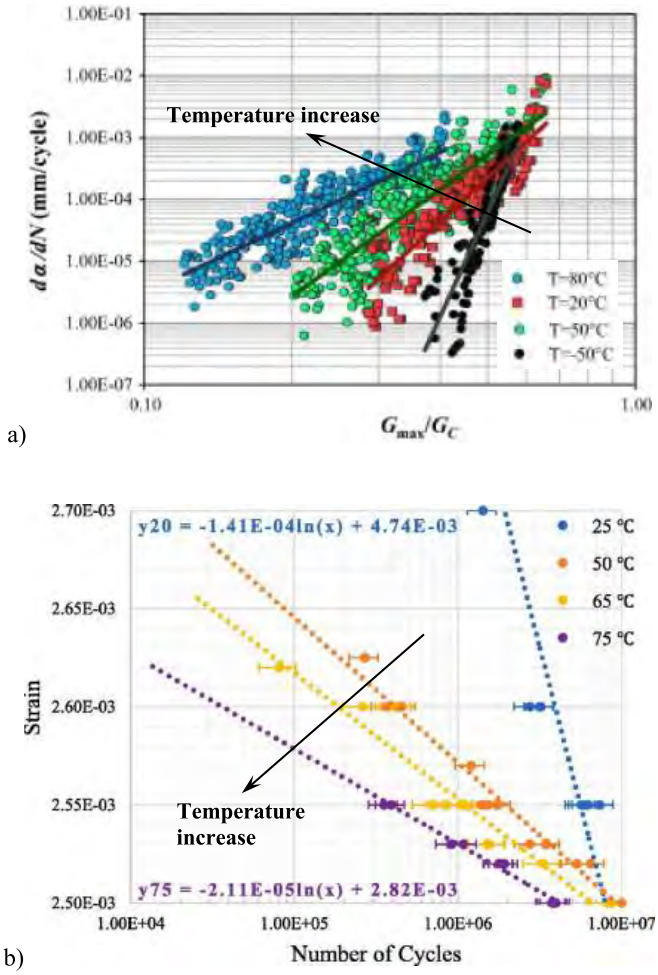

FIGURE 3 | (a) Bi-logarithmic plot of fatigue delamination growth rate (da/dN) vs. normalized energy release rate for different temperatures (adapted from [56]); (b) Fatigue life curves for different temperatures [57]. [Colour figure can be viewed at wileyonlinelibrary.com]

From the cooling systems mentioned in the literature, the use of airflow from fans/blowers has proven to be a simple, economical, and efficient technique for situations in which the thermal heat rate generated is generally less than 5 kW [14]. For example, fatigue studies performed by Katunin and Wachla [12] at 30 Hz, without cooling and cooled by airflow (at room temperature) at rates of 5.5 m/s and 1.5 m/s, revealed that the presence of airflow at 5.5 m/s almost doubled the fatigue life compared to that obtained without cooling (see Figure 4). In this case, the mechanical fatigue process controls the final failure and degradation of the specimens as a result of the heat being removed from their surfaces by air cooling. Furthermore, the authors concluded that it is a strategy that can be implemented for very high cycle fatigue tests with suitable air flow rates. In another study, Bartelt et al. [59] used two fans to cool the specimens that were tested at frequencies between 20 Hz and 80 Hz. For the same frequency range, Adams and Horst [60, 61] carried out studies in which the test rig was housed in an air-conditioned chamber with a constant temperature of 20 ± 1.5 °C.

Apinis [62] carried out fatigue tests at 400 Hz to obtain fatigue lives of up to 10^8 cycles and, due to the temperature observed on the surface of the specimens (over 50 °C), a water jet cooling system was implemented. To preserve the structural integrity of the specimen against humidity, it was covered with a thin layer of wax. In this case, because the rate of thermal heat generated on the surface of the specimen was higher, the authors had to use a cooling element with a higher specific heat than air. However, the most recent ultrasonic fatigue testing systems that operate at frequencies of 20 kHz, theoretically reaching 10^8 cycles in <2 h, lead to much higher thermal heat rates in the specimens, and the literature, in this case, suggests adopting the pulse-pause air cooling technique (see Figure 5) [63].

In addition to the cooling fluid, the process also includes sequences of pulses and pauses to maintain the specimen's temperature between room temperature and a value below the glass transition temperature (T_g) to avoid harmful thermal effects. For example, some studies in the literature suggest this

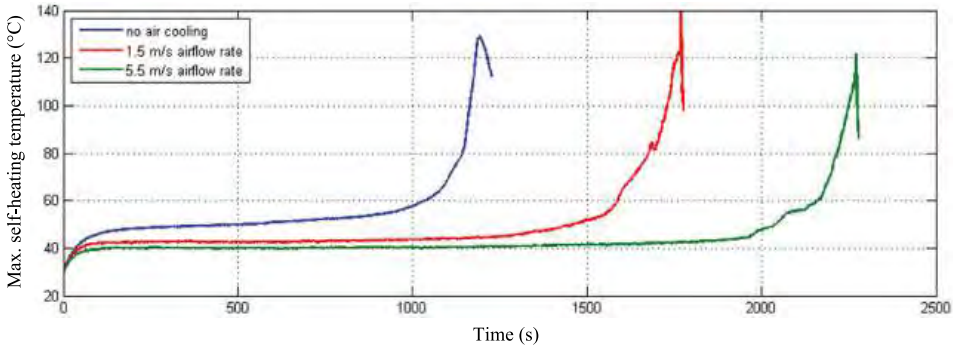

FIGURE 4 | Historical self-heating temperature curves for scenarios with and without air cooling (adapted from [12]). [Colour figure can be viewed at wileyonlinelibrary.com]

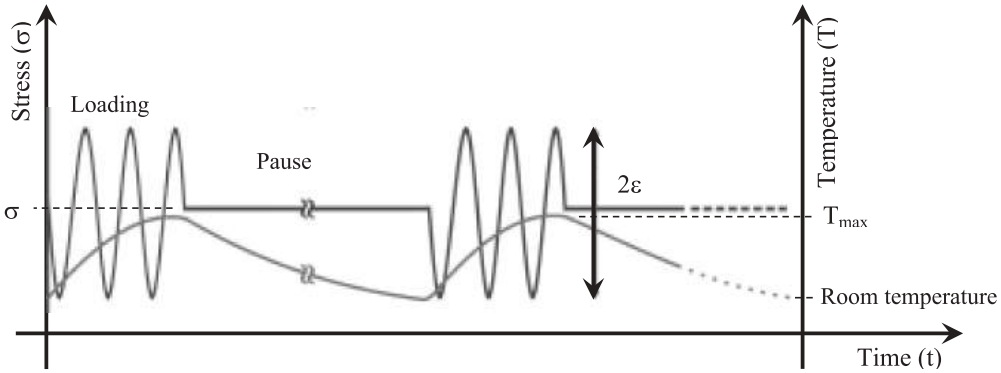

FIGURE 5 | Schematic principle of the pulse-pause air cooling technique for VHCF tests on composites (adapted from [4]).

technique combined with dry compressed air [2–4, 8, 63–65], or with a Peltier ring-type cooler (also known as a thermoelectric-based air cooler) [66].

Regardless of the success obtained with the pulse-pause technique used alone or together with air cooling, it is inevitable that the tests will take longer because the pause reduces the effective frequency of the test. Therefore, it is not surprising that the literature presents various studies in which the authors focus on minimizing pause time or on more efficient systems than those that use only air cooling. In terms of the pulse-pause technique, the lengths are typically between 25 and 250 ms (500–5000 cycles) for the pulses and 25 to 2000 ms for the pauses, depending on the damping of the material being tested [55, 67]. Based on the literature, for example, Flore et al. [2] and Premanand et al. [68] reported typical pulse–pause ratios of 1:20 for glass-fiber reinforced composites (GFRP) and 1:10 for carbon-reinforced composites (CFRP), respectively. In the first case, Flore et al. [2] using pulse lengths of 100 ms (corresponding to around 2000 cycles) and pause lengths of 2000 ms, which promote effective frequencies of 1 kHz, combined with pressurized air-cooling obtained maximum temperatures below 25 °C for quasi-unidirectional GFRP composites. On the other hand, for carbon fiber-reinforced Polyether-ketone-ketone (CF-PEKK) composites, Premanand and Balle [68] used sequences of 200 ms of ultrasonic pulses and 2000 ms of pause, obtaining temperature increases of up to 10 °C. For sequences of a similar magnitude, Miyakoshi et al. [65] found ΔT below 25 °C for a composite produced with T800S carbon fiber prepreg and a thermosetting epoxy resin.

However, these ratios are not unanimous in the literature because, for example, values of 1:20 were also used by Weibel et al. [69, 70] in CF-PEKK, CF-epoxy composites, and carbon fiber fabric-reinforced polyphenylene sulfide (CF-PPS), and by Balle et al. [71] in CF-epoxy composites. Furthermore, although they do not mention the temperature values obtained throughout the test, Lee et al. [66] studied the very high cycle fatigue of a PA66-GF30 GFRP composite using 300 ms pulses and 3000 ms pauses. In this context, the literature reports a comprehensive study carried out by Premanand and Balle [13] on the effect of the pulse-pause sequence on the self-heating response of a CF/PEKK composite and, for this purpose, different cyclic amplitudes (40 μm, 45 μm, and 50 μm) and pause periods (1000 ms, 2000 ms, and 4000 ms) were considered. From this study, authors observed that when cyclic amplitudes are combined with pause times that provide temperature increases of less than 20 °C, no significant thermal effects occur and, consequently, these conditions become ideal for carrying out tests in very high cycle fatigue (*VHCF*) regimes. However, they also emphasized that this conclusion cannot be generalized, because it depends on: Heat dissipation from the composite due to the type of fibers and their combination; Glass transition temperature of the polymer; and Fatigue damage mechanisms. On the other hand, when cyclic amplitudes lead to the appearance of damage capable of interacting with the self-heating phenomenon, such as delamination which activates frictional heating, authors suggest that the control of pause times based on the self-heating temperature should only be valid until damage appears [13]. The results found by the authors are summarized in Figure 6 in terms of time versus temperature curves for all the conditions analyzed during a window of 1 min.

The curves have the shape of a sawtooth, where the peaks are related to the ultrasonic pulses and the valleys to the ultrasonic pauses. Based on a detailed analysis of the curves furthest apart, it is noticed that the temperature increase is less than 5 °C for the specimen tested with a cyclic amplitude of 40 μm and a pause time of 4 s. This is because the heat generated during the test is dissipated during the pause time, i.e. before the next pulse begins. On the other hand, for the specimen tested with cyclic amplitudes of 50 μm and pause times of 1 s, the ultrasonic sequences lead to temperature increases close to 25 °C because the pause time is too short to dissipate the thermal energy generated during an impulse. Furthermore, it should also be noted that both the specimens tested with a cyclic amplitude of 45 μm and a pause time of 1 s and the specimens tested with a cyclic amplitude of 50 μm and a pause time of 2 s have a stabilization temperature very close to 18 °C. Based on these findings, the authors concluded that the self-heating temperature depends on the cyclic amplitude and interval length between pulses.

Regarding more efficient systems than those using conventional air cooling, Premanand et al. [10] used two nozzles to blow compressed air onto the surface of the specimen. Before proposing a new cooling system, Cui et al. [1] addressed the need to use cooling systems and reported that, when CF-PEEK composites are tested without any cooling system, the temperature easily reaches values above 90 °C, but using compressed cold air, the temperature is limited to 40 °C. For carbon fiber/epoxy

composites, the temperature increases 106 °C in 7 s and reaches a maximum of 190 °C, even with the use of compressed air, evidencing that this system is not efficient for carrying out tests under acceptable conditions. However, when compressed cold air is combined with the intermittent ultrasonic loading method, these authors also found no significant benefits because the temperature rises to 42 °C after the first loading cycle, 60.5 °C after the second loading cycle, 78 °C after 7.85×10^6 cycles and exceeds 100 °C for 10^7 cycles. Therefore, to absorb more heat and cool the compressed air, they proposed a new cooling system based on vaporizing liquid nitrogen. According to Figure 7, the sample is cooled by air circulating through a system inside a liquid nitrogen tank, which absorbs the heat and lowers the temperature of the airflow. Using this method, maximum temperatures can be reached in the specimen below 40 °C for a load frequency of around 19.73 kHz. Finally, the benefits obtained can be summarized in Figure 8, comparing the compressed cooling system with intermittent loading and liquid nitrogen cooling.

Wang et al. [72] analyzed the fatigue response to high and very high cycles of a honeycomb sandwich structure with faces made of carbon fiber composites (0/90/45/−45) and observed, that using frequencies between 18.5 and 20.5 kHz and the traditional compressed air cooling system, the specimens were severely damaged (see Figure 9), but using cryogenic nitrogen blown over the surface of the specimen and the pulse-pause method, no more than 40 °C was observed (a value within the requirements).

4 | Discussion and Critical Analysis

As evidenced in Table 1, the thermal conductivity of a neat polymer or a fiber-reinforced polymer composite can be significantly improved by incorporating fillers, especially if they are thermally conductive, such as carbon allotropes (e.g., carbon fiber, CNT, GNP, CNF), ceramics (e.g., BN), and metals (e.g., Cu, Ag, Au).

Moreover, literature recognizes that increasing the filler content increases the thermal conductivity (*TC*) and, in general, only for fractions higher than 80 vol.% is it possible to obtain a *TC* higher than 20 W/(m × K). However, from the point of view of the mechanical performance of composite materials, these values are very high and compromise their structural integrity. In

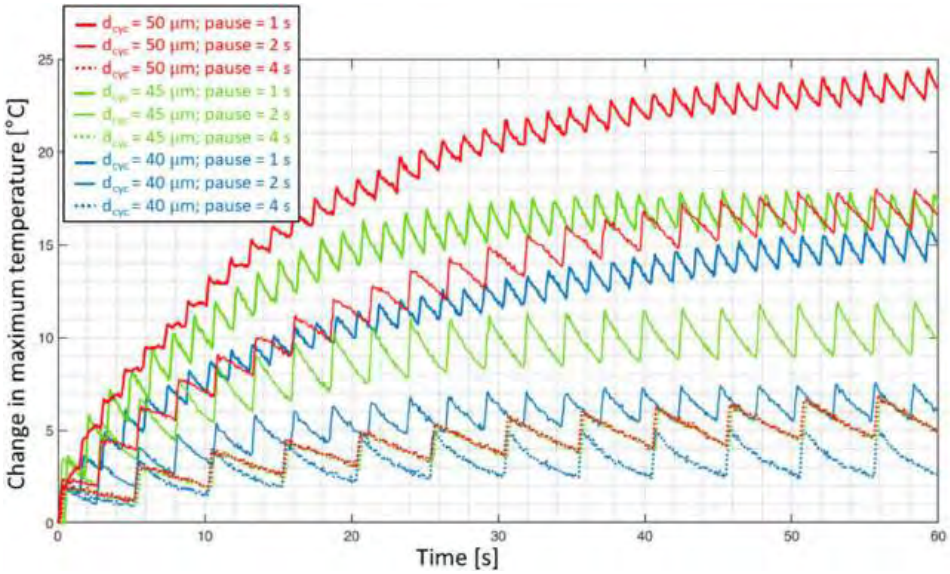

FIGURE 6 | Time versus temperature curves for different conditions analyzed [13]. [Colour figure can be viewed at wileyonlinelibrary.com]

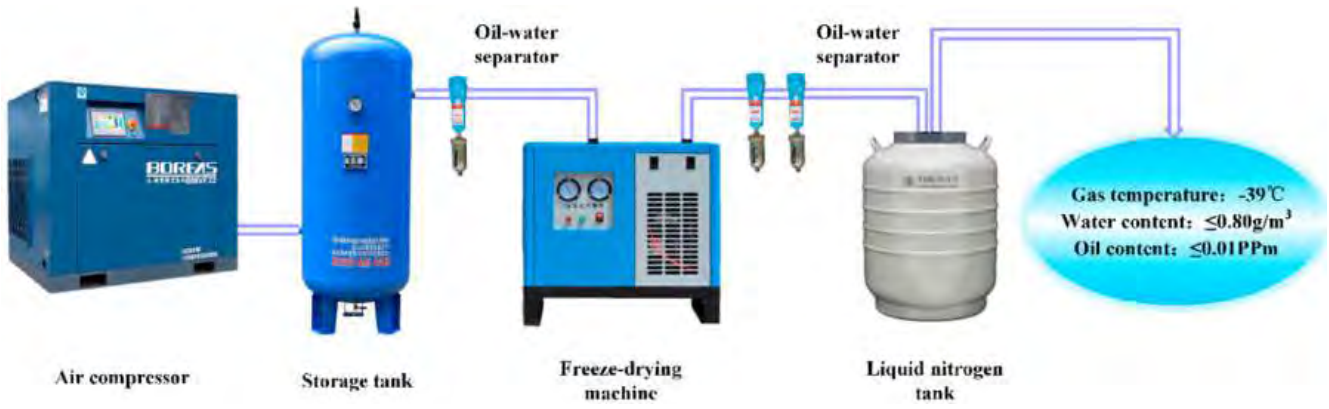

FIGURE 7 | Liquid nitrogen cooling system proposed by Cui et al. [1]. [Colour figure can be viewed at wileyonlinelibrary.com]

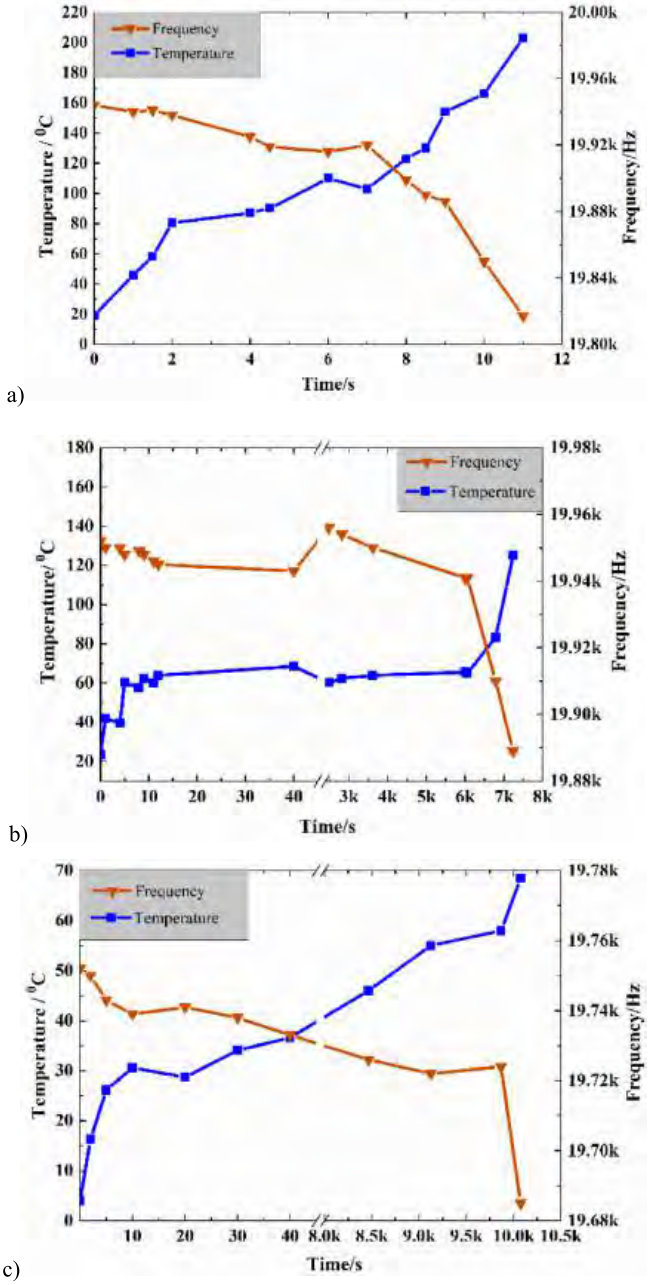

FIGURE 8 | Evolution of the temperature (blue) and the frequency (red) using: (a) compressed cold air; (b) intermittent loading; (c) liquid nitrogen cooling (adapted from [1]). In panels b and c, k indicates 10^3. [Colour figure can be viewed at wileyonlinelibrary.com]

fact, in addition to the filler content that affects the material's properties, the size, shape, aspect ratio, particle distribution, and degree of orientation of the non-spherical particles in relation to the applied stress are also parameters to be taken into consideration [73].

According to studies carried out by Ferreira et al. [73] involving silica particles with sizes of 10 and 350 μm, the tensile strength of the composite is affected by the size and volume fraction of the particles. In the first case, for example, the tensile strength increases with decreasing particle size, because the interfacial area increases and promotes a more effective bond between the reinforcement and matrix. On the other hand, a higher volume fraction promotes agglomerations/aggregations that affect the interfacial area and, consequently, the mechanical engagement of the polymer chains with the nanoparticles decreases. Furthermore, the literature also reports theoretical models for predicting the mechanical strength of composites and, for a volume fraction greater than 0.2, most of them lead to similar predictions and highlight a decrease in strength compared to the matrix material [74–76]. Ferreira et al. [73] also observed that the particle's shape also affects the mechanical strength, because particles with sharp edges lead to much higher stress concentration factors than rounder particles. Moreover, they observed that the composites filled with the smallest particles (10 μm) had lower toughness (K_c) than the composite with the largest particles (350 μm), but both with an improved fracture toughness compared to the unfilled matrix. Finally, in other studies, the authors observed that increasing the particle size promotes shorter fatigue lives due to a reduction in initiation life, and the fatigue crack propagation rate increases with increasing particle size [77, 78]. Boonyapookana et al. [79] analyzed the response to fatigue crack growth of an epoxy composite reinforced with silica particles and observed a predominantly time-dependent behavior evidenced by the almost overlapping of the K_{max}-da/dN curves into a single one. In terms of damage mechanisms, micro-cracks formed in front of the main crack, which joined together to grow. This process was repeated throughout the fatigue tests.

Azimi et al. [80] observed that, especially near the threshold regime, the fatigue crack propagation resistance of a rubber-epoxy composite is improved by approximately one order of magnitude when smaller rubber particles (0.2 μm) are used instead of higher rubber particles (1.5 μm). This was explained by the authors due to the fact that when the plastic zone's size increases in relation to the rubber particles' sizes, the mechanisms of cavitation/shear of the rubber and expansion of the plastic voids become active. Furthermore, the behavior close to the threshold is influenced by the morphology of the mixture and the particles' size, but not by the volume fraction, although the opposite occurs for the slope of the Paris-Erdogan power law.

Regarding the effect of particle shape on fatigue response, Verma and Sharma [81] observed that the fatigue life of epoxy nanocomposites filled with spherical alumina nanoparticles was 14 to 28 times higher than that of unfilled composites and those reinforced with rod-shaped alumina nanoparticles, concluding that spherical geometry is more effective as a filler material for improving fatigue behavior. Moreover, compared to spherical alumina nanoparticles, the rod-shaped geometry has a greater propensity to produce agglomerates for higher filler contents. Epoxy composites filled with spherical nanoparticles also evidenced higher resistance to fatigue crack growth due to reduced stress levels at the particle-matrix interface as a consequence of the larger surface area. Finally, regardless of reinforcement geometry, microcracking, crack bifurcation, and crack bowing were the most frequently observed damage mechanisms. In another study, Kane et al. [82] found that for hydroxyapatite (HA) reinforced high-density polyethylene (HDPE), the fatigue life increased when the micro-whiskers were used instead of microparticles with a mean diameter of 1.3 ± 0.4 μm (comparable to the width of the micro-whiskers). The fatigue life of composites with micro-whiskers is shown to be four to five times longer,

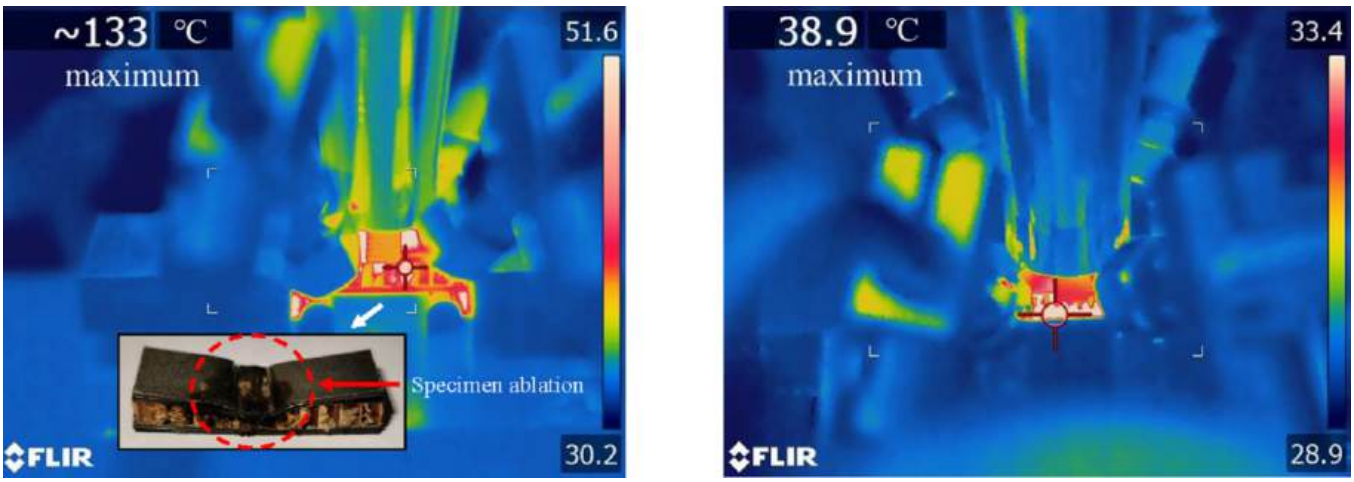

FIGURE 9 | (a) Conventional compressed air cooling; (b) Cryogenic nitrogen and intermittent loading [72]. [Colour figure can be viewed at wileyonlinelibrary.com]

and authors justify this improvement by the fact that composites reinforced with micro-whiskers are more tolerant to damage due to a lower stiffness loss, creep, and energy dissipation compared to reinforcement with micro-particles.

Another finding of the study carried out by Kane et al. [82] is related to the reinforcement content, and, in this case, the authors observed that composites containing 40 vol.% HA presented lower fatigue lives compared to the composites with 20 vol.% HA, but this decrease was more significant for composites containing micro-particles. Chisholm et al. [83] found that nanocomposites with 1.5 wt.% SiC nanoparticulate had better fatigue performance than those with 3.0 wt.%. For a stress ratio of 0.1 and compared to the unreinforced composite, Boonyapookana et al. [79] observed a 26% increase in ΔK_{th} when silica microparticles (average size 20–30 μm) were added. This benefit was due to the increase in micro-cracking ahead of the main crack and deflection of the crack.

Verma et al. [84] conducted a literature review on the fatigue behavior of particle-reinforced polymer composites and concluded that the mechanical properties of composites are significantly influenced by the type of reinforcing material and the manufacturing process. For example, the size and shape of the reinforced materials have a detrimental effect on the various mechanical properties. However, composite materials containing nanofillers cannot be produced using standard techniques for producing microparticle-based composites, because nanoparticles tend to form agglomerates if not processed appropriately. According to the authors, smaller particles are preferable to larger ones, as long as they are properly dispersed, because by being present in greater numbers in the composite they block and/or delay the propagation of the fatigue crack and improve the material's fatigue performance. In this case, these two factors are very important for the composite's fatigue properties. Based on this evidence, while micro-fillers generally only improve fracture toughness, nano-fillers are preferable in terms of fatigue because they increase fatigue life and ΔK_{th}. In this case, increasing the volume fraction is favorable, as long as the nanofillers are well dispersed and the absence of agglomerations/aggregations is guaranteed, because, in this case, the interfacial area between the polymer matrix and the nanoparticles decreases and, consequently, only a few polymer molecules penetrate between the nanoparticles [85, 86]. Furthermore, according to the literature, agglomerations/aggregations are considered defects responsible for significant stress concentrations in nanocomposites that dramatically affect mechanical properties [85, 87–89]. In this context, when the nanofillers are functionalized, they disperse more uniformly in the composite and the coupling agents or silanes used also modify the contact surface, providing a strong chemical bond between the fillers and matrix [84, 90]. For example, Zhao et al. [91] observed slight improvements in terms of fracture toughness or fracture energy, but very significant benefits in terms of the fatigue crack growth rate when the alumina nanoparticles were surface treated with silane and well dispersed in an epoxy matrix. In this case, the Paris law constants (C and m) decreased from 42.1×10^{-3} and 10 for the neat resin to 0.39×10^{3} and 7 for the untreated Al_2O_3/epoxy nanocomposites, and to 0.07×10^{-3} and 5 for the treated Al_2O_3/epoxy nanocomposites [91].

Based on this discussion, it is possible to conclude that thermal conductivities higher than 20 W/(m × K), obtained for filler contents higher than 80%, are incompatible with long fatigue lives and with the mechanical performance in general of polymer-based composites. From the point of view of structural integrity, fatigue strength is only maximized with the use of nano-scale fillers properly dispersed in the matrix. However, for these ratios, it is very difficult, if not impossible, to avoid agglomerates that act as defects and stress concentration points that affect the properties of the composites.

Therefore, Lokanathan et al [39] state that it is possible to obtain a thermal conductivity of more than 10 W/(m × K) using filler fractions of less than 10 vol.%, provided that they are based on carbon (particularly graphene) and/or boron nitride. In this case, these values are perfectly suited to the mechanical requirements where Bortz et al. [92] found benefits in terms of fracture toughness with the addition of 0.5 and 1.0 wt.% of carbon nanofibers (CNFs) of around 66% and 78%, respectively, compared to neat resin, while, in terms of fatigue life, these values were around 180% and 365%, respectively, for a stress level of 20 MPa.

TABLE 1 | Summary of the benefits achieved by incorporating different types of fillers to enhance the thermal conductivity.

Authors	Composites	Filler	Percentages	Highlights
Wang et al. [40]	Polyacrylate	Long CuNWs	From 0 to 0.9 vol.%	Compared to the neat composite, an improvement of 1350% in thermal conductivity was obtained with 0.9 vol.%.
		Short CuNWs	From 0 to 1.5 vol.%	Compared to the neat composite, an improvement of 350% in thermal conductivity was achieved with 1.5 vol.%.
		AgNWs	From 0 to 1.1 vol.%	Compared to the neat composite, an improvement of 650% was obtained with 1.1 vol.%.
Balachander et al. [41]	Polydimethylsiloxane	Gold nanowires	From 0 to 3 vol.%	Compared to the neat composite, an increase of about 30 times was obtained.
Yu et al. [42]	CF/epoxy	Copper spheres	Volume fractions were controlled by varying the width of the unit cell.	Composites periodically filled with copper spheres and coated with aluminum foils present thermal conductivities through-thickness of 0.6 to 7.6 ± 0.6 W/mK, i.e., improvements of 12 times compared to the unmodified ones.
Hu et al. [43]	Poly (vinylidene fluoride)	hBN and MWCNTs-SiO_2	From 0 to 30 wt.%	Compared to the neat composite, 25 wt.% of hBN/MWCNTs-SiO2 provided improvements of about 586% in thermal conductivity and 25% in tensile strength due to the 3D networks obtained through the synergy of the fillers.
Bozlar et al. [49]	Al_2O_3-epoxy	MWCNTs	From 0 to 0.4 wt.%	By adding just 0.15 wt.% of MWCNTs, they obtained thermal conductivity values around 1.3 times higher.
Yu et al. [50]	Epoxy	SWCNTs + GNPs	2.5 wt.% + 7.5 wt.%	The thermal conductivity increased 5-fold compared to the neat resin, and the fillers' hybridization showed a strong synergistic effect with results superior to those obtained with single fillers.
Teng et al. [51]	Epoxy	BN flakes + MWCNTs	30 vol.% + 1 vol.%	The synergistic effect of the hybrid filler increased the thermal conductivity by around 743%, significantly more than the advantage of using single fillers.
Im et al. [52]	GO-epoxy	MWCNTs	0.36 wt.%	Hybridization increased thermal conductivity by 140% due to the 3D network structures created and the consequent synergistic effect on thermal transport properties.
TabkhPaz et al. [53]	Polystyrene (PS)	hBN/and CNT	From 0.3 to 13.15 vol.%	For hybrid composites with 3.1 vol.% CNT/hBN (1.55 vol.% each), the increase in thermal conductivity was 290%, while for the same filler content, it was 170% and 250% for single CNT and hBN fillers, respectively.

(Continues)

TABLE 1 | (Continued)

Authors	Composites	Filler	Percentages	Highlights
Yu et al. [54]	Polycarbonate (PC)	GNP and MWCNT	From 0 to 20.0 wt.%	The improvements in thermal conductivity of the hybrid composites with 18 wt.% GNPs and 2 wt.% MWCNTs were 23% and 479% compared to those of the composites with 20 wt.% GNPs and the neat polymer, respectively. The synergistic effect was produced by the formation of an efficient 3D thermally conductive network among the incorporated nanocarbon fillers.

Zhou et al. [93] observed that increasing the CNFs content up to 2 wt.% in an epoxy matrix nanocomposite increases its fatigue life, reaching one order of magnitude for the tensile stress of 35.75 MPa and two orders of magnitude for 42.5 MPa. The fatigue crack propagation response of fullerene–epoxy nanocomposites analyzed by Rafiee et al. [94] showed that the Paris law constants (C and m) decreased from 0.8308 and 8.262 for the neat resin to 0.0266 and 6.8497 for the nanocomposites reinforced with 1 wt.% of fullerene. Zhang et al. [95] studied the effects of MWCNTs dimensions (length and diameter) on the fatigue behavior of epoxy matrix nanocomposites and observed a significant improvement when the length is kept constant (10–20 μm) and the diameter decreases from 50–70 to 5–8 nm, or when the diameter is kept constant (10–20 nm) and the length increases from 1–2 to 10–20 μm. In this context, according to Figure 10, the results were optimized for a diameter of 5–8 nm and a length of 10–20 μm with a fatigue crack growth rate around 10 times lower than that observed for the neat epoxy. Therefore, higher aspect ratios are favorable to more efficient load transfer and higher toughness [96].

In this study, authors also evaluated the benefits of the surface treatment and, for this purpose, subjected the MWCNTs (as they were received) to a plasma polymerization in order to coat them with an ultra-thin layer of poly (methyl methacrylate) (PMMA). An average thickness of around 2–3 nm was obtained by adjusting the power of the plasma generator and deposition time. Therefore, for a content of 0.25 wt.% of MWCNTs and for the lowest values of ΔK (see Figure 11), the crack growth rate of the nanocomposites coated with PMMA was around 4 times lower than that observed for untreated nanocomposites and 20 times lower than that of neat epoxy [95]. The authors observed that the decrease in growth rate is related to the bridges created by the MWCNTs between the two faces of the crack, which dissipates energy through the frictional pull-out of the nanotubes from the epoxy matrix during propagation. However, when MWCNTs were coated with PMMA, their adhesion to the matrix increased, as did their dispersion in the polymer, which explains the lower crack growth rate observed compared to the other nanocomposites. However, it should be noted that the literature refers to the

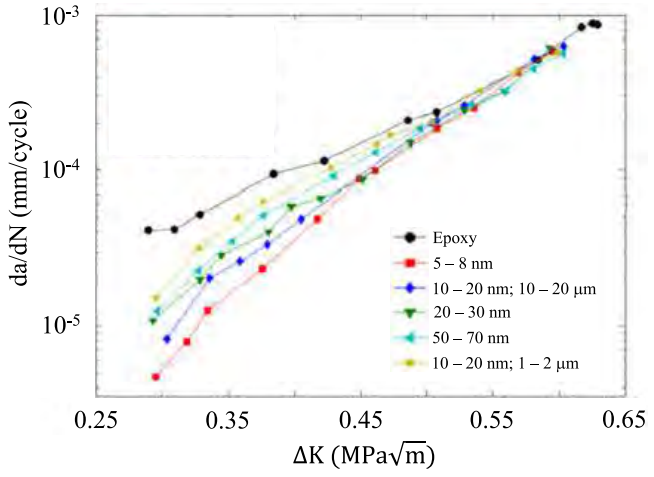

FIGURE 10 | Effects of the MWCNTs dimensions on the fatigue crack growth rate versus ΔK curves (adapted from [95]). [Colour figure can be viewed at wileyonlinelibrary.com]

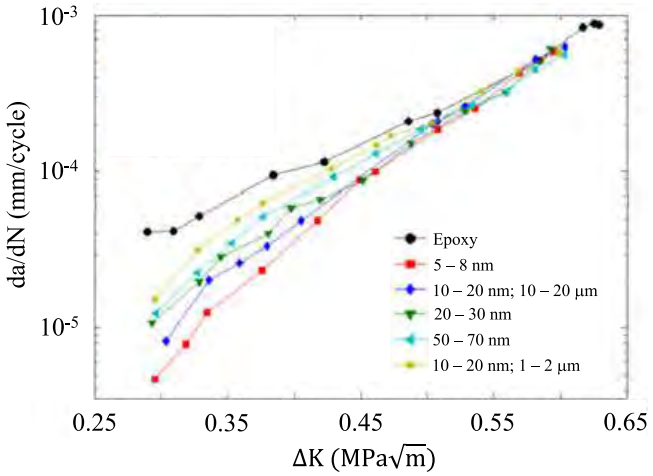

FIGURE 11 | Effect of MWCNTs coating on the fatigue crack growth rate versus ΔK curves (adapted from [95]). [Colour figure can be viewed at wileyonlinelibrary.com]

existence of an ideal amount of coupling agent so as not to affect thermal conductivity [15].

Bortz et al. [97] studied the matrix-dominated fatigue response of a composite reinforced with carbon fibers ($[\pm 45]_6$) and observed that only for 1 wt.% of CNFs did the average fatigue life increase by between 150% and 670% for fully compressive, tensile and tensile-dominated loads. Fenner and Daniel [98] investigated a carbon fabric/epoxy composite with 0.5 wt.% of MWCNTs and, compared to the neat matrix, authors found improvements of around 20% in the interlaminar shear strength, 180% in terms of fracture toughness, one order of magnitude in the shear fatigue life and a factor of 2 for the fatigue crack growth rate. According to the authors, these improvements resulted from a combination of energy-absorbing mechanisms of the nano-reinforcements (i.e. frictional pull-out of the nanotubes from the epoxy matrix as reported in [95]) and changes in the morphology of the crack surface. On the other hand, Böger et al. [99] analyzed the fatigue response of glass fiber-reinforced epoxy laminates and observed that just 0.3 wt.% of MWCNTs led to benefits of one order of magnitude in the fatigue life compared to the unmodified composite ($R = 0.1$), but these benefits were even higher for $R = -1$, especially for the high cycle fatigue regime. In the study carried out by Grimmer and Dharan [100], they observed that adding just 1 wt.% of CNTs to a glass fiber-epoxy composite improved its high-cycle fatigue strength by around 60% to 250%, depending on the loading condition. Moreover, the hysteresis loops evidenced a decrease in their area compared to the composite with neat resin. Also in this study, the increase in fatigue life was explained by energy-absorbing mechanisms (CNTs pulled out of the matrix or simply fractured).

Therefore, this discussion demonstrates clearly that adding small fractions of carbon-based nanofillers to neat resins or fiber-reinforced resins can result in a significant increase in their fatigue life and, consequently, make these materials more suitable for applications involving very high cycle fatigue regimes. These values are usually between 0.25 wt.% and 1.0 wt.%, although the literature also mentions benefits for higher contents, between 3 wt.% and 20 wt.%, but involving resins with certain specificities (such as viscosity, and different interfacial adhesion and physical interactions [101]) [102]. In addition to improvements in mechanical properties, the literature also mentions benefits in terms of thermal conductivity with these nano-reinforcements, which facilitates heat dissipation within the composite [103–105]. According to Berber et al. [106], for example, the thermal conductivity of carbon nanotubes is around 6600 W/(m × K) at room temperature, a value comparable to that of a hypothetical isolated graphene monolayer or graphite, but which depends on the temperature. However, this value can vary significantly because it depends on its structure, form, and method of synthesis [107]. In terms of graphene, its thermal conductivity at room temperature can vary between 2000 and 6000 W/(m × K), but with a perfect structure it is over 5000 W/(m × K), among the highest thermal conductivity of all known materials [108, 109]. In this case, these values are in line with those reported by Lokanathan et al [39], for filler fractions of less than 10 vol.%, and are ideal for obtaining composites with extremely high thermal conductivities and significantly improved mechanical properties (especially for obtaining long fatigue lives).

However, these benefits can be improved by taking advantage of the synergistic effect, which consists of using different fillers, and with different sizes and/or dimensions, to establish long thermal conductive paths with relatively low filler content [109]. For example, according to Yu et al [50], the synergistic effects obtained by replacing the point contacts between SWCNTs/SWCNTs or GNPs/GNPs with linear contacts obtained between CNT and GNPs improved the *TC* from 0.85 W/(m × K) of composites reinforced with SWCNTs and 1.49 W/(m × K) with GNPs to 1.75 W/(m × K) with hybridized fillers in a 3:1 ratio (GNPs:CNT). Therefore, these synergistic effects of combining graphene with other highly heat-conducting filler materials prove to be a very efficient strategy for dissipating heat and, at the same time, improving the dispersion of graphene into polymeric matrices. In this context, the large surface area of the graphene platelets helps the dispersion of the CNT, and the CNT decreases the formation of large-size stacked GNPs sheets and the π-π stacking in GNPs [110–112]. Furthermore, these benefits extend to the mechanical performance of the composites and, in particular, to fatigue strength. Shokrieh et al. [113], for example, found that composites reinforced with GNPs and CNFs present, compared to those with neat resin, improvements in fatigue life by 24 and 27.4 times, respectively, but when the fillers were hybridized in a 1:1 ratio the benefits reached values of around 37.2 times. Li et al. [114] also observed that hybridization is preferable to composites reinforced with only single nanoparticles, because it promotes longer fatigue lives. A similar conclusion was found by Papageorgiou et al. [115] when they hybridized GNPs with short carbon fibers to reinforce a PEEK matrix composite.

In this context, adding fillers not only enhances the thermal conductivity but also improves the mechanical properties of the composite. The synergistic benefits are more pronounced in composites reinforced with high thermally conductive hybrid fillers, where combining different types, such as CNFs with GNPs, improves the dispersion and contact networks among the polymer chains and reinforcement. This hybridization reduces filler agglomeration, and forms interconnected thermal conduction pathways, allowing for efficient heat transfer, and

thereby reducing the localized heating by less mismatches in the coefficient of thermal expansion (CTE) between the fibers and the adjacent polymer matrix [14]. This desirably minimizes the heat storage rate inside the fatigue-loaded composite specimen, maintaining a mechanically driven fatigue process. Additionally, the nanofillers contribute to improving the stiffness and toughness of the composite, delaying crack initiation and propagation, which are fundamental to the fatigue life of composites within the VHCF regime. Therefore, the combined effects of improved thermal management and mechanical properties lead to superior fatigue performance by mitigating both thermal and mechanical degradation, thereby prolonging the fatigue life of the tested composite.

Based on this discussion, which has been duly consolidated by the literature, it can be concluded that, when the design requirements do not allow the selection of the most suitable composite material for a very specific purpose, the use of nanofillers is a very favorable option. In this case, they not only allow the dissipation of the self-heating in the composite, but also maximize the mechanical properties and, in particular, the fatigue strength (where polymers generally have a weak response). This can be done inclusively with very low filler contents, as long as they are carbon-based and well dispersed in the matrix. However, due to the demands for increasingly efficient decisions right from the design stage, traditional fatigue testing is proving to be a problem due to the long testing times and associated costs. To overcome this problem, more and more ultrasonic fatigue systems are appearing, reducing test times by around 100 times [55], but, for which, the methodology described above is insufficient to minimize the negative consequences of the self-heating phenomenon on the lifetime of tested composite specimens. Therefore, it is necessary to use external cooling systems to prevent thermal fatigue from being associated with the mechanical fatigue of the composite and, consequently, accelerating the emerging damage mechanisms [9, 10]. Table 2, for example, summarizes the cooling methodologies used in the VHCF.

A suitable cooling system should be selected based on the energy associated with self-heating and the energy generated by damage, information that is not widely available in the literature. For this purpose, Amraei et al. [117] developed a validated numerical model for simulating the self-heating effect in polymer-matrix composites (PMCs) by incorporating the oscillatory shear rheometry data. They highlighted the necessity of considering radiative heat flux as an environmental factor, particularly in scenarios involving high stress/strain loading, to determine the self-heating temperature response accurately using the proposed numerical model. They demonstrated that the temperature variation across the thickness in thin PMCs remains below 4 °C, which is negligible. This confirms that surface temperature measurements are sufficient for assessing the heat generation induced by friction and damage in the thin PMCs. Additionally, the numerical results facilitated the assessment of heat generation rate evolution across the fatigue cycles. In another study, Huang et al. [118] determined the heat generation rate per unit volume in a composite laminate both experimentally and numerically. Authors assumed that the heat generated during a fatigue test comes from internal friction, which does not cause any damage, and from irreversible changes such as delaminations, crack propagation, etc. In the first case, it comes from the viscoelastic behavior of the polymer and both the interfaces between adjacent layers of the laminate and the fiber/matrix, while the heat generated rate from damage only arises for stress levels above the fatigue limit (see Figure 12a).

Therefore, the heat generated rate depends on the stress level and increases with increasing stress applied (see Figure 12a). The other exception is the study carried out by Premanand et al. [67], but in this case in terms of the heat dissipation rate, with evolution in distinct phases as shown in Figure 12b. It is notorious that the heat dissipation rate increases linearly up to a temperature of around 50 °C and a very significant increase after 65 °C due to non-stationary self-heating. In this regime, in addition to heat dissipation caused by viscoelastic hysteresis, macro cracks and the appearance of new damage also occur. On the other hand, in the interval between 50 °C and 65 °C the heat dissipation rate varied around 1.5 MJ/($m^3 \times s$) due to the accumulation of damage around the critical self-heating temperature.

These results prove clearly that it is necessary to cool specimens when they are tested using ultrasonic fatigue systems. According to the studies available in the literature, the most common methodology is the pulse-pause technique and although there is a suggestion to adopt ratios of 1:20 for glass fiber-reinforced composites and 1:10 for carbon-reinforced composites, it is not unanimous among the various published studies. In this context, Premanand and Balle [13] studied the effect of different cyclic amplitudes (40 μm, 45 μm, and 50 μm) combined with different pause periods (1000 ms, 2000 ms, and 4000 ms) and concluded, based on Figure 13, that for a pause time of 4 s between pulses, the temperature increase was around 7 °C regardless of the cyclic amplitude. In this case, the tests met the failure criterion (10^8) because the pause time was sufficient to dissipate the energy generated during the ultrasonic pulse in the form of heat.

For the pause time of 2 s, the temperatures increased by 42.9%, 71.4%, and 185.7% for the cyclic amplitudes of 40, 45, and 50 μm, respectively, due to the greater amount of energy supplied to the specimen. In this case, only the 40 μm/2 s condition met the failure criterion (10^8), because in the others the failure occurred in 8×10^7 cycles (for 45 μm/2 s) and 7.1×10^7 cycles (for 50 μm/2 s) due to the resonance frequency of the ultrasonic system dropped below 19.5 kHz. This shows that, in the latter two cases, not all the energy generated was dissipated in the form of heat, but some of it contributed to triggering/accelerating the fatigue mechanisms. Finally, for a pause time of 1 s, three different behaviors are observed. For 40 μm, the temperature was around 17 °C until a fatigue life of 10^8 cycles was reached, while for 45 μm, the failure criterion was reached at around 8.4×10^7 for a temperature between 18–19 °C. Finally, for 50 μm, the non-stationary regime occurred, with the temperature gradually increasing to 26 °C and suddenly to 35 °C at the moment of final collapse (6.67×10^7 cycles). For all cyclic amplitudes (40, 45, and 50 μm) the energy stored in the form of heat is higher than for the other pause times (2 s and 4 s), denoting that most of the energy generated is dissipated through damage and not heat.

This comprehensive study carried out by the authors makes it clear that the pulse-pause technique can be used effectively to prevent excessive self-heating and, consequently, the thermal fatigue associated with mechanics. However, although the

TABLE 2 | Summary of cooling methodologies used in the VHCF.

Authors	Testing conditions	Composite	Frequency [Hz]	Highlights
Effect of the ambient temperature				
Charalambous et al. [56]	−50 °C, 20 °C, 50 °C, 80 °C	CF/epoxy	5	The delamination crack propagated two orders of magnitude faster at 80 °C compared to the room temperature.
Voudouris et al. [57]	25 °C, 50 °C, 65 °C, 75 °C	GF/epoxy	395	Higher ambient temperatures decreased fatigue life by intensifying the competition between mechanical and thermal effects.
External cooling systems				
Cui et al. [1]	Compressed air cooling.	CF/epoxy	20,000	The authors observed that compressed air cooling is not efficient, not even when combined with intermittent ultrasonic loading, because the temperature increases to undesirable values. Therefore, to absorb more heat and cool the compressed air, they proposed a cooling system based on liquid nitrogen vaporization. In this case, temperatures do not exceed 40 °C.
Katunin and Wachla [12]	Without cooling and cooled by airflow at room temperature at 5.5 m/s and 1.5 m/s.	GF/epoxy	30	The presence of airflow at 5.5 m/s almost doubled the fatigue life compared to that obtained without cooling.
Bartelt et al. [59]	The test rig was housed in an air-conditioned chamber at 20 ± 1.5 °C and two fans for cooling the specimens were used.	GF/epoxy	20 to 80	The mean surface temperature of the specimens was kept below 25 °C.
Adams and Horst [60, 61]	The test rig was housed in an air-conditioned chamber at 20 ± 1.5 °C and additional airflow cooling at 20 °C for the highest load levels.	GF/epoxy	25 to 80	Specimen heating was negligible for cross-ply laminates but, for high-load testing of angle-ply laminates, additional airflow cooling was required because the temperature reached about half the T_g due to inner friction surfaces and higher bending strain.
Apinis [62]	A water jet cooling system and a thin layer of wax were used to preserve the structural integrity of the specimen against moisture.	GF/epoxy CF/epoxy	400	Due to the high rate of thermal heat generated on the surface of the specimen, it was necessary to use a cooling element with a higher specific heat than air.
Pulse/pause sequences				
Backe et al. [4]	Sequences of t = 200 ms with a cooling time of t = 2000 ms.	CF/PPS	20,000	The temperature increased by only 5 °C in the undamaged samples, but when damage appeared (delaminations between layers and transversal cracks) this value increased to 45 °C.

(Continues)

TABLE 2 | (Continued)

Authors	Testing conditions	Composite	Frequency [Hz]	Highlights
Premanand and Balle [68]	Sequences of t = 200 ms with a cooling time of t = 2000 ms.	CF/PEKK	20,200	Temperature was always below the T_g of the material, including at the interface between specimen and booster. The tests were carried out under uniaxial loading conditions and the specimen bonded to the booster.
Pulse/pause sequences with external cooling systems				
Flore et al. [2]	Sequences of t = 100 ms with a cooling time of t = 2000 ms and dry pressurized air cooling.	GF/epoxy	20,000	Temperatures below 25 °C have been reached, but the effective frequency drops to just 1 kHz.
Premanand and Balle [8]	Sequences of t = 200 ms with a cooling time of t = 600 ms and t = 100 ms with a cooling time of t = 2000 ms for tests under uniaxial and bending loading conditions, respectively, and compressed air cooling.	CF/PEKK	20,200	Stationary self-heating temperature below 10 °C and reached after 120 s for all cyclic amplitudes in tests under uniaxial loading conditions, while for bending loads this value was reached after 180 s.
Premanand et al. [10]	Sequences of t = 250 ms with a cooling time of t = 1500 ms and compressed air cooling.	CF/PEKK	20,200	To have a more efficient system than those that use conventional air cooling, the authors used two nozzles to blow compressed air onto the surface of the specimen.
Premanand and Balle [13]	Different cyclic amplitudes (40 μm, 45 μm, and 50 μm) and pause periods (1000 ms, 2000 ms, and 4000 ms) were considered.	CF/PEKK	20,200	The authors concluded that the self-heating temperature depends on the cyclic amplitude and interval length between pulses, and it is not possible to generalize the results because they depend on the heat dissipation of the composite (due to the type of fibers and their combination), the glass transition temperature of the polymer, and the fatigue damage mechanisms.
Backe et al. [63]	Pulse/pause sequences and compressed air cooling.	CF/PPS	20,000	The authors only report pulse and pause sequences to keep the specimens well below the T_g of the material (≈90 °C), but without quantifying the values used.
Hosoi et al. [64]	Sequences of t = 200 ms with a cooling time of t = 2000 ms, and air cooling.	CF/epoxy	20,000	The stationary self-heating temperature was always below 20 °C for all cyclic amplitudes, which was well below the T_g of the material.
Miyakoshi et al. [65]	Sequences of t = 200 ms with a cooling time of t = 2000 ms and dry compressed air cooling.	CF/epoxy	20,000	The maximum temperature was below the T_g of the material, but the values depended on the material used in the metal tab that connects the sample to the horn end of the testing machine. The tests were carried out under uniaxial loading conditions.

(Continues)

TABLE 2 | (Continued)

Authors	Testing conditions	Composite	Frequency [Hz]	Highlights
Lee et al. [66]	Sequences of t = 300 ms with a cooling time of t = 3000 ms and air cooling.	GF/PA66	20,000	No reference was made to the temperature increase observed in this study. However, the authors used a Peltier ring cooler for higher efficiency.
Weibel et al. [69, 70]	Pulse/pause sequences and compressed air cooling.	CF/epoxy CF/PPS	20,000	A pulse-pause ratio of 1:20 was used (without specifying the respective values), which corresponded to an effective frequency of ~1 kHz. Self-heating due to increased internal friction between crack surfaces led to a temperature increase of up to 50% of T_g.
Balle et al. [71]	Pulse/pause sequences and dry compressed air cooling.	CF/epoxy	20,000	Although no values were specified, the pulse-pause ratio of 1:20 used corresponded to an effective frequency of ~1 kHz and a temperature increase occurred due to internal friction between crack surfaces.
Wang et al. [72]	Cryogenic nitrogen blown over the surface of the specimen and pulse-pause sequences	Sandwiches	20,000	No temperatures higher than 40 °C were observed.
Amraei et al. [116]	Natural air cooling was used for the low-frequency tests and pulse-pause sequence with forced air cooling for the ultrasonic tests. Pulse-pause ratio of 1:6 (pulse-pause sequences of 50 ms and 300 ms for IATs, and 250 ms and 1500 ms for CATs) was used.	CF/PEKK	50 & 20,200	For IATs the self-heating temperature did not exceed 30 °C for 50 Hz and 52 °C for 20.2 kHz, but for CATs it was below 110 °C, values lower than the T_g of the composite.
Effect of nanoparticles				
Ding and Cheng [3]	Silica nanoparticles (20 nm).	CF/epoxy	20,000	The authors obtained significant increases in the fatigue strength of carbon/epoxy laminates when the matrix was reinforced by silica nanoparticles. However, they do not report any effect of the nanoparticles on temperature or cooling.

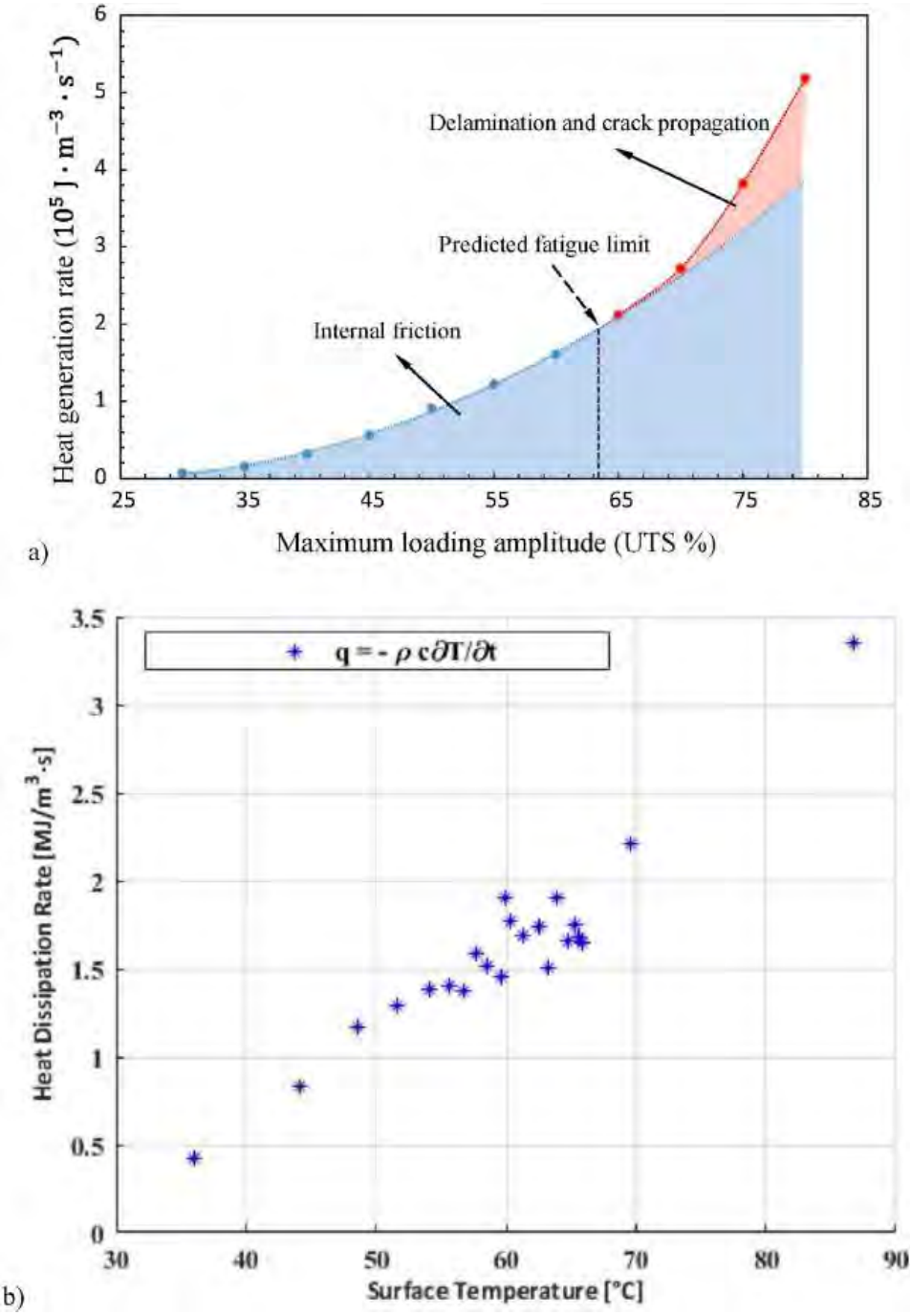

FIGURE 12 | a) Heat generation rates for different loading amplitudes [118]: b) Heat dissipation rates for different surface temperatures [67]. [Colour figure can be viewed at wileyonlinelibrary.com]

heating of the specimen depends on the cyclic amplitude and interval length between pulses, there are no values that can be generalized for materials of the same family, because the pause time depends on the heat dissipation of the composite, glass transition temperature of the composite, and the damage mechanisms involved in the fatigue process [13]. In this case, given the specific nature of each composite, it is suggested that preliminary tests be carried out to determine the interval length between pulses.

Nevertheless, despite the effectiveness of this technique, it cannot be ignored that the long pauses between pulses result in longer tests due to the lower effective frequencies that are used. Therefore, a balance must be established between the pause time adopted and an adequate and effective cooling system. The cheapest system reported in the literature is dry compressed air, where some authors even suggest that it can be directed through nozzles to the regions of the specimen where damage is most likely to occur. In the case of more demanding situations, for example, when the thermal energy generated rate is greater than 5 kW [14], as reported in the study carried out by Cui [1], there are also recommendations to use cooling systems that involve water instead of air, due to its high thermal capacity and low cost. Although it has not yet been used, Amraei and Katunin

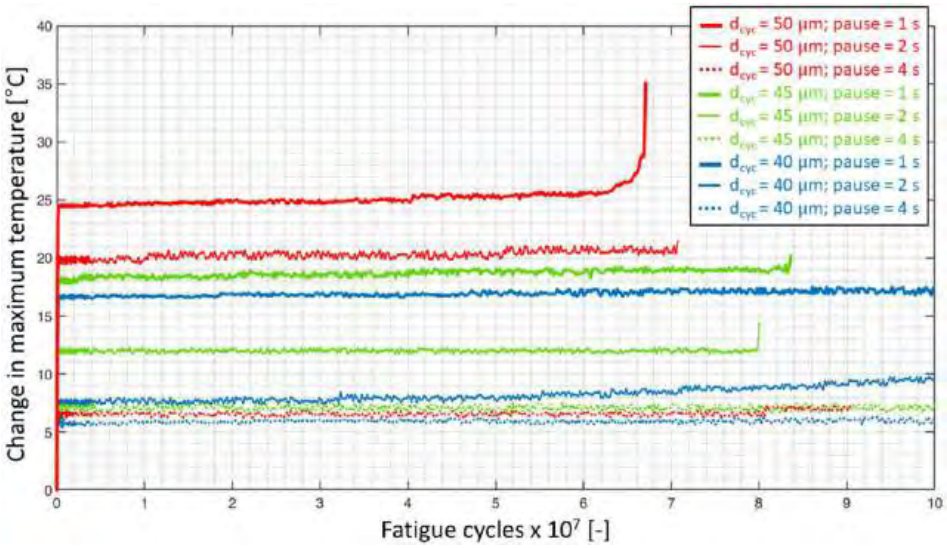

FIGURE 13 | Specimen surface temperature versus fatigue life [13]. [Colour figure can be viewed at wileyonlinelibrary.com]

[14] even suggested using water-based nanofluids because the nanoparticles used significantly increase the fluid's thermal conductivity. In this context, Apinis [62] used a water jet cooling system but emphasized the need to preserve the structural integrity of the specimen against humidity. For this purpose, the specimen was covered with a thin layer of wax, but there is no evidence that this can affect the heat dissipation of the specimen. A vaporization system is also indicated by Amraei and Katunin [14], but there is no evidence that this methodology cannot affect the structural integrity of the specimen. Finally, the literature also suggests implementing nitrogen-based cooling systems but injecting the gas at regular intervals to prevent the matrix from becoming brittle [14]. However, there are no studies on how long these cooling intervals should be so that the polymer does not become brittle.

In this context, it is suggested that further studies be carried out in the future on these methodologies to eliminate these gaps, because, given the current knowledge, the use of dry compressed air systems remains the safest.

5 | Conclusions

In this study, a critical analysis of cooling approaches of composite structures being tested in the fatigue regime has been provided. The problem originates from the appearance of the self-heating effect, which reveals a significant influence on tested composite structures, accelerating the fatigue process. This causes structural and mechanochemical changes in a tested material and leads to a premature failure of a tested structure. The problem of the appearance of the self-heating effect is starting to become critical when carrying out accelerated VHCF tests. This is due to the very high loading frequencies that govern the generation of heat during loading.

Two general approaches for limiting the self-heating effect were considered: modification of a material system to obtain better thermal conductivity, and thus, better heat transfer during the appearance of the self-heating effect; and surface cooling of a tested structure for minimizing the overall self-heating effect. In the first case, the analysis of the possibility of adding various fillers to composites was performed taking into account not only the thermal conductivity performance but also the benefits of incorporating additional fillers in terms of mechanical and thermal performance of a resulting composite. This approach underlines the benefits of hybridizing reinforcing composite materials to achieve this goal. Furthermore, the limitations defined, and the suggestions related to the fillers' content in composites make it possible to evaluate the benefits and multifunctionality of such solutions in the framework of practical applications, especially modifications of systems involving traditional materials for composite components. Nevertheless, reducing the self-heating effect through the modifications of the material systems has limited performance in light of the amount of thermal energy generated during fatigue loading at higher frequency levels. Therefore, this approach is targeting the applications where the external cooling cannot be applied due to operational reasons.

The second approach discussed in this paper is based on the forced cooling of a composite structure surface using various media and technologies. In this case, the specific limitations addressing the physical performance of external cooling systems and interval loading demonstrate the possibility of increasing fatigue life by limiting the influence of the self-heating effect, which has been confirmed by numerous experimental studies performed previously.

The provided critical analysis on the possibilities of reducing the influence of the self-heating effect on the fatigue life of composite structures working under fatigue loading, including accelerated fatigue regimes, clarifies the practical possibilities of implementing various cooling techniques with their physical limitations. This makes it possible to implement them both in laboratory conditions as well as in numerous applications where the appearance of the self-heating belongs to the typical working conditions of composite components.

Acknowledgments

The first author would like to acknowledge the grant BPN/ULM/2023/1/00119/U/00001 awarded to him by NAWA - Narodowa Agencja Wymiany Akademickiej. This research was also sponsored by national funds through FCT – Fundação para a Ciência e a Tecnologia, under the project UIDB/00285/2020 and LA/P/0112/2020. The second author would like to acknowledge the COST Action HISTRATE (CA21155) for the motivation of this study.

Data Availability Statement

Data sharing is not applicable to this article as no new data were created or analyzed in this study.

References

1. W. Cui, X. Chen, C. Chen, L. Cheng, J. Ding, and H. Zhang, "Very High Cycle Fatigue (VHCF) Characteristics of Carbon fiber Reinforced Plastics (CFRP) Under Ultrasonic Loading," *Materials* 13 (2020): 908.

2. D. Flore, K. Wegener, H. Mayer, U. Karr, and C. C. Oetting, "Investigation of the High and Very High Cycle Fatigue Behaviour of Continuous Fibre Reinforced Plastics by Conventional and Ultrasonic Fatigue Testing," *Composites Science and Technology* 141 (2017): 130–136.

3. J. Ding and L. Cheng, "Ultra-High Three-Point Bending Fatigue Performance of Nano-Silica-Reinforced CFRP," *International Journal of Fatigue* 145 (2021): 106085.

4. D. Backe, F. Balle, and D. Eifler, "Fatigue Testing of CFRP in the Very High Cycle Fatigue (VHCF) Regime at Ultrasonic Frequencies," *Composites Science and Technology* 106 (2015): 93–99.

5. D. Backe and F. Balle, "Ultrasonic Fatigue and Microstructural Characterization of Carbon fiber Fabric Reinforced Polyphenylene Sulfide in the Very High Cycle Fatigue Regime," *Composites Science and Technology* 126 (2016): 115–121.

6. P. Shabani, F. Taheri-Behrooz, S. S. Samareh-Mousavi, and M. M. Shokrieh, "Very High Cycle and Gigacycle Fatigue of fiber-Reinforced Composites: A Review on Experimental Approaches and Fatigue Damage Mechanisms," *Progress in Materials Science* 118 (2021): 100762.

7. L. Ding, X. Cheng, C. Chen, and K. Chen, "Liu, a Review on Ultra-High Cycle Fatigue of CFRP," *Composite Structures* 256 (2021): 113058.

8. A. Premanand and F. Balle, "Stress and Strain Calculation Method for Orthotropic Polymer Composites Under Axial and Bending Ultrasonic Fatigue Loads," *Ultrasonics* 135 (2023): 107130.

9. A. Katunin, A. Wronkowicz, M. Bilewicz, and D. Wachla, "Criticality of Self-Heating in Degradation Processes of Polymeric Composites Subjected to Cyclic Loading: A Multiphysical Approach," *Archives of Civil and Mechanical Engineering* 17 (2017): 806–815.

10. A. Premanand, M. Rienks, and F. Balle, "Damage Assessment During Ultrasonic Fatigue Testing of a CF-PEKK Composite Using Self-Heating Phenomenon," *International Journal of Fatigue* 180 (2024): 108084.

11. A. Katunin, "Domination of Self-Heating Effect During Fatigue of Polymeric Composites," *Procedia Structural Integrity* 5 (2017): 93–98.

12. A. Katunin and D. Wachla, "Minimizing Self-Heating Based Fatigue Degradation in Polymeric Composites by air Cooling," *Procedia Structural Integrity* 18 (2019): 20–27.

13. A. Premanand and F. Balle, "Influence of Pulse-Pause Sequences on the Self-Heating Behavior in Continuous Carbon fiber-Reinforced Composites Under Ultrasonic Cyclic Three-Point Bending Loads," *Materials* 15 (2022): 3527.

14. J. Amraei and A. Katunin, "Recent Advances in Limiting Fatigue Damage Accumulation Induced by Self-Heating in Polymer–Matrix Composites," *Polymers* 14 (2022): 5384.

15. S. N. Leung, "Thermally Conductive Polymer Composites and Nanocomposites: Processing Structure-Property Relationships," *Composites Part B: Engineering* 150 (2018): 78–92.

16. V. Cecen, I. H. Tavman, M. Kok, and Y. Aydogdu, "Epoxy- and Polyester-Based Composites Reinforced With Glass, Carbon and Aramid Fabrics: Measurement of Heat Capacity and Thermal Conductivity of Composites by Differential Scanning Calorimetry," *Polymer Composites* 30 (2009): 1299–1311.

17. D. P. H. Hasselman and L. F. Johnson, "Effective Thermal Conductivity of Composites With Interfacial Thermal Barrier Resistance," *Journal of Composite Materials* 21 (1987): 508–515.

18. H. Wu and L. T. Drzal, "High Thermally Conductive Graphite Nanoplatelets/Polyetherimide Composite by Precoating: Effect of Percolation and Particle Size," *Polymer Composites* 34 (2013): 2148–2153.

19. S. Kemaloglu, G. Ozkoc, and A. Aytac, "Thermally Conductive Boron Nitride/SEBS/EVA Ternary Composites: "Processing and Characterization,"" *Polymer Composites* 31 (2010): 1398–1408.

20. J. F. Fu, L. Y. Shi, D. S. Zhang, Q. D. Zhong, and Y. Chen, "Effect of Nanoparticles on the Performance of Thermally Conductive Epoxy Adhesives," *Polymer Engineering and Science* 50 (2010): 1809–1819.

21. O. M. Khan, S. N. Leung, E. Chan, H. E. Naguib, F. Dawson, and V. Adinkrah, "Effects of Microsized and Nanosized Carbon Fillers on the Thermal and Electrical Properties of Polyphenylene Sulfide Based Composites," *Polymer Engineering and Science* 53 (2013): 2398–2406.

22. Y. Yang, D. Li, G. Si, Q. Liu, and Y. Chen, "Improved Thermal and Mechanical Properties of Carbon fiber Filled Polyamide 46 Composites," *Journal of Polymer Engineering* 37 (2017): 345–353.

23. Y.-M. Chen and J.-M. Ting, "Ultra High Thermal Conductivity Polymer Composites," *Carbon* 40 (2002): 359–362.

24. S. Li, T. Yang, H. Zou, M. Liang, and Y. Chen, "Enhancement in Thermal Conductivity and Mechanical Properties via Large-Scale Fabrication of Boron Nitride Nanosheets," *High Performance Polymers* 29 (2017): 315–327.

25. R. F. Hill and P. H. Supancic, "Thermal Conductivity of Platelet-Filled Polymer Composites," *Journal of the American Ceramic Society* 85 (2002): 851–857.

26. S. N. Leung, O. M. Khan, E. Chan, et al., "Analytical Modelling and Characterization of Heat Transfer in Thermally Conductive Polymer Composites Filled With Spherical Particulates," *Composites Part B: Engineering* 45 (2013): 43–49.

27. E.-C. Cho, J.-H. Huang, C.-P. Li, et al., "Graphene-Based Thermoplastic Composites and Their Application for LED Thermal Management," *Carbon* 102 (2016): 66–73.

28. H. Zhu, Y. Li, Z. Fang, et al., "Highly Thermally Conductive Papers With Percolative Layered Boron Nitride Nanosheets," *ACS Nano* 8 (2014): 3606–3613.

29. H.-J. Hong, S. M. Kwan, D. S. Lee, et al., "Highly Flexible and Stretchable Thermally Conductive Composite Film by Polyurethane Supported 3D Networks of Boron Nitride," *Composites Science and Technology* 152 (2017): 94–100.

30. X. Wang and P. Wu, "Highly Thermally Conductive Fluorinated Graphene Films with Superior Electrical Insulation and Mechanical Flexibility," *ACS Applied Materials & Interfaces* 11 (2019): 21946–21954.

31. C. Yu, Q. Zhang, J. Zhang, et al., "One-Step in Situ Ball Milling Synthesis of Polymer-Functionalized few-Layered Boron Nitride and Its Application in High Thermally Conductive Cellulose Composites," *ACS Applied Nano Materials* 1 (2018): 4875–4883.

32. K. Wu, J. Fang, J. Ma, et al., "Achieving a Collapsible, Strong, and Highly Thermally Conductive Film Based on Oriented Functionalized Boron Nitride Nanosheets and Cellulose Nanofiber," *ACS Applied Materials & Interfaces* 9 (2017): 30035–30045.

33. J. Wang, Y. Wu, Y. Xue, et al., "Super-Compatible Functional Boron Nitride Nanosheets/Polymer Films With Excellent Mechanical Properties and Ultra-High Thermal Conductivity for Thermal Management," *Journal of Materials Chemistry C* 6 (2018): 1363–1369.

34. Y.-F. Huang, Z.-G. Wang, H.-M. Yin, et al., "Highly Anisotropic, Thermally Conductive, and Mechanically Strong Polymer Composites With Nacre-Like Structure for Thermal Management Applications," *ACS Applied Nano Materials* 1 (2018): 3312–3320.

35. X. Zeng, J. Sun, Y. Yao, R. Sun, J.-B. Xu, and C.-P. Wong, "A Combination of Boron Nitride Nanotubes and Cellulose Nanofibers for the Preparation of a Nanocomposite With High Thermal Conductivity," *ACS Nano* 11 (2017): 5167–5178.

36. Z. Zhu, C. Li, E. Songfeng, et al., "Enhanced Thermal Conductivity of Polyurethane Composites via Engineering Small/Large Sizes Interconnected Boron Nitride Nanosheets," *Composites Science and Technology* 170 (2019): 93–100.

37. L. M. Guiney, N. D. Mansukhani, A. E. Jakus, S. G. Wallace, R. N. Shah, and M. C. Hersam, "Three-Dimensional Printing of Cytocompatible, Thermally Conductive Hexagonal Boron Nitride Nanocomposites," *Nano Letters* 18 (2018): 3488–3493.

38. J. Zhang, X. Wang, C. Yu, et al., "A Facile Method to Prepare Flexible Boron Nitride/Poly (Vinyl Alcohol) Composites With Enhanced Thermal Conductivity," *Composites Science and Technology* 149 (2017): 41–47.

39. M. Lokanathan, P. V. Acharya, A. Ouroua, S. M. Strank, R. E. Hebner, and V. Bahadur, "Review of Nanocomposite Dielectric Materials With High Thermal Conductivity," *Proceedings of the IEEE* 109 (2021): 1364–1397.

40. S. Wang, Y. Cheng, R. Wang, J. Sun, and L. Gao, "Highly Thermal Conductive Copper Nanowire Composites With Ultralow Loading: Toward Applications as Thermal Interface Materials," *ACS Applied Materials & Interfaces* 6 (2014): 6481–6486.

41. N. Balachander, I. Seshadri, R. J. Mehta, et al., "Nanowire-Filled Polymer Composites With Ultrahigh Thermal Conductivity," *Applied Physics Letters* 102 (2013): 093117.

42. G.-C. Yu, L.-Z. Wu, L.-J. Feng, and W. Yang, "Thermal and Mechanical Properties of Carbon fiber Polymer-Matrix Composites With a 3D Thermal Conductive Pathway," *Composite Structures* 149 (2016): 213–219.

43. B. Hu, H. Guo, Q. Wang, et al., "Enhanced Thermal Conductivity by Constructing 3D-Networks in Poly (Vinylidene Fluoride) Composites via Positively Charged Hexagonal Boron Nitride and Silica Coated Carbon Nanotubes," *Composites. Part A, Applied Science and Manufacturing* 137 (2020): 106038.

44. N. Wu, S. Che, H.-W. Li, C.-N. Wang, X.-J. Tian, and Y.-F. Li, "A Review of Three-Dimensional Graphene Networks for use in Thermally. Conductive Polymer Composites: Construction and Applications," *New Carbon Materials* 36 (2021): 911–926.

45. W. Yu, Y. Qi, Y. Zhou, L. Chen, H. Du, and H. Xie, "Synergistic Improvement of Thermal Transport Properties for Thermoplastic Composites Containing Mixed Alumina and Graphene Fillers," *Journal of Applied Polymer Science* 133 (2016): 43242.

46. S. Y. Pak, H. M. Kim, S. Y. Kim, and J. R. Youn, "Synergistic Improvement of Thermal Conductivity of Thermoplastic Composites With Mixed Boron Nitride and Multi-Walled Carbon Nanotube Fillers," *Carbon* 50 (2012): 4830–4838.

47. C.-C. Teng, C. M. Ma, K.-C. Chiou, and T.-M. Lee, "Synergetic Effect of Thermal Conductive Properties of Epoxy Composites Containing Functionalized Multi-Walled Carbon Nanotubes and Aluminum Nitride," *Composites Part B: Engineering* 43 (2012): 265–271.

48. K. Kim and J. Kim, "Exfoliated Boron Nitride Nanosheet/MWCNT Hybrid Composite for Thermal Conductive Material via Epoxy Wetting," *Composites Part B: Engineering* 140 (2018): 9–15.

49. M. Bozlar, D. He, J. Bai, Y. Chalopin, N. Mingo, and S. Volz, "Carbon Nanotube Microarchitectures for Enhanced Thermal Conduction at Ultralow Mass Fraction in Polymer Composites," *Advanced Materials* 22 (2010): 1654–1658.

50. A. Yu, P. Ramesh, X. Sun, E. Bekyarova, M. E. Itkis, and R. C. Haddon, "Enhanced Thermal Conductivity in a Hybrid Graphite Nanoplatelet–Carbon Nanotube Filler for Epoxy Composites," *Advanced Materials* 20 (2008): 4740–4744.

51. C.-C. Teng, C.-C. M. Ma, K.-C. Chiou, T.-M. Lee, and Y.-F. Shih, "Synergetic Effect of Hybrid Boron Nitride and Multi-Walled Carbon Nanotubes on the Thermal Conductivity of Epoxy Composites," *Materials Chemistry and Physics* 126 (2011): 722–728.

52. H. Im and J. Kim, "Thermal Conductivity of a Graphene Oxide–Carbon Nanotube Hybrid/Epoxy Composite," *Carbon* 50 (2012): 5429–5440.

53. M. TabkhPaz, S. Shajari, M. Mahmoodi, D.-Y. Park, H. Suresh, and S. S. Park, "Thermal Conductivity of Carbon Nanotube and Hexagonal Boron Nitride Polymer Composites," *Composites Part B: Engineering* 100 (2016): 19–30.

54. J. Yu, H. K. Choi, H. S. Kim, and S. Y. Kim, "Synergistic Effect of Hybrid Graphene Nanoplatelets and Multi-Walled Carbon Nanotube Fillers on the Thermal Conductivity of Polymer Composites and Theoretical Modeling of the Synergistic Effect," *Composites. Part A, Applied Science and Manufacturing* 88 (2016): 79–85.

55. S. Stanzl-Tschegg, "Very High Cycle Fatigue Measuring Techniques," *International Journal of Fatigue* 60 (2014): 2–17.

56. G. Charalambous, G. Allegri, and S. R. Hallett, "Temperature Effects on Mixed Mode I/II Delamination Under Quasi-Static and Fatigue Loading of a Carbon/Epoxy Composite," *Composites. Part A, Applied Science and Manufacturing* 77 (2015): 75–86.

57. G. Voudouris, D. Di Maio, and I. A. Sever, "Experimental Fatigue Behaviour of CFRP Composites Under Vibration and Thermal Loading," *International Journal of Fatigue* 140 (2020): 105791.

58. M. Bartkowiak, M. Kizak, W. Liebig, and K. Weidenmann, "Fatigue Behavior of Hybrid Continuous-Discontinuous fiber-Reinforced Sheet Molding Compound Composites Under Application-Related Loading Conditions," *Composites Part C: Open Access* 8 (2022): 100265.

59. M. Bartelt, P. Horst, and S. Heimbs, "Effects of an Enhanced Fibre–Matrix Adhesion on the Fatigue Behaviour of Composite Materials Under Very High Cycle Fatigue," *CEAS Aeronautical Journal* 14 (2023): 753–763.

60. T. J. Adam and P. Horst, "Very High Cycle Fatigue Testing and Behavior of GFRP Cross- and Angle-Ply Laminates," in *Fatigue of Materials at Very High Numbers of Loading Cycles*, ed. H. J. Christ (Wiesbaden: Springer Spektrum, 2018), 511–532.

61. T. J. Adam and P. Horst, "Fatigue Damage and Fatigue Limits of a GFRP Angle-Ply Laminate Tested Under Very High Cycle Fatigue Loading," *International Journal of Fatigue* 99 (2017): 202–214.

62. R. Apinis, "Accceleration of Fatigue Tests of Polymer Composite Materials by Using High-Frequency Loadings," *Mechanics of Composite Materials* 40 (2004): 107–118.

63. D. Backe, F. Balle, T. B. Helfen, et al., "Ultrasonic Fatigue Testing System Combined With Online Nondestructive Testing for Carbon Fiber Reinforced Composites," Suppl. Proc. Vol. 2: Materials Properties, Characterization, and Modeling, TMS 2012, Orlando, FL, USA, (2012): 855–863.

64. A. Hosoi, T. Suzuki, K. Kosugi, et al., "Very High-Cycle Fatigue Characteristics of Cross-Ply CFRP Laminates in Transverse Crack Initiation," in *ICAF 2019 – Structural Integrity in the age of Additive Manufacturing. ICAF 2019. Lecture Notes in Mechanical Engineering*, eds. A. Niepokolczycki and J. Komorowski (Cham: Springer, 2020), 838–846.

65. T. Miyakoshi, T. Atsumi, K. Kosugi, A. Hosoi, T. Tsuda, and H. Kawada, "Evaluation of Very High Cycle Fatigue Properties for Transverse Crack Initiation in Cross-Ply Carbon fiber-Reinforced Plastic Laminates," *Fatigue and Fracture of Engineering Materials and Structures* 45 (2022): 2403–2414.

66. C. S. Lee, H. J. Kim, A. Amanov, J. H. Choo, Y. K. Kim, and I. S. Cho, "Investigation on Very High Cycle Fatigue of PA66-GF30 GFRP Based on fiber Orientation," *Composites Science and Technology* 180 (2019): 94–100.

67. A. Premanand, T. Rogala, D. Wachla, et al., "Fatigue Strength Estimation of a CF/PEKK Composite Through Self-Heating Temperature Analysis Using Cyclic Bending Tests at 20 kHz," *Composites Science and Technology* 243 (2023): 110218.

68. A. Premanand and F. Balle, "Development of an Axial Loading System for Fatigue Testing of Textile-Composites at Ultrasonic Frequencies," *Materials Letters: X* 13 (2022): 100131.

69. D. Weibel, F. Balle, and D. Backe, "Ultrasonic Fatigue of CFRP - Experimental Principle, Damage Analysis and Very High Cycle Fatigue Properties," *Key Engineering Materials* 742 (2017): 621–628.

70. D. Weibel, T. Backe, and F. Balle, "Fatigue Properties and Damage of CF-PPS From High to Very High Cycles," In Proceedings of the 22nd International Conference on Composite Materials (ICCM22), Melbourne-Australia, August 11–16, 2019, paper 295, 2019.

71. F. Balle, D. Weibel, and D. Backe, "Fatigue Testing of Carbon Fibre Reinforced Epoxy Based Composites at Ultrasonic Frequencies and Damage Monitoring Under VHCF Loading," In Proceedings of the 7th International Conference on Very High Cycle Fatigue (VHCF7), Dresden-Germany, July 3–5, 2017, 14–21, 2017.

72. C. Wang, X. Chen, L. Cheng, and J. Ding, "High-Cycle and Very-High-Cycle Fatigue Properties of CFRP-Aramid Honeycomb Sandwich Structure in Three-Point Bending," *International Journal of Fatigue* 155 (2022): 106576.

73. M. Ferreira, J. D. Costa, and C. Capela, "Fracture Assessment of PMMA/Si Kitchen Sinks Made From Acrylic Casting Dispersion," *Theoretical and Applied Fracture Mechanics* 26 (1997): 105–116.

74. S. Sahu and L. J. Broutman, "Mechanical Properties of Particulate Composites," *Polymer Engineering and Science* 12 (1972): 91–100.

75. L. Nicolais, E. Drioli, and R. F. Landel, "Mechanical Behaviour and Permeability of ABS/Glass Bead Composites," *Polymer* 14 (1973): 21–26.

76. S. Ahmed and F. R. Jones, "A Review of Particulate Reinforcement Theories for Polymer Composites," *Journal of Materials Science* 25 (1990): 4933–4942.

77. J. D. Costa, J. M. Ferreira, and C. Capela, "Fatigue Behaviour of PMMA/Silica Acrylic Casting Dispersions," *Materials Science and Technology* 17 (2001): 1657–1663.

78. F. V. Antunes, J. M. Ferreira, J. D. Costa, and C. Capela, "Fatigue Life Predictions in Polymer Particle Composites," *International Journal of Fatigue* 24 (2002): 1095–1105.

79. A. Boonyapookana, K. Nagata, and Y. Mutoh, "Fatigue Crack Growth Behavior of Silica Particulate Reinforced Epoxy Resin Composite," *Composites Science and Technology* 71 (2011): 1124–1131.

80. H. R. Azimi, R. A. Pearson, and R. W. Hertzberg, "Fatigue of Rubber-Modified Epoxies: Effect of Particle Size and Volume Fraction," *Journal of Materials Science* 31 (1996): 3777–3789.

81. V. Verma and C. Sharma, "Fatigue Behavior of Epoxy Alumina Nanocomposite – Role of Particle Morphology," *Theoretical and Applied Fracture Mechanics* 110 (2020): 102807.

82. R. J. Kane, G. L. Converse, and R. K. Roeder, "Effects of the Reinforcement Morphology on the Fatigue Properties of Hydroxyapatite Reinforced Polymers," *Journal of the Mechanical Behavior of Biomedical Materials* 1 (2008): 261–268.

83. N. Chisholm, H. Mahfuz, V. K. Rangari, A. Ashfaq, and S. Jeelani, "Fabrication and Mechanical Characterization of Carbon/SiC-Epoxy Nanocomposites," *Composite Structures* 67 (2005): 115–124.

84. V. Verma, A. K. Pandey, and C. Sharma, "Fatigue Behavior of Particulate-Reinforced Polymer Composites: A Review," in *Advanced Materials and Manufacturing Processes*, (London: CRC Press, Taylor & Francis Group, 2021): 154–171.

85. X. Ma, Y. Zare, and K. Y. Rhee, "A two-Step Methodology to Study the Influence of Aggregation/Agglomeration of Nanoparticles on Young's Modulus of Polymer Nanocomposites," *Nanoscale Research Letters* 12 (2017): 621.

86. P. Santos, A. P. Silva, and P. N. B. Reis, "Effect of Carbon Nanofibers on the Viscoelastic Response of Epoxy Resins," *Polymers* 15 (2023): 821.

87. Y. Zare, "Study of Nanoparticles Aggregation/Agglomeration in Polymer Particulate Nanocomposites by Mechanical Properties," *Composites Part A: Applied Science and Manufacturing* 84 (2016): 158–164.

88. Y. Zare, "Modeling the Yield Strength of Polymer Nanocomposites Based Upon Nanoparticle Agglomeration and Polymer–Filler Interphase," *Journal of Colloid and Interface Science* 467 (2016): 165–169.

89. Y. Zare, K. Y. Rhee, and D. Hui, "Influences of Nanoparticles Aggregation/Agglomeration on the Interfacial/Interphase and Tensile Properties of Nanocomposites," *Composites: Part B* 122 (2017): 41–46.

90. D. K. Shukla, S. V. Kasisomayajula, and V. Parameswaran, "Epoxy Composites Using Functionalized Alumina Platelets as Reinforcements," *Composites Science and Technology* 68 (2008): 3055–3063.

91. S. Zhao, L. S. Schadler, H. Hillborg, and T. Auletta, "Improvements and Mechanisms of Fracture and Fatigue Properties of Well-Dispersed Alumina/Epoxy Nanocomposites," *Composites Science and Technology* 68 (2008): 2976–2982.

92. D. R. Bortz, C. Merino, and I. Martin-Gullon, "Carbon Nanofibers Enhance the Fracture Toughness and Fatigue Performance of a Structural Epoxy System," *Composites Science and Technology* 71 (2011): 31–38.

93. Y. Zhou, F. Pervin, and S. Jeelani, "Effect Vapor Grown Carbon Nanofiber on Thermal and Mechanical Properties of Epoxy," *Journal of Materials Science* 42 (2007): 7544–7553.

94. M. A. Rafiee, F. Yavari, J. Rafiee, and N. Koratkar, "Fullerene–Epoxy Nanocomposites-Enhanced Mechanical Properties at low Nanofiller Loading," *Journal of Nanoparticle Research* 13 (2011): 733–737.

95. W. Zhang, R. C. Picu, and N. Koratkar, "The Effect of Carbon Nanotube Dimensions and Dispersion on the Fatigue Behavior of Epoxy Nanocomposites," *Nanotechnology* 19 (2008): 285709.

96. I. Srivastava and N. Koratkar, "Fatigue and Fracture Toughness of Epoxy Nanocomposites," *JOM* 62 (2010): 50–57.

97. D. R. Bortz, C. Merino, and I. Martin-Gullon, "Augmented Fatigue Performance and Constant Life Diagrams of Hierarchical Carbon fiber/Nanofiber Epoxy Composites," *Composites Science and Technology* 72 (2012): 446–452.

98. J. S. Fenner and I. M. Daniel, "Hybrid Nanoreinforced Carbon/Epoxy Composites for Enhanced Damage Tolerance and Fatigue Life," *Composites. Part A, Applied Science and Manufacturing* 65 (2014): 47–56.

99. L. Böger, J. Sumfleth, H. Hedemann, and K. Schulte, "Improvement of Fatigue Life by Incorporation of Nanoparticles in Glass Fibre Reinforced Epoxy," *Composites Part A: Applied Science and Manufacturing* 41 (2010): 1419–1424.

100. C. S. Grimmer and C. K. H. Dharan, "High-Cycle Fatigue of Hybrid Carbon Nanotube/Glass fiber/Polymer Composites," *Journal of Materials Science* 43 (2008): 4487–4492.

101. P. S. P. Santos, A. Maceiras, S. Valvez, and P. N. B. Reis, "Mechanical Characterization of Different Epoxy Resins Enhanced With Carbon Nanofibers," *Frattura ed Integrità Strutturale* 15 (2021): 198–212.

102. P. Santos, A. P. Silva, and P. N. B. Reis, "The Effect of Carbon Nanofibers on the Mechanical Performance of Epoxy-Based Composites: A Review," *Polymers* 16, no. 15 (2024): 2152.

103. M. Kumar, P. Kumar, and S. S. Bhadauria, "Interlaminar Fracture Toughness and Fatigue Fracture of Continuous fiber-Reinforced Polymer Composites With Carbon-Based Nanoreinforcements: A Review," *Polymer-Plastics Technology and Materials* 59 (2020): 1041–1076.

104. N. G. Sahoo, H. K. F. Cheng, J. Cai, et al., "Improvement of Mechanical and Thermal Properties of Carbon Nanotube Composites Through Nanotube Functionalization and Processing Methods," *Materials Chemistry and Physics* 117 (2009): 313–320.

105. M. Moniruzzaman and K. I. Winey, "Polymer Nanocomposites Containing Carbon Nanotubes," *Macromolecules* 39 (2006): 5194–5205.

106. S. Berber, Y.-K. Kwon, and D. Tománek, "Unusually High Thermal Conductivity of Carbon Nanotubes," *Physical Review Letters* 84 (2000): 4613–4616.

107. B. Kumanek and D. Janas, "Thermal Conductivity of Carbon Nanotube Networks: A Review," *Journal of Materials Science* 54 (2019): 7397–7427.

108. A. Alofi and G. P. Srivastava, "Thermal Conductivity of Graphene and Graphite," *Physical Review B* 87 (2013): 115421.

109. X. Huang, C. Zhi, Y. Lin, et al., "Thermal Conductivity of Graphene-Based Polymer Nanocomposites," *Materials Science & Engineering R: Reports* 142 (2020): 100577.

110. L. Yue, G. Pircheraghi, S. A. Monemian, and I. Manas-Zloczower, "Epoxy Composites With Carbon Nanotubes and Graphene Nanoplatelets—Dispersion and Synergy Effects," *Carbon* 78 (2014): 268–278.

111. S. Chatterjee, F. Nafezarefi, N. H. Tai, L. Schlagenhauf, F. A. Nüesch, and B. T. T. Chu, "Size and Synergy Effects of Nanofiller Hybrids Including Graphene Nanoplatelets and Carbon Nanotubes in Mechanical Properties of Epoxy Composites," *Carbon* 50 (2012): 5380–5386.

112. J. M. Parente, R. Simões, A. P. Silva, and P. N. B. Reis, "Impact of the Curing Temperature on the Manufacturing Process of Multi-Nanoparticle-Reinforced Epoxy Matrix Composites," *Materials* 17 (2024): 1930.

113. M. M. Shokrieh, M. Esmkhani, A. R. Haghighatkhah, and Z. Zhao, "Flexural Fatigue Behavior of Synthesized Graphene/Carbonnanofiber/Epoxy Hybrid Nanocomposites," *Materials and Design* 62 (2014): 401–408.

114. F. Li, Y. Hua, C.-B. Qu, H.-M. Xiao, and S.-Y. Fu, "Greatly Enhanced Cryogenic Mechanical Properties of Short Carbon fiber/Polyethersulfone Composites by Graphene Oxide Coating," *Composites. Part A, Applied Science and Manufacturing* 89 (2016): 47–55.

115. D. G. Papageorgiou, M. Liu, Z. Li, C. Vallés, R. J. Young, and I. A. Kinloch, "Hybrid Poly (Ether Ether Ketone) Composites Reinforced With a Combination of Carbon Fibres and Graphene Nanoplatelets," *Composites Science and Technology* 175 (2019): 60–68.

116. J. Amraei, T. Rogala, A. Katunin, et al., "Thermomechanical Fatigue Behavior of CF/PEKK Composite Under low and Ultrasonic Frequencies," *Composites Part B: Engineering* 281 (2024): 111539.

117. J. Amraei, A. Katunin, and M. Lipińska, "Numerical Simulation and Experimental Validation of Self-Heating of Polymer-Matrix Composites During low-Cycle Fatigue Loading," *International Journal of Fatigue* 188 (2024): 108510.

118. J. Huang, C. Garnier, M.-L. Pastor, and X. Gong, "Investigation of Self-Heating and Life Prediction in CFRP Laminates Under Cyclic Shear Loading Condition Based on the Infrared Thermographic Data," *Engineering Fracture Mechanics* 229 (2020): 106971.

Paper III

Numerical simulation and experimental validation of self-heating of polymer-matrix composites during low-cycle fatigue loading

International Journal of Fatigue 188 (2024) 108510

Contents lists available at ScienceDirect

International Journal of Fatigue

journal homepage: www.elsevier.com/locate/ijfatigue

Numerical simulation and experimental validation of self-heating of polymer-matrix composites during low-cycle fatigue loading

Jafar Amraei [a,*], Andrzej Katunin [a], Magdalena Lipińska [b]

[a] Department of Fundamentals of Machinery Design, Faculty of Mechanical Engineering, Silesian University of Technology, Konarskiego 18A, 44-100 Gliwice, Poland
[b] Institute of Polymer and Dye Technology, Faculty of Chemistry, Lodz University of Technology, Stefanowskiego 16, 90-537 Łódź, Poland

ARTICLE INFO

Keywords:
Polymer-matrix composites (PMCs)
Rheological properties
Thermomechanical fatigue
Self-heating effect
Residual flexural stiffness

ABSTRACT

This study addressed gaps in understanding the physics underlying the self-heating phenomenon — a potential factor contributing to acceleration of fatigue life degradation in polymer-matrix composites (PMCs). Through developing a validated numerical model and implementation of oscillatory shear rheometry data, this research sought to enhance predictive capabilities. It aimed to implement an energy-based approach to predict the thermomechanical fatigue performance of PMCs, emphasizing self-heating temperature prediction. This includes addressing the absence of a physical framework to quantify the heat generation rate in response to prolonged fatigue loading. The findings highlighted the necessity of considering the radiative heat flux as an environmental factor in accurately determining self-heating temperature via the numerical model, and demonstrating negligible temperature variations through the PMC thickness. Furthermore, a temperature-stress approach was introduced to demonstrate the relation between the applied stress amplitude and the thermal response, alongside extracting residual flexural stiffness of tested PMCs under various stress amplitudes.

1. Introduction

Self-heating phenomenon, described as a temperature growth process, occurs in fatigue-loaded PMC structures such as wind turbine blade sections [1,2], and carbon fiber-reinforced (CFRP) composite gear [3,4]. The severity of self-heating temperature depends on (i) operational and environmental factors (e.g., ambient temperature) [5–8], (ii) material types [9–12], and (iii) loading parameters (e.g., loading frequency, applied stress/strain ratio) [4,13–18]. If the self-heating temperature increase is maintained within the safe range (usually below 5 °C with respect to the room temperature [19]), it is feasible to implement this phenomenon for damage inspection using nondestructive testing (NDT) techniques such as self-heating based vibrothermography (SHVT), without jeopardizing the structural integrity [18–20]. In SHVT, the process is driven by the self-heating phenomenon caused by resonant excitation within the tested PMCs, allowing for the observation of local temperature distribution on the tested specimen's surface and aiding in damage inspection [19,20].

On the other hand, subjecting PMCs with low thermal conductivity to high stress and/or frequency loading leads to the accumulation of a large amount of volumetric internal heat [4]. This accelerates the stiffness degradation of PMCs through damage accumulation at different scales, ranging from micro- to macro-scale. At the microscale, for example, the higher coefficient of thermal expansion of polymers compared to fibers leads to residual thermal stresses at the interface/interphase region between the reinforcement and bulk polymer. The residual stress acts as a catalyst in increasing the self-heating temperature [21]. This results in chemical degradation and softening of cross-linked networks [22], reduction in intermolecular forces, and consequently, debonding and crack in the interphase zone [23,24]. These effects can be assessed using the bulk dissipation model and near-crack dissipation analysis [25–27]. In micro- and macro-scales, PMC specimens applied to fatigue loading may experience crack nucleation, matrix cracking, single fiber breakage, open cracks, macro cracks, and delaminations [28–30]. The irretrievable formation of microcracks and microdelaminations occurs continuously as entropy is released, aligning with the second law of thermodynamics (Clausius inequality statement) [31]. The evolution of macroscopic damage, triggered by the accumulation of microcracks and microdelaminations, ultimately leads to sudden fatigue failure. Therefore, a comprehensive understanding of these damage mechanisms is vital to reliably simulate the self-heating phenomenon.

The self-heating phenomenon is generally explained by the following

* Corresponding author.
E-mail address: jafar.amraei@polsl.pl (J. Amraei).

https://doi.org/10.1016/j.ijfatigue.2024.108510
Received 14 April 2024; Received in revised form 12 June 2024; Accepted 12 July 2024
Available online 14 July 2024

Nomenclature

T_g	Glass transition temperature
T_{ref}	Reference temperature
α_T	Temperature-dependent shift factor
E_a	Activation energy
R_a	Universal gas constant
f	Loading frequency
n	Number of Prony parameters
g_i	Relaxation modulus
τ_i	Relaxation time
G_∞	Long-term shear modulus
G_0	Initial shear modulus
$\tan\delta$	Dissipation factor
σ_d	Standard deviation
b	Width
H	Thickness
L	Length
A_s	Cross-section
I	Moment inertia
P	Force
W	Displacement
ε_{yy}	Bending strain
γ_{yz}	Shear strain
A	Helmholtz free energy
ρ	Density
σ	Cauchy stress tensor
$\dot{q}$	Heat generation rate
T_a	Ambient temperature
e	Emissivity
β	Stephan-Boltzman constant
C_p	Heat capacity
K	Thermal conductivity
V_d	Velocity
E	Young's modulus
ν	Poisson's ratio
M	Torque
θ	Angular displacement
G^*	Complex shear modulus
G'	Storage shear modulus
G''	Loss shear modulus
R^2	Determination coefficient
f_r	Reduced frequency
N	Total number of nodes
ζ	Unitless residual temperature
T_s	Stabilized self-heating temperature

three phases. Phase I involves a rapid temperature growth in a relatively short period of time. Phase II is characterized by a stabilized self-heating temperature over prolonged fatigue loading, while phase III marks a sudden increase in self-heating temperature, corresponding to fatigue damage accumulation, formation of new friction surfaces in the appeared crack front, while finally leading to thermal fatigue failure [4]. One of the parameters characterizing the self-heating phenomenon used in our previous studies is the critical self-heating temperature [32]. This parameter signifies a temperature value at which rapid damage propagation begins, accelerating fatigue damage accumulation and eventually resulting in premature thermal fatigue degradation (i.e., non-stationary self-heating regime) [4]. For this purpose, Katunin [32] reported the critical self-heating temperature of glass fiber-reinforced polymer (GFRP) composite using numerous physical quantities in the range of 60–83 °C, with the glass transition temperature (T_g) of 120 °C. In another study, Turczyn et al. [33] illustrated physical–chemical changes in a tested PMC leading to an insignificant structural degradation below the self-heating temperature of 80 °C, while 30 % degradation occurred at the temperature of 95 °C because of the cross-linking chain degradation [34]. Performing fatigue tests poses several challenges. On the one hand, experimental investigation on the self-heating effect by altering loading parameters and ambient temperature is both time-consuming and costly, and controlling the parameter of self-heating temperature evolution captured by infrared camera and post-processing of the data is also quite challenging, particularly during prolonged fatigue testing durations. On the other hand, results obtained from experiments in the presence of the self-heating effect may exhibit significant deviations under different testing conditions. Therefore, developing a reliable model to address these challenges is of paramount importance.

Understanding the physics and modeling of the self-heating phenomenon within fatigue experiments is crucial. For this purpose, Di Maio et al. [35] focused on numerical modeling and experimental validation of the observed temperature evolution on the CFRP specimen surface induced by delamination growth using the virtual crack closure technique (VCCT). In another study, Demleitner et al. [36] utilized passive thermography alongside Bayesian optimization to define key parameters for self-heating in impacted glass/epoxy composites. Ly et al. [37] developed a numerical viscoelastic constitutive model using the thermodynamic laws to study the self-heating effect that appeared in high-density polyethylene (HDPE)-carbon composite under cyclic loading with the low-frequency, i.e., 0.1 and 1 Hz. Nonetheless, the model was not validated experimentally. Sevenois et al. [38] numerically investigated the influence of self-heating on the thermoviscoplastic behavior of representative volume element of a unidirectional carbon-polyamide 6 composite under monotonic loading. The influence of frequency was not taken into consideration in their study. De Lima et al. [39] implemented a numerical-experimental concept based on a curve-fitting procedure for investigating the self-heating effect in viscoelastic dampers under cyclic loading. Furthermore, Sapozhnikov et al. [40] developed an analytical self-heating model under three-point bending. In another study [41], researchers examined how loading frequency affected self-heating temperature. Despite their success in evaluating temperature distribution, the developed model has a limitation. The approach of substituting convection heat flux for all boundaries may not always be suitable, especially in scenarios where at least one boundary remains unaffected by fluid interaction. Moreover, Huang et al. [42] conducted an experimental–numerical study to quantify the relation between heat generation rate and applied shear stress of angle-ply CFRP composite. The fatigue experiments were conducted at a low frequency (5 Hz), with a focus on the phase II of the fatigue damage accumulation. Likewise, Lahuerta et al. [43] carried out an experimental–numerical investigation to predict the self-heating temperature of thick GFRP laminates (i.e. 10 mm, 20 mm, and 30 mm) under low frequencies, ranging from 0.25 Hz to 2.5 Hz. However, the assumption of uniform heat generation in their analysis may diminish the accuracy of the results, particularly in scenarios with high-stress amplitude. In response to these challenges, we formulated and developed the numerical model, considering all the limitations outlined above, thereby improving the predictability of the self-heating phenomenon.

In the current study, the thermomechanical fatigue behavior of PMCs is investigated with a focus on the self-heating phenomenon. Incorporating thermoviscoelastic properties from rheometric experiments into a validated numerical model aims to bridge existing knowledge gaps and offers a deeper understanding of the phenomenology of self-heating in glass/epoxy composites subjected to fatigue loading. Furthermore,

constructing *S–N* curves, determining the residual flexural stiffness, and analyzing the relationship between stress amplitude and self-heating temperature response are pivotal steps toward comprehensively understanding the thermomechanical fatigue characteristics of PMCs.

2. Theoretical background

2.1. Modeling of linear thermoviscoelastic behavior of PMCs

2.1.1. Time-temperature superposition

Time-temperature superposition (TTS) principle [44] is often used to extend the mechanical performance evaluation across different time and frequency scales in PMCs. This principle assumes that temperature and time affect the mechanical properties similarly in PMCs with simple thermal rheological behavior. In other words, TTS aligns isothermal curves at different frequencies into a continuous curve using the temperature-dependent horizontal shift factor (a_T) [45]. The determination of a_T, governed by the Arrhenius equation linked to the side chain motion, is applicable to the temperature below T_g, where the fatigue tests are performed. Integrating from the reference temperature (T_{ref}) to the considered temperature (T) establishes the final form of the Arrhenius equation (see Eq. (1)).

$$ln(a_T) = \frac{E_a}{R_a}\left(\frac{1}{T} - \frac{1}{T_{ref}}\right), \tag{1}$$

where E_a is activation energy of the tested PMC and R_a is the universal gas constant with the value of 8.314 J/mol K.

2.1.2. Estimating thermoviscoelastic response of PMCs using Prony series

The generalized Maxwell model, represented by Prony series, estimates the linear viscoelastic behavior of PMCs. The frequency-dependent Prony series used in [46] can mathematically be rewritten as frequency-temperature-dependent Prony series [47]:

$$G'(T,\omega) = G_\infty + G_0\sum_{i=1}^{n}\left(\frac{g_i\tau_i^2 a_T^2\omega^2}{1+\tau_i^2 a_T^2\omega^2}\right), \tag{2}$$

$$G''(T,\omega) = G_0\sum_{i=1}^{n}\left(\frac{g_i\tau_i a_T\omega}{1+\tau_i^2 a_T^2\omega^2}\right), \tag{3}$$

where ω denotes the angular frequency, defined as $2\pi f$, with f representing the loading frequency applied in rheometric test, n denotes the number of required Prony parameters, i.e., g_i and τ_i. The parameter g_i represents the relaxation modulus at each relaxation time τ_i, indicating how much the material relaxes under an applied load over time. G_∞ is the long-term shear modulus obtained from static test, while G_0 is the initial shear modulus at time $t = 0$ of a relaxation test. Such shear moduli can be converted to each other using Prony parameter of g_i as follows:

$$G_\infty = G_0\left(1 - \sum_{i=1}^{n} g_i\right), \tag{4}$$

$$G_0 = \frac{G_\infty}{1-\sum_{i=1}^{n} g_i}. \tag{5}$$

Estimated Prony parameter of g_i should be positive and in sum less than one, i.e., $\sum_{i=1}^{n} g_i < 1, g_i > 0$. For optimizing Prony parameters, n is an arbitrarily selected number, and g_i, τ_i and G_0 are initially assumed. Storage and loss moduli (G' and G'') are then estimated using Eqs. (2) and (3) and compared with the extracted data from a torsional rheometer. The errors will finally be minimized using the given objective function (OF) programmed in MATLAB software.

$$\frac{\left(G'_{ms}-G'_{es}\right)^2}{\sigma_d\left(G'_{ms}\right)} + \frac{\left(G''_{ms}-G''_{es}\right)^2}{\sigma_d\left(G''_{ms}\right)} + \frac{\left(\tan\delta_{ms}-\tan\delta_{es}\right)^2}{\sigma_d\left(\tan\delta_{ms}\right)} = \min(OF), \tag{6}$$

where $\tan\delta_{es}$ denotes the dissipation factor estimated by Eq. (7), *ms* and *es* indices show the measured data from experiments and estimated data using minimization algorithm, respectively, and σ_d indicates the standard deviations for each of these three measured values.

$$\tan\delta_{ms} = \frac{\sum_{i=1}^{n}\left(\frac{g_i\tau_i a_T\omega}{1+\tau_i^2 a_T^2\omega^2}\right)}{1-\sum_{i=1}^{n} g_i + \sum_{i=1}^{n}\left(\frac{g_i\tau_i a_T\omega}{1+\tau_i^2 a_T^2\omega^2}\right)}. \tag{7}$$

2.2. Heat generation induced by fatigue loading for thermal analysis

In case of a supported cantilever beam with the width b, thickness H, and a span L subjected to a point load P at its free end, the displacement at an imaginary cross-section y from the fixed end or holder is a combination of bending (W_b) and shear (W_s) displacements (i.e., $W = W_b + W_s$) [48]:

$$W(y,T,f) = \frac{P}{6IE_y(T,f)} + \frac{3PL}{2A_sG(T,f)}, \tag{8}$$

where

$$\varepsilon_{yy} = -z\frac{\partial^2 W}{\partial y^2}, \tag{9}$$

$$\gamma_{yz} = \frac{3P}{2AG'(T,f)}\left[1-4\left(\frac{z}{H}\right)^2\right], \tag{10}$$

where ε_{yy} and γ_{yz} denote the bending and shear strains, respectively, z is the distance from the neutral axis, A_s denote the cross-section, I is the moment inertia. The equivalent strain can be obtained via:

$$\varepsilon = \sqrt{\varepsilon_{yy}^2 + 3\gamma_{yz}^2}. \tag{11}$$

By implementing the second law of thermodynamics and Helmholtz free energy A, the heat generation rate $\dot{q}$ can be calculated by [49]:

$$\dot{q} = \left[\left(\sigma - \frac{\partial A}{\partial \varepsilon}\right) : \dot{\varepsilon} - \rho\frac{\partial A}{\partial \gamma} : \dot{\gamma} - \frac{K\nabla T.\nabla T}{T}\right], \tag{12}$$

where σ is the Cauchy stress tensor, ρ is density, ε is the equivalent strain, and γ is a vector of internal variables. The first term on the right-hand side indicates the mechanical energy dissipation resulting from the inelastic deformation, the second term represents the irreversible stored energy, and the third term stands for convective heat flux via PMC boundary. Nevertheless, it is quite challenging to quantify the heat generation using Eq. (12). The main root of this difficulty can be sought in measuring Helmholtz free energy as a function of strain, temperature, and internal variables, i.e., $\sigma = \sigma(\varepsilon, T, \gamma)$. Alternatively, the heat generation rate induced within fatigue experiments can be correlated with the viscoelastic behavior of any arbitrary PMC as follows [50]:

$$\dot{q} = 3\pi f\varepsilon_0^2 G'', \tag{13}$$

where ε_0 is the thermomechanical strain amplitude, determined by Eq. (11).

2.3. Modeling of self-heating phenomenon

According to the thermodynamic principle and assuming that the mass density and heat capacity of a PMC specimen are independent of the thermodynamic state, the energy equation for a fatigue-loaded PMC specimen applied to a control volume (V) can be expressed in the following form [51]:

$$\int\left(\rho C_p\frac{\partial T}{\partial t}\right)dV + \left[\int\left(-K\nabla^2 T\right)dV\right] = \int \dot{q}dV, \tag{14}$$

where C_p is the heat capacity and K is the thermal conductivity of PMC specimen. The right-hand side term represents the heat generation rate across the specimen volume, while the left-hand side term within the bracket illustrates the heat release/dissipation through volumetric conduction. The last term of left-hand side is the internal storage energy rate over the specimen volume, which manifests as an increase in temperature through the thickness of a specimen, termed as the self-heating effect.

The thermal initial condition (IC) is stated as zero temperature rise at the beginning of the test, thus:

$$T(x,y,z,t=0)=T_a. \tag{15}$$

The boundary conditions (BCs) assumed thermal insulation at the lower end of the specimen due to the real test condition. Therefore, the thermal BCs are given by:

$$-K_x\frac{\partial T}{\partial x}\Big|_{x=+\frac{b}{2}} = -K_x\frac{\partial T}{\partial x}\Big|_{x=-\frac{b}{2}} = h(T-T_a)+e\beta\left(T^4-{T_a}^4\right), \tag{16}$$

$$-K_y\frac{\partial T}{\partial y}\Big|_{y=0}=0;\ -K_y\frac{\partial T}{\partial y}\Big|_{y=L} = h(T-T_a)+e\beta\left(T^4-{T_a}^4\right), \tag{17}$$

$$-K_z\frac{\partial T}{\partial z}\Big|_{z=+\frac{H}{2}} = -K_z\frac{\partial T}{\partial z}\Big|_{z=-\frac{H}{2}} = h(T-T_a)+e\beta\left(T^4-{T_a}^4\right). \tag{18}$$

where h is the heat transfer coefficient on the surface of the PMC specimen, e is the emissivity, and β is the Stephan-Boltzman constant. The value of h for natural air cooling at room temperature (RT) in the laboratory is assumed to be 8.1 W/m^{2}K [52], while h is dependent on the specimen's movement velocity (V_d) under pure bending. Therefore, velocity-dependent h factor exposed to natural air cooling can be determined via [53]:

$$h(y)=8.1+40.7V_d, \tag{19}$$

where V_d for a cantilever beam is node-based and varies along the specimen's length. It can be computed by $V_d=2\pi fW$, with W obtained from Eq. (8). Assuming temperature independence for K in glass/epoxy composites, as specified in the manufacturer's datasheet, with uniform values across all directions (i.e., $K_x=K_y=K_z=K$), C_p exhibits temperature dependency with units of J/kg.K, and can be derived from [54]:

$$C_p=828.7+2.71T \tag{20}$$

where T is given in °C. Incorporating IC and BCs into the energy law (see Eq. (14)) and applying a suitable solution strategy as described in Section 4, the model simulates the self-heating phenomenon.

3. Material and preliminary experiments

3.1. Tested material and its properties

The tested GFRP specimens were manufactured from a 14-layered epoxy-based unidirectional laminate reinforced with a plain weave E-glass fabric weighing 200 g/m^2, sourced from Izo-Erg S.A. (Gliwice, Poland), identified as EP GC 201. The material properties of the specimens and the surrounding environment are outlined in Table 1.

Table 1
Material properties of the tested specimens.

Properties		GFRP	Ref.
Young's modulus [MPa]	E_x	27170	[55,56]
	E_y	24203.61	
Poisson's ratio [–]	ν_{yx}	0.166	
Density [kg/m^3]	ρ	1978.3	
Initial shear modulus [MPa]	G_0	6079.56	Current study
Long-term shear modulus [MPa]	G_∞	3172.18	
Thermal conductivity [W/m·K]	K	0.442	[57]
Heat capacity at RT [J/kg·K]	C_p	891	[54]

3.2. Measuring shear moduli

Dynamic rheological measurements of GFRP specimens were conducted using ARES-G2 rheometer by TA Instruments (New Castle, DE, USA). ARES-G2 experimental setup including the torsional clamp fixture is depicted in Fig. 1. The rheometer, equipped with the separate motor and transducer designs, allows the motor to apply deformation independently from the torque measurement on the transducer. This separation ensures that the test results remain unaffected by the motor's inertia, decoupling the required moment of inertia to move the motor from the torque measurements. The experiments were conducted using torsional oscillation mode, utilizing a rectangular geometry with dimensions of 50 mm in length, 10 mm in width, and 2.4 mm in thickness, with a span length of 34 mm. Measurements of storage and loss shear moduli were taken at temperatures ranging from 25 °C to 175 °C, covering 18 frequencies between 0.01 Hz and 99 Hz. The tests were conducted with a consistent oscillation strain of 0.001 % to ensure adherence to the linear viscoelastic region. Such tests are necessary to determine the heat generation rate, resulting from Eq. (13), which is essential for solving the energy equation (Eq. (14)).

3.3. Processing of experimental data

The rheometer independently measured the torque M and the angular displacement θ [58]. The data acquired were implemented as inputs for Eq. (21), and a MATLAB (MathWorks, USA) code was developed to determine the complex shear modulus.

$$G^*=\frac{M}{\theta}\frac{3L}{bH^3g_{sv}}. \tag{21}$$

The parameter g_{sv} is given by [57]:

$$g_{sv}=1-\frac{192}{\pi^5}\frac{H}{b}\left[\tanh\left(\frac{\pi}{2}\frac{H}{b}\right)+0.004524\right]. \tag{22}$$

The storage and loss shear moduli, denoted as G' and G'', respectively, can be derived from Eq. (21). Fig. 2 illustrates the exemplary storage and loss moduli, along with tanδ, derived from rheometric measurements after postprocessing for the loading frequency of 30 Hz.

Rheometric experiments were each subjected to a consistent heating rate of 2 °C/min. The Arrhenius plot (Fig. 3) presented the experiment-derived values $1000/T_g$ versus logarithmized excitation frequency values. Linear regression analysis was applied to determine the slope from the Arrhenius plot using the measured data. Activation energy value was obtained by multiplying the slope with the universal gas constant (see Eq. (1)). The activation energy was estimated to be 661.46 kJ/mol, with a determination coefficient R^2 of 0.928, indicating the accuracy of the fitting for the regression curves of T_g. Activation energy value was then implemented to determine shift factor values, α_T, based on the Arrhenius law (Eq. (1)) as a function of temperature, presented in Fig. 4.

3.4. Constructing master curves

To construct the master curves for thermoviscoelastic GFRP composite using rheometric experiments, several steps were followed. The raw data from all frequencies were first processed to obtain frequency-domain curves at various temperatures. Using the kinetic Arrhenius model, the reference temperature was then set at 140 °C, the lowest among the 18 values for T_g acquired from experiments. This conservative selection ensures the model covers the most extreme temperature conditions encountered in the experiments, resulting in a robust estab-

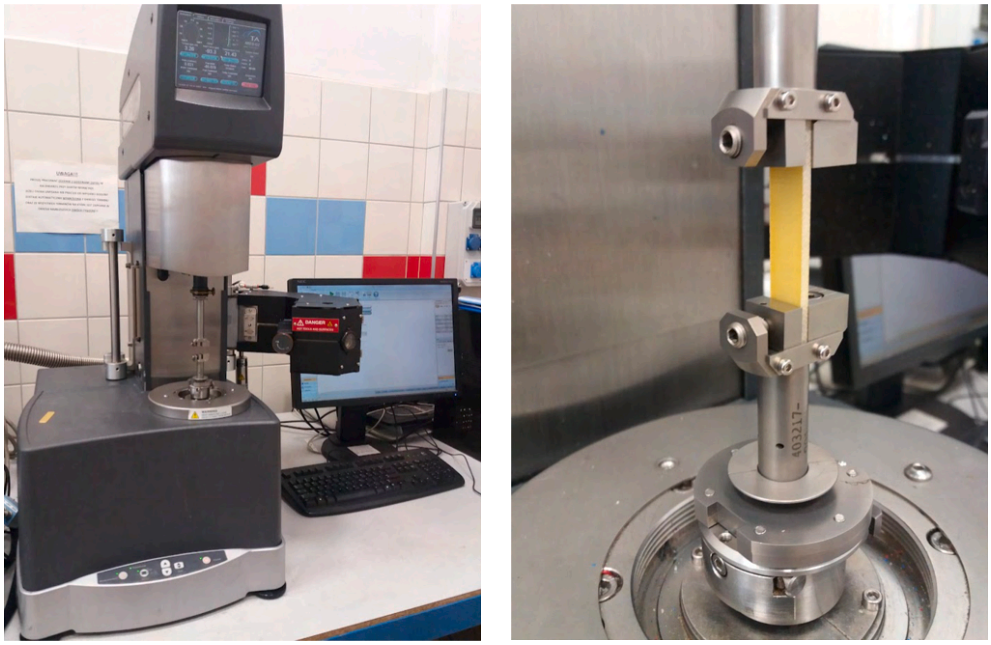

Fig. 1. Rheometer test-rig: (a) ARES-G2 facility, (b) torsional clamp fixture.

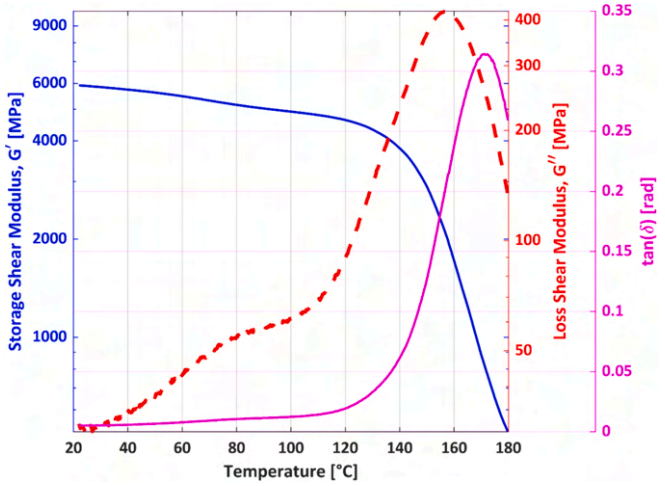

Fig. 2. Exemplary results of the determination of storage and loss moduli alongside tan δ at 30 Hz.

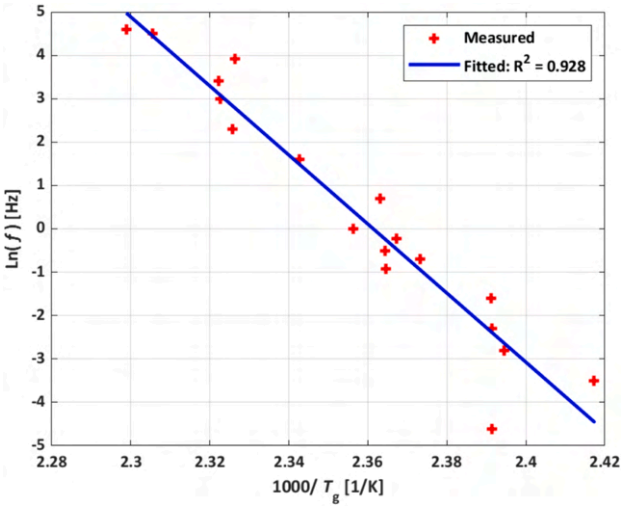

Fig. 3. Arrhenius plot illustrating ln(f) versus 1000/T at a heating rate of 2 °C/min.

lishment of the final frequency domain across an arbitrary temperature range. The curves were then horizontally shifted with the temperature step of 5 °C relative to reference using Eq. (1). Finally, the master curves for storage and loss shear moduli, along with the damping factor tanδ, across a broad frequency spectrum, considered as the reduced frequency (f_r), were constructed based on the criterion of curve smoothness among all 18 datasets. These curves are depicted in Figs. 5, and 6. Eq. (23) illustrates f_r corresponding to the measured frequency at an arbitrary temperature as follows:

$$f_r = a_T(T)f \text{ or } f\omega_r = a_T(T)\omega. \tag{23}$$

To represent thermoviscoelastic behavior of the investigated PMCs with required accuracy, up to 75 Prony series with corresponding coefficients were taken into account. Employing the minimization objective function (see Eq. (6), the optimal number of the Prony series was identified as 44, with the initial and long-term shear moduli values provided in Table 1, and coefficients given in Table A.1 in Appendix A. The loss shear modulus, pivotal in determining the heat generation rate (see Eq. (13)), was then mathematically formulated and quantified using the 44 Prony series. Fig. 7 demonstrates a good agreement between the loss modulus obtained from the Prony series and the master curve.

4. Solution method for numerical self-heating model and simulation results

4.1. Assumptions and strategy for solving

This section aims to simulate the self-heating phenomenon in a fatigue-loaded PMC specimen, employing a thermomechanical coupling analysis grounded in the thermodynamic principles. The numerical methodology utilized for this purpose is outlined using the finite difference (FD) approach, with a schematic representation provided in

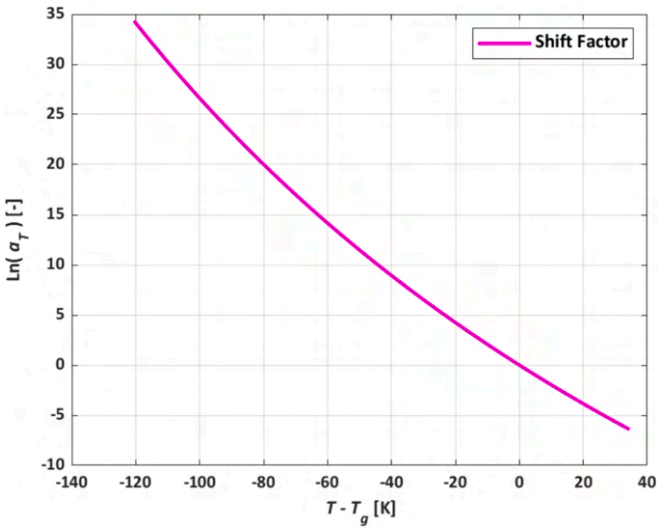

Fig. 4. Temperature-dependent shift factor.

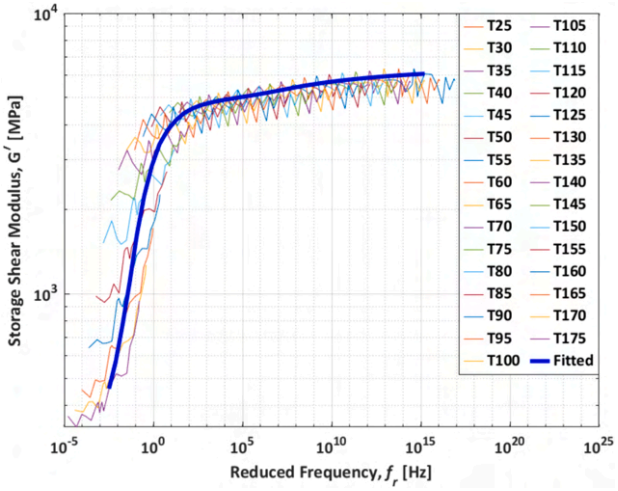

Fig. 5. Master curve representing storage shear modulus versus reduced frequency.

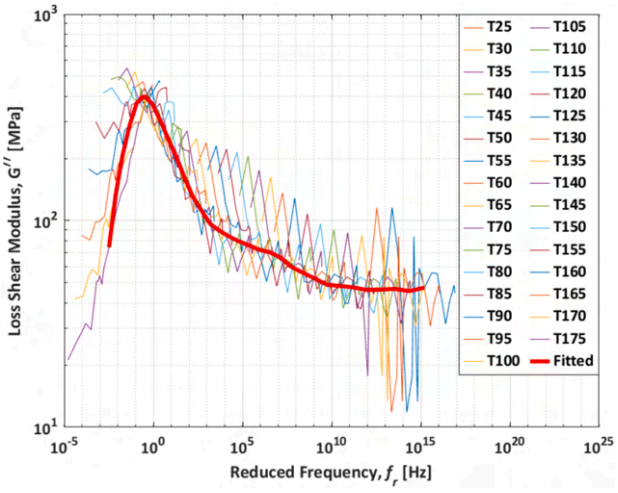

Fig. 6. Master curve illustrating shear loss modulus versus reduced frequency.

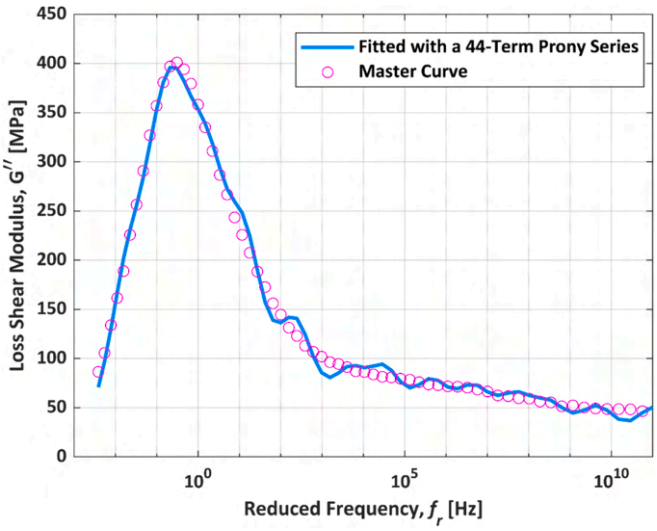

Fig. 7. Evaluating the loss shear modulus via Prony series versus the master curve.

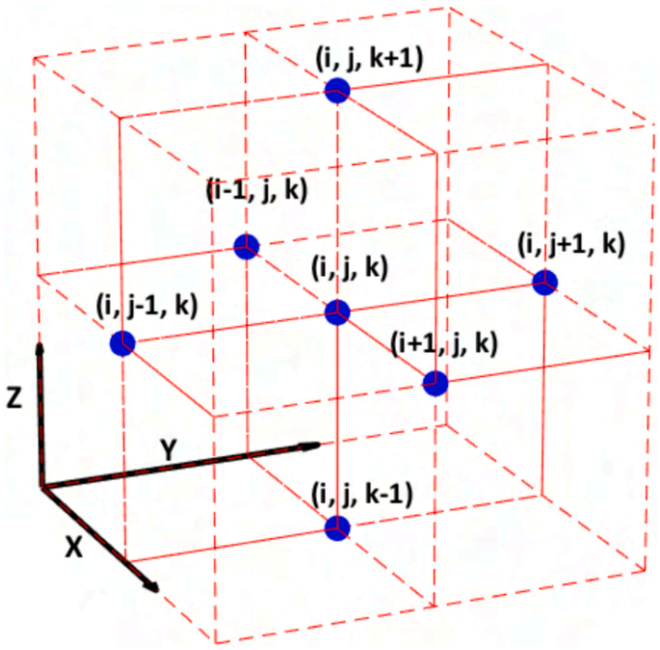

Fig. 8. Schematic representation of nodal spacing in x-, y-, and z-directions via central finite difference approximation, including central node at (x, y, z) corresponding to (i,j,k).

Fig. 8, see Ref. [59] for further details.

A FD code was developed to facilitate the numerical simulation of the self-heating phenomenon within a three-dimensional (3D) geometric model of a pure bending PMC specimen. The simulated specimen mimics the geometric dimensions of the experiments, featuring a width of 10 mm, length of 40 mm, and thickness of 2.4 mm. Preliminary simulations highlighted the significant influence of mesh size on the results, particularly when $\Delta z > 0.4$ mm and $\Delta x = \Delta y > 1$ mm. To address this dependency, the model was discretized into 19,200 elements using a hexahedral mesh, ensuring the lack of dependency on mesh size with $\Delta x = \Delta y = 0.5$ mm, and $\Delta z = 0.2$ mm.

Temporal discretization was crucial for accommodating the harmonic loading signal. Therefore, a time step Δt of $1/(4f)$ was chosen at a loading frequency of 30 Hz, resulting in $\Delta t = 8.3$ ms. Despite increasing

the computational time, which ensured a more realistic simulation. Mechanical and thermal BCs were then set to replicate the real fatigue testing conditions. The bottom of the specimen was clamped and thermally insulated at $y = 0$, while the top at $y = L$ was subjected to fully reversed fatigue loading applied in the z direction. Additionally, the contribution of radiative heat transfer (i.e., T^4) was estimated using a Taylor series expansion around the ambient temperature (T_a) by: $4T_a{}^3T - 3T_a{}^4$. The nodal-based heat transfer coefficient on the specimen's surface using Eq. (19), under various stress amplitudes, was then determined and depicted in Fig. 9.

As presented in the flowchart in Fig. 10, the thermal analysis began by estimating the displacement and strain (i.e., deformation) distributions at RT, followed by considering a 44-term Prony series as input. The heat generation rate was then computed based on these distributions. To ensure the stability of the temperature field across successive time steps, a convergence criterion, termed as the unitless residual temperature, was implemented:

$$\left(\frac{\sum_{n=1}^{N}\left|T_n^{m+1}-T_n^{m}\right|^2}{\sum_{n=1}^{N}\left|T_n^{m+1}\right|^2}\right)^{0.5} \le \zeta, \tag{24}$$

where N is the total number of nodes, $m+1$ and m are current and previous time steps, respectively. This criterion, expressed by Eq. (24), ensured that the residual temperature or the discrepancy between successive temperature fields remained below an acceptable threshold ($\zeta = 10^{-6}$), as recommended for energy residual in [60]. Iterative convergence of the thermal field was continued until convergence was achieved, ensuring the accurate determination of the self-heating temperature for each node at each time step. Subsequently, thermo-viscoelastic properties, including storage and loss moduli, were updated based on the new self-heating temperature field. Consequently, the updated thermomechanical displacement and strain fields served as input for calculating the heat generation rate at the subsequent time step, and finally extracting the nodal-based temperature.

4.2. Simulation results

This section analyzes the self-heating temperature distribution across the specimen thickness and examines the effect of radiation heat flux on this temperature profile. Measurement techniques, such as infrared (IR) cameras, solely capture surface temperatures, leaving the internal self-heating temperature variations unexplored. To bridge this gap, six regions of interest (ROIs) were considered to numerically investigate the temperature profiles across both cross-sectional and longitudinal dimensions of the specimen. Three ROIs were defined near the lower clamp in the cross-section (XZ-plane) and three along the length of the specimen in the YZ-plane, as depicted in Fig. 11a and b, respectively. Assuming the symmetry of temperature distribution under fully reversed bending, ROIs were defined across half of the specimen's thickness. The temporal evolution of self-heating temperature across fatigue load cycles was determined in ROIs 1 to 3, while ROIs 4 to 6 aimed at presenting the temperature distribution at the end of fatigue loading along the specimen's length.

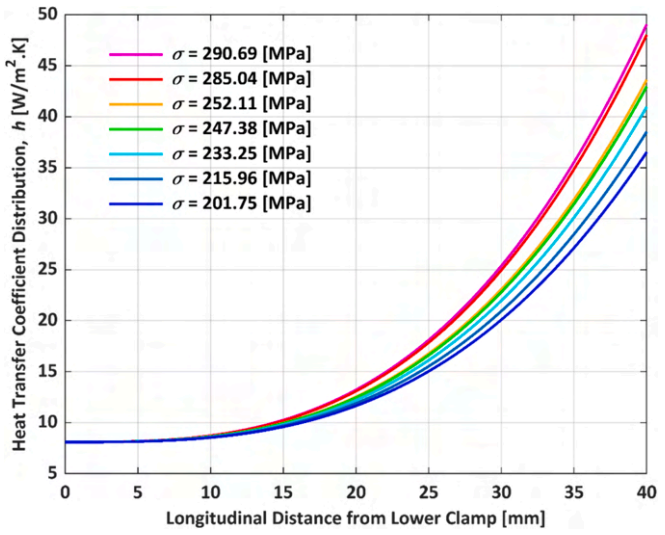

Fig. 9. Convective heat transfer coefficient with stress levels across the length of the specimen.

In alignment with the experimental results, simulations prioritized the critical scenario, focusing on premature fatigue failure at a bending stress amplitude of 285.04 MPa according to the experimental investigations. The unitless residual temperature (ζ) resulting from such a stress level was determined and depicted in Fig. 12. It remains below the defined threshold ($\zeta < 10^{-6}$), signifying the thermal field convergence throughout the fatigue load cycle. The heat generation rates illustrated in Fig. 13, during fatigue load cycles in ROIs 1 to 3 were determined under such a stress level. ROI1 exhibited significantly higher heat generation attributed to the elevated thermomechanical strain/stress. Conversely, ROI3 demonstrated negligible heat generation, linked to no bending stress and only shear stress at the neutral axis ($z = 0$), peaking at 4.28 MPa, approximately 66 times lower than the bending stress magnitude. However, this trend of shear stress magnitude is anticipated to intensify in thicker specimens, implying that heat generation from shear strain in thick specimens could be remarkable under specific loading conditions, which falls outside the scope of the current study. Fig. 14 illustrates the relationship between the heat generation rate per unit volume per cycle and the temperature increase across ROIs 1 to 3. This trend closely mirrors the pattern observed in the heat generation rate versus load cycles in Fig. 13.

Fig. 15a and b depict numerical simulation results on the specimen surface alongside experimental results shown in Fig. 15c. Fig. 16a and b compare the cross-sectional temperature profiles with and without considering the radiative heat flux near the clamp. Similarly, Fig. 17a and b show temperature profiles in the middle of the specimen's length. Fig. 18 compares the relative temperatures of ROIs 1 to 3 in scenarios including and excluding radiation's effect, while Fig. 19 provides a similar comparison for ROIs 4–6.

Although ROI3 exhibits negligible heat generation (see Fig. 13), it lacks direct interaction with the environment through radiation and convection heat transfer. As a result, the influence of radiation and convection on ROI3 is omittable. By contrast, a portion of heat from ROI1 dissipates through radiation and convection, with some transferred to ROI3 via conduction, while the rest is stored and appeared in the form of a self-heating temperature. Despite its negligible heat generation, the transferred conductive heat flux to ROI3 contributes to temperature elevation in this region. This temperature rise is similar to that of ROIs 1 and 2 due to the balanced thermodynamic heat transfer (see Fig. 18). On the other side, the elevated self-heating temperatures correlate with the increased radiative heat flux, driven by radiation's temperature dependency, leading to reduced heat storage within ROI1. Consequently, this results in a relatively lower amount of conductive heat flux from ROI1 to ROI3, leading to less heat being stored in ROI3 and ultimately lower temperature enhancement in ROIs compared to scenarios excluding the influence of radiation. In detail, with radiation taken into account in simulations, ROI1 registers temperatures 3.93 °C and 6.69 °C higher than ROI2 and ROI3 (i.e., 109.96 °C vs. 106.03 °C and 103.27 °C), respectively. Excluding radiation's effect, ROI1 maintains temperatures 2.10 °C and 3.60 °C higher than ROI2 and ROI3 (117 °C vs. 114.90 °C and 113.41 °C), see Figs. 15, 16, and 17. In other words, the temperature difference between ROI1 and ROIs 2 and 3 with radiation is roughly double that without radiation, attributed to reduced heat dissipation into the environment and increased conductive heat

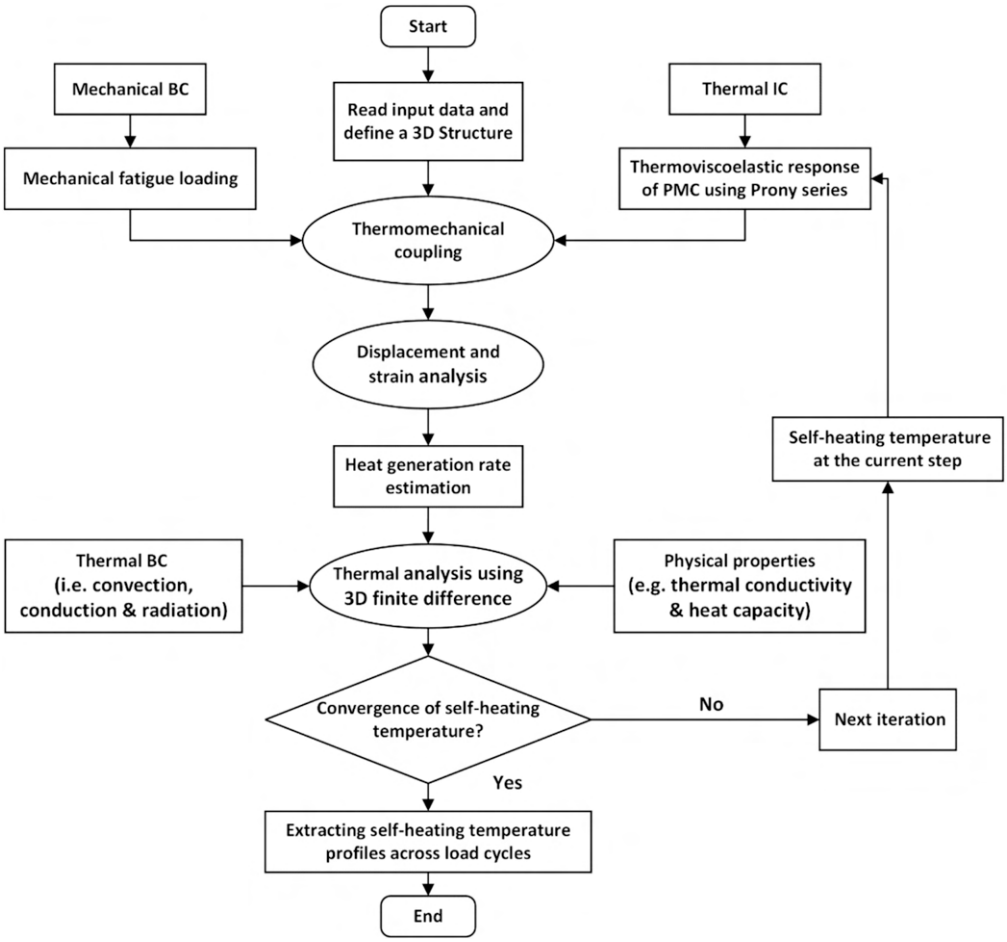

Fig. 10. Flowchart for modeling of self-heating in a fatigue-loaded PMC specimen.

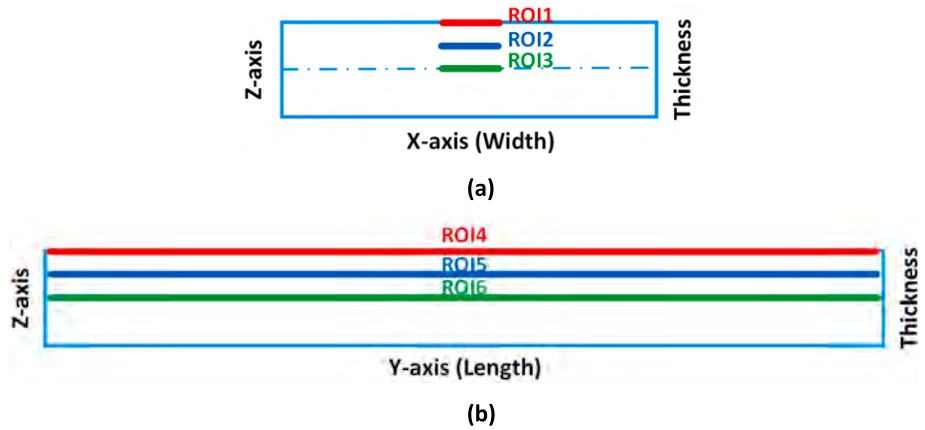

Fig. 11. ROIs defined (a) close to lower clamp in XZ plane (y = 0), (b) in YZ plane along specimen's length (x = 0).

flux through the specimen's thickness, resulting in a more uniform temperature distribution. Additionally, the relative temperature profiles obtained from the numerical simulations in the absence of radiation reached the critical temperature (T_g) of 140 °C at the ambient temperature of 23 °C after 17,900 cycles. Nevertheless, simulation results considering radiation remained 7 °C below T_g even after undergoing an additional 1000 cycles (i.e., 18,900 cycles), as illustrated in Fig. 18. Fig. 19 depicts the influence of radiation across the specimen's length for ROIs 4–6. The effect of radiation is more pronounced near the clamp, decreasing along the specimen's length.

5. Experimental validation

5.1. Experimental setup and experiment conduction

The fatigue tests were conducted using a custom-designed testing rig shown in Fig. 20a, b and c, wherein each specimen was clamped within a thermally insulated bakelite holder under a consistent torque of 20 Nm to maintain consistent testing conditions. Each specimen had a rectangular geometry with dimensions of 100 mm in length, 10 mm in width, and 2.4 mm in thickness. The specimens were tested using a span length

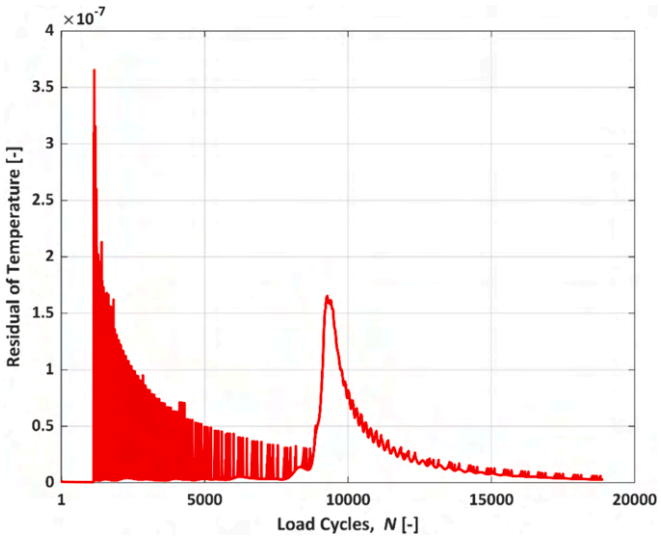

Fig. 12. The unitless residual temperature versus load cycle.

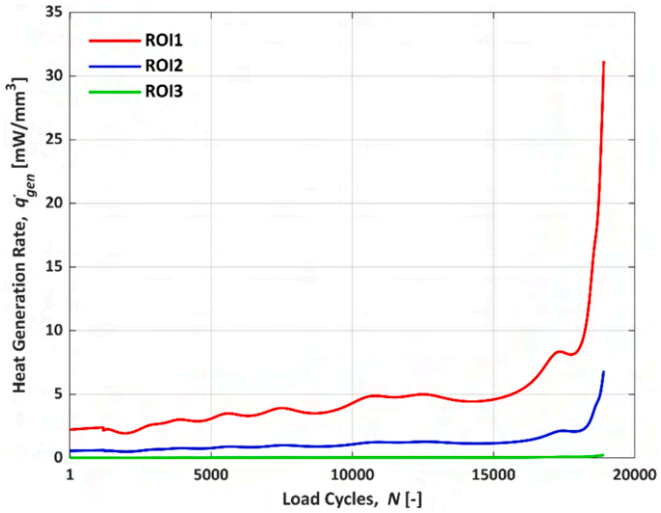

Fig. 13. Heat generation rate across fatigue load cycles for ROIs 1–3.

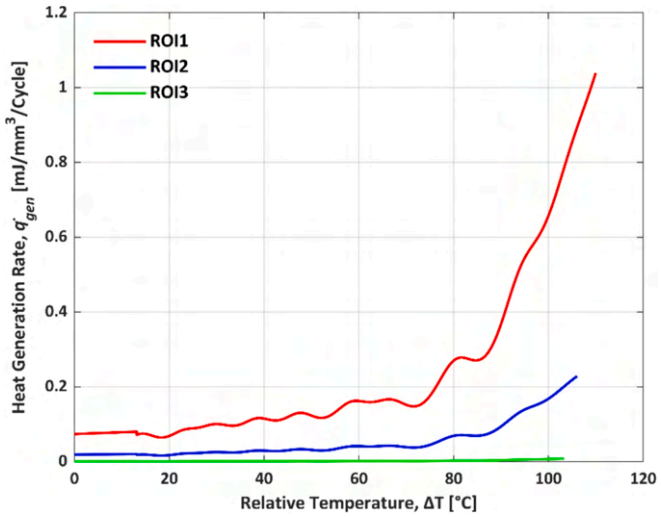

Fig. 14. Heat generation rate versus temperature increase for ROIs 1–3.

of 40 mm. Detailed information about the tested GFRP specimens, including their properties and manufacturing process, is provided in Section 3.1. Excitation of the specimens was achieved using a TIRA® TV-51120 electrodynamic shaker, connected to the force sensor (PCB Piezotronics® 208C03) via a stringer. The shaker generated controlled vibrational displacement, transmitted through the stringer to the tested specimen. The force sensor measured the force corresponding to the applied displacement. Additionally, vibration velocity was measured using the single-point laser Doppler vibrometer Polytec® PDV-100, while force and vibration signals were captured at a 2 kHz sample rate through the multi-channel data acquisition card (NI® DAQ Card 6062E) linked to a PC. The shaker parameters were regulated using a dedicated in-house application. Temperature monitoring during tests was facilitated by the InfraTec® VarioCAM® hr IR camera, having a microbolometric detector with a pixel resolution of 640 × 480 pixels. To ensure precise temperature measurements, specimens were coated with black matt heat-resisting silicone enamel with an emissivity of 0.98. These measures ensured controlled conditions and accurate data collection throughout the experimental procedure. Specimens were subjected to cyclic loading in a fully reversed bending mode at a constant frequency of 30 Hz. The average of force amplitudes ($\overline{P}_{max}$), with values ranging from 47 N to 70 N in 23 steps, were varied to observe changes in the maximum self-heating temperature on the specimen surface, corresponding to the defined ROI1 in numerical simulations, which occurred near the bakelite holder. The force was converted to stress using the cantilever beam stress formulas recommended for thin composite laminates:

$$\sigma = \frac{6\overline{P}_{max}L}{bH^2}. \tag{25}$$

5.2. Comparison of numerical and experimental results

The comparison between numerical simulations and experimental results aimed to assess the effectiveness of the developed numerical model under three stress levels, as depicted in Fig. 21. Considering the computational constraints linked to the small time increment (i.e., 8.3 ms) and its consequential effect on simulation duration, the analyses were limited to a maximum of 30,000 load cycles. It is evident that relative self-heating temperatures exponentially increase from the beginning up to 10,000 cycles in both experiments and simulations. However, the discrepancies in values are notable within this loading range. Numerical results consistently indicated lower temperature values compared to experimental data. This inconsistency between numerical simulations and experimental measurements is attributed to the assumption of a constant force amplitude throughout the simulations (i.e., similar to the low-frequency fatigue testing facilities), contrasting with decreasing the force amplitude applied by the shaker within load cycles (as illustrated in Fig. 22). Notably, as the number of cycles increased, the discrepancy between both sets of results diminished. This convergence became evident between both numerical and experimental results as the temperature stabilization was achieved after several thousand cycles, wherein the tested specimen typically tolerates prolonged load cycles.

6. Thermomechanical fatigue of the PMC under fully reversed bending

6.1. Constructing S–N curve

To construct the semi-logarithmic *S–N* curve, the force data captured by the force sensor (e.g., shown in Fig. 22) was postprocessed. The highest peak force within each cycle was identified, and the average of these peaks was calculated as the force amplitude ($\overline{P}_{max}$ or $\overline{P}_{min}$, with equal magnitudes). The stress amplitude was then derived from the force amplitude using Eq. (25).

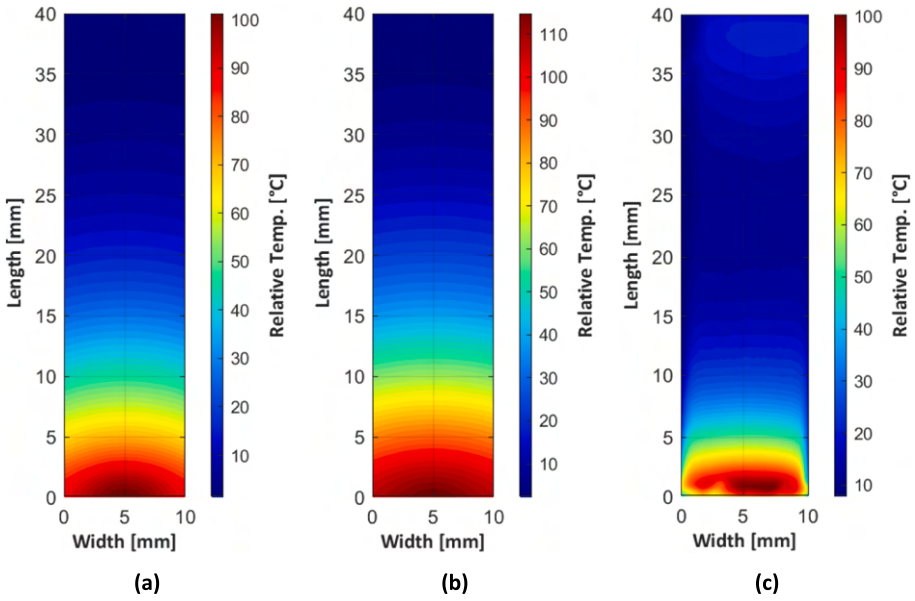

Fig. 15. Relative temperature profiles on the specimen surface from (a) simulations including radiation, (b) simulations excluding radiation, and (c) experiment.

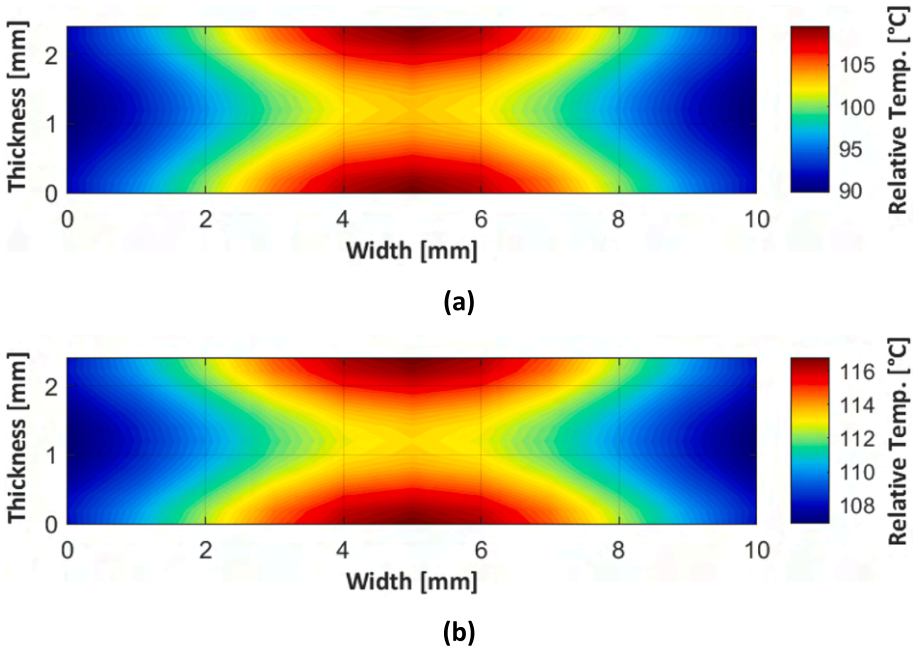

Fig. 16. Relative temperature profiles near the clamp from numerical simulations: (a) with radiation, and (b) without radiation.

Constructing a semilog-linear *S–N* model across a broad spectrum of fatigue cycles requires numerous experiments, which is a time-consuming task. Therefore, the conducted constant amplitude tests (CATs) were limited to half a million fatigue cycles in this study. The semi-logarithmic *S–N* curve in Fig. 23 shows the CAT results extracted until sudden failure, subjected to fully reversed bending. The equation derived from the regression curve fitting procedure on the experimental *S-N* data yielded a determination coefficient (R^2) of 0.934.

6.2. Thermomechanical fatigue response

In addition to establishing *S-N* curve as a measure of mechanical fatigue response in the tested PMC, it is crucial to comprehend its thermomechanical fatigue response. Prior investigations have primarily concentrated on the stabilized self-heating temperature increase of the PMCs. For this purpose, the thermographic approach (i.e.,$T-\sigma$ curve) has been widely implemented to estimate the fatigue strength of PMCs [17,61]. In $S-N$ domain, the term of fatigue strength denotes the stress threshold causing sudden failure within specified cycles, while in the stabilized temperature-based thermographic approach, it indicates the stress level correlated with changes in thermal response resulting from accumulating fatigue damage [4,61]. Nonetheless, in the present study, analyzing the registered self-heating temperature curves under the specific fatigue loading conditions illustrated three key terms: (i) the rise in the stabilized self-heating temperature compared to the ambient temperature (i.e., ΔT_{sa}), (ii) the variation between the maximum temperature recorded by the IR camera at the abrupt failure and the stabilization temperature (i.e., ΔT_{fs}), and (iii) the difference between the maximum temperature at the sudden failure and the ambient temperature, which are outlined by Eqs. (26)–(28) and illustrated in Fig. 24.

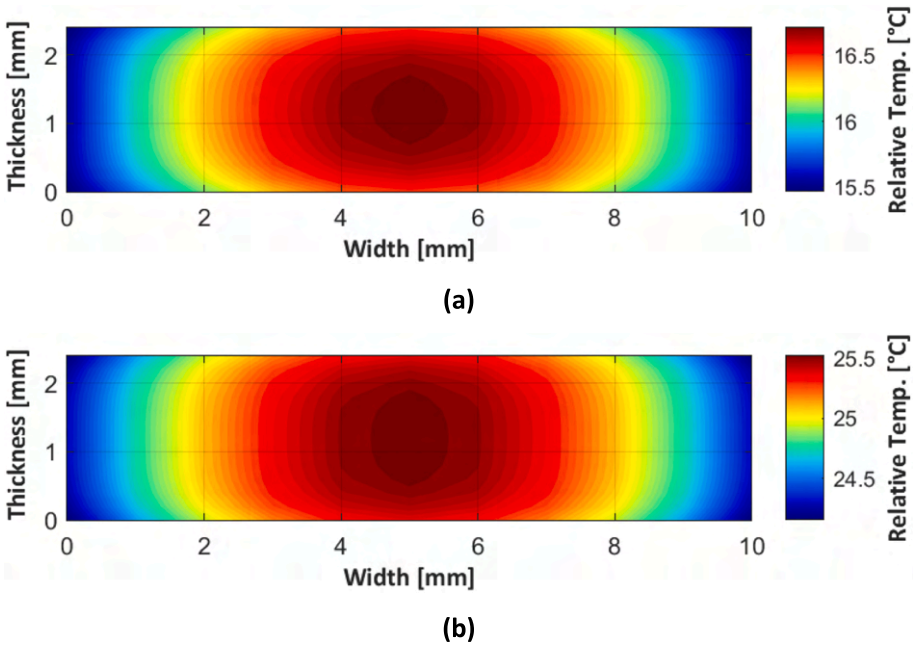

Fig. 17. Relative temperature profiles at the midsection from numerical simulations: (a) with radiation, and (b) without radiation.

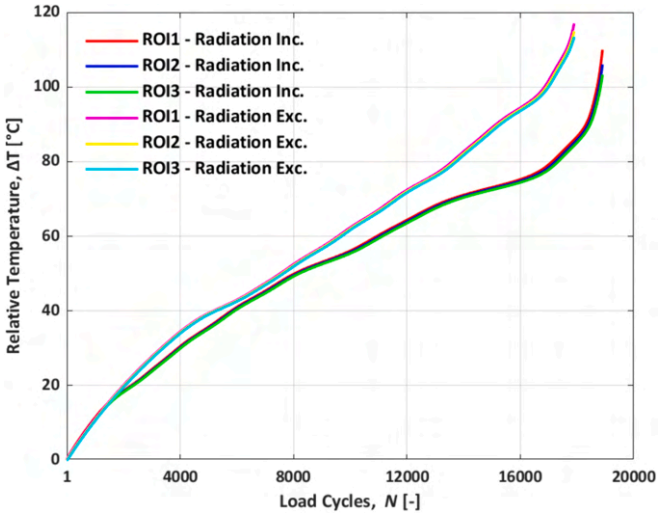

Fig. 18. Temperature evolution for ROIs 4 to 6 versus load cycles, including and excluding the influence of radiation.

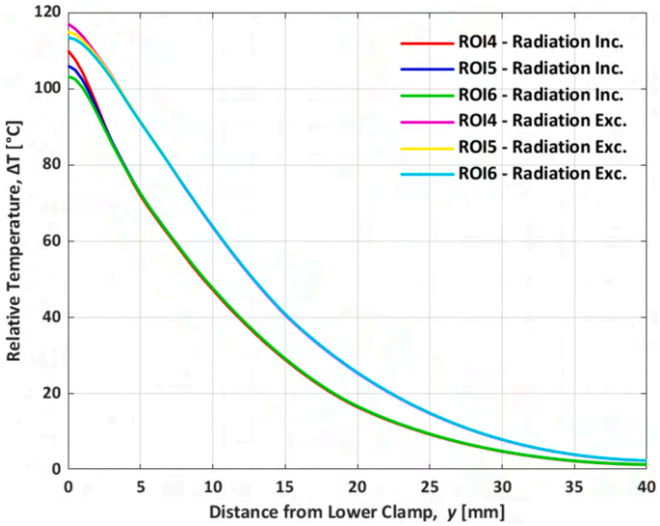

Fig. 19. Temperature rise for ROIs 4 to 6 with and without radiation's effect over load cycles.

$$\Delta T_{sa} = T_s - T_a, \tag{26}$$

$$\Delta T_{fs} = T_f - T_s, \tag{27}$$

$$\Delta T_{fa} = T_f - T_a, \tag{28}$$

where T_a is the ambient temperature, T_s is the the stabilized self-heating temperature, and is the maximum registered temperature on the specimen surface during fatigue testing.

The temperature profiles corresponding to different stress amplitudes until sudden failure are presented in Fig. 25. It was observed that enhancing the relative self-heating temperature (ΔT_{sa}) significantly reduces the residual life of tested PMCs. For example, raising ΔT_{sa} from 8 °C to 11.3 °C limited the lifespan from $444 \bullet 10^3$ to $247 \bullet 10^3$ load cycles, while an increase to 13.5 °C reduced it by approximately five times to $85 \bullet 10^3$ load cycles. With a temperature increase of 20 °C, the specimen could endure only $50 \bullet 10^3$ load cycles, whereas with a 30 °C increase, it could endure merely $19 \bullet 10^3$ load cycles. Therefore, the greater stabilized self-heating temperature resulting from higher stress amplitude shortened the duration of the second phase, making a larger portion of the process occur in the third phase.

Linear regression was employed to model the three aforementioned parameters represented by Eqs. (26)–(28) in relation to the stress amplitude (see Fig. 26). The slopes of the regression lines, along with the determination coefficient R^2, are detailed in Table 2. The analysis illustrated that the slope of the fitted line for ΔT_{fs} is marginally greater than that of ΔT_{sa}, maintaining a constant vertical offset of 11.3 °C for ΔT_{fs} above ΔT_{sa}. Furthermore, the slope of the regression line for ΔT_{fa} is roughly double that of both ΔT_{sa} and ΔT_{fs} individually, and is equivalent to the sum of both.

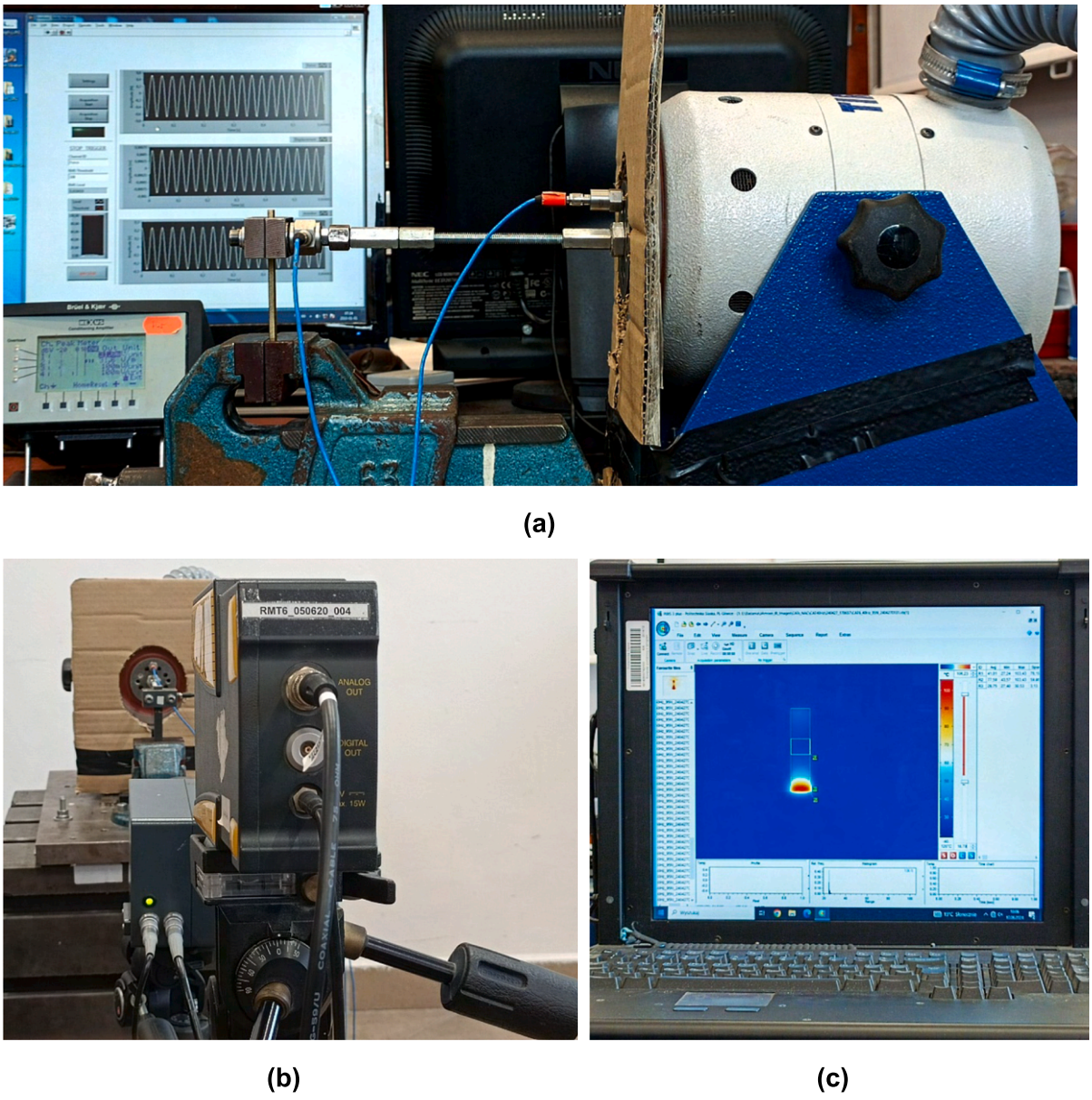

Fig. 20. Experimental test-rig: (a) and (b) Clamped specimen with measurement devices and control setup, and (c) PC and IR software.

6.3. Residual flexural stiffness under thermomechanical conditions

Determining the flexural stiffness D is prioritized due to its direct influence on measuring the bending behavior and structural integrity. Analyzing the residual flexural stiffness of typical PMCs in a cantilever beam configuration subjected to fully reversed fatigue bending in the presence of the self-heating effect highlights the complex and mixed interplay between mechanical integrity and thermal response. To mathematically estimate this parameter, the displacement amplitude W_{max} can be first computed using Eq. (8). Given the negligible heat generation resulting from pure shear strain in ROI3 shown in Figs. 13 and 14, the shear term in Eq. (8) can then be disregarded for simplicity. Rewriting Eq. (8) allows for the determination of the residual modulus E_y as a function of force P_{max} and displacement amplitudes for a thin laminated composite per load cycle:

$$E_y(T,f) = \frac{L^3}{3I}\left(\frac{P_{max}}{W_{max}}\right)_{cycle}. \tag{29}$$

The residual stiffness of a tested PMC can ultimately be determined by:

$$D(T,f) = \frac{E_y(T,f)H^3}{12\left(1-\nu_{xy}\nu_{yx}\right)}, \tag{30}$$

where ν_{yx} is the longitudinal Poisson's ratio given in Table 1, and ν_{xy} can be achieved through:

$$\nu_{xy} = \frac{E_x}{E_y}\nu_{yx}. \tag{31}$$

The study investigated the interaction between residual flexural stiffness and fatigue cycles across eight stress amplitudes, ranging from 201.75 MPa to 285.04 MPa, in the presence of self-heating, as depicted in Fig. 27. The results showed a correlation among the stress amplitude, fatigue cycle, and residual flexural stiffness of the PMC. A consistent pattern emerged, revealing a decline in residual flexural stiffness with increasing fatigue cycles across all stress amplitudes. Lower stress amplitudes exhibited a more gradual decrease in flexural stiffness, indicating relatively higher resistance to thermomechanical fatigue-induced degradation. However, higher stress amplitudes exhibited a more

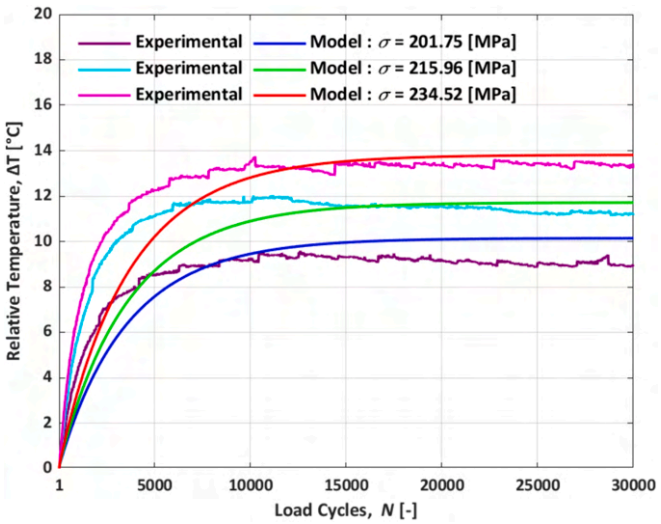

Fig. 21. Comparison of extracted results from the numerical model and experiments at three load levels.

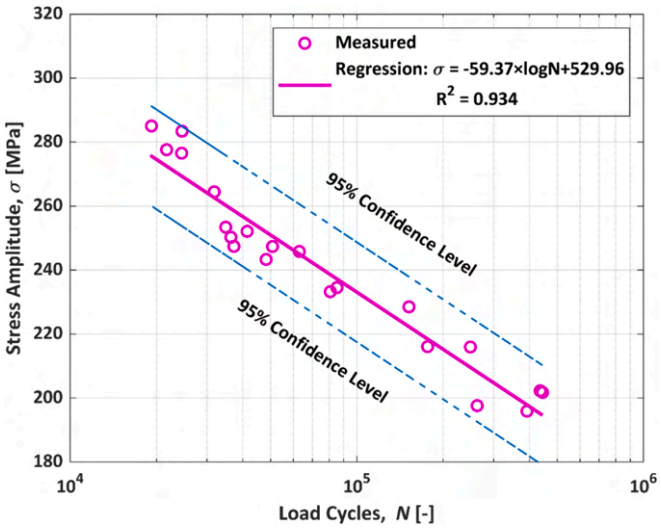

Fig. 23. *S-N* curve estimated at loading frequency of 30 Hz under fully reversed fatigue bending.

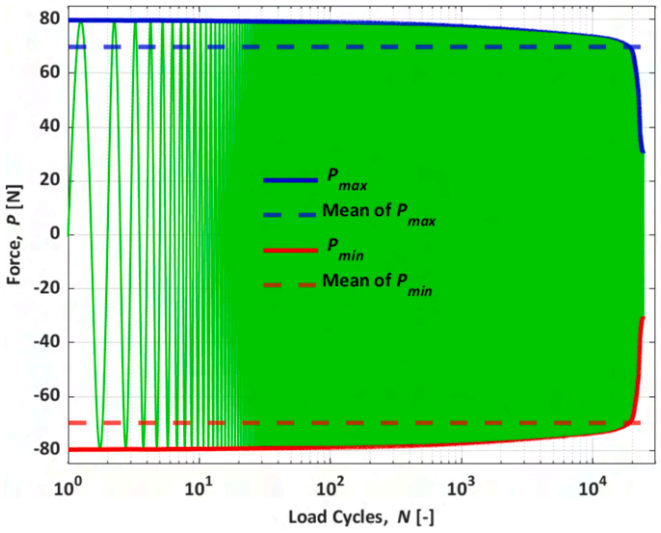

Fig. 22. Exemplary illustration of force data recorded by the force sensor (depicted in green) alongside the calculated mean force amplitude derived from the identified maximum peak force within each cycle.

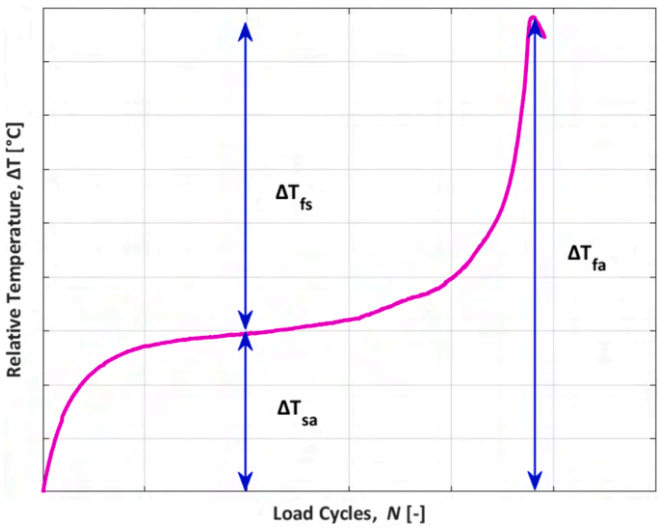

Fig. 24. Schematic illustration of three key characteristics in analyzing the thermomechanical fatigue response of the PMC.

pronounced reduction in residual flexural stiffness, resulting from accelerated fatigue damage. Furthermore, higher stress amplitudes intensified the self-heating temperature, see. Fig. 26, thereby accelerating molecular mobility and consequently leading to crosslinking degradation of polymer chains, fiber–matrix debonding, delamination, and ultimately fiber breakage according to the literature.

7. Discussion

Results obtained from the implemented numerical simulation provided a deeper understanding of the self-heating temperature distribution across the thickness of a tested PMC and highlighted the impact of radiation heat flux. In thin PMCs, like the one tested with a thickness of 2.4 mm under high-stress amplitude, the temperature variation between the surface near the clamp (ROI1) and the neutral axis (ROI2) remained under 4 °C when the radiation effect was considered, and below 7 °C when radiation effect was excluded. This indicates that the surface temperature measurement suffices for thin-tested PMCs, as confirmed across ROIs 1 to 6. However, for thicker specimens, this temperature difference may be more pronounced and necessitates consideration in future investigations. The absence of radiative heat flux in the simulations led to increased temperature values across all ROIs due to reduced heat dissipation into the environment. However, the incorporation of radiation effects into numerical models significantly enhanced the accuracy of temperature predictions, highlighting its importance in capturing real-world thermomechanical fatigue behavior.

Furthermore, *S-N* curve was constructed for the fully reversed bending conditions in our study, offering comprehension of the PMC's mechanical fatigue response. Our experimental setup also allowed us to observe the thermomechanical fatigue response of the tested PMCs. Moreover, three different key features were introduced for a better understanding of the relation between the applied stress amplitude and the thermal response, see Fig. 24 and Eqs. (26)–(28). The increase in relative stabilized self-heating temperature (ΔT_{sa}) as found to significantly reduce the residual life of the tested PMCs. In other words, a higher stabilized self-heating temperature resulting from the increased stress amplitude drastically shortened the duration of the second phase, which is pivotal in fatigue characterization as it typically involves a longer load duration for the tested PMC. Linear regression analysis revealed useful

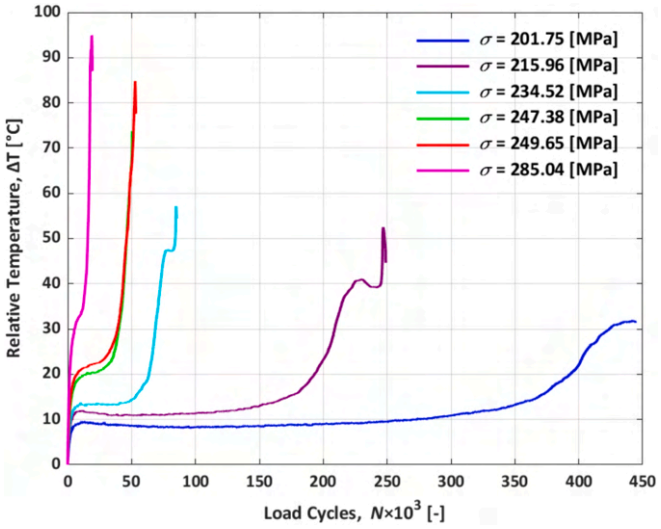

Fig. 25. Temperature profile evolution until the abrupt failure, measured under different stress amplitudes.

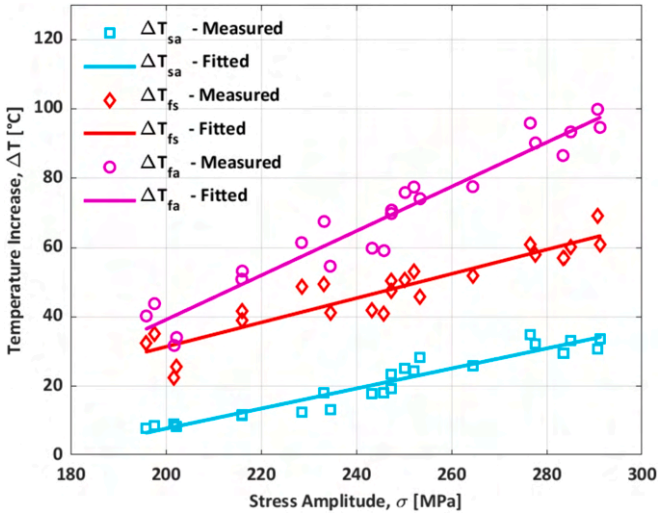

Fig. 26. Temperature rise versus applied stress amplitude.

Table 2
Relationship between temperature variation and stress amplitude.

Regression line equation	R^2
$\Delta T_{sa} = 0.29\sigma - 50.03$	0.922
$\Delta T_{fs} = 0.35\sigma - 38.71$	0.846
$\Delta T_{fa} = 0.64\sigma - 88.74$	0.933

relationships between the mentioned three thermal parameters (see Eqs. (26)–(28)) and the applied stress amplitude. The slopes of the regression lines for ΔT_{sa}, ΔT_{fs} and ΔT_{fa} were determined. The slope of the regression line for ΔT_{fa} was roughly double that of ΔT_{sa} and ΔT_{fs} individually, highlighting a synergistic effect of stress amplitude on thermal response. Such linear regression models are feasible for stress levels above the fatigue limit or fatigue strength. However, if the applied stress levels cover a wide spectrum, including below the fatigue limit as well, implementing a bilinear model similar to the thermographic approach (i.e.,$T-\sigma$) is recommended. Additionally, a correlation among stress amplitude, fatigue cycle, and residual flexural stiffness was identified, highlighting the relationship between mechanical integrity and thermal

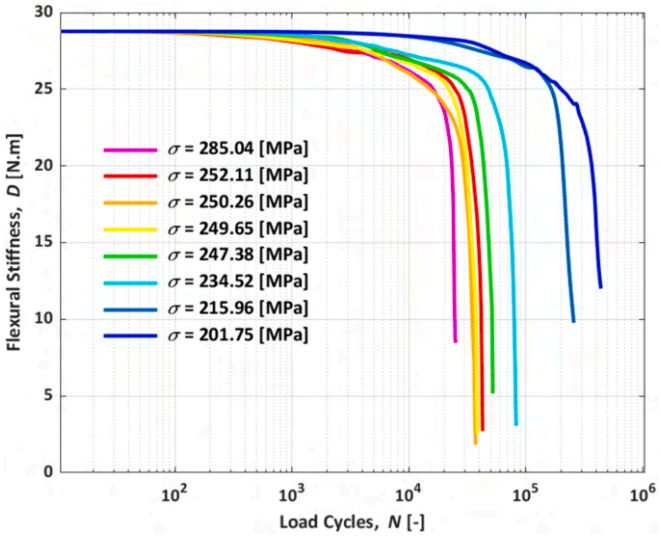

Fig. 27. Residual flexural stiffness resulted from applied stress amplitudes.

effects. The decrease in residual flexural stiffness as fatigue cycles increase, especially under higher stress amplitudes, emphasized the key role of self-heating in accelerating stiffness degradation.

8. Conclusions

This study shed light on better understanding the complex thermo-mechanical fatigue behavior of PMCs, with particular attention given to the issue of self-heating. The synergy between experimental characterization and numerical modeling has led to valuable achievements in deeper comprehension of the phenomenology of self-heating in fatigue-loaded PMCs.

The results highlighted the necessity of considering radiative heat flux as an environmental factor for accurately determining self-heating temperatures in numerical models. The study revealed that the temperature variation across the thickness remained minimal in thin PMCs, thus confirming the sufficiency of surface temperature measurements for the thin-tested PMCs.

Moreover, the experimental results demonstrated a correlation between the stress amplitude, and three key relative self-heating temperatures (i.e. ΔT_{sa}, ΔT_{fs}, and ΔT_{fa}) of the tested PMCs. Additionally, a correlation between fatigue lifetime and residual flexural stiffness under different stress amplitudes was identified, emphasizing the role of self-heating in accelerating stiffness degradation.

These findings offer useful guidance for a better understanding of the self-heating phenomenon, enhancing predictability, improving the accuracy of numerical modeling, and ultimately mitigating thermal fatigue in structural PMCs in the future. The findings are also crucial for designing durable PMCs in structural applications. Accurate simulation of temperature distributions aids in the excitation of the tested specimen using a multi-harmonic vibrational signal to uniformly distribute the self-heating temperature on the tested specimen surface for its damage inspection using the developed self-heating based vibrothermography (SHVT) technique.

CRediT authorship contribution statement

Jafar Amraei: Writing – review & editing, Writing – original draft, Validation, Software, Methodology, Investigation, Funding acquisition, Formal analysis, Data curation, Conceptualization. **Andrzej Katunin:** Writing – review & editing, Writing – original draft, Methodology, Investigation, Conceptualization. **Magdalena Lipińska:** Writing – review & editing, Investigation.

Declaration of competing interest

The authors declare that they have no known competing financial interests or personal relationships that could have appeared to influence the work reported in this paper.

Data availability

Data will be made available on request.

Acknowledgements

The publication is supported under the Excellence Initiative – Research University Program of the Silesian University of Technology, grant no. 32/014/SDU/10-22-48, year 2022.

Appendix

Table A.1. Prony parameters extracted for the thermoviscoelastic modeling of glass/epoxy composite

i	τ_i [ms]	g_i [−]
1	5.815E-03	0.0218
2	9.679E-09	0.0002
3	1.154E+03	0.0075
4	6.138E+02	0.0081
5	2.941E-06	0.0121
6	3.409E-08	0.0138
7	1.154E+03	0.0075
8	6.137E+02	0.0081
9	6.795E-01	0.0367
10	4.751E-07	0.0122
11	1.154E+03	0.0075
12	6.137E+02	0.0081
13	3.530E-04	0.0190
14	1.399E-09	0.0149
15	5.946E+01	0.0076
16	6.139E+02	0.0081
17	3.544E-02	0.0201
18	2.226E-11	0.0233
19	5.946E+01	0.0076
20	6.138E+02	0.0081
21	3.486E-05	0.0169
22	6.106E-06	0.0030
23	1.154E+03	0.0075
24	6.133E+02	0.0081
25	1.167E+03	0.0075
26	1.149E+03	0.0075
27	1.154E+03	0.0075
28	6.138E+02	0.0081
29	9.111E+01	0.0074
30	1.580E+02	0.0074
31	6.365E+01	0.0074
32	1.118E+03	0.0073
33	1.582E+02	0.0074
34	1.030E+02	0.0074
35	6.365E+01	0.0074
36	1.423E+03	0.0089
37	1.581E+02	0.0074
38	1.580E+02	0.0074
39	8.722E+03	0.0211
40	1.424E+03	0.0089
41	1.884E+03	0.0123
42	1.884E+03	0.0123
43	8.722E+03	0.0211
44	3.774E+02	0.0089

References

[1] Ming Y, Duan Y, Zhang S, Zhu Y, Wang B. Self-heating 3D printed continuous carbon fiber/epoxy mesh and its application in wind turbine deicing. Polym Test 2020;82:106309.
[2] Tongchitpakdee C, Benjanirat S, Sankar LN. Numerical simulation of the aerodynamics of horizontal axis wind turbines under yawed flow conditions 2005; 127:464–74.
[3] Zorko D, Tavčar J, Bizjak M, Šturm R, Bergant Z. High cycle fatigue behaviour of autoclave-cured woven carbon fibre-reinforced polymer composite gears. Polym Test 2021;102:107339.
[4] Amraei J, Katunin A. Recent advances in limiting fatigue damage accumulation induced by self-heating in polymer-matrix composites. Polymers 2022;14(24): 5384.
[5] Voudouris G, Di Maio D, Sever IA. Experimental fatigue behaviour of CFRP composites under vibration and thermal loading. Int J Fatigue 2020;140:105791.
[6] Charalambous G, Allegri G, Hallett SR. Temperature effects on mixed mode I/II delamination under quasi-static and fatigue loading of a carbon/epoxy composite. Compos A Appl Sci Manuf 2015;77:75–86.

[7] Katunin A, Wachla D. Minimizing self-heating based fatigue degradation in polymeric composites by air cooling. Proc Struct Integr 2019;18:20–7.
[8] Gagani AI, Monsås AB, Krauklis AE, Echtermeyer AT. The effect of temperature and water immersion on the interlaminar shear fatigue of glass fiber epoxy composites using the I-beam method. Compos Sci Technol 2019;181:107703.
[9] Knoll J, Riecken BT, Kosmann N, Chandrasekaran S, Schulte K, Fiedler B. The effect of carbon nanoparticles on the fatigue performance of carbon fibre reinforced epoxy. Compos A Appl Sci Manuf 2014;67:233–40.
[10] Wang C, Chen X, Cheng L, Ding J. High-cycle and very-high-cycle fatigue properties of CFRP-aramid honeycomb sandwich structure in three-point bending. Int J Fatigue 2022;155:106576.
[11] Katunin A, Wachla D, Santos P, Reis PN. Fatigue life assessment of hybrid bio-composites based on self-heating temperature. Compos Struct 2023;304:116456.
[12] Katunin A, Bilewicz M, Wachla D, Amraei J, Viana J. Investigation of fracture mechanisms of self-reinforced polypropylene/polycarbonate composites subjected to fatigue loading. Materials Science Forum. 2022. Trans Tech Publ. 1075: p. 65-70.
[13] Backe D, Balle F. Ultrasonic fatigue and microstructural characterization of carbon fiber fabric reinforced polyphenylene sulfide in the very high cycle fatigue regime. Compos Sci Technol 2016;126:115–21.
[14] Tao Y, Stevens CA, Bilotti E, Peijs T, Busfield JJ. Fatigue of carbon cord-rubber composites: effect of frequency, R ratio and life prediction using constant life models. Int J Fatigue 2020;135:105558.
[15] Vassilopoulos AP. The history of fiber-reinforced polymer composite laminate fatigue. Int J Fatigue 2020;134:105512.
[16] Katunin A, Pivdiablyk I, Gornet L, Rozycki P. A hybrid method for determination of fatigue limit and non-destructive evaluation of composite structures after low-velocity impact loading. Compos B Eng 2022;238:109898.
[17] Premanand A, Rogala T, Wachla D, Amraei J, Katunin A, Khatri B, et al. Fatigue strength estimation of a CF/PEKK composite through self-heating temperature analysis using cyclic bending tests at 20 kHz. Compos Sci Technol 2023;243:110218.
[18] Grammatikos SA, Kordatos EZ, Matikas TE, Paipetis AS. On the fatigue response of a bonded repaired aerospace composite using thermography. Compos Struct 2018;188:461–9.
[19] Katunin A, Wachla D. Analysis of defect detectability in polymeric composites using self-heating based vibrothermography. Compos Struct 2018;201:760–5.
[20] Katunin A, Wronkowicz-Katunin A, Wachla D. Impact damage assessment in polymer matrix composites using self-heating based vibrothermography. Compos Struct 2019;214:214–26.
[21] Fard MY, Raji B, Pankretz H. Correlation of nanoscale interface debonding and multimode fracture in polymer carbon composites with long-term hygrothermal effects. Mech Mater 2020;150:103601.
[22] Katunin A, Krukiewicz K, Turczyn R. Evaluation of residual cross-linking caused by self-heating effect in epoxy-based fibrous composites using Raman spectroscopy. Chemik 2014;68(11):957–66.
[23] Amraei J, Jam JE, Arab B, Firouz-Abadi RD. Effect of interphase zone on the overall elastic properties of nanoparticle-reinforced polymer nanocomposites. J Compos Mater 2019;53(9):1261–74.
[24] Amraei J, Jam JE, Arab B, Firouz-Abadi RD. Modeling the interphase region in carbon nanotube-reinforced polymer nanocomposites. Polym Compos 2019;40(S2):E1219–34.
[25] Zhang T, Lin S, Yuk H, Zhao X. Predicting fracture energies and crack-tip fields of soft tough materials. Extreme Mech Lett 2015;4:1–8.
[26] Zhao X. Multi-scale multi-mechanism design of tough hydrogels: building dissipation into stretchy networks. Soft Matter 2014;10(5):672–87.
[27] Zhang W, Hu J, Tang J, Wang Z, Wang J, Lu T, et al. Fracture toughness and fatigue threshold of tough hydrogels. ACS Macro Lett 2018;8(1):17–23.
[28] Rose M, Niverty S, Schmidt B, Kästner M, Zimmermann M, Chawla N. X-ray computer tomography (XCT) of fatigue damage in laser-machined versus milled carbon fiber reinforced polymer matrix composites. Eng Fract Mech 2021;252:107820.
[29] Colombo C, Vergani L. Influence of delamination on fatigue properties of a fibreglass composite. Compos Struct 2014;107:325–33.
[30] Colombo C, Bhujangrao T, Libonati F, Vergani L. Effect of delamination on the fatigue life of GFRP: A thermographic and numerical study. Compos Struct 2019;218:152–61.
[31] Guo Q, Guo X, Fan J, Syed R, Wu C. An energy method for rapid evaluation of high-cycle fatigue parameters based on intrinsic dissipation. Int J Fatigue 2015;80:136–44.
[32] Katunin A, Wronkowicz A, Bilewicz M, Wachla D. Criticality of self-heating in degradation processes of polymeric composites subjected to cyclic loading: a multiphysical approach. Arch Civil Mech Eng 2017;17(4):806–15.
[33] Turczyn R, Krukiewicz K, Katunin A. Spectroscopic evaluation of structural changes in composite materials subjected to self-heating effect. Compos Struct 2018;204:192–7.
[34] Katunin A, Krukiewicz K. Physicochemical analysis of self-heating of glass-epoxy composites cured by novolac. Chemik 2012;66:1326–31.
[35] Di Maio D, Voudouris G, Sever I. Investigation of fatigue damage growth and self-heating behaviour of cross-ply laminates using simulation-driven dynamic test. Int J Fatigue 2022;155:106617.
[36] Demleitner M, Albuquerque RQ, Sarhadi A, Ruckdäschel H, Eder MA. Bayesian optimization-based prediction of the thermal properties from fatigue test IR imaging of composite coupons. Compos Sci Technol 2024;248:110439.
[37] Ly M, Khan KA, Muliana A. Modeling self-heating under cyclic loading in fiber-reinforced polymer composites. J Mater Eng Perform 2020;29(2):1321–35.
[38] Sevenois RD, Hao P, Van Paepegem W, Gilabert FA. Numerical study on the effect of matrix self-heating on the thermo-visco-plastic response of continuous fiber-reinforced polymers under transverse tensile loading. Polymers 2022;14(10):1941.
[39] De Lima A, Rade D, Lacerda H, Araújo C. An investigation of the self-heating phenomenon in viscoelastic materials subjected to cyclic loadings accounting for prestress. Mech Syst Sig Process 2015;58:115–27.
[40] Sapozhnikov S, Shabley A, Ignatova A. Predicting the kinetics of hysteretic self-heating of GFRPs under high-frequency cyclic loading. Compos Struct 2019;226:111214.
[41] Ignatova A, Bezmelnitsyn A, Olivenko N, Kudryavtsev O, Sapozhnikov S, Shavshina A. Prediction of GFRP self-heating kinetics under cyclic bending. Mech Compos Mater 2023:1–16.
[42] Huang J, Garnier C, Pastor M-L, Gong X. Investigation of self-heating and life prediction in CFRP laminates under cyclic shear loading condition based on the infrared thermographic data. Eng Fract Mech 2020;229:106971.
[43] Lahuerta F, Nijssen R, Van Der Meer F, Sluys L. Experimental–computational study towards heat generation in thick laminates under fatigue loading. Int J Fatigue 2015;80:121–7.
[44] Ferry JD. Viscoelastic properties of polymers. third ed. John Wiley & Sons. New York; 1980.
[45] Krauklis AE, Akulichev AG, Gagani AI, Echtermeyer AT. Time–temperature–plasticization superposition principle: predicting creep of a plasticized epoxy. Polymers 2019;11:1848.
[46] Abouhamzeh M, Sinke J, Jansen K, Benedictus R. Kinetic and thermo-viscoelastic characterisation of the epoxy adhesive in GLARE. Compos Struct 2015;124:19–28.
[47] Fazekas B, Burkhart C, Staub S, Thielen S, Andrä H, Goda TJ, et al. Radial shaft seals: How ageing in oil and hyper-viscoelasticity affect the radial force and the numerically predicted wear. Tribol Int 2023;186:108601.
[48] Ahmed AM, Rifai AM. Euler-bernoulli and timoshenko beam theories analytical and numerical comprehensive revision. Euro J Eng Technol Res 2021;6(7):20–32.
[49] Huang J, Yang H, Liu W, Zhang K, Huang A. Confidence level and reliability analysis of the fatigue life of CFRP laminates predicted based on fracture fatigue entropy. Int J Fatigue 2022;156:106659.
[50] Dinzart F, Molinari A, Herbach R. Thermomechanical response of a viscoelastic beam under cyclic bending; self-heating and thermal failure. Arch Mech 2008;60(1):59–85.
[51] Hajshirmohammadi B, Khonsari M. An approach for fatigue life prediction based on external heating. Int J Mech Sci 2021;204:106510.
[52] Acikgoz O, Kincay O. Experimental and numerical investigation of the correlation between radiative and convective heat-transfer coefficients at the cooled wall of a real-sized room. Energ Build 2015;108:257–66.
[53] Ignatova A, Bezmelnitsyn A, Olivenko N, Kudryavtsev O, Sapozhnikov S, Shavshina A. Prediction of GFRP self-heating kinetics under cyclic bending. Mech Compos Mater 2023;58(6):787–802.
[54] Kalogiannakis G, Van Hemelrijck D, Van Assche G. Measurements of thermal properties of carbon/epoxy and glass/epoxy using modulated temperature differential scanning calorimetry. J Compos Mater 2004;38(2):163–75.
[55] Katunin A, Wachla D. Determination of fatigue limit of polymeric composites in fully reversed bending loading mode using self-heating effect. J Compos Mater 2019;53(1):83–91.
[56] Lopes H, dos Santos JA, Katunin A. Identification of material properties of a laminated plate from measurements of natural frequencies and modal rotations. Proc Struct Integrity 2019;17:971–8.
[57] Izo-Erg SA. Measurement of thermal conductivity and coefficient of thermal expansion of glass/epoxy plates. Internal Document 2008.
[58] Franck A. Evaluation of the correct Modulus in Rectangular Torsion. TA-Instruments application note APN024 V2. https://www. tainstruments. com/pdf/literature/APN024. pdf.
[59] Abdoh D, Zhang Y, Ademiloye A, Kodur V, Liew K. Modeling of heating and cooling behaviors of laminated glass facades exposed to fire with three-dimensional flexibilities. Compos Struct 2023;314:116961.
[60] Kothari R, Hemmingsen CS, Voigt NV, La Seta A, Nielsen KK, Desai NB, et al. Numerical and experimental analysis of instability in high temperature packed-bed rock thermal energy storage systems. Appl Energy 2024;358:122535.
[61] Amraei J, Rogala T, Katunin A, Premanand A, Kokot G, Wachla D, et al. Thermomechanical fatigue behavior of CF/PEKK composite under low and ultrasonic frequencies. Compos B Eng 2024;281:111539.

Paper IV

Thermomechanical fatigue behavior of CF/PEKK composite under low and ultrasonic frequencies

Composites Part B 281 (2024) 111539

Contents lists available at ScienceDirect

Composites Part B

journal homepage: www.elsevier.com/locate/composites

Thermomechanical fatigue behavior of CF/PEKK composite under low and ultrasonic frequencies

Jafar Amraei [a], Tomasz Rogala [a], Andrzej Katunin [a,*], Aravind Premanand [b], Grzegorz Kokot [c], Dominik Wachla [a], Wacław Kuś [c], Marcin Bilewicz [d], Bilal Khatri [b], Frank Balle [b,e,f]

[a] Department of Fundamentals of Machinery Design, Faculty of Mechanical Engineering, Silesian University of Technology, Konarskiego 18A, Gliwice, 44-100, Poland
[b] Department for Sustainable Systems Engineering (INATECH), Faculty of Engineering, Albert-Ludwigs-Universität Freiburg, Freiburg, 79110, Germany
[c] Department of Computational Mechanics and Engineering, Faculty of Mechanical Engineering, Silesian University of Technology, Konarskiego 18A, Gliwice, 44-100, Poland
[d] Department of Engineering Materials and Biomaterials, Faculty of Mechanical Engineering, Silesian University of Technology, Konarskiego 18A, Gliwice, 44-100, Poland
[e] Freiburg Materials Research Center (FMF), Freiburg, 79110, Germany
[f] Fraunhofer Institute for High Speed Dynamics, Ernst Mach Institute (EMI), Freiburg, 79110, Germany

ARTICLE INFO

Keywords:
Polymer-matrix composites (PMCs)
Fatigue
Thermal analysis
Heat dissipation
Fractography

ABSTRACT

This study aimed to extract the thermomechanical fatigue behavior of a CF/PEKK composite under low and ultrasonic frequency fatigue tests (LFFTs and UFFTs) in the presence of the self-heating effect. Preliminary increasing amplitude tests (IATs) were performed to obtain the minimum load level at which the self-heating is observable. Extracting the fatigue strength from T-σ curves for three mean stress levels resulted in constructing S-N curves for the LFFT regime at different load levels using a shift procedure. However, combining LFFT and UFFT results via S-N curve was impractical, while joining such results through the heat dissipation rate ($\dot{q}$) was feasible for various constant amplitude tests and IATs. The derived σ-$\dot{q}$ curves from combining LFFT and UFFT results and comparing the fracture mechanisms of CF/PEKK composite using fractography would make a step for bridging the transition zone between LFFTs and UFFTs and making the results transferable. The microscopy images obtained from fractography also confirmed the similarities of fatigue fracture mechanisms between LFFTs and UFFTs.

1. Introduction

Polymer-matrix composites (PMCs), such as carbon and glass fiber reinforced polymers (CFRPs and GFRPs) are increasingly gaining attention in the fields of energy and transportation (e.g., e-vehicles, aviation and wind power plants) due to their superior strength- and stiffness-to-weight ratios, excellent durability, good environmental resistance and design flexibility [1,2]. Nevertheless, such structures are still over-designed because of the absence of knowledge to guarantee the nonoccurrence of remarkable fatigue damage accumulation over prolonged fatigue loading [3]. This is due to a lack of knowledge on the structural behavior of PMCs after billions of fatigue loading cycles and how this relates to their well-established low-cycle fatigue behavior. To evaluate such behavior, prolonged testing is necessary.

Fatigue life assessment of PMCs in the very-high-cycle-fatigue (VHCF) (i.e. 10^7 or above) at conventional loading frequency, i.e., 5 Hz or below is impractical. For example, performing a single fatigue experiment up to 10^9 cycles will take more than 6 years at cyclic frequency of 5 Hz., which is approximately one-fifth of the typical service lifetime of an aircraft [4].

To address this issue and perform the fatigue experiments at a feasible time, an accelerated ultrasonic fatigue technique can be implemented [5–7]. However, the question of the compatibility of VHCF at ultrasonic frequency with high-cycle fatigue (HCF) at conventional frequencies (up to 50 Hz) still remains open. A particular problem in the evaluation of such compatibility is the presence of the self-heating effect.

1.1. Self-heating effect in PMCs

When cyclic stress is applied to a PMC, the strain response comes with a phase lag due to the viscoelastic nature of polymers or vice versa. The heat generated due to hysteresis leads to temperature increase

* Corresponding author.
E-mail address: andrzej.katunin@polsl.pl (A. Katunin).

https://doi.org/10.1016/j.compositesb.2024.111539
Received 23 December 2023; Received in revised form 11 April 2024; Accepted 7 May 2024
Available online 10 May 2024

on the specimen surface under fatigue loading, termed as self-heating effect. This phenomenon consists of three phases [2,8]. In phase I, a rapid temperature growth occurs on the specimen surface after some fatigue cycles, the rate of which is dependent on the applied stress/strain level. This is followed by a stabilized self-heating temperature with an almost constant value for most of the test duration (phase II). This stabilized temperature is proportional to the applied stress loading [9]. Within the final phase (phase III), the self-heating temperature suddenly increases, corresponding to the fatigue damage accumulation and thermal fatigue failure [10]. This degradation process, in the presence of the self-heating effect, is driven by numerous parameters such as material properties (e.g., mechanical stiffness, thermomechanical properties) and fatigue loading parameters (e.g., loading frequency, stress ratio, mean stress) [10]. In the case of ultrasonic frequency fatigue test (UFFT), the influence of the self-heating effect is even more evident [8,11], and therefore, the steps to avoid overheating of the tested specimen need to be considered. For this purpose, the authors of [5,12] implemented a pulse-pause sequence and forced air cooling to minimize the influence of self-heating temperature, which allows performing a fatigue test up to 10^9 cycles in 12 days.

The structural performance of the PMC subjected to fatigue loading was described by the critical self-heating temperature in previous studies [13,14] as a material property. For a typical fatigue test, the critical self-heating temperature is defined as the temperature interval at which rapid damage propagation begins. Above this threshold, i.e., in the non-stationary self-heating regime occurring within the third phase [10], the failure of the specimen is dominated by thermal effects. The phenomenon of self-heating and the determination of its criticality interval were studied by several research groups using various physical quantities (see, e.g., [15]). The sensitivity of various approaches regarding structural changes that appeared after exceeding the self-heating temperature were presented in [16].

1.2. Dependency of fatigue behavior of PMCs on loading parameters

Regardless of the type of PMCs, their fatigue behavior can be influenced by the environmental conditions (e.g. ambient temperature, humidity) [17–19] and loading parameters (e.g. direction of applied loading, stress ratio, mean stress, and frequency) [12,20,21]. For this purpose, several studies have investigated the fatigue behavior of GFRP specimens under axial loading at different stress ratios (R) and low frequencies (≤15 Hz) [22–25]. The authors of the mentioned studies reported that increasing R at the same stress level led to longer fatigue life, while the slope of S-N curve dropped with more scattered responses. Additionally, different R resulted in different damage distributions. Damage was uniformly distributed along the specimens under $R = 0.5$, while damage zones were severe and localized at $R = 0.1$ and caused continuous stiffness degradation. Numerous researchers studied the effect of frequency on the fatigue behavior of the PMCs. They reported a decrease in the fatigue lifespan with increasing testing frequencies (up to 100 Hz) due to the self-heating effect [21,26–31]. However, Adam and Horst [32] conducted fatigue tests on glass/epoxy specimens at a low-frequency range (25–50 Hz). They observed that similar fatigue lives at those two frequencies by maintaining the increase of self-heating temperature (up to 15 °C).

1.3. Thermodynamic-based method for estimating the fatigue strength

Constructing a conventional S-N curve for a PMC requires many experiments at different load levels, which is time-consuming and costly [33]. To address this issue, Rosa and Risitano [34] developed an accelerated thermodynamic-based method for estimating the fatigue strength of materials, known as the temperature-stress (T-σ) curve based on stabilized self-heating temperature (phase II). This approach requires more advanced facilities (e.g., the IR camera) to capture the thermal response of the fatigue-loaded specimen.

The fatigue limit, typically derived from S-N curve, represents the maximum stress threshold below which structural integrity remains unaffected and endure an infinite number of cycles. However, S-N curves obtained for composite materials usually do not exhibit a fatigue limit [35]. The conventional fatigue limit term can be replaced by the fatigue strength for PMCs to address this issue. This term within S-N domain is defined as a stress level above which sudden failure occurs under specific cycles. For the thermographic approach, it is the stress level above which a change in the thermal response is observed arising due to fatigue damage accumulation. Therefore, capturing the benefits of both approaches is of primary importance. Numerous researchers implemented the thermographic approach (i.e., T-σ curve) for estimating the fatigue strength of PMCs [33,36–41].

The authors in [8] recently used this approach to evaluate the fatigue strength of a CF/PEKK composite under three-point (3P) bending at the ultrasonic frequency. In another study, Katunin et al. [38] developed a hybrid approach by taking advantage of rapid Risitano's model as well as the non-destructive testing technique based on self-heating developed previously within the group in order to estimate the fatigue strength values and identify damage of CFRP and GFRP composites at different applied impact energies. They later determined the fatigue strength of hybrid bio-composites (i.e., glass/flax, Kevlar/flax, and carbon/flax) with the aim of critical self-heating temperature and acoustic emission methods and justified the obtained results through fracture mechanisms analysis using microscopy [14]. These studies prove this approach's effectiveness for determining fatigue strength.

1.4. Comparability of fatigue results at different loading frequencies

The loading frequency during fatigue testing can greatly influence the fatigue behavior of the material under test. Fatigue tests below a loading frequency of 100 Hz, termed low-frequency fatigue tests (LFFTs), which are usually force-controlled, can show contrasting results compared to ultrasonic frequency fatigue tests (UFFTs). The latter is usually carried out in a displacement-controlled manner at loading frequencies of 20 kHz in a pulse-pause pattern, leading to effective loading frequencies of up to 3 kHz. A few studies implemented both techniques for the same PMCs with similar stacking sequences to understand how the results extracted from these test systems are comparable. Ueki [42] compared the fatigue performance of the plain-woven glass/epoxy specimens using the developed accelerated cantilever bending fatigue test (ACBFT) at a loading frequency of 230 Hz and 1 Hz. All the tests were performed at $R = -1$. They extracted S-N curves from three testing conditions for conventional frequency fatigue tests (CFFTs): (i) at room temperature (20–25 °C), (ii) ACBFT at low temperature (specimen: 8–15 °C; ambient: 0 °C), and (iii) ACBFT at high temperature (specimen: 40–60 °C; ambient: 30 °C). They demonstrated that the fatigue strength obtained from ACBFT declined by approximately 10% to 20% at a higher temperature than room temperature. They also reported that the fatigue behavior of the specimens under CFFTs and ACBFTs was quite similar under the appropriate temperature control on the specimen surface.

Lee et al. [7] conducted a large number of fully reversed axial fatigue experiments on glass/polyamide (GF30/PA66) specimens at room temperature (RT) at both conventional (3 Hz) and ultrasonic (20 kHz) frequencies. CFFTs were conducted at stress levels of 35% up to 55% of the maximum yield strength, and UFFTs were carried out at 30% up to 40%. They used similar specimen geometry for CFFTs and UFFTs. The self-heating of the specimen for the UFFT experiments was limited by employing 300 ms pulse and 3000 ms pause times and an active thermoelectric cooler. Their findings show a comparatively lower slope for the UFFT results for the same stress levels. In another study, Flore et al. [43] performed experiments on the unidirectional glass/epoxy specimens using both conventional (10 Hz) and ultrasonic axial fatigue tests, with $R = 0.1$. They also reported a lower slope in S-N curve and a lower fatigue strength for UFFTs. Such a discrepancy may result from various types of damage (e.g., microcracks and fiber–matrix debonding) as well as the frequency-dependent cyclic softening of the matrix during UFFTs.

Table 1
Material properties of CF/PEKK laminate [8].

Fabric type	5H satin woven fabric
Ply thickness	0.31 ± 0.01 mm
Layup	$[0/90/0/90/0/90/\underline{0}]_s$
Areal density	280 g/m^2
Fiber volume fraction	50%
Glass transition temperature	160 °C
Melting temperature	337 °C
Ultimate tensile strength 0°	776 MPa
Ultimate compressive strength 0°	585 MPa
Specific heat	1425 J kg^{-1} K^{-1}

1.5. Motivation

Presently, limited studies have compared LFFT and UFFT results. These chiefly pertain to GFRP composites under axial fatigue loading. The comparability and transferability of fatigue results for composites between the LFFTs and UFFTs is challenging and still remains open for investigation. Nevertheless, the current state of knowledge presented in the background provides the motivation for this study, which aims to highlight the problem of transferability between the results obtained from LFFT and UFFT and offer a potential solution. This study aims to investigate an aerospace-relevant CF/PEKK composite material, compare its behavior under 3P bending LFFT and UFFT conditions, and report on the transferability of the results from CATs and IATs performed at vastly different loading frequencies. Additionally, the frequency and self-heating-related differences in thermomechanical behavior and fatigue fracture mechanisms are analyzed as the potential factors, allowing to elaborate a reliable frequency-independent fatigue strength estimation method in the further studies for CF/PEKK composite. This investigation would promote the interpretation of the thermomechanical fatigue behavior of a CF/PEKK composite under low and ultrasonic frequencies.

2. Specimens and testing methodologies

2.1. Specimens preparation

Laminates of carbon fibers in 5-harness satin fabric architecture with poly-ether-ketone-ketone (PEKK) as a polymer matrix were manufactured by Toray Advanced Composites (Nijverdal, The Netherlands) and used in this investigation. PEKK is a semi-crystalline polymer with a glass transition (T_g) and melting point (T_m) of about 160 °C and 340 °C, respectively. The manufacturer ultrasonically C-scanned the laminates to show a defect-free consolidation process. The composite laminate consists of 13 layers of fabrics symmetrically stacked in alternating 0° and 90° warp fiber orientations with a single 0° layer in the center. A laminate thickness of 4.1 mm was achieved after the consolidation process. More information on the composite material can be found in the previous studies by the authors [5,8]. Table 1 shows the material properties of the CF/PEKK laminate provided by the manufacturer.

The CF/PEKK specimens must be designed to be excited during resonance vibrations under transverse-bending eigenmode at an oscillation frequency of 20 kHz. Modal and harmonic analyses were conducted using Ansys Workbench software to determine the suitable specimen geometry for realizing ultrasonic cyclic bending with a 3P bending loading condition. A specimen volume of 34.0 × 15.0 × 4.1 mm^3 with a span length of 18.6 mm was thus adapted for fatigue testing at ultrasonic [5,8,44] as well as for low-frequency fatigue testing.

2.2. Low-frequency fatigue testing setup

CF/PEKK specimens were examined using constant and increasing amplitude tests using the electromechanical Instron ElectroPuls E10000 (High Wycombe, UK) test system with ±0.5% of the indicated load accuracy. All of the LFFTs were carried out in force control mode. The loading waveforms, according to Table 2, were established and controlled by the electromechanical testing system. An ambient temperature of 23 °C was maintained for the laboratory where the test system is located. The ambient temperature around the testing system was also monitored using the precision thermometer TM-917 (Lutron, Coopersburg, USA) with resistive probe PT-100. Observations of the surface temperature evolution of the specimens during testing were carried out using a VarioCAM hr infrared (IR) camera (Infratec, Dresden, Germany) with the Carl-Zeiss F1.0/focal length 50 mm lens. The IR images captured using the IR camera with a resolution of 640 × 480 pixels were initially pre-processed using Irbis 3 plus software (Infratec, Dresden, Germany) and finally exported to MATLAB (MathWorks, USA) environment for further data processing. The entire fatigue testing setup is presented in Fig. 1. The same specimen size was adapted for LFFTs and UFFTs under 3P bending loading conditions [8]. The fixture shown in Fig. 2 has the same span length (18.6 mm) and radius (5 mm) for the loading nose (5 mm), and the support shoulders used in UFFT system [8].

2.3. Testing procedure

According to the recommendations [10], fatigue experiments on GFRPs exposed to natural air cooling should be performed at the loading frequency below 10 Hz to make the influence of frequency on the self-heating temperature negligible, which decelerates the fatigue testing. Nevertheless, applying such a loading frequency on CF/PEKK composite seems conservative. The main causative factor contributing to this may be the higher thermal conductivity value of CF/PEKK composite compared to GFRPs. This plays a key role in dissipating greater heat into the surroundings, leading to a lower rate of internal heat storage and, consequently, a lower self-heating temperature on the specimen surface. For this purpose, IATs, as the initial trials, were conducted at the loading frequency ranging from 5 Hz up to 50 Hz in order to find the maximum loading frequency at which the self-heating temperature is primarily dominated by mechanical loading and not by loading frequency. It was observed that even at the upper limit of the interval (i.e., 50 Hz), the induced self-heating temperature by frequency was negligible. This allowed to accelerate the fatigue experiments and perform the entire LFFT experiments at 50 Hz.

The experimental procedure was proceeded by measuring the emissivity of the CF/PEKK specimens. An indirect technique using a reference material with known emissivity was implemented. The emissivity of the CF/PEKK, was than measured with the value of 0.91 ± 0.01 and then considered for all experiments.

The captured thermograms using an IR camera contain regions of interest (ROIs). The ROIs defined in LFFTs are presented in Fig. 3 and comprise five regions on its lateral face: the entire lateral face of the specimen (R4), the central region located at the bottom of lateral face (R1), the lateral regions close to the right and left side of the fixture (R2, R3) respectively, and the lateral region near the loading nose (R5). Due to the characteristics of the 3P bending test, the most interesting lateral region is (R1), while other ROIs were used to observe any potentially undesirable side effects (e.g., friction or movement of the specimen at low loads). For every ROI, the maximum temperature change was registered. Since no side effects have been observed in other ROIs during tests, only the maximum temperature from R1 was analyzed for further data processing within LFFT results. Similarly, the ROIs were defined in UFFTs. An example of the determined ROIs was discussed and presented in the paper [8].

The experimental testing procedure included two steps: conducting CATs and IATs. In the first step, CATs were performed at the mean load of 2.5 kN (283 MPa) for five different amplitudes (i.e., 2.25 kN (255 MPa), 2 kN (226 MPa), 1.8 kN (204 MPa), 1.5 kN (170 MPa) and 1 kN (113 MPa) up to one million loading cycles for constructing S-N curve, and consequently estimating the fatigue strength of CF/PEKK

Fig. 1. Test rig for LFFT.

Fig. 2. In-house designed fixture for 3P bending loading condition with broken CF/PEKK specimen.

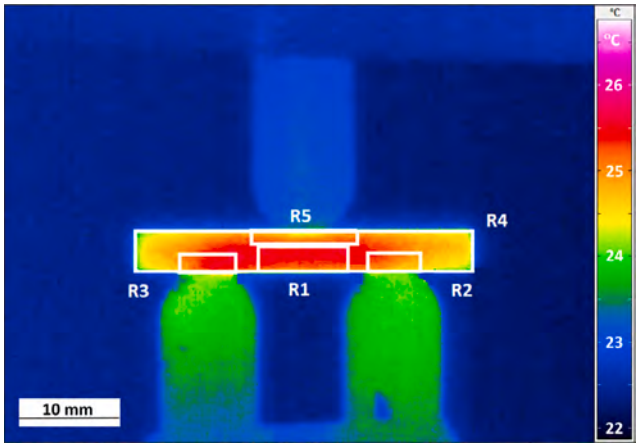

Fig. 3. ROIs defined on the exemplary thermogram registered during IAT-1B test.

composite in LFFT regime. Additionally, the CATs were used for building S-N curve consisting of LFFT and UFFT results. In the second step, IATs were first performed at the same mean load (i.e., 283 MPa) for combining the results from both LFFTs and UFFTs with the same mean force, as well as for validating the extracted fatigue strength from the thermographic approach (i.e., temperature-stress curve) with S-N curve.

For conducting IAT at the mean load of 283 MPa, 14 loading levels shown in Table 2 were considered to estimate the fatigue strength from the stress-temperature curve reliably. The applied forces within performing LFFTs have been converted to the maximal bending stress using the relation, referring to the recommendation by ASTM D7264/D7264M-15:

$$\sigma = 3/2\left(\frac{FL}{bh^2}\right) \tag{1}$$

where L, b, and h are the tested specimen's span length, width, and thickness. According to the preliminary test results from CATs, one specimen could not tolerate such load levels without fatigue failure. To address this issue, such load levels were divided into two groups and were equally applied to the two different specimens with the same mean force of 283 MPa (see the testing conditions in Table 2 for IAT-1A and IAT-1B). Additionally, to understand the influence of mean loading on the fatigue strength, IATs were performed for two more mean force values, i.e., 3 kN (340 MPa) and 3.5 kN (396 MPa). Based on the preliminary CATs and monotonic tests for compression failure mode [8], the level of maximum applied load should not exceed the ultimate compressive strength of the specimen. For this reason, 11 load levels were considered for the mean loads of 340 MPa and 396 MPa

Table 2
Settings for performing increasing amplitude tests (IATs) under loading frequency of 50 Hz.

Index	Initial load N [MPa]	Amp. load step N [MPa]	No. of steps [–]	ΔN [cycles]	Unloading duration between each Two Amp. levels [min]
IAT-1A	3300 [374.2]	200 [22.7]	7	$3.5{\cdot}10^4$	10
IAT-1B	3400 [385.6]	200 [22.7]	7	$3.5{\cdot}10^4$	10
IAT-2	3900 [442.2]	100 [11.3]	10	$3.5{\cdot}10^4$	10
IAT-3	4400 [498.9]	100 [11.3]	10	$3.5{\cdot}10^4$	10

with the same level of force step of 100 N or 11 MPa (IAT-2 and IAT-3, respectively). It should be mentioned that the number of cycles per loading block was set to 35 000, corresponding to a loading duration of 700 s. Derived from preliminary investigations, such a number of cycles was enough to achieve self-heating temperature stabilization. Furthermore, the unloading duration between the two loading blocks was set to 600 s to allow the tested specimen to return to the ambient temperature. Next, the IR camera was applied to register the thermal response in ROIs with the framerate of 1 Hz by acquiring the thermograms with a resolution of 480 × 640 pixels. The acquisition parameters of thermograms were as follows: distance from IR camera to the CF/PEKK specimen 0.47 m, emissivity 0.91, environmental and path temperatures 23 °C.

2.4. Ultrasonic frequency testing setup

The fatigue experiments at ultrasonic cyclic frequencies were carried out at the INATECH facility at the University of Freiburg. The ultrasonic fatigue test system consists of loading nose and support units with the same radius (R = 5 mm) as the LFFT system. An in-house test system constructed using the ultrasonic resonance components supplied by Herrmann Ultraschalltechnik GmbH, (Karlsbad, Germany) was used for testing the CF/PEKK specimens at frequencies of about 20.2 ± 0.02 kHz. The description of the UFT system for the 3P bending loading conditions can be found in the previous works performed by the authors [5,8,44]. The experiments are displacement-controlled since the cyclic loading is applied using the inverse piezoelectric effect with maximum cyclic displacement amplitude up to 57 μm [5]. Thus, only the mean displacements can be increased in order to increase the maximum displacements or stresses on the CF/PEKK material. In the previous investigation [8], a monotonic displacement of 150 μm was realized for all the fatigue experiments. In the current study, increasing amplitude experiments were performed at monotonic displacements of 250 μm, and 300 μm with a pulse and pause durations of 250 ms and 1500 ms, respectively. Furthermore, three constant amplitude experiments were performed at a monotonic displacement of 300 μm with pulse and pause durations of 50 ms and 300 ms. Thus, the effective frequency remains unchanged compared to the previous investigation [8].

2.5. Fractography

The fractographic analysis of the specimens after LFFT was performed on Leica DVM6 digital microscope (Weltzar, Germany) with the ring lighting and the magnification varying in the range of ×22 to ×500, depending on the observed defects. Additionally, the side lighting was applied to improve the visibility of the surface topography.

Initially, the images were collected as a Z stack, which was then converted into two-dimensional images using Leica Application Suite dedicated software to improve the depth of focus, which was especially important to visualize defects in specimens after LFFT. The specimens were initially tested with a microscope to check for any initial damage before starting LFFT. The only damage observed in undamaged specimens was the cracks on the boundaries resulting from cutting, which do not influence the development of damage mechanisms during LFFT.

The CF/PEKK specimens tested under ultrasonic loading conditions do not break into two halves, unlike the monotonic or LFFT experiments. This is because UFFT experiments are displacement-controlled and terminated after a global stiffness drop of ≈15% occurs in the presence of macroscopic damage, such as delamination. The failed specimens were embedded in epoxy. These epoxy samples were ground and polished using the Streurs LaboPol-30 system (Willich, Germany). A SiC #320 (fineness number) sheet was used to grind the specimen surface. MD-Largo and MD-DAC sheets were used to polish the surface of the CF/PEKK specimens for the standard polishing time recommended by Streurs. This procedure was already presented in the previous investigation of the authors and can be found in [5]. The prepared samples were then observed under a light optical digital microscope of type Zeiss Smartzoom 5 from Carl Zeiss AG (Oberkochen, Germany).

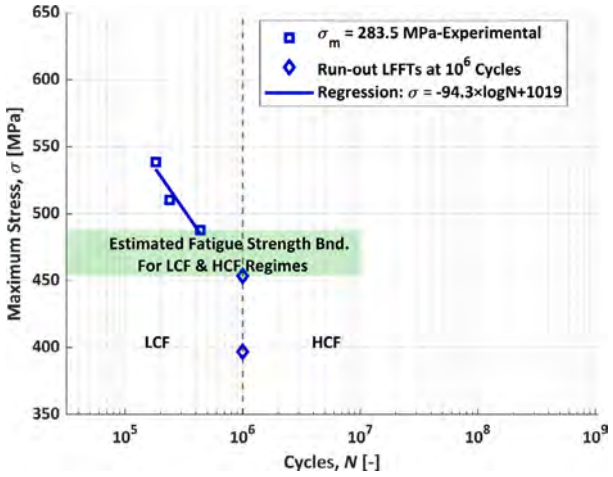

Fig. 4. *S-N* curve estimated for the mean stress of 283.5 MPa (2.5 kN) with the predicted zone of fatigue strength estimated based on LFFTs.

3. Results of fatigue tests

This section presents and discusses the acquired results and their analysis. In Section 3.1, the fatigue strength of a tested composite is first evaluated and validated in the LFFT regime based on analysis of *S-N* curves and IR-thermography approaches. In Section 3.2, the influence of mean load on the fatigue strength of the tested composite is assessed using a novel approach based on the IR-thermography. The derived shifting factors from the bilinear IR thermography curves are then implemented to construct *S-N* curve for further mean loads. Furthermore, in Section 3.3, the LFFT and UFFT results are compared regarding the critical self-heating temperature concept. In Section 3.4, the thermomechanical fatigue behavior of the CF/PEKK composite is characterized by combining the LFFT and UFFT results.

3.1. Fatigue strength estimation using *S-N* and IR-thermography

The logarithmic *S-N* curve in Fig. 4 shows the results of CATs for LFFT. The tests were conducted at 50 Hz under mean stress of 283 MPa until final failure or run-out when the number of cycles reaches 10^6 cycles, which is commonly recognized as a boundary between Low Cycle Fatigue (LCF) and High Cycle Fatigue (HCF) regimes.

Estimation of the full logarithmic *S-N* model in HCF or VHCF is a time-consuming process, which requires numerous sets of experiments

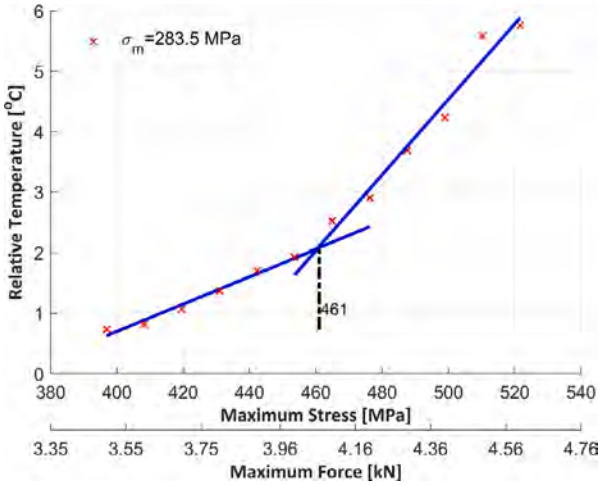

Fig. 5. Fatigue strength estimated for mean stress of 283.5 MPa (2.5 kN) in LFFTs.

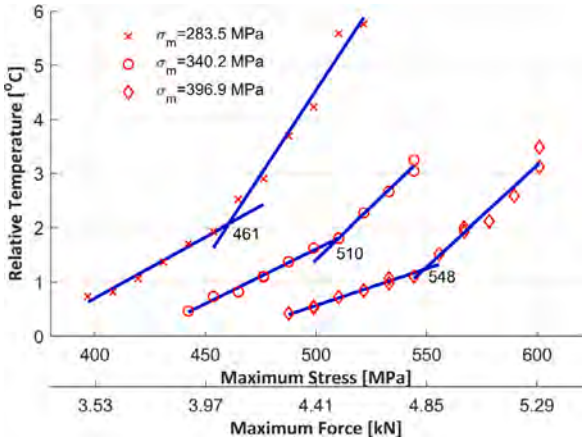

Fig. 6. Fatigue strengths estimated for mean stresses of 283.5 MPa (represented by (crosses), 340.2 MPa (circles), and 396.9 MPa (diamonds) in LFFT tests.

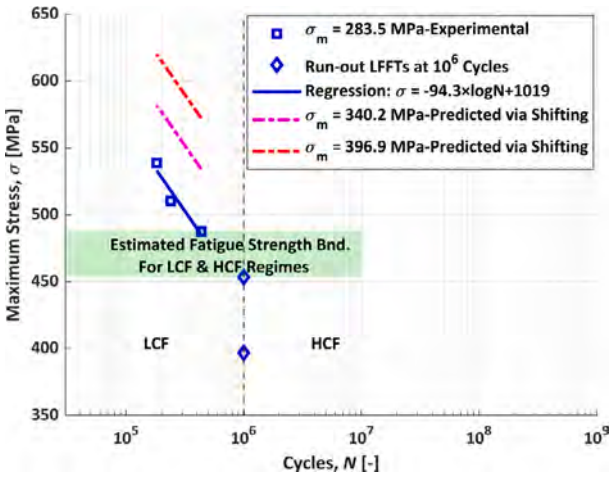

Fig. 7. Fatigue strength zone (i.e., the region between LCF and HCF) extracted from S-N curve under LFFTs for mean stress of 283.5 MPa, and shifting S-N curves for the mean stresses of 340.2 MPa (squares) and 396.9 MPa (circles) according to the values estimated from T-σ curves.

to obtain a model with appropriate statistical significance [35,45]. An alternative accelerated approach is a thermographic method, proved by many research studies [34,37,46–51], which, by the observation of the relative temperature changes for different stresses, allows acquiring information on fatigue-related behavior of composite materials [48].

The thermographic approach procedure requires performing IATs, for which stabilization of the self-heating temperature should be observed for different loads for an adequate period of time. Based on Luong's method [52] with some further modifications presented in [50], the temperature-stress (T-σ) diagram in this study has been constructed for two increasing amplitude tests, IAT-1A and IAT-1B, with the use of two tested specimens. Some points for lower loads with the limited ability to observe the thermal response in relation to noise level were omitted. The combined results of both tests can be observed in Fig. 5. The presented bilinear model was built using the minimum average Root Mean Square Error (RMSE) criteria [50] obtained for both lines of this model. The estimated fatigue strength at the intersection of both lines is 461 MPa, which refers to the applied load of 4.07 kN.

The comparison of the fatigue strength obtained from S-N curve for 50 Hz with the fatigue strength of 461 MPa and derived by the thermographic approach allows finding the corresponding fatigue cycles of $8.25 \cdot 10^5$ for the fatigue strength obtained using the thermographic approach.

3.2. The influence of mean stress effect on fatigue behavior

To extend the fatigue strength results to other conditions of fatigue experiments, e.g., the influence of different mean stress, it is essential to apply different shifting procedures or correction factors using various approaches. In the classical approach, to model the mean stress effect based on S-N curves and fatigue failure criteria [35], the effect can be modeled using different models defined in the domain of the Constant Life Diagrams (CLD). In CLDs the relation between the stress amplitude and the mean stress is not always linear [53]. In a further modification of this approach, S-N curves are collected for different constant stress ratios and finally, the mean stress effect is approximated using piecewise linear models [45,54] or any other nonlinear models [53,55–57]. These methods usually require more input data [35,45,55], which, in turn, requires performing numerous CATs. This section shows the concept of the implemented method for estimating the mean stress effect on estimating HCF strength based on the thermographic approach.

Fig. 6 presents T-σ diagram for different mean stresses: 283.5 MPa, which correspond to 2.5 kN, related to IAT-1A and IAT-1B data previously shown in Fig. 5, and also for 340 MPa (3.0 kN) based on the data from IAT-2, and 397 MPa (3.5 kN) using IAT-3 experimental data. Applying the same procedure as in the results presented in Fig. 5, bilinear models were constructed and fatigue strengths were estimated for the mean loads. The results are presented in Fig. 7 and correspond to 461 MPa, 510 MPa, and 548 MPa for subsequent mean stresses of 283 MPa, 340 MPa, and 397 MPa. The difference between the fatigue strengths derived for mean stress of 283 MPa (2.5 kN) and 340 MPa (3.0 kN) equals 49 MPa, while the difference between the fatigue strengths obtained for 340 MPa (3.0 kN) and 397 MPa (3.5 kN) equals 38 MPa. The differences between subsequent tests performed for different mean stress values were used as vertical shifting factors in the S-N model presented in Fig. 7. The presented shifting procedure is limited by ultimate strengths in the range of LCF of the analyzed composite.

3.3. Estimating the critical self-heating temperature interval for LFFT and UFFT

The concept of critical self-heating temperature was implemented in the previous studies by this research group [13,14,16] for damage evaluation in fatigue-loaded PMC specimens under the low-frequency regime. This indicates the temperature interval above which a noticeable thermomechanical change begins. This section aims to estimate

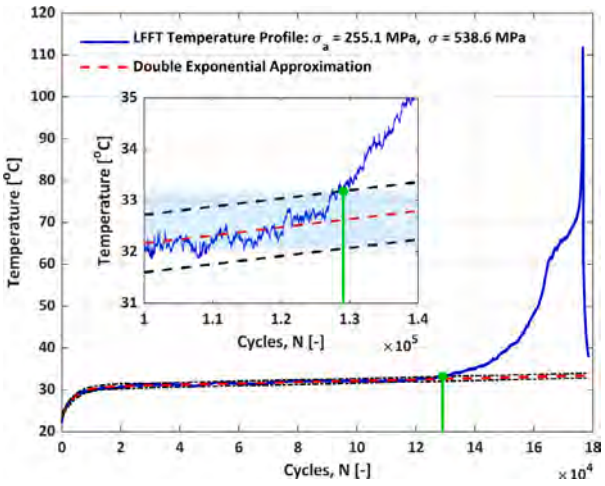

Fig. 8. Critical temperature analysis for LFFT with $\sigma_a = 255.1$ MPa and $\sigma = 538.6$ MPa. (For interpretation of the references to color in this figure legend, the reader is referred to the web version of this article.)

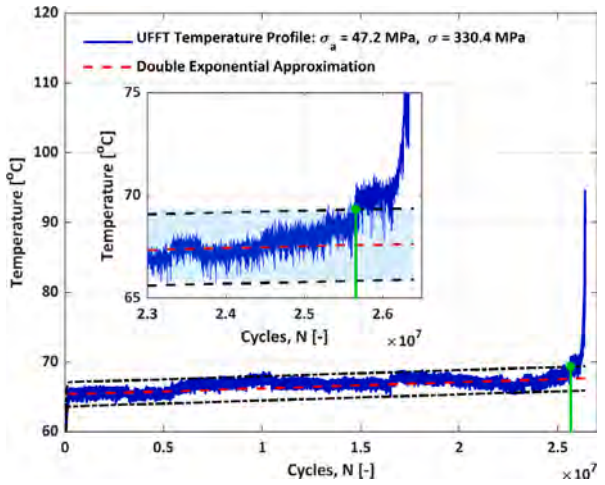

Fig. 9. Critical temperature analysis for UFFT with $\sigma_a = 47.2$ MPa and $\sigma = 330.7$ MPa. (For interpretation of the references to color in this figure legend, the reader is referred to the web version of this article.)

the critical self-heating temperature intervals for both LFFT and UFFT regimes. This allowed to evaluate how the obtained temperature intervals are comparable for both regimes. For this reason, the critical temperature intervals were estimated for CF/PEKK composite at the mean load of 283 MPa and three different stress amplitudes (σ_a) provided in Table 3 for both, LFFT and UFFT regimes.

The interval of critical self-heating temperature was identified based on a time series of temperature, which was extracted from thermograms registered during constant amplitude experiments of LFFT (Section 2.3) and UFFT (Section 2.4). In particular, the mentioned time series were formed using maximum temperatures from the ROI at the bottom center of the tested specimen (see Fig. 3) in both cases. Finally, a six series of self-heating temperatures (three series for each LFFT and UFFT) were obtained. Due to the sequenced structure, the UFFT time temperature series were preprocessed before estimating the critical self-heating temperature intervals. In particular, data samples with a maximum temperature value for each pulse-pause sequence were selected in order to form a new UFFT time temperature series, and the LFFT time–temperature series were used directly.

Identification of the interval for the critical self-heating temperature for each temperature time series was performed by means of

Table 3
Results of estimating critical self-heating temperature interval ranges for performed LFFT and UFFT constant amplitude experiments.

	σ_a [MPa]	σ [MPa]	L_{CT} [°C]	U_{CT} [°C]	N_{CT} [–]
LFFT	255.1	538.6	32.1	33.2	$1.29 \cdot 10^5$
	226.8	510.3	28.0	29.2	$1.37 \cdot 10^5$
	204.1	487.6	27.1	27.5	$1.30 \cdot 10^5$
UFFT	47.2	330.7	65.8	69.3	$2.57 \cdot 10^7$
	45.9	329.4	55.3	57.7	$4.82 \cdot 10^7$
	44.6	328.1	48.9	55.2	$2.37 \cdot 10^7$

double-exponential approximation (dashed red line in Figs. 8 and 9, respectively) [50]. This approach distinguishes three distinct phases of the self-heating temperature evolution. Two points were defined in the double-exponential approximation model. The first one indicates the end of the first phase, which can be determined directly using estimated parameters of the double-exponential model [50]. The second one indicates the end of the second phase and is recognized as a location, where the self-heating temperature profile begins deviating from the double-exponential approximation model (see Figs. 8 and 9). In [13,14,16], this temperature is defined as critical temperature, which is a function of different factors (e.g., number of cycles, stress levels) for the beginning of noticeable damage accumulation.

According to disturbances observed in self-heating temperature profiles (especially in temperature series from UFFTs), it is more rational to use an interval of the critical self-heating temperature instead of a single value reported in [13,14,16]. In this approach, the interval is indicated by two boundary values, which are the upper (U) and lower (L) symmetrical offsets (two dashed black lines in Figs. 8 and 9) from the double-exponential approximation. These are estimated in the following way:

$$L(N) = \hat{T}(N) - 3\,SD_{2nd} \tag{2}$$

$$U(N) = \hat{T}(N) + 3\,SD_{2nd} \tag{3}$$

where:

$$SD_{2nd} = \frac{1}{N_{2nd}}\sqrt{\sum \left(r(N_{2nd}) - \bar{r}(N_{2nd})\right)} \tag{4}$$

$$r(N_{2nd}) = \hat{T}(N_{2nd}) - T(N_{2nd}) \tag{5}$$

$$\bar{r}(N_{2nd}) = \frac{1}{N_{2nd}}\sum r_i(N_{2nd}) \tag{6}$$

and N is the number of fatigue cycles, N_{2nd} is the number of fatigue cycles in the second phase of self-heating evolution, $T(N)$ indicates the self-heating temperature profile, $\hat{T}(N)$ is the double-exponential approximation of self-heating temperature evolution. Based on above, the upper bound ($U(N)$) and $T(N)$ is used to find an intersection (green asterisk point in Figs. 8 and 9), which indicates the lower and upper offset of the critical self-heating temperature (i.e., the L_{CT} and U_{CT}), respectively, and corresponding number of fatigue cycles (N_{CT}).

This approach was applied to estimated intervals of the critical self-heating temperature for conducted LFFT and UFFT constant amplitude experiments. All the obtained results for CATs within LFFTs and UFFTs are presented in Table 3, and the exemplary results have been shown in Figs. 8 and 9. Results presented in Table 3 show that the range of the interval of the critical self-heating temperature is growing in accordance with the level of load amplitude σ_a. Looking at the obtained results, one can conclude the greater range of critical self-heating temperature interval for UFFTs compared to LFFTs (i.e., interval of 48.9–69.3 °C compared to 27.1–33.2 °C, respectively), despite applying the lower amplitude of stress within UFFTs. Such a discrepancy between the extracted intervals can be rooted in different loading frequencies, cooling conditions, etc. Therefore, the critical self-heating temperature concept for LFFT and UFFT regimes in 3P bending testing cannot be implemented directly and requires modification and further investigation. We refer to this issue in the next subsection by combining LFFT and UFFT with the concept of heat dissipation rate.

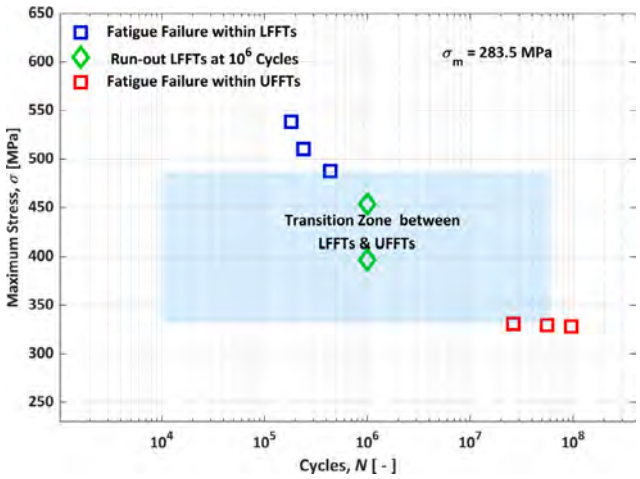

Fig. 10. Combining the fatigue behavior of CF/PEKK composite under LFFT and UFFT regimes through S-N curve.

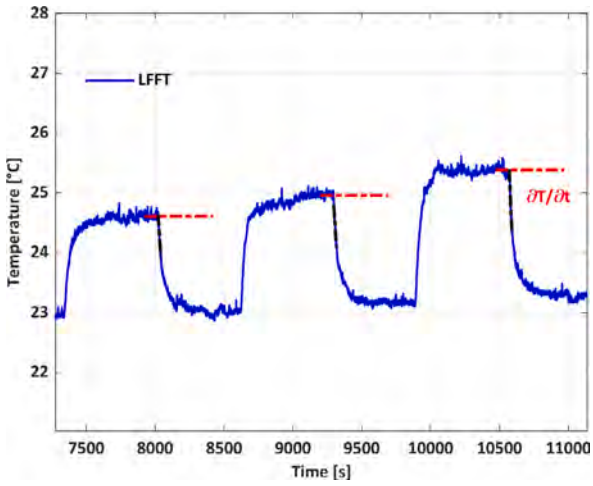

Fig. 11. The exemplary Temperature - Time response of L3000 (see Table 4) under stress amplitude 170.1 MPa, 181.4 MPa and 192.8 MPa for evaluating of heat dissipation rate in LFFT regime.

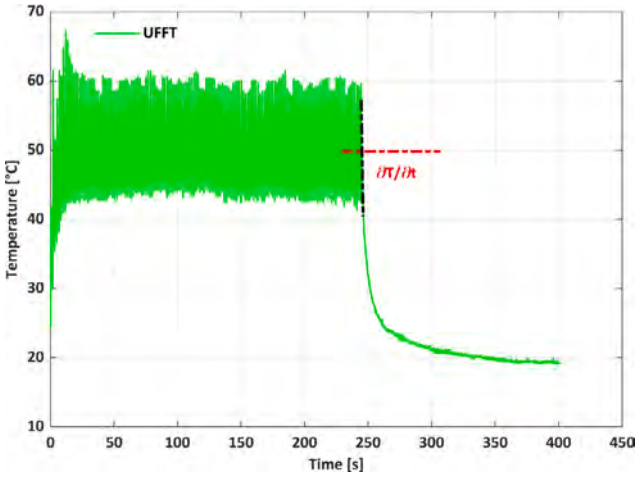

Fig. 12. The exemplary thermal response of U300 (see Table 4) under stress amplitude 44.6 MPa for determining heat dissipation rate in UFFT regime.

3.4. Combining LFFT and UFFT results for thermomechanical fatigue analysis

Due to the time-consuming nature of VHCF testing at low frequencies, a straightforward strategy consists of simultaneously utilizing UF and LF techniques to combine both test results and construct S-N curve. For this purpose, CATs were conducted on CF/PEKK composite specimens, subjecting them to various load amplitudes while maintaining a constant mean load of 283 MPa (2.5 kN or a static deflection of 300 μm), for up to 10^6 and 10^8 cycles within LF and UF techniques, respectively. The stress ratio range for CATs within LFFTs falls between 0.05 and 0.43, while this ratio for UFFTs spans from 0.71 to 0.72 (i.e., $0.05 \leq R_{LFFTs} \leq 0.43$, and $0.71 \leq R_{UFFTs} \leq 0.72$, respectively). The results are presented in Fig. 10. A vivid and primary outcome from the figure is a transition zone between LFFT and UFFT results. On one hand, constructing the transition zone through LF testing requires extensive testing time. On the other hand, technological limitations also restrict the application of higher loads in the UFFT technique.

A viable path can be found in the representation of the thermomechanical fatigue behavior of the CF/PEKK composite under both LF and UF experiments by utilizing the concept of heat dissipation rate. This approach quantitatively assesses the specimen's response subjected to fatigue loading. In prior investigation [8], the parameter $\dot{q}$ was assessed within the context of a non-stationary self-heating scenario at the pulse-pause boundaries for CATs, using the following equation:

$$\dot{q} = -\rho c \frac{\partial T}{\partial t} \tag{7}$$

where ρ is the mass density, c is the specific heat, T is the temperature, and t is time. In the current study, $\dot{q}$ is evaluated for the stationary self-heating regime, but at the end of each loading block, allowing for sufficient cooling of the tested specimen using the applied technology until the specimen's temperature approaches the ambient temperature (e.g., 23 °C for LFFTs). This mitigates the potential negative influence of additional surface-temperature rise led by frictional heat on the experimental setup, particularly in the case of UFFTs, and consequently enhances the accuracy of the obtained results. Figs. 11 and 12, respectively, illustrate the exemplary temperature history curves of LFFT and UFFT alongside their corresponding linear regressions, allowing us to determine the heat dissipation rate. According to the post-processing of the LFFT results, a constant window of 20 thermograms registered at a framerate of 1 Hz was considered for constructing the regression line. Performing similar post-processing for UFFT results, the constant window length of 48 thermograms acquired at the IR camera's 32 Hz framerate was adopted to align with the pause duration within each pulse-pause sequence similarly. Considering such constant window lengths for LFFTs and UFFTs provided high-accuracy results with reduced data scattering.

Heat dissipation rate ($\dot{q}$) is intrinsically dependent on several key variables, including loading frequency (f), oscillation displacement/force amplitude (δ_a/F_a), and the implemented cooling technique (CT). Distinguishing the effects of such parameters on the results obtained from LF and UF technologies is challenging. Among the mentioned factors, however, the mechanical loading from LF (forced control) and UF (displacement control) can be adopted using the oscillation displacement amplitude presented in [8] for the monotonic and dynamic test results. This adaptation assumes a negligible influence on the accuracy of the converted results. The influence of frequency and applied cooling technique (FCT) can be assumed and then determined as a combined and scalable factor, which makes results obtained for both LFFTs and UFFTs transferable and equivalent. This approach simplifies the interplay of such factors in the comparative analysis of LF and UF technologies.

To quantify the dependency of $\dot{q}$ on oscillation amplitude, a campaign of IATs was first performed with the same mean load of 283 MPa. The stress ratio range for IATs within LFFTs spans from 0.11 to 0.59, while this ratio for UFFTs varies between 0.67 and 0.88 (i.e., $0.11 \leq$

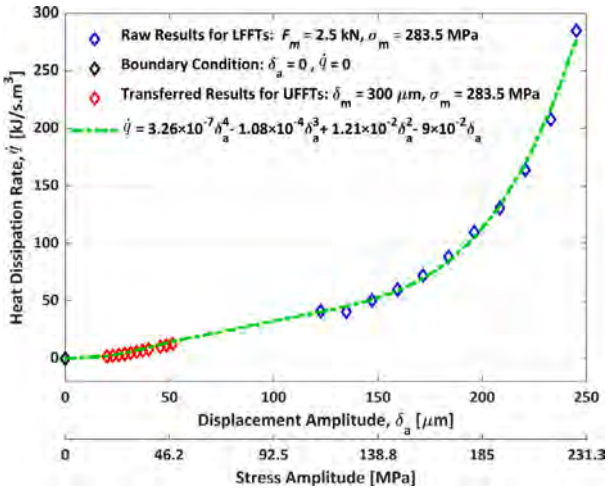

Fig. 13. The dependency of heat dissipation rate on loading amplitude within LFFT and UFFT regimes.

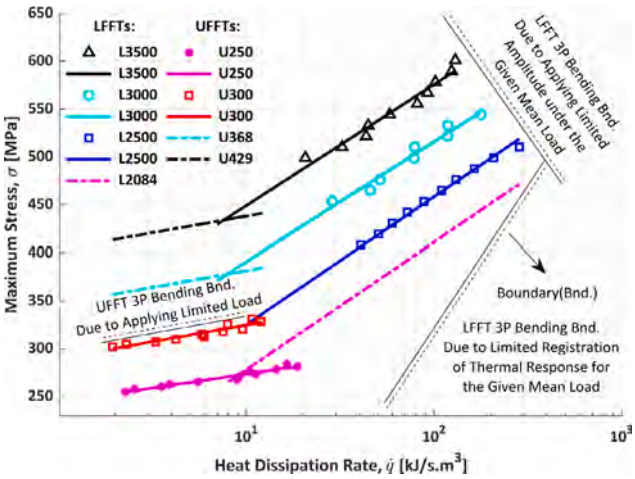

Fig. 14. Combining the thermomechanical fatigue behavior of CF/PEKK composite under LFFT and UFFT regimes through stress-heat dissipation rate curves. (For interpretation of the references to color in this figure legend, the reader is referred to the web version of this article.)

$R_{LFFTs} \leq 0.59$, and $0.67 \leq R_{UFFTs} \leq 0.88$, respectively). Applying such a wide range of loading provided a comprehensive coverage of the potentialities in performing 3P bending tests. This is crucial in characterizing the thermomechanical fatigue behavior of CF/PEKK composite under different stress conditions, aiding in understanding the durability, potential failure modes, and fracture mechanisms. The heat dissipation rate over the determined spectrum of transferred displacement amplitudes (utilizing the relationship between displacement and force) is presented in Fig. 13. Furthermore, it is assumed that the heat dissipation rate is negligible when the displacement amplitude is zero, denoted as $\delta_a = 0$, implying $\dot{q} = 0$ under such a condition. This zero-displacement scenario is considered the lower boundary condition (LBC), while data extracted from LFFTs performed at the higher displacement amplitudes are considered the upper boundary condition (UBC). Using LBC and UBC results, a quadratic fit (4th-order polynomial) was implemented to model $\dot{q}$ with satisfactory accuracy, yielding a RMSE of 4.4 kJ/s m^3 with the data obtained from LFFT experiments and LBC, as well as with the standard deviation (SD) of 3.57 kJ/s m^3.

Given that the available UF technique can apply the displacement amplitude in the range of 51.4 μm at 90 percent of power generation as the upper limit, located within the spectrum bounded by LBC and UBC, it is reasonable to infer that when conducting LFFTs within this specific amplitude range, the heat dissipation rate can predictably be estimated through the quadratic formula. The raw results for $\dot{q}$ obtained from UFFTs were divided by their counterparts derived from LFFTs, considering the same displacement amplitudes. This energy ratio, denoted by $\dot{q}_{ratio}$ as follows,

$$\dot{q}_{ratio} = \frac{\dot{q}_{UFFT}}{\dot{q}_{LFFT}} \tag{8}$$

This serves as an indicator of the cumulative effects of frequency and applied cooling technique. Noticeably, the average value of this ratio (i.e., $\dot{q}_{ratio}$) was calculated to be 2107. To put it another way, the FCT ratio signifies that the interplay of frequency and cooling system in UFFT accelerates the heat dissipation rate by a factor of 2107 compared to conducting the same test with LFFT system. Following this adjustment, the combination of frequency and cooling technique can be regarded as a unified and scalable factor in the analysis of heat dissipation rate.

To analyze the thermomechanical fatigue behavior of the CF/PEKK composite, the tested specimens were subjected to various mean and amplitude loads (see Tables 2 and 4). Considering the above-mentioned assumptions and applying $\dot{q}_{ratio}$, the heat dissipation rate for an equivalent mean load of 283 MPa was first evaluated based on results from IATs for both LFFT (2.5 kN) and UFFT (300 μm), demonstrated by the blue and red squares in Fig. 14, respectively. The test conditions are presented in Table 4. It should be mentioned that the applied mean load of 283 MPa, represents slightly over one-third of the CF/PEKK ultimate strength (811 MPa [5]), which is insufficient for the comprehensive thermomechanical fatigue characterization of such a composite. To address this, the capabilities/boundaries of performing 3P bending testing using both low and ultrasonic frequency techniques have been illustrated in Fig. 14. As can be extracted from Fig. 14, the UFFT technique offers the opportunity to apply a lower level of mean load, while the LFFT method provides the opportunity to apply a higher level of mean load. By implementing such benefits, both higher and lower mean loads were applied to the tested specimens. UFFTs were performed under the highest possible mean load of 283 MPa (300 μm) and the lower mean load of 236 MPa (250 μm). Both applied mean loads enabled the thermal response registration using an IR camera. On the other side, according to the preliminary LFFT results, the lowest amplitude load that registered a thermal response was 102 MPa (900 N), while the amplitude load level leading to failure below 10^6 cycles was 240 MPa (1.8 kN). As the limitation of conducting 3P bending testing, the applied amplitude loading must not exceed the mean load value. Considering such limitations regarding the testing technique and the necessity for thermal response registration, the tested specimens were additionally applied to higher mean loads (i.e., 340 MPa and 397 MPa) using the LFFT technique. Taking the advantages of UFFTs, the thermomechanical fatigue behavior of σ-$\dot{q}$ curve was predicted for LFFTs for the lower mean load of 236 MPa (i.e., 2.08 kN or 250 μm). Using LFFTs, by contrast, σ-$\dot{q}$ curves were predicted for higher mean loads of 340 MPa and 397 MPa (368 μm and 429 μm), which surpass the capabilities of existing UFFT technology.

3.5. Fractographic analysis

The results of the fractographic analysis demonstrated fracture mechanisms typical for the applied loading and investigated composites. The propagation of a crack in the normal direction to the surface where the loading was applied was accompanied by extended delaminations at different depths, which were mostly propagated through the matrix-reinforcement interface. The selected images of the failed specimens are presented in Fig. 15. In one of the tested cases (see Fig. 15(c)), the transverse matrix crack was observed for the unbroken specimen after LFFT (the runout), which demonstrates the influence of shear loading during LFFT.

Table 4
Defining the annotations for LFFTs and UFFTs.

Anno	LFFTs (50 Hz)	Anno	UFFTs (20 kHz)
L3500	F_m = 3.5 [kN], δ_m = 429 [μm], σ_m = 396.9 [MPa] Predicted by: $\sigma = 126.5 \cdot \log(\dot{q}) + 322.7$ [MPa]	U250	δ_m = 250 [μm], F_m = 2.08 [kN], σ_m = 236.3 [MPa] Predicted by: $\sigma = 29.3 \cdot \log(\dot{q}) + 244.3$ [MPa]
L3000	F_m = 3 [kN], δ_m = 368 [μm], σ_m = 340.2 [MPa] Predicted by: $\sigma = 125 \cdot \log(\dot{q}) + 3265.7$ [MPa]	U300	δ_m = 300 [μm], F_m = 2.5 [kN], σ_m = 283.5 [MPa] Predicted by: $\sigma = 34.5 \cdot \log(\dot{q}) + 290.2$ [MPa]
L2500	F_m = 2.5 [kN], δ_m = 300 [μm], σ_m = 283.5 [MPa] Predicted by: $\sigma = 133 \cdot \log(\dot{q}) + 192.4$ [MPa]	U368	δ_m = 368 [μm], F_m = 3 [kN], σ_m = 340.2 [MPa] Predicted by: $\sigma = 34.5 \cdot \log(\dot{q}) + 346.9$ [MPa]
L2084	F_m = 2.08 [kN], δ_m = 250 [μm], σ_m = 236.3 Predicted by: $\sigma = 133 \cdot \log(\dot{q}) + 145.2$ [MPa]	U429	δ_m = 429 [μm], F_m = 3.5 [kN], σ_m = 396.9 [MPa] Predicted by: $\sigma = 34.5 \cdot \log(\dot{q}) + 403.6$ [MPa]

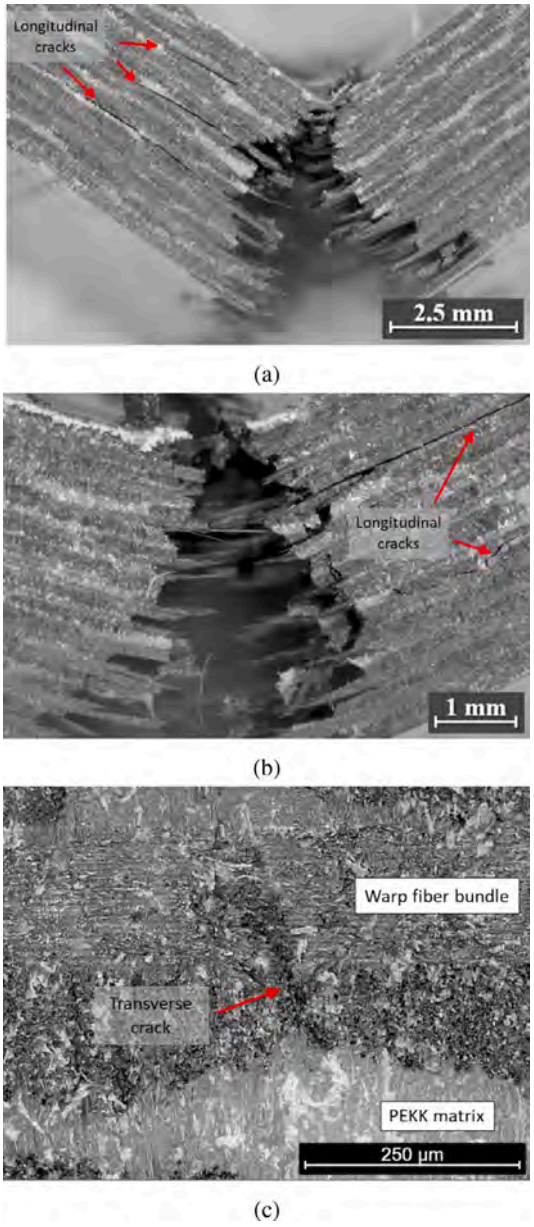

Fig. 15. The selected results of fractographic analysis of specimens after LFT.

The microscopy of the CF/PEKK specimen tested at a cyclic normal stress amplitude of 44.6 MPa revealed damage due to compressive, tensile, and shear stresses in the central region at the top and bottom layers. Warp fiber bundle kinking (Fig. 16a) is typical for local compressive stresses directly under the loading nose. Further, interlaminar delamination was observed between the loading nose and right-side support pin (see Fig. 16c). A single transverse crack along the weft bundle in the central region at the bottom layer observed during microscopy is shown in Fig. 16b.

The microscopic results from the specimen tested at a cyclic normal stress amplitude of 45.9 MPa shown in Fig. 17 showed damage features in the same regions as the specimen tested cyclic stress amplitude of 44.6 MPa. Fig. 17a shows a stitched image with nine windows showing the damage locations. Here, a transverse crack grew from the warp fiber bundle fracture at the top center of the CF/PEKK specimen (see Fig. 17b). The delamination due to cyclic shear stresses was much longer between the loading nose and right-side support unit, as shown in Fig. 17c,d, and e.

The similarities in fracture mechanisms can be noticed for both types of loading, i.e., LFFT and UFFT. In both cases, the inter-laminar delamination and transverse cracking through the entire composite layup is clearly observable, manifesting the domination of shear and tension/compression stresses during loading. This, in particular, demonstrates the mechanical nature of fatigue fracture. Thus, the self-heating effect did not dominate the fatigue process. This corresponds with the $T - \sigma$ curves presented in Section 3.1, representing mechanically-dominated fatigue of tested specimens. In both cases, the observed temperatures during loading were less than 50% of T_g, which can be considered as a transition point between mechanically- and thermally-driven fatigue according to the previous observations (see, e.g., [10,13]). Therefore, it can be concluded that the damage mechanisms in both LFFT and UFFT are driven by mechanical fatigue. The resulting fracture mechanisms demonstrate similarities for UFFT and LFFT, which confirms the possibility of interchangeable transferability between both types of loading. The LFFTs are force-controlled, resulting in the specimens' failure into two halves. As mentioned earlier, the UFFTs are displacement-controlled, with stiffness loss between 15–20% due to damage. This is the only difference marked on the macroscopic failure of the specimens under two different loading conditions. Otherwise, the microscopic and macroscopic damage features and their locations on the specimens agree.

4. Discussion and conclusions

A novel T-σ approach is proposed to capture the mean stress effect and then construct S-N curves without performing the CATs. To the knowledge of the authors, this method was not previously used and reported for altering or shifting S-N curves. The method is based on the assumption that a change in the thermomechanical behavior of composite materials, represented by the change of relative temperature, occurs due to a self-heating effect or the presence of damage and that estimated fatigue strength. Therefore, any change in the loading conditions should be reflected in the change in the fatigue strength during observation of the thermomechanical behavior of the tested specimen using the thermographic method. This assumption refers to LFFTs, where results are primarily affected by mechanical loading, and consequently, the influence of loading frequency is negligible.

In comparison to classical approaches [35,56,57], the method presented in Section 3.2 allowed to estimate the shifting factor for constructing S-N curves subjected to different mean stresses in an accelerated way. The applied thermographic method led to determining the fatigue strength, which corresponds to the initiation of a change in

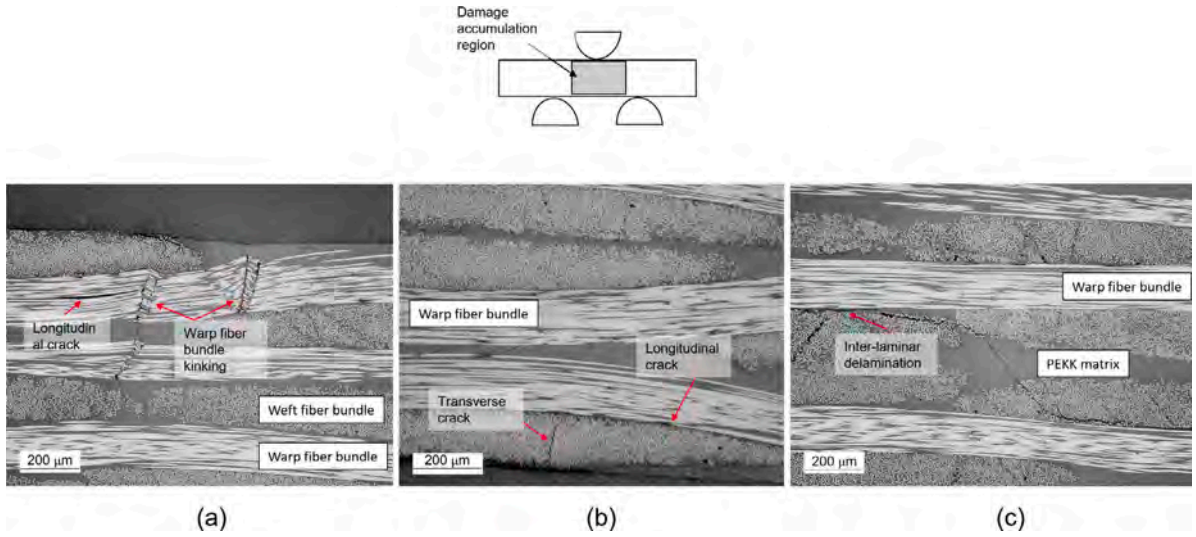

Fig. 16. (a) Wrap fiber bundle kinking at top due to compression, (b) transverse and longitudinal cracks due to tension, and (c) delamination due to shear.

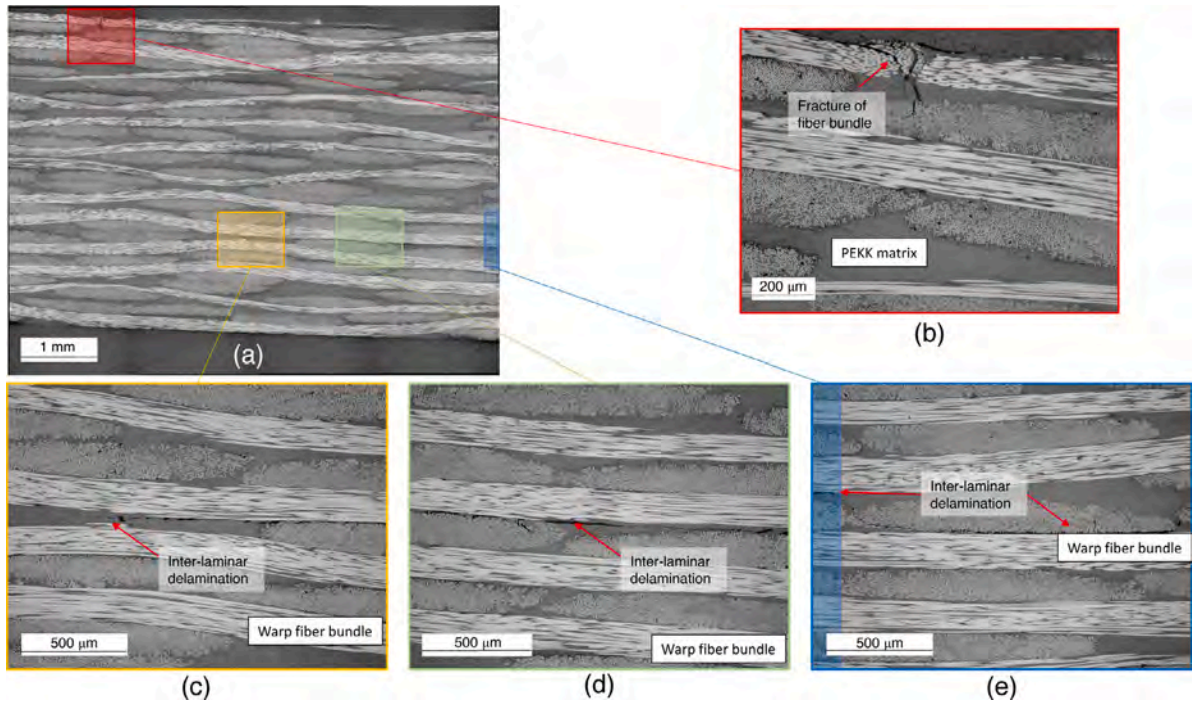

Fig. 17. (a) Wrap fiber bundle kinking at the top due to compression, delamination due to cyclic shear stresses (c) close to the specimen center, (d) a little away from the specimen center, and (e) and further away from specimen center.

the thermomechanical response of the specimen. Having constructed at least one S-N curve, the proposed method allowed to estimate the shift of this curve into a region corresponding to another mean stress condition. Estimating the shifting factor requires performing IATs for the mean stress corresponding to the already constructed S-N curve and another one corresponding to the new mean stress conditions. After obtaining two separate fatigue strengths for both mean stress conditions, the shifting factor can be estimated as a difference between the fatigue strengths. These values allow the vertical shifting of S-N curve to the region corresponding to the new mean stress conditions. The shift process depends on the accuracy of both estimated fatigue strengths using a thermographic approach estimated for two different mean stresses.

The feasibility of using S-N curve as a conventional approach for predicting the fatigue strength of CF/PEKK composite across low- to very-high-cycle fatigue regimes was evaluated. Given the inherent challenges of conducting VHCF testing at low frequencies, a practical approach was introduced involving the simultaneous implementation of LFFT and UFFT techniques (up to 10^6 and 10^8 cycles, respectively) to combine the test results and consequently construct S-N curve. Analyzing the extracted results from CATs using both techniques illustrated a significant finding: a transition zone between LFFT and UFFT for CF/PEKK composite. Therefore, implementing the traditional S-N curve for addressing and characterizing this transition zone was impractical, owing to the time required for LFFT testing and technological limitations in applying higher loads in UFFT. Therefore, one of the key objectives of the research was to introduce and adapt the concept of heat dissipation rate to quantitatively evaluate the thermomechanical response of the CF/PEKK composite under various IATs subjected to

different mean loads using LFFT and UFFT techniques. The study considered the influence of key parameters, including loading frequency, oscillation, and cooling techniques, via introducing a scalable factor ($\dot{q}_{ratio}$) for transferring the obtained results from UFFTs to LFFTs at similar amplitude displacement. To quantify the heat dissipation rate for LFFTs and UFFTs at the same amplitude displacement, the 4th-order polynomial function was implemented as a trial to interpret the relationship between the heat dissipation rate to the amplitude displacement. Notably, the study highlighted a substantial acceleration in the heat dissipation rate in UFFT due to the interplay of frequency and cooling systems, approximately 2100 times greater than the extracted average results from LFFTs.

The fracture mechanisms observed from examining specimens after both LFFTs and UFFTs demonstrated numerous similarities, primarily in the domination of mechanical fatigue and the typical character of damage initiation and propagation in CFRP structures. This initially confirms the transferability of the results between LFFTs and UFFTs.

The study, therefore, provides a foundation for a comprehensive understanding of thermomechanical fatigue behavior in CF/PEKK composites and paves the way for future research in this field. Moreover, the research demonstrates the capabilities and limitations of 3P bending testing using low and ultrasonic frequency test systems for various mean and amplitude loads. These findings have strong implications for the characterization of thermomechanical fatigue behavior in composite materials and offer valuable insights for guiding future investigations in this domain.

CRediT authorship contribution statement

Jafar Amraei: Writing – review & editing, Writing – original draft, Software, Methodology, Investigation, Formal analysis, Data curation, Conceptualization. **Tomasz Rogala:** Conceptualization, Methodology, Experiments, Data curation, Formal analysis, Software, Writing – original draft preparation, Writing – review and editing. **Andrzej Katunin:** Writing – review & editing, Writing – original draft, Project administration, Methodology, Funding acquisition, Formal analysis, Conceptualization. **Aravind Premanand:** Writing – original draft, Resources, Investigation, Formal analysis, Data curation, Conceptualization. **Grzegorz Kokot:** Writing – review & editing, Investigation. **Dominik Wachla:** Writing – review & editing, Writing – original draft, Software, Formal analysis, Data curation, Conceptualization. **Wacław Kuś:** Writing – review & editing, Investigation. **Marcin Bilewicz:** Writing – review & editing, Investigation. **Bilal Khatri:** Writing – review & editing, Conceptualization. **Frank Balle:** Writing – review & editing, Project administration, Methodology, Funding acquisition, Conceptualization.

Declaration of competing interest

The authors declare that they have no known competing financial interests or personal relationships that could have appeared to influence the work reported in this paper.

Data availability

Data will be made available on request.

Acknowledgments

The authors acknowledge the support of all the ultrasonic-related activities by the Walter-and-Ingeborg-Herrmann Foundation and German Research Foundation (DFG) for supporting the initiation of collaboration between the authors.

References

[1] Bakis CE, Bank LC, Brown VL, Cosenza E, Davalos JF, Lesko JJ, Machida A, Rizkalla SH, Triantafillou TC. Fiber-reinforced polymer composites for construction—State-of-the-art review. J Compos Constr 2002;6(2):73–87.
[2] Ferdous W, Ngo TC, Nguyen KTQ, Ghazlan A, Mendis P, Manalo A. Effect of fire-retardant ceram powder on the properties of phenolic-based GFRP composites. Composites B 2018;155:414–24.
[3] Harris B. Fatigue in composites: science and technology of the fatigue response of fibre-reinforced plastics. Woodhead Publishing; 2003.
[4] Dursun T, Soutis C. Recent developments in advanced aircraft aluminium alloys. Mater Des (1980-2015) 2014;56:862–71.
[5] Premanand A, Balle F. Influence of pulse–pause sequences on the self-heating behavior in continuous carbon fiber-reinforced composites under ultrasonic cyclic three-point bending loads. Materials 2022;15(10):3527.
[6] Wang C, Chen X, Cheng L, Ding J. High-cycle and very-high-cycle fatigue properties of CFRP-aramid honeycomb sandwich structure in three-point bending. Int J Fatigue 2022;155:106576.
[7] Lee CS, Kim HJ, Amanov A, Choo JH, Kim YK, Cho IS. Investigation on very high cycle fatigue of PA66-GF30 GFRP based on fiber orientation. Compos Sci Technol 2019;180:94–100.
[8] Premanand A, Rogala T, Wachla D, Amraei J, Katunin A, Khatri B, Rienks M, Balle F. Fatigue strength estimation of a CF/PEKK composite through self-heating temperature analysis using cyclic bending tests at 20 kHz. Compos Sci Technol 2023;243:110218.
[9] Santonocito D, Foti P, Risitano G, Berto F. Fatigue damage assessment in AM polymers evaluating their energy release. Procedia Struct Integr 2021;34:211–20.
[10] Amraei J, Katunin A. Recent advances in limiting fatigue damage accumulation induced by self-heating in polymer–matrix composites. Polymers 2022;14(24):5384.
[11] Balle F, Backe D. Very high cycle fatigue of carbon fiber reinforced polyphenylene sulfide at ultrasonic frequencies. In: Fatigue of materials at very high numbers of loading cycles: Experimental techniques, mechanisms, modeling and fatigue life assessment. Springer; 2018, p. 441–61.
[12] Backe D, Balle F, Eifler D. Fatigue testing of CFRP in the Very High Cycle Fatigue (VHCF) regime at ultrasonic frequencies. Compos Sci Technol 2015;106:93–9.
[13] Katunin A, Wronkowicz A, Bilewicz M, Wachla D. Criticality of self-heating in degradation processes of polymeric composites subjected to cyclic loading: A multiphysical approach. Arch Civ Mech Eng 2017;17(4):806–15.
[14] Katunin A, Wachla D, Santos P, Reis PN. Fatigue life assessment of hybrid bio-composites based on self-heating temperature. Compos Struct 2023;304:116456.
[15] Kahirdeh A, Khonsari MM. Energy dissipation in the course of the fatigue degradation: Mathematical derivation and experimental quantification. Int J Solids Struct 2015;77:74–85.
[16] Katunin A. Criticality of the self-heating effect in polymers and polymer matrix composites during fatigue, and their application in non-destructive testing. Polymers 2018;11(1):19.
[17] Voudouris G, Di Maio D, Sever IA. Experimental fatigue behaviour of CFRP composites under vibration and thermal loading. Int J Fatigue 2020;140:105791.
[18] Bartkowiak M, Kizak M, Liebig WV, Weidenmann KA. Fatigue behavior of hybrid continuous-discontinuous fiber-reinforced sheet molding compound composites under application-related loading conditions. Composites C 2022;8:100265.
[19] Chen K, Kang G, Lu F, Chen J, Jiang H. Effect of relative humidity on uniaxial cyclic softening/hardening and intrinsic heat generation of polyamide-6 polymer. Polym Test 2016;56:19–28.
[20] Vassilopoulos AP. The history of fiber-reinforced polymer composite laminate fatigue. Int J Fatigue 2020;134:105512.
[21] Shabani P, Taheri-Behrooz F, Samareh-Mousavi SS, Shokrieh MM. Very high cycle and gigacycle fatigue of fiber-reinforced composites: A review on experimental approaches and fatigue damage mechanisms. Prog Mater Sci 2021;118:100762.
[22] Movahedi-Rad AV, Keller T, Vassilopoulos AP. Stress ratio effect on tension-tension fatigue behavior of angle-ply GFRP laminates. Int J Fatigue 2019;126:103–11.
[23] Deniz ME, Aydin F. Determination of fatigue life of the unidirectional GFRP/Al hybrid composite laminates. Composites B 2019;166:580–7.
[24] Manjunatha CM, Taylor AC, Kinloch AJ, Sprenger S. The tensile fatigue behavior of a GFRP composite with rubber particle modified epoxy matrix. J Reinf Plast Compos 2010;29(14):2170–83.
[25] Radhakrishnan PM, Ramajeyathilagam K. Effect of stress ratio on tension-tension fatigue behaviour of woven angle ply GFRP laminates. Int J Fatigue 2023;172:107633.
[26] Al-Hmouz IA. The effect of loading frequency and loading level on the fatigue behavior of angle-ply carbon/PEEK thermoplastic composites (Ph.D. thesis), Concordia University; 1997.
[27] Mallick PK, Zhou Y. Effect of mean stress on the stress-controlled fatigue of a short E-glass fiber reinforced polyamide-6, 6. Int J Fatigue 2004;26(9):941–6.
[28] Crowther MF, Wyatt RC, Phillips MG. Creep-fatigue interactions in glass fibre/polyester composites. Compos Sci Technol 1989;36(3):191–210.

[29] Tong X, Chen X, Xu J-S, Zheng Y, Zhi S-J. The heat build-up of a polymer matrix composite under cyclic loading: Experimental assessment and numerical simulation. Int J Fatigue 2018;116:323–33.
[30] Justo J, Marin JC, Paris F, Canas J. The effect of frequency on fatigue behavior of graphite epoxy composites. In: Proceedings of the ECCM16-16th European conference on composite materials, Seville, Spain. 2014, p. 22–6.
[31] Mini KM, Lakshmanan M, Mathew L, Mukundan M. Effect of fibre volume fraction on fatigue behaviour of glass fibre reinforced composite. Fatigue Fract Eng Mater Struct 2012;35(12):1160–6.
[32] Adam TJ, Horst P. Fatigue damage and fatigue limits of a GFRP angle-ply laminate tested under very high cycle fatigue loading. Int J Fatigue 2017;99:202–14.
[33] Huang J, Pastor ML, Garnier C, Gong XJ. A new model for fatigue life prediction based on infrared thermography and degradation process for CFRP composite laminates. Int J Fatigue 2019;120:87–95.
[34] La Rosa G, Risitano A. Thermographic methodology for rapid determination of the fatigue limit of materials and mechanical components. Int J Fatigue 2000;22(1):65–73.
[35] Flore D, Wegener K. Modelling the mean stress effect on fatigue life of fibre reinforced plastics. Int J Fatigue 2016;82(3):689–99.
[36] Peyrac C, Jollivet T, Leray N, Lefebvre F, Westphal O, Gornet L. Self-heating method for fatigue limit determination on thermoplastic composites. Procedia Eng 2015;133:129–35.
[37] Colombo C, Libonati F, Pezzani F, Salerno A, Vergani L. Fatigue behaviour of a GFRP laminate by thermographic measurements. Procedia Eng 2011;10:3518–27.
[38] Katunin A, Pivdiablyk I, Gornet L, Rozycki P. A hybrid method for determination of fatigue limit and non-destructive evaluation of composite structures after low-velocity impact loading. Composites B 2022;238:109898.
[39] Huang J, Pastor ML, Garnier C, Gong X. Rapid evaluation of fatigue limit on thermographic data analysis. Int J Fatigue 2017;104:293–301.
[40] Montesano J, Fawaz Z, Bougherara H. Use of infrared thermography to investigate the fatigue behavior of a carbon fiber reinforced polymer composite. Compos Struct 2013;97:76–83.
[41] Huang J, Garnier C, Pastor ML, Gong X. Investigation of self-heating and life prediction in CFRP laminates under cyclic shear loading condition based on the infrared thermographic data. Eng Fract Mech 2020;229:106971.
[42] Ueki Y. High-speed bending-fatigue testing of composite materials. In: IOP conference series: materials science and engineering, vol. 388, IOP Publishing; 2018, 012008, (1).
[43] Flore D, Wegener K, Mayer H, Karr U, Oetting CC. Investigation of the high and very high cycle fatigue behaviour of continuous fibre reinforced plastics by conventional and ultrasonic fatigue testing. Compos Sci Technol 2017;141:130–6.
[44] Premanand A, Balle F. Stress and strain calculation method for orthotropic polymer composites under axial and bending ultrasonic fatigue loads. Ultrasonics 2023.
[45] Vassilopoulos AP, Manshadi AP, Keller T. Influence of the constant life diagram formulation on the fatigue life prediction of composite materials. Int J Fatigue 2010;32(4):659–96.
[46] Mandegarian S, Samareh-Mousavi SS, Taheri-Behrooz F. Experimental investigation on in-plane shear fatigue failure criteria of $\pm 45^{o}$ angle-ply carbon epoxy composite. Int J Fatigue 2022;160:106873.
[47] Mirzaei AH, Shokrieh MM. Evolution of the temperature rise and damage in laminated composites with stress concentration under fatigue loading. Composites B 2023;254:110607.
[48] Quaresimin M. Fatigue of woven composite laminates under tensile and compressive loading. In: ECCM-10; composites for the future. 2002, 10th European Conference on Composite Materials ; Conference date: June 3-7, 2002, Brugge, Belgium.
[49] Yu F, Zhou B, Xin W, Zhang X. Fatigue life prediction for the main spar with wrinkle defects of a wind turbine blade. Fatigue Fract Eng Mater Struct 2021;44:2764–80.
[50] Katunin A, Wachla D. Determination of fatigue limit of polymeric composites in fully reversed bending loading mode using self-heating effect. J Compos Mater 2019;53(1):83–91.
[51] Li A, Huang J, Zhang C. Enabling rapid fatigue life prediction of short carbon fiber reinforced polyether-ether-ketone using a novel energy dissipation–based model. Compos Struct 2021;272:114227.
[52] Luong MP. Fatigue limit evaluation of metals using an infrared thermographic technique. Mech Mater 1998;28(1):155–63.
[53] Kassapoglou C. Fatigue life prediction of composite structures under constant amplitude loading. J Compos Mater 2007;41(22):2737–54.
[54] Philippidis TP, Vassilopoulos AP. Life prediction methodology for GFRP laminates under spectrum loading. Composites A 2004;35(6):657–66.
[55] Vassilopoulos AP, Manshadi AP, Keller T. Piecewise non–linear constant life diagram formulation for FRP composite materials. Int J Fatigue 2010;32(10):1731–8.
[56] Kawai M, Koizumi M. Nonlinear constant fatigue life diagrams for carbon epoxy laminates at room temperature. Composites A 2007;38(11):2345–53.
[57] Boerstra GK. The multislope model: a new description for the fatigue strength of glass reinforced plastic. Int J Fatigue 2007;29(8):1571–6.

Paper V

Fatigue strength estimation of a CF/PEKK composite through self-heating temperature analysis using cyclic bending tests at 20 kHz

Composites Science and Technology 243 (2023) 110218

Contents lists available at ScienceDirect

Composites Science and Technology

journal homepage: www.elsevier.com/locate/compscitech

Fatigue strength estimation of a CF/PEKK composite through self-heating temperature analysis using cyclic bending tests at 20 kHz

Aravind Premanand [a,*], Tomasz Rogala [b], Dominik Wachla [b], Jafar Amraei [b], Andrzej Katunin [b], Bilal Khatri [a], Michael Rienks [a], Frank Balle [a,c,d]

[a] Department for Sustainable Systems Engineering (INATECH), Faculty of Engineering, Albert-Ludwigs-Universität Freiburg, Freiburg, 79110, Germany
[b] Department of Fundamentals of Machinery Design, Silesian University of Technology, Konarskiego 18A, Gliwice, 44-100, Poland
[c] Freiburg Materials Research Center (FMF), Freiburg, 79110, Germany
[d] Fraunhofer Institute for High Speed Dynamics, Ernst Mach Institute (EMI), Freiburg, 79110, Germany

ARTICLE INFO

Keywords:
Very high cycle fatigue
Self-heating effect
Fatigue strength estimation
Ultrasonic fatigue testing
Carbon fiber reinforced polymers
Material characterization

ABSTRACT

Very high cycle fatigue (VHCF) testing at conventional frequencies is highly time-consuming and unrealistic for large sample sizes. Though testing at ultrasonic frequencies can accelerate the testing, any undesirable thermal effect arising from testing at 20 kHz can cause significant heat generation in the specimens, increasing the likelihood of thermally induced failure. When mitigated, the temperature behavior during ultrasonic fatigue testing may conversely provide knowledge of the fatigue behavior of the composite. We study this hypothesis in this work by estimating the fatigue strength of a CF/PEKK composite through its temperature evolution during 3-point bending tests at 20 kHz with different cyclic load amplitudes. The fatigue strength of the composite was estimated using the temperature characteristics from an increasing cyclic amplitude test. This estimation was validated with four constant cyclic amplitude tests. Further, the estimation model was extended to different pulse–pause sequences by two constant cyclic amplitude tests. The results indicate a reliable and rapid method for fatigue life estimation as a material property. Finally, the criticality of the self-heating phenomenon during the non-stationary self-heating condition was evaluated.

1. Introduction

Carbon-fiber reinforced polymers (CFRPs) used in the aircraft industry today are over-designed for safety to ensure low working strains, so that no significant local damage appears during the material's service life [1]. Several material and loading factors affect the fatigue lives of such laminated composites with continuous fiber reinforcements. These include the matrix and fiber materials, the laminate composition and layup architecture, service conditions (environment temperature, humidity, etc.) as well as loading conditions (such as loading direction, loading ratio, mean load, and frequency). To efficiently design composite structures for the desired service-life time, the damage mechanisms as a result of the actual loading conditions need to be studied. A comprehensive understanding of the fatigue failure mechanisms in these composites can lead to the development of reliable methods to predict their service life in the presence of defects and damage. This is critical to ensure the long-term operation of such composite structures in sectors such as aerospace, where knowledge about the condition of structural elements after the prolonged operation are highly desired to prepare maintenance plans [2,3]. Currently, the accurate prediction of the fatigue life of such materials is difficult based on the available theoretical and empirical models.

One potential approach to study the effect of fatigue loading on defects in the material is to perform experiments in the very high cycle fatigue (VHCF) regime (greater than 10^7 cycles per test). At conventional testing frequencies (up to 50 Hz), this can lead to unrealistic testing times. By increasing the loading frequency into the ultrasonic regime (up to 20 kHz), the testing period can be significantly reduced. In such a fatigue testing system, tests up to 10^9 cycles can be performed within two weeks [4]. However, these tests can lead to rapid temperature increases due to the high loading frequency, termed self-heating, which can adversely affect the results due to thermally induced fatigue damage and significantly reduced fatigue performance.

The self-heating phenomenon appears due to the viscoelastic response of a polymer matrix in composites during cyclic loading, which results in hysteresis and energy dissipation. A major part of this energy is dissipated in the form of heat, and the temperature inside the material increases. This increase in temperature is mostly dependent on the level of the applied stress and the cyclic loading frequency

* Corresponding author.
E-mail address: aravind.premanand@inatech.uni-freiburg.de (A. Premanand).

https://doi.org/10.1016/j.compscitech.2023.110218
Received 17 February 2023; Received in revised form 14 July 2023; Accepted 14 August 2023
Available online 19 August 2023

and may lead to accelerated structural degradation and fatigue failure. Previous studies (Katunin et al. [5–7]) demonstrated that the self-heating temperature might reach or even exceed the glass-transition temperature, which leads to the premature failure of composites.

Thermal fatigue damage accumulation induced by the self-heating of polymer–matrix composites (PMCs) under cyclic loading is an active topic of research. A recent review by Amraei and Katunin [8] addresses the self-heating effect and summarizes the investigations into various cooling techniques. One such technique applicable to ultrasonic fatigue testing systems is the so-called pulse–pause method, where the cyclic loading is paused for a defined amount of time to allow the sample to cool down, and stay below a certain threshold, and avoid thermal damage. Recent investigations into ultrasonic fatigue tests report pulse–pause ratios of 1:20 for glass-fiber reinforced composite (GFRP) specimens (Flore et al. [9]) and 1:10 for CFRP specimens (Premanand and Balle [10]). In the latter publication, the pulse–pause ratio was kept constant throughout the test duration, and the specimens were cooled using dry compressed air to limit the surface temperature below 30 °C. In a separate study, Premanand and Balle [11] looked at the influence of different pause-times (1000 ms, 2000 ms, and 4000 ms) on CFRP specimens under 3-point fatigue bending conditions using a tailor-made testing setup originally reported by Backe et al. [4]. Longer pause-times, though suitable for keeping the temperature-rise below a certain threshold, increase the test duration by several times. A thorough investigation into the self-heating behavior as well as a versatile testing setup incorporating variable pulse–pause ratios can lead to reliable experimental results while keeping the test duration within a realizable time frame.

1.1. Self-heating phenomenon and its influence on the fatigue performance of composites

The self-heating effect can manifest in one of two scenarios depending on the magnitude and frequency of the cyclic loading. In the first of these, the increased specimen surface temperature during the first fatigue phase can stabilize at an elevated level until the onset of damage or final failure [12]. This stabilization, termed stationary self-heating, is a result of the thermal equilibrium reached between the heat generated due to viscoelastic damping and the rate of heat dissipation through convection [6]. Beyond a certain loading magnitude and/or frequency, the rate of heat generation surpasses that of the dissipation, resulting in non-stationary self-heating and significantly accelerated damage accumulation. The two self-heating behaviors result in different fracture and failure mechanisms [13]: Mechanical degradation is the chief contributor to failure in the case of stationary self-heating, whereas thermal degradation dominates for non-stationary self-heating.

1.2. Estimation of fatigue limit for low cycle fatigue

Depending on the maximum number of cycles being tested, a low-cycle fatigue-testing campaign can take several months, even without taking replication tests into account. In contrast, a single uninterrupted ultrasonic fatigue experiment up to 10^9 cycles at a pulse–pause ratio of 100–2000 ms would take close to 12 days. Additionally, the results from such a set of experiments are only applicable to the specific composite type with its constituent materials, fiber–matrix-ratio, and lay-up sequence [14]. Conventionally, the so-called Woehler or S–N curves are used to characterize and compare the fatigue life performance of different materials. This curve plots failure cycles against the applied loading amplitudes to predict the fatigue limit. Here, the fatigue limit is defined as the stress level below which no significant damage can occur for an unlimited number of cycles. Above this fatigue limit value, structural integrity is reduced, or failure propagation appears. In case the material does not exhibit a distinct fatigue limit, the term fatigue strength is often used. The fatigue strength is defined as the stress level at which damage occurs for a specified number of cycles.

An alternative method to S–N curves to more rapidly determine the fatigue limit of materials or mechanical components was reported by Rosa and Risitano [15], known as the temperature–stress curve. This method estimates the fatigue limit for high cyclic stress-amplitudes by measuring the increased temperature during fatigue loading, arising due to the release of plastic energy. The resulting fatigue limit estimates were found to be in good agreement with those determined through S–N curves while requiring a much smaller number of specimens. This method has since been used to determine the fatigue limit for a variety of material systems and shapes. Quaresimin [16] evaluated the high cycle fatigue strength of a woven CF/epoxy composite under tension–compression axial loading and found that the thermographic method was in good agreement with the data from Woehler curves. Colombo et al. [17] used this method to study the fatigue behavior of GFRPs under axial loading at a stress ratio (R) of 0.1. Montesano et al. [18] estimated the fatigue limit of tri-axially braided carbon fiber reinforced polymers under axial loading at $R = 0.1$. Yu et al. [19] successfully applied the Risitano method to estimate the fatigue limit of the main spar of a wind turbine blade with wrinkle defects. Katunin and Wachla [20] used this method to determine the fatigue limit in a GFRP under fully reversed bending loading while also recording the acoustic emission events that reflect the progressive damage evolution. The results indicated a rapid increase in acoustic emissions above the fatigue limit determined using the Risitano method. They later combined the Risitano method with the non-destructive evaluation of impact damage in CFRP and GFRP structures, validated using X-ray CT inspections [21]. These studies validate the use of this method for the evaluation of fatigue limit or fatigue strength in parallel to the conventional S–N curve method. This thermographic method, originally applied to metals, is thus applicable to composites as long as an evident change in the stabilized temperature occurs for different stress levels. Here, the increase in temperature is caused by the non-linear elastic and plastic behavior of the composite material or by other internal dissipation mechanisms [16] and is dependent on the testing frequency and stress levels but not on the fatigue damage evolution. Damage evolution results in a temperature rise before failure, even for low-stress amplitudes. However, during the initial part of the fatigue experiments, a plateau in the temperature trend can always be identified for the stationary self-heating condition, which corresponds to the fatigue loading of the composite material.

In addition to the Risitano method, the fatigue behavior can also be estimated using a temperature/failure-cycle curve over a series of tests [22]. To extract this curve, three different temperature-related fatigue phases have to be assumed. Shortly after the start of the test, phase I exhibits a rapid temperature increase on the specimen surface, the rate of which is dependent on the loading level. In phase II, the temperature stabilizes and remains at an almost constant value for most of the test duration. This constant surface temperature is directly proportional to the applied stress amplitude [23]. As the specimen enters phase III, the temperature increases rapidly, leading to the final fatigue failure. The temperature-cycle curve was used by Mandegarian et al. [24] to determine the in-plane shear fatigue behavior of a $[\pm 45]_s$ angle-ply CFRP composite under step-wise increasing load-amplitude conditions at $R = -1$. They reported the cycles-to-failure as a function of the applied stress amplitude for different stress-ratios between 0.4 and 0.8. Another recent study by Li et al. [25] used the temperature–stress curve to predict the fatigue limit of a carbon-fiber-reinforced polyetheretherketone (CF/PEEK) composite through a combination of its thermodynamic response and the fatigue damage observed.

1.3. Criticality of self-heating temperature during cyclic loading with pulse–pause sequence

Ratner and Korobov [26] defined the critical self-heating concept as a critical stress leading to thermal fracture, or vice versa. This

concept was also described by Gumenyuk and Karnaukhov [27] as the temperature beyond which the temperature growth profile becomes unstable, resulting in the softening of viscoelastic materials such as GFRPs and CFRPs. Katunin [5] defined this concept as a measure of the structural degradation in PMC materials subjected to fatigue loading. The methods of determining the critical self-heating temperature were reviewed in [7]. In parallel, Kahirdeh and Khonsari [28] suggested using acoustic emissions as a function of the thermal response for evaluating the structural degradation of PMCs under fully-reversed bending loading. The methods of determining the critical self-heating temperature were reviewed in [7].

The critical self-heating temperature in polymer composites is the temperature at which damage initiates. Below this temperature, the sample is considered to be in the stationary self-heating regime, and consequently, above it the structures experience non-stationary self-heating [7]. In a previous study by the authors [11], a temperature rise beyond 60 °C during ultrasonic fatigue loading of a carbon-fiber-reinforced polyetherketoneketone (CF/PEKK) composite (with a glass transition temperature T_g of 160 °C) resulted in a transition from stationary to non-stationary self-heating. The final damage evolution in the CF/PEKK specimen with non-stationary self-heating behavior was a result of thermomechanical degradation. For an experiment conducted with the same cyclic amplitude at a frequency of 20 kHz and a longer pause time resulted in a stationary self-heating temperature below 60 °C. Here, the damage observed was caused only by mechanical fatigue. This observation on the influence of the critical self-heating temperature on final fatigue failure is synonymous with the study of Katunin and Wronkowicz [29].

1.4. Motivation and research goal

Flore et al. [9] investigated the high-cycle fatigue (HCF) and VHCF behavior of continuous GFRPs using conventional and ultrasonic fatigue experiments under axial loading conditions. An absence of knowledge of CFRPs under these loading conditions, especially for three-point bending, drives the need for the current investigation. Such studies can reduce the gap between different fatigue methods used for characterizing composites in the HCF and VHCF regimes. This study proposes an approach to enable the results from distinct fatigue experiments and methodologies to be compared. Understanding the failure mechanisms and estimating the fatigue limit as a material property in the VHCF regime using ultrasonic fatigue testing will help bridge the gap between low-cycle, high-cycle, and very-high-cycle fatigue behaviors of composites. This, in turn, will allow the adjustment and validation of the methods described in this study to establish a reliable and vastly faster fatigue testing technique.

2. Materials and experimental setup

2.1. Composite material and its properties

For this study, a CF/PEKK composite laminate manufactured by Toray Advanced Composites (Nijverdal, The Netherlands) with a 5-harness satin CF fabric was chosen. PEKK is a semi-crystalline thermoplastic polymer belonging to the polyaryletherketone (PAEK) family. It exhibits a melting temperature (T_m) of about 337 °C and a glass transition temperature (T_g) of around 160 °C, making it suitable for elevated-service temperature applications such as primary and secondary load-carrying structures in the aerospace and automobile sectors. The absence of critical manufacturing impecrfections such as voids and defects in the laminate was confirmed through ultrasonic C-scans provided by the manufacturer. Table 1 shows the material properties of the CF/PEKK laminate provided by the manufacturer.

The satin weave fabric layers were stacked up with alternating 0° and 90° orientations in a symmetrical sequence (see Fig. 1), given in Table 1. Here, the 0° and 90° denote the orientation of warp fiber bundles with respect to the loading direction, and the single 0_f excluded from the stack symmetry is denoted with an underscore. The thickness of the consolidated laminate was measured and is 4.05 ± 0.05 mm.

Table 1
Material properties of CF/PEKK laminate.

Fabric type	5H satin woven fabric
Ply thickness	0.3 mm
Number of plies	13
Layup	$[0/90/0/90/0/90/\underline{0}]_s$
Area weight	[a]280 g/m^2
Fiber volume fraction	[a]50%
Glass transition temperature	[b]160 °C
Melting temperature	[b]337 °C
Ultimate tensile strength 0°	[a]776 MPa
Ultimate compressive strength 0°	[a]585 MPa
Specific heat	[c]1425 J kg^{-1} K^{-1}

[a]Values obtained from [30].
[b]Values obtained from [31].
[c]Values obtained from [32].

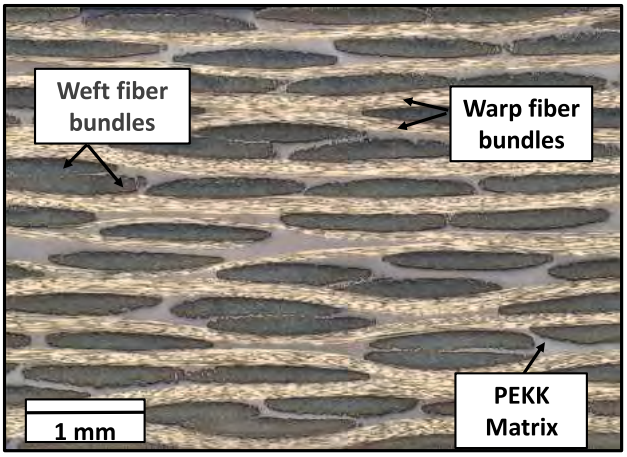

Fig. 1. A representative micrograph of the 13-layer CF/PEKK laminate cross-section, stacked using 5-harness satin CF fabrics.

Table 2
Values of elastic constants and mass density used for orthotropic material model of CF/PEKK material.

E_{11} [GPa]	58	G_{12} [GPa]	4.80	ν_{12} [–]	0.05
E_{22} [GPa]	58	G_{13} [GPa]	5.70[a]	ν_{13} [–]	0.5[a]
E_{33} [GPa]	13[a]	G_{23} [GPa]	5.70[a]	ν_{23} [–]	0.5[a]
ρ [kg/m^3]	1530				

[a]Values are estimated using the micro-mechanics model developed at the University of Twente [34].

2.2. Specimen geometry for ultrasonic fatigue testing

To ensure resonance during cyclic loading of the specimen at ultrasonic frequencies, a transverse bending eigenmode of the sample close to 20 kHz [33] was required. This was simulated in the Ansys Workbench software using a homogeneous orthotropic model with six elastic moduli, three Poisson's ratios, and mass density as the input parameters. This yielded sample dimensions of 34 × 15 × 4.05 mm^3 (see Fig. 2a) and a natural frequency of 20.2 kHz. Table 2 lists the simulation input parameters used to determine the optimal sample size.

The span length for the three-point bending tests was obtained by determining the two nodes along the specimen length, where displacements are zero using the Ansys harmonic analysis tool. The simulation was performed for an applied sinusoidal oscillation of 50 μm at a frequency of 20.2 kHz and yielded a span length of 18.6 mm (see Fig. 2b).

2.3. Monotonic tests

Monotonic tests were carried out prior to the ultrasonic fatigue tests to obtain insights into the monotonic failure load and mode of failure.

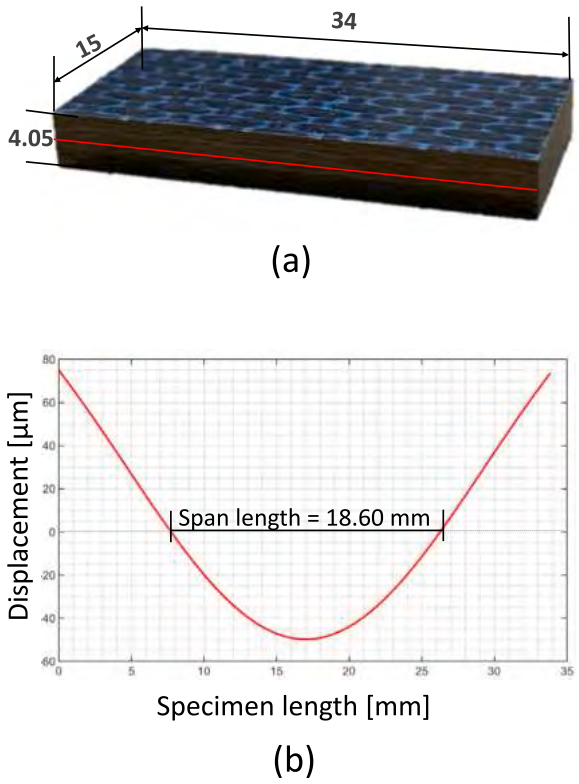

Fig. 2. (a) The geometry of the CF/PEKK specimens designed to oscillate at an applied frequency of 20 kHz with dimensions in mm (b) The span length of 18.6 mm obtained using the Ansys harmonic analysis tool for 3-point bending tests.

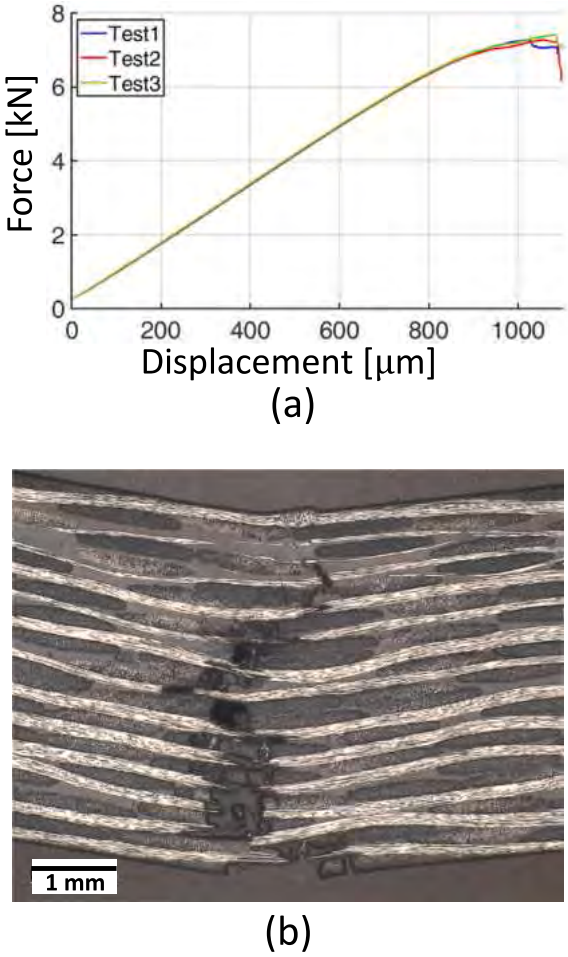

Fig. 3. (a). The force–displacement response of the CF/PEKK specimens under monotonic loading (b) Post-failure specimen cross-section after a monotonic three-point bending test.

These experiments were performed in the Zwick/Roell Z010 testing machine (Ulm, Germany) with a 10 kN load cell under displacement control at a rate of 1 mm/min. A span length of 18.6 mm was chosen to allow the monotonic loading conditions to be comparable to their fatigue-loading counterparts. An indenter of radius 5 mm and support pins of radius 2 mm were used.

The monotonic 3-point bending tests exhibited failure forces of 7330 ± 63 N at displacements of 1100 ± 17 µm (Fig. 3a). The failure initiation was observed in the bottom half of the specimens (Fig. 3b), propagating towards the top half, indicating a purely bending stress-related failure mode. No cracks were found in the contact areas of the loading nose or the support units, confirming that shear stresses are not critical for the chosen specimen geometry. Thus, the monotonic apparent bending strength and secant modulus were calculated using the homogeneous beam theory (suggested by ASTM D7264/D7264M-15) to be 811.05 ± 6.97 MPa and 12.36 ± 0.02 GPa respectively. This result was previously published in [11].

2.4. Ultrasonic fatigue testing setup

An ultrasonic fatigue test setup was developed in-house at INATECH using the ultrasonic load train manufactured by Herrmann Ultraschalltechnik GmbH (Karlsbad, Germany). This setup can apply cyclic displacement amplitudes of up to 57 µm at frequencies between 19.5 kHz and 20.5 kHz using a 4.8 kW digital ultrasonic generator. The cyclic response of the specimen was monitored using the Polytec CLV2534 single-point laser doppler vibrometer (LDV) (Waldbronn, Germany) at a frame rate of 500 kHz (Fig. 4). Further details are described in [11].

The temperature evolution on the specimen surface during ultrasonic oscillations was monitored by means of active thermography, using a Micro-Epsilon TIM640 (Ortenburg, Germany) infra-red (IR) camera at a resolution of 640 × 480 pixels. The maximum temperatures in four different regions of interest (ROIs) were continuously recorded using a LabView®program at the maximum frame rate of the IR camera of 32 Hz. Fig. 5 shows a representative thermogram during ultrasonic fatigue with four defined ROIs and the corresponding maximum temperature evolution in each ROI.

2.5. Increasing amplitude experiments

Three-point bending experiments with step-wise increasing oscillatory loads were conducted at 12 different cyclic amplitudes. The oscillations are realized by the ultrasonic generator in terms of the percentage of maximum possible amplitude, which is 57 µm. For example, 4 µm oscillation amplitude correlates to 7% of generator amplitude. For the test, cyclic oscillations were applied from ±4 µm to ±48 µm in increments of ±4 µm. These increasing amplitudes correspond to a starting normal stress amplitude of 3.7 MPa up to 44.1 MPa in steps of 3.7 MPa. Each step comprised 2.02 × 10^5 cycles, with pulse and pause times of 250 ms and 1.75 s, respectively. An additional 20 ms each was added around the pulse time for ramp-up (also called as onset time of the pulse) and ramp-down (offset) to accommodate for the time the oscillatory system requires to reach the desired amplitude. The resonance frequency measured by LDV was found to be in the range between 20 180 to 20 220 Hz, which corresponds to 5040 to 5055 cycles per pulse-time of 250 ms. After the completion of one step, the test was paused to allow the specimen to cool down to room temperature before stepping up to the next amplitude. To ensure continuous contact between the loading nose and the specimen, a monotonic displacement

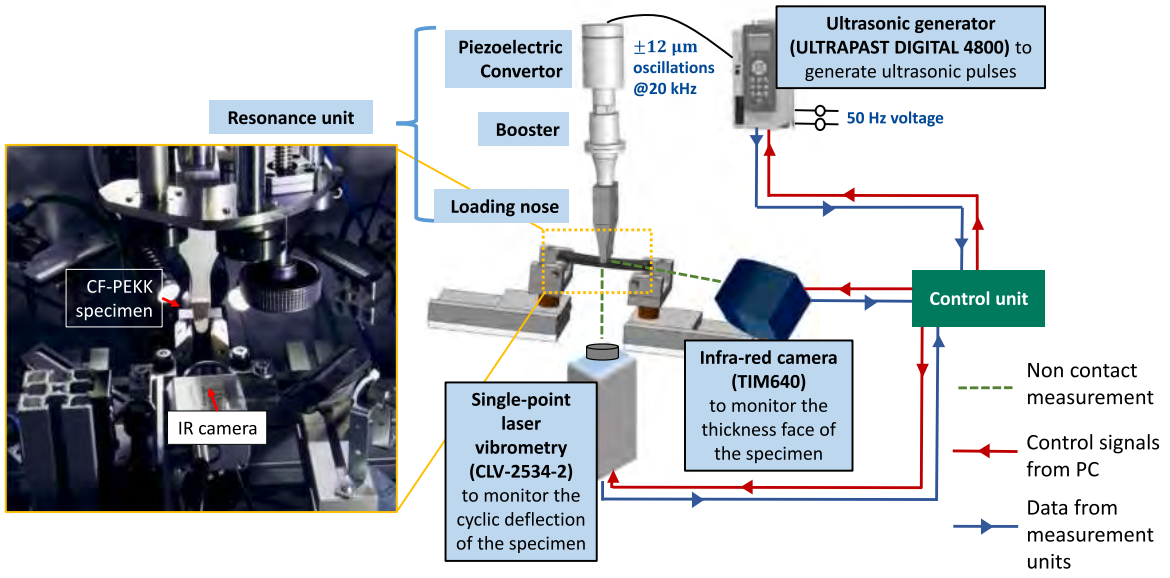

Fig. 4. An overview of the ultrasonic three-point bending fatigue testing setup.

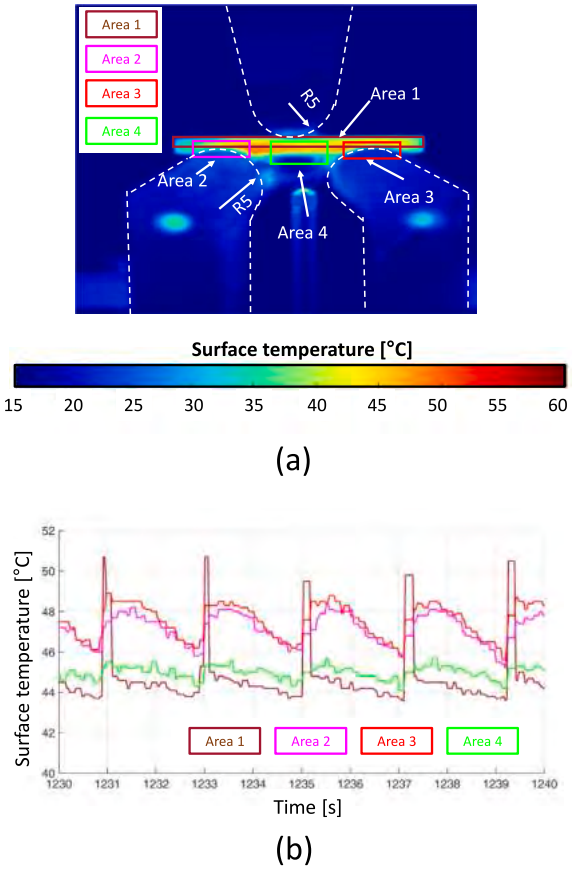

Fig. 5. (a) An IR thermal image with 4 different regions of interest on the specimen for continuous temperature measurement (b) The corresponding temperature evolution as a function of time for the different regions during the pulse–pause sequence.

of 150 µm, corresponding to a normal stress of 200 MPa, was applied for each test. Fig. 6 shows a graphical representation of the increasing amplitude experiments. The data from the increasing amplitude experiment was used to develop a methodology for estimating the fatigue strength of the CF-PEKK composite.

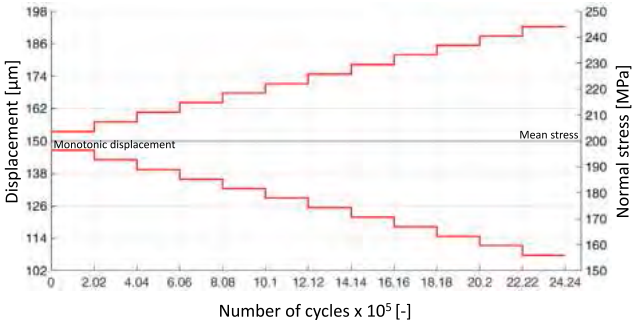

Fig. 6. Increasing amplitude experiments.

Table 3
Pulse–Pause and load settings for cases constant-amplitude loading.

Case	Pulse duration	Pause duration	Oscil. amplitude
I	250 ms	1.85 s	±48.0 µm
II	250 ms	1.25 s	±51.4 µm

2.6. Constant amplitude experiments

Two constant-load cyclic fatigue experiments were performed to represent the stationary and non-stationary self-heating conditions respectively. The data from the two experiments were used to extend the applicability of the fatigue strength estimation model developed using the increasing amplitude test. Both tests were performed at the same pulse-time of 250 ms. To achieve the stationary self-heating condition, a mean stress of 200 MPa and a stress amplitude of 44.4 MPa was applied with a pause-time of 1.85 seconds. For the non-stationary self-heating condition, a mean stress of 200 MPa and a stress amplitude of 47.6 MPa and a pause-time of 1.25 s was set. The two cases are described in Table 3 and shown in Fig. 7.

The maximum temperatures at the 4 ROIs as well as the resonance data from the generator were recorded for all the ultrasonic pulses until failure. The experiments were terminated when

- the maximum surface temperature exceeded 160 °C (T_g of PEKK) or when

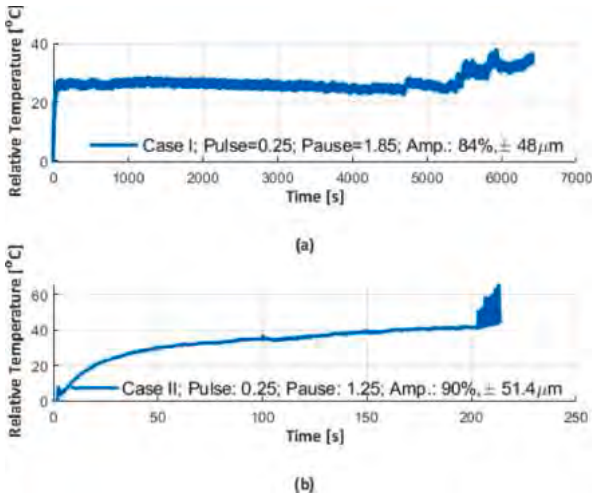

Fig. 7. Temperature profile evolution until the specimen damage in the constant amplitude tests ((a) Case I and (b) Case II).

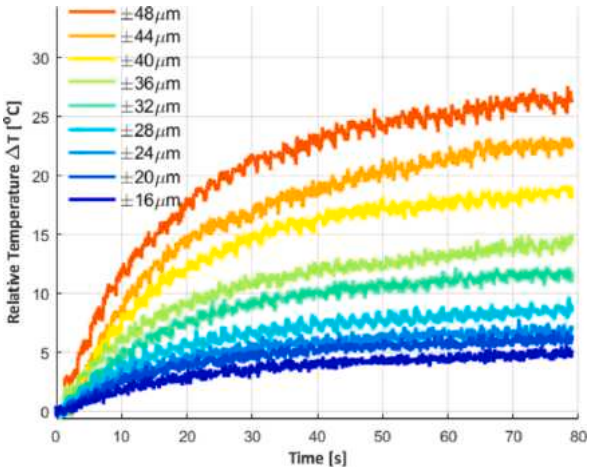

Fig. 8. Selected self-heating temperature profiles measured in the bottom center part of the specimen (area 4).

- the resonance frequency dropped below 19.5 kHz due to loss of stiffness, which is the minimum resonance frequency that can be applied by the ultrasonic fatigue testing system.

Fig. 5a shows a thermal image of the specimen under test with the ROIs marked as colored squares, capturing a comprehensive temperature response of the CF/PEKK specimen. The contact points of the specimen with the loading nose and the support units can (areas 1, 2, and 3) lead to an additional surface-temperature rise due to frictional heat. A previous study [11] was carried out with a termination criterion of 80 °C. As the current work was designed to characterize the self-heating behavior due to viscoelasticity as well as due to friction, a higher temperature limit was set to include temperature evolution during the final fatigue phase of the CF/PEKK specimens.

2.7. Microscopy

After failure, the specimens were cut into two length-wise halves, embedded in epoxy, and ground and polished using the Struers LaboPol-30 system (Willich, Germany). The prepared cross-sections were observed using the Zeiss Smartzoom 5 light optical microscope (Oberkochen, Germany).

3. Results and discussion

3.1. Preliminary analyses and assumptions

This section details the results observed in the bottom center region (ROI no. 4), which was chosen to avoid or minimize the influence of the observation of any other source, e.g. friction between the supports or the loading nose and the specimen. Measurement data was collected using the acquisition system based on the LabVIEW® programming environment and processed in Matlab. Next, the following operations were performed on the imported signals:

- Temperature readings from the IR camera for two different places in the facility operational space (see photo in Fig. 4) were used to calculate the average ambient temperature for each sample. Later, this temperature trend was removed from the observed temperature profiles.
- The time–temperature profiles for different experiments were time-shifted to synchronize their initial pulses. The profiles were additionally tail-trimmed to the time–temperature profile with the shortest duration.
- After removing the influence of the ambient temperatures, there was still a bias (up to 1 °C in peak value) between the specimen's temperature and the ambient temperature before the start of the test. The relative temperature as such, refers to the initial temperature of the specimen. This initial temperature was calculated on the average of the first ten samples measured with the IR camera just before the first pulse–pause sequence began.

3.2. Estimation of fatigue strength based on increasing amplitude experiments

The results of the increasing load-amplitude experiment were used for the estimation of fatigue strength based on a similar approach presented by Katunin and Wachla [20], Huang et al. [35] based on the Luong method [36]. The data presented describe the initial increase in temperature (phase I) of the CF/PEKK specimen and a certain part of the steady state of temperature evolution (phase II) during the bending fatigue test conducted at the VHCF test facility operating at 20 kHz. The term fatigue strength is used here in comparison to the commonly used fatigue limit as the experimental validation is carried out so far up to 10^9 cycles.

Fig. 8 shows the self-heating temperature evolution profiles measured in the bottom central part of the specimen (Area 4). The temperature responses for small displacements (between 4 μm and 12 μm) have been excluded from the analysis due to their high variance relative to the total temperature increase due to self-heating. The temperatures presented in Fig. 8 are relative to the temperature of the specimen at the beginning of the test, so as to remove the influence of the ambient temperature from the measurement data. Profiles for different displacements contain similar numbers of pulse–pause cycles.

Each of the profiles was modeled using a double-exponential approximation model, which can be used to describe the temperature profile in the first phase (initial increase) and the second phase (steady-state temperature stabilization).

$$T(t) = \Gamma_1 \exp(\Lambda_1 t) + \Gamma_2 \exp(\Lambda_2 t), \tag{1}$$

where two terms indicate the behavior of the first and second phases respectively. Γ_2 is the relative specimen temperature at the time t_s, $|\Gamma_1|$ is the temperature increase at the time t_s, and Λ_1 and Λ_2 represent specimen heat-gradient in the first and second phases respectively.

The model represents the temperature evolution. To characterize the pulse–pause profiles, these profiles were initially pre-processed according to the procedure described below. To avoid the influence of local peaks in the thermal response during a pulse–pause sequence,

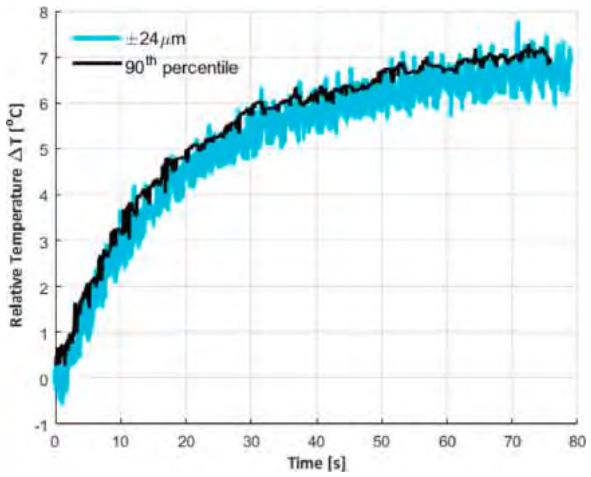

Fig. 9. The selected self-heating temperature profile (in blue) and its 90 percentile moving average.

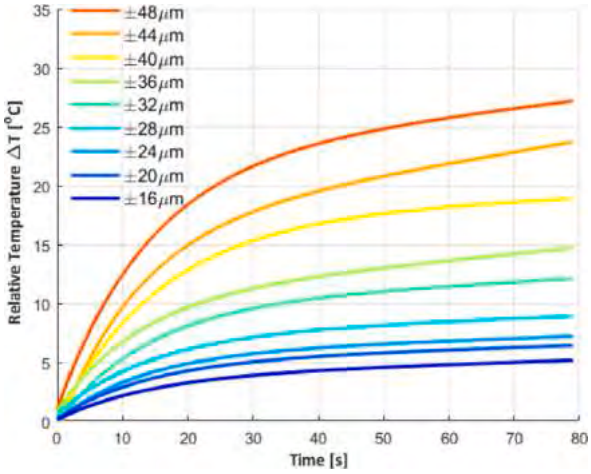

Fig. 10. Double-exponential approximation of the self-heating temperature profiles from Fig. 8.

higher percentile moving averages between 60 and 99% were calculated, and all of them lead to the same fatigue strength. Higher percentile average models lead to a better fit of bilinear models used to determine the fatigue strength. To this end, the 90th percentile moving average was finally used. Fig. 9 presents an example of the 90th percentile moving average with a dynamically changing window length, calculated using the formula:

$$wL_i = cI_i[wL_{min} - cI_{max}], \qquad i = 1...(N - wL_{max}), \tag{2}$$

where i is the sample number, wL_i is the instantaneous window length, I_i is the instantaneous slope of the heating profile, I_i is the maximum slope of the heating profile, wL_{min} is the minimum required window length and c is a coefficient based on the quotient of the selected window length range and the slope of the heating profile. The double exponential approximation models obtained for every 90th percentile waveform are shown in Fig. 10.

Table 4 presents results from the approximation of the selected self-heating temperature profiles using the double exponential model according to Eq. (1). Here RMSE is the root mean square error of residuals and R^2 represents the coefficient of determination. The time t_s indicates the time instant where the first term of the double exponential model in Eq. (1) starts to dominate over the second term.

To establish the beginning of the second phase of the temperature evolution, the temperature responses were temporarily treated as a

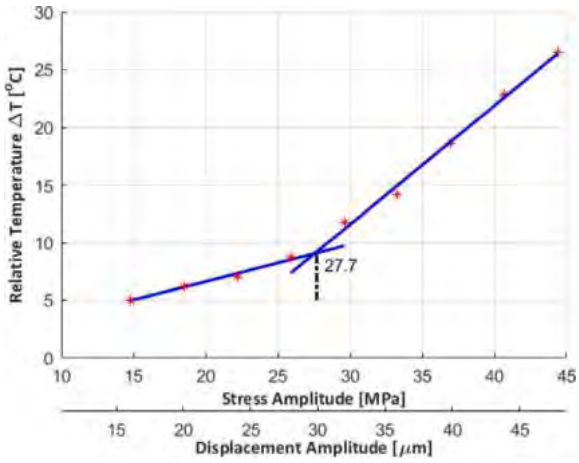

Fig. 11. Fatigue strength estimation based on the self-heating temperature that occurs during three-point bending at 20 kHz.

model of the inertia system of first order [37] with the steady-state temperatures (denoted as A) recorded at 80 s. Next, the time constants T were estimated for each profile. The longest time constant was observed for the maximum displacement amplitude profile of 48 μm at 17 s. After this, the boundary between the first phase (unsteady) and the second phase (steady-state) was established using 4 times the time constant (4T = 68 s), which is equivalent to $A(1 - \exp(t/T))100\% \approx 98.2\%$ of A. Since the time constant for other profiles was lower, they were also in the second phase at the time (4T). Finally, $t_h = 70$ s was used in further analysis.

The self-heating temperatures obtained for each model at t_h were plotted against the applied load to determine the fatigue strength using the Luong method [36]. This method interpolates the experimental results along two lines and determines the fatigue strength at the intersection of these lines. The interpolated experimental data were thus divided into two groups based on the minimum average root mean square errors of both lines [20]. The result is shown in Fig. 11 and the estimated fatigue strength equals 27.7 MPa, which refers to a displacement amplitude 30 μm according to Fig. 6.

3.3. Evaluation of the variability of fitting parameters

During the increasing load-amplitude experiment (see Section 2.5), temperature measurements were taken using thermal imaging (in 2.25 s-intervals) as well as using the IR camera (at 32 Hz, see Fig. 5). The variability between parameters of the double-exponential models used here was evaluated for temperature regression history data (for justification of the assumed model see [5]). In the absence of a significant difference between the parameters of the approximation models, the thermal images captured during the experiment would have to be used for the optimization of the ROI sizes and locations for a more precise evaluation of the fatigue strength.

To evaluate the variability of the fitting parameters, the thermal images captured during the increasing load-amplitude experiment were processed. First, the maximum temperatures measured within Area 4 (see Fig. 5a) were identified and normalized to remove the effect of the ambient temperature for the nine loading levels between 16 μm and 48 μm. The resulting temperature profiles are presented in Fig. 12 as discrete points. Based on these profiles, the fitting parameters of the double-exponential model (Γ_1, Λ_1, Γ_2 and Λ_2, see Eq. (1)) were identified and are presented in Table 5.

In order to evaluate variability between the same types of parameters of the double-exponential model (see Tables 4 and 5), the following random variables were introduced:

$$\theta_1(i) = \Gamma_{1(img)}(i) - \Gamma_{1(cam)}(i), \tag{3}$$

Table 4
The results of the approximation of selected self-heating temperature profiles.

Disp. Amp. [μm]	StressL Amp. [MPa]	Γ_1 [°C]	Λ_1 [°C/s]	Γ_2 [°C]	Λ_2 [°C/s]	RMSE	R^2	t_s [s]
16	14.8	−3.82	−0.069	3.92	0.0035	0.0865	0.995	28.7
20	18.5	−4.94	−0.071	5.15	0.0028	0.0960	0.996	28.6
24	22.2	−5.78	−0.076	5.83	0.0027	0.1169	0.995	31,0
28	25.9	−6.83	−0.070	7.41	0.0024	0.1677	0.993	26.6
32	29.6	−10.18	−0.072	9.94	0.0025	0.1723	0.997	36.5
36	33.3	−10.12	−0.077	10.99	0.0037	0.1617	0.998	22.4
40	37.0	−17.36	−0.064	17.22	0.0012	0.2518	0.998	44.6
44	40.7	−18.37	−0.078	17.33	0.0040	0.3385	0.997	33.0
48	44.4	−21.65	−0.069	22.64	0.0023	0.3092	0.998	30.1

Table 5
The results of approximation of selected self-heating temperature profiles processed from thermal images.

Disp. Amp. [μm]	Γ_1 [°C]	θ_1 [°C]	Λ_1 [°C/s]	θ_2 [°C/s]	Γ_2 [°C]	θ_3 [°C]	Λ_2 [°C/s]	θ_4 [°C/s]	RMSE	R^2
16	−3.75	0.07	−0.096	−0.027	3.68	−0.24	0.0048	0.0013	0.2365	0.972
20	−5.23	−0.29	−0.075	−0.004	5.30	0.15	0.0026	−0.0002	0.2187	0.984
24	−6.14	−0.36	−0.071	0.005	6.19	0.36	0.0014	−0.0013	0,2511	0,982
28	−6.84	−0.01	−0.086	−0.016	6.85	−0.56	0.0039	0.0015	0.2517	0.986
32	−9.34	0.84	−0.070	0.002	9.27	−0.67	0.0023	−0.0002	0.1865	0.996
36	−11.25	−1.13	−0.079	−0.002	11.67	0.68	0.0037	0.0000	0.2389	0.996
40	−15.17	2.19	−0.064	0.000	15.29	−1.93	0.0019	0.0007	0.2415	0.997
44	−16.22	2.15	−0.077	0.001	15.82	−1.51	0.0037	−0.0003	0.3215	0.997
48	−20.60	1.05	−0.069	0.000	20.78	−1.86	0.0027	0.0004	0.2834	0.998

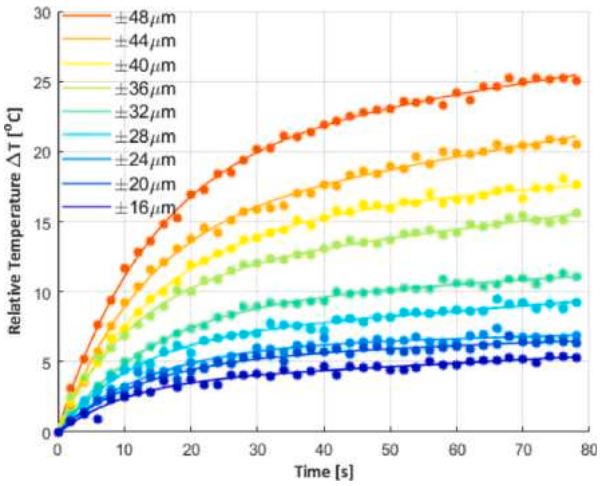

Fig. 12. Selected self-heating temperature profiles extracted from thermal images and their approximation models.

$$\theta_2(i) = \Lambda_{1(img)}(i) - \Lambda_{1(cam)}(i), \tag{4}$$

$$\theta_3(i) = \Gamma_{2(img)}(i) - \Gamma_{2(cam)}(i), \tag{5}$$

$$\theta_4(i) = \Lambda_{2(img)}(i) - \Lambda_{2(cam)}(i), \tag{6}$$

where the subscript *img* indicates model parameters related to the temperature profiles processed using thermal images and the subscript *cam* indicates those from the temperature profiles acquired directly from IR camera. The particular values for each random variable were presented in Table 5 as well.

An initial statistical analysis was performed on the data sets associated with the random variables θ_1, θ_2, θ_3 and θ_4 (see Table 5). The following statistical features were estimated: Minimum and maximum values, data range, mean and median values, standard deviation, and variance. The results obtained are presented in Table 6. A detailed analysis did not reveal any tendencies and dependencies and will require the use of more advanced statistical tools.

Since the number of samples in a sequence is small for all random variables considered (9 values per feature), the application of typical

Table 6
Results of the basic statistical analysis.

	θ_1	θ_2	θ_3	θ_4
Min.	−1.13	−2.70	−1.93	−1.3
Max.	2.19	0.50	0.68	1.5
Range	3.32	3.20	2.61	2.8
Mean	0.50	−0.46	−0.62	0.2
Median	0.07	0.00	−0.56	0.0
St. dev.	1.14	1.03	0.96	0.9
Variance	1.31	0.01	0.93	0.0

tests (e.g., Shapiro–Wilk test [38]) for verification data normality is inadequate. For this reason, a qualitative analysis based on quantile plots for a Gaussian distribution was carried out. To conduct quantile–quantile plot analysis, the theoretical quantiles z_i were calculated using the following formula [39]:

$$z_i = \Phi^{-1}\left(\frac{i-0.5}{n}\right), \tag{7}$$

where $\Phi(\cdot)$ is the standard normal quantile function [40,41], n is the sample size and i is the quantile index.

Next, the sample quantiles y_i were sorted in ascending order and associated with adequate theoretical quantiles (7) forming a set of data (z_i, y_i) for the quantile–quantile (Q–Q) plots, shown in Fig. 13. The analysis of the Q–Q plots is based on the observation of linearity between the theoretical quantiles of a standardized Gaussian distribution and the empirical quantiles, i.e., if the Q–Q points lie on a line, it means that the data follows a Gaussian distribution.

The quantile–quantile plot analysis (Fig. 13) of the Gaussian distribution confirms that the empirical distribution of random variables θ_1, θ_3 and θ_4 is very similar to the Gaussian distribution. For θ_2 the conclusion is questionable.

To confirm that the mean value of the considered random variables is equal to 0, the one-sample t-test was carried out. The t-test is applicable for populations with a Gaussian distribution and unknown standard deviations. Taking into account the evaluation of the models' fitting parameters, the following null hypothesis H_0 and alternative hypothesis H_1 were assumed:

- H_0: $\mu = 0$, i.e. mean values of features $\theta_1, \theta_2, \theta_3, \theta_4$ is equal to 0,
- H_1: $\mu \neq 0$, i.e. mean values of features $\theta_1, \theta_2, \theta_3, \theta_4$ is not equal to 0.

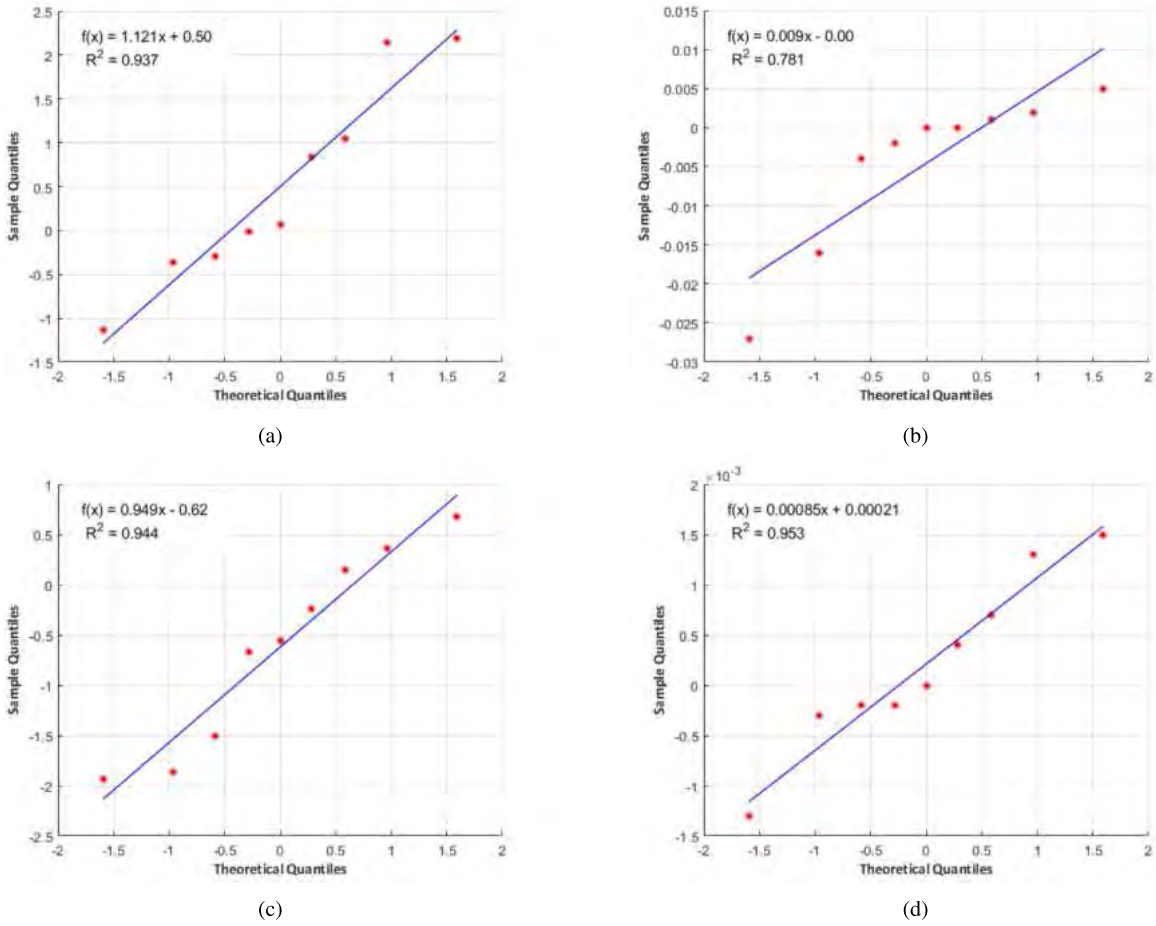

Fig. 13. Qualitative analysis for the Gaussian distribution of random variables: (a) θ_1, (b) θ_2, (c) θ_3 and (d) θ_4.

Table 7
Results of the one sample *t*-test.

	θ_1	θ_2	θ_3	θ_4
Sample size	9	9	9	9
Degrees of freedom ν	8	8	8	8
Significance level α	0.05	0.05	0.05	0.05
Critical value $t_{.025}$	−2.306	−2.306	−2.306	−2.306
Critical value $t_{.975}$	2.306	2.306	2.306	2.306
Mean	0.5011	−0.0046	−0.6200	0.0002
Statistic t	1.3146	−1.3273	−1.3613	0.7283
p-Value	0.2251	0.2211	0.0899	0.4872

To test the null hypothesis, the test statistic t and its degrees of freedom were calculated using established formulae [40,41]. These showed critical values $t_{.025}$ and $t_{.975}$ for the two-tailed test and a significance level $\alpha = 0.05$ using the tables of values from Student's t-distribution. The results of testing the mean are presented in Table 7.

The data from the Table 7 reveal that the absolute value of t statistic for all considered random variables is higher than the corresponding p-Value and it is in the range of critical values of $t_{.025}$ and $t_{.095}$ as well. Above means that for all considered random variables, hypothesis H_0 cannot be rejected with the significance level of $\alpha = 0.05$. Therefore, the assumed optimization of the ROI sizes and locations using thermal images captured within the increasing amplitude experiment can be performed.

3.4. Experimental validation of fatigue strength in the VHCF regime

After estimating the fatigue strength of the CF-PEKK material to be 27.7 MPa, four constant amplitude experiments were conducted to experimentally validate this finding. All four experiments were conducted with a mean stress of 200 MPa, a pulse time of 250 ms, and a pause time of 1500 ms. The experiment performed at a cyclic stress amplitude of 27.7 MPa was considered a run-out as no damage was observed up to 10^9 loading cycles. Later, two specimens were tested at a cyclic stress amplitude of 31.5 MPa—one resulted in a run-out, and the other failed after 4.2×10^8 loading cycles. The fourth specimen, tested at a cyclic stress amplitude of 33 MPa, also failed after 4.2×10^8 cycles. The change in relative temperature against the number of cycles for the three different stress amplitudes is shown in Fig. 14. For all these experiments, the maximum surface temperatures on the previously defined ROIs were recorded as a function of time throughout the entire duration of the experiments. To realize this plot, the peak temperature during each ultrasonic pulse was retrieved using a MATLAB routine. Therefore, each data point in Fig. 14 corresponds to the maximum surface temperature during one ultrasonic pulse, which corresponds to the maximum temperature reached after every 5050 fatigue cycles. The relative temperature was then determined from these peak values by removing the trend of ambient temperature and initial surface temperature of the specimens.

It can be inferred from this set of experiments that the fatigue strength of the CF-PEKK specimen is close to the cyclic stress amplitude of 31.5 MPa as one experiment led to a run-out while the other failed after 4.2×10^8 cycles. The maximum surface temperature for the failed specimens rose up to 80 °C due to the occurrence of damage, after which the experiments were stopped. These four experiments confirm

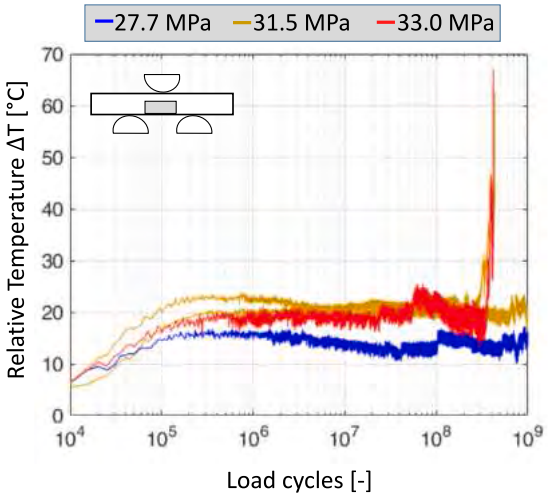

Fig. 14. Evolution of relative temperature on the surface of CF-PEKK specimens for different stress amplitudes.

Table 8
Pulse–Pause and load settings for cases using in shifting procedure.

Case	Pulse duration	Pause duration	Oscil. amplitude
A	250 ms	1.5 s	±40.0 μm
B	250 ms	1.25 s	±40.0 μm

that the fatigue strength of the CF-PEKK is within 10% of the estimated value of 27.7 MPa.

3.5. Extension of the fatigue strength estimation concept for variable pause duration

Based on the results observed for the increasing load-amplitude test discussed in Section 3.2, which was performed for pulse and pause-times of 250 ms and 1.75 s respectively, this section extends the fatigue strength estimation concept for a different pause-time. For this, an assumption was made that the fatigue strength is a material property and should be independent of the pause-time chosen. Different pause times should lead to a range of relative temperature changes, which may allow the determination of fatigue strength.

The shifting procedure was shown using two cases shown in Table 8, recorded for two tests at constant load-amplitudes with a pulse time of 250 ms. These two tests differed in their pause times: 1.5 s and 40 μm for Case A, and 1.25 s and 40.0 μm for Case B, The time–temperature profiles obtained from these tests were pre-processed similarly to the procedure discussed in Section 3.2. Fig. 15 shows models of the temperature evolution observed for the first phase and part of the second phase during cyclic loading. These profiles were smoothed using an average percentile and modeled using two exponential models. The profiles were then compared with the corresponding profiles from the increasing load-amplitude tests.

For a valid comparison of the cases shown in Table 8 with different pause-times, the relative temperatures for both tests needed to be correlated for the same:

- displacement amplitude conditions,
- number of cycles in every pulse, and
- the same steady-state condition of the temperature evolution in the second phase. Here, this refers to the 4 times the time constant, as discussed in Section 3.2.

Based on the temperature recorded at the respective 4T points shown in Fig. 15, the absolute difference in relative temperature between the two cases and the reference relative temperature from the

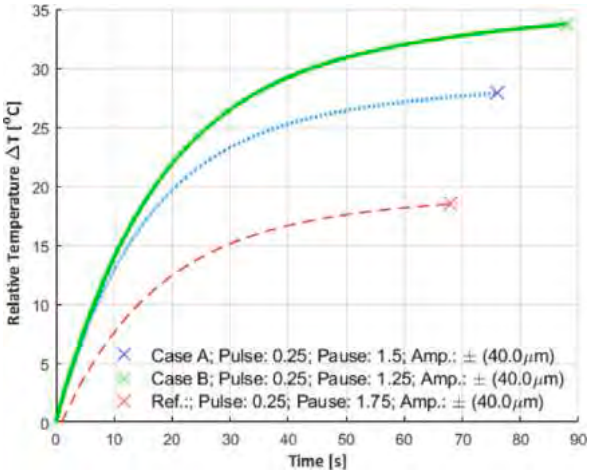

Fig. 15. Models of the temperature profiles for the same load but different pause times up to 4 times the time constant of individual profiles.

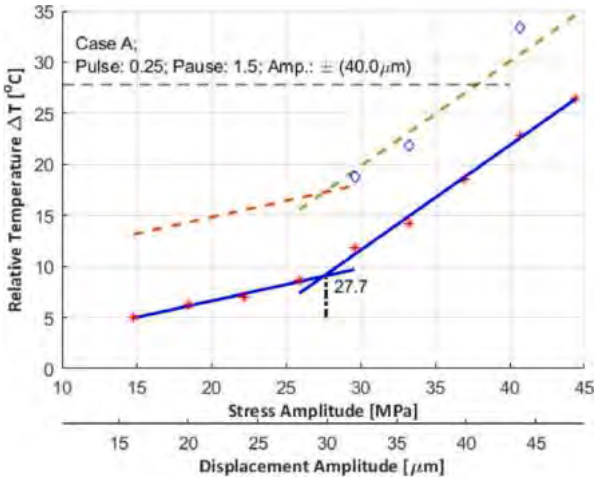

Fig. 16. Vertical shift of the bilinear model for the Case A. The red star points represent experimental data used for the estimation of the bilinear model (solid blue lines). The dashed line represents the shifted bilinear model, and the diamond points represent the experimental data obtained for the pause time of 1.5 s.

increasing amplitude test was estimated for case A:

$$\Delta T_{mA} = T_{ref} - T_{caseA} = 9.3\ ^{\circ}\mathrm{C}. \tag{8}$$

and case B correspondingly.

$$\Delta T_{mB} = T_{ref} - T_{caseB} = 15.2\ ^{\circ}\mathrm{C}. \tag{9}$$

The temperature differences ΔT_{mA} and ΔT_{mB} were used to shift the bilinear model vertically and are presented in Figs. 16 and 17 correspondingly.

In order to validate the approximation of the vertical shifting procedure, additional experiments were performed for the settings which correspond to the pause times for case A and case B. Figs. 16 and 17, contain blue diamonds points which represent validation points of the proposed procedure. For case A, a relative error of 7% was estimated, excluding the relative error of a bilinear model. Adequately for Case B, an error was 15%. The proposed method of using the thermographic approach in the estimation of fatigue strength and corresponding temperature for different pauses time is an approximation. This approximation depends on the quality of the estimation of the bilinear model, accuracy in the estimation of the vertical shifting value as well as on variance of the estimated fatigue strength.

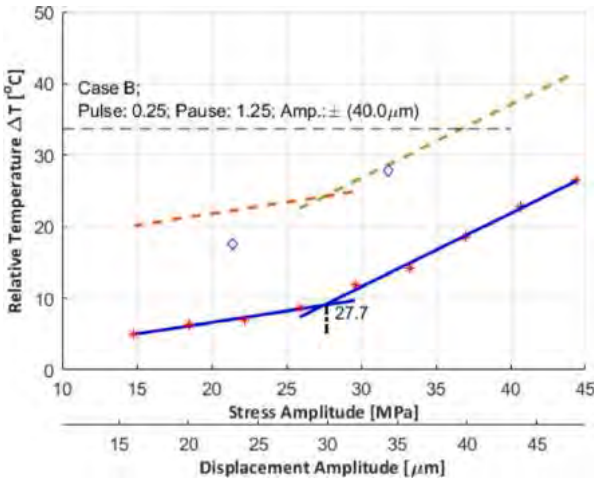

Fig. 17. Vertical shift of the bilinear model for the Case B. Red star points represent experimental data used for the estimation of the bilinear model (solid blue lines). The dashed line represents the bilinear shifted model and the diamond points represent experimental data obtained for the pause time of 1.25 s. experimentally.

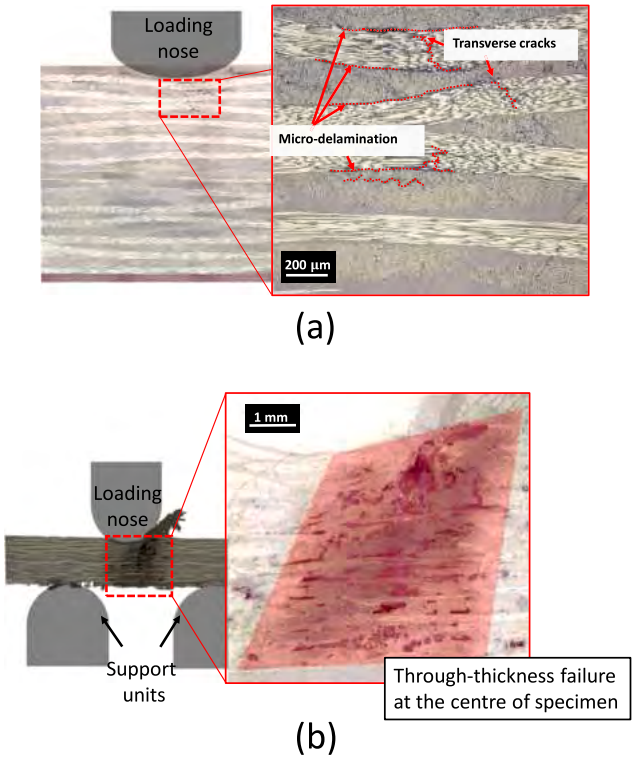

Fig. 18. The optical micrographs of the failed CF/PEKK specimens tested under (a) the stationary (Case I), and (b) non-stationary self-heating conditions (Case II).

3.6. Micrography for the constant load-amplitude experiments

From Fig. 18a and b it can be inferred that the damage was initiated at the top of the CF/PEKK specimens. For the specimen tested at ±48 μm with a pause time of 1.85 s (Case I), micro-delaminations and transverse cracks can be observed up to a depth of three plies from the top. For the specimen tested at ±51.4 μm with a pause time of 1.25 s (Case II), the damage was observed to travel across the entire specimen thickness with matrix de-cohesion failure (shown in the red-shaded region).

The damage in the specimen tested at ±51.4 μm with a pause of 1.25 s is catastrophic with significant structural damage due to the simultaneous loss of resonance and localized thermally induced softening of the PEKK matrix during the final ultrasonic pulse. One potential reason for such a failure could be the existence of a critical self-heating temperature. On the other hand, the absence of the thermally induced polymer softening mechanism in the specimen tested at ±48 μm with a pause time of 1.85 s could have limited the damage from propagating across the entire thickness. In other words, for the stationary self-heating condition, the temperature does not exceed the critical self-heating temperature. This condition could have limited the CF/PEKK specimen from significant structural damage. It should be noted here that the constant amplitude experiment with the non-stationary self-heating condition is rather invalid due to the strong influence of temperature on the fatigue of the CF/PEKK specimen. However, an insight into the critical self-heating temperature can be used in the future as a threshold value to avoid thermal effects along with mechanical fatigue.

To test the hypothesis of localized softening of the PEKK matrix during the final phase (failure) for the non-stationary self-heating condition the rate of energy dissipation at different ultrasonic pulses during ultrasonic cyclic loading was estimated.

3.7. Estimation of rate of energy dissipation for approximating the critical self-heating temperature

The critical self-heating temperature may be approximated through the rate of energy dissipation of the specimen during fatigue loading. Using the classical non-stationary heat transfer equation, the variation in the dissipated energy q with time [42] for a certain material can be given as:

$$q = w - \rho \frac{du}{dt}, \tag{10}$$

where ρ is the material density, w is the total mechanical work per unit volume and u is the specific internal energy, which includes both energy components related to and not related to damage: E_d and E_{nd} respectively. For a particular material, the heat dissipation rate can be given as:

$$\rho \frac{du}{dt} = E_{nd} + E_d = \rho c \frac{\partial T}{\partial t} + E_d, \tag{11}$$

where c is the specific heat and T is the temperature. The energy dissipation rate can be determined through dynamic mechanical analysis or estimated directly from the curves of self-heating temperature history. The procedure originally proposed by Meneghetti and Quaresimin [43,44] was adopted here based on the temperature drop rate using the dissipated energy q and E_{nd}, just after the ultrasonic pulses. Inserting Eq. (11) into Eq. (10) and considering that after the end of an ultrasonic pulse, the mechanical energy is no longer supplied to the CF/PEKK specimens and the damaging processes stop, Eq. (10) takes the following form:

$$q = -\rho c \frac{\partial T}{\partial t}. \tag{12}$$

Based on Eq. (12), it can be assumed that the energy dissipation in short intervals at the pulse–pause boundary is the same if the variations in the temperature field of the specimen are neglected. This energy dissipation rate can be obtained from the slope of the linear regression line of the cooling curve [45]. For the non-stationary constant load-amplitude test (Case II), temperature curves were extracted from the thermograms obtained at different pulses, and the slope of the linear regression at the start of the pause phase was determined. Then, using Eq. (12) and the specific heat and density of the CF/PEKK specimens (see Tables 1 and 2) the cooling rate was estimated. Fig. 19 shows a representative temperature history curve and its linear regression, based on which the cooling rate was evaluated.

Fig. 20 shows the average dissipated energy for all the pulse–pause sequences (each pulse consists of 5050 fatigue cycles) during the non-stationary constant load-amplitude test. The data of the first two

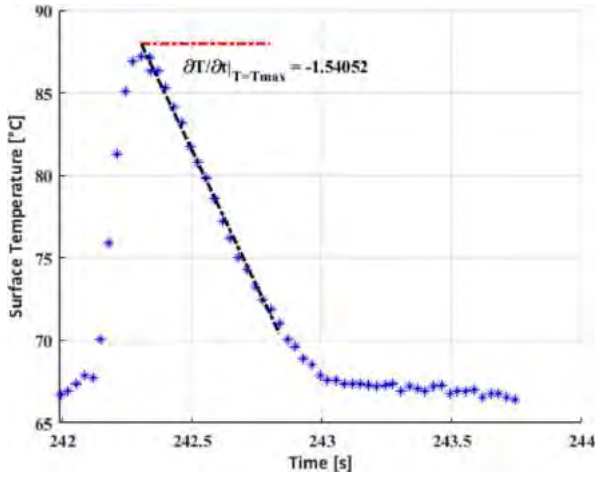

Fig. 19. An example for estimating the cooling rate based on the slope of linear regression of the temperature at the start of a pause phase.

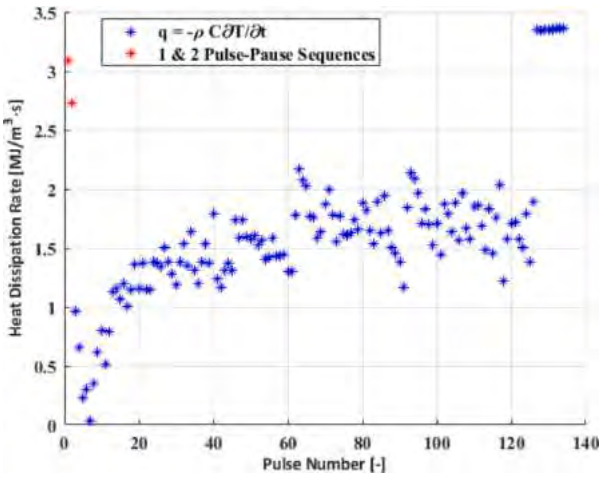

Fig. 20. Variation of the heat dissipation rate during the consecutive pulses for the non-stationary constant load-amplitude test.

pulse–pause sequences (shown in red) have been excluded from the analysis, as these could have resulted from frictional heating due to the self-alignment of the specimen at the start of the experiment. For the remaining points, constant window averages with window lengths of 2, 4, 6, and 12 were applied to the raw data. Fig. 21 shows the results from the average with a window length of 6, as it showed the least amount of scattering.

From Fig. 21 it can be seen that the higher heat dissipation rate occurs after ≈65 °C due to non-stationary self-heating. Distinct phases of energy dissipation can be identified from this figure: A linear increase up to about ≈50 °C and a sharp increase after ≈65 °C. This temperature range can be hypothesized to be related to the fatigue limit, based on the previous work of the authors [20]. The heat dissipation rate varies around 1.5 MJ/m^3 s between 50 °C and 65 °C. This may be the result of the damage accumulation on the specimen surface as the critical self-heating temperature. Above this temperature, the sharper temperature increase can be attributed to polymer softening, the formation of macrocracks, and the appearance of new surfaces in the failure region of the CF-PEKK specimen in addition to the heat dissipation caused by viscoelastic hysteresis. The heat dissipation analysis of such non-stationary self-heating experiments can provide an upper self-heating temperature limit for future fatigue tests at constant load amplitudes.

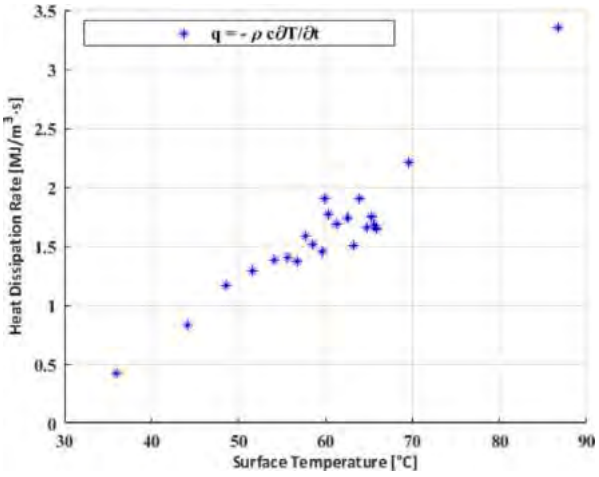

Fig. 21. Heat dissipation rates indicating the self-heating temperature after a moving average with a constant window length of 6.

4. Conclusions

This study investigated the self-heating behavior of a CF/PEKK composite at ultrasonic frequencies in the VHCF regime, in particular its thermal response and structural degradation. This accelerated fatigue testing at 20 kHz enables a significant shortening of the testing time, making it economically reasonable. A consequence of this high loading frequency is the pronounced influence of the self-heating effect, which is unavoidable even in the presence of active air-cooling and the use of pulse–pause sequences for loading. On the other hand, this temperature increase due to self-heating can serve as a sensitive indicator for the structural degradation of the specimen over the course of the test. This method has been applied in numerous studies to estimate the fatigue limit in the LCF regime. In this study, it was experimentally confirmed that this critical evaluation method can be effectively adapted to VHCF tests (up to 10^9 cycles).

It should be noted that in contrast to LCF testing, the evaluation of fatigue strength for VHCF testing at ultrasonic frequencies requires data pre-processing due to the vastly different local self-heating dynamics under pulse–pause loading. A methodology was developed to incorporate this and additional variables particular to ultrasonic VHCF testing such as the pause duration. Based on this methodology, it is possible to evaluate the test results on a fatigue strength plot and determine if the loading parameters result in a temperature response above or below the estimated fatigue strength. Since this analysis is based only on the second-phase self-heating response (see Section 3.5), the evaluation can be performed in a fast and reliable manner.

Furthermore, it was shown that the fatigue strength estimated in this work remained independent of changes in the experimental parameters used, which implies that the fatigue strength can be considered a material property for VHCF testing at ultrasonic frequencies. This was also confirmed by experiments as well as the statistical tests performed on the approximation model features of the temperature history curves (see Section 3.3). The results of the statistical analysis lay the foundation for further optimization of the ROIs for the self-heating temperature measurements for future VHCF tests.

The microscopic observations of the two specimens tested under the stationary (Case I) and non-stationary (Case II) constant cyclic amplitudes indicate that the failure occurred near the middle of the specimen. However, for the non-stationary case, matrix de-cohesion was observed due to polymer softening. This led to more severe damage due to the specimen experiencing non-stationary self-heating, compared to the specimen tested under stationary self-heating conditions. The relevance of micrography in this study in observing the locations

of damage initiation for the two loading cases, which were observed to be consistent.

The estimation of the energy dissipation, used previously in LCF testing, was successfully adapted to the non-stationary self-heating experiment (Case II). The heat dissipation characteristic as a function of the structural degradation yielded a threshold temperature near ≈65 °C. This temperature could represent the critical self-heating temperature and is related to the fatigue strength. The correlation between the self-heating temperature and fatigue strength for VHCF testing must be further examined and planned for future studies.

CRediT authorship contribution statement

Aravind Premanand: Conceptualization, Methodology, Experiments, Data curation, Writing – original draft, Writing – review & editing. **Tomasz Rogala:** Conceptualization, Methodology, Data curation, Formal analysis, Software, Writing – original draft, Writing – review & editing. **Dominik Wachla:** Conceptualization, Methodology, Data curation, Formal analysis, Software, Writing – original draft. **Jafar Amraei:** Conceptualization, Methodology, Data curation, Formal analysis, Software, Writing – original draft. **Andrzej Katunin:** Conceptualization, Methodology, Formal analysis, Writing – original draft, Writing – review & editing, Project administration. **Bilal Khatri:** Conceptualization, Writing – original draft, Writing – review & editing. **Michael Rienks:** Software, Implementation. **Frank Balle:** Conceptualization, Methodology, Writing – review & editing, Project lead, Funding acquisition.

Declaration of competing interest

The authors declare that they have no known competing financial interests or personal relationships that could have appeared to influence the work reported in this paper.

Data availability

Data will be made available on request.

Acknowledgments

The authors acknowledge the support of all the ultrasonic-related activities by the Walter-and-Ingeborg-Herrmann Foundation and German Research Foundation (DFG) in the framework of the project (493632129) for supporting the initiation of collaboration between the authors. The authors would also like to thank the Carl Zeiss Foundation for supporting the research project (SCHARF).

References

[1] Bryan Harris, Fatigue in Composites: Science and Technology of the Fatigue Response of Fibre-Reinforced Plastics, in: Woodhead Publishing Series in Composites Science and Engineering, vol. Number 16, Woodhead Publishing Limited, Cambridge, England, 2003.

[2] Yasushi Miyano, Masayuki Nakada, Kazuyoshi Nishigaki, Prediction of long-term fatigue life of quasi-isotropic CFRP laminates for aircraft use, Int. J. Fatigue 28 (2006) 1217–1225.

[3] John Tomblin, Waruna Seneviratne, Determining the Fatigue Life of Composite Aircraft Structures Using Life and Load-Enhancement Factors, techreport DOT/FAA/AR-10/6, U.S. Department of Transportation, Federal Aviation Administration, Washington, DC, 2011.

[4] Daniel Backe, Frank Balle, Ultrasonic fatigue and microstructural characterization of carbon fiber fabric reinforced polyphenylene sulfide in the very high cycle fatigue regime, Compos. Sci. Technol. 126 (2016) 115–121.

[5] Andrzej Katunin, Critical self-heating temperature during fatigue of polymeric composites under cyclic loading, Compos. Theory Pract. 12 (1) (2012) 72–76.

[6] Andrzej Katunin, Angelika Wronkowicz, Marcin Bilewicz, Dominik Wachla, Criticality of self-heating in degradation processes of polymeric composites subjected to cyclic loading: A multiphysical approach, Arch. Civ. Mech. Eng. 17 (2017) 806–815.

[7] Andrzej Katunin, Criticality of the self-heating effect in polymers and polymer matrix composites during fatigue, and their application in non-destructive testing, Polymers 11 (1) (2018) 19.

[8] Jafar Amraei, Andrzej Katunin, Recent advances in limiting fatigue damage accumulation induced by self-heating in polymer–matrix composites, Polymers 14 (24) (2022) 5384.

[9] Dominik Flore, Konrad Wegener, Herwig Mayer, Ulrike Karr, Claus C Oetting, Investigation of the high and very high cycle fatigue behaviour of continuous fibre reinforced plastics by conventional and ultrasonic fatigue testing, Compos. Sci. Technol. 141 (2017) 130–136.

[10] Aravind Premanand, Frank Balle, Development of an axial loading system for fatigue testing of textile-composites at ultrasonic frequencies, Mater. Lett.: X 13 (2022) 100131.

[11] Aravind Premanand, Frank Balle, Influence of pulse–pause sequences on the self-heating behavior in continuous carbon fiber-reinforced composites under ultrasonic cyclic three-point bending loads, Materials 15 (2022) 3527.

[12] Andrzej Katunin, Marcin Bilewicz, Dominik Wachla, Jafar Amraei, Julio Viana, Investigation of fracture mechanisms of self-reinforced polypropylene/polycarbonate composites subjected to fatigue loading, in: Mater. Sci. Forum, 1075, Trans Tech Publ, 2022, pp. 65–70.

[13] Andrzej Katunin, Criticality of the self-heating effect in polymers and polymer matrix composites during fatigue, and their application in non-destructive testing, Polymers 11 (1) (2018) 19.

[14] Zvi Hashin, Assa Rotem, A fatigue failure criterion for fiber reinforced materials, J. Compos. Mater. 7 (1973) 448–464.

[15] Giusy La Rosa, Antonino Risitano, Thermographic methodology for rapid determination of the fatigue limit of materials and mechanical components, Int. J. Fatigue 22 (2000) 65–73.

[16] Marino Quaresimin, Fatigue of woven composite laminates under tensile and compressive loading, in: ECCM-10; Composites for the Future, 2002, 10th European Conference on Composite Materials ; Conference date: June 3-7, 2002, Brugge, Belgium.

[17] Chiara Colombo, Flavia Libonati, Flavio Pezzani, Antonio Salerno, Laura Vergani, Fatigue behaviour of a GFRP laminate by thermographic measurements, Procedia Eng. 10 (2011) 3518–3527.

[18] John Montesano, Zouheir Fawaz, Habiba Bougherara, Use of infrared thermography to investigate the fatigue behavior of a carbon fiber reinforced polymer composite, Compos. Struct. 97 (2013) 76–83.

[19] Fangai Yu, Bo Zhou, Wen Xin, Xueyan Zhang, Fatigue life prediction for the main spar with wrinkle defects of a wind turbine blade, Fatigue Fract. Eng. Mater. Struct. 44 (2021) 2764–2780.

[20] Andrzej Katunin, Dominik Wachla, Determination of fatigue limit of polymeric composites in fully reversed bending loading mode using self-heating effect, J. Compos. Mater. 53 (2019) 83–91.

[21] Andrzej Katunin, Ivanna Pivdiablyk, Laurent Gornet, Patrick Rozycki, A hybrid method for determination of fatigue limit and non-destructive evaluation of composite structures after low-velocity impact loading, Composites B 238 (2022) 109898.

[22] Pietro Foti, Dario Santonocito, Paolo Ferro, Giacomo Risitano, Filippo Berto, Determination of fatigue limit by static thermographic method and classic thermographic method on notched specimens, Procedia Struct. Integr. 26 (2020) 166–174.

[23] Dario Santonocito, Pietro Foti, Giacomo Risitano, Filippo Berto, Fatigue damage assessment in AM polymers evaluating their energy release, Procedia Struct. Integr. 34 (2021) 211–220.

[24] Sepanta Mandegarian, Seyed Sina Samareh-Mousavi, Fathollah Taheri-Behrooz, Experimental investigation on in-plane shear fatigue failure criteria of±45° angle-ply carbon epoxy composite, Int. J. Fatigue 160 (2022) 106873.

[25] Aijia Li, Jia Huang, Chao Zhang, Enabling rapid fatigue life prediction of short carbon fiber reinforced polyether-ether-ketone using a novel energy dissipation–based model, Compos. Struct. 272 (2021) 114227.

[26] S.B. Ratner, V.I. Korobov, Self-heating of plastics during cyclic deformation, Polymer Mech. 1 (3) (1965) 63–68.

[27] B.P. Gumenyuk, V.G. Karnaukhov, Dynamic behavior of viscoelastic bodies during harmonic excitation, Sov. Appl. Mech. 16 (7) (1980) 623–628.

[28] Ali Kahirdeh, Michael M. Khonsari, Criticality of degradation in composite materials subjected to cyclic loading, Composites B 61 (2014) 375–382.

[29] Andrzej Katunin, Angelika Wronkowicz, Characterization of failure mechanisms of composite structures subjected to fatigue dominated by the self-heating effect, Compos. Struct. 180 (2017) 1–8.

[30] Toray cetex TC1200 PEEK product data sheet, 2022, https://www.toraytac.com/media/7765d981-1f9f-472d-bf24-69a647412e38/Pr7gdw/TAC/Documents/Data_sheets/Thermoplastic/UD%20tapes,%20prepregs%20and%20laminates/Toray-Cetex-TC1200_PEEK_PDS.pdf. Accessed on 29.11.2022.

[31] Toray cetex TC1320 PEKK product data sheet, 2022, https://www.toraytac.com/media/409dcc72-6aff-4643-86b8-20b5f464f038/lNO6TA/TAC/Documents/Data_sheets/Thermoplastic/UD%20tapes,%20prepregs%20and%20laminates/Toray-Cetex-TC1320_PEKK_PDS.pdf. Accessed on 29.11.2022.

[32] Wouter Grouve, Weld strength of laser-assisted tape-placed thermoplastic composites, Univ. Twente (2012).

[33] Daniel Backe, Frank Balle, Dietmar Eifler, Fatigue testing of CFRP in the very high cycle fatigue (VHCF) regime at ultrasonic frequencies, Compos. Sci. Technol. 106 (2015) 93–99.
[34] Richard de Vries, Edwin Lamers, Sebastiaan Wijskamp, Blasimir Villa Rodriguez, Remko Akkerman, Micromechanics modeller, 2021, https://www.utwente.nl/en/et/ms3/research-chairs/pt/Tools/Files/U20MM%20background%20information.pdf, Accessed on 30.11.2021.
[35] Andrzej Katunin, Angelika Wronkowicz, Dominik Wachla, Impact damage assessment in polymer matrix composites using self-heating based vibrothermography, Compos. Struct. 214 (2019) 214–226.
[36] Minh Phong Luong, Fatigue limit evaluation of metals using an infrared thermographic technique, Mech. Mater. 28 (1) (1998) 155–163.
[37] Henrik Niemann, Robert Miklos, A simple method for estimation of parameters in first order systems, J. Phys. Conf. Ser. 570 (1) (2014) 012001.
[38] Samuel Shapiro, Martin Wilk, An analysis of variance test for normality (complete samples), Biometrika 52 (3–4) (1965) 591–611.
[39] Dominik Wachla, Andrzej Katunin, Modelling fatigue with self-heating of polymeric composites based on statistical analysis of temperature profiles, Compos. Theory Pract. 18 (4) (2018) 202–209.
[40] Yadolah Dodge, The Concise Encyclopedia of Statistics, in: Springer Reference, Springer, 2008.
[41] George Snedecor, William Cochran, Statistical Methods, Wiley-Blackwell, 1989.
[42] Mehdi Naderi, Ali Kahirdeh, Michael M. Khonsari, Dissipated thermal energy and damage evolution of glass/epoxy using infrared thermography and acoustic emission, Composites B 43 (3) (2012) 1613–1620.
[43] Giovanni Meneghetti, Marino Quaresimin, Fatigue strength assessment of a short fiber composite based on the specific heat dissipation, Composites B 42 (2) (2011) 217–225.
[44] Giovanni Meneghetti, Analysis of the fatigue strength of a stainless steel based on the energy dissipation, Int. j. fatigue 29 (1) (2007) 81–94.
[45] Andrzej Katunin, Evaluation of criticality of self-heating of polymer composites by estimating the heat dissipation rate, Mech. Compos. Mater. 54 (1) (2018) 53–60.

Paper VI

Thermomechanical fatigue life assessment of polymer-matrix composites via entropy-based damage evolution and stiffness degradation under different frequencies

Composites Part B 298 (2025) 112353

Contents lists available at ScienceDirect

Composites Part B

journal homepage: www.elsevier.com/locate/compositesb

Thermomechanical fatigue life assessment of polymer-matrix composites via entropy-based damage evolution and stiffness degradation under different frequencies

Jafar Amraei *, Andrzej Katunin

Department of Fundamentals of Machinery Design, Faculty of Mechanical Engineering, Silesian University of Technology, Konarskiego 18A, 44-100, Gliwice, Poland

ARTICLE INFO

Handling Editor: Prof. Ole Thomsen

Keywords:
Fracture fatigue entropy
Fatigue strength
Lifetime prediction
Self-heating effect
Acoustic emission
Stiffness degradation
Frequency effect

ABSTRACT

This study assessed the fatigue performance of glass/epoxy composite by exploring the role of loading frequency (20–50 Hz) on fatigue strength, lifespan, and damage evolution. Implementing bilinear thermographic approaches ($\Delta T-\sigma$ and $\dot{q}-\sigma$) highlighted a remarkable fatigue strength reduction as frequency increased. At higher frequencies (40 Hz and 50 Hz), the discrepancies in fatigue strength values resulting from thermographic methods were more pronounced than at lower frequencies. The determined fatigue strengths at higher frequencies were then compared to those obtained from the standard $S-N$ curves as a reference. The analysis demonstrated the closer alignment of $\dot{q}-\sigma$ results with the reference $S-N$ curves. The unfeasibility of bilinear models at higher frequency under high-stress levels necessitated establishing a new trilinear $\dot{q}-\sigma$ model. The developed model aimed to assess the fracture fatigue entropy (FFE), alongside the entropy-based damage index (EDI) as a normalized indicator for damage evolution across low-, intermediate-, and high-cycle-fatigue regimes, facilitating the FFE-based $S-N$ curves validated with the experimental $S-N$ data. The new EDI-based $S-N$ curves were then established at different levels of damage accumulation. Damage evolution was captured via real-time acoustic emission (AE) monitoring synchronized with the registered thermal responses, enabling the identification of critical fatigue cycles, where rapid damage accumulation begins, alongside determining the boundaries that indicate abrupt failure. Correlating the AE-identified critical boundaries with the stiffness reduction enabled the establishment of $S-N$ curves based on various controlled degradation levels, bridging the knowledge gap and establishing a refined methodology for thermomechanical fatigue analysis of polymer-matrix composites (PMCs).

1. Introduction

Polymer matrix composites (PMCs) are increasingly utilized in industries such as aerospace, automotive, and wind energy owing to their exceptional strength-to-weight ratio, stiffness, and fatigue endurance/strength [1]. Evaluating and mimicking the prolonged fatigue performance of PMCs under typical operating conditions at low frequencies ($\leq$10 Hz) remains challenging due to the time-consuming and costly nature of traditional fatigue tests [2,3]. Therefore, there is a compelling need for accelerated fatigue testing methods that retain reliability while reducing testing durations.

Increasing the testing frequency offers an attractive pathway for accelerating fatigue life assessments, while it introduces complexities, primarily linked to the self-heating effect [3–8]. This phenomenon originates from the viscoelastic nature of polymers used in PMCs. Nevertheless, for a fatigue-loaded PMC specimen, it is driven by the thermoviscoelastic response. The out-of-phase lag between stress and strain during cyclic loading induces dissipation processes in a material, being a direct consequence of the viscoelastic nature of a polymeric matrix. Due to its low thermal conductivity, a large amount of dissipated energy is converted to heat storage, leading to a temperature increase and, consequently, structural changes in PMCs, including significant acceleration of fatigue degradation processes under certain conditions [4]. The self-heating temperature history curve is represented by three characteristic phases [4,9]: (i) an initial phase of rapid temperature rise, (ii) a steady phase with temperature stabilization, and (iii) the final phase where the tested PMC reaches a critical self-heating temperature [6,10], beyond which the rapid damage accumulation occurs, leading to

* Corresponding author.
E-mail address: jafar.amraei@polsl.pl (J. Amraei).

https://doi.org/10.1016/j.compositesb.2025.112353
Received 18 November 2024; Received in revised form 10 February 2025; Accepted 26 February 2025
Available online 27 February 2025

a sharp temperature increase, microstructural damage, and eventual fatigue failure [6]. The intensity of the self-heating effect is influenced by several factors, including the loading parameters (e.g., stress ratio, frequency) [11–14], material properties (e.g., polymer and fiber types) [15,16], alongside the environmental factors (e.g. ambient temperature and moisture) [17–19]. Minimizing or limiting self-heating temperature can be achieved by cooling the surface of fatigue-loaded PMCs using efficient cooling techniques [6,9]. Within the framework of accelerating fatigue testing through higher loading frequencies, studies primarily performed ultrasonic frequency fatigue testing (UFFT) around 20 kHz within the very-high-cycle fatigue (VHCF) regime. To limit the self-heating effect, researchers in Refs. [9,20] used a pulse-pause method alongside forced air cooling. Lee et al. [21] incorporated a Peltier ring-type cooling based on a pulse-pause approach. Wang et al. [22] utilized both cryogenic nitrogen cooling and pulse–pause method, see Ref. [4] for further details. Nevertheless, VHCF tests are typically conducted at relatively low-stress amplitudes, e.g. up to ±49.1 MPa with a corresponding displacement amplitude of ±54.2 μm [15]. Fatigue testing should be extended under moderate and high-stress amplitudes to comprehensively capture the thermomechanical fatigue behavior of PMCs. This may be achieved using standard testing facilities such as servo-hydraulic systems operating at the maximum frequency of 100 Hz [3]. As a step forward in addressing this limitedly studied testing scenario, performing experiments under natural air cooling enables analysis of how temperature rise correlates with both frequency and applied stress/strain level, aiding in selecting the appropriate and cost-effective cooling methods based on the level of determined heat and temperature growth.

The stress-life ($S-N$) and strain-life ($\varepsilon-N$) methods are often utilized for evaluating the durability and longevity of fatigue-loaded PMCs [23,24]. The former is typically used for force-controlled fatigue tests, maintaining a constant stress amplitude throughout cycles [25]. Nevertheless, the latter is usually implemented for displacement-controlled tests, including ultrasonic- and shaker-based tests [9,26], where strain remains constant during the test [27]. To compare both methods, Ferreira et al. [28] conducted fatigue tests on glass fiber-reinforced polypropylene composites using both displacement- and stress-controlled modes at a frequency of 10 Hz. They presented the results in the form of the $S-N$ and $\varepsilon-N$ curves, and reported less than 5 % discrepancy between those two methods, highlighting the comparability and transferability of findings extracted from the $S-N$ and $\varepsilon-N$ curves for assessing the fatigue behavior of PMCs. However, higher frequency in displacement-controlled fatigue tests may lead to thermal nonlinearities in PMCs due to their low thermal conductivity and viscoelastic behavior [4,29], making accurate strain measurement more challenging. Assuming the comparability of the $S-N$ and $\varepsilon-N$ models for the fatigue life assessment of PMCs, instead of developing the $\varepsilon-N$ curves under the displacement-controlled scenario, a viable strategy at higher frequencies is to construct the $S-N$ curves based on the maximum stress level that the PMC specimen tolerates [6]. To achieve this, the maximum force measured by a force sensor can be correlated with the applied displacement, thereby enabling the conversion of force into stress [26].

To estimate the fatigue strength of PMCs, the thermographic methods have gained significant attention primarily due to advancements in non-contact infrared thermography [30–40], serving as an alternative to the time-consuming and costly $S-N$ curves. Thermographic methods encompass the temperature rise-stress ($\Delta T-\sigma$) and heat dissipation rate-stress ($\dot{q}-\sigma$) approaches, which shorten the experimental duration and facilitate the rapid estimation of fatigue strength in PMCs [41]. $\Delta T-\sigma$ approach evaluates the fatigue strength of the tested PMC by measuring the stabilized temperature increases corresponding to a wide range of stress levels without requiring extensive time or large datasets. Within this approach, fatigue strength is defined as the stress level above which the PMC exhibits a noticeable increase in thermal response, attributed to the accumulation of fatigue-induced damage [9]. Numerous studies have demonstrated the utility of this method in predicting the fatigue strength of numerous PMCs, including carbon fiber-reinforced polymers (CFRPs), glass fiber-reinforced polymers (GFRPs), and other PMCs [30–40]. Similarly, $\dot{q}-\sigma$ approach offers an accelerated and efficient way to evaluate the fatigue strength of PMCs [42,43]. The fatigue strength determined from this thermographic approach is identified at the stress level above which the rate of heat dissipation accelerates, highlighting the critical boundary where rapid cumulative damage begins. In summary, both methods offer advantages depending on the material and application, with $\Delta T-\sigma$ excelling in simplicity and speed, while $\dot{q}-\sigma$ approach, requiring further analysis, but may deliver a more in-depth assessment of fatigue behavior. However, this represents a key gap in the literature, highlighting the need for further research to evaluate which approach provides higher accuracy.

Alongside the fatigue strength estimation at 10^6 cycles [7,34,44], the fatigue life assessment of PMCs plays a key role in ensuring performance across different fatigue regimes, ranging from low-cycle fatigue (LCF) to VHCF [6]. As opposed to the widely used standard $S-N$ curves, which rely on abrupt failure, implementing the entropy concept as a thermodynamic framework can yield a more comprehensive analysis by incorporating the results derived from $\dot{q}-\sigma$ approach [45]. Entropy generation, governed by the second law of thermodynamics (Clausius–Duhem inequality) [46], is a function of loading types [47], ambient temperature [48], stress level, and loading frequency [49,50]. For fatigue-loaded PMCs, entropy generation may arise from different fracture mechanisms such as matrix cracking, fiber breakage, debonding, and delamination [51]. Several studies have implemented entropy-based models for fatigue life prediction in PMCs [15,34,52,53]. By applying the first and second laws of thermodynamics, Naderi and Khonsari [51] developed a theoretical framework to assess the fracture fatigue entropy (FFE) as a material property. FFE is chiefly driven by the accumulated irreversible energy resulting from the damage evolution until reaching its critical threshold at the final fracture [52]. Their findings were further supported by Mohammadi and Mahmoudi [46], who proposed a micromechanical model for evaluating FFE, demonstrating that the FFE value remains relatively constant regardless of the fracture mechanism, whether the damage is caused by fiber breakage or polymer matrix cracking. Huang et al. [34] employed heat generation, which encompasses both recoverable and non-recoverable energy to evaluate FFE and subsequently the lifetime of CFRP specimens. When determining FFE for PMCs, internal friction resulting from the fiber-matrix interphase, the interlaminar region between adjacent layers is often regarded as a recoverable process with negligible impact on fatigue life [53]. For this reason, they implemented a quadratic function to separate the internal heat friction from the entire heat generation including damage. Furthermore, Premanand et al. [15] implemented the FFE concept for lifetime prediction within the VHCF regime. All previous works assumed constant heat capacity (C_p) when implementing the $\dot{q}-\sigma$ approach for evaluating FFE, but incorporating temperature-dependent C_p is critical for accurately modeling and quantifying the heat dissipation rate. This refinement can thereby lead to a more reliable determination of entropy generation, which is a key factor in comprehending damage evolution under fatigue loading. Furthermore, prior studies used the entropy concept and proposed mainly one mean value for FFE within all fatigue regimes, while it is essential to develop a comprehensive approach for evaluating FFE from low-, to high-cycle fatigue regimes.

Most existing studies focused on low-frequency ($\leq$15 Hz) or ultrasonic ($\sim$ 20 kHz) fatigue testing, leaving a key gap in understanding how moderate frequencies affect fatigue strength, lifetime, and damage evolution of PMCs, with particular attention to the role of self-heating in accelerating the integrity degradation. This research addresses this gap by analyzing the fatigue performance of PMCs at a frequency range of 20–50 Hz. Moreover, while previous studies have applied

thermographic approaches (i.e., $T-\sigma$ and $\dot{q}-\sigma$) individually, assessing the sensitivity of fatigue strength determination using both methods remains essential for the same tested PMC. Furthermore, this study also seeks to improve the quantification of heat dissipation rates by implementing temperature-dependent C_p, allowing for a more accurate determination of FFE across different fatigue regimes. On the other side, constructing standard $S-N$ curves primarily account for abrupt failure, yet such criteria are unsuitable for in-service PMC design. A viable strategy is to evaluate the fatigue performance of PMCs based on their allowable stiffness degradation levels, rather than relying solely on final failure. To achieve this, the current study seeks to incorporate real-time acoustic emission (AE) monitoring during fatigue testing, capturing the initiation and damage evolution. By correlating AE data with the level of stiffness reduction, it facilitates the development of $S-N$ curves based on the permissible level of stiffness degradation in PMCs. This research not only bridges a fundamental knowledge gap in the literature, but establishes a refined methodology for enhancing the predictive accuracy to assess the durability and structural integrity of fatigue-loaded PMCs.

2. Theoretical framework of irreversible thermodynamic processes

Heat generation in PMCs during cyclic loading is governed by its thermoviscoelastic behavior resulting from the nature of a polymer matrix of a composite, and the most of dissipated energy is converted into heat. The heat transfer equation over a control volume is given by Ref. [54]:

$$\int\left(\rho C_p\frac{\partial T}{\partial t}\right)dV+\left[\int\left(-K\nabla^2T\right)dV\right]=\int\dot{q}_{gen}dV, \tag{1}$$

where ρ is the density, C_p is the heat capacity, and K is the thermal conductivity of PMC specimen. $\dot{q}_{gen}$ denotes the volumetric heat generation rate, which is proportional to the thermomechanical strain amplitude ε_0, frequency f, and the dynamic shear loss modulus $G''(f,T)$ [55]:

$$\dot{q}_{gen}=3\pi f\varepsilon_0^2G''(f,T). \tag{2}$$

The detailed relationships for the thermoviscoelastic response and heat generation due to the self-heating effect have been presented in the previous authors' study [26]. In accordance with the first law of thermodynamics for a control volume, a part of the heat generation is released into the environment, with the rest being stored within the tested PMC. When a fatigue-loaded PMC specimen goes under the stabilization self-heating temperature (phase II), the rate of heat storage ($\dot{q}_s$) balances with the rate of heat dissipated into the environment ($\dot{q}$), which is given by Ref. [56]:

$$\dot{q}_s=\dot{q}=-\rho C_p\frac{\partial T}{\partial t}(t=t_u), \tag{3}$$

where $\partial T/\partial t$ refers to the cooling rate at time (t_u) when the tested PMC is unloaded from the applied fatigue stress, and goes under either natural or forced cooling [6], see Fig. 1 for more details. C_p, as a function of temperature for the glass/epoxy composite, is given by Ref. [57]:

$$C_p=828.7+2.71T, \tag{4}$$

where T is given in °C. When the applied stress level remains below the fatigue strength (σ_{FS}), the primary mechanism for heat dissipation is internal friction (i.e., $\dot{q}=\dot{q}_f$), which is considered as a recoverable process [53]. However, when the applied stress exceeds the fatigue strength, the heat arises due to internal friction and fatigue damage ($\dot{q}_d$), corresponding to reversible and irreversible thermodynamic processes, respectively, and can be expressed as follows:

$$\dot{q}=\dot{q}_{f+d}=\dot{q}_f+\dot{q}_d. \tag{5}$$

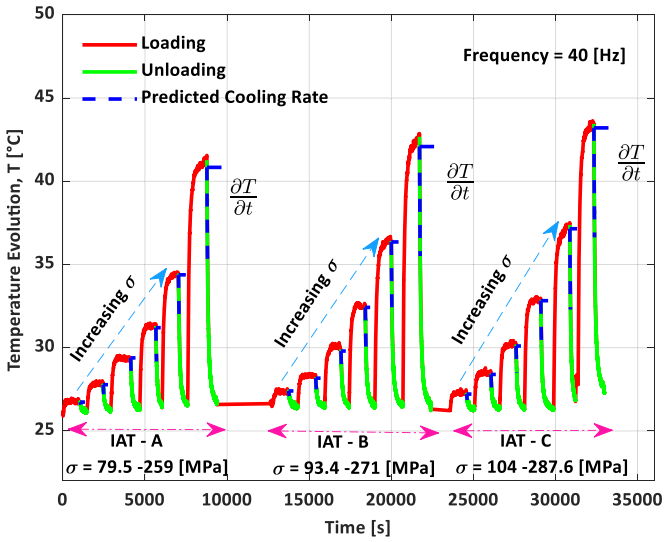

Fig. 1. Exemplary temperature-time responses of three fatigue-loaded PMCs (IAT-A, IAT-B, and IAT-C) at 40 Hz under various stress levels, ranging from 79.5 MPa to 287.6 MPa.

The heat dissipation rate led by damage ($\dot{q}_d$) can then be determined as a function of stress (σ) using:

$$\dot{q}_d=\dot{q}_{f+d}(\sigma\geq\sigma_{FS})-\dot{q}_f(\sigma<\sigma_{FS}). \tag{6}$$

On the other side, the entropy generation resulting from heat conduction and internal variables within the stabilization regime can be negligible, accounting for only 5–10 % of the entropy generated by plastic dissipation [58]. By excluding these effects and implementing the second law of thermodynamics [46], the total volumetric entropy generation (γ) can then be expressed as [34]:

$$\gamma=\mathrm{FFE}=\int_{t_0}^{t_f}\dot{\gamma}dt=\int_{t_0}^{t_f}\frac{\dot{q}_d}{T}dt. \tag{7}$$

For a single load level scenario resulting in a stabilized temperature, e.g. each block of temperature response within loading and unloading illustrated in Fig. 2, the FFE is given by Ref. [34]:

$$\mathrm{FFE}=\frac{N_f\dot{q}_d}{fT_s}, \tag{8}$$

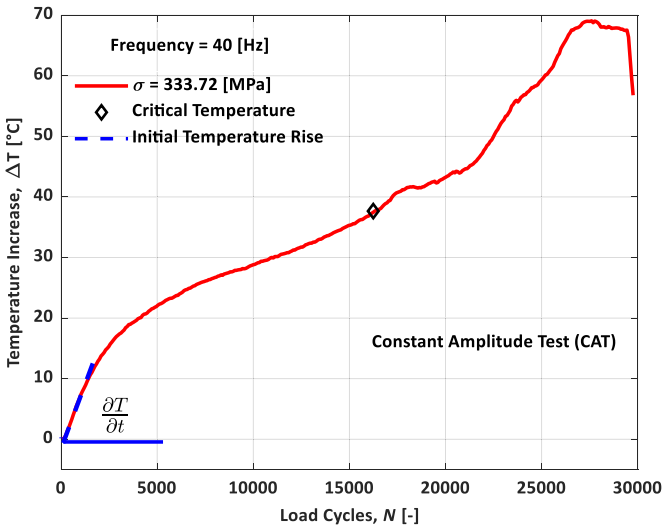

Fig. 2. Exemplary temperature-cycle history of CAT at 40 Hz under applied stress of 333.72 MPa.

where N_f represents the number of cycles until failure, T_s is the stabilized temperature measured on the Kelvin scale, and f indicates the frequency. By generalizing Eq. (8), the cumulative entropy generated for multiple load levels or increasing amplitude tests (IATs) can be expressed as follows [49]:

$$\mathrm{FFE} = \sum_{i=1}^{m} \frac{N_i \dot{q}_{di}}{f_i T_{si}}, \tag{9}$$

where m represents the number of load levels, N_i is the number of cycles, T_{si} is the stabilized temperature in Kelvin, $\dot{q}_{di}$ indicates the damage-induced heat dissipation rate, and f_i is the loading frequency at the $i-$th step. Once FFE value [51] is determined from fatigue tests, it becomes possible to estimate N_f for any arbitrary stress level above the fatigue strength ($\sigma \geq \sigma_{FS}$) using Eq. (10). However, to apply Eq. (10), it is essential to establish the correlation among stabilized temperature, heat dissipation, and stress level, which is discussed in Section 4.1.

$$N_f(\sigma) = \mathrm{FFE}\ \frac{f T_s(\sigma)}{\dot{q}_d(\sigma)}. \tag{10}$$

Nevertheless, for constant amplitude testing (CAT) scenarios under high-stress levels, the application of Meneghetti's approach [56] to measure the cooling rate for heat dissipation quantification becomes unfeasible. This challenge arises due to the rapid temperature increase registered in the third phase of the self-heating temperature evolution [6], linked to the fatigue damage accumulation in the tested PMC, complicating the reliable cooling rate determination at the end of the fatigue test. A viable strategy for determining the heat dissipation rate is to implement the initial temperature rise instead of the cooling rate, which is equivalent [40,49,59]. Furthermore, the temperature drastically increases under applied high-stress levels without even reaching stabilization within the LCF regime, as demonstrated in Fig. 2. Thus, using the critical temperature, characterized as the point above which temperature markedly increases due to rapid damage propagation [6,10] (see Fig. 2), in Eqs. (8) and (10) may be more feasible for determining the FFE value under CAT scenarios. This is justified by noting that the stabilized temperature serves as an indicator for the transition between phases II and III under lower stress levels within the entire fatigue testing, while the critical temperature similarly marks this transition/boundary at higher stress levels [4,16].

3. Materials and experimental procedure

The tested GFRP specimens consisted of 14 layers of unidirectional epoxy-based laminate, reinforced with a 200 g/m^2 plain weave E-glass fabric. The composite was sourced from Izo-Erg S.A. (Gliwice, Poland) under the designation EP GC 201, with the material properties presented in Table 1. Specimens were prepared in a rectangular geometry, with dimensions of 100 ± 0.4 mm in length, 10 ± 0.1 mm in width, and 2.4 ± 0.05 mm in thickness, with a span length of 39 mm.

The fatigue experiments were performed using a customized shaker-based cantilever bending apparatus with the stress ratio of $R = -1$ in displacement-controlled mode, similar to the previous works of the authors, see the details, e.g., in Ref. [26]. A schematic representation of the customized laboratory test rig is shown in Fig. 3. The PMC specimen (1) was clamped at both ends, with an effective length of 39 mm between the grips. The lower clamp (2), made of thermally insulating material, was fixed and tightened with a torque of 20 Nm to achieve consistent test conditions throughout the experiment. The upper grip (3) applied load to the specimen through a stringer (4) linked to the TIRA® TV-51120 electrodynamic shaker (5). The shaker was powered by a TIRA® BAA 500 amplifier (6), which controlled the sine-wave excitation signal generated by a multichannel data acquisition system (7). A PCB Piezotronics® T352C34 accelerometer (8) was employed to monitor the acceleration of the PMC specimen during testing, alongside a PCB Piezotronics® 208C03 force sensor (9) that recorded the force. The acceleration data were then integrated twice to obtain the displacement. The force and acceleration sensors were connected to a signal conditioner (Brüel & Kjær Nexus 2693), facilitating data acquisition at a sampling rate of 1652 Hz using a multi-channel card (NI® DAQ Card 6062E) linked to a PC (10) using a custom-built LabVIEW application. The fatigue tests, performed at room temperature, included both IATs at frequencies of 20 Hz, 30 Hz, 40 Hz, and 50 Hz, alongside CATs at 40 Hz and 50 Hz. The maximum bending stress for each load level, used in constructing $S-N$ curves and thermographic methods, was determined by:

$$\sigma = \frac{6PL}{bH^2}, \tag{11}$$

where P denotes the maximum force measured by force sensor within IATs and CATs, L is the span length, with b representing the width and H the thickness of the specimen, respectively.

The surface temperature of PMC during testing was recorded using an InfraTec® VarioCAM® infrared camera (11) with the Carl-Zeiss F1.0/focal length 50 mm lens. The frame rate of thermal registration for IATs was set to 1 Hz, while for CATs was set between 0.5 and 2 Hz, depending on the test duration, with shorter tests using a higher frame rate, and vice versa. The camera featured a microbolometric detector with a resolution of 640 × 480 pixels, and the approximate geometric resolution of the thermal imaging in this study was 5 pixels/mm for both IAT and CAT scenarios. To enhance the accuracy of thermal response, PMCs were coated with a black matte heat-resistant silicone enamel with an emissivity of 0.98. Similarly to the methodology used by authors in their previous study in synchronization with thermal data registration [16], AE data were simultaneously collected with a Vallen® AMSY-5 system (12), with the AEP4 preamplifier and the AE sensor VS700-D (13), functioning in the frequency range of 150–800 kHz, attached to the specimen with a thermoplastic adhesive. The recorded AE signals, in cascade form, were processed through Vallen® Visual AE software to assess the fatigue-induced degradation process.

Two regions of interest (ROIs) were established for assessing the temperature data for IAT and CAT scenarios based on the symmetry of the temperature distribution under fully reversed bending with respect to the midplane of the tested specimen in the cantilever beam mode. According to Fig. 3(b), ROI1 was defined to cover the entire surface of the tested PMC specimen, with dimensions of 10 x 39 mm^2. This region was selected to capture the overall thermal response of the specimen throughout the fatigue test. ROI2, with dimensions of 10 × 10 mm^2, was placed near the lower clamp, where the maximum stress is applied. Although ROI1 was considered to monitor the entire surface for any unexpected thermal behavior, it was observed that the maximum self-heating temperature consistently occurred at the bottom of the specimen, within ROI2.

Table 1
Material properties of the tested glass/epoxy composite.

Properties		GFRP	Ref.
Young's moduli [MPa]	E_x	27170	[26,60]
	E_y	24203.61	
Poisson's ratio [−]	ν_{yx}	0.166	
Density [kg/m^3]	ρ	1978.3	
Ultimate tensile strength [MPa]	σ_u	413	
Dynamic shear modulus [MPa]	G	6079.56	
Long-term shear modulus [MPa]	G_∞	3172.18	
Heat capacity at RT [J/kg·K]	C_p	891	[57]

4. Results and discussion

Fig. 4 illustrates a schematic workflow outlining the sequential steps of the study, beginning with IATs (Section 4.1) to assess fatigue strength using thermographic methods. To achieve this, the bilinear $\Delta T - \sigma$

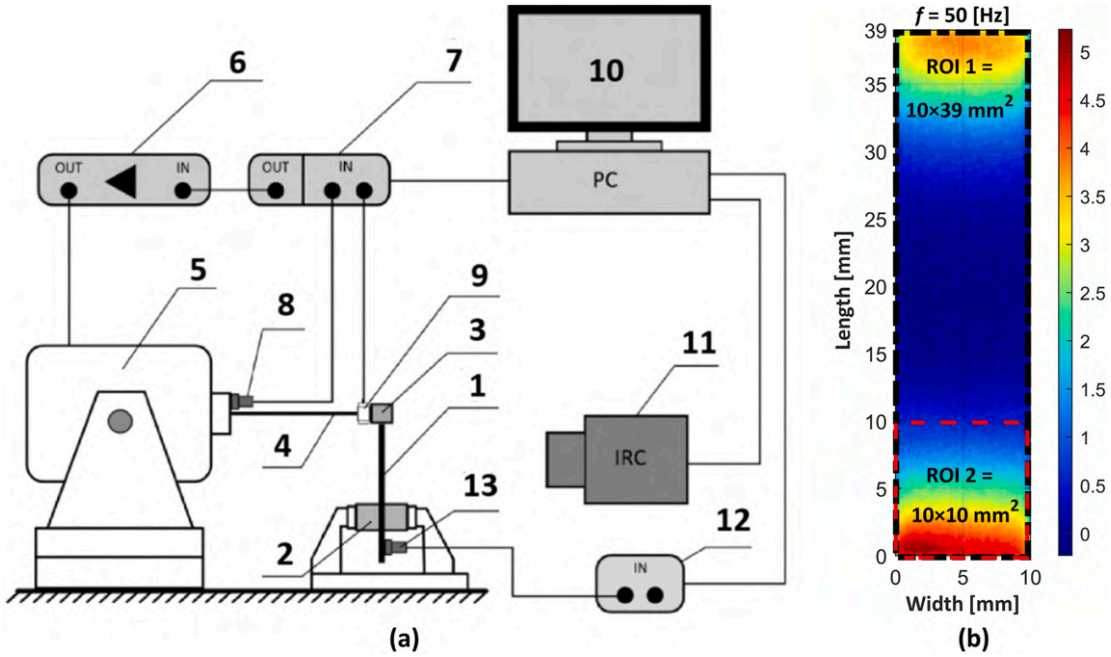

Fig. 3. (a) Schematic representation of the customized laboratory test rig, adopted from Ref. [16]; (b) Definition of ROIs on the exemplary thermogram registered during CAT under maximum stress of 271 MPa at a frequency of 50 Hz.

approach (Section 4.1.1), and the bilinear $\dot{q}-\sigma$ approach (Section 4.1.2), incorporating both constant- and temperature-dependent C_p, are applied. Furthermore, Section 4.1.3 evaluates the sensitivity of thermography-based approaches in predicting fatigue strength, which serves as the first objective of this study. In the second step, the CATs were conducted. By monitoring the real-time AE response of the fatigue-loaded PMC specimen, the critical boundary where rapid damage accumulation occurs is identified. A novel methodology based on this AE-determined critical boundary is then proposed to construct the $S-N$ curve, serving as the second objective of the study presented in Section 4.2. Furthermore, the fatigue life index corresponding to the AE-identified critical boundary at each loading level is used to determine the associated critical self-heating temperature, based on the temperature history of the PMC specimen. The results from IAT and CAT, obtained within the same calibration range for the equipment (i.e., IR camera, accelerometer, and force sensor), are subsequently combined to develop a trilinear thermographic model (i.e. $\dot{q}-\sigma$), as outlined in Section 4.3. The trilinear $\dot{q}-\sigma$ model facilitates a comprehensive evaluation of fracture fatigue entropy (FFE) (Section 4.3) across different loading regimes. This entropy-based approach is further extended to introduce a novel entropy-based damage index (EDI). The EDI concept offers an alternative methodology for constructing the $S-N$ curves based on the progressive damage accumulation from initiation to final failure, see Sections 4.4 and 4.5. Additionally, by applying the measured force and the displacement determined via twice-integrated acceleration data, the dynamic Young's modulus is calculated in Section 4.6.1. This enables the construction of a new $S-N$ curve as the function of permissible stiffness degradation level in Section 4.6.2, serving as the last aim of study.

4.1. Estimation of fatigue strength using thermography-based approaches

This section evaluates the sensitivity of fatigue strength estimation using two bilinear thermography-based approaches: (i) the temperature rise-stress $(\Delta T-\sigma)$ and (ii) heat dissipation rate-stress $(\dot{q}-\sigma)$. The assessment is conducted across four loading frequencies (20 Hz, 30 Hz, 40 Hz, and 50 Hz). Notably, the influence of heat capacity C_p is disregarded in the $\Delta T-\sigma$ model, while the role of either constant or temperature-dependent C_p is considered in the $\dot{q}-\sigma$ method.

Preliminary experiments were conducted to identify the necessary number of cycles for each specified load level for a campaign of IATs. The results indicated that conducting IATs with $40 \bullet 10^3$ cycles at each load level would be sufficient to achieve a stabilized self-heating temperature across the examined frequencies of 20 Hz, 30 Hz, 40 Hz, and 50 Hz. Following the preliminary tests, IATs were conducted across a broad range of stress levels, e.g., from 105 MPa to 410 MPa for 20 Hz, within 24 steps to capture stabilized temperatures for each loading frequency. Preliminary results from CATs demonstrated that a single PMC specimen could not endure the wide stress range (105–410 MPa) without breaking. To mitigate the likelihood of specimen breakage, the wide stress range was divided into three groups, with each group consisting of 8 steps applied to a separate specimen at each frequency (see Fig. 1 for IAT-A, IAT-B, and IAT-C at 40 Hz demonstrating 18 load levels out of a total of 24 levels). This configuration facilitated the testing of 12 PMCs within IAT scenarios under four different frequencies. The methodology was designed to preserve specimen integrity throughout the experiments. The unloading duration of 8–12 min between successive loading blocks was implemented to ensure that the tested PMCs returned to ambient temperature before applying the next loading sequence. This cooling period was crucial to mitigate the influence of cumulative thermal effects from prior loading cycles on the thermal and mechanical responses of the fatigue-loaded PMC specimen. The unloading duration was selected based on preliminary tests, which showed that the time required for the specimens to cool down is a function of the applied stress level and loading frequency. Higher stress levels and frequencies resulted in greater heat generation, necessitating longer unloading periods to allow the specimens to dissipate heat into the environment and return to the ambient temperature. This procedure ensured consistent initial conditions for each loading block, thereby improving the reliability and accuracy of the experimental data. It is noteworthy that any data points where the self-heating temperature did not stabilize were excluded from the analysis. For subsequent analysis, up to 20 representative measurement points, as depicted in Fig. 3, were selected from the 24 recorded points for each loading frequency.

In the current study, the fatigue strength is determined based on the intersection of two characteristic lines (i.e., line I, and line II) derived

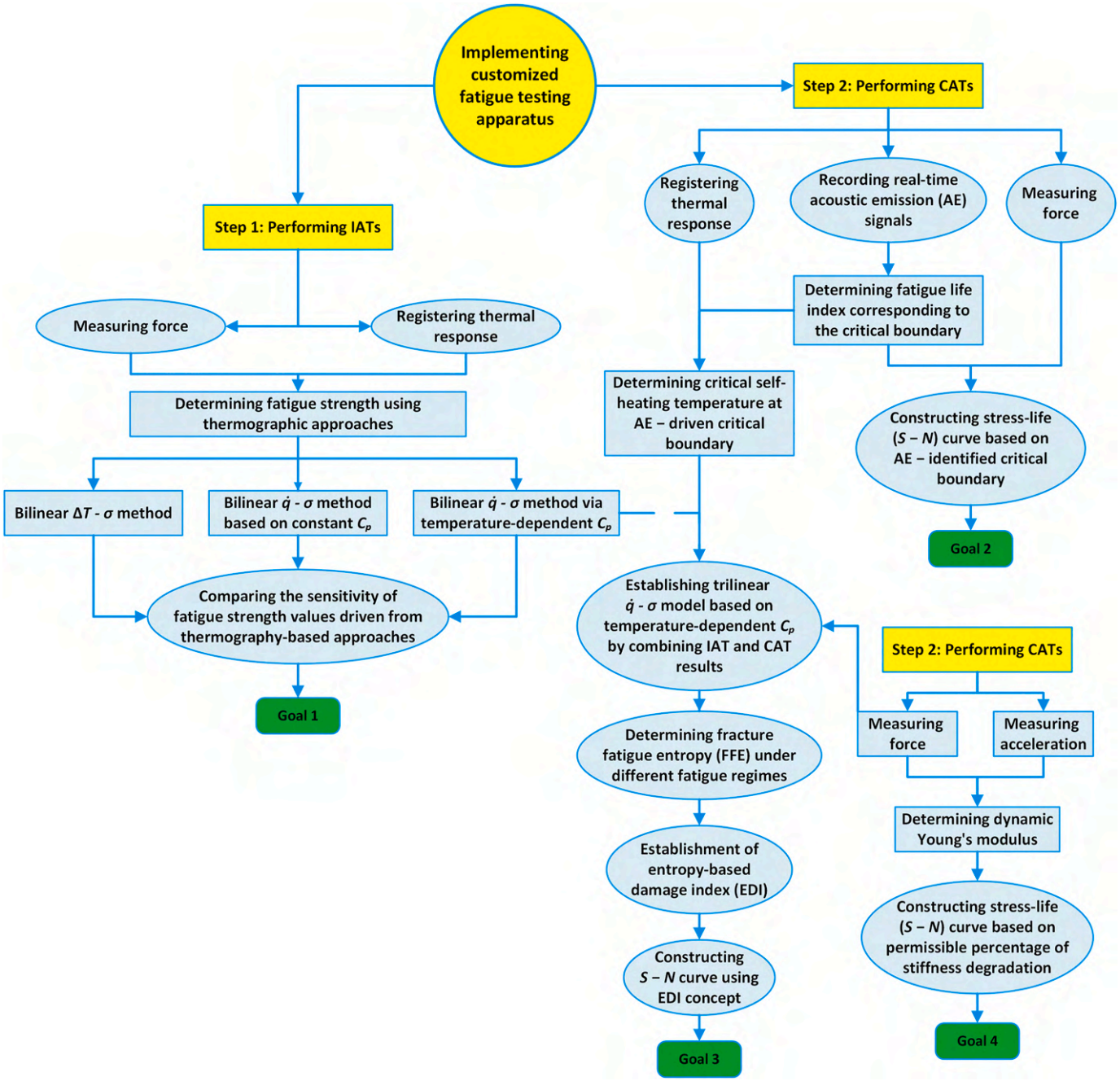

Fig. 4. Schematic workflow of the thermomechanical fatigue assessment of tested PMCs.

from the thermal response data registered during the fatigue experiments. The iterative process of constructing a bilinear model begins with selecting an initial trial stress value and categorizing the measured points into two groups—those below and those above this threshold. Separate linear approximations are then applied to each group to establish two trend lines, with their intersection point serving as the next trial stress value. The error, defined as the difference between successive trial stress values, guides the adjustment process: if the error is positive, the trial stress is increased; if negative, it is decreased. Additionally, in each trial, the root mean square error (RMSE) is computed to assess the accuracy of the approximation. The iteration continues until the RMSE reaches its minimum value, and the bilinear models are then constructed for the experimental data at each frequency. This approach allows for capturing the relationship between the temperature rise and the applied stress across different frequencies more accurately [6]. To evaluate the overall accuracy of the constructed bilinear model, the determination coefficient (R^2) was then calculated for each line individually. The overall coefficient of goodness estimation for the entire bilinear model for each frequency ($\overline{R}^2$), was finally computed as the mean value of two lines (i.e., $\overline{R}^2 = 0.5(R_I^2 + R_{II}^2)$) [33]. This averaging strategy shows the overall goodness of the bilinear model.

4.1.1. *Dependency of fatigue strength on loading frequency using $\Delta T - \sigma$ approach*

The fatigue strengths, determined using the bilinear $\Delta T - \sigma$ method, showed a notable decreasing trend with increasing frequency, as illustrated in Fig. 5. At 20 Hz, the fatigue strength was highest with the value of 264.4 MPa, decreasing significantly to 219 MPa at 30 Hz, then to 173.2 MPa at 40 Hz, and finally to 120 MPa at 50 Hz, representing a 55

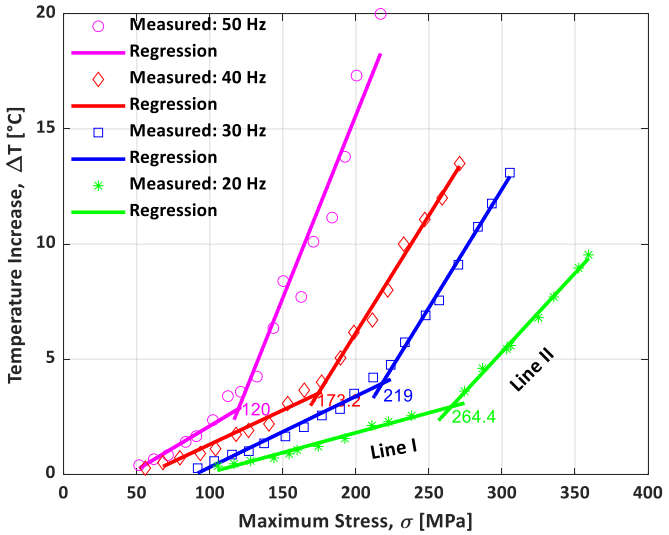

Fig. 5. Estimation of fatigue strength in glass/epoxy composite using $\Delta T-\sigma$ approach at different loading frequencies.

% reduction compared to the value at 20 Hz.

Table 2 displays these predictive regression lines, along with their corresponding $\overline{R}^2$ and RMSE, illustrating the relationship between temperature rise and applied stress at each frequency. At 20 Hz and 30 Hz, the models fit well, with high $\overline{R}^2$ (above 0.98) and low RMSE (0.1 °C and 0.2 °C, respectively). However, accuracy decreased at higher frequencies; at 50 Hz, $\overline{R}^2$ decreased to 0.914, and RMSE increased to 1 °C, indicating greater prediction error. Table 2 also illustrates the temperature rise at fatigue strength (ΔT_{FS}), increasing from 2.9 °C at 20 Hz to 4 °C at 30 Hz, then unexpectedly decreasing at higher frequencies.

At lower frequencies, the relatively lower hysteretic heat due to the viscoelastic response of the polymer, dissipates more uniformly into the surroundings, resulting in a less noticeable rise in temperature on the specimen surface. Consequently, fatigue damage accumulates gradually. In contrast, at higher frequencies, the relatively low thermal conductivity of PMCs, combined with a larger phase lag between stress and strain, causes a significant portion of the dissipated energy to remain within the PMC specimen, leading to higher temperatures. Additionally, the mismatch in the coefficient of thermal expansion (CTE) between the fibers and the polymer matrix causes localized thermal hotspots and consequently stress concentrations. These thermal stresses, interacting with the applied mechanical stresses, contribute to stress concentrations and may lead to the initiation and propagation of damage. With the rise in temperature due to increased frequency, the polymer matrix may undergo a weakening of polymer chain interactions, initiating microstructural degradation processes like matrix cracking, fiber-matrix debonding, and delamination. Thus, the fatigue damage evolution is not solely influenced by loading frequency but results from the complex interplay between thermal stresses, and mechanical loading. This interaction is more pronounced at higher frequencies, where rapid temperature increases can intensify degradation mechanisms, leading to a reduction in fatigue strength.

Table 2
Estimation of frequency-dependent bilinear $\Delta T-\sigma$ curves.

Frequency [Hz]	Line I estimated by	Line II estimated by	RMSE [°C]	$\overline{R}^2$	ΔT_{FS} [°C]
20	$\Delta T = 0.017 \bullet \sigma - 1.66$	$\Delta T = 0.069 \bullet \sigma - 15.24$	0.13	0.985	2.92
30	$\Delta T = 0.031 \bullet \sigma - 2.78$	$\Delta T = 0.103 \bullet \sigma - 18.48$	0.22	0.981	3.99
40	$\Delta T = 0.030 \bullet \sigma - 1.69$	$\Delta T = 0.102 \bullet \sigma - 14.25$	0.29	0.967	3.52
50	$\Delta T = 0.038 \bullet \sigma - 1.71$	$\Delta T = 0.159 \bullet \sigma - 16.13$	1.00	0.914	2.87

4.1.2. *Sensitivity of fatigue strength estimation using thermography-based approaches*

To build on the analysis presented in Section 4.1.1, this Section introduces the $\dot{q}-\sigma$ approach, incorporating both constant and temperature-dependent C_p to assess the sensitivity of the thermography-based methods for determining the fatigue strength of the tested PMCs under the same frequencies. Fig. 1 illustrates exemplary temperature-time responses for three fatigue-loaded PMCs (IAT-A, IAT-B, and IAT-C) tested at 40 Hz under various stress levels, along with their corresponding linear regression lines used to determine the heat dissipation rate. Based on post-processing across all four loading frequencies, a consistent window of 37 thermograms, recorded at a frame rate of 1 Hz, was selected to construct the regression line. The results of these predictive models using constant C_p are illustrated in Fig. 6 and Table 3, while the results of scenarios implementing temperature-dependent C_p are presented in Fig. 7 and Table 4. According to Tables 3 and 4, RMSE values for the constant heat capacity model ranged from 3.8 mW/cm^3 to 8.4 mW/cm^3, while for the temperature-dependent C_p model, RMSE values were slightly higher, ranging from 6.8 mW/cm^3 to 9.9 mW/cm^3. Such minimized RMSE values resulted in high predictive accuracy across all loading frequencies. For both models, the determined $\overline{R}^2$ values were 0.953 or above, indicating a good-fitting model.

The $\dot{q}-\sigma$ method consistently predicted higher fatigue strengths than the $\Delta T-\sigma$ method, with the discrepancy becoming more pronounced at higher frequencies. At 20 Hz, the $\dot{q}-\sigma$ model predicted values of 270.3 MPa (constant C_p) and 273.3 MPa (temperature-dependent C_p), slightly exceeding the value of 264.4 MPa derived from $\Delta T-\sigma$. As frequency increased, the difference grew for both constant and temperature-dependent C_p, respectively: 1.8 % at 30 Hz, 6.7 % and 7.9 % at 40 Hz, and 19.3 % and 20.7 % at 50 Hz. These results indicate that the influence of C_p becomes more pronounced at higher frequencies, particularly temperature-dependent C_p. Additionally, the heat dissipation rates showed a vivid upward trend with increasing frequency for both constant and temperature-dependent C_p scenarios, indicating a correlation between higher frequencies and increased energy dissipation. The results obtained from both $\Delta T-\sigma$ and $\dot{q}-\sigma$ approaches demonstrated a decline in fatigue strength with rising frequency, but the $\dot{q}-\sigma$ approach consistently predicted higher values than that of $\Delta T-\sigma$,

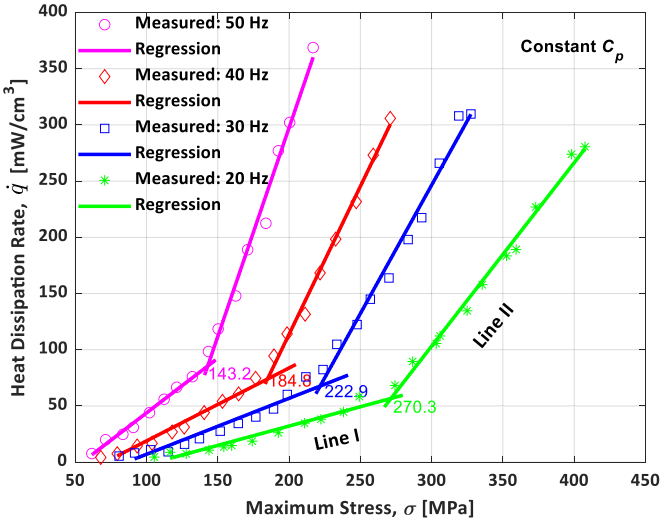

Fig. 6. Estimation of fatigue strength in glass/epoxy composite using $\dot{q}-\sigma$ approach at constant C_p under different loading frequencies.

Table 3
Estimating bilinear $\dot{q}-\sigma$ curves as a function of frequency with constant C_p.

Frequency [Hz]	Line I estimated by	Line II estimated by	RMSE $[mW/cm^3]$	$\overline{R}^2$	$\dot{q}_{FS}$ $[mW/cm^3]$
20	$\dot{q}=0.347\bullet\sigma-37.12$	$\dot{q}=1.495\bullet\sigma-342.03$	3.80	0.965	55.40
30	$\dot{q}=0.498\bullet\sigma-42.83$	$\dot{q}=2.287\bullet\sigma-439.50$	8.42	0.953	68.86
40	$\dot{q}=0.649\bullet\sigma-46.00$	$\dot{q}=2.631\bullet\sigma-412.42$	5.20	0.984	74.56
50	$\dot{q}=0.972\bullet\sigma-53.44$	$\dot{q}=3.714\bullet\sigma-445.27$	8.41	0.986	86.85

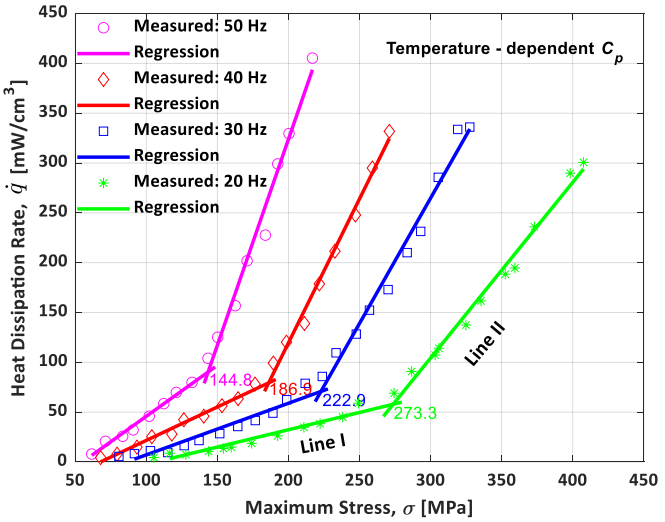

Fig. 7. Estimation of fatigue strength in glass/epoxy composite using $\dot{q}-\sigma$ approach considering temperature-dependent C_p at various loading frequencies.

Table 4
Bilinear $\dot{q}-\sigma$ curve estimation as a function of frequency and temperature-dependent C_p.

Frequency [Hz]	Line I estimated by	Line II estimated by	RMSE $[mW/cm^3]$	$\overline{R}^2$	$\dot{q}_{FS}$ $[mW/cm^3]$
20	$\dot{q}=0.347\bullet\sigma-37.11$	$\dot{q}=1.763\bullet\sigma-424.70$	6.77	0.962	57.66
30	$\dot{q}=0.518\bullet\sigma-44.67$	$\dot{q}=2.515\bullet\sigma-489.71$	9.69	0.950	60.41
40	$\dot{q}=0.671\bullet\sigma-45.43$	$\dot{q}=2.890\bullet\sigma-458.48$	5.76	0.986	79.20
50	$\dot{q}=1.022\bullet\sigma-56.41$	$\dot{q}=4.132\bullet\sigma-502.73$	9.94	0.985	89.85

especially at higher frequencies when incorporating temperature-dependent C_p. This highlights the necessity of comparing the results obtained from $\Delta T-\sigma$ and $\dot{q}-\sigma$ methods, at higher frequencies, using the standard $S-N$ curve as a reference to assess the reliability of these methods.

4.1.3. Comparative analysis of fatigue responses driven from $S-N$ curves and thermography-based approaches

This section compares the fatigue strength values derived from both AE-based $S-N$ curves and thermography-based methods for glass/epoxy composites. Furthermore, the AE-based $S-N$ curves are employed to estimate the fatigue life cycles (N_{FS}) corresponding to the fatigue limit/strength values extracted from the thermography-based approaches.

Due to the relatively high discrepancy in the estimated fatigue strength values from $\Delta T-\sigma$ and $\dot{q}-\sigma$ approaches at higher frequencies (40 Hz and 50 Hz), the $S-N$ curves for these frequencies were established as the primary reference for evaluating the accuracy of thermographic approaches. The $S-N$ curves were constructed using experimental data from 17 CATs within a wide range of stress levels at each frequency, spanning from 218.3 MPa to 379.1 MPa for 40 Hz and from 172.9 MPa to 309 MPa for 50 Hz, as illustrated in Fig. 8.

At 40 Hz, the predicted fatigue strength by the $S-N$ curve at 10^6 load cycles is 241.1 MPa, significantly higher than 186.9 MPa derived from the $\dot{q}-\sigma$ approach and 173.2 MPa from the $T-\sigma$ approach, representing discrepancies of approximately 22.4 % and 28.1 %, respectively. Similarly, at 50 Hz, fatigue strength from the $S-N$ curve is 192.5 MPa, compared to 144.8 MPa from the $\dot{q}-\sigma$ method and 120 MPa from the $\Delta T-\sigma$ approach, with discrepancies of 24.8 % and 37.5 %, respectively. Furthermore, a vivid trend is observed with a notable decline in fatigue strength as frequency increases from 40 Hz to 50 Hz, with the $S-N$ curve showing a reduction of 20.2 %, the $\dot{q}-\sigma$ approach reflecting a decrease of 22.5 %, and the $\Delta T-\sigma$ approach demonstrating a more significant drop of 30.7 %. This highlights the advantage of implementing $\dot{q}-\sigma$ approach, offering a higher accuracy in fatigue analysis of PMCs, particularly at higher frequencies where thermal effects become more pronounced.

Furthermore, Table 5 presents the predicted fatigue life cycles (N_{FS}) derived from the linear regression models at 40 Hz and 50 Hz (see equations in Fig. 8), corresponding to the fatigue strength values extracted from the thermography-based approaches (i.e. $\Delta T-\sigma$, and $\dot{q}-\sigma$). To achieve this, the thermographic-driven fatigue strength values were substituted into the linear regression models extracted from AE-based $S-N$ curves at final failure, illustrated in Fig. 8. The results indicate that the fatigue life index associated with the fatigue strength values is consistently close to 10^7 cycles, with slight variations depending on the approach used. For example, for the $\Delta T-\sigma$ method, the fatigue life index is just above 10^7 cycles, with values of $1.3\bullet10^7$ cycles at 40 Hz and $2.6\bullet10^7$ cycles at 50 Hz. In contrast, for the $\dot{q}-\sigma$ approach, the fatigue life index is slightly below 10^7 cycles, with values ranging from $7.7\bullet10^6$ to $9.1\bullet10^6$ cycles, depending on whether a constant or temperature-dependent C_p is considered. Despite these minor differences, the results consistently illustrate that the fatigue life index corresponding to the thermography-based fatigue strength remains in the vicinity of 10^7 cycles.

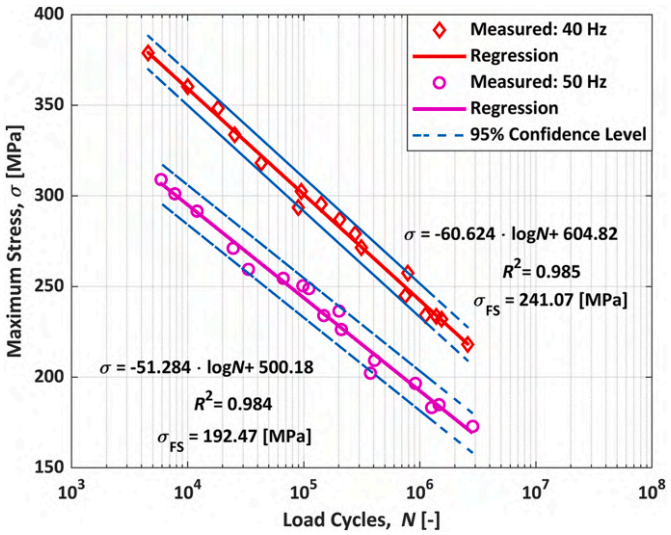

Fig. 8. Standard S–N curves constructed for glass/epoxy composite under fully reversed bending at loading frequencies of 40 Hz, and 50 Hz.

Table 5
Predicted fatigue life cycles derived from $S-N$ curves corresponding to the fatigue limit/strength values driven from the thermography-based approaches.

Frequency [Hz]	$\Delta T-\sigma$ approach		$\dot{q}-\sigma$ approach			
			Constant C_p		Temperature-dependent C_p	
	σ_{FS} [MPa]	N_{FS} [−]	σ_{FS} [MPa]	N_{FS} [−]	σ_{FS} [MPa]	N_{FS} [−]
40	173.23	$1.32 \bullet 10^7$	184.81	$8.48 \bullet 10^6$	186.85	$7.73 \bullet 10^6$
50	120.00	$2.59 \bullet 10^7$	143.17	$9.14 \bullet 10^6$	144.80	$8.50 \bullet 10^6$

4.2. Establishment of $S-N$ curve based on AE-identified critical damage boundaries

This section implements AE analysis to identify the critical damage accumulation boundaries, thereby introducing a novel methodology for constructing the $S-N$ curve based on the criticality of AE data. Unlike the standard $S-N$ approach, primarily considering the final stage of failure, the proposed criticality-based AE method relies on the boundaries where the damage is progressively accumulated throughout the lifespan of the fatigue-loaded PMC specimen. During the preliminary study, several AE features were evaluated, including total counts of hit-cascade (CCNT), true energy (ETE), cumulative energy (CENY), and peak amplitude (ALIN). Among these, CCNT was identified as the most sensitive feature/indicator of early microstructural changes and microcrack growth, the finding was also confirmed by previous studies (e.g., Ref. [16]). Figs. 9 and 10 present the AE data collected from fatigue testing of glass/epoxy composite specimens subjected to frequencies of 40 Hz and 50 Hz, respectively. The results are categorized into three fatigue regimes: low-cycle fatigue (LCF) with less than 10^5 cycles, intermediate-cycle fatigue (ICF) ranging from 10^5 to 10^6 cycles, and high-cycle fatigue (HCF) beyond 10^6 cycles [61]. While these classifications may not be universally standardized, they establish a valuable framework for assessing the fatigue behavior of PMCs within the current study. Given the primary focus of the study on these fatigue regimes, this classification was implemented to effectively describe the observed thermomechanical fatigue response of tested PMCs in the presence of the self-heating phenomenon—a potential contributor in accelerating fatigue damage accumulation, and thereby, the lifetime degradation.

The stress ranges defining LCF, ICF, and HCF vary with frequency. For 40 Hz, LCF ranges from 318.2 to 378.8 MPa, ICF consists of 244.9–302.5 MPa, and HCF includes 218.1–234.2 MPa. However, for 50 Hz, LCF ranges from 259.5 to 309 MPa, ICF involves 196.6–254.5 MPa, and HCF corresponds to stress levels below 196.6 MPa. According to the following classification, in Fig. 9, the AE data at 40 Hz are shown with (a-b) representing LCF, (c-e) indicating ICF, and (f) covering HCF regimes. Similarly, Fig. 10 shows AE results at 50 Hz, with (a-c) referring to LCF, (d-e) covering ICF, and (f) corresponding to HCF. In Figs. 9 and 10, the abrupt fatigue failure events are marked by the peak values of CCNT feature, alongside the critical boundary, denoted by black dashed lines, where significant damage accumulation begins. Using the identified criticality boundary values derived from the CCNT feature for different stress levels at frequencies of 40 Hz and 50 Hz, a new strategy for constructing the $S-N$ curve can be established. This approach provides straightforward information on the permissible number of cycles a tested PMC can endure at a given stress level before entering the accelerated fatigue damage phase.

The $S-N$ curves represented in Fig. 11 and Table 6 derived from final failure events (denoted by diamonds in Figs. 9 and 10) predict slightly higher fatigue strengths at 10^6 cycles for both frequencies of 40 Hz and 50 Hz compared to the criticality-based $S-N$ curves. The fatigue strength under 40 Hz is estimated at 241.1 MPa based on the final failure, versus 222.9 MPa from the criticality-based $S-N$ curve, showing a 7.5 % discrepancy. This highlights that the criticality-based $S-N$ method tends to predict a lower value, owing to identifying the fatigue damage at an earlier stage of degradation thereby providing a more conservative estimation that is key to preventing sudden failures. On the other side, both methods indicate a reduction in fatigue strength as the frequency increases. For the final failure-based $S-N$ curve, the fatigue strength decreases by 20.2 % when increasing from 40 Hz (241.1 MPa) to 50 Hz (192.5 MPa). Similarly, the criticality-based $S-N$ method demonstrates a 20.3 % reduction in fatigue strength, decreasing from 222.9 MPa at 40 Hz to 177.5 MPa at 50 Hz. These closely aligned results highlight the effectiveness of the criticality-based $S-N$ approach in assessing and capturing the frequency-dependent fatigue behavior of PMCs. Despite these findings, a critical question arises regarding how the $S-N$ curves derived from final failure and the criticality of AE data correlate with the stiffness degradation of the tested PMC. Establishing such a relationship will enhance the predictive capabilities in fatigue assessments, given that stiffness degradation serves as an indicator of structural integrity and residual service life of PMCs.

It should be mentioned that the recording of AE events and thermal imaging was synchronized throughout the fatigue testing process, with both techniques employed to monitor the same underlying damage accumulation mechanisms. The AE data provides real-time information on the initiation and progression of damage, while thermal images highlight the temperature distribution across the specimen, which is a direct result of energy dissipation due to internal friction and other damage processes. As damage accumulates, both the AE signals and thermal responses exhibit distinct patterns, which are closely associated with the same degradation mechanisms.

4.3. Analysis of fracture fatigue entropy across different loading regimes

The entropy analysis shows how fatigue damage evolves across different stress levels, frequencies, and thermal responses [49,50]. This section applies the FFE concept for thermomechanical fatigue life assessment of PMCs across different fatigue regimes (LCF, ICF, and HCF). As a preliminary step, the FFE values were derived from the heat dissipation analysis based on IATs illustrated in Fig. 1 based on Eq. (9), and discussed in Section 4.1 for frequencies of 20 Hz, 30 Hz, 40 Hz, and 50 Hz. Three PMC specimens (labeled as IAT-A, IAT-B, and IAT-C) were tested at each frequency, see Fig. 1, with the determined FFE values presented in Table 7. The mean FFE value ($\overline{\text{FFE}}$) calculated across all frequencies is 4.0 ± 1.6 J/(cm^3·K). Implementing $\overline{\text{FFE}}$ value derived from the IATs to construct $S-N$ curve is feasible only within specific stress ranges (up to 271 MPa at 40 Hz and 217 MPa at 50 Hz, as shown in Fig. 7). On the other side, the fatigue strengths at 10^6 cycles derived from Fig. 8, yield 241.1 MPa at 40 Hz and 192.5 MPa at 50 Hz, while covering stress ranges up to 378.9 MPa and 309 MPa, respectively. This implies that in IAT scenarios, the stress levels inducing damage above the fatigue strength ($\sigma \geq \sigma_{FS}$) partially align with the low-stress ranges illustrated in Fig. 8, leaving a significant portion of the high-stress range uncovered (from 271 MPa to 378.9 MPa under 40 Hz, and from 241.1 MPa to 309 MP under 50 Hz) when compared to Fig. 8 as the reference. This highlights that relying on a single $\overline{\text{FFE}}$ value derived from Eq. (10) and the bilinear $\dot{q}-\sigma$ model within IATs, similar to other studies [34,53], is unfeasible for fatigue life assessment under intermediate- and high-stress levels corresponding to LCF and ICF regimes, respectively, at 40 Hz and 50 Hz. Thus, the illustrated $\dot{q}-\sigma$ curves in Fig. 7, need to be extended to cover a broader stress range at 40 Hz and 50 Hz. To achieve

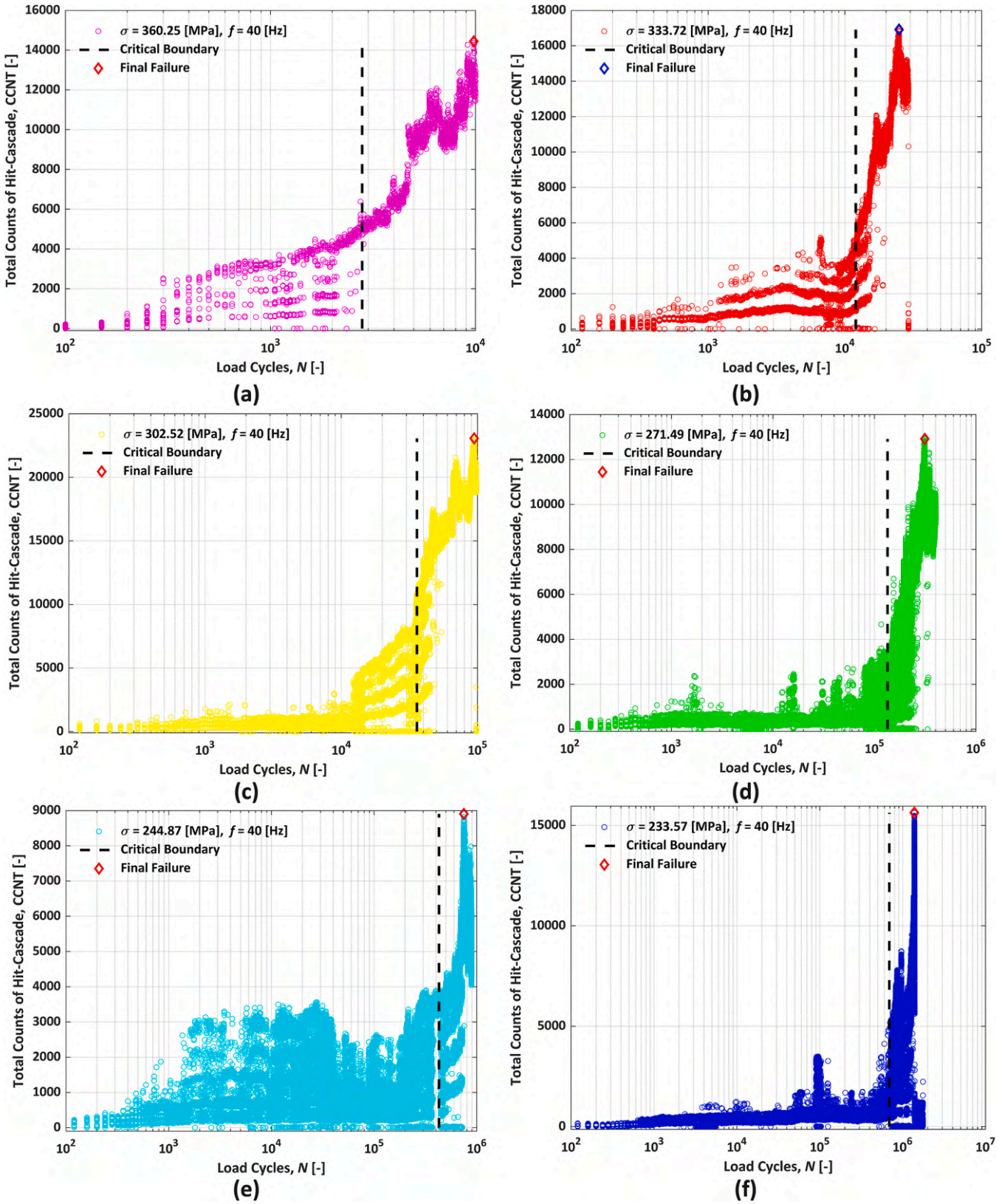

Fig. 9. AE results from fatigue testing of glass/epoxy composite at 40 Hz for different loading regimes: (a–b) LCF, (c–e) ICF, (f) HCF.

this, the analysis is extended by incorporating CAT results at a wide stress range. In other words, combining IATs and CATs results in exploring regime-based FFE values/trends as a function of frequency and stress.

Notably, the stabilized temperature was utilized to evaluate FFE for IAT scenarios by Eq. (9), as presented in Table 7. However, within CATs—particularly at medium and high-stress levels—it may be more rational to consider the critical temperature in Eqs. (8) and (10), as

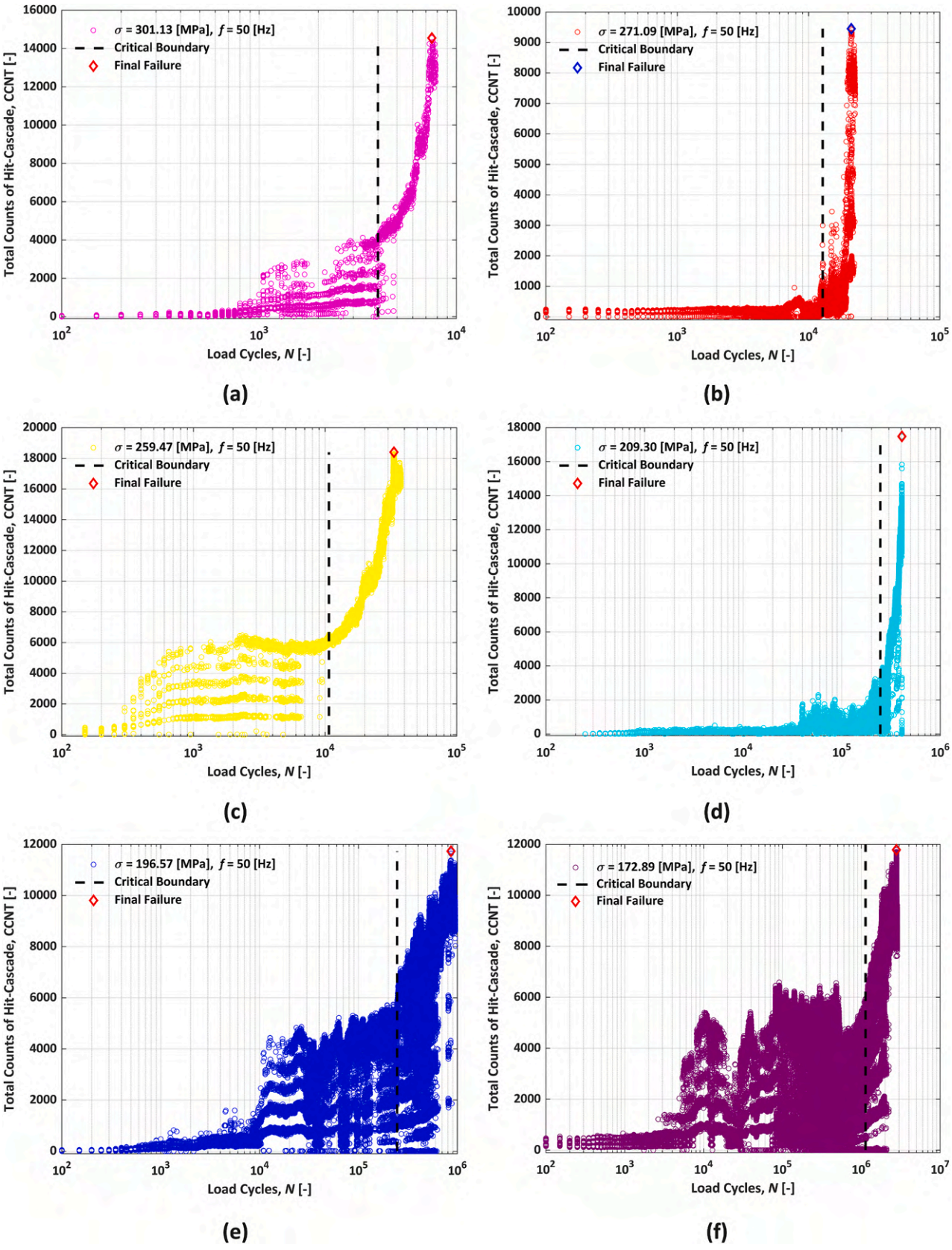

Fig. 10. AE results extracted during fatigue testing of glass/epoxy composite at 50 Hz for different loading regimes: (a–c) LCF, (d–e) ICF, (f) HCF.

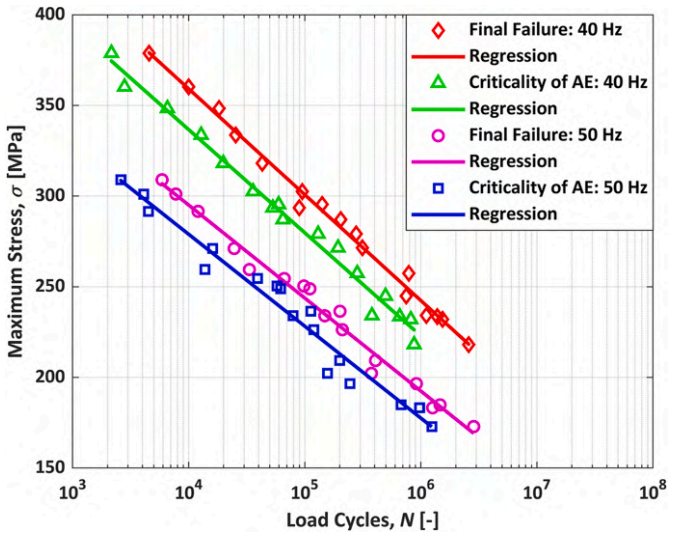

Fig. 11. $S-N$ curves for glass/epoxy composite constructed based on final failure and the criticality of AE features at frequencies of 40 Hz and 50 Hz.

stabilization does not occur, see Fig. 2, as also confirmed in Ref. [62]. For the CAT scenario, FFE values were determined using Eq. (8), where the critical temperature is utilized instead of the stabilized temperature. Since the AE and thermal responses are recorded simultaneously during fatigue testing, the critical temperature and AE-identified critical boundary correspond to the same stages of damage evolution, with their occurrence in similar fatigue life index. In other words, the number of cycles at critical boundaries of AE data shown in Figs. 9 and 10 for 40 Hz and 50 Hz, respectively, synchronized with the thermal responses illustrated in Fig. 12(a) and (b), are implemented to determine the corresponding critical temperatures. Such critical temperatures, confirmed in Refs. [6,10], are also presented in Fig. 12(a) and (b) for frequencies of 40 Hz and 50 Hz, respectively, derived from a series of temperature evolution profiles for CATs shown in Section 4.1.

Fig. 13 shows the exemplary infrared image sequences for the PMC specimen at the stress level of 271 MPa, with frequencies of 40 Hz (a-c) and 50 Hz (a'-c'). The thermographic images correspond to (a, a') at the onset of loading after 10^3 cycles, (b, b') at the critical boundary, identified at 133.7 • 10^3 cycles for 40 Hz and 10.3 • 10^3 cycles for 50 Hz, and (c, c') at final failure, occurring at 403 • 10^3 cycles for 40 Hz and 24.8 • 10^3 cycles for 50 Hz. The thermograms vividly illustrate how the temperature profiles are influenced by the change in frequency at the same stress level, increasing from 40 Hz to 50 Hz in the corresponding images from (a) to (a'), (b) to (b'), and (c) to (c').

By Incorporating CAT results at medium and high-stress levels along with the critical temperature responses from Fig. 12, the correlation between applied stress and temperature response for 40 Hz and 50 Hz frequencies can be derived from Fig. 14. The correlation has been utilized to determine the FFE in the further stages of the study. Note that the temperature scale is in Kelvin.

Fig. 15 illustrates the quantified heat dissipation rate ($\dot{q}$) by incorporating IATs and CATs over a wide range of stress levels for loading frequencies of 40 Hz and 50 Hz. Analysis of the results revealed that the

Table 7
FFE values derived from IAT analysis for different loading frequencies.

Parameter [J/cm^3.K]	Sample ID	20 Hz	30 Hz	40 Hz	50 Hz
FFE	IAT-A	2.673	5.729	5.647	5.598
	IAT-B	2.242	5.139	1.625	2.641
	IAT-C	2.919	3.056	6.415	3.863
$\overline{FFE}$	Average	2.6 ± 0.3	4.6 ± 1.1	4.6 ± 2.1	4.0 ± 1.2
			4.0 ± 1.6		

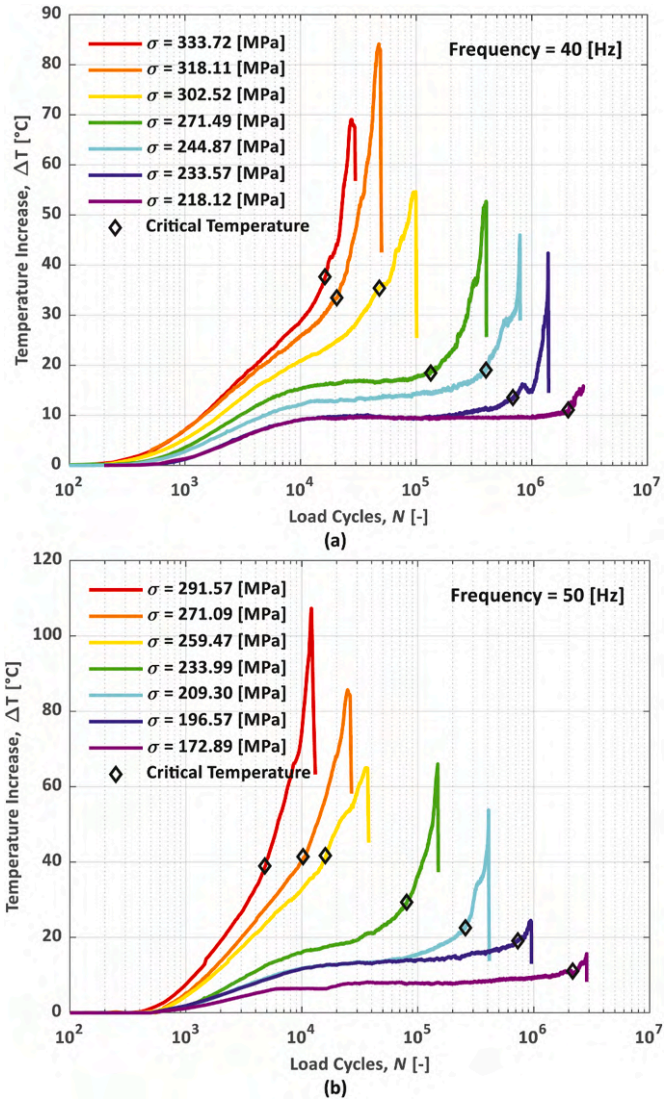

Fig. 12. Temperature profile evolution, incorporating critical temperature values determined through AE analysis for various stress levels under: (a) 40 Hz, and (b) 50 Hz.

Table 6
Estimated $S-N$ curves based on the criticality of AE and final failure.

Criterion	Frequency [Hz]	Estimating $S-N$ curve by	R^2	σ_{FS} [MPa]
Criticality of AE	40	$\sigma = -56.865 \bullet \log N + 564.09$	0.982	222.90
	50	$\sigma = -50.691 \bullet \log N + 481.69$	0.965	177.54
Final failure	40	$\sigma = -60.624 \bullet \log N + 604.82$	0.985	241.07
	50	$\sigma = -51.284 \bullet \log N + 500.18$	0.984	192.47

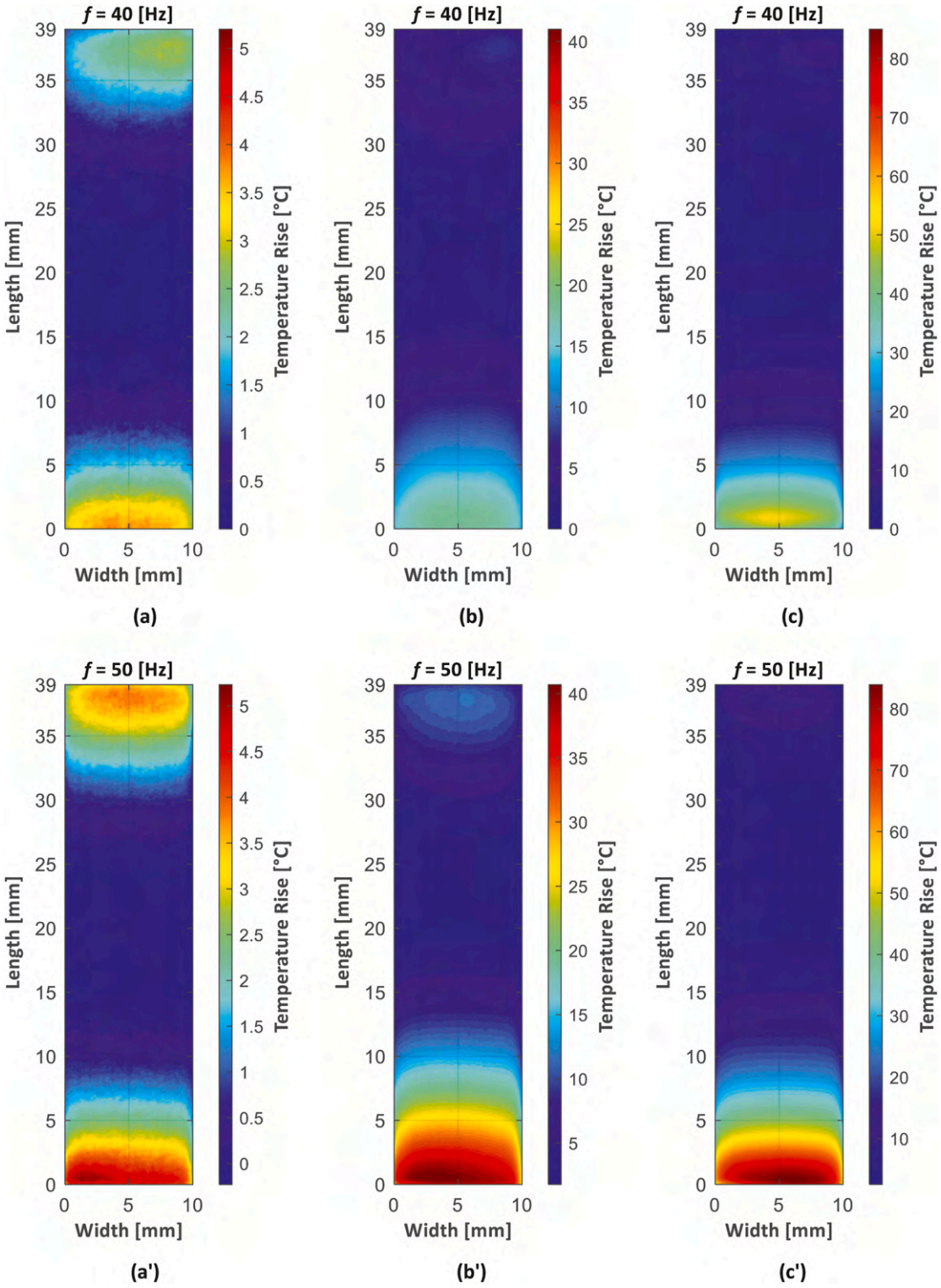

Fig. 13. Infrared thermograms registered for the fatigue-loaded PMC specimen under maximum stress of 271 MPa, for frequencies of 40 Hz (a–c) and 50 Hz (a'-c'), with images corresponding to (a, a') after 1000 cycles, (b, b') at the critical points, and (c, c') at the final failure stages.

previously employed bilinear model, as presented in Section 4.1 (e.g., Fig. 7), was insufficient for correlating heat dissipation rates across the broad range of applied stress, especially at higher stress levels. This limitation is primarily owing to the significant increase in heat dissipation at the higher stress levels, which the bilinear model failed to capture. To refine the accuracy of predictions, the trilinear model was developed by minimizing the RMSE value for the experimental data at each loading frequency, via adopting the approach used for the bilinear model in Section 4.1 depicted in Fig. 7. To assess the overall accuracy of the trilinear model, the average determination coefficient ($\overline{R}^2$), was then determined as the mean value of the three lines (i.e., $\overline{R}^2 = \left(R_I^2 + R_{II}^2 + R_{III}^2\right)/3$) for each loading frequency [33]. This model implements all results extracted from both IATs and CATs, enabling a more rational correlation between the applied stress and the corresponding heat

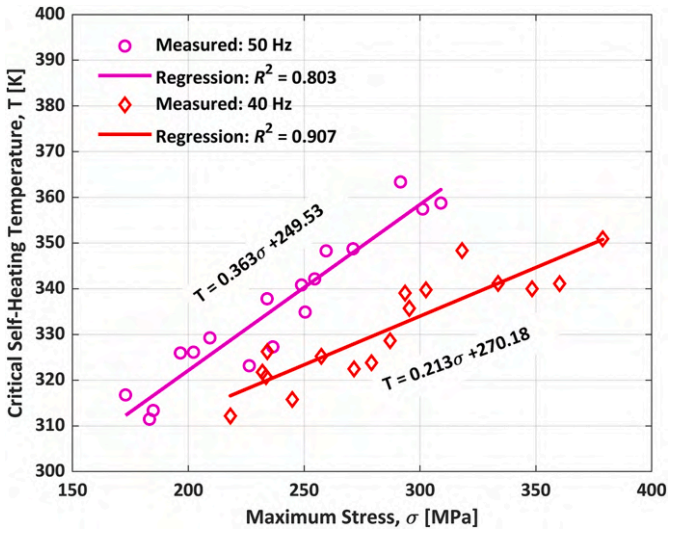

Fig. 14. Correlating applied stress with the critical temperature response at 40 Hz and 50 Hz.

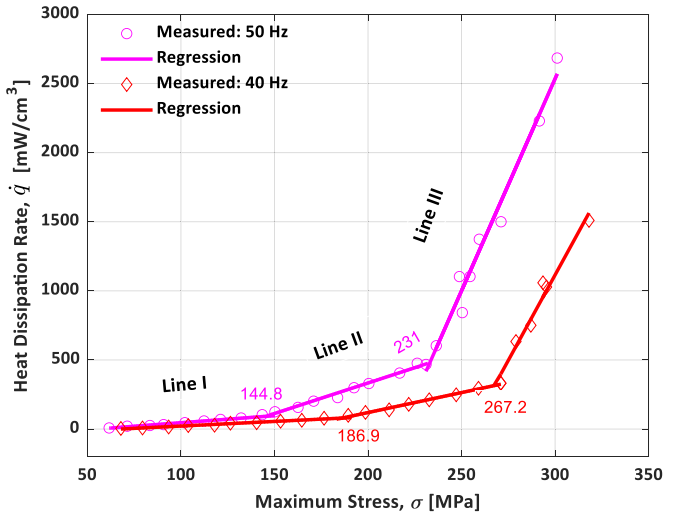

Fig. 15. Developing the trilinear $\dot{q} - \sigma$ model incorporating temperature-dependent heat capacity at loading frequencies of 40 Hz and 50 Hz.

dissipation rate. One key enhancement of the trilinear model is the incorporation of temperature-dependent C_p in assessing heat dissipation, as depicted in Fig. 7. This is even more significant at higher stress levels, where thermal responses are more pronounced, and C_p varies linearly with temperature, see Eq. (4).

The results of these established trilinear models using temperature-dependent C_p are illustrated in Fig. 15 and Table 8. As the loading frequency increased from 40 Hz to 50 Hz, the RMSE value doubled, rising from 31.2 mW/cm^3 at 40 Hz to 63.8 mW/cm^3 at 50 Hz. Despite this increase, the minimized RMSE values resulted in $\overline{R}^2$ value of 0.98 or above for both frequencies, indicating a well-fitting model. The applied stress levels (corresponding to lines I and II under IATs, and line III under CATs) ranged from 67.9 MPa to 318.1 MPa at 40 Hz, and from 61.6 MPa to 301.1 MPa at 50 Hz. The validity region of the estimated lines in Table 8 is demonstrated by the intervals (values in red and magenta colors) between the lines for both frequencies, as depicted in Fig. 15.

Table 8
Trilinear $\dot{q} - \sigma$ curve estimation using temperature-dependent C_p for 40 Hz and 50 Hz.

Frequency [Hz]	$\dot{q}$ - Line I [mW/cm^3]	$\dot{q}$ - Line II [mW/cm^3]	$\dot{q}$ - Line III [mW/cm^3]	RMSE [mW/cm^3]	$\overline{R}^2$
40	0.671 • σ – 45.43	2.890 • σ – 458.48	24.723 • σ – 6301.65	31.24	0.980
50	1.022 • σ – 56.41	4.132 • σ – 502.73	30.689 • σ – 6671.58	63.79	0.982

Further analysis implements Eq. (6), and (7), along with the findings from Figs. 14 and 15, and Table 8 for evaluating the cumulative entropy across LCF, ICF, and HCF regimes. Fig. 16(a) and (b) present the determined cumulative entropy evolutions for frequencies of 40 Hz and 50 Hz, respectively. The results demonstrate how entropy evolves as a function of the load cycle, stress level, and frequency for different fatigue regimes until the final fracture, referred to as FFE [51]. An analysis of the FFE values across a wide range of stress levels (applied within CATs) under 40 Hz and 50 Hz in Fig. 17 reveals three distinct trends, each corresponding to a different fatigue regime. As a simplification, consistent with other studies [15,34,46], FFE can still be treated as a material property, with the mean value differing across fatigue regimes.

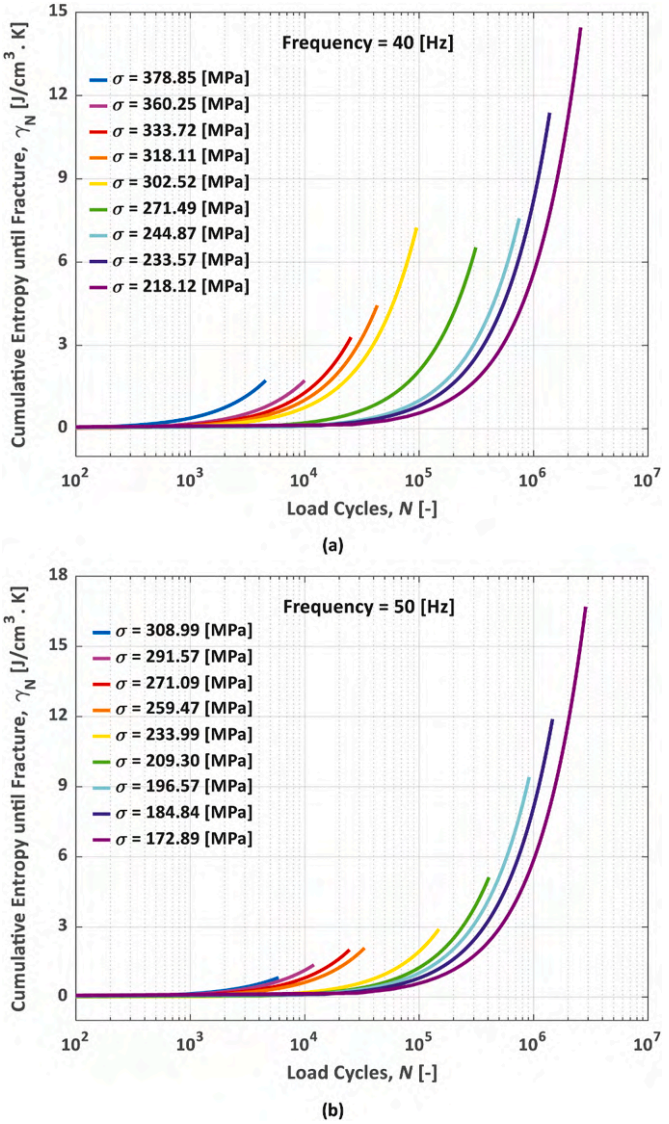

Fig. 16. Entropy evolution of the tested PMCs until eventual fracture across a wide spectrum of stress levels at loading frequencies of: (a) 40 Hz, and (b) 50 Hz.

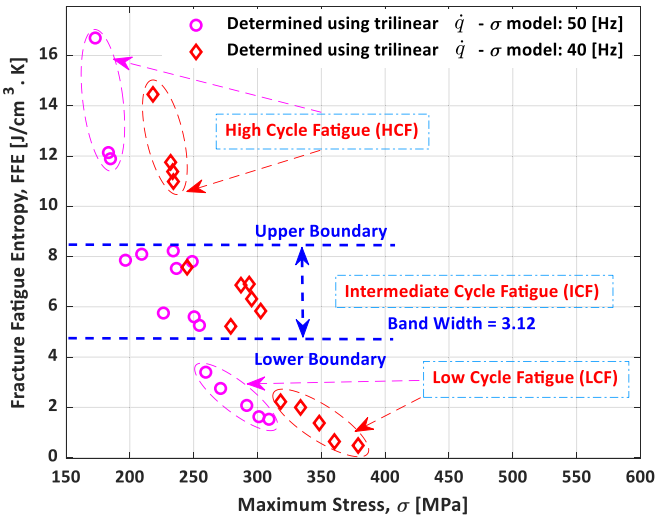

Fig. 17. Determination of FFE for different loading regimes at frequencies of 40 Hz and 50 Hz.

Table 9
Mean values of fracture fatigue entropy ($\overline{\text{FFE}}$) across different loading regimes.

Fatigue regime	$\overline{\text{FFE}}$ [J/cm^{3}K]	Frequency [Hz]	Validity of stress range [MPa]
LCF	1.8 ± 0.9	40	$318.11 \leq \sigma \leq 378.78$
		50	$259.47 \leq \sigma \leq 309.00$
ICF	6.5 ± 1.2	40	$244.87 \leq \sigma \leq 302.52$
		50	$196.57 \leq \sigma \leq 254.52$
HCF	12.8 ± 2.1	40	$218.12 \leq \sigma \leq 234.16$
		50	$172.89 \leq \sigma < 196.57$

This simplification highlights the applicability of regime-based $\overline{\text{FFE}}$ value as a reliable characteristic for assessing the fatigue response of tested PMCs under different loading frequencies and stress levels. Accordingly, Table 9 lists the mean FFE values ($\overline{\text{FFE}}$) for LCF, ICF, and HCF regimes.

Within the LCF regime, characterized by relatively high-stress levels (e.g. 360.3 MPa and 378.9 MPa for 40 Hz; 291.6 MPa and 309 MPa for 50 Hz), cumulative entropy illustrated in Fig. 16(a) and (b) exhibits a rapid growth from the early stages of fatigue lifespan. The rapid entropy accumulation at lower cycles correlates with notable energy dissipation for high-stress levels (see Fig. 15). The $\overline{\text{FFE}}$ value for the LCF regime, as seen in Tables 9 and is (1.8 ± 0.9 J/(cm^3·K)), lower than that of ICF and HCF regimes due to the fewer cycles to failure; however, the rate of entropy accumulation per cycle is significantly greater. This highlights the likelihood of severe damage occurring per cycle, linked to crack initiation and propagation, within the LCF regime.

Entropy accumulation within the ICF regime progresses more slowly as the stress level decreases. Compared to the rapid entropy growth in the LCF regime, the ICF shows a more gradual entropy increase, with the applied stress between 302.5 MPa and 271.5 MPa at 40 Hz, and between 234 MPa and 209.3 MPa at 50 Hz, as illustrated in Fig. 16(a) and (b). This behavior is linked to a moderate level of energy dissipation (see Fig. 15), and highlighting more cycles is necessary to reach the final fracture/failure. According to Table 9, the accumulated entropy in the ICF regime ranged between those of LCF and HCF. The $\overline{\text{FFE}}$ value within the ICF regime is 6.5 ± 1.2 J/(cm^3·K), greater than those for LCF, demonstrating a more steady rise that may be due to the balance between mechanical and thermal energy dissipation throughout fatigue cycles. Among all the fatigue regimes, the slowest entropy accumulation occurs in the HCF regime under relatively lower stress levels. Despite minimal energy dissipation per cycle, the large number of cycles to failure results in cumulative entropy exceeding that of the LCF and ICF regimes. Consequently, the determined $\overline{\text{FFE}}$ value for HCF is the highest, approximately double that of ICF and seven times higher than LCF.

4.4. Comparative analysis of standard and FFE-based $S-N$ curves

This section presents the development of $S-N$ curves based on the $\overline{\text{FFE}}$, denoted as FFE for simplicity, serving as an accelerated approach for fatigue life estimation of PMCs. To accomplish this, three average FFE values, determined for different fatigue regimes (LCF, ICF, and HCF) as shown in Table 9, have been implemented. The obtained FFE-based $S-N$ curves are then compared with the standard $S-N$ curves at final failure, indicated by the peak value of CCNT feature marked by diamonds in Figs. 9 and 10. The analysis was conducted at two frequencies, 40 Hz and 50 Hz, to assess the consistency between these two methods.

For the LCF regime, up to 10^5 cycles, the FFE-based $S-N$ curve predicts slightly fewer cycles at the equivalent stress levels compared to the standard $S-N$ curve for both loading frequencies, as shown in Fig. 18. The deviation, however, is insignificant, and remains within an acceptable range, indicating that the FFE method can be a viable tool for life prediction within the LCF regime. This tiny difference may be attributed to the sensitivity of considering the mean FFE value in the LCF regime, where the higher entropy accumulation rate per cycle leads to significant early-stage damage in the fatigue process due to the dominance of the self-heating effect, as highlighted in Section 4.3. This contributes to a more conservative life prediction, yielding fewer cycles compared to the standard $S-N$ curves. In the ICF regime, spanning from 10^5 to 10^6 cycles, the gap between the FFE-based and standard $S-N$ curves diminish considerably. The primary reason for this better alignment may be rooted in a more balanced distribution of mechanical and thermal energy over the fatigue cycles compared to the LCF regime, enhancing its potential as a predictive tool within the ICF scenarios.

As the applied stress level decreases further within the HCF regime (10^6 cycles or above), the FFE-based curves align almost perfectly with the standard $S-N$ curves for both loading frequencies. As can be extracted from Fig. 18 and Table 10, the fatigue strength predictions at 10^6 cycles obtained from both FFE-based $S-N$ curves and the standard $S-N$ model are closely aligned, particularly at the loading frequency of 40 Hz. For this frequency, the fatigue strength prediction from the FFE-based method is 241.8 MPa, while the standard $S-N$ approach predicts a nearly identical value of 241.1 MPa, indicating a negligible

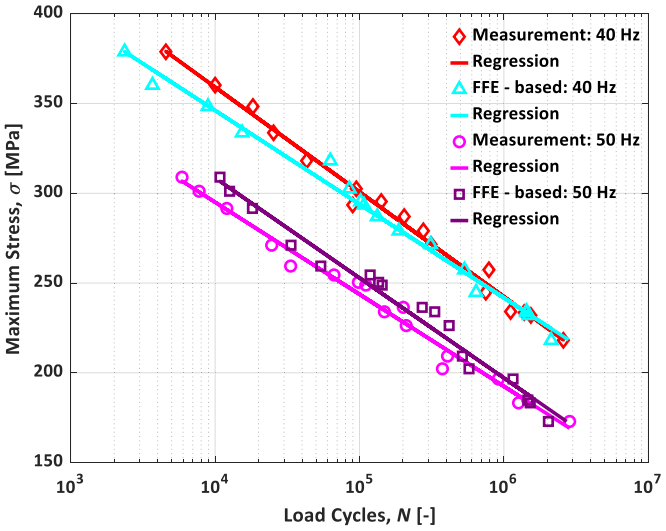

Fig. 18. Comparison of constructed S–N curves between the conventional method and the developed trilinear $\dot{q}-\sigma$ model for loading frequencies of 40 Hz and 50 Hz.

Table 10
Estimated $S-N$ curves based on FFE and final failure.

Criterion	Frequency [Hz]	Estimating $S-N$ curve by	R^2	σ_{FS} [MPa]
FFE-based	**40**	$\sigma = -52.207 \bullet \log N + 554.99$	0.989	241.75
	50	$\sigma = -55.726 \bullet \log N + 531.47$	0.978	197.11
Final failure	**40**	$\sigma = -60.624 \bullet \log N + 604.82$	0.985	241.07
	50	$\sigma = -51.284 \bullet \log N + 500.18$	0.984	192.47

discrepancy. However, at a higher frequency of 50 Hz, there is a slightly higher difference between the two methods. The FFE-based approach estimates a fatigue strength of 197.1 MPa, while the standard $S-N$ curve predicts a slightly lower value of 192.5 MPa, resulting in an insignificant difference of approximately 2.4 %. This good convergence between two curves in the HCF regime can be explained by the lower entropy generation per cycle in HCF over the prolonged fatigue life where damage progresses more gradually as a result of more evenly distributed energy dissipation.

The comparative analysis reveals that while the FFE-based $S-N$ curves slightly underestimate the number of cycles in the LCF regime, this approach demonstrates a good agreement with the standard $S-N$ curves in both ICF and HCF regimes. This highlights that the FFE approach, with further refinement, holds the potential as an alternative methodology for fatigue life prediction, potentially offering deeper insight into the thermomechanical damage processes occurring during fatigue loading.

4.5. Establishment of $S-N$ curves using entropy-based damage index

The application of FFE concept, which has shown its effectiveness in characterizing fatigue behavior across the LCF, ICF, and HCF regimes, can be further extended into the entropy-based damage index (EDI). The EDI is determined by dividing the cycle-dependent cumulative entropy (γ_N), shown in Fig. 16(a) and (b), by the FFE values (at the final fracture) presented in Fig. 15 across various stress levels for 40 Hz and 50 Hz (i.e. EDI $= \gamma_N/\text{FFE}$). This index provides a normalized and dimensionless measure of damage accumulation throughout the fatigue life, where the EDI with the value of 1 represents the final fracture. Fig. 19(a) and (b) depict the evolution of EDI over fatigue cycles for various stress levels at frequencies of 40 Hz and 50 Hz, respectively, covering the LCF, ICF, and HCF regimes. The progressive damage accumulation has been shown at intervals corresponding to 10 %, 20 %, 40 %, 60 %, 80 %, and 100 % of the EDI, represented by diamond and circle markers on the graphs.

The number of fatigue cycles associated with each EDI value is then extracted and implemented to establish the new $S-N$ curves based on different EDI levels, as illustrated in Fig. 20(a) and (b) at the frequencies of 40 Hz and 50 Hz, respectively. The estimated linear regressions for various EDI levels, based on Fig. 20(a) and (b), are presented in Table 11. At 40 Hz, the EDI-based $S-N$ curves have a slope of approximately −58.78, with intercepts rising from 535 at 10 % EDI to 593.5 at final fracture (100 % EDI), while at 50 Hz, the slope is around −49.90, with intercepts increasing from 442.65 at 10 % EDI to 492.3at 100 % EDI. A notable finding is that the established $S-N$ curves for different EDI levels illustrate similar slopes for each loading frequency, despite the shifting based on the percentage of accumulated damage. These shifts highlight the changes in the damage accumulation process in the fatigue-loaded PMC, where higher shift values are associated with accelerated damage, and consequently a shorter operational lifespan, and vice versa.

A comparison between the EDI-based $S-N$ curves and standard $S-N$ curves highlight some key differences in the representation of fatigue life. As opposed to the standard $S-N$ curves reflecting the fatigue cycles at the final fracture, i.e., EDI = 100 %; the EDI-based curves provide a continuous measure of the damage evolution at different stages. This is critical for applications where identifying the early stages of fatigue damage is vital for their predictive maintenance and life extension strategies. In other words, the incorporation of the FFE and EDI concepts provides a comprehensive framework for predicting fatigue life across different fatigue regimes and loading frequencies.

4.6. Analysis of thermomechanical fatigue behavior of PMCs using stiffness degradation

4.6.1. Load-displacement correlation and stiffness degradation curves

To obtain a comprehensive understanding of the thermomechanical fatigue behavior of PMCs, it is crucial to understand how stiffness degrades under different stress levels and loading frequencies. Assuming the geometric stability and a constant Poisson's ratio, the dynamic Young's modulus E serves as a representative indicator of stiffness

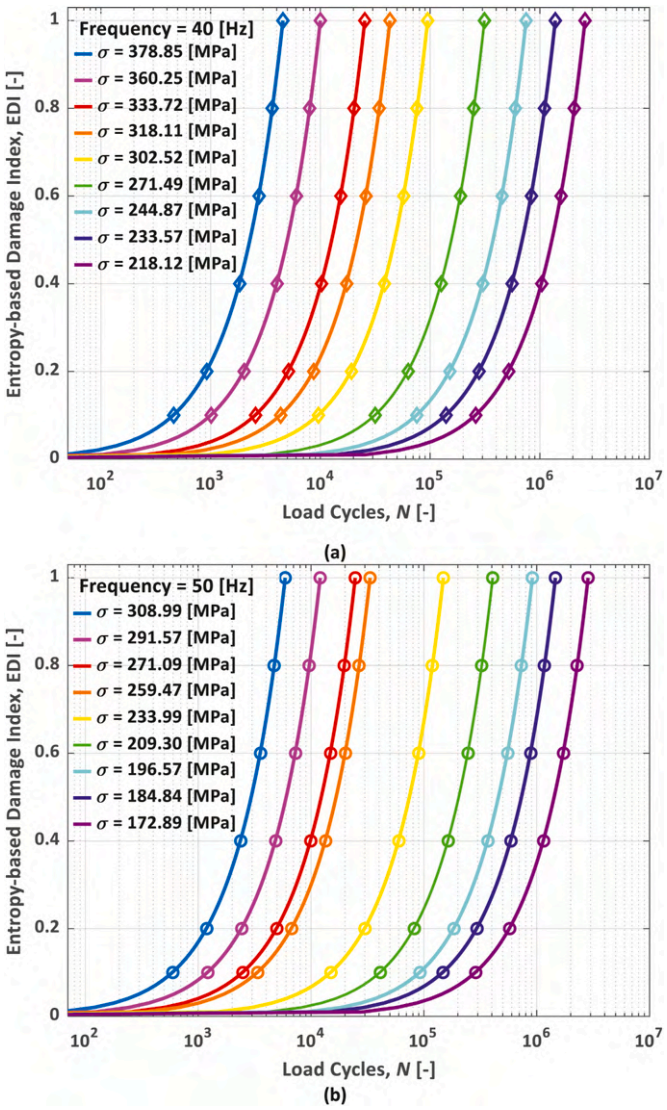

Fig. 19. Evolution of entropy-based damage index of the tested PMC from the initial stage to sudden fracture under different stress levels at loading frequencies of: (a) 40 Hz, and (b) 50 Hz.

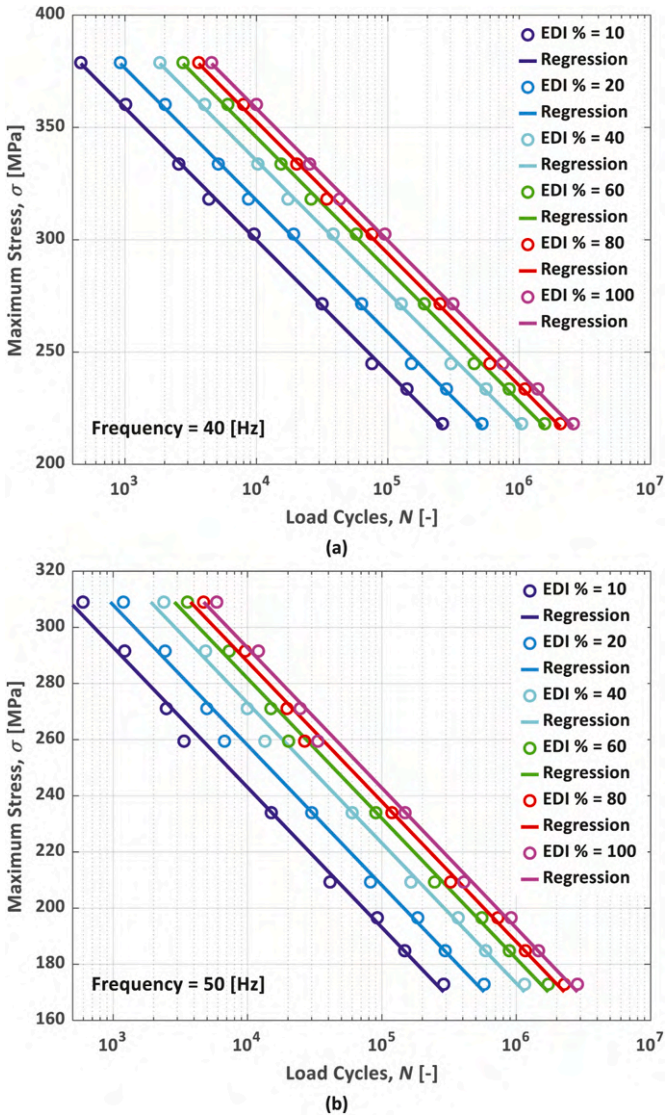

Fig. 20. Construction of $S-N$ curves using different EDI percentages for: (a) 40 Hz, and (b) 50 Hz.

Table 11
Estimated $S-N$ curve based on different EDI levels.

Frequency [Hz]	EDI% [−]	Estimating $S-N$ curve by	R^2
40	10	$\sigma = -58.781 \bullet \log N + 535.02$	0.999
	20	$\sigma = -58.780 \bullet \log N + 552.71$	0.999
	40	$\sigma = -58.776 \bullet \log N + 570.38$	0.999
	60	$\sigma = -58.775 \bullet \log N + 580.72$	0.999
	80	$\sigma = -58.774 \bullet \log N + 587.74$	0.999
	100	$\sigma = -58.774 \bullet \log N + 593.50$	0.999
50	10	$\sigma = -49.908 \bullet \log N + 442.65$	0.994
	20	$\sigma = -49.907 \bullet \log N + 457.67$	0.994
	40	$\sigma = -49.906 \bullet \log N + 472.69$	0.994
	60	$\sigma = -49.905 \bullet \log N + 481.47$	0.994
	80	$\sigma = -49.905 \bullet \log N + 487.43$	0.994
	100	$\sigma = -49.905 \bullet \log N + 492.32$	0.994

degradation [26]. This parameter can be determined using the cantilever beam formula, based on the relationship established between maximum force over each fatigue cycle P_{max} recorded by the force sensor and maximum displacement δ_{max} obtained by integrating the measured acceleration data twice over a wide range of load levels [26]:

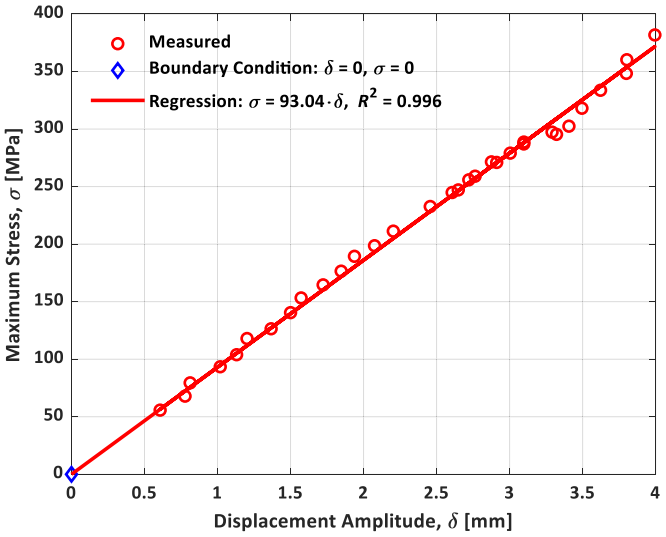

Fig. 21. Correlation between stress and displacement using test results of 40 Hz and 50 Hz.

$$E = \frac{L^3}{3I}\left(\frac{P_{max}}{\delta_{max}}\right)_{cycle}, \tag{12}$$

where L is the length and I is the moment inertia of the tested PMC. To establish the correlation between the maximum stress and the displacement amplitude for further analysis, it is assumed that the stress is negligible when the displacement amplitude δ is zero (i.e., $\delta = 0, \sigma = 0$) [6], serving as the boundary condition, indicated by a diamond in Fig. 21. Accordingly, a linear correlation between the maximum stress and the displacement amplitude was identified using the measured data from 40 Hz to 50 Hz, indicating that a displacement amplitude of 1 mm corresponds to a stress level of 93 MPa. Using this correlation along with the measured maximum force and Eq. (12), the dynamic Young's modulus is evaluated across all fatigue regimes. Fig. 22(a) and (b) show the evolution of dynamic Young's modulus over fatigue cycles at 40 Hz and 50 Hz, respectively. The graphs illustrate various levels of stiffness degradation, from 10 % to 50 %, marked by circles to illustrate the degradation trend better. Notably, final failures occurred at approximately 50–60 % stiffness degradation.

4.6.2. *Establishment of $S-N$ curves based on stiffness degradation*

The $S-N$ curves were then established based on different levels of stiffness degradation (SD): 10 %, 20 %, 30 %, 40 %, and 50 %, at frequencies of 40 Hz and 50 Hz, as illustrated in Fig. 23(a) and (b), respectively. These Figures demonstrate the permissible number of cycles a fatigue-loaded PMC can endure under an arbitrary stress level, based on different SD levels at 40 Hz and 50 Hz. Table 12 presents the estimated linear regressions corresponding to the $S-N$ curves across different SD levels for 40 Hz and 50 Hz. At 40 Hz, increasing SD from 10 % to 50 % slightly reduces the $S-N$ curve slopes by 5.2 % and raises the intercepts by 1.1 %, while at 50 Hz, these changes are more substantial, with a 6.4 % slope reduction and a 2.8 % intercept rise. This interplay between slope and intercept for both frequencies confirms a vivid trend of increased endurance at higher permissible SD levels, while the comparison indicates a more pronounced decrease in the fatigue lifespan of the tested PMC at 50 Hz, confirming the PMC specimen endures fewer cycles before failure at a higher frequency.

The relationship between the critical values determined from AE analysis (shown in Figs. 9 and 10) and the SD levels remains still unsolved. To address this, SD-based $S-N$ curves have been established, incorporating AE-based critical values, as illustrated in Fig. 23(a) and (b) for 40 Hz and 50 Hz. Within the LCF, ICF, and HCF regimes at 40 Hz,

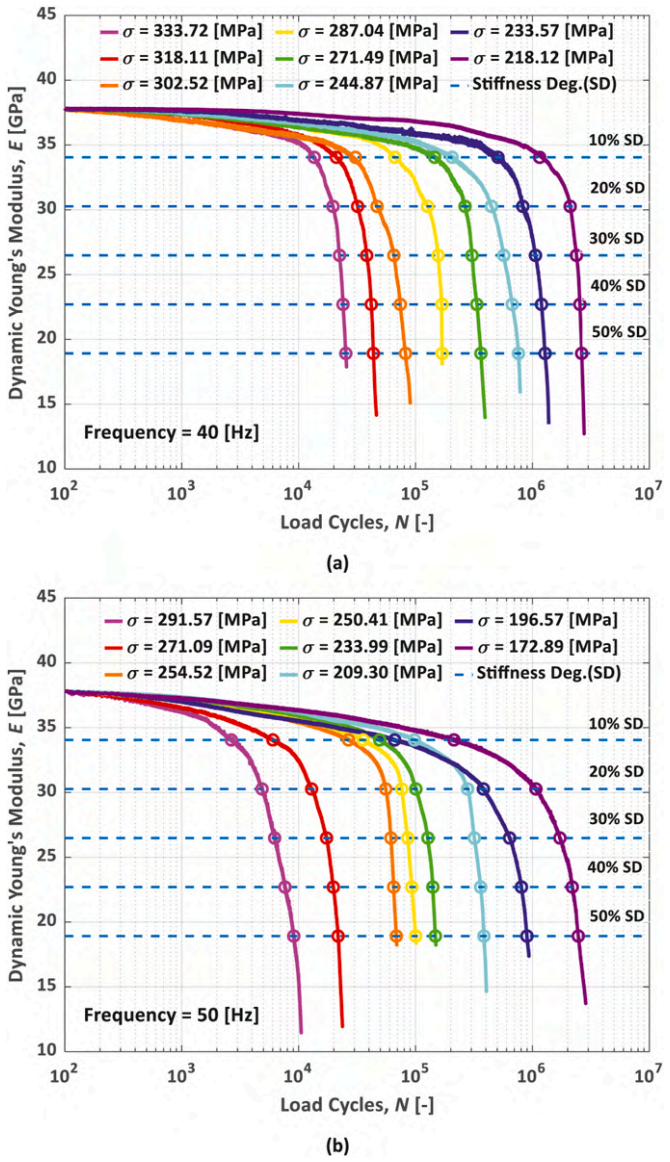

Fig. 22. Evolution of the dynamic Young's modulus degradation up to abrupt failure, with annotations indicating different degradation levels (10 % SD, 20 % SD, 30 % SD, 40 % SD, and 50 % SD) at various stress levels for frequencies of: (a) 40 Hz and (b) 50 Hz.

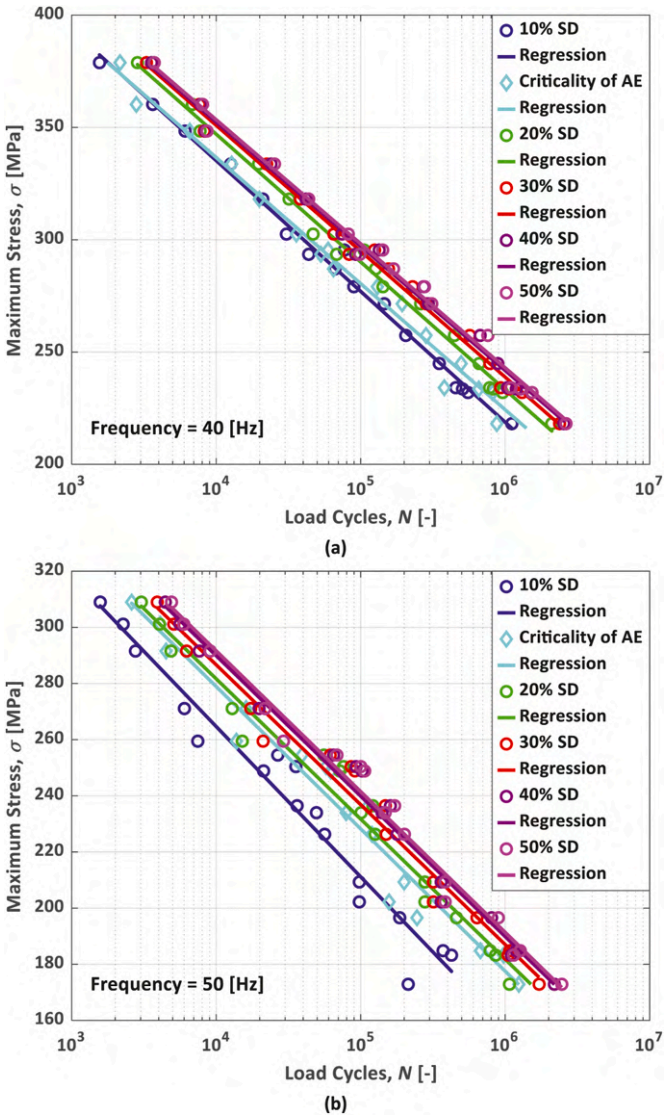

Fig. 23. Constructing $S-N$ curves using various SD levels for: (a) 40 Hz, and (b) 50 Hz.

Table 12
Estimated $S-N$ curve based on different stiffness degradation (SD) levels.

Frequency [Hz]	SD% [−]	Estimated by	R^2
40	10	$\sigma = -58.230 \bullet \log N + 568.16$	0.993
	20	$\sigma = -56.895 \bullet \log N + 574.58$	0.992
	30	$\sigma = -56.032 \bullet \log N + 575.05$	0.993
	40	$\sigma = -55.310 \bullet \log N + 573.64$	0.992
	50	$\sigma = -55.213 \bullet \log N + 574.28$	0.992
50	10	$\sigma = -53.534 \bullet \log N + 478.82$	0.957
	20	$\sigma = -49.934 \bullet \log N + 481.41$	0.971
	30	$\sigma = -49.810 \bullet \log N + 485.90$	0.978
	40	$\sigma = -50.012 \bullet \log N + 489.94$	0.984
	50	$\sigma = -50.123 \bullet \log N + 492.14$	0.983

AE-based critical values correlated with the SD levels of approximately 11 %, 12 %, and 13 %, respectively. This gradual increase in degradation (up to 2 %) from the LCF to HCF regime can be attributed to the influence of creep during prolonged fatigue cycles [63]. Notably, increasing the frequency to 50 Hz led to increased SD levels, with roughly 19 % in the LCF and ICF regimes, and 18 % in the HCF regime. This greater degradation at higher frequency can be explained by the self-heating dominance, and thereby a higher energy dissipation rate (see Fig. 15). This intensifies the non-recovery mechanisms in PMCs, e.g. polymer chain degradation, delamination, and fiber breakage, further contributing to increased stiffness degradation [4]. On the other side, the SD levels showed the opposite trend at 40 Hz and 50 Hz. At 40 Hz, the SD level increased by roughly 2 % from the LCF to HCF regimes due to the creep effect [63], while at 50 Hz, there was a slight decrease in degradation, dropping by 1 % from the LCF to HCF regime. While creep remains a contributing factor at 50 Hz, the lower SD level may likely be attributed to the reduced self-heating effect resulting from the lower stress levels (see Fig. 15), enabling the partial recovery of polymer chain movement and fiber-matrix interactions, thereby mitigating the damage evolution, and making the impact of self-heating slightly more pronounced than that of creep. For the VHCF regime based on the criticality of AE, stiffness degradation is projected to reach the threshold levels of 14 % at 40 Hz and 18 % at 50 Hz. This SD threshold (14–18 %) is significant as a potential test termination criterion, as monitoring degradation within this range is crucial to prevent catastrophic failure, especially in ultrasonic fatigue testing setups designed for VHCF and giga-cycle fatigue (GCF) regimes [6].

5. Conclusion

This study successfully addressed a fundamental gap in understanding the thermomechanical fatigue response of PMCs by examining the impact of loading frequency, ranging from 20 Hz to 50 Hz, on fatigue strength, lifespan, and damage evolution. The standard $S-N$ curves derived from final failure events, marked by the peak CCNT AE feature in Figs. 9 and 10, as well as the results obtained from thermographic approaches for estimation fatigue strength ($\Delta T-\sigma$ and $\dot{q}-\sigma$) all demonstrated a pronounced decline in fatigue strength as frequency increased. Nevertheless, the determined fatigue strength from the $\Delta T-\sigma$ method resulted in a larger discrepancy compared to the reference $S-N$ at higher frequencies, which is likely due to neglecting the influence of heat capacity, thereby highlighting the higher reliability of $\dot{q}-\sigma$ method for thermomechanical fatigue assessment of PMCs.

Incorporating temperature-dependent heat capacity within the $\dot{q}-\sigma$ approach was essential for accurately quantifying heat dissipation rates, thereby facilitating a better evaluation of entropy generation. This refined framework resulted in the construction of trilinear $\dot{q}-\sigma$ model over the wide spectrum of stress levels at frequencies of 40 Hz and 50 Hz. Unlike the bilinear model, primarily used in previous studies to estimate one $\overline{\mathrm{FFE}}$ value within all fatigue regimes using IAT results, the trilinear model provided a more reliable determination of $\overline{\mathrm{FFE}}$ values across different fatigue regimes (LCF, ICF, and HCF) by implementing both IAT and CAT results. The $\overline{\mathrm{FFE}}$ value within the ICF regime reached 6.5 ± 1.2 J/(cm^3·K), approximately four times greater than the LCF regime (1.8 ± 0.9 J/(cm^3·K)) and about half of the HCF regime (12.8 ± 2.1 J/(cm^3·K)). These findings highlighted that the $\overline{\mathrm{FFE}}$ varies significantly with the fatigue regime, showing relatively minor sensitivity to frequency.

The development of a trilinear $\dot{q}-\sigma$ model enabled the construction of $S-N$ curves using the $\overline{\mathrm{FFE}}$ values across LCF, ICF, and HCF regimes, validated through the standard $S-N$ curves derived from real-time AE monitoring at the point of abrupt fracture (see Figs. 9 and 10). Using the entropy concept, new $S-N$ curves were further developed based on various EDI levels, extending from 10 % to 100 % (i.e., final failure). As opposed to standard $S-N$ curves that depict fatigue cycles at the final failure, the EDI-based curves facilitate a continuous evaluation of damage at various stages. The incremental rise in stress level for each EDI percentage illustrated the transition process from damage initiation to ultimate fracture. In addition to EDI-based $S-N$ curves, the $S-N$ curves were constructed for different SD levels ranging from 10 % to 50 % under frequencies of 40 Hz and 50 Hz, indicating the permissible number of cycles that a fatigue-loaded PMC specimen can endure under a given stress level depending on SD levels. Correlating AE-identified critical values with SD-based $S-N$ curves showed a stiffness degradation threshold of 11–13 % at 40 Hz, which increased to 18–19 % at 50 Hz, exceeding the 40 Hz threshold by over 1.5 times. Implementing AE analysis alongside the EDI-based and SD-based $S-N$ frameworks aid in improving predictive maintenance and strategies for prolonging the lifespan of tested PMCs.

CRediT authorship contribution statement

Jafar Amraei: Writing – review & editing, Writing – original draft, Validation, Software, Methodology, Investigation, Funding acquisition, Formal analysis, Data curation, Conceptualization. **Andrzej Katunin:** Writing – review & editing, Methodology, Conceptualization.

Declaration of competing interest

The authors declare that they have no known competing financial interests or personal relationships that could have appeared to influence the work reported in this paper.

Acknowledgments

The publication is supported under the statutory funds of the Silesian University of Technology, grant no. 10/060/BKM24/2053, year 2024. The authors would like to thank their colleagues, Dr Dominik Wachla for the fruitful discussions on data curation, and Dr Krzysztof Lis for his assistance with specimen preparation from the Silesian University of Technology.

Data availability

Data will be made available on request.

References

[1] Borda F, Ingarao G, Ambrogio G, Gagliardi F. Cumulative energy demand analysis in the current manufacturing and end-of-life strategies for a polymeric composite at different fibre-matrix combinations. J Clean Prod 2024;449:141775.
[2] Backe D, Balle F, Eifler D. Fatigue testing of CFRP in the very high cycle fatigue (VHCF) regime at ultrasonic frequencies. Compos Sci Technol 2015;106:93–9.
[3] Shabani P, Taheri-Behrooz F, Samareh-Mousavi SS, Shokrieh MM. Very high cycle and gigacycle fatigue of fiber-reinforced composites: a review on experimental approaches and fatigue damage mechanisms. Prog Mater Sci 2021;118:100762.
[4] Amraei J, Katunin A. Recent advances in limiting fatigue damage accumulation induced by self-heating in polymer–matrix composites. Polymers 2022;14(24):5384.
[5] Mortazavian S, Fatemi A, Mellott SR, Khosrovaneh A. Effect of cycling frequency and self-heating on fatigue behavior of reinforced and unreinforced thermoplastic polymers. Polym Eng Sci 2015;55(10):2355–67.
[6] Amraei J, Rogala T, Katunin A, Premanand A, Kokot G, Wachla D, Kuś W, Bilewicz M, Khatri B, Balle F. Thermomechanical fatigue behavior of CF/PEKK composite under low and ultrasonic frequencies. Compos B Eng 2024;281:111539.
[7] Mortazavian S, Fatemi A. Fatigue of short fiber thermoplastic composites: a review of recent experimental results and analysis. Int J Fatig 2017;102:171–83.
[8] Sapozhnikov S, Shabley A, Ignatova A. Predicting the kinetics of hysteretic self-heating of GFRPs under high-frequency cyclic loading. Compos Struct 2019;226:111214.
[9] Premanand A, Rogala T, Wachla D, Amraei J, Katunin A, Khatri B, Rienks M, Balle F. Fatigue strength estimation of a CF/PEKK composite through self-heating temperature analysis using cyclic bending tests at 20 kHz. Compos Sci Technol 2023;243:110218.
[10] Katunin A, Wronkowicz A, Bilewicz M, Wachla D. Criticality of self-heating in degradation processes of polymeric composites subjected to cyclic loading: a multiphysical approach. Arch Civ Mech Eng 2017;17(4):806–15.
[11] Amjadi M, Fatemi A. Creep and fatigue behaviors of High-Density Polyethylene (HDPE): effects of temperature, mean stress, frequency, and processing technique. Int J Fatig 2020;141:105871.
[12] Wu H, Song J, Yue L, Yu X, Zhu Y. Experimental investigation on the influence of self-heating effect on the fatigue behavior of aluminum-CFRP riveted-bonded hybrid joints. Polym Compos 2024;45(11):10098–112.
[13] Kuleyin H, Gümrük R, Çalışkan S. Fatigue behavior of polymethyl methacrylate/acrylonitrile butadiene styrene blends including blend composition, stress ratio, frequency, and holding pressure effects. Int J Fatig 2024;187:108483.
[14] De Lima A, Rade D, Lacerda H, Araújo C. An investigation of the self-heating phenomenon in viscoelastic materials subjected to cyclic loadings accounting for prestress. Mech Syst Signal Process 2015;58:115–27.
[15] Premanand A, Rienks M, Balle F. Accelerated estimation of the very high cycle fatigue strength and life of polymer composites under ultrasonic cyclic three-point bending. Mater Des 2024;240:112872.
[16] Katunin A, Wachla D, Santos P, Reis PN. Fatigue life assessment of hybrid bio-composites based on self-heating temperature. Compos Struct 2023;304:116456.
[17] Charalambous G, Allegri G, Hallett SR. Temperature effects on mixed mode I/II delamination under quasi-static and fatigue loading of a carbon/epoxy composite. Compos Appl Sci Manuf 2015;77:75–86.
[18] Voudouris G, Di Maio D, Sever IA. Experimental fatigue behaviour of CFRP composites under vibration and thermal loading. Int J Fatig 2020;140:105791.
[19] Gagani AI, Monsås AB, Krauklis AE, Echtermeyer AT. The effect of temperature and water immersion on the interlaminar shear fatigue of glass fiber epoxy composites using the I-beam method. Compos Sci Technol 2019;181:107703.
[20] Backe D, Balle F. Ultrasonic fatigue and microstructural characterization of carbon fiber fabric reinforced polyphenylene sulfide in the very high cycle fatigue regime. Compos Sci Technol 2016;126:115–21.
[21] Lee CS, Kim HJ, Amanov A, Choo JH, Kim YK, Cho IS. Investigation on very high cycle fatigue of PA66-GF30 GFRP based on fiber orientation. Compos Sci Technol 2019;180:94–100.
[22] Wang C, Chen X, Cheng L, Ding J. High-cycle and very-high-cycle fatigue properties of CFRP-aramid honeycomb sandwich structure in three-point bending. Int J Fatig 2022;155:106576.
[23] Tao G, Xia Z. Mean stress/strain effect on fatigue behavior of an epoxy resin. Int J Fatig 2007;29(12):2180–90.

[24] Di Maio D, Voudouris G, Sever I. Investigation of fatigue damage growth and self-heating behaviour of cross-ply laminates using simulation-driven dynamic test. Int J Fatig 2022;155:106617.
[25] Colombo C, Vergani L. Influence of delamination on fatigue properties of a fibreglass composite. Compos Struct 2014;107:325–33.
[26] Amraei J, Katunin A, Lipińska M. Numerical simulation and experimental validation of self-heating of polymer-matrix composites during low-cycle fatigue loading. Int J Fatig 2024;188:108510.
[27] Mahboob Z, Bougherara H. Strain amplitude controlled fatigue of Flax-epoxy laminates. Compos B Eng 2020;186:107769.
[28] Ferreira J, Costa J, Reis P, Richardson M. Analysis of fatigue and damage in glass-fibre-reinforced polypropylene composite materials. Compos Sci Technol 1999;59 (10):1461–7.
[29] Mirzaei A, Shokrieh M. Simulation and measurement of the self-heating phenomenon of carbon/epoxy laminated composites under fatigue loading. Compos B Eng 2021;223:109097.
[30] Huang J, Pastor M-L, Garnier C, Gong X-J. A new model for fatigue life prediction based on infrared thermography and degradation process for CFRP composite laminates. Int J Fatig 2019;120:87–95.
[31] Colombo C, Libonati F, Pezzani F, Salerno A, Vergani L. Fatigue behaviour of a GFRP laminate by thermographic measurements. Procedia Eng 2011;10:3518–27.
[32] Katunin A, Pivdiablyk I, Gornet L, Rozycki P. A hybrid method for determination of fatigue limit and non-destructive evaluation of composite structures after low-velocity impact loading. Compos B Eng 2022;238:109898.
[33] Huang J, Pastor M-L, Garnier C, Gong X. Rapid evaluation of fatigue limit on thermographic data analysis. Int J Fatig 2017;104:293–301.
[34] Huang J, Garnier C, Pastor M-L, Gong X. Investigation of self-heating and life prediction in CFRP laminates under cyclic shear loading condition based on the infrared thermographic data. Eng Fract Mech 2020;229:106971.
[35] Grammatikos SA, Kordatos EZ, Matikas TE, Paipetis AS. On the fatigue response of a bonded repaired aerospace composite using thermography. Compos Struct 2018; 188:461–9.
[36] Colombo C, Bhujangrao T, Libonati F, Vergani L. Effect of delamination on the fatigue life of GFRP: a thermographic and numerical study. Compos Struct 2019; 218:152–61.
[37] La Rosa G, Risitano A. Thermographic methodology for rapid determination of the fatigue limit of materials and mechanical components. Int J Fatig 2000;22(1): 65–73.
[38] Palumbo D, De Finis R, Demelio PG, Galietti U. A new rapid thermographic method to assess the fatigue limit in GFRP composites. Compos B Eng 2016;103:60–7.
[39] De Finis R, Palumbo D, Galietti U. Evaluation of damage in composites by using thermoelastic stress analysis: a promising technique to assess the stiffness degradation. Fatig Fract Eng Mater Struct 2020;43(9):2085–100.
[40] Pathak P, Gururaja S, Kumar V, Nuttall D, Mahmoudi A, Khonsari M, Vaidya U. Examining infrared thermography based approaches to rapid fatigue characterization of additively manufactured compression molded short fiber thermoplastic composites. Compos Struct 2025;351:118610.
[41] Teng Z. Thermo-based fatigue life prediction: a review. Fatig Fract Eng Mater Struct 2023;46(9).
[42] Zaeimi M, De Finis R, Palumbo D, Galietti U. Fatigue limit estimation of metals based on the thermographic methods: a comprehensive review. Fatig Fract Eng Mater Struct 2024;47(3):611–46.
[43] Maquin F, Pierron F. Heat dissipation measurements in low stress cyclic loading of metallic materials: from internal friction to micro-plasticity. Mech Mater 2009;41 (8):928–42.
[44] Demilly K, Cavoit J, Marco Y, Moreau G, Dolo G, Carrere N. Estimating fatigue life of carbon/epoxy composites: a rapid method coupling thermo-mechanical analysis and residual strength. Fatig Fract Eng Mater Struct 2024;47(6):1856–67.
[45] Ghane E, Mohammadi B. Entropy-damage mechanics for the failure investigation of plain weave fabric composites. Compos Struct 2020;250:112493.
[46] Mohammadi B, Mahmoudi A. Developing a new model to predict the fatigue life of cross-ply laminates using coupled CDM-entropy generation approach. Theor Appl Fract Mech 2018;95:18–27.
[47] Mehdizadeh M, Khonsari M. On the application of fracture fatigue entropy to multiaxial loading. Int J Fatig 2021;150:106321.
[48] Amooie MA, Khonsari M. On the effect of environmental temperature on fracture fatigue entropy. Int J Fatig 2023;168:107411.
[49] Mehdizadeh M, Khonsari M. On the application of fracture fatigue entropy to variable frequency and loading amplitude. Theor Appl Fract Mech 2018;98:30–7.
[50] Amooie MA, Lijesh K, Mahmoudi A, Azizian-Farsani E, Khonsari MM. On the characteristics of fatigue fracture with rapid frequency change. Entropy 2023;25 (6):840.
[51] Naderi M, Khonsari M. On the role of damage energy in the fatigue degradation characterization of a composite laminate. Compos B Eng 2013;45(1):528–37.
[52] Mahmoudi A, Mohammadi B. On the evaluation of damage-entropy model in cross-ply laminated composites. Eng Fract Mech 2019;219:106626.
[53] Huang J, Yang H, Liu W, Zhang K, Huang A. Confidence level and reliability analysis of the fatigue life of CFRP laminates predicted based on fracture fatigue entropy. Int J Fatig 2022;156:106659.
[54] Hajshirmohammadi B, Khonsari M. An approach for fatigue life prediction based on external heating. Int J Mech Sci 2021;204:106510.
[55] Dinzart F, Molinari A, Herbach R. Thermomechanical response of a viscoelastic beam under cyclic bending; self-heating and thermal failure. Arch Mech 2008;60 (1):59–85.
[56] Meneghetti G, Quaresimin M. Fatigue strength assessment of a short fiber composite based on the specific heat dissipation. Compos B Eng 2011;42(2): 217–25.
[57] Kalogiannakis G, Van Hemelrijck D, Van Assche G. Measurements of thermal properties of carbon/epoxy and glass/epoxy using modulated temperature differential scanning calorimetry. J Compos Mater 2004;38(2):163–75.
[58] Lemaitre J, Chaboche J-L. Mechanics of solid materials. Cambridge university press; 1994.
[59] Amooie MA, Wilson PJ, Mahmoudi A, Azizian-Farsani E, Khonsari MM. On the measurement of total entropy generation for determining fatigue fracture. Int J Fatig 2024;189:108578.
[60] Amraei J, Katunin A, Wachla D, Lis K. Damage assessment in composite plates using extended non-destructive self-heating based vibrothermography technique. Measurement 2025;241:115670.
[61] Cao F, Chandran KR. The role of crack origin size and early stage crack growth on high cycle fatigue of powder metallurgy Ti-6Al-4V alloy. Int J Fatig 2017;102: 48–58.
[62] Wang X, Crupi V, Jiang C, Feng E, Guglielmino E, Wang C. Energy-based approach for fatigue life prediction of pure copper. Int J Fatig 2017;104:243–50.
[63] Vassilopoulos AP. The history of fiber-reinforced polymer composite laminate fatigue. Int J Fatig 2020;134:105512.

Paper VII

Synergistic effects of graphene nanoplatelets and carbon nanofibers on thermomechanical fatigue response of modified glass/epoxy composites

Highlights

1. Incorporating GNPs enhanced low-cycle fatigue but weakened high-cycle durability.
2. Hybrid GNP-CNF fillers improved fatigue performance across all fatigue regimes.
3. GNPs and hybrid GNPs-CNFs mitigated self-heating and prolonged fatigue lifetime.
4. MPD-based $\Delta T - \sigma$ and $\dot{q} - \sigma$ methods offered robust fatigue strength assessment.

Synergistic Effects of Graphene Nanoplatelets and Carbon Nanofibers on Thermomechanical Fatigue Response of Modified Glass/Epoxy Composites

Jafar Amraei[1,*], Tomasz Rogala[1], Andrzej Katunin[1], Izabela Barszczewska-Rybarek[2], João M. Parente[3], Paulo N.B. Reis[4]

[1] Department of Fundamentals of Machinery Design, Faculty of Mechanical Engineering, Silesian University of Technology, Konarskiego 18A, 44-100 Gliwice, Poland

[2] Department of Physical Chemistry and Technology of Polymers, Faculty of Chemistry, Silesian University of Technology, Strzody 9 Str., 44-100 Gliwice, Poland

[3] Centre for Mechanical and Aerospace Science and Technologies (C-MAST), Universidade da Beira Interior, Rua Marquês d'Ávila e Bolama, 6201-001, Covilhã, Portugal

[4] University of Coimbra, CEMMPRE, ARISE, Department of Mechanical Engineering, 3030-788 Coimbra, Portugal

[*] Corresponding author: jafar.amraei@polsl.pl, +48 32 237 13 75

Abstract

This study explored the synergistic role of graphene nanoplatelets (GNPs) and carbon nanofibers (CNFs) on the thermomechanical fatigue performance of modified glass fiber-reinforced polymer (GFRP). Three composite materials were investigated including unmodified GFRP, GFRP modified with GNPs (0.75 wt.% GNPs), and GFRP modified with hybrid nano-reinforcements (0.375+0.375 wt.% GNPs and CNFs). Their fatigue strengths were assessed using two thermography-based approaches (i.e. $\Delta T - \sigma$, and $\dot{q} - \sigma$), with the minimum curvature radius (MCR) and maximum perpendicular distance (MPD) procedures individually incorporated into each approach. The results extracted from thermographic approaches highlighted the negative influence of GNPs on fatigue strength, while HNPs contributed to fatigue strength improvement. The $S - N$ curves were constructed as a reference to assess the reliability of fatigue strengths derived from thermographic approaches. Unlike the MCR, incorporating MPD analysis into $\Delta T - \sigma$ and $\dot{q} - \sigma$ approaches demonstrated good alignment with fatigue strength values derived from $S - N$ curves. Nevertheless, the introduced MPD-based $\dot{q} - \sigma$ approach provided a more reliable strategy for assessing the fatigue strengths of these composites. Moreover, the $S - N$ curve analysis, supported by thermal responses and microscopic observations, illustrated that while GNPs

enhanced the low-cycle fatigue performance, incorporating HNPs notably improved the life of modified GFRP composite across both low- and high-cycle regimes.

Keywords: Fatigue strength, thermographic-based fatigue assessment, self-heating effect, hybridization, nanofillers

Nomenclature

Symbol	Definition
T	Temperature
T_g	Glass-transition temperature
T_p	Peak temperature
σ	Maximum stress
P	Maximum force
L	Span length of the specimen
W	Width of the specimen
h	Thickness of the specimen
ΔT	Temperature rise
$\dot{q}$	Heat dissipation rate
N	Number of cycles
R^2	Determination coefficient
ΔH	Post-curing heat
$S - N$	Stress-life
$\varepsilon - N$	Strain-life
σ_{FS}	Fatigue strength
r_{min}	Minimum radius of the curvature
d_{max}	Maximum perpendicular distance
$f(x)$	Exponential function
a, b, c	Coefficients
A	Slope of the chord line
B	Intercept of the chord line
σ_{FS}^{MCR}	Fatigue strength based on maximum curvature radius
σ_{FS}^{MPD}	Fatigue strength based on maximum perpendicular distance
ρ	Density
C_p	Heat capacity
V_i	Volume fraction of an arbitrary material
W_i	Weight fraction of an arbitrary material

1. Introduction

Laminated composites are becoming popular alternatives to traditional metal-based materials in a wide range of engineering applications due to their higher specific strength and modulus, fatigue strength, corrosion resistance, design flexibility, and long-term durability [1]. In recent years, nanoparticles have been extensively utilized for strengthening matrices mechanically and providing composites with multifunctional capabilities [2]. Several studies have shown that incorporating low content of nanoparticles provides substantial benefits without affecting significantly density or production methods, which is attributed to their greater surface area-to-volume ratio and stronger physical and chemical interactions with polymer matrices [3-7].

Among the diverse types of nanoparticles, carbon-based allotropes are distinguished owing to their exceptional mechanical, electrical, and thermal properties [8-13]. In this context, the literature also highlights that incorporating hybrid nanoparticles (HNPs) into composites improves their performance by synergizing the unique benefits of each type of nanoparticle. These advantages can be obtained in multiple aspects, with notable gains in mechanical properties such as fatigue strength. For example, Böger et al. [14] hybridized silica nanoparticles with multi-walled carbon nanotubes (MWCNTs) and obtained benefits of several orders of magnitude in fatigue life. Furthermore, Li et al. [15] hybridized CNFs with graphene oxide (GO) and found longer fatigue lives compared to those achieved with individual nanoparticle types. Using a semi-crystalline thermoplastic polyetheretherketone (PEEK) matrix, Papageorgiou et al. [16] achieved similar findings when hybridizing GNPs with short carbon fibers. However, according to Yue et al. [17] and Parente et al. [8], this hybridization is fully efficient only when the different nanoparticles are combined in specific proportions due to the synergistic effects between them.

Fatigue, a primary type of loading in engineering components and structures, can result in progressive damage during loading cycles [18-21]. In other words, this form of loading affects load-bearing structures throughout their operational lifespan, regardless of the type of material used in such structures. Despite extensive research and numerous fatigue models developed to address fatigue behavior, as highlighted in [22, 23], fatigue remains one of the main problems of polymer-matrix composites (PMCs) due to their complex internal architecture and their sensitivity to numerous external factors such as temperature and loading frequency. Particularly, the predictability of the fatigue behavior of PMCs reinforced with HNPs is more crucial due to their puerile state [24]. Nevertheless, the traditional techniques for evaluating the fatigue behavior of PMCs are primarily based on $S - N$ curves at low frequencies (10 Hz or below) [25];

a methodology that is quite time-consuming, especially for high- and very-high-cycle fatigue (HCF and VHCF) experiments [26]. Therefore, there is a need for accelerated fatigue testing techniques that ensure reliability while reducing testing times.

To accelerate the fatigue life assessment of PMCs, increasing the testing frequency is a viable strategy; however, it introduces challenges, mainly due to the self-heating effect in the form of temperature growth [26, 27]. This phenomenon results from the phase lag (out-of-phase oscillations) between stress and strain during cyclic loading, attributed to the viscoelastic nature of polymers, which generate heat. Unlike metals, polymers, and PMCs have significantly lower thermal conductivity, allowing only a portion of the generated heat to dissipate into the surroundings by convection and radiation [28]. The remaining heat accumulates within the structure, leading to a rise in temperature known as self-heating temperature. For this purpose, Amraei et al. [29] developed a validated numerical model to simulate the self-heating phenomenon in PMCs by utilizing oscillatory shear rheometry data along with the first and second principles of thermodynamics. Their findings highlighted the critical role of incorporating radiative heat flux as an environmental factor, particularly under high stress/strain levels, to accurately capture the self-heating temperature response. Additionally, they demonstrated that the temperature variation across the thickness of thin PMCs, 2.4 mm in thickness and a length-to-thickness ratio of 16, is less than 4°C, which can be negligible compared to the temperature increase of 100°C under high load level. This result confirms that surface temperature measurements, which are currently feasible to record using an infrared camera, are sufficient to assess heat generation and subsequently quantify and distinguish the contributions of friction and damage-induced heat in PMCs [30]. If the increase of self-heating temperature is kept within a safe limit (typically below 5 °C relative to the room temperature (RT) [31]), this phenomenon can be implemented as an alternative heat source for damage detection using nondestructive testing (NDT) methods, such as self-heating-based vibrothermography (SHVT), without degrading the structural integrity [31]. Otherwise, this may dominate the fatigue process, and lead to premature structural failure [32]. Depending on the mode of the development of the self-heating effect (stationary or nonstationary behavior of the temperature response after the transient exponential growth), also the fracture mechanisms differ [23, 32]. Loading frequency is a key factor influencing dissipated energy; higher frequencies result in greater heat generation (see, e.g., [28]). This is especially important in the context of accelerated fatigue tests under high frequency, affecting the intensity and mechanisms of structural degradation. In other words, when the self-heating temperature during fatigue is relatively high, it can influence not only the mechanical degradation but also introduce chemical changes in the

polymeric matrix of a composite [33]. Therefore, it is essential to find solutions to minimize or limit the self-heating effect. A comprehensive overview of methods to limit the self-heating effect discusses various approaches, including forced cooling with air, nitrogen, and other media [28]. For example, Amraei et al. [26] evaluated the thermomechanical fatigue response of CF/PEKK composites under two different conditions: (i) at a loading frequency of 50 Hz with natural air cooling, and (ii) at ultrasonic frequency (20.2 kHz) using a pulse-pause sequence combined with forced air cooling. Fractographic analysis demonstrated similarities in fatigue fracture mechanisms between the low-frequency and ultrasonic-frequency tests when the temperature generated during ultrasonic testing (20.2 kHz) was controlled using a pulse-pause ratio of 1:6, with pulse and pause durations of 250 ms and 1500 ms, respectively. In addition to the implementation of the cooling techniques, the authors in [28] highlighted the material modification as a potential strategy to mitigate the self-heating effect. By appropriately selecting the type, shape, and content of fillers in the composite structure, it is possible to not only enhance the fatigue life of the composite materials but also improve the mechanisms for dissipating the thermal energy generated by the self-heating effect into the environment.

Advances in understanding the self-heating effect have led to the development of thermography-based approaches to rapidly estimate fatigue strength or, in other studies, the fatigue limit. The concept of determining the fatigue strength/limit through increasing amplitude tests (IATs) under sequential stress levels was first introduced by Luong [34], Rosa and Risitano [35], called temperature rise-stress ($\Delta T - \sigma$). According to this groundbreaking methodology, fatigue strength is identified as the stress level at which a significant temperature rise occurs, corresponding to the beginning of rapid thermal and structural degradation. For instance, Luong's classical method relies on bilinear regression to determine fatigue strength at the intersection of two fitted lines. Numerous other studies have recently implemented thermographic approaches to assess the fatigue strength in PMCs [26, 36-41]. For example, Palumbo et al. [39] and De Finis et al. [38] proposed an approach relying on the detailed analysis of thermal signals, including thermoelastic responses, to identify the fatigue strength of PMCs. Meanwhile, Huang et al. [42] proposed alternative curve-fitting methods, each potentially suitable for modeling the thermomechanical fatigue response of specific polymers and PMCs. Recently, Dolbachian et al. [41] implemented the knee method, where the maximum perpendicular distance (MPD) of data points from the chord was used for the determination of the fatigue strength. Therefore, it is crucial to select the appropriate thermographic approach for determining fatigue strength.

To the authors' knowledge, only a limited number of studies have explored the role of hybridization in PMCs considering their thermomechanical response during fatigue loading. The introductory studies performed by the authors in [23] support the relevance and importance of further investigation in this direction. The current study focuses on investigating the influence of nanoparticles on the thermomechanical fatigue response of composite materials, by considering the self-heating effect. For this purpose, three types of composite materials were examined: glass fiber reinforced polymer (GFRP) used as a reference, and its two modifications – GFRP modified with GNPs (GFRP-GNPs), and GFRP modified with GNPs and CNFs (GFRP-HNPs). The carbon allotropes were selected due to their superior mechanical and thermal properties, which improve fatigue resistance and promote higher thermal conductivity, enabling more efficient heat dissipation into the surroundings. Besides the determination of fatigue behavior, the glass transition temperature (T_g) and post-curing reaction heat are determined using the differential scanning calorimetry (DSC) technique to confirm the benefits of hybridization of PMCs via such carbon allotropes. The outcomes of this study highlight the potential strategies for enhancing the fatigue life of PMCs via the incorporation of nanoparticles during the manufacturing process.

2. Materials and experimental procedure

Composite laminates were produced with ten layers of plain weave bi-axial 0/90 E-glass fabric (195 g/m^2 areal density) and a bi-component matrix composed of an SR 8100 epoxy resin and SD8824 hardener, both supplied by Sicomin (Châteauneuf-les-Martigues, France). The hand lay-up technique was used to obtain plates with overall dimensions of 330×330×2 mm^3 and with all reinforcing fabrics aligned in the same direction. This system was placed inside a vacuum bag and then subjected to a load of 2.5 kN for 24 hours in a hydraulic press to ensure a constant fiber volume fraction and uniform laminate thickness. During the first four hours, the bag was connected to a vacuum pump to remove air bubbles. Finally, the laminates were post-cured at 40°C for 24 hours.

Based on the same methodology, two more laminates were produced with the same matrix reinforced with GNPs and another with a hybrid reinforcement involving GNPs and CNFs. The GNPs and CNFs were supplied by Graphnest (Sever do Vouga, Portugal) and Merck (Algés, Portugal), respectively. For this purpose, and for each configuration, the nanoparticles were mixed at room temperature (RT) with the resin, using a mechanical mixer at 1000 rpm and an ultrasonic bath, for 3 hours. Subsequently, the

hardener was added to the system using the same mixer at 300 rpm, for five minutes, followed by degassing of the mixture in a vacuum chamber to remove air bubbles introduced throughout the manufacturing system. Note that the applied nano-reinforcement contents consisted of 0.75 wt.% GNP and 0.375+0.375 wt.% GNP and CNFs, respectively, because according to Parente et al. [8], these contents were those that maximized the mechanical performance of the resin. The study showed that the viscosity of the resin is less affected by the addition of GNPs than by CNFs. This difference arises from the structural characteristics of the materials, CNFs being thin and long, while GNPs are flat and capable of sliding over each other with ease. Furthermore, it was also shown that the bending performance is superior when the composites are nano-reinforced with GNPs, which led to its adoption in this study instead of CNFs. On the other hand, filler hybridization is a very effective strategy to increase thermal conductivity due to the thermally conductive network that is created in polymer matrices involving fillers of various sizes and/or shapes [43]. Therefore, based on this information, the advantages of hybridizing 0.375+0.375 wt.% of GNPs and CNFs were also examined, as previous studies [8] have shown that this configuration optimizes the bending performance of the composite. Finally, although the literature also suggests that it is common practice to use surface treatments (silane-based coupling agents or surface functionalization) on nanoparticles to reduce their thermal contact resistance and improve dispersion in the matrix [43], Leung [44] observed that these benefits are achieved only for very specific concentrations and depend on nanoparticle/matrix compatibility. However, since the goal of this study is not to evaluate the impact of surface treatments, the nanoparticles were used in their supplied form to assess their actual effect on the self-heating response of the composites, ensuring that the results are not influenced by a suboptimal treatment. Despite everything, the methodology adopted to disperse the nanoparticles (described in more detail in [8]) proved to be effective and, as Figure 1 shows, the absence of voids or holes is also evident.

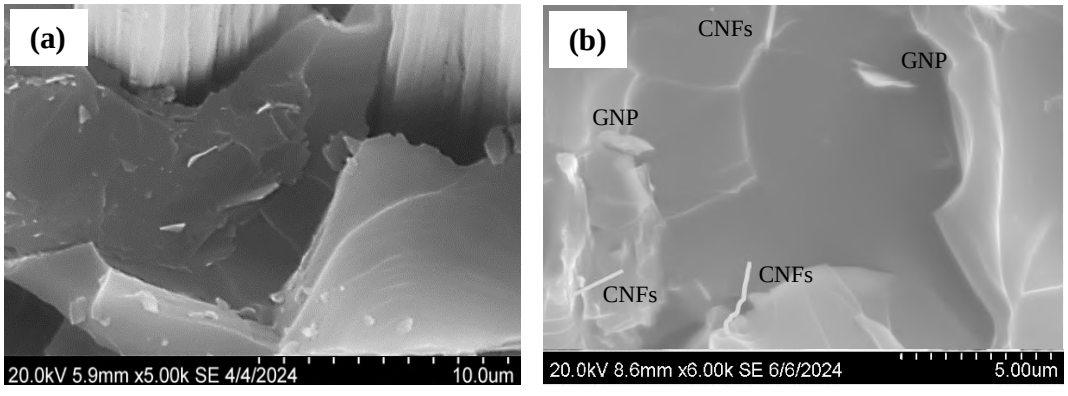

Figure 1. SEM images for composite laminates with (a) 0.75 wt.% GNP, and (b) of 0.375+0.375 wt.% of GNPs and CNFs.

These plates were then used to obtain 100×10×2 mm^3 specimens for fatigue tests, which were carried out using a specially designed test apparatus. Figure 2 illustrates a schematic representation of all components involved in the experimental setup, see Ref. [29] for the experimental apparatus.

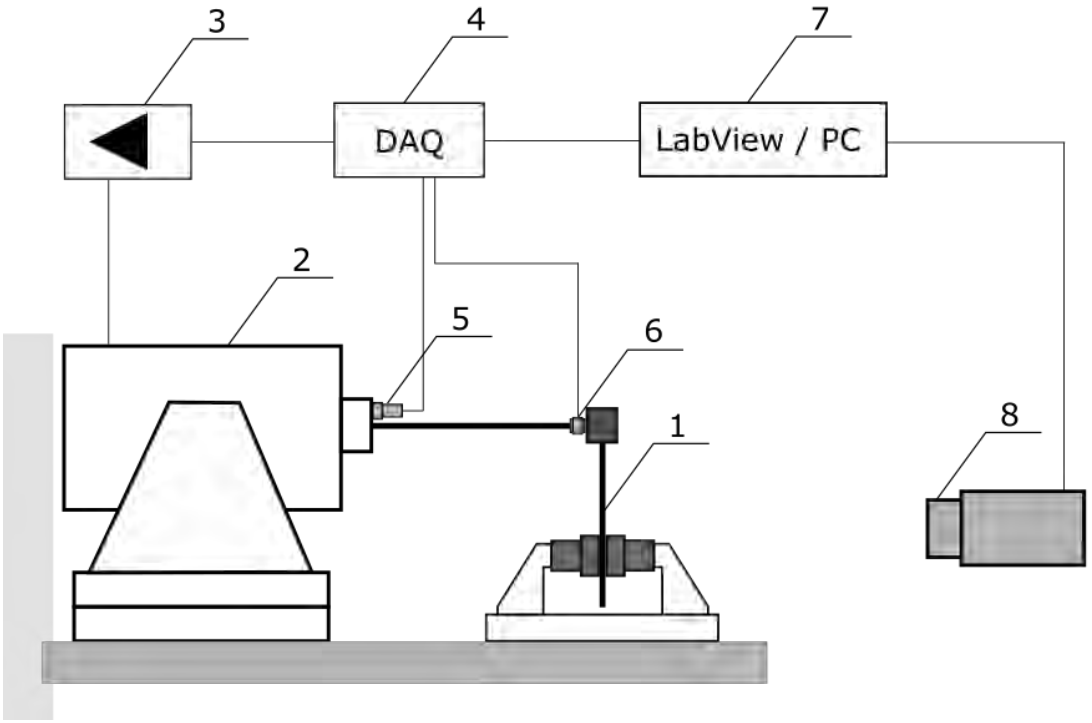

Figure 2. Schematic view of the customized laboratory test equipment.

The tested specimen (1) was bi-clamped at its ends, with an effective length of 31 mm, achieved by adjusting the distance between the two grips. The specimen in the lower grip was secured with a torque of 20 Nm to ensure the same testing conditions. The upper grip imposes displacement on the specimen through a stringer connected to the TIRA® TV-51120 electrodynamic shaker (Schalkau, Germany) (2). The shaker was powered and controlled by the TIRA® BAA 500 amplifier (Schalkau, Germany) (3), which amplifies the sine-wave excitation signal produced by a multichannel signal acquisition system (4). During operation, the PCB Piezotronics® T352C34 accelerometer (Depew, NY, USA) (5) and the

PCB Piezotronics® 208C03 force sensor (Depew, NY, USA) (6) were used to measure the acceleration and force, respectively. The data acquisition system was based on the NI® cDAQ-9174 USB compact DAQ chassis (Austin, TX, USA), equipped with the NI® 9234 Sound and Vibration module (Austin, TX, USA) and the NI® 9263 Voltage Output module (Austin, TX, USA). These components were connected to the transducers via the Brüel & Kjaer Nexus 2693 CCLD signal conditioner (Nærum, Denmark). The system was controlled by a custom LabView application running on a PC (9), which control also the InfraTec® VarioCAM® hr infrared camera (Dresden, Germany) equipped with a microbolometric detector (8) via the dedicated software IRBIS 3 plus.

While most of previous studies have carried out fatigue testing under force-controlled conditions, the current study implemented shaker-based displacement-controlled fatigue testing at room temperature. For this purpose, Ferreira et al. [45] compared fatigue testing methods for glass fiber-reinforced polypropylene composites by using both displacement- and force-controlled modes at a frequency of 10 Hz. Their results, presented as stress-life ($S - N$) and strain-life ($\varepsilon - N$) curves, illustrated less than a 5% difference between the two testing methods, highlighting these curves can be reliably compared and used to assess the fatigue behavior of PMCs. Nevertheless, displacement-controlled tests necessitate alternative failure criterion, such as tracking stiffness reduction. In the current study, the test failure criterion was defined as a 20% decrease in dynamic stiffness relative to the initial value, consistent with recommendations from [26] and other studies [46, 47].

The prepared specimens were initially coated with a thin layer of black paint with an emissivity of 0.98 [29] to facilitate thermal camera measurements. Thermograms captured using an infrared (IR) camera for two regions of interest (ROIs) were analyzed: the entire face of the specimen and the region at the bottom of the side face near the lower grip. Due to the characteristics of the cantilever beam under fully reversed bending tests, the most critical region was the bottom face, where the maximum stress occurred. The ROI, encompassing the entire face, was also used to monitor any potential localized heat hotspots. Since the maximum temperature was consistently recorded at the bottom of the tested specimen, only the temperature from this region was used for further data analysis.

The load range used in the increasing amplitude tests (IAT) was selected based on the step-wise procedure. The minimum self-heating temperature response was considered about 0.5°C above the RT and, subsequently, the loading process continued incrementally until reaching the highest load level at which the temperature remained stabilized. Beyond this threshold, the temperature history curves illustrated non-stationary behavior, indicating increased thermal effects that could lead to failure, and

these conditions were therefore excluded from further IAT analysis. Additionally, load blocks in the range of 40×10^3 cycles for all composites were used to ensure the stabilized self-heating temperature. In constructing the IAT curves, more than one specimen of the same material was typically tested. For lower load levels, individual specimens were often reused (based on the tolerance of such load levels without fatigue failure based on preliminary tests), whereas for higher loads—due to the potential for material degradation under high load levels—each specimen was tested only once. The resolution of acquired infrared images was 480×640 pixels, the distance from IR camera to the tested specimens was set at 0.39 m, and the environmental and path temperatures maintained at constant room temperature. Different load values were used, which were converted to maximum bending stress using the following relation:

$$\sigma = \frac{6\ P\ L}{W\ h^2}, \tag{1}$$

where P is the maximum force, L is the span length (31 mm), W is the width, and h is the thickness of the specimen.

The DSC tests were performed using the Mettler Toledo 3 differential scanning calorimeter (Columbus, OH, USA). The specimens of each material were prepared in the powder form, with an amount of 2 mg. The tests were performed in the temperature range 10-260°C, at the heating rate 10K/min to determine the glass transition temperature (T_g) and post-curing reaction heat for each tested material.

3. Results and discussion

3.1. DSC results

To evaluate the thermal properties of tested composites and differences in characteristic temperatures depending on the additives used for hybridization, the DSC tests were performed. The acquired scans are presented in Figure 3. In this figure, the black color represents the unmodified GFRP composite, the red color corresponds to the GFRP-GNPs composite, and the blue color indicates the GFRP modified with GNPs and CNFs (GFRP-HNPs).

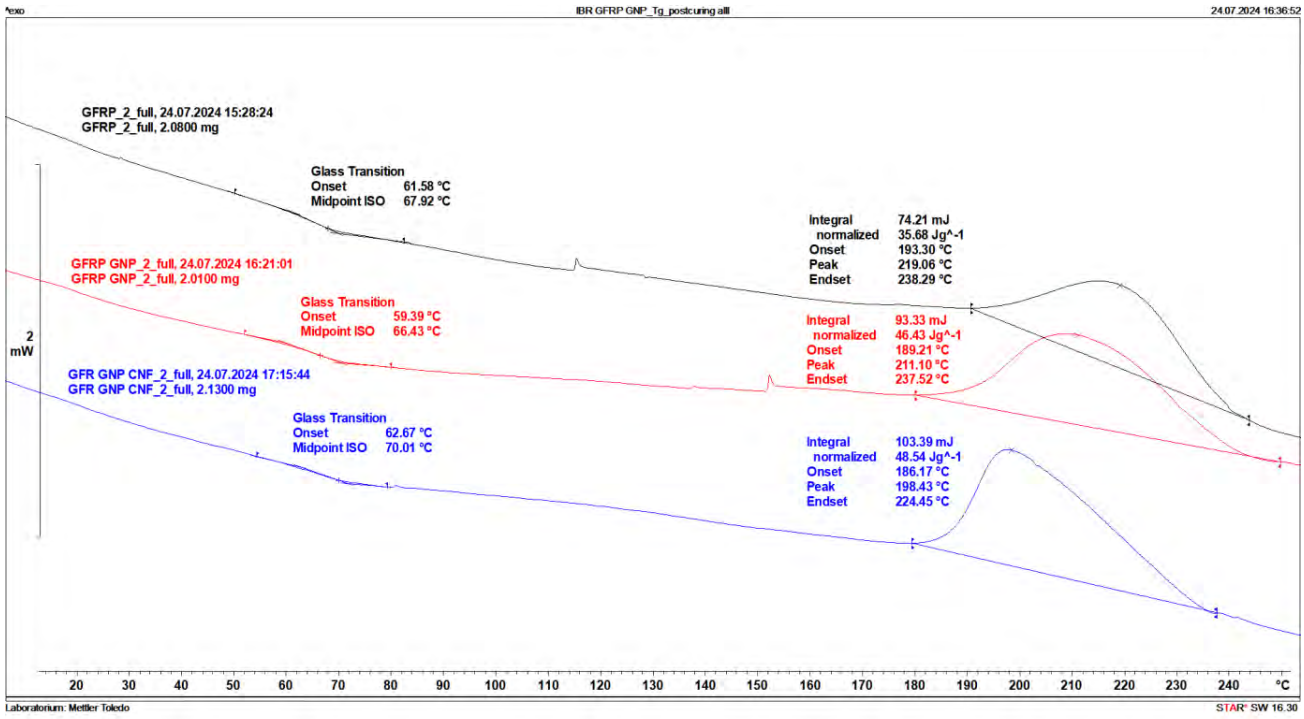

Figure 3. The DSC scan of the tested materials.

The endothermic step present at the beginning of DSC plots allowed to determine the glass-transition temperature (T_g). It is noticed that the lowest T_g is observable for GFRP with addition of GNP, the higher T_g is observed for GFRP without additives, while the highest value was observed for hybrid composite specimens. The successive exothermal peak observable in thermograms appeared due to the post-curing reaction in the epoxy matrices of tested materials. It is observable that the additives influence the post-curing reaction parameters. The onset and peak temperatures decrease, while the reaction heat increases with respect to pure GFRP specimens.

Incorporating GNPs into the GFRP reduced the glass transition temperature by 2%. Further addition of CNFs resulted in a 3% increase in T_g, in comparison to GFRP. This shows that the addition of GNPs as well as GNPs-CNFs does not negatively affect the functional properties of composites, regarding the maintaining of physical and mechanical properties as a function of temperature. They remain in a glassy state to practically the same temperature as the GFRP composite. Additionally, an increase in the T_g for GFRP-HNPs indicates a slightly beneficial effect of hybrid GNPs-CNFs reinforcement on the polymer

matrix. Their presence probably limits the segmental mobility of polymer network chains, which results in the increase in the T_g.

On the other hand, the addition of GNPs as well as GNPs-CNFs decreased peak temperature (T_p) and increased post-curing heat (ΔH). A 4% and 9% reduction were observed for T_p, whereas a 30 and 36% rise was observed for ΔH, respectively for GNPs and GNPs-CNFs. These changes suggest that the addition of GNPs as well as GNPs-CNFs decrease crosslink density in the epoxy matrix.

In summary, the acquired results from DSC tests indicate that although HNPs probably influence the structure of the polymeric matrix of tested composites [33], by decreasing their crosslink density, they do not adversely affect the T_g, whose value is important for maintaining stable functional properties for a suitable temperature range.

3.2. Frequency effect on increasing amplitude tests

The existing literature reports that frequency has a significant effect on the fatigue life of PMCs mainly due to hysteretic heating. This confirms that the selection of loading frequency is a critical step in the high-cycle fatigue of composite materials. While increasing the frequency can reduce the test duration, it may also intensify the self-heating phenomena, which if excessive, can mask the fatigue response of these materials.

Therefore, it is crucial to identify the maximum loading frequency that could accelerate fatigue testing without allowing self-heating to dominate the thermal response. For this purpose, preliminary tests were carried out in a frequency range of 35 to 45 Hz, with the step of 5 Hz, and the temperature increase (ΔT) was measured as a function of the applied stress (σ) for different frequencies. In this context, the thermal response (ΔT) of the nano-modified GFRP composite with GNPs was measured. It is worth mentioning that this analysis considered only this composite typology because the hybrid architecture is expected to bring benefits in terms of mitigating the self-heating temperature and, consequently, mask the comparability of the fatigue response of both composites. The results are presented in Figure 4 as a function of the applied maximum stress, while Table 1 provides the summary of approximate linear models derived from these tests. The linear regression models for each frequency exhibited a high coefficient of determination (R^2 = 0.971 or above), indicating the reliable goodness-of-fit between stress and thermal response across all three tested frequencies for the GFRP-GNPs composite. Finally, although this section focused solely on GFRP modified with GNPs, the results suggest that they can be extended to other configurations, such as unmodified GFRP composite, or GFRP modified with hybrid nanofillers

(CNFs-GNPs). This assumption is supported by the consistent basic architecture of the composites analyzed, consisting of the same types of fiberglass reinforcement and epoxy resin matrix.

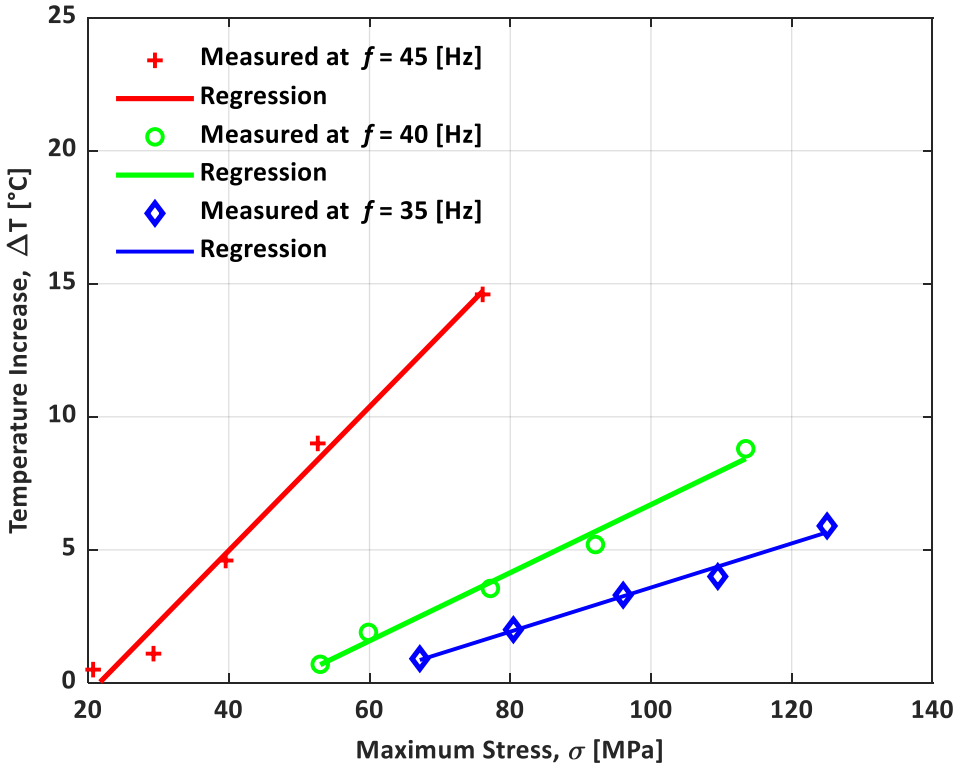

Figure 4. Loading frequency effect on the thermomechanical fatigue response of GFRP-GNP composites.

Table 1: Estimated models for the stabilized thermal response (ΔT) at different frequencies.

Frequency [Hz]	Approximated by	R^2	Load range [MPa]
45	$\Delta T = 0.270 \cdot \sigma - 5.832$	0.971	$20.7 \leq \sigma \leq 76.1$
40	$\Delta T = 0.128 \cdot \sigma - 6.099$	0.983	$53.0 \leq \sigma \leq 113.5$
35	$\Delta T = 0.083 \cdot \sigma - 4.706$	0.986	$67.2 \leq \sigma \leq 125.0$

It is notorious that, among the tested frequencies, 45 Hz resulted in the highest temperature increase, reflecting a pronounced thermal effect and leading to premature fatigue failure due to excessive self-heating. On the other hand, the 40 Hz loading frequency showed a relatively lower temperature increase, reducing the likelihood of self-heating effects significantly affecting the fatigue response. For example, considering an initial stress level of 75 MPa, the ΔT value observed for 40 Hz is around 75.7% lower (4.1 times lower) than that obtained for 45 Hz (14.42°C), but only about 2.3 times higher than that for 35

Hz (1.52°C). Therefore, the loading frequency of 40 Hz allows fatigue tests to be performed faster and without excessive self-heating, i.e., with a thermal response within a range in which the mechanical behavior of the GFRP-GNP composite is not significantly affected by thermally activated phenomena.

3.3. Results for increasing amplitude tests at 40 Hz

Achieving the stabilized self-heating temperature is vital for applying methods to determine fatigue strength, as highlighted in Refs. [26, 35, 42, 46]. For this purpose, and as reported in Section 2, preliminary tests were performed, and the results highlighted that temperature stability, for all materials and stress levels, was achieved in the range of 40×10^3 cycles.

The preliminary analysis of the results obtained from increasing amplitude tests indicated that the bilinear model [35] failed to reliably fit the experimental results. Nevertheless, as shown in Figure 5, the exponential regression approach was found to suitably fit the measured data obtained from the three composite materials. Once the parameters of the exponential model were adjusted, the fatigue strength was evaluated using two procedures: (i) the minimum curvature radius (MCR) and (ii) the maximum perpendicular distance (MPD) from the chord connecting the initial and final points to the approach line constructed for the measured data. It is noteworthy that the MPD procedure, detailed in [41], is a novel method developed to corroborate the MCR results and extend its applicability to nanoparticle-reinforced composites.

In brief, the fatigue strength estimation using the MCR procedure was preceded by normalization of the experimental data, followed by approximation using the following exponential formula:

$$\Delta T = a \cdot \exp(b \cdot \sigma) + c, \tag{2}$$

where, ΔT represents the temperature increase, calculated as the difference between the initial surface temperature of the specimen and the temperature measured after achieving the steady-state condition of the thermal response. The σ corresponds to the maximum stress applied to the specimen. a, b, and c represent coefficients determined through the exponential curve fitting. Once the exponential approximation provided a satisfactory goodness-of-fit, the minimum radius of the curvature $r_{\min}$ was calculated using the following formula [42]:

$$r_{\min} = \frac{\left[1 + \left(\frac{\mathrm{d}f(x)}{\mathrm{d}(x)}\right)^2\right]^{\frac{3}{2}}}{\left|\frac{\mathrm{d}^2 f(x)}{\mathrm{d}x^2}\right|}, \tag{3}$$

where $f(x)$ is the exponential function fitted in accordance with Eq. (2). After estimating the fatigue strength, the normalized data was denormalized and plotted on the original scale.

Similar to the MCR, the MPD procedure employed the same exponential approximation to fit and encompass the full range of maximum stresses represented in the dataset. However, in the MPD procedure, a chord line was then drawn to connect both ends of the approximation. The maximum perpendicular distance $d_{\max}$ between each point sampled from the approximation and the chord was determined using the formula extracted from the reconstruction method described in Ref. [41]:

$$d_{\max} = \arg\max_{\sigma} \frac{|A \cdot \sigma + \Delta T + B|}{\sqrt{(A^2 + 1)}}, \tag{4}$$

where, *A* and *B* represent the slope and intercept of the chord line, respectively. To implement the MCR and MPD procedures, the fatigue load was incrementally increased in stepwise manner, ensuring that temperature stabilization conditions were observable within IAT scenarios for all three composite types.

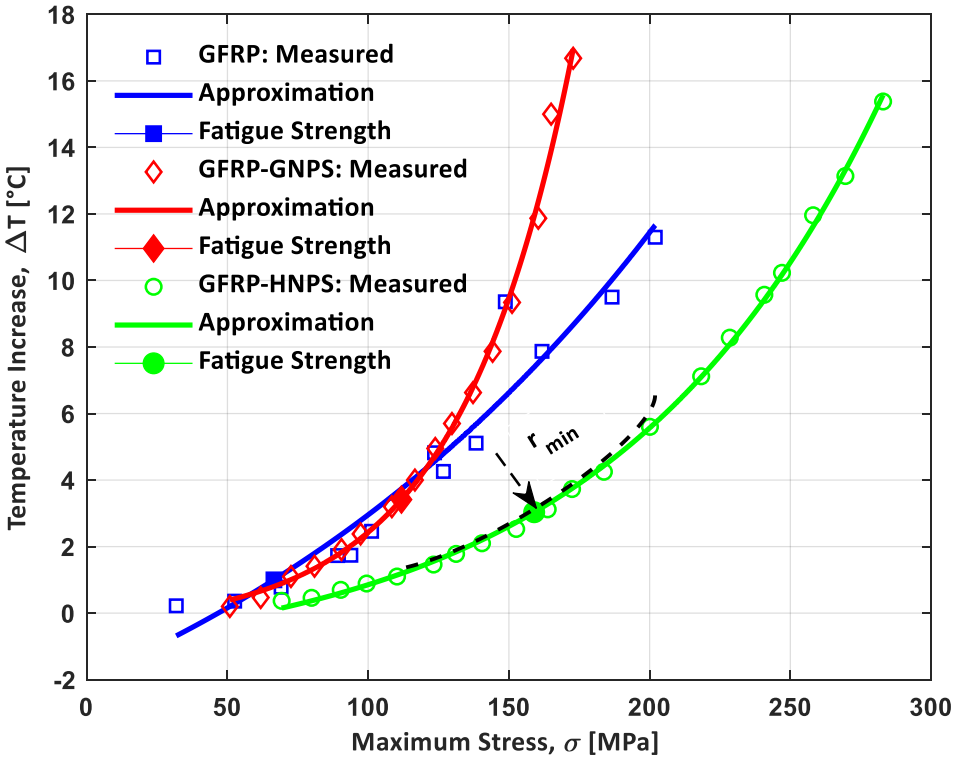

(a)

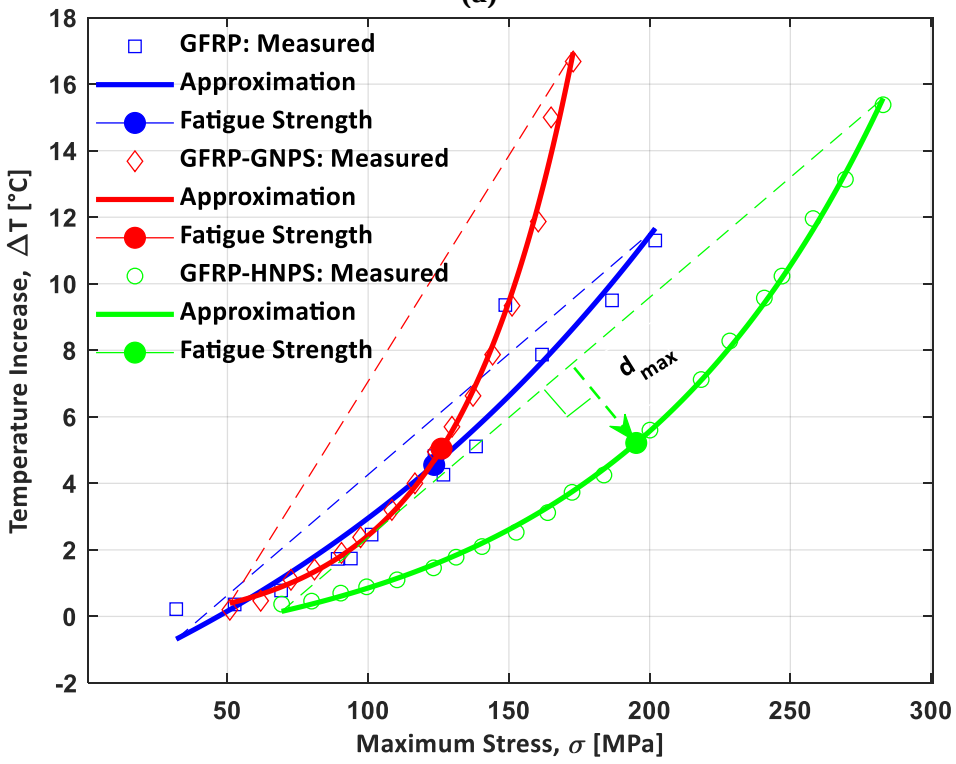

(b)

Figure 5. Fatigue strength estimations for GFRP (blue), GFRP-GNPs (red), and GFRP-HNPs (green), derived using: (a) MCR, and (b) MPD procedures.

By applying the MCR to the $\Delta T - \sigma$ approach, the estimated fatigue strengths are 66.5 MPa for unmodified GFRP, 111.8 MPa for GFRP nano-modified with GNPs (GFRP-GNPs), and 159 MPa for the GFRP laminates with hybrid nano-reinforcements (GFRP-HNPs), as shown in Figure 5(a) and Table 2. However, when the MPD procedure is incorporated into the $\Delta T - \sigma$ approach, the predicted fatigue strengths are slightly higher: 123.5 MPa for unmodified GFRP, 126.1 MPa for GFRP-GNPs, and 195.3 MPa for GFRP-HNPs. The comparison between the two methods demonstrates that the MPD-based $\Delta T - \sigma$ approach predicts the higher fatigue strength values for all analyzed composites, with increases of 57 MPa (46.1%) for unmodified GFRP, 14.2 MPa (12.7%) for GFRP-GNPs, and 36.3 MPa (22.9%) for GFRP-HNPs, as shown in Figure 5(b) and Table 2. Therefore, these results highlight the impact of the chosen method on the predicted fatigue strength of composite materials, emphasizing the importance of selecting an appropriate method for an accurate estimation.

Table 2. Exponential regression equations used to estimate the thermal response (ΔT) and fatigue strength (σ_{FS}) for all composites at 40 Hz.

Type of composite	Estimated ΔT in [℃] by	σ_{FS}^{MCR}[MPa]	σ_{FS}^{MPD}[MPa]
GFRP	$\Delta T = 3.37 \cdot \exp(0.28 \cdot \sigma) - 3.50$	66.5	123.5
GFRP-GNPs	$\Delta T = 0.85 \cdot \exp(0.94 \cdot \sigma) - 1.22$	111.8	126.1
GFRP-HNPs	$\Delta T = 1.17 \cdot \exp(0.70 \cdot \sigma) - 1.46$	159.0	195.3

It is noticed that adding GNPs into the glass/epoxy composite (i.e., GFRP-GNPs) increased the fatigue strength by approximately 68.1% compared to the unmodified GFRP composite when predicted using the MCR method, and by 2.1% when using the MPD method. On the other hand, the addition of hybrid nanoparticles (i.e., 0.375 wt.% GNPs and 0.375 wt.% CNPs) to the glass/epoxy composite led to an increase in fatigue strength by around 139% and 58.1% according to the MCR and MPD procedures, respectively. This significant improvement aligns with findings in the literature, where several authors have reported that hybridization enhances the fatigue response more effectively than the use of a single type of nanoparticle [15, 16, 49]. Shokrieh et al. [49], for example, studied the fatigue response of composites reinforced with carbon nanofibers plus graphene and observed that the fatigue life increased, respectively, 24 and 27.4 times compared to composites with a neat matrix. However, when they hybridized the two nanoparticles (CNF+GNP) in a 1:1 ratio, the improvements were around 37.2 times. According to the authors, while GNPs increased stiffness, CNFs increased strength. Therefore, hybridization with nanoparticles of different geometric shapes enables the CNFs to reduce π-π stacking

and agglomeration of GNPs, providing better mechanical properties due to the resulting synergistic effect [8, 17, 50]. However, the literature did not report on the advantages of the synergistic effect on heat dissipation and its subsequent impact on fatigue response. This gap will be addressed and discussed in detail in the following section.

3.4. Fatigue strength determination using heat dissipation concept

In Section 3.3, both MCR and MPD procedures were applied within the thermographic framework of the $\Delta T - \sigma$ approach to determine the fatigue strengths of unmodified GFRP, GFRP-GNPs, and GFRP-HNPs composites. Building upon this analysis, this section intends to incorporate the concept of heat dissipation rate ($\dot{q}$) as an alternative to the temperature increase parameter (ΔT). By substituting ΔT with $\dot{q}$, the MCR- and MPD-based $\dot{q} - \sigma$ approaches are then established.

According to the literature [26, 48], the heat dissipation rate can be calculated by:

$$\dot{q} = \rho C_p \frac{\partial T}{\partial t}, \tag{5}$$

where ρ is the density and C_p is the specific heat capacity of the tested specimen. For the GFRP composite, the experimentally obtained density was around 1704.3 $\mathrm{kg/m^3}$ and the heat capacity at room temperature is 891 J/kg·°C [51]. However, it is also necessary to determine these two parameters for GFRP-GNPs and GFRP-HNPs composites. In each case, the aim is to determine the volume fractions and heat capacity of the nanoparticles (GNPs and CNFs) relative to the GFRP.

The volume fraction of a given component in the composite can be obtained by the ratio of its weight fraction and respective density, compared to the overall volume of all the constituents. The general equation for determining the volume fraction V_i of any material "i" in the composite is:

$$V_i = \frac{\frac{W_i}{\rho_i}}{\sum\left(\frac{W_i}{\rho_i}\right)}, \tag{6}$$

where W_i is the weight fraction of material "i", and ρ_i is its density. The sum in the denominator accounts for the contributions of all components in the composite.

For the GFRP-GNPs composite, assuming the neglect of void content, the volume fraction of graphene nanoplatelets (V_{GNP}) can be obtained by the following equation:

$$V_{GNP} = \frac{\frac{W_{GNP}}{\rho_{GNP}}}{\frac{W_{GNP}}{\rho_{GNP}} + \frac{1 - W_{GNP}}{\rho_{GFRP}}}. \quad (7)$$

The term $(1 - W_{GNP})/\rho_{GNP}$ represents the remaining mass fraction occupied by the GFRP. For the GFRP-HNPs (i.e. GFRP-GNPs-CNFs) composite, the volume fractions of both the graphene nanoplatelets and carbon nanofibers must be considered. In this case, the equation for the volume fraction of GNPs (V_{GNP}^{H}) and CNFs (V_{CNF}^{H}) is given by:

$$V_{GNP}^{H} = \frac{\frac{W_{GNP}}{\rho_{GNP}}}{\frac{W_{GNP}}{\rho_{GNP}} + \frac{W_{CNF}}{\rho_{CNF}} + \frac{1 - W_{GNP} - W_{CNF}}{\rho_{GFRP}}}, \quad (8)$$

$$V_{CNF}^{H} = \frac{\frac{W_{CNF}}{\rho_{CNF}}}{\frac{W_{GNP}}{\rho_{GNP}} + \frac{W_{CNF}}{\rho_{CNF}} + \frac{1 - W_{GNP} - W_{CNF}}{\rho_{GFRP}}}. \quad (9)$$

The densities of GNPs and CNFs are 2000 kg/m^3 and 1970 kg/m^3, respectively [52, 53]. In the manufactured GFRP-GNPs composite, the GNP content is 0.075 wt.%, while for the GFRP-HNPs composite, the weight fractions are 0.375 wt.% GNPs and 0.375 wt.% CNFs. Therefore, using Eqs. (7) to (9), the volume fraction of GNPs (V_{GNP}) in the GFRP-GNPs composite is calculated as 0.64%, while the volume fractions of both GNPs and CNFs in the GFRP-HNPs composite are 0.32% each.

Moreover, for the GFRP-GNPs composite, the specific heat capacity $C_p^{GFRP-GNP}$ is calculated using a rule of mixtures similar to the approach for determining volume fractions with the assumption of zero void content, as follows:

$$C_p^{GFRP-GNP} = V_{GNP} \times C_p^{GNP} + (1 - V_{GNP}) \times C_p^{GFRP}. \quad (10)$$

Following a similar approach, the specific heat capacity of the GFRP-HNPs composite ($C_p^{GFRP-HNP}$) can be determined by:

$$C_p^{GFRP-HNP} = V_{GNP}^{H} \times C_p^{GNP} + V_{GNP}^{H} \times C_p^{GNP} + (1 - V_{GNP}^{H} - V_{CNF}^{H}) \times C_p^{GFRP}. \quad (11)$$

Considering the specific heat capacities for GNPs and CNFs of 670 J/kg·°C and 860 J/kg·°C, respectively [54, 55] and applying Eqs. (10) and (11) together with the calculated volume fractions of the nanoparticles, the heat capacities of the GFRP-GNPs and GFRP-HNPs composites are around 889.6 J/kg·°C and 890.2 J/kg·°C, respectively.

In addition to the heat capacities previously obtained for the composites, the temperature history curves obtained from IATs are also necessary to determine the heat dissipation rate. For this purpose, and as an example of the procedure adopted, Figure 6 shows the temperature-time profiles for the GFRP-HNPs composite subjected to stresses ranging between 123.2 MPa (for the lowest stabilized temperature rise) and 283.3 MPa (for the highest). Note that the stress value refers to the maximum stress measured by the force sensor at the beginning of the displacement-controlled test, and the temperature profiles include both loading and unloading phases. To quantify the heat dissipation rate ($\dot{q}$), according to Eq. (5) for the IAT scenario, it is necessary to determine the temperature gradient ($\partial T / \partial t$) just after stopping the test, i.e., the cooling rate illustrated in Figure 6. See Ref. [56] for more details. On the other hand, to estimate the cooling rates (highlighted in green shown in Figure 6), a consistent window of 25 thermograms recorded at a frame rate of 1 Hz was considered for all composites during post-processing. A linear regression, represented by the dashed blue line (equivalent to the cooling rate), was then constructed based on the minimized root mean square error (RMSE) criterion. The slope of the estimated cooling rate at each load block was then implemented into Eq. (5).

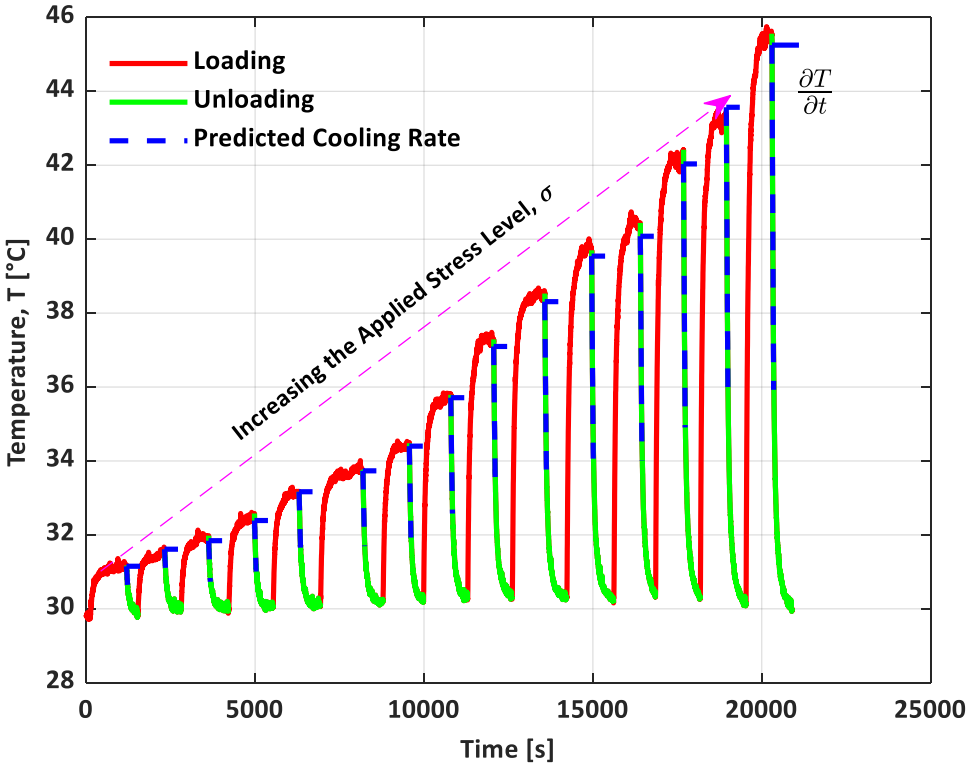

Figure 6. Temperature-time response of the GFRP-HNPs composite at various stress levels, from 123.2 MPa corresponding to the lowest temperature rise to 283.3 MPa for the highest, used for determining the heat dissipation rate.

Based on the methodology described above, the dependence of the heat dissipation rate ($\dot{q}$) on the stabilized self-heating temperature rise (ΔT) was analyzed for three types of composites (GFRP, GFRP-GNPs, and GFRP-HNPs) under the loading frequency of 40 Hz. The results are summarized in Figure 7, and the corresponding regression models used for the estimation are presented in Table 3. A good precision was found by good coefficients of determination (R^2) of 0.880 for GFRP, 0.994 for GFRP-GNPs, and 0.999 for GFRP-HNPs should be highlighted.

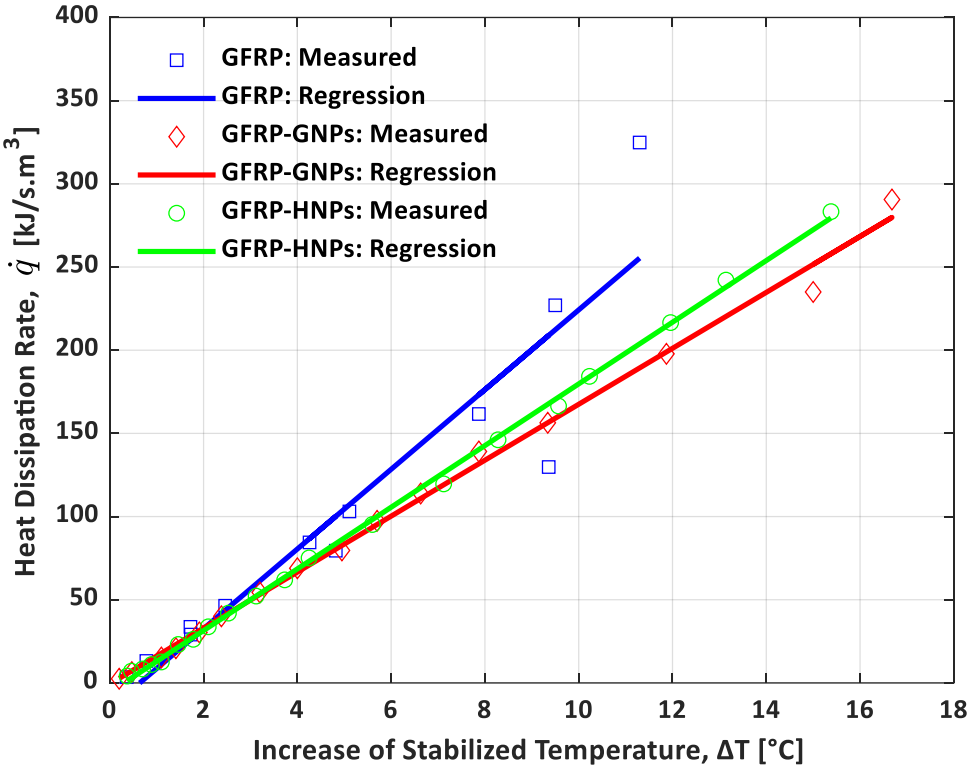

Figure 7: Dependency of the heat dissipation rate ($\dot{q}$) on the increase of stabilized self-heating temperature (ΔT) for GFRP, GFRP-GNP, and GFRP-HNP composites (marked as blue, red, and green colors, respectively) for 40 Hz.

Table 3. Predicted relationships between heat dissipation rate ($\dot{q}$) and stabilized temperature rise (ΔT).

Type of composite	Estimated by:	R^2
GFRP	$\dot{q} = 23.954 \cdot \Delta T - 15.308$	0.880
GFRP-GNPs	$\dot{q} = 16.813 \cdot \Delta T - 0.635$	0.994
GFRP-HNPs	$\dot{q} = 18.534 \cdot \Delta T - 5.599$	0.999

To quantify this dependency and compare the response of the composites, the slope values were analyzed, and it was possible to conclude that the GFRP composite, with the highest slope of 23.95, had a heat dissipation rate that was around 29.8% higher than that of GFRP-GNPs, which had a slope of 16.81, and 22.6% higher than that of GFRP-HNPs, whose slope was measured at 18.53. On the other hand, the GFRP-HNPs composites, with a slope of 18.53, had heat dissipation about 10.2% lower than that of the GFRP-GNPs composite. These differences highlight the critical role of choosing suitable reinforcement strategies to improve the thermal management capabilities and, consequently, the thermomechanical

fatigue characteristics of composites. Moreover, this study also shows the importance of investigating the relationship between applied stress and heat dissipation response.

Subsequently, based on the concept of heat dissipation rate ($\dot{q}$), the authors analyzed the feasibility of implementing $\dot{q}$ as an alternative parameter to the ΔT for determining the fatigue strength. In other words, the authors evaluated whether the fatigue strength derived from the $\Delta T - \sigma$ approach, which depends on the relationship between the temperature change (ΔT) and the applied stress (σ), can alternatively be determined by $\dot{q} - \sigma$ approach, which relies on the relationship between the heat dissipation ($\dot{q}$) and the applied stress (σ). For this purpose, the same procedures described above will be applied, i.e., the minimum curvature radius (MCR) and the maximum perpendicular distance (MPD). The results from MCR- and MPD-based $\dot{q} - \sigma$ approaches are summarized in Figure 8, while the predictive relationships between heat dissipation rate ($\dot{q}$) and applied maximum stress (σ) for all composites are presented in Table 4. These functions serve as predictive models for estimating fatigue strength based on the heat dissipation rate, similar to the approach used for $\Delta T - \sigma$.

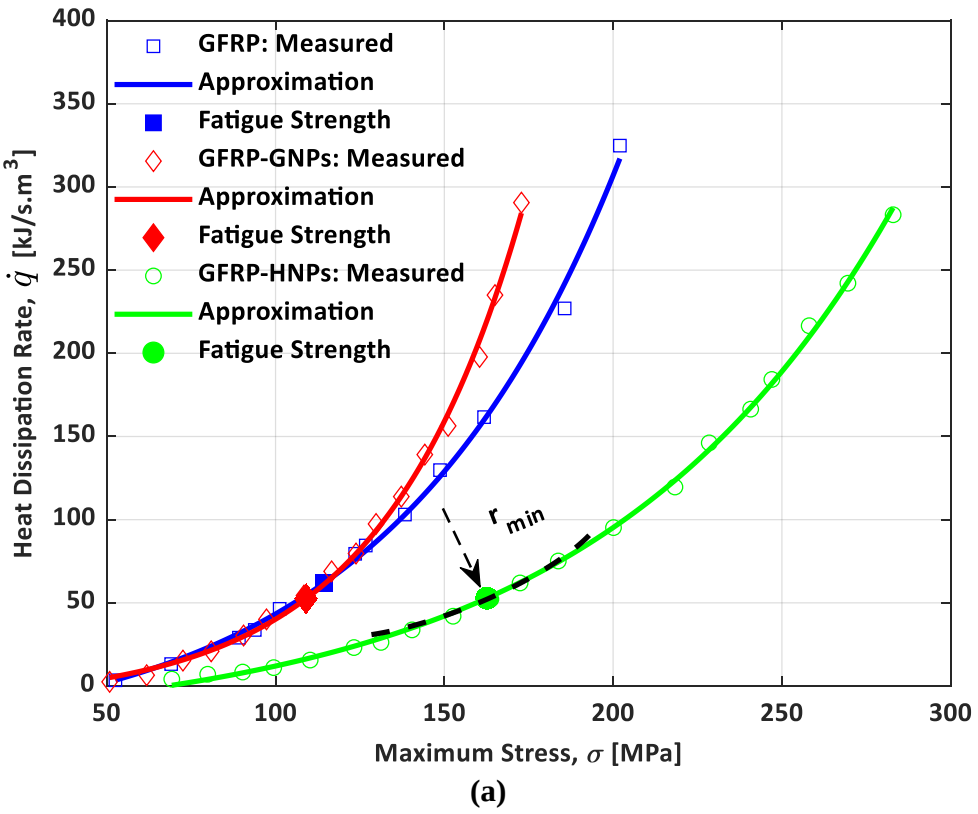

(a)

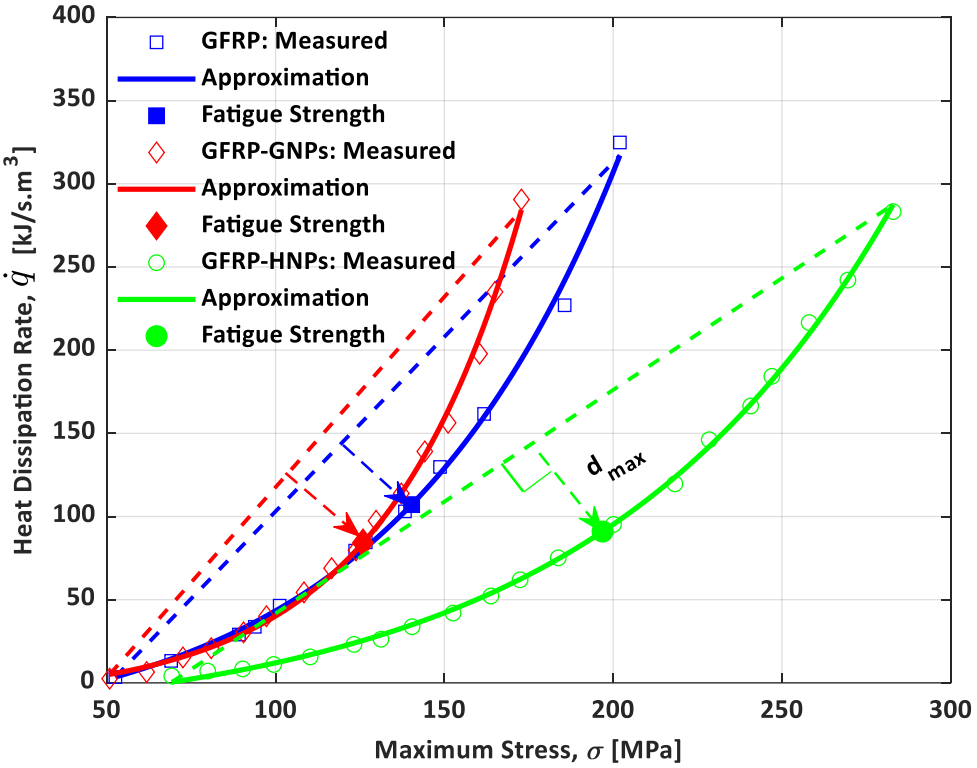

(b)

Figure 8. Estimated fatigue strength for GFRP composite marked in blue, GFRP-GNPs composite marked in red, and GFRP-HNPs marked in green.

Table 4. Equations used to estimate ($\dot{q}$) and fatigue strength (σ_{FS}) for all composites and 40 Hz.

Type of composite	Estimated $\dot{q}$ in [kJ/s. m^3] by	σ_{FS}^{MCR}[MPa]	σ_{FS}^{MPD}[MPa]
GFRP	$\dot{q} = 18.44 \cdot \exp(0.01462 \cdot \sigma) - 36.24$	114.4	140.3
GFRP-GNPs	$\dot{q} = 4.455 \cdot \exp(0.02425 \cdot \sigma) - 10.21$	109.0	125.9
GFRP-HNPs	$\dot{q} = 12.57 \cdot \exp(0.01138 \cdot \sigma) - 27.22$	162.6	196.9

Similar to the $\Delta T - \sigma$ approach, the results show that the fatigue strength determined by the $\dot{q} - \sigma$ method also depends on the implemented methodology, i.e., MCR and MPD procedures. According to Table 4, when the MPD-based $\dot{q} - \sigma$ method is used, the predicted fatigue strength is 140.3 MPa for the GFRP composite. In comparison, this value is 11.4% lower for the GFRP-GNPs composite, while 40.3% higher for the GFRP-HNPs composite. For the MCR-based $\dot{q} - \sigma$ method, the corresponding values are 114.4 MPa for the GFRP composite, 4.9% lower for the GFRP-GNPs composite, while 42.1% higher for the GFRP-HNPs composite. Therefore, the MPD-based $\dot{q} - \sigma$ approach predicts higher fatigue strength

values for all composites studied with differences ranging from 15.5% to 22.6% higher, which is in line with the previous analysis performed in Section 3.3, i.e. $\Delta T - \sigma$ approach. However, the reliability of the MCR and MPD procedures in the determination of fatigue strength must be further assessed.

Finally, in Table 5 a comparison of the fatigue strength obtained by the $\Delta T - \sigma$ and $\dot{q} - \sigma$ approaches have been presented. It is notorious that both approaches yield relatively similar results, except for the unmodified GFRP, with the maximum discrepancy among all composites. For unmodified GFRP composite, when the MCR procedure was incorporated into the $\Delta T - \sigma$ and $\dot{q} - \sigma$ approaches, the maximum error found between MCR-based $\Delta T - \sigma$ and $\dot{q} - \sigma$ approaches, which was roughly 46.1% (between 66.5 and 123.46 MPa).

Table 5. Comparison of the fatigue strength (σ_{FS}) obtained by the $\Delta T - \sigma$ and $\dot{q} - \sigma$ approaches.

Type of composite	$\dot{q} - \sigma$ approach		$\Delta T - \sigma$ approach	
	σ_{FS}^{MCR}[MPa]	σ_{FS}^{MPD}[MPa]	σ_{FS}^{MCR}[MPa]	σ_{FS}^{MPD}[MPa]
GFRP	114.4	140.3	66.5	123.5
GFRP-GNPs	109.0	125.9	111.8	126.1
GFRP-HNPs	162.6	196.9	159.0	195.3

Although the fatigue strength values were derived from the thermographic approaches (i.e., $\Delta T - \sigma$ and $\dot{q} - \sigma$) based on MCR and MPD procedures, the reliability of the MCR and MPD procedures needs to be assessed. In other words, this still remains unsolved whether the MCR- or MDP-based procedure incorporated in the $\Delta T - \sigma$ and/or $\dot{q} - \sigma$ approach yields more reliable fatigue strength estimations. To address this, it is necessary to perform constant amplitude fatigue tests and construct $S - N$ curves (stress vs. number of cycles to failure) for each composite material. These $S - N$ curves would serve as a reference to compare the predictions from both methods at 10^6 cycles.

3.5 Uncertainty analysis of the determined fatigue strengths

To estimate the uncertainty of fatigue strength values derived from different thermography-based approaches presented in the study (Sections 3.3, and 3.4), the procedure outlined in (JCGM GUM-1:2023) [57] with the specified parts was adopted. The uncertainties associated with input values (e.g., maximum stress, stabilized temperature, and heat dissipation rate) were determined using the law of propagation of uncertainty based on (JCGM 100:2008) [58]. The uncertainty in the maximum bending

stress was estimated using this law for Eq. (1). The following values of the input uncertainties were used: $u_c = 0.05$ mm for width, thickness and effective length, and $u_F = 0.02$ N for the force sensor. The resulting stress uncertainties varied depending on factors such as applied load, with values of $u_{s(\mathrm{GFRP})} = [3.7, 9.7]$ MPa for GFRP composites and $u_{s(\mathrm{GFRP-GNPs})} = [3, 10.1]$ MPa and $u_{s(\mathrm{GFRP-HNPs})} = [3.8, 15.9]$ MPa for GFRP-GNPs and GFRP-HNPs composites, respectively. To estimate the uncertainty of relative temperature, the precision value of the thermal camera was taken, which for the relative measurements yields $u_{\Delta T} = 0.06$ °C. The uncertainty of the density in the heat dissipation rate formula (Eq. (5)) was established based on the repeated measurements of the densities and equals $u_\rho = 26.4\ \mathrm{kg/m^3}$. The uncertainty propagation for heat dissipation rate for individual measurement points primarily falls within the range of $u_{\dot{q}} = [60.7\ 60.95]\ \mathrm{kJ/s.m^3}$ for all considered composite materials, with minor deviations.

For derived uncertainties $u_{\Delta T}$, u_σ, and $u_{\dot{q}}$, the normal distributions for these quantities were assumed. The propagation of the distributions to estimate fatigue strengths variability using different approaches $\sigma_{FS}^{MCR}(\dot{q} - \sigma)$, $\sigma_{FS}^{MPD}(\dot{q} - \sigma)$, $\sigma_{FS}^{MCR}(\Delta T - \sigma)$, and $\sigma_{FS}^{MPD}(\Delta T - \sigma)$ was then conducted. Since the fatigue strength estimation procedures are relatively complex — the further propagation of distributions was performed using the Monte Carlo method, following the guidelines of (JCGM 101:2008) [59]. The Monte Carlo simulation was performed for 2×10^3 trials for each approach, ensuring accuracy of 0.5% for stipulated coverage probability of 95%. For random sampling, the Latin Hypercube was selected. Table 6 presents the uncertainties corresponding to the fatigue strength values derived from the thermography-based approaches in Table 5. Furthermore, this Table shows 95% of the probabilistically symmetric coverage interval endpoints.

Table 6. Comparing the uncertainties corresponding to the $\Delta T - \sigma$ and $\dot{q} - \sigma$ approaches, along with 95% coverage intervals.

Type of composite	Statistics	$\dot{q} - \sigma$ approach		$\Delta T - \sigma$ approach	
		σ_{FS}^{MCR}[MPa]	σ_{FS}^{MPD}[MPa]	σ_{FS}^{MCR}[MPa]	σ_{FS}^{MPD}[MPa]
GFRP	**Uncertainty**	±5.9	±6.6	±6.4	±5.9
	95% coverage interval	[104.9, 127.9]	[127.9, 153.2]	[53.6, 78.8]	[111.6, 134.8]
GFRP-GNPs	**Uncertainty**	±6.8	±7.5	±6.8	±7.7
	95% coverage interval	[98.2, 124.7]	[112.6, 133.8]	[98.9, 125.5]	[98.2, 124.7]
GFRP-HNPs	**Uncertainty**	±9.2	±14	±8.9	±11.0
	95% coverage interval	[144.7, 180.8]	[168.7, 221.4]	[141.7, 176.7]	[144.7, 180.8]

3.6 Thermomechanical fatigue analysis based on *S*-*N* curves, thermal data and microscopic observations

In addition to the $S-N$ curves being crucial for understanding the fatigue response of the composite materials under analysis, the results obtained from $\Delta T-\sigma$ and $\dot{q}\ -\sigma$ methods are validated. The $S-N$ curves corresponding to 20% stiffness degradation for unmodified GFRP, GFRP-GNPs, and GFRP-HNPs composite materials were based on the results of various constant amplitude tests (CATs) at the loading frequency of 40 Hz, and are shown in Figure 9, while the estimated $S-N$ curves for each composite and respective fatigue strength are summarized in Table 7.

Based on the CATs performed on the unmodified GFRP, a bilinear $S-N$ curve was identified, indicating the existence of two fatigue regimes, shown by Line I and Line II in Figure 9. The transition point between these two regimes, denoted as Point A, occurs at a stress level of 193.4 MPa for around 2.1×10^4 cycles. Above this threshold (Line I) corresponding to a relatively high-stress range and higher heat dissipation rates (see Figure 8), the self-heating effect becomes more pronounced, thereby accelerating the fatigue degradation of the GFRP specimens. The slope of Line I of the $S-N$ curve is steeper, with a magnitude approximately 5 times higher than the slope of Line II. This indicates that fatigue life rapidly decreases at higher stress levels due to the adverse effects of heat dissipation, or more concisely internal heat storage. Above 2.1×10^4 cycles (Line II), the influence of self-heating diminishes, and the fatigue degradation of the GFRP slows down. As a result, the slope of the $S-N$ curve in Line II is much gentler, indicating that the fatigue life of GFRP increases more significantly at lower stress levels. The fatigue life at 10^7cycles correspond to a stress level of 168.4 MPa.

Incorporating GNPs into the GFRP composite significantly altered the fatigue behavior, particularly in the low-cycle fatigue regime. The addition of GNPs extended the fatigue life of the composite, particularly in the range of 10^3 cycles up to 1.8×10^5 cycles (Point B), where the $S-N$ curve shows a noticeable improvement compared to unmodified GFRP. The slope of the $S-N$ curve for GFRP-GNPs, up to the transition point at 2.1×10^4 cycles (Point A), is approximately 20% less steep than that of the unmodified GFRP (-36.5 vs. -43.8). This reduced slope indicates that GNPs provide an advantage in fatigue life by mitigating the self-heating effects during the early stages of fatigue. The role of GNPs in this regime is very beneficial, because the lower slope shows a slower degradation rate, leading to an extended fatigue life. However, from 2.1×10^4 cycles to 1.8×10^5 cycles, the slope of the $S-N$ curve for GFRP-GNPs becomes four times steeper than the slope for unmodified GFRP (-36.533 vs. -9.436). This steep increase suggests that the benefits of GNPs diminish with an increasing number of cycles, causing

the fatigue performance of GFRP-GNPs to deteriorate significantly. At 1.8×10^5 cycles, the $S-N$ curves for GFRP and GFRP-GNPs converge, after which the fatigue life of GFRP- GNPs declines more rapidly compared to unmodified GFRP. At 168.4 MPa, while unmodified GFRP maintained its endurance up to 10^7 cycles, GFRP-GNPs failed after only 5×10^5 cycles, approximately 20 times fewer than GFRP at the same stress level. This result indicates that although GNPs enhance fatigue life in the low-cycle regime, they may not be the viable candidate for improving the fatigue performance of GFRP in the high-cycle regime. This can be explained by the interplay between mechanical fatigue and thermal effects under different stress conditions. At high stresses, the self-heating phenomenon leads to a significant rise in temperature, where GNPs demonstrate their effectiveness by dissipating heat, thereby reducing the adverse effects of thermal fatigue. In contrast, at low stresses, corresponding to the high-cycle regime, the self-heating effect becomes less pronounced, and GNPs offer limited benefits in mitigating mechanical fatigue. This interpretation might be supported by the DSC findings presented in Section 3.1 and the heat dissipation analyses detailed in Section 3.3 (See Figure 8).

The addition of GNPs and CNFs into GFRP (GFRP-HNPs) led to an improvement in fatigue performance across the entire range of fatigue regimes tested, from 10^3 cycles up to 2.6×10^6 cycles. The slope of the $S-N$ curve for GFRP-HNPs was approximately 64.6% lower than that of unmodified GFRP (-15.5 vs. -43.8) up to 2.1×10^4 cycles, indicating an improvement in fatigue behavior during the low-cycle regime. This highlights that the addition of hybrid nanoparticles reduced the rate of fatigue damage accumulation by improving the chemical bonding and reducing the heat dissipation rate (see Figure 8). Above 2.1×10^4 cycles, the slope for GFRP-HNPs (-15.5) remained more advantageous than the reduced slope of unmodified GFRP (-9.4), although the difference was less significant. This shows that GFRP-HNPs composite maintained its superior fatigue resilience in the high-cycle regime as well, though the rate of improvement was less pronounced compared to the low-cycle regime. These findings indicate that while GFRP-GNPs perform well in low-cycle fatigue, they are quickly outperformed by GFRP-HNPs in higher cycles. These findings regarding the superior thermomechanical fatigue response may be supported by the DSC results presented in Section 3.1, which indicate the highest T_g value for the GFRP-HNPs composite. Additionally, the heat dissipation analysis in Section 3.3 (Figure 8) revealed that GFRP-HNPs exhibit the lowest heat dissipation rate. As a result, less proportion of heat is stored within the tested GFRP-HNPs specimen, leading to reduced temperature rise and limiting the damage induced by thermal effects, thereby prolonging the fatigue life of the GFRP-HNPs composite compared to other composite types. As highlighted by Shokrieh et al. [49], GNPs contribute to increased stiffness, whereas CNFs

improve strength. In this regard, the hybridization of nanoparticles with different geometric shapes mitigates agglomeration (particularly of GNPs) and significantly extends fatigue life due to the synergistic effects achieved.

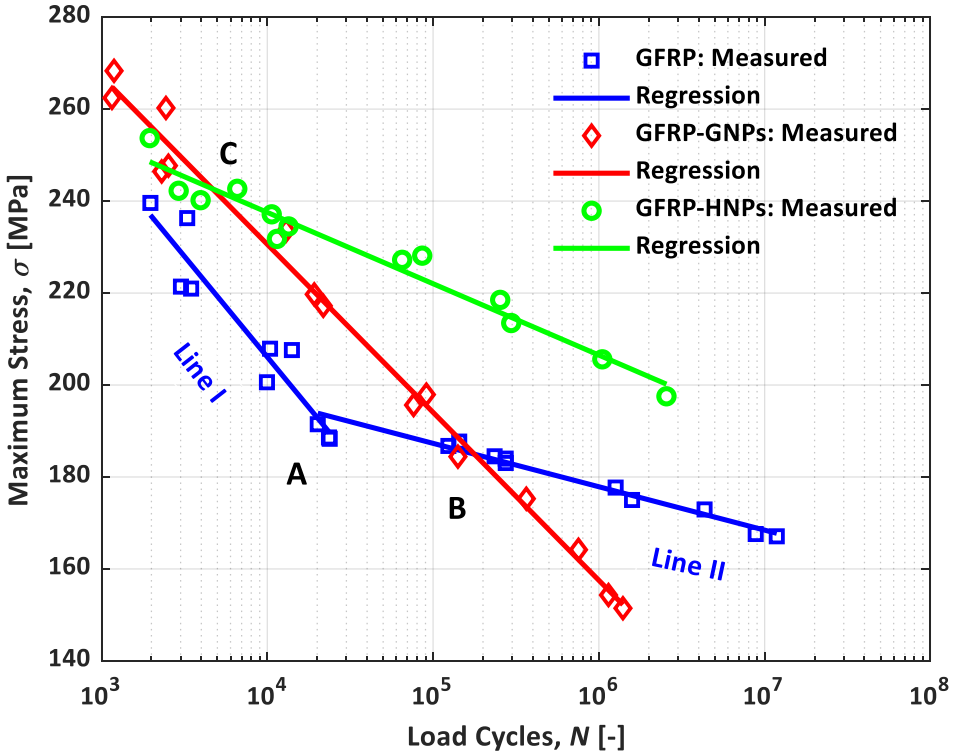

Figure 9. Constructed $S-N$ curves for three different composite materials.

Table 7. Estimated $S-N$ curves and fatigue strengths (σ_{FS}) corresponding to 10^6 load cycles for three different composite materials.

Type of composite material	Estimated by	R^2	σ_{FS} [MPa]
GFRP	$\sigma_I = -43.783 \cdot \log N + 381.234$	0.9118	177.9
	$\sigma_{II} = -9.436 \cdot \log N + 234.495$	0.9488	
GFRP-GNPs	$\sigma = -36.533 \cdot \log N + 376.721$	0.9834	157.5
GFRP-HNPs	$\sigma = -15.517 \cdot \log N + 299.614$	0.9545	206.5

To clarify the benefits achieved with nanoparticles, the damage mechanisms were analyzed and are shown in Figure 10. From a macroscopic point of view, Figure 10(a) shows that the observed damage

mechanisms are transversal to all the composites studied and are characterized by some broken fibers in the lower clamped region of the specimens accompanied by delaminations along them. This evidence is also confirmed in Figure 10(b) for GFRP composite, where it can be concluded that the delaminations result from the combined action between the stress concentrations resulting from the fiber breakage and the fibers/matrix debonding [60]. However, as shown in Figure 10(c), when graphene is added to the matrix, the delamination resistance increases due to the reinforcement of the fiber/matrix interface. In this context, the intralaminar failure of the fiber/matrix interface occurs with the breaking of numerous fiber/matrix bridges (promoted by graphene nanoplatelets), which, by increasing the debonding strength and toughness of the resin, improves the load transfer between fibers and matrix [61, 62]. In fact, a lower number of delaminations is noticeable, which is in line with the literature [63, 64]. These benefits are even greater with the hybridization of nano-reinforcements with different geometric shapes (high aspect ratio with higher surface area) because, as shown in Figures 10(d) and 10(e), it promotes a more robust nanoparticle network (3-dimensional network) as well as a synergistic effect [65]. This evidence is quite noticeable in Figure 10(d), where the synergistic effect provides strong adhesion and mechanical interaction between the epoxy resin and the fibers. Furthermore, the nanoparticles act as a protective layer around the fiber and help to divert stress concentration away from the fiber surface [66]. Consequently, all these benefits lead to an increase in fatigue life.

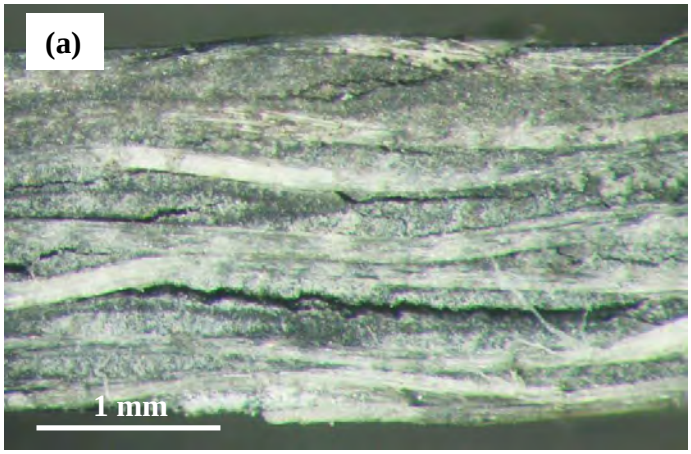

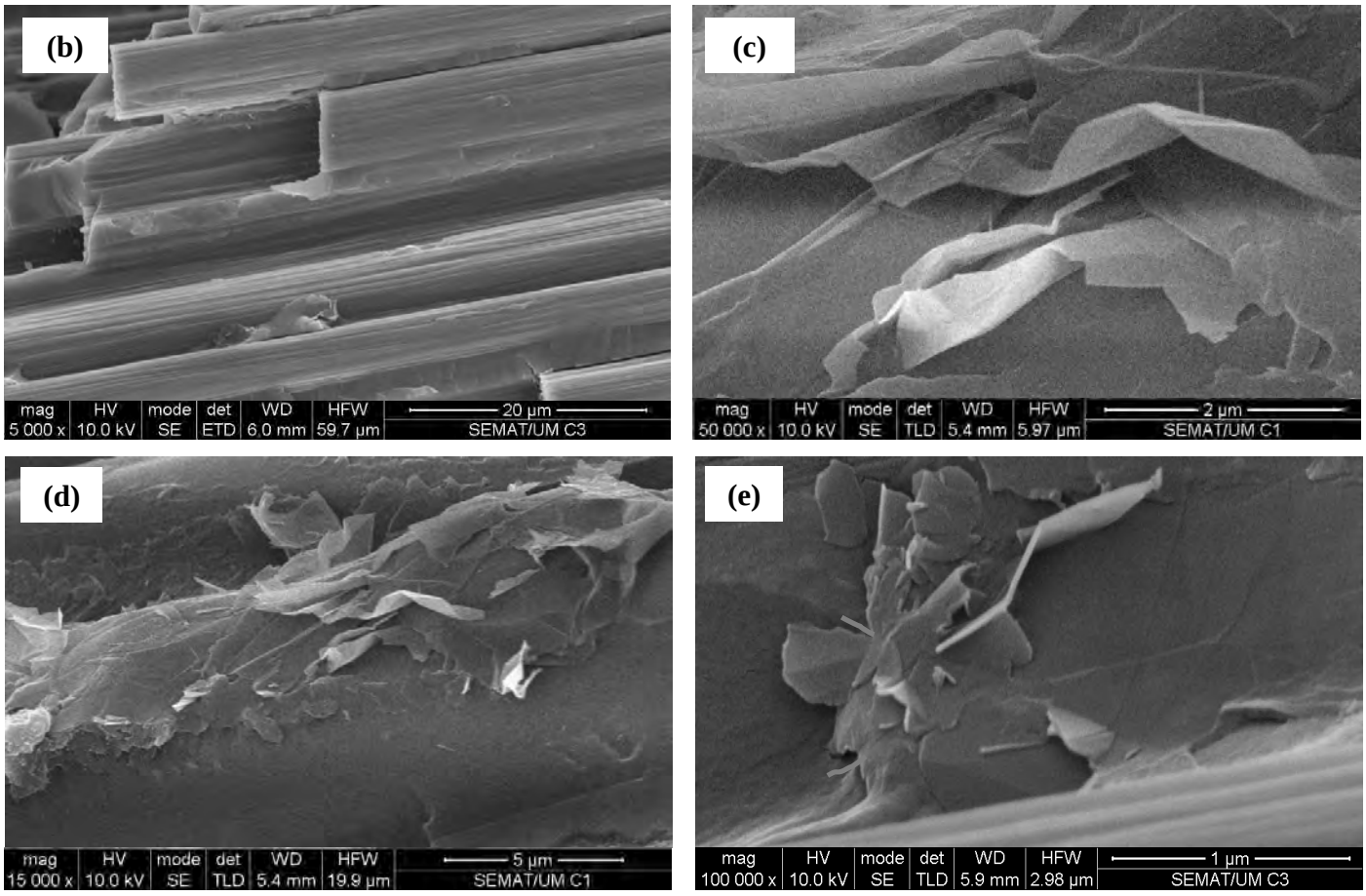

Figure 10. (a) Lateral view of the typical failure mechanisms observed for all specimens, (b) Front view of the typical failure mechanisms observed for all specimens, (c) SEM image for unmodified GFRP composite, (d) SEM image for GFRP-GNPs composite, and (e) SEM image for GFRP-HNPs composite.

In addition to the improvements reported previously, the literature also highlights the benefits obtained with the nanoparticles in terms of mitigating the self-heating temperature and, consequently, improving the fatigue strength [43]. For this purpose, the thermal responses of the entire surfaces of all composite types are compared for two different stress levels, and Figure 11 presents the registered IR images corresponding to the stiffness degradation of 20% for three types of fatigue-loaded PMC specimens. Figures 11(a-c) correspond to the stress level of 198.7 ± 1.4 MPa, showing (a) unmodified GFRP, (b) GFRP-GNPs, and (c) GFRP-HNPs. Similarly, Figure 11(d-f) corresponds to the stress level of 219.7 ± 1.0 MPa, illustrating (d) unmodified GFRP, (e) GFRP-GNPs, and (f) GFRP- HNPs. In Figure 11(b) and (e), the addition of GNPs clearly demonstrates a significant reduction in the magnitude of temperature

rise, particularly in the critical region (bottom) of the tested specimen. This effect is observed across the entire surface of the specimen for both stress levels, effectively mitigating the thermal response. From Figure 11(c) and (f), it is evident that incorporating HNPs further reduces the temperature rise magnitude and provides superior control over the thermal response across the entire specimen surface compared to GNPs, for both stress levels.

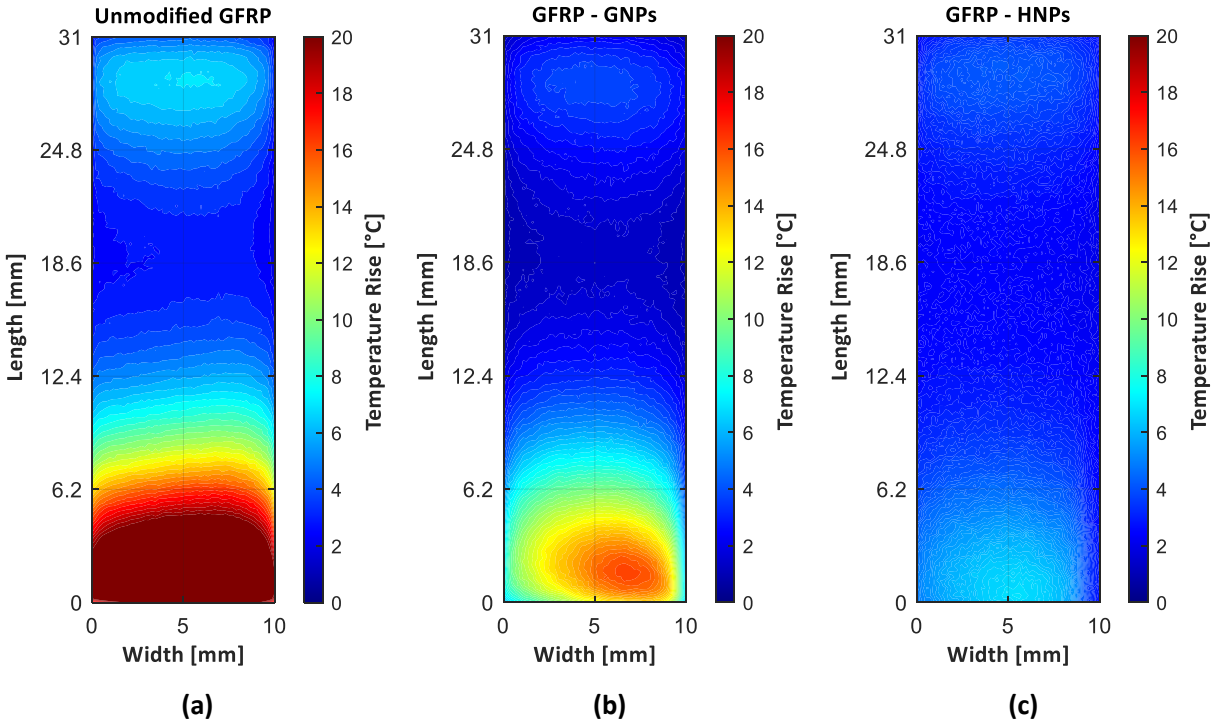

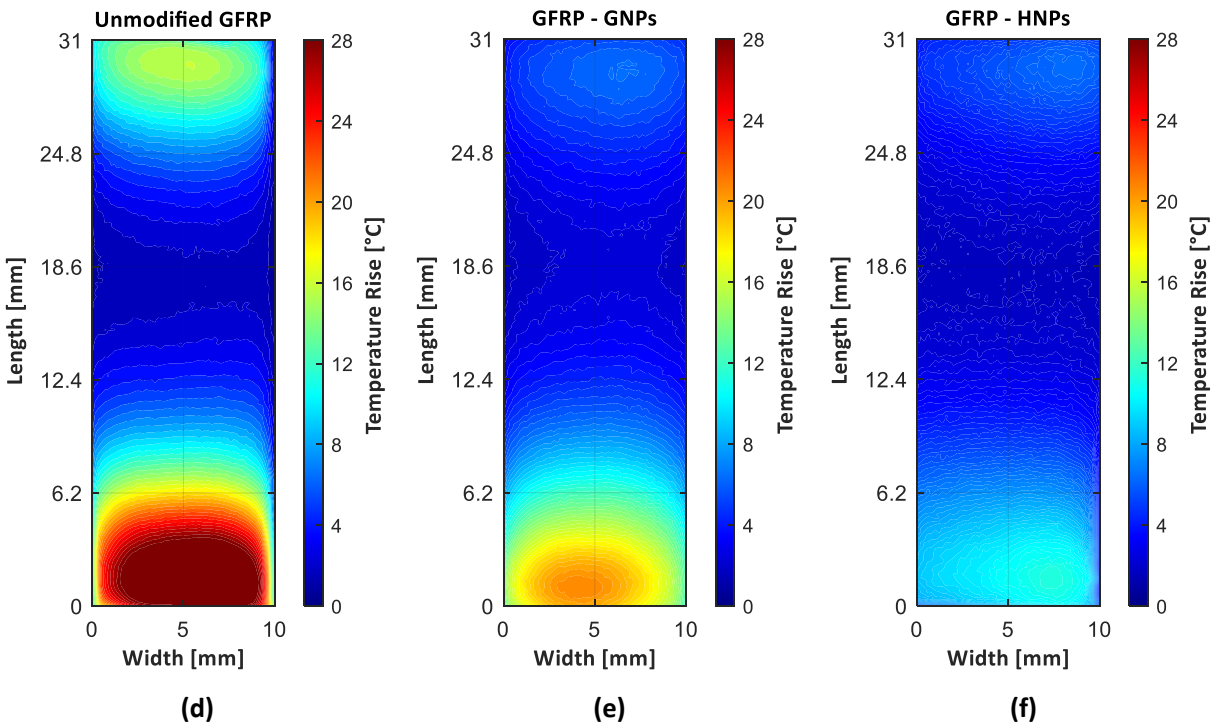

Figure 11. Recorded IR images corresponding to the stress level of 198.69 ± 1.36 MPa, for (a) unmodified GFRP, (b) GFRP-GNPs, and (c) GFRP-HNPs, and the stress level of 219.73 ± 1.00 MPa, for (d) unmodified GFRP, (e) GFRP-GNPs, and (f) GFRP-HNPs.

By controlling and reducing the temperature rise, and consequently limiting the heat dissipation rate, the fatigue lifetime of the tested specimens significantly improved, see Figures 9 and 11. According to Figure 8, under the stress level of 198.7±1.4 MPa, the fatigue life extended from 1×10^4 cycles (for unmodified GFRP) to 9.1×10^3 cycles with the addition of GNPs (approximately 9 times greater), and further to 2.6×10^6 cycles with HNPs (257 times higher). Similarly, under a stress level of 219.7±1.0 MPa, the fatigue life increases from 3.5×10^3 cycles (for unmodified GFRP) to 1.9×10^4 cycles with GNPs (approximately 5-fold increase), and to 2.5×10^5 cycles with HNPs (a 73-fold increase). These findings highlight the beneficial role of adding nanocarbon allotropes, particularly the hybridization of GNPs and CNFs, in enhancing the thermomechanical fatigue performance of modified GFRP composites. The combination of CNFs with GNPs improves the distribution and contact networks between the epoxy chains and glass fibers. This hybridization reduces filler agglomeration and establishes interconnected thermal conduction pathways, facilitating effective heat transfer. This, in turn, minimizes localized heating (see Figure 11) due to a reduced mismatch in the coefficient of thermal expansion (CTE) between

the fibers and the polymer matrix [28]. As a result, the rate of heat accumulation in fatigue-loaded HNPs-GFRP specimens is minimized (see Figure 8), preserving the mechanical fatigue process. The mitigation of the thermal response directly contributed to the substantial improvement in fatigue lifetime, highlighting the potential of these materials for advanced structural applications. Additionally, the incorporation of nanofillers increases the stiffness of the composite, which delays the initiation and growth of cracks, essential for prolonging the fatigue lifespan of the GFRP-HNPs composite.

To compare the results from the $\Delta T - \sigma$ and $\dot{q} - \sigma$ approaches using both MCR- and MDP-based procedures in Sections 3.3 and 3.4, with the reference values derived from the standard $S - N$ curve, the derived fatigue strengths from the thermographic approaches for each composite material type are compared with values derived from the $S - N$ curves at 10^6 cycles.

For GFRP, the $S - N$ curve predicted the fatigue strength value of 177.9 MPa. In comparison, the MCR- and MPD-based $\Delta T - \sigma$ approaches estimated it to be 66.5 MPa and 123.5 MPa, resulting in remarkably lower fatigue strength values than the reference value derived from the $S - N$ curve, by approximately 62.6% and 30.6%, respectively. Nevertheless, the MCR-and MPD-based $\dot{q} - \sigma$ approaches predicted 114.4 MPa and 140.3 MPa. These values are relatively higher than the values extracted from $\Delta T - \sigma$, but still lower than the value derived from the $S - N$ curve, with deviations of 35.7% and 21.1%, respectively. For GFRP-GNPs, the fatigue strength predicted by the $S - N$ curve is 157.5 MPa. The $\Delta T - \sigma$ approach estimated 111.8 MPa and 126.1 MPa using the MCR and MPD procedures, respectively, yielding values approximately 29.0% and 20.0% lower than the $S - N$ reference value. Similarly, the MCR-and MPD-based $\dot{q} - \sigma$ methods predicted 109 MPa and 125.9 MPa, which correspond to deviations of 30.8% and 20.0% from the $S - N$ prediction. In the case of GFRP-HNPs, the $S - N$ curve predicted a fatigue strength of 206.5 MPa. Comparatively, the MCR-and MPD-based $\Delta T - \sigma$ approaches predicted fatigue strength values of 159 MPa and 195.3 MPa, which are respectively 23.0% and 5.4% lower than the reference value obtained from the $S - N$ curve. Similarly, the MCR-and MPD-based $\dot{q} - \sigma$ approaches estimated slightly higher values of 162.6 MPa and 196.9 MPa compared to the $\Delta T - \sigma$, yet below the reference value derived from the $S - N$ curve by 21.2% and 4.6%, respectively.

In summary, while both $\dot{q} - \sigma$ and $\Delta T - \sigma$ methods provided reasonable estimations of fatigue strength, incorporating the MPD procedure generally yielded predictions closer to the $S - N$ curve than the MCR procedure for all three types of composite materials. Additionally, the $\dot{q} - \sigma$ approach aligns more closely with the $S - N$ curve predictions compared to the $\Delta T - \sigma$ method, especially for GFRP, reflecting its superior reliability in estimating fatigue strength. This highlights that incorporating heat

dissipation rate as a predictive parameter provides a more accurate representation of the fatigue behavior of composites. Therefore, implementing the $\dot{q} - \sigma$ method and MPD-based analysis stand out as reliable tools for evaluating fatigue strength of polymeric composite materials.

4. Final remarks and conclusions

This study presented a comprehensive analysis of fatigue strength prediction methodologies for GFRP, GFRP-GNP, and GFRP-HNP composites, using the thermographic approaches (i.e., $\Delta T - \sigma$ and $\dot{q} - \sigma$). To achieve this, exponential regressions were employed to reliably model the thermal responses under various applied stress levels. The minimum curvature radius (MCR) and maximum perpendicular distance (MPD) procedures were individually incorporated into the $\Delta T - \sigma$ and $\dot{q} - \sigma$ methods to determine the fatigue strengths of three types of composite materials. The analysis illustrated notable differences in predictive accuracy using MCR and MPD procedures. Compared to the MCR-based thermographic methods, the MPD-based thermographic approaches yielded higher strength predictions, aligning more closely with the standard $S - N$ curves derived from constant amplitude fatigue test. The results show that the MPD-based $\dot{q} - \sigma$ approach provided relatively accurate fatigue strength estimations, particularly for GFRP when compared to the results from $S - N$ curves. These findings highlight that incorporating MPD-based analysis into the $\dot{q} - \sigma$ approach offers a reliable methodology for assessing the fatigue strength of polymeric composite materials.

Furthermore, an uncertainty analysis of fatigue strength values derived from the thermography-based methods was conducted using Monte Carlo simulation to quantify variability. The results indicated that the variability introduced by different approaches in fatigue strength estimation is comparable and had a limited range, with slightly higher uncertainty observed in the $\dot{q} - \sigma$ based methods. However, the mutual differences in uncertainty levels and coverage intervals between the corresponding methods do not impact the overall conclusion that the MPD-based $\dot{q} - \sigma$ approach provides relatively more accurate estimations.

As can be extracted from the standard $S - N$ curve illustrated in Figure 9, while the addition of GNPs to GFRP led to beneficial effects in low-cycle fatigue, it adversely affects high-cycle fatigue behavior. In contrast, the hybridization of GNPs and CNFs significantly enhanced the fatigue performance of modified GFRP composite across both low- and high-cycle- fatigue regimes due to the positive synergistic effects of hybrid nanofillers in mitigating localized self-heating heating, thereby prolonging the fatigue life of tested GFRP modified with HNPs.

Thermal imaging analysis illustrated that the inclusion of nanofillers effectively controlled the thermal response of the modified composites during fatigue loading. While the inclusion of GNPs reduced the localized temperature rise, especially in critical regions, the addition of hybrid nanofillers (GNPs + CNFs in a 1:1 ratio) achieved a more uniform and substantial temperature reduction across the entire surface. The mitigation of the thermal response directly contributed to the substantial improvement in fatigue lifetime. For example, under a stress level of 198.7±1.4 MPa, the addition of GNPs significantly enhanced the fatigue lifetime of GFRP specimens, increasing it from 1×10^4 cycles to 9.1×10^4 cycles—an approximately 9-fold improvement. This demonstrates the effectiveness of GNPs in reducing self-heating and delaying fatigue degradation in the low-cycle regime. On the other hand, the incorporation of HNPs resulted in an even more pronounced improvement, extending the fatigue lifetime to 2.56×10^6 cycles— by over 250 times increase compared to unmodified GFRP. These findings, supported by microscopic observations, highlight the potential of carbon allotropes, particularly hybrid GNPs-CNFs, in limiting in mitigating thermally induced crack initiation and propagation, thereby significantly extending the fatigue lifespan of the modified composites. The DSC analysis supported these findings, with HNPs achieving the highest glass transition temperature (T_g).

Compared to GFRP, GFRP-GNPs showed better fatigue performance only in the low cycle number regime, and their performance deteriorated significantly when the cycle number exceeded 2.1×10^4. The lower T_g value of GFRP-GNPs than that of GFRP suggests that GNPs provided a reinforcing effect in the early stages of fatigue testing. When the cycle number exceeded 2.1×10^4, the segmental mobility in the epoxy matrix probably increased, which resulted in the worsening of the fatigue behavior in the high cycle number regime. On the contrary, GFRP-HNPs showed better fatigue performance across the entire range of fatigue regimes tested, in comparison to both GFRP and GFRP-GNPs. This observation allows to conclude that hybridization of GNPs and CNFs decreases mobility of the epoxy polymer network chains resulting in the excellent fatigue performance of a GFRP-HNPs composite, as evidenced by the highest T_g among all composites studied.

The results of DSC tests also demonstrated that more heat has been released during the post-curing reaction of GFRP-GNPs and GFRP-HNPs composites, compared to GFRP composite. This observation can be attributed to a decrease in the cross-link density in the epoxy matrix. The results from the fatigue behavior tests suggest that the decreased cross-link density did not have a negative effect on the fatigue performance, throughout the entire fatigue cycle of GFRP-HNPs composites, and at early stages of

fatigue tests of GFRP-GNPs composites. However, the presence of GNPs deteriorated the fatigue behavior of the composite in the high-cycle regime.

Overall, the $\dot{q} - \sigma$ method proves to be a promising tool for estimating fatigue strength and capturing the thermomechanical behavior of PMCs modified with nanoparticles, offering greater reliability than $\Delta T - \sigma$ approach. The implementation of hybrid nanoparticles offers a superior strategy for enhancing fatigue strength, making them suitable for applications requiring long-term durability under cyclic loading. Therefore, optimal material selection and reinforcement strategies are crucial for improving the fatigue performance of composite materials under different loading conditions.

CRediT authorship contribution statement

Jafar Amraei: Conceptualization, Methodology, Investigation, Data curation, Validation, Formal analysis, Software, Writing-original draft preparation, Writing-review and editing. **Tomasz Rogala**: Conceptualization, Methodology, Data curation, Formal analysis, Software, Writing-original draft preparation, Writing-review and editing. **Andrzej Katunin**: Conceptualization, Methodology, Formal analysis, Writing-original draft preparation, Writing-review and editing. **Izabela Barszczewska-Rybarek:** Investigation, Formal analysis, Writing-original draft preparation, Writing-review and editing. **João M. Parente:** Resources**,** Writing-review and editing. **Paulo N. B. Reis:** Conceptualization, Methodology, Investigation, Formal analysis, Writing-original draft preparation, Writing-review and editing, Project administration, Funding acquisition.

Acknowledgments

The last author would like to acknowledge the grant BPN/ULM/2023/1/00119/U/00001 awarded to him by NAWA - Narodowa Agencja Wymiany Akademickiej. This research was also sponsored by national funds through FCT – Fundação para a Ciência e a Tecnologia, under projects UID/00285/2020 - Centre for Mechanical Engineering, Materials and Processes and LA/P/0112/2020. João M. Parente thanks FCT—Fundação para a Ciência e a Tecnologia for the grant UI/BD/151477/2021 (DOI: 10.54499/UI/BD/151477/2021). Finally, the authors would also like to thank Graphenest for kindly supplying the graphene used in this study.

References

[1] K.S. Boparai, R. Singh and M. Hashmi, *Reinforced non-conventional material composites: A comprehensive review.* Advances in Materials and Processing Technologies, 2021. **7**(2): p. 333-342.

[2] R.F. Gibson, *A review of recent research on mechanics of multifunctional composite materials and structures.* Composite structures, 2010. **92**(12): p. 2793-2810.

[3] J.-J. Luo and I.M. Daniel, *Characterization and modeling of mechanical behavior of polymer/clay nanocomposites.* Composites science and technology, 2003. **63**(11): p. 1607-1616.

[4] E.P. Giannelis, *Polymer layered silicate nanocomposites.* Advanced materials, 1996. **8**(1): p. 29-35.

[5] S. Saber-Samandari, A.A. Khatibi and D. Basic, *An experimental study on clay/epoxy nanocomposites produced in a centrifuge.* Composites Part B: Engineering, 2007. **38**(1): p. 102-107.

[6] M. Zamanian, M. Mortezaei, B. Salehnia and J. Jam, *Fracture toughness of epoxy polymer modified with nanosilica particles: Particle size effect.* Engineering Fracture Mechanics, 2013. **97**: p. 193-206.

[7] B. Soltannia, K. Duke, F. Taheri and P. Mertiny, *Quantification of the effects of strain rate and nano-reinforcement on the performance of adhesively bonded single-lap joints.* Reviews of Adhesion and Adhesives, 2019. **7**(1).

[8] J.M. Parente, R. Simoes, A.P. Silva and P.N. Reis, *Impact of the Curing Temperature on the Manufacturing Process of Multi-Nanoparticle-Reinforced Epoxy Matrix Composites.* Materials, 2024. **17**(8): p. 1930.

[9] J. Jam and M. Ahangari, *Effect of carbon nanotubes on the rheological and electrical percolation of PP/EPDM blend.* Polymer-Plastics Technology and Engineering, 2012. **51**(14): p. 1474-1482.

[10] P. Zamani, L.F. da Silva, R.M. Nejad, D.G. Moghaddam and B. Soltannia, *Experimental study on mixing ratio effect of hybrid graphene nanoplatelet/nano-silica reinforcement on the static and fatigue life of aluminum-to-GFRP bonded joints under four-point bending.* Composite Structures, 2022. **300**: p. 116108.

[11] P. Santos, A.P. Silva and P.N. Reis, *The Effect of Carbon Nanofibers on the Mechanical Performance of Epoxy-Based Composites: A Review.* Polymers, 2024. **16**(15): p. 2152.

[12] P. Santos, A. Silva and P. Reis, *Effect of Carbon Nanofibers on the Strain Rate and Interlaminar Shear Strength of Carbon/Epoxy Composites. Materials 2023, 16, 4332*. 2023.

[13] A. Jafarpour, M.S. Farahani and M. Haghighi-Yazdi, *Numerical investigation of oriented CNFs effects on thermo-mechanical properties and curing residual stresses field of polymeric nanocomposites.* Mechanics of Materials, 2019. **138**: p. 103176.

[14] L. Böger, J. Sumfleth, H. Hedemann and K. Schulte, *Improvement of fatigue life by incorporation of nanoparticles in glass fibre reinforced epoxy.* Composites Part A: Applied Science and Manufacturing, 2010. **41**(10): p. 1419-1424.

[15] F. Li, Y. Hua, C.-B. Qu, H.-M. Xiao and S.-Y. Fu, *Greatly enhanced cryogenic mechanical properties of short carbon fiber/polyethersulfone composites by graphene oxide coating.* Composites Part A: Applied Science and Manufacturing, 2016. **89**: p. 47-55.

[16] D.G. Papageorgiou, M. Liu, Z. Li, C. Vallés, R.J. Young and I.A. Kinloch, *Hybrid poly (ether ether ketone) composites reinforced with a combination of carbon fibres and graphene nanoplatelets.* Composites Science and Technology, 2019. **175**: p. 60-68.

[17] L. Yue, G. Pircheraghi, S.A. Monemian and I. Manas-Zloczower, *Epoxy composites with carbon nanotubes and graphene nanoplatelets–Dispersion and synergy effects.* Carbon, 2014. **78**: p. 268-278.
[18] G. Voudouris, D. Di Maio and I.A. Sever, *Experimental fatigue behaviour of CFRP composites under vibration and thermal loading.* International Journal of Fatigue, 2020. **140**: p. 105791.
[19] D. Di Maio, G. Voudouris and I. Sever, *Investigation of fatigue damage growth and self-heating behaviour of cross-ply laminates using simulation-driven dynamic test.* International Journal of Fatigue, 2022. **155**: p. 106617.
[20] F. Magi, D. Di Maio and I. Sever, *Damage initiation and structural degradation through resonance vibration: Application to composite laminates in fatigue.* Composites Science and Technology, 2016. **132**: p. 47-56.
[21] D. Zorko, J. Tavčar, M. Bizjak, R. Šturm and Z. Bergant, *High cycle fatigue behaviour of autoclave-cured woven carbon fibre-reinforced polymer composite gears.* Polymer Testing, 2021. **102**: p. 107339.
[22] R. Talreja, *Damage and fatigue in composites–a personal account.* Composites Science and Technology, 2008. **68**(13): p. 2585-2591.
[23] A. Katunin, D. Wachla, P. Santos and P.N. Reis, *Fatigue life assessment of hybrid bio-composites based on self-heating temperature.* Composite Structures, 2023. **304**: p. 116456.
[24] Y.-M. Jen and W.-L. Ni, *Effect of dispersing multiwalled carbon nanotubes and graphene nanoplatelets hybrids in the matrix on the flexural fatigue properties of carbon/epoxy composites.* Polymers, 2022. **14**(5): p. 918.
[25] A.P. Vassilopoulos, *The history of fiber-reinforced polymer composite laminate fatigue.* International Journal of Fatigue, 2020. **134**: p. 105512.
[26] J. Amraei, T. Rogala, A. Katunin, A. Premanand, G. Kokot, D. Wachla, W. Kuś, M. Bilewicz, B. Khatri and F. Balle, *Thermomechanical fatigue behavior of CF/PEKK composite under low and ultrasonic frequencies.* Composites Part B: Engineering, 2024. **281**: p. 111539.
[27] P. Shabani, F. Taheri-Behrooz, S.S. Samareh-Mousavi and M.M. Shokrieh, *Very high cycle and gigacycle fatigue of fiber-reinforced composites: A review on experimental approaches and fatigue damage mechanisms.* Progress in Materials Science, 2021. **118**: p. 100762.
[28] J. Amraei and A. Katunin, *Recent advances in limiting fatigue damage accumulation induced by self-heating in polymer–matrix composites.* Polymers, 2022. **14**(24): p. 5384.
[29] J. Amraei, A. Katunin and M. Lipińska, *Numerical simulation and experimental validation of self-heating of polymer-matrix composites during low-cycle fatigue loading.* International Journal of Fatigue, 2024. **188**: p. 108510.
[30] J. Huang, C. Garnier, M.-L. Pastor and X. Gong, *Investigation of self-heating and life prediction in CFRP laminates under cyclic shear loading condition based on the infrared thermographic data.* Engineering Fracture Mechanics, 2020. **229**: p. 106971.
[31] J. Amraei, A. Katunin, D. Wachla and K. Lis, *Damage assessment in composite plates using extended non-destructive self-heating based vibrothermography technique.* Measurement, 2025. **241**: p. 115670.
[32] A. Katunin and A. Wronkowicz, *Characterization of failure mechanisms of composite structures subjected to fatigue dominated by the self-heating effect.* Composite Structures, 2017. **180**: p. 1-8.
[33] R. Turczyn, K. Krukiewicz and A. Katunin, *Spectroscopic evaluation of structural changes in composite materials subjected to self-heating effect.* Composite Structures, 2018. **204**: p. 192-197.

[34] M.P. Luong, *Fatigue limit evaluation of metals using an infrared thermographic technique*. Mechanics of materials, 1998. **28**(1-4): p. 155-163.
[35] G. La Rosa and A. Risitano, *Thermographic methodology for rapid determination of the fatigue limit of materials and mechanical components.* International journal of fatigue, 2000. **22**(1): p. 65-73.
[36] C. Colombo and L. Vergani, *Influence of delamination on fatigue properties of a fibreglass composite.* Composite Structures, 2014. **107**: p. 325-333.
[37] C. Colombo, T. Bhujangrao, F. Libonati and L. Vergani, *Effect of delamination on the fatigue life of GFRP: A thermographic and numerical study.* Composite Structures, 2019. **218**: p. 152-161.
[38] R. De Finis, D. Palumbo and U. Galietti, *Evaluation of damage in composites by using thermoelastic stress analysis: A promising technique to assess the stiffness degradation.* Fatigue & Fracture of Engineering Materials & Structures, 2020. **43**(9): p. 2085-2100.
[39] D. Palumbo, R. De Finis, P.G. Demelio and U. Galietti, *A new rapid thermographic method to assess the fatigue limit in GFRP composites.* Composites Part B: Engineering, 2016. **103**: p. 60-67.
[40] A. Katunin, I. Pivdiablyk, L. Gornet and P. Rozycki, *A hybrid method for determination of fatigue limit and non-destructive evaluation of composite structures after low-velocity impact loading.* Composites Part B: Engineering, 2022. **238**: p. 109898.
[41] L. Dolbachian, W. Harizi, I. Gnaba and Z. Aboura, *Rapid fatigue limit estimation of smart polymer–matrix composite under self-heating bending tests using an innovative automatic approach: Knee method.* International Journal of Fatigue, 2024: p. 108684.
[42] J. Huang, M.-L. Pastor, C. Garnier and X. Gong, *Rapid evaluation of fatigue limit on thermographic data analysis.* International Journal of Fatigue, 2017. **104**: p. 293-301.
[43] P. Reis, A. Katunin and J. Amraei, Critical Analysis of the Systems Used to Reduce Self-Heating in Polymer Composites Subjected to Very High Cycle Fatigue Regimes. Fatigue & Fracture of Engineering Materials & Structures, 2025. In press. https://doi.org/10.1111/ffe.14561
[44] S.N. Leung, Thermally conductive polymer composites and nanocomposites: Processing-structure-property relationships. Composites Part B: Engineering, 2018. 150: p. 78-92.
[45] J. Ferreira, J. Costa, P. Reis and M. Richardson, *Analysis of fatigue and damage in glass-fibre-reinforced polypropylene composite materials.* Composites science and technology, 1999. **59**(10): p. 1461-1467.
[46] L. Maragoni, G. Modenato, N. De Rossi, L. Vescovi and M. Quaresimin, *Effect of fibre waviness on the compressive fatigue behavior of woven carbon/epoxy laminates.* Composites Part B: Engineering, 2020. **199**: p. 108282.
[47] J. Huang, L. Guo, L. Chen, Z.-X. Wang and J. Li, *Damage evolution of 3D woven carbon/epoxy composites under the tension–compression fatigue loading based on multi damage information.* International Journal of Fatigue, 2022. **154**: p. 106566.
[48] A. Premanand, T. Rogala, D. Wachla, J. Amraei, A. Katunin, B. Khatri, M. Rienks and F. Balle, *Fatigue strength estimation of a CF/PEKK composite through self-heating temperature analysis using cyclic bending tests at 20 kHz.* Composites Science and Technology, 2023. **243**: p. 110218.
[49] M. Shokrieh, M. Esmkhani, A. Haghighatkhah and Z. Zhao, *Flexural fatigue behavior of synthesized graphene/carbon-nanofiber/epoxy hybrid nanocomposites.* Materials & Design (1980-2015), 2014. **62**: p. 401-408.
[50] S. Chatterjee, F. Nafezarefi, N. Tai, L. Schlagenhauf, F. Nüesch and B. Chu, *Size and synergy effects of nanofiller hybrids including graphene nanoplatelets and carbon nanotubes in mechanical properties of epoxy composites.* Carbon, 2012. **50**(15): p. 5380-5386.

[51] G. Kalogiannakis, D. Van Hemelrijck and G. Van Assche, *Measurements of thermal properties of carbon/epoxy and glass/epoxy using modulated temperature differential scanning calorimetry.* Journal of composite materials, 2004. **38**(2): p. 163-175.
[52] T. Varol and A. Canakci, *The effect of type and ratio of reinforcement on the synthesis and characterization Cu-based nanocomposites by flake powder metallurgy.* Journal of Alloys and Compounds, 2015. **649**: p. 1066-1074.
[53] M. Shokrieh, A. Daneshvar, S. Akbari and M. Chitsazzadeh, *The use of carbon nanofibers for thermal residual stress reduction in carbon fiber/epoxy laminated composites.* Carbon, 2013. **59**: p. 255-263.
[54] S.A. Zonouzi and S.A. Bonab, *Improvement of the performance of thermal energy storage systems with conical annular enclosure using magnetic field.* Applied Thermal Engineering, 2024. **245**: p. 122906.
[55] S. Wang, Y.H. Ng, K.H. Tan and A. Dasari, *Thermal properties of carbon nanofibers enhanced lightweight cementitious composite under high temperature.* Construction and Building Materials, 2021. **307**: p. 124358.
[56] G. Meneghetti and M. Quaresimin, *Fatigue strength assessment of a short fiber composite based on the specific heat dissipation.* Composites Part B: Engineering, 2011. **42**(2): p. 217-225.
[57] BIPM, IEC, IFCC, ILAC, ISO, IUPAC, IUPAP, and OIML. *Guide to the expression of uncertainty in measurement — Part 1: Introduction.* Joint Committee for Guides in Metrology, JCGM-GUM-1:2023. URL: https://www.bipm.org/documents/20126/2071204/JCGM_GUM-1.pdf [accessed 14 February 2025].
[58] BIPM, IEC, IFCC, ILAC, ISO, IUPAC, IUPAP, and OIML. *Evaluation of measurement data — Guide to the expression of uncertainty in measurement.* Joint Committee for Guides in Metrology, JCGM-100:2008. URL: https://www.bipm.org/documents/20126/2071204/JCGM_GUM-1.pdf [accessed 14 February 2025].
[59] BIPM, IEC, IFCC, ILAC, ISO, IUPAC, IUPAP, and OIML. *Evaluation of measurement data — Supplement 1 to the "Guide to the expression of uncertainty in measurement" — Propagation of distributions using a Monte Carlo method.* Joint Committee for Guides in Metrology, JCGM-101:2008. URL: https://www.bipm.org/documents/20126/2071204/JCGM_101_2008_E.pdf, [accessed 14 February 2025].
[60] J. Watanabe, F. Tanaka, R. Higuchi, H. Matsutani, H. Okuda and T. Okabe, A study of stress concentrations around fiber breaks in unidirectional CF/epoxy composites using double-fiber fragmentation tests. Advanced Composite Materials, 2018. 27(6): p. 575-587.
[61] M. Ali Charfi, R. Mathieu, J.-F. Chatelain, C. Ouellet-Plamondon and G. Lebrun, Effect of graphene additive on flexural and interlaminar shear strength properties of carbon fiber-reinforced polymer composite. Journal of Composites Science, 2020. 4(4): p. 162.
[62] X. Zhang, X. Fan, C. Yan, H. Li, Y. Zhu, X. Li and L. Yu, Interfacial microstructure and properties of carbon fiber composites modified with graphene oxide. ACS applied materials & interfaces, 2012. 4(3): p. 1543-1552.
[63] A. Sayam, A.M. Rahman, M.S. Rahman, S.A. Smriti, F. Ahmed, M.F. Rabbi, M. Hossain and M.O. Faruque, A review on carbon fiber-reinforced hierarchical composites: mechanical performance, manufacturing process, structural applications and allied challenges. Carbon Letters, 2022. 32(5): p. 1173-1205.
[64] J. Parente, A. Silva and P. Reis, The influence of carbon and glass fiber hybridization combined with a graphene-enhanced epoxy matrix on bending fatigue response. International Journal of Fatigue, 2025. 193: p. 108782.

[65] S. Chatterjee, F. Nafezarefi, N. Tai, L. Schlagenhauf, F. Nüesch and B. Chu, Size and synergy effects of nanofiller hybrids including graphene nanoplatelets and carbon nanotubes in mechanical properties of epoxy composites. Carbon, 2012. 50(15): p. 5380-5386.
[66] O. Shishkina, V. Romanov, Y. Abdin, S.V. Lomov and L. Gorbatikh, Stress distribution around a broken carbon fibre and how it is affected by carbon nanotubes in the interface region. Composite Interfaces, 2019. 26(6): p. 507-524.

Paper VIII

Damage assessment in composite plates using extended non-destructive self-heating based vibrothermography technique

Measurement 241 (2025) 115670

Contents lists available at ScienceDirect

Measurement

journal homepage: www.elsevier.com/locate/measurement

Damage assessment in composite plates using extended non-destructive self-heating based vibrothermography technique

Jafar Amraei [a,*], Andrzej Katunin [a], Dominik Wachla [a], Krzysztof Lis [b]

[a] Department of Fundamentals of Machinery Design, Faculty of Mechanical Engineering, Silesian University of Technology, Konarskiego 18A, 44-100 Gliwice, Poland
[b] Department of Machine Technology, Faculty of Mechanical Engineering, Silesian University of Technology, Konarskiego 18A, 44-100 Gliwice, Poland

ARTICLE INFO

Keywords:
Self-heating based vibrothermography
Non-destructive testing
Resonant vibration
Damage quantification
Image processing

ABSTRACT

Self-heating based vibrothermography (SHVT) is a promising non-destructive technique for inspecting polymer-matrix composites (PMCs) in circumstances with limited external heating feasibility, functioning under the resonant frequency excitation. This study broadened the applicability of SHVT technique for two-dimensional (2D) PMCs by examining its sensitivity and effectiveness in detecting and quantifying damage within 2D laminated composites across nine different scenarios. A two-step algorithm based on the concepts of the boundary of effective thermograms, and the maximal temperature ratio was proposed to methodically choose the optimal raw thermogram from a large set of registered thermograms for each scenario. The issues linked to blurred damage signatures in the raw infrared (IR) images adversely affected the overall sensitivity and accuracy of SHVT. Implementing the algorithm based on central moments improved the overall damage detectability using this technique. Additionally, the introduced hit/miss metric enabled the damage identification and quantification for all scenarios.

1. Introduction

The increasing utilization of polymer matrix composites (PMCs) in the mobility field (e.g., aerospace, aircraft, automotive, and naval industries) can be attributed to their superior strength- and stiffness-to-weight ratios, excellent durability, good environmental resistance and design flexibility [1,2]. Maintaining PMC structures throughout their lifespan is essential. Periodically inspecting PMCs using non-destructive testing (NDT) methods is paramount. Among the developed NDT techniques [3–6], infrared thermography (IRT) distinguishes itself owing to its capacity for rapid and uncomplicated inspection of PMCs and its effectiveness in detecting diverse forms of external and internal damage [7–10]. Thermographic testing includes a two-step process [11]. A tested structure is first subjected to thermal excitation, typically achieved using high-power halogen flash lamps, optical heaters, lasers, or similar heat sources. Following this excitation, the thermal response of the structure is registered and evaluated using an infrared (IR) camera [12,13]. Numerous techniques fall under the umbrella of IRT, which can broadly be categorized as either active or passive [3,14–16]. Active IRT methods function in the presence of an external heating source to stimulate the tested structure and register thermal data disruptions using the IR camera. Nonetheless, passive ones concentrate on examining the energy dissipation from the specimen, primarily aiming to detect and localize damage within the tested specimens [3,14,15]. Various IRT techniques applicable to PMCs have been presented in detail in [6,16]. Among them, Pulsed Thermography (PT) employs short heating pulses, while Step-Heating Thermography (SHT) implements longer ones for excitation. By contrast, Lock-in Thermography (LIT) uses a sinusoidal heating wave with frequency modulation, providing enhanced subsurface damage sensitivity in comparison to pulse IRT techniques [17]. Vibrothermography (VT) implements a unique excitation mechanism, relying on the energy dissipation process to detect and identify the damage. A mechanical elastic wave propagates through the tested PMC, dissipating energy at the damaged locations, leading to localized heating registered by an IR camera. This wave typically falls within the sonic and ultrasonic frequency range [18–21], with energy dissipation arising from frictional interactions occurring at defect interfaces or stress in the vicinity of the defect sites, see [20,22,23] for further information.

VT excels in identifying complex defects and crack types by inducing heat and addressing challenges often encountered by alternative NDT techniques. VT has been successfully applied for inspecting the diverse categories of defects and cracks in PMCs, consisting of debonds [10],

* Corresponding author.
E-mail address: jafar.amraei@polsl.pl (J. Amraei).

https://doi.org/10.1016/j.measurement.2024.115670
Received 28 May 2024; Received in revised form 14 August 2024; Accepted 3 September 2024
Available online 6 September 2024

Nomenclature

E_x, E_y, E_z	Young's moduli
G_{xy}, G_{yz}, G_{xz}	Shear moduli
ν_{xy}, ν_{yz}, ν_{xz}	Poisson's ratio
ρ	Density
V_c	Cutting speed
f	Feed rate
L	Length
W	Width
e	Base of the natural logarithm
T_s	Stabilized self-heating temperature
T_{max}	Maximum value of registered self-heating temperature
T_{min}	Minimum value of registered self-heating temperature
$\overline{T}_{ratio}^{max}$	Maximal value of temperature ratio
$\overline{T}_{ratio}$	Temperature ratio per thermogram
$\overline{T}_{FBD}$	Mean value of temperature of the damage region per thermogram
$\overline{T}_{FBD}^{min}$	Minimal value of the mean temperature of the damage per thermogram
$\overline{T}_{P-FBD}$	Mean value of temperature obtained by subtracting the plate area from the damage region per thermogram
$\overline{T}_{P-FBD}^{min}$	Minimal value of mean temperature obtained by subtracting the plate area from the damage area among all thermograms
A_t	True area of damage
A_i	Identified area of damage
A_R	Ratio between the areas identified and true damage regions
A_{hit}	Identified damage coincided with the true damage location
A_{miss}	Non-coinciding area with true damage location

closed cracks [24], and vertical open cracks oriented orthogonally to the inspected surface [25], surface-breaking and fatigue-induced cracks [26–29], delamination [30], impact damage [31], corrosion [32] and other [33]. In certain situations, where the application of external excitation sources is unfeasible, e.g., single-sided access or limited accessibility to specific regions of the inspected specimen [34], the non-destructive self-heating based vibrothermography (SHVT) technique can alternatively be implemented [35]. In SHVT, the process is driven by the self-heating phenomenon, termed as a temperature increase, induced by resonant excitation within tested PMCs. This phenomenon stems from the phase lag between the applied stress and the strain amplitude response, due to the viscoelasticity of PMCs [36], or vice versa, occurring during mechanical vibrations [37,38]. The authors of [5,28,39,40], excited the PMC specimen at resonant frequencies for crack localization and crack propagation monitoring and were likewise employed by the authors of [41]. Their study involved the application of absorptive viscoelastic coatings on metallic test specimens, enabling the observation of the self-heating at the ultrasonic frequency range. SHVT technique was successfully implemented in the inspection of PMC elements with numerous defect types, consisting of simulated cracks, flat bottom holes [15], and low-velocity impact damage (LVID) [42]. In another study, Katunin et al. [7] presented a hybrid technique, similar to the concept of SHVT. This technique combined the advantages of a rapid thermographic approach introduced for determining the fatigue limit of impact-damaged PMCs, alongside non-destructively assessing the extent of impact damage. The X-ray computed tomography NDT was carried out to confirm the existence of internal damage and identify its geometric properties within the tested specimens. The detectability thresholds were defined for the hybrid method to indicate the stress levels required for identifying LVID across various impact energies. The findings demonstrated that LVID is detectable during fatigue limit tests, even at the earliest stages of visibility. Moreover, the rise in self-heating temperature required for detection measured below the threshold that would cause damage.

Further enhancements in LVID detectability can be achieved via image processing techniques applied to thermograms. Heat transfer processes, especially thermal diffusion between damaged zones and their surroundings, can negatively influence the SHVT inspections. Such diffusion frequently leads to obscured or concealed damage indications in thermograms, lowering the sensitivity and complicating the damage identification. To overcome these challenges and improve the sensitivity of SHVT technique to various damage types, it is of primary significance to apply additional processing on the raw thermograms [34].

Recent advancements have led to the development of diverse image post-processing methodologies aimed at enhancing defect detection capabilities [10,43–57]. These techniques have evolved from initial endeavors focused on noise reduction to more sophisticated methods. For example, Thermographic Signal Reconstruction (TSR) introduced by Shepard et al. [43] offered the potential to make IR results comparable with other high-resolution and high-sensitivity NDT methods [34]. Additionally, *k*-space filtering [44], Differential Absolute Contrast (DAC) [53,54], and Principal Component Thermography (PCT) [55,56] enhanced the inspection of damage in laminated composites, including barely visible impact damage (BVID) [44,57]. In this context, Wei et al. [10] employed VT to detect debonding defects in Thermal Barrier Coatings (TBCs). Utilizing thermal image sequences and algorithms such as TSR, Principal Component Analysis (PCA), and Fast Fourier Transform (FFT), it was possible to extract defect-related information successfully. According to their findings, among the post-processing algorithms, the primary component within the PCA showed the most pronounced temperature contrast and Signal-to-Noise Ratio (SNR). This allowed the successful detection of the tested structure featuring a 2 mm-diameter debond at a 0.5 mm coating thickness. In addition, Katunin and Wachla [15] evaluated the efficiency of SHVT technique in detecting defects, specifically estimating the depth at which a defect could be detected. For this purpose, a series of specimens with flat-bottomed holes (FBHs) of different depths and shapes were examined. They implemented the thermal gradient technique, as a simple image post-processing algorithm, to improve the raw thermograms. Their findings highlighted the ability of SHVT technique for defect detectability at depths as low as 1.75 mm, corresponding to 60 % of the specimen's thickness. In other words, the defects were less detectable or not as prominently detected beyond this depth. Subsequently, Wronkowicz et al. [34] implemented three sets of post-processing techniques (i.e., algorithms based on statistical features, temperature profile trend estimation, and similarity maps) to enhance the damage detectability of one-dimensional (1D) composite elements. From a qualitative assessment spanning over 30 approaches, nine sensitive post-processing methods were chosen. These methods notably enhanced damage detection compared to analyzing raw thermograms alone, highlighting their essential role in damage identification. Additionally, the authors of [42] evaluated the sensitivity of SHVT technique in identifying and measuring the LVID in 1D composite elements. They showed that SHVT technique is sensitive enough to detect LVID, particularly for impact energy levels below 10 J, which can be addressed to the so-called tool drop impact damage in aircraft ground maintenance practice (see, e.g., [58]). Moreover, applying numerous IR image enhancement techniques remarkably improved the detectability, making the undetectable damage signatures visible in raw IR images. Among 16 tested image post-processing algorithms, root-mean-square (RMS), root-sum-of-squares

(RSS), central moments, principal component thermography (PCT), and partial least-squares regression (PLSR) showed the highest sensitivity and accuracy regarding damage detection and quantification. Nevertheless, despite extensive research efforts, there remains a challenge in achieving a global assessment of sensitivity and accuracy, particularly in the quantification of damage.

Previous research efforts in our group primarily concentrated on 1D composite beams in the context of SHVT. Nevertheless, neither an objective strategy was developed for selecting effective thermograms from a large set of registered images, nor a reliable approach was established for damage quantification in composite elements using the SHVT technique. This study addresses several challenges that distinguish it from prior works. First, the issues related to the sensitivity of SHVT technique to the noise and the stabilization of temperature distribution within thermographic images, which may obscure the damage signatures during inspection, are addressed. For this purpose, a new methodology is established for selecting the clearest thermograms to see structural damage from a large dataset (i.e., several hundred or even thousands of images) captured by an infrared (IR) camera during testing. Additionally, damage detectability is enhanced by implementing a novel image post-processing algorithm to identify the best raw thermogram. Finally, a new metric, termed the hit/miss metric, is introduced, enabling both qualitative and quantitative assessment of damage with high accuracy. This study emphasizes that the discussed advancements in measurements and IR thermogram processing are vital for refining and broadening the SHVT technique's application to damage inspection in 2D laminated composite structures, which are more commonly used than 1D elements. These advancements open up new possibilities for inspecting polymeric composite structures with a potential application in inspections of aircraft structures with single-sided access.

2. Specimens, numerical simulations, and experiments

2.1. Specimen preparation

Specimens used in this study were prepared by cutting them from sheets with thicknesses of 0.5 mm, 0.75 mm, and 1 mm to the dimensions of 240 mm × 240 mm. These sheets were made of E-glass-fabric-reinforced epoxy composite with an areal density of 200 g/m^2, featuring 3, 5, and 6 layers, respectively, and were manufactured by Izo-Erg S.A. in Gliwice, Poland. The material properties of the specimens are presented in Table 1.

Nine specimens were considered in the study, which consisted of flat bottom damage (FBD) extruded to the depths of 10 %, 25 %, and 50 % of the total thickness of the specimens (see Table 2). FBD depths were precisely extruded using a 3-axis CNC milling machine equipped with a high-speed spindle (24 krpm) and positioning accuracy of 0.01 mm, according to the scheme shown in Fig. 1.

Depending on the FBD depth, milling was carried out in three stages:

Implementing a Vollhartmetall (VHM)-type solid carbide cutter with a 4 mm diameter and 2 teeth, a coarse milling process was executed, leaving a 0.05 mm allowance at the FBD base. The process employed a spiral FBD selection strategy with 10 % coverage of the previously milled path, operating at a cutting speed (V_c) of 110 m/min (8750 rpm) and a feed rate (f) of 0.03 mm/tooth (525 mm/min), ensuring a depth of approximately 0.3 mm per pass.

Finishing milling was conducted with the following parameters: a cutting speed of 110 m/min (8750 rpm) and a feed rate of 0.01 mm/tooth (175 mm/min). A spiral FBD selection strategy was applied, covering 10 % of the previously milled path.

Finishing milling of the FBD corners (with a radius of 0.5 mm) using a VHM-type solid carbide cutter with a diameter of 1 mm and one blade, operating at a cutting speed of 50 m/min (16000 rpm) and feed rate of 0.005 mm/tooth (80 mm/min).

The second step was implemented to increase the FBD depth accuracy, reduce the flatness deviation, and improve the roughness of FBD. It is worth mentioning that the first step was skipped for smaller milling depths. To achieve the appropriate thermal emissivity, the laminated composite plates were covered by the silicone-based heat-resistant black matt coating from the Dragon Poland Sp. z. o.o. (Cracow, Poland) before being inspected by the SHVT technique, resulting in a thermal emissivity of 0.98. In addition to achieving uniform emissivity and optical absorption, this enhances the authenticity of inspections by replicating the coating typically applied to in-service composite components, preventing the weave pattern from being directly visible during inspection [44].

Table 1
Material properties of specimens and other equipment simulated in numerical modal analysis [36,59,60].

Properties		GFRP	Al	Steel
Young's moduli, GPa	E_x	27.17	71.7	200
	E_y	24.20		
	E_z	10		
Shear moduli, GPa	G_{xy}	3.17	–	–
	G_{yz}	3.17		
	G_{xz}	3.17		
Poisson's ratio, –	ν_{xy}	0.166	0.33	0.30
	ν_{yz}	0.30		
	ν_{xz}	0.30		
Density, kg/m^3	ρ	2245.90	2810	7850

Table 2
Damage scenarios.

Scenarios	Plate thickness, mm	Damage depth, mm	Damage depth-through thickness, %
1	0.5	0.05	10
2		0.13	25
3		0.25	50
4	0.75	0.08	10
5		0.19	25
6		0.38	50
7	1	0.10	10
8		0.25	25
9		0.50	50

2.2. Numerical simulations

The goal of performing preliminary numerical simulations was to extract the mode shapes of laminated composite plates, including the FBD with the material properties given in Table 1, and the details on the scheme in Fig. 1. The numerical modal analysis begins with meshing of the model of a tested composite plate using commercial ANSYS® workbench software. The simulations were conducted for the model of the plate with dimensions of 220 mm in length (L) and 240 mm in width (W) due to the presence of fixtures. Nine scenarios were considered, consisting of three different thicknesses and three FBD depths, see Fig. 1 and Table 2 for details. Owing to the experimental similarity, where the lower edge is fixed by the fixture, a fixed–fixed boundary condition (BC) was accounted for its effect to reduce the computational runtime. The fixture, composed of aluminum (Al) and steel, possesses the material properties outlined in Table 1, with all contacts assumed to be bonded connections. The upper fixture connected to the shaker had all degrees of freedom (DOFs), including rotations and displacements, constrained, except for displacement in Z-direction parallel to the shaker's movement. Furthermore, the right and left sides of the tested plate were assigned to the free-free BCs, enabling unrestricted movement for them. Automated dense triangular meshes were utilized for the numerical simulations. To determine the optimal mesh size, simulations were conducted for the laminated composite plate with 1 mm thickness and

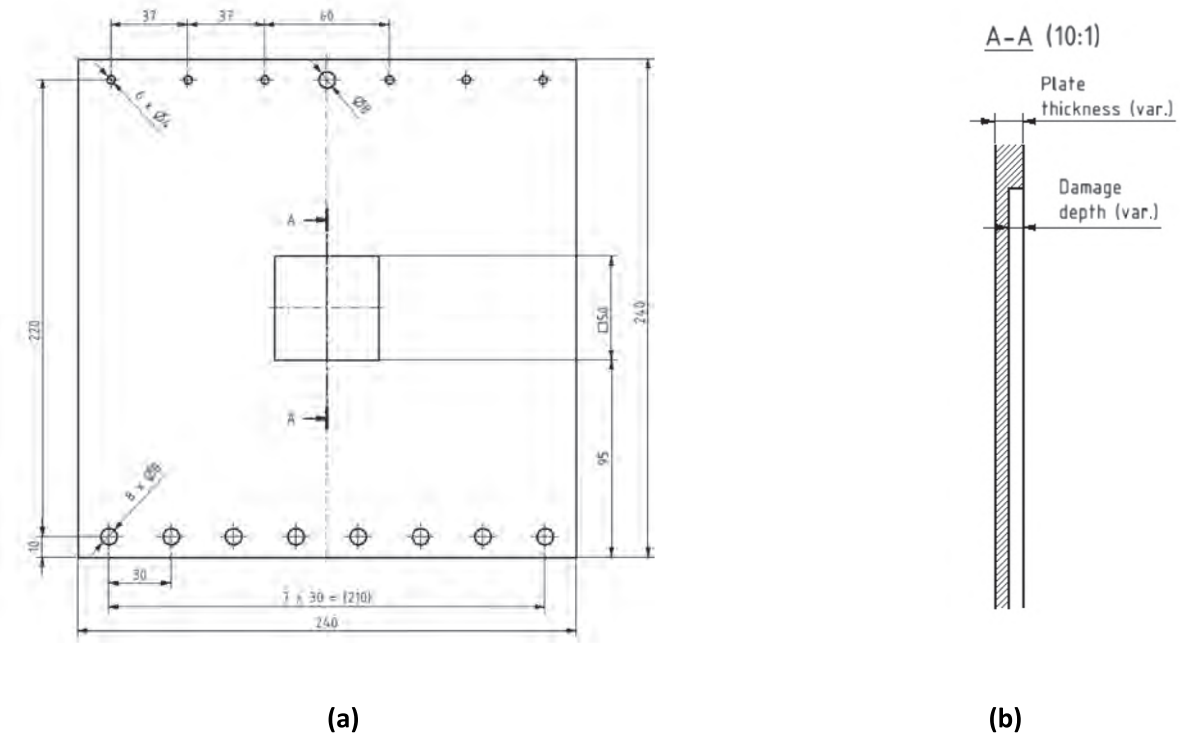

Fig. 1. Scheme and dimensions of the tested specimen: (a) main view, and (b) section AA, respectively.

50 % FBD depth, as an example, using mesh sizes ranging from 0.5 mm to 10 mm. The convergence of the mesh was assessed by examining the variation in the first six natural frequencies of the composite plate across these different mesh sizes, illustrated in Fig. 2. The results indicated that the frequency values converged at a mesh size of 2 mm, suggesting that further refinement beyond this point did not lead to significant improvements in accuracy. Therefore, a 2 mm mesh size was sufficient to accurately capture the resonant frequencies of all scenarios presented in Table 2 for the composite plates. As an example, in a 1 mm thick specimen with a 50 % FBD depth, the mesh contained 116,240 nodes and 47,797 tetrahedral elements.

Mode shapes extracted from finite element analysis (FEA), corresponding to the first six fundamental resonant frequencies of the tested specimen, are presented in Fig. 3. In this example, the laminated composite plate has a thickness of 1 mm and a 50 % FBD depth. The six mode shapes across all scenarios illustrated similarity, as opposed to the different natural frequency values depending on the thickness of a laminate. The main advantage of these numerical simulations is to strategically introduce damage, thereby improving the likelihood of damage detectability using SHVT technique in laminated composite structures. The primary cause behind this is attributed to the higher deflection amplitude occurring at the resonance frequencies of the tested specimen. The location of FBD was established at the center of the tested specimen, where deflection is at its highest, for the nine scenarios, presented in Table 2, using the first mode shape.

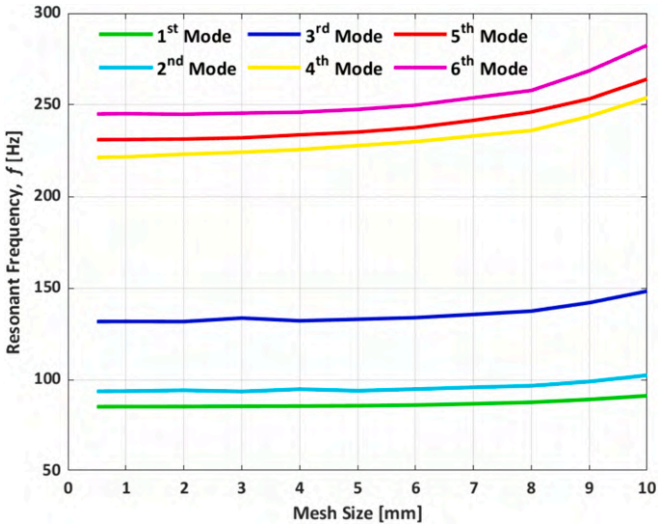

Fig. 2. Influence of mesh refinement on the first six resonant frequencies for a laminated composite plate with 1 mm thickness and 50 % FBD depth, based on numerical simulations.

2.3. Experimental test rig and testing procedure

The experimental studies were performed on the own-designed testing rig presented in Fig. 4(a). The specimen, after covering with the coating was mounted in the aluminum frame, which holds the specimen from the top and bottom sides by bolted connection. The bottom edge of the specimen was fully fixed to the steel brick through the lower fixture, while on the top edge, the fixture that fixed the specimen was connected to the electrodynamic shaker TIRA® TV-51120 (Schalkau, Germany) through the steel stinger. Between the stinger and the tested specimen, the force sensor PCB Piezotronics® 208C02 (Depew, NJ, USA) was used to acquire the reference signal for modal analysis (see Fig. 4(b)). The measured signal from the force sensor was amplified using the Brüel & Kjær Nexus 2693-0I4 conditioning amplifier (Nærum, Denmark). The measurements of vibration velocity were performed using the Polytec® PSV-400 scanning laser Doppler vibrometer (Waldbronn, Germany) connected through the data acquisition and control unit Polytec® PSV-W-400 to the PC with dedicated software. This software was used to set the parameters of modal analysis as well as to generate excitation signals. The excitation signals were amplified using TIRA® BAA 500 shaker amplifier and then transferred to the shaker.

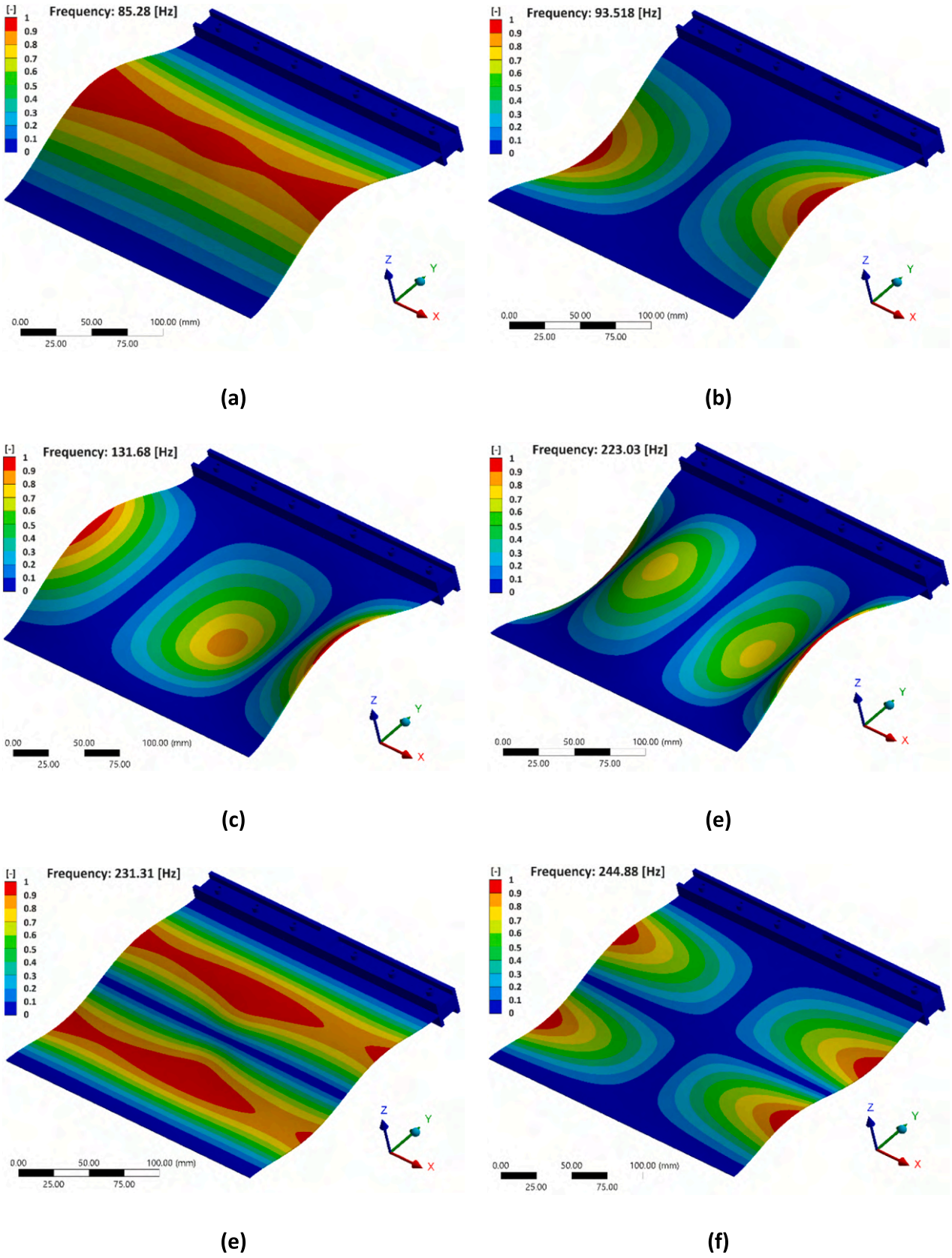

Fig. 3. Illustrating the first six mode shapes of the laminated composite plate with 1 mm thickness and 50 % FBD depth: (a) first, (b) second, (c) third, (d) fourth, (e) fifth, and (f) sixth mode shapes, respectively.

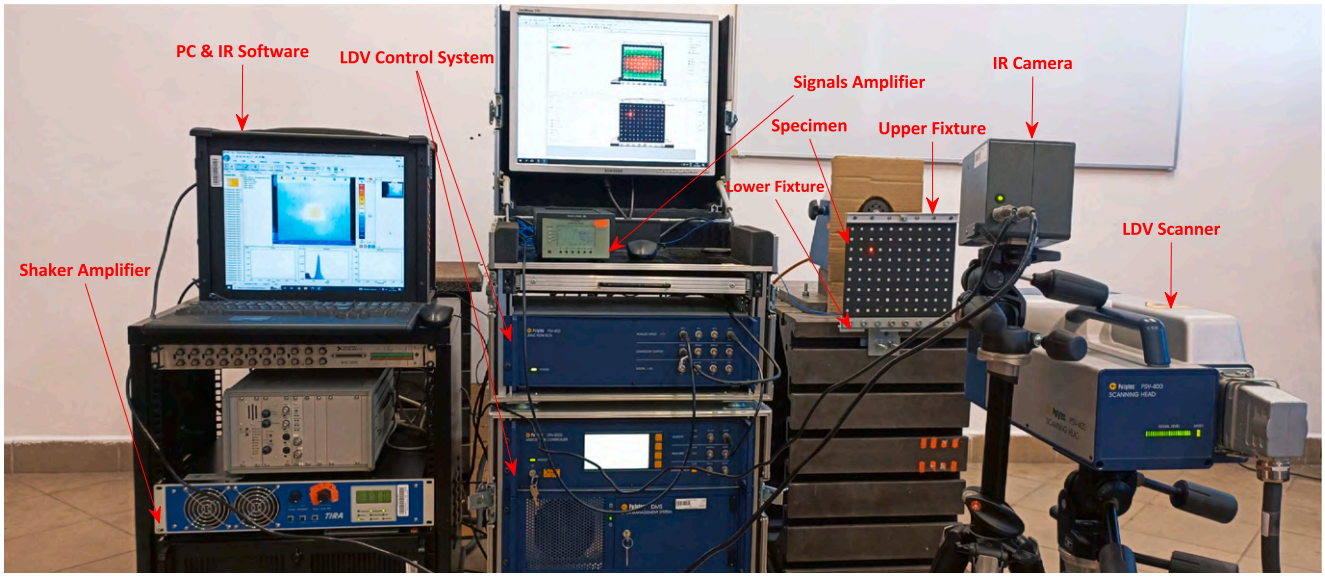

(a)

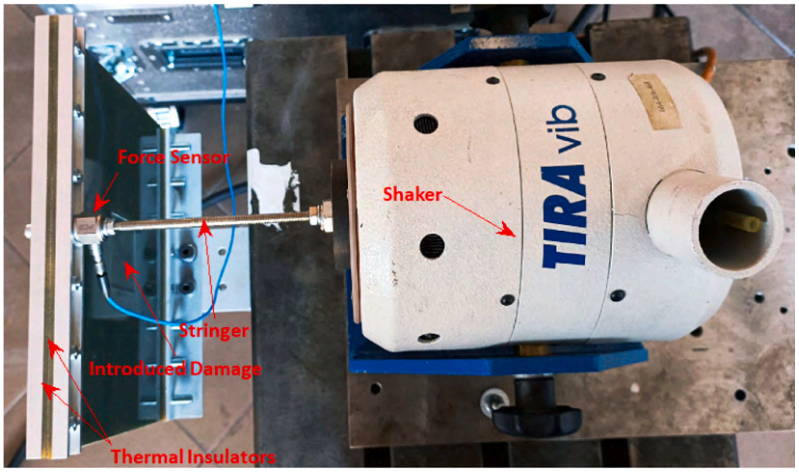

(b)

Fig. 4. The experimental setup: (a) the main view of the testing rig, and (b) the top view of the specimen and shaker assembly, respectively.

The testing procedure consisted of two steps: first, the modal analysis was performed to acquire the natural frequencies of vibration of the tested specimens; and next, the specimen was excited with the determined natural frequencies without unmounting from the fixing frame to retain the BCs from the modal analysis. Before starting the tests, the square fragments of a reflective tape were stuck to the scanned surface of a plate to ensure appropriate focus of the laser beam of the scanning head of a vibrometer. The scanned surface of the specimen was always the opposite one to the surface with an introduced FBD. From the preliminary tests, it was decided to use 9×11 equidistant measurement points, which was enough to precisely determine the natural frequencies of vibration.

The modal analysis was performed across a frequency spectrum of 0 to 300 Hz, with a resolution of 0.25 Hz to accurately capture vibrational characteristics. The excitation was performed using a 50 % burst random signal, which allowed excitation in the wide frequency range. The exemplary frequency response function (FRF) and coherence function from the performed modal analyses is presented in Figs. 5, and 6, respectively. It can be noticed that the first and fifth bending mode shapes, as the exemplary experimental results, are presented in Fig. 7(a) and 7(b). The preliminary loading tests on this natural frequency determined from the modal analysis show that only in the case of the fundamental natural frequency (i.e., first mode shown in Fig. 7(a)), the magnitude of excitation is appropriate to initiate the self-heating effect. Due to this, it was decided to use the first natural frequency only in the next studies. The fundamental natural frequencies determined for all considered scenarios are presented in Table 3. It should be mentioned that the vibrational loads applied across all nine scenarios yielded a maximum deformation magnitude of 12 μm for the first mode, while the displacement magnitude for higher modes was approximately 2 μm, as demonstrated in Fig. 7(b), which is six times lower than that of the first mode.

After determining the natural frequencies for the tested plates, the second step of testing was applied, namely, the specimens were excited at their fundamental natural frequencies to initiate the self-heating effect, and the thermal response was captured by the VarioCam® hr IR

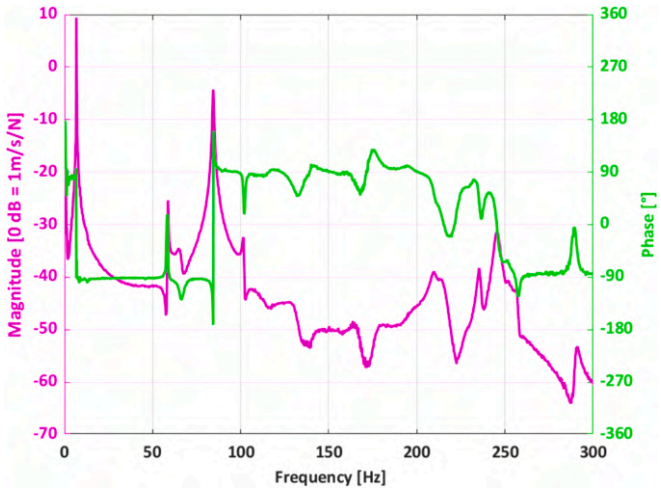

Fig. 5. The experimental FRF of 1 mm thick specimen with 50 % FBD depth.

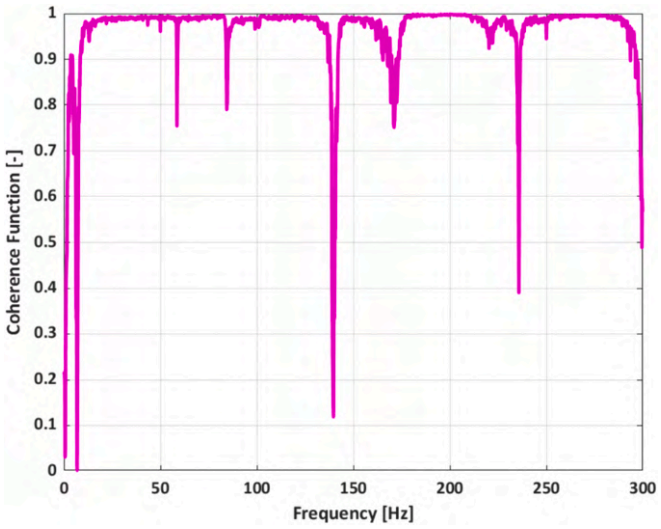

Fig. 6. The coherence function of 1 mm thick specimen with 50 % FBD depth.

camera (Dresden, Germany) with the microbolometric IR detector and resolution of 640 × 480 pixels. During each test, a sequence of a minimum of 400 thermograms was acquired with a sampling rate of 1 Hz. Moreover, to account for environmental influences, the ambient temperature was continuously monitored via thermocouples during thermogram registration.

3. Damage detection and identification

3.1. Issues in damage detection and sensitivity of the technique

During performing SHVT experiments under the resonance frequency excitation, the specimen surface undergoes a rapid temperature growth owing to the high stress concentration and/or displacement amplitude, followed by temperature stabilization over numerous vibration cycles in a stationary self-heating condition. The absence of a standardized testing duration for SHVT arises from the reliance of the technique on the thermomechanical properties of the tested laminated composite. Nonetheless, the reasonable testing time covers both rapid and stabilized periods. Derived from the findings of previous endeavors [15,34,42], a few minutes of testing after the rapid temperature growth would be sufficient. To evaluate the damage using SHVT technique, the registered thermograms for all nine scenarios have been demonstrated in Figs. 8 and 9 for two different moments of testing (i.e., 40th and 120th, respectively).

Within the nine scenarios across all recorded IR images, FBD was detectable in eight cases, excluding the 0.5 mm-thick plate with 10 % FBD depth (see Fig. 8(a) and 9(a)). The registered thermograms at the earlier moment (i.e., 40th) showed better damage detectability, contrasting with thermograms captured afterward (i.e., 120th). This might be primarily attributed to recording 120th − IR images near the self-heating temperature stabilization region, where the least temperature variation occurs, i.e., the noise and uniformity of temperature distribution surrounding FBD provoked challenges for identification and quantification. These problems contribute to the difficulties in globally assessing the sensitivity and accuracy of the SHVT technique understood as clear detectability of damage and sharpness of the detected damage signatures.

3.2. Procedure to identify the best raw thermograms

Although some minutes of performing SHVT testing would be enough for damage identification in such laminated composite plates, several hundred thermograms may be registered during this period. It is, therefore, of primary significance to identify the best raw thermograms for effective damage detection among all the acquired raw thermograms within this interval. For this purpose, the following two-step algorithm is developed. The effective boundary of registered raw thermograms was first determined similar to the methodology implemented for calculating

Table 3
Vibrational resonant frequencies (f) of the laminate composite plates under experiments, denoted in Hz.

Plate thickness, mm →	0.5	0.75	1
FBD depth, % ↓	f [Hz]	f [Hz]	f [Hz]
10	44	62.25	84
25	44.5	61.75	84.5
50	44.5	64.25	84.75

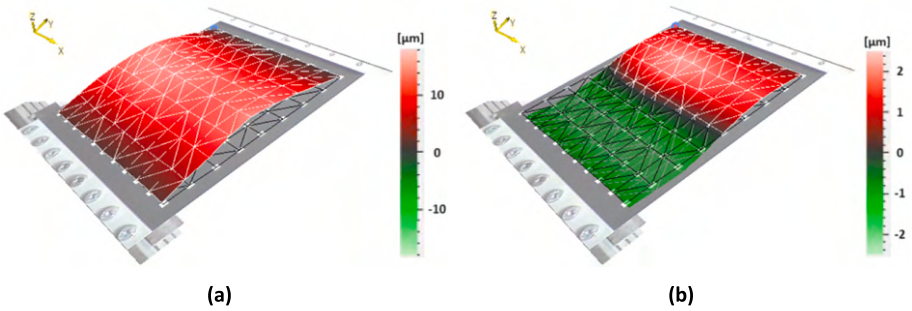

Fig. 7. The first and fifth mode shapes of the 1 mm thick specimen with 50 % FBD depth.

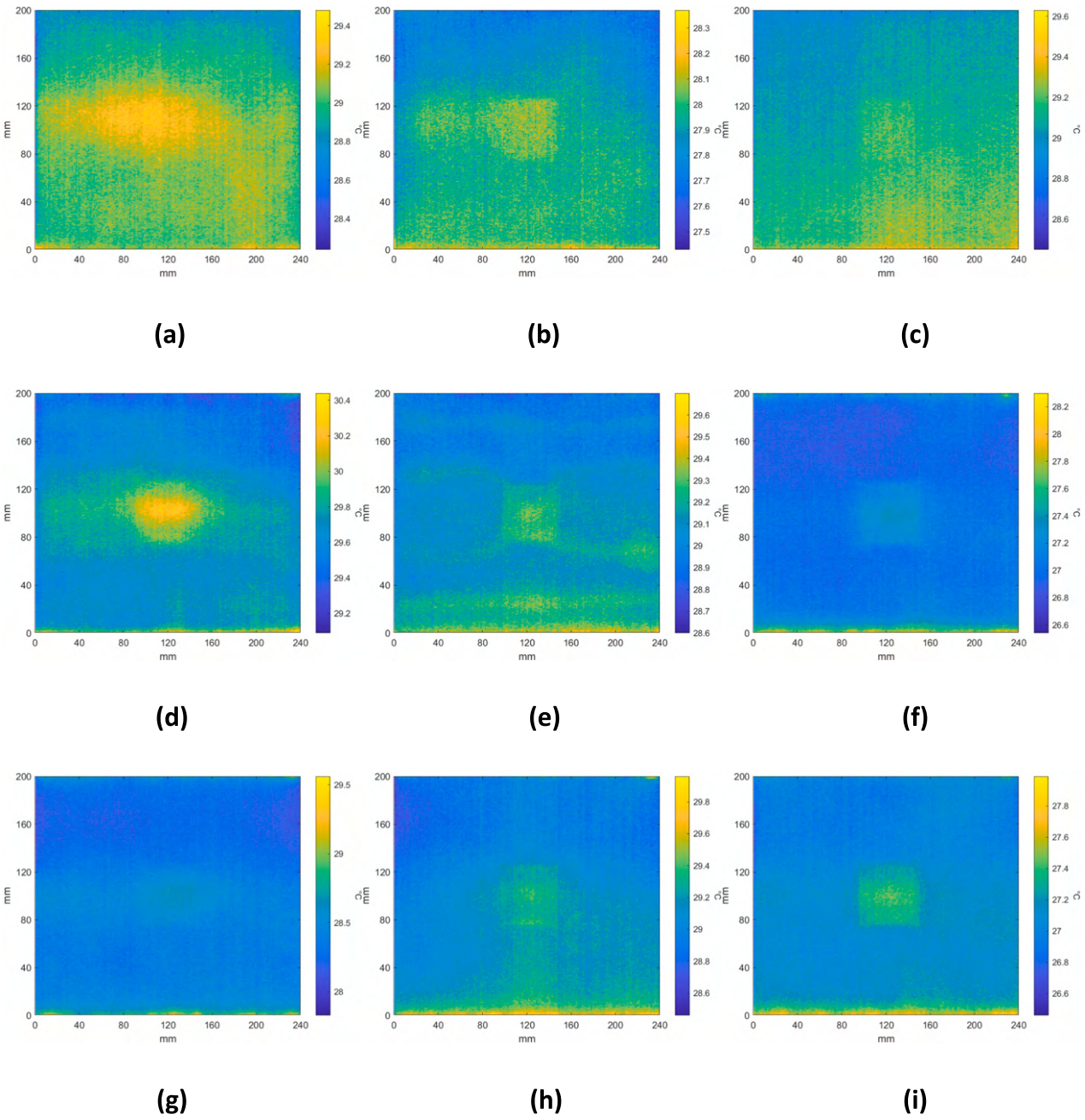

Fig. 8. The selected thermograms at 40th second of testing recorded for plates (a-c) 0.5 mm, (d-f) 0.75 mm, (g-i) 1 mm, each row from left to right consisting of 10 %, 25 %, 50 % damage depth.

the thermal time constant [61–63], while the best raw thermogram was then selected based on an introduced maximal value of temperature ratio ($\overline{T}^{max}_{ratio}$) for each scenario.

The first step involved determining the optimal period aligned with the boundary of effective thermograms (BET), which occurred at the outset of SHVT testing when the self-heating temperature gradient reached its peak. BET, a dynamic parameter, is an indicator for transferring a high amount of heat inside the tested laminated plate in a short timeframe. Preliminary test results highlighted the enhanced damage detection capabilities associated with the dynamic thermal response observed in the tested specimen within the BET interval. Therefore, during image post-processing, BET was established as the maximum permissible number of recorded thermograms for damage identification. This assists not only in selecting the optimal raw thermograms but also in further image processing procedures, see Section 4. Fig. 10 illustrates an exemplary temperature history curve for the acquired maximum self-heating temperature, across the entire specimen surface of interest as the region of interest, over the inspection interval marked as a colored asterisk. BET for the tested laminated plate involving FBD was quantified following two manners: (i) the number of thermograms required for the registered self-heating temperature to stabilize (Eq. (1)), (ii) the number of thermograms needed for the registered self-heating temperature to reach its maximum value (Eq. (2)), as follows:

$$\frac{T_{max} - T}{T_{max} - T_{min}} \geq \frac{1}{e}. \tag{1}$$

$$\frac{T_s - T}{T_s - T_{min}} \geq \frac{1}{e}. \tag{2}$$

Applying each criterion, which is consistent with the concept of thermal

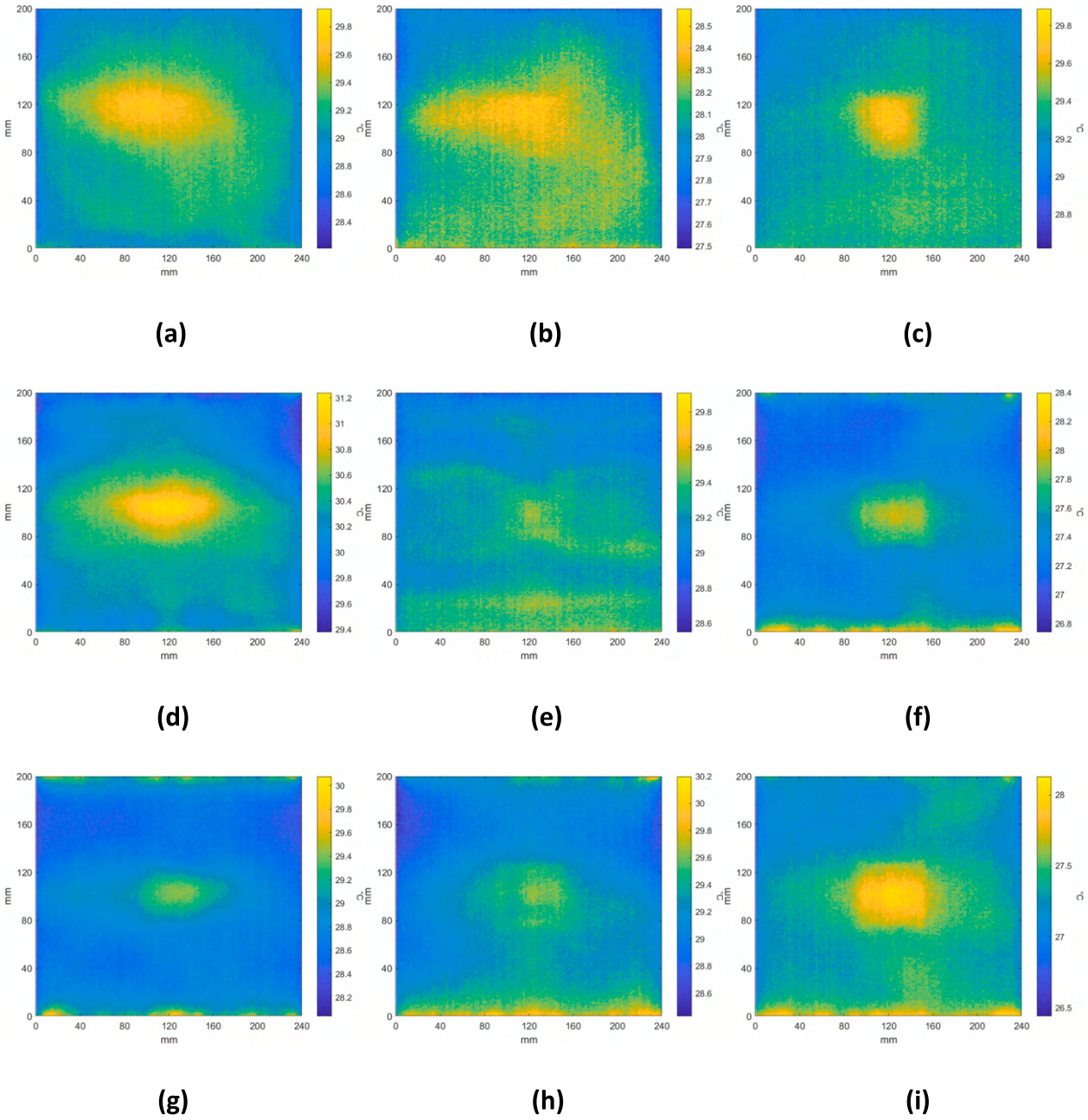

Fig. 9. The selected thermograms at 120th second of testing recorded for plates (a-c) 0.5 mm, (d-f) 0.75 mm, (g-i) 1 mm, each row from left to right consisting of 10 %, 25 %, 50 % damage depth.

time constant, yields a different result for BET. The value $1/e$, where e is the base of the natural logarithm, is known as one thermal time constant, and holds significance as it corresponds to approximately 63.2 % of the maximum or stabilized self-heating temperature. As an illustrative example for a 1 mm-thick laminated composite with the 50 % FBD depth shown in Fig. 10, the BET based on maximum self-heating temperature is 55, while employing the stabilized self-heating temperature sets BET at 116. The choice of criterion has a significant influence on the defined boundary on the interval of observation. Detailed results for all nine scenarios are presented in Table 4 for both approaches. As can be concluded, implementing BET based on T_{max} characterized by its conservative nature, offers a broader spectrum of thermograms, as opposed to using the stabilized self-heating temperature (see Fig. 10 for more details). In other words, considering the maximum self-heating temperature will enhance the capability of handling unexpected variations and transient thermal events.

In the second step, the best raw thermogram for each scenario is selected based on the maximal value of mean value of temperature ratio ($\overline{T}^{max}_{ratio}$), which is simplified to the maximal temperature ratio throughout the paper, calculated across the effective registered thermograms within BET, using the proposed formula:

$$\overline{T}^{max}_{ratio} = \max(\overline{T}_{ratio}) \tag{3}$$

where $\overline{T}_{ratio}$ represents the temperature ratio for each registered thermogram, determined using the following equation:

$$\overline{T}_{ratio} = \frac{\Delta\overline{T}_{FBD}}{\Delta\overline{T}_{P-FBD}} = \frac{\overline{T}_{FBD} - \overline{T}^{min}_{FBD}}{\overline{T}_{P-FBD} - \overline{T}^{min}_{P-FBD}}. \tag{4}$$

where $\overline{T}_{FBD}$ is the mean value of temperature of the FBD for each recorded thermogram, i.e., one value per thermogram. $\overline{T}^{min}_{FBD}$ denotes the

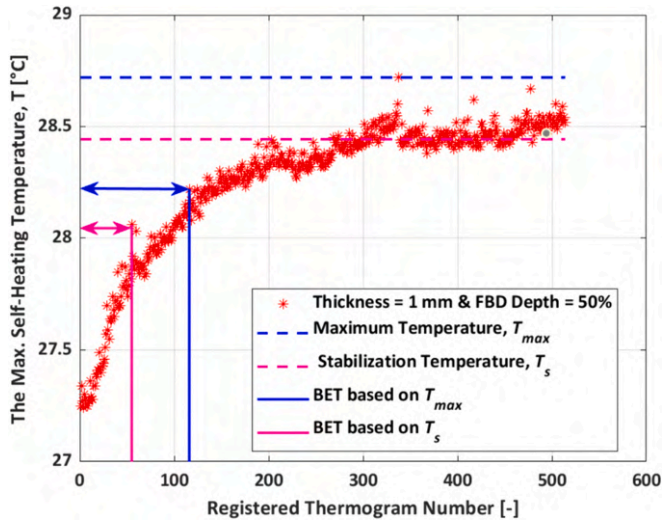

Fig. 10. The boundary of effective thermograms determined using stabilized and maximum self-heating temperature evolution over registered thermograms.

Table 4
The established BET based on stabilized and maximum self-heating temperature.

Plate thickness, mm →	0.5		0.75		1	
FBD depth, % ↓	BET using T_s	BET using T_{max}	BET using T_s	BET using T_{max}	BET using T_s	BET using T_{max}
10	41	45	45	59	35	49
25	43	48	33	77	60	60
50	57	92	51	80	55	116

minimal value of the mean temperature of the FBD, which typically occurs at the starting point of the test, i.e. close to the ambient temperature. This represents a constant value for each of the nine scenarios. $\overline{T}_{P-FBD}$ is the mean value of temperature obtained by subtracting the values for the whole laminated plate from the values of damage (FBD) for every recorded thermogram in each scenario, $\overline{T}^{min}_{P-FBD}$ represents the minimal value of mean temperature value extracted in the same manner and remaining constant across each of the nine scenarios. Similar to $\overline{T}^{min}_{FBD}$, $\overline{T}^{min}_{P-FBD}$ generally occurs at the beginning of the tests.

Considering the effective dimensions of the tested plate (240 mm × 200 mm) and the fixtures occupying the upper and lower edges, the length of FBD is equivalent to either 84 or 85 pixels (i.e. 50 mm corresponding to either 84 or 85 pixels), as determined by post-processing. This correspondence depends on the distance of the IR camera from the tested specimen during SHVT experiments.

As mentioned above, the second step aims to identify the value of $\overline{T}^{max}_{ratio}$ in each scenario. This methodologically offers the best raw thermogram, avoiding the huge under- or over-identification area corresponding to the actual FBD region. Exemplary results for the specimens with thicknesses of 0.5 mm, 0.75 mm, and 1 mm, each with a 50 % FBD depth, are depicted in Fig. 11(a-c), respectively. Table 5 lists the best raw thermograms for all nine scenarios, identified through the two-step proposed algorithm. The corresponding thermograms, categorized by plate thickness and damage depth, are shown in Fig. 12: (a-c) 0.5 mm, (d-f) 0.75 mm, and (g-i) 1 mm. Each row, from left to right, represents different damage depths of 10 %, 25 %, and 50 %, respectively. Additionally, thermograms registered within the stabilization phase, although exhibiting greater sharpness in some cases, tended to demonstrate an overestimation of the true damage size. Such thermograms had relatively lower $\overline{T}_{ratio}$ values, which should not be considered as the most

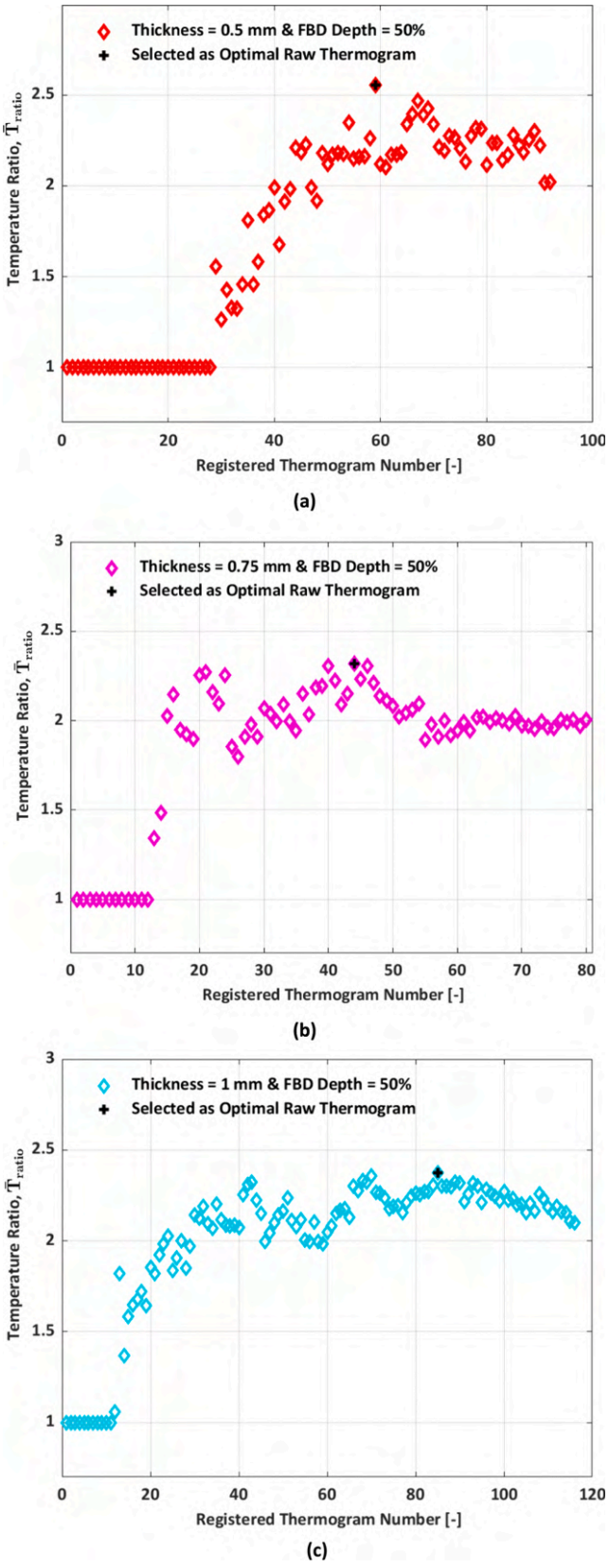

Fig. 11. The determined temperature ratio and marked the optimal raw thermogram for (a) 0.5 mm, (b) 0.75 mm and (c) 1 mm −thick laminated plate with the 50 % FBD depth.

Table 5
The indices of the best raw thermograms from collected sequences.

Plate thickness, mm →	0.5	0.75	1
FBD depth, % ↓			
10	23	24	42
25	32	68	50
50	59	44	85

appropriate thermograms, highlighting the reliability of the results obtained from the proposed two-step algorithm in such conditions.

4. Enhancing damage identification and quantification

The enhancement procedure was based on the application of image processing algorithms to the thermograms selected in the first step of the proposed algorithm (i.e. BET). The sequence of thermograms was considered in processing algorithms, where the number of the best thermograms determined in the previous step was considered as a boundary of set of processed thermograms. Another boundary was always set as 1. The selection of such a set of thermograms is justified by the highest temperature gradient at the beginning of excitation, which

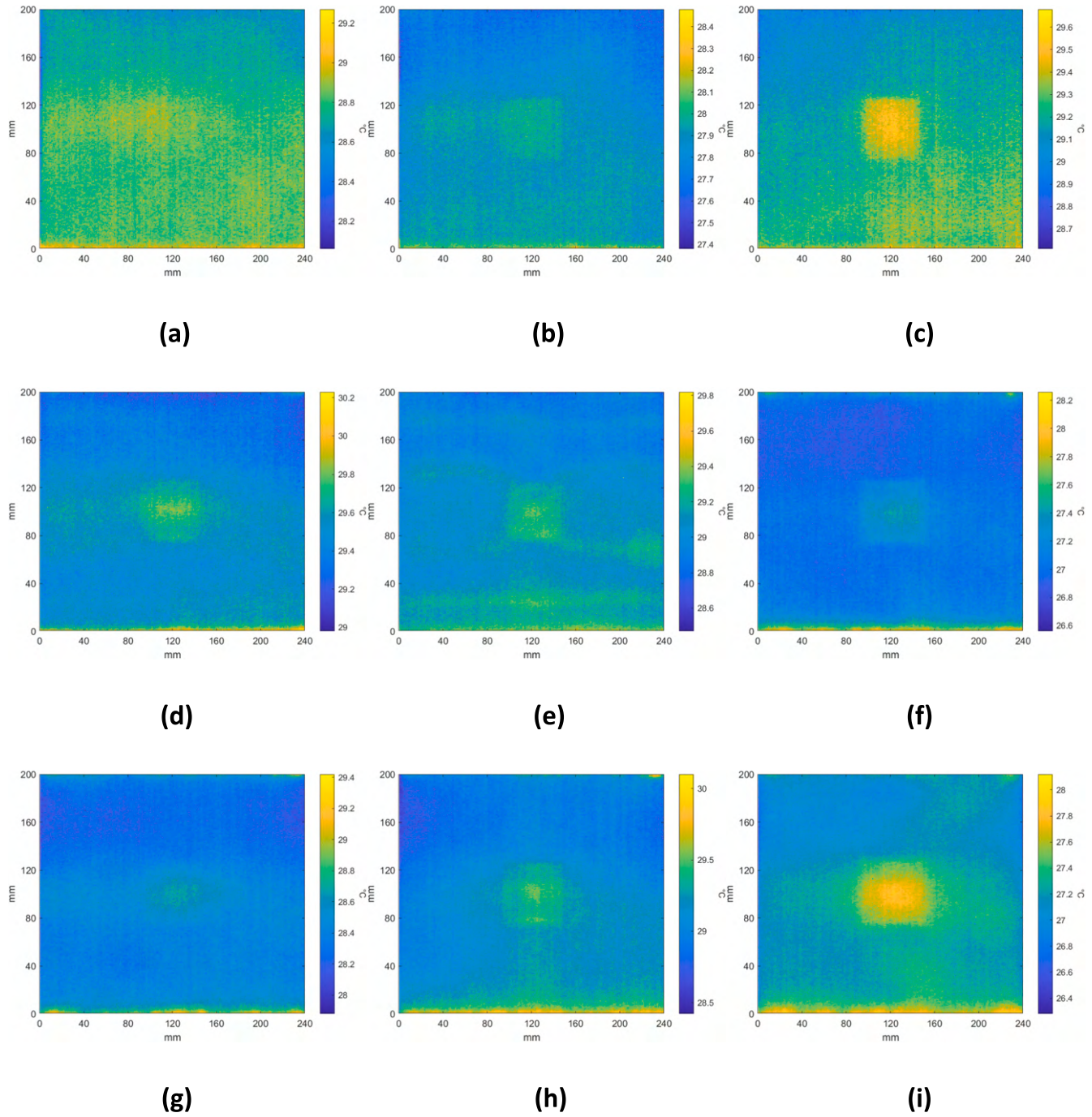

Fig. 12. Selected best thermograms from collected sequences for the plates with a thickness of (a-c) 0.5 mm; (d-f) 0.75 mm; (g-i) 1 mm and the damage depth of 10 %, 25 %, and 50 %, respectively, in each row from left to right.

resulted in high sharpness of the edges of damage to be identified. In the later period of excitation, the gradient is much smaller, which results in temperature stabilization and tending to the thermal balance. This, in turn, results in the blurring of boundaries of damage signature in thermograms.

In the preliminary study, several processing algorithms were applied, including statistical features (mean absolute deviation, median absolute deviation, central moments, kurtosis, skewness, root-mean-squared, root-sum-of-squares, crest factor, peak-to-peak, peak-to-root-mean-squared) and more advanced metrics often applicable for processing of thermograms (gradients, Laplacian, Hessians, wavelet transform, principal component thermography, partial least-squares regression, thermographic signal reconstruction). The mathematical description of these algorithms can be found in [42]. The performed analysis demonstrated satisfactory results for several algorithms, namely, mean absolute deviation, peak-to-peak, peak-to-root-mean-squared, central

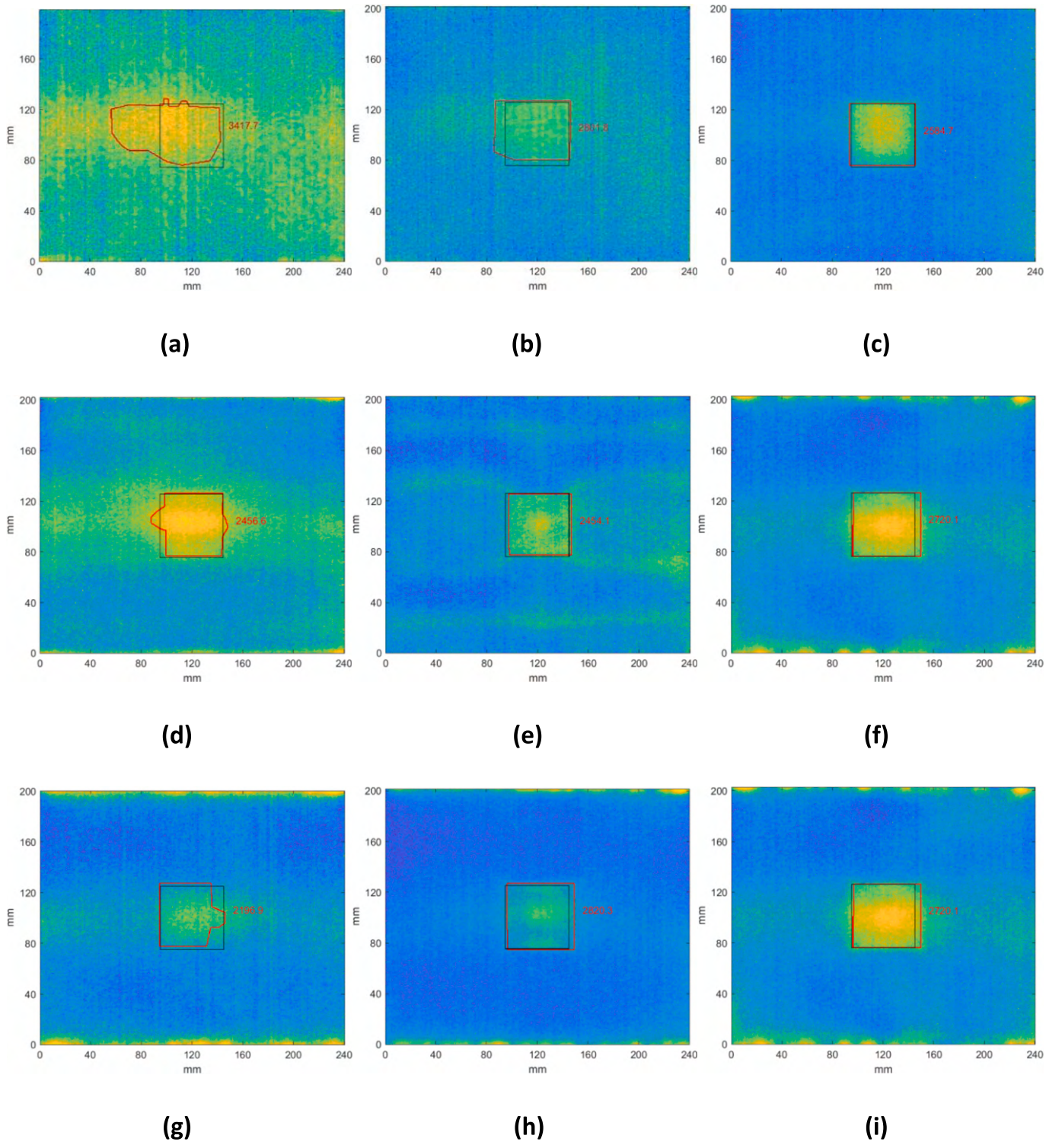

Fig. 13. The results of enhancement of selected thermograms with the quantified damaged regions for the plates with a thickness of (a-c) 0.5 mm; (d-f) 0.75 mm; (g-i) 1 mm and the damage depth of 10 %, 25 %, and 50 %, respectively, in each row from left to right.

moments, principal component thermography, and partial least-squares regression. The criteria of selection of the processing algorithm in further studies were focused on the improvement of damage detectability, accuracy of estimation of damage shape, and reduction of noise. According to these criteria, the best algorithm selected for further studies was based on the estimation of central moments, which is in agreement with the previous results achieved in [42].

In the applied algorithm, odd central moments up to 8th were calculated for a given thermogram, since only odd central moments were sensitive to damage, while higher-order moments were characterized by much less sensitivity to damage, i.e., the damage signatures are not recognizable for them. Next, the values within the resulting images were raised to the power of 0.01 and summed up to further improve the distinguishability between damaged and healthy regions on tested plates.

To quantify damage in the considered plates the contours of the identified damage signatures were manually circumscribed using the polygons. The assumed boundaries between healthy and damaged regions were perceptually determined based on a sudden change of colors on the enhanced thermograms. The resulting images are presented in Fig. 13, where the red line describes the identified boundary, while the black line describes the true contour of a damage obtained from proportion (considering dimensions of a plate determined from thermograms). In every case, the determined area of damage in mm^2 was provided on the images.

The overall improvement of the analyzed thermograms is noticed. It is especially well visible for the cases with 10 % and 25 % damage depth (cf. Figs. 12 and 13), which makes detection, identification, and quantification of damage possible for smaller damage. To compare the results of quantification, the ratio between the areas of identified A_i and true A_t damage regions was calculated according to the formula:

$$A_R = \frac{A_i - A_t}{A_t} \bullet 100\%. \tag{5}$$

The results are presented in Table 6. Although in the cases with the damage depth of 25 % and 50 % the accuracy of determination of a damage shape is very good (see Fig. 13), in the cases with the damage depth of 10 % the shapes of identifiable damage are far from true damage shapes and locations. Due to this, the hit/miss metric was introduced, which determines the amount of area of identified damage that coincides with a true damage location A_{hit}, and the amount of area that is not coinciding with the true damage location A_{miss}:

$$A_{hit} = A_i \cap A_t \bullet 100\%. \tag{6}$$

$$A_{miss} = (A_i \cup A_t) \backslash A_t \bullet 100\%. \tag{7}$$

Note that incoincidences are calculated for both areas within the area of a true damage location and for the areas outside a true damage location. The determined values of this metric are presented in Table 6. For the damage depth of 10 %, notable inaccuracies are evident, as shown by increased A_{miss} and lower A_R percentages in Table 6. The large inconsistencies in the quantitative results for flat damage at the 10 % depth, specifically at 0.1 mm or less, as depicted in Fig. 13 (a), (d), and (g) with damage depths of 0.05 mm, 0.075 mm, and 0.1 mm, respectively, can primarily be attributed to insufficient thermal contrast. This consequently leads to a lower signal-to-noise ratio and reduced accuracy in damage quantification. Additionally, the flat morphology of the damage likely contributes to weaker thermal signals, complicating accurate detection. This limitation should be considered when applying this technique to materials with tiny damage depths, and additional procedure(s) may be necessary to complement the detection of such small damage depths. By contrast, for the damage at 25 % and 50 % depths, the quantification is significantly more accurate. The A_{hit} values are higher, and the A_{miss} values are lower, indicating a more reliable identification of the true shape of the simulated damage and its location. This improved performance at greater depths can be attributed to the increased thermal contrast, which enhances the ability of the method to detect and accurately quantify the damage.

5. Conclusions

The recorded temperature rise on the surface of 2D laminated composites, remaining below 2 °C without affecting the structural changes, confirms the non-destructive nature of SHVT. This technique identified the FBD in eight out of nine scenarios, with the exception of the thinner laminated plate with 10 % FBD depth, demonstrating its effectiveness. Variations in thermogram quality were observed, especially at the beginning of the SHVT experiments due to non-uniform temperature distribution and noise during stabilization, leading to blurred damage signatures. To address these challenges, a two-step algorithm was developed, combining BET and the peak value of temperature ratio. This method helped to successfully select the optimal raw thermograms as well as to determine the effective acquisition time boundaries of the thermograms' sequence, with the optimal assessment period occurring at the beginning of a test. The upper boundary of thermograms for damage enhancement in each scenario was established by BET value in each scenario, chosen for having the highest temperature gradient and leading to more precise and sharper identification of damaged edges. Among various statistical features and more advanced processing algorithms like PCT or PLSR, the algorithm based on central moments showed a remarkable improvement in damage detectability, accuracy of damage shape estimation, and noise reduction. Additionally, it is more computationally efficient, as it avoids the need for advanced thermogram transformations.

The proposed hit/miss metric assessed the accuracy of identified damage properties (location and area) with the actual introduced damage. This provides an effective approach for precise comparison of identified and introduced damage dimensions and locations in tested composite plates. The proposed enhancement algorithm combined with hit/miss metric allowed improving damage detectability and quantification for all considered cases, which was not possible by analyzing raw thermograms only. The study suggests that SHVT, with the proposed enhancements, is a promising tool for both laboratory and field inspections of composite structures, especially where traditional thermal excitation methods are impractical. Future research will focus on refining the excitation methods, enhancing thermogram processing algorithms, as well as identification of low velocity impact damage in PMCs.

CRediT authorship contribution statement

Jafar Amraei: Writing – review & editing, Writing – original draft, Software, Project administration, Validation, Methodology,

Table 6
The results of damage quantification from enhanced thermograms.

Plate thickness, mm →	0.5			0.75			1		
FBD depth, % ↓	A_R, %	A_{hit}, %	A_{miss}, %	A_R, %	A_{hit}, %	A_{miss}, %	A_R, %	A_{hit}, %	A_{miss}, %
10	36.708	81.39	71.02	−1.736	90.92	14.00	−12.124	80.63	24.29
25	12.072	91.17	27.25	1.836	91.94	11.91	12.812	97.22	15.81
50	3.388	97.46	6.00	8.804	96.85	12.61	11.612	94.80	19.62

Investigation, Funding acquisition, Formal analysis, Data curation, Conceptualization. **Andrzej Katunin:** Writing – review & editing, Writing – original draft, Software, Methodology, Formal analysis, Data curation, Conceptualization. **Dominik Wachla:** Writing – review & editing, Writing – original draft, Software, Methodology, Investigation, Conceptualization. **Krzysztof Lis:** Writing – review & editing, Writing – original draft, Software, Investigation, Conceptualization.

Declaration of competing interest

The authors declare that they have no known competing financial interests or personal relationships that could have appeared to influence the work reported in this paper.

Data availability

Data will be made available on request.

Acknowledgements

The publication is supported under the Excellence Initiative – Research University Program of the Silesian University of Technology, grant no. 32/014/SDU/10-22-48, year 2022.

References

[1] C.E. Bakis, L.C. Bank, V. Brown, E. Cosenza, J. Davalos, J. Lesko, A. Machida, S. Rizkalla, T. Triantafillou, Fiber-reinforced polymer composites for construction—State-of-the-art review, J. Compos. Constr. 6 (2) (2002) 73–87.
[2] W. Ferdous, T.D. Ngo, K.T. Nguyen, A. Ghazlan, P. Mendis, A. Manalo, Effect of fire-retardant ceram powder on the properties of phenolic-based GFRP composites, Compos. B Eng. 155 (2018) 414–424.
[3] O. Ahmed, X. Wang, M.-V. Tran, M.-Z. Ismadi, Advancements in fiber-reinforced polymer composite materials damage detection methods: Towards achieving energy-efficient SHM systems, Compos. B Eng. 223 (2021) 109136.
[4] G.F. Gomes, F.A. de Almeida, A.C. Ancelotti Jr, S.S. da Cunha Jr, Inverse structural damage identification problem in CFRP laminated plates using SFO algorithm based on strain fields, Eng. Comput. 37 (4) (2021) 3771–3791.
[5] G.F. Gomes, F.A. de Almeida, S.S. da Cunha, A.C. Ancelotti, An estimate of the location of multiple delaminations on aeronautical CFRP plates using modal data inverse problem, Int. J. Adv. Manuf. Technol. 99 (2018) 1155–1174.
[6] L.A. de Oliveira, G.F. Gomes, J.L.J. Pereira, M.B. Francisco, A. Demarbaix, S. S. Cunha Jr, New trends of damage detection and identification based on vibrothermography in composite materials, J. Nondestr. Eval. 42 (3) (2023) 57.
[7] A. Katunin, I. Pivdiablyk, L. Gornet, P. Rozycki, A hybrid method for determination of fatigue limit and non-destructive evaluation of composite structures after low-velocity impact loading, Compos. B Eng. 238 (2022) 109898.
[8] J. Segers, S. Hedayatrasa, E. Verboven, G. Poelman, W. Van Paepegem, M. Kersemans, In-plane local defect resonances for efficient vibrothermography of impacted carbon fiber-reinforced polymers (CFRP), NDT and E Int. 102 (2019) 218–225.
[9] F. Jensen, J.F. Jerg, M. Sorg, A. Fischer, Active thermography for the interpretation and detection of rain erosion damage evolution on GFRP airfoils, NDT and E Int. 135 (2023) 102778.
[10] Q. Wei, J. Huang, J. Zhu, L. Zhuo, C. Li, Experimental investigation on detection of coating debonds in thermal barrier coatings using vibrothermography with a piezoceramic actuator, NDT and E Int. 137 (2023) 102859.
[11] A. Katunin, A concept of thermographic method for non-destructive testing of polymeric composite structures using self-heating effect, Sensors 18 (1) (2017) 74.
[12] C. Ibarra-Castanedo, J.-M. Piau, S. Guilbert, N.P. Avdelidis, M. Genest, A. Bendada, X.P. Maldague, Comparative study of active thermography techniques for the nondestructive evaluation of honeycomb structures, Res. Nondestr. Eval. 20 (1) (2009) 1–31.
[13] J. Huang, Q. Wei, L. Zhuo, J. Zhu, C. Li, Z. Wang, Detection and quantification of artificial delaminations in CFRP composites using ultrasonic thermography, Infrared Physics Technology 130 (2023) 104579.
[14] R.B. Heslehurst, Defects and damage in composite materials and structures, CRC Press, 2014.
[15] F. Ciampa, P. Mahmoodi, F. Pinto, M. Meo, Recent advances in active infrared thermography for non-destructive testing of aerospace components, Sensors 18 (2) (2018) 609.
[16] A. Katunin, D. Wachla, Analysis of defect detectability in polymeric composites using self-heating based vibrothermography, Compos. Struct. 201 (2018) 760–765.
[17] C. Ibarra-Castanedo, M. Genest, S. Guibert, J.-M. Piau, X.P. Maldague, A. Bendada, Inspection of aerospace materials by pulsed thermography, lock-in thermography, and vibrothermography: a comparative study. Thermosense XXIX, SPIE, 2007.
[18] G.K. Geetha, D.R. Mahapatra, Modeling and simulation of vibro-thermography including nonlinear contact dynamics of ultrasonic actuator, Ultrasonics 93 (2019) 81–92.
[19] L. Pieczonka, F. Aymerich, G. Brozek, M. Szwedo, W. Staszewski, T. Uhl, Modelling and numerical simulations of vibrothermography for impact damage detection in composites structures, Structural Control Health Monitoring 20 (4) (2013) 626–638.
[20] R. Yang, Y. He, Optically and non-optically excited thermography for composites: a review, Infrared Physics Technology 75 (2016) 26–50.
[21] F. Mevissen, M. Meo, Ultrasonically stimulated thermography for crack detection of turbine blades, Infrared Physics Technology 122 (2022) 104061.
[22] F. Mabrouki, M. Thomas, M. Genest, A. Fahr, Frictional heating model for efficient use of vibrothermography, NDT and E Int. 42 (5) (2009) 345–352.
[23] J. Renshaw, J.C. Chen, S.D. Holland, R.B. Thompson, The sources of heat generation in vibrothermography, NDT and E Int. 44 (8) (2011) 736–739.
[24] K. Truyaert, V. Aleshin, K. Van Den Abeele, Qualitative analysis of a 3D multiphysics model for nonlinear ultrasonics and vibration induced heating at closed defects, Res. Nondestr. Eval. 33 (1) (2022) 17–32.
[25] A. Mendioroz, K. Martínez, R. Celorrio, A. Salazar, Characterizing the shape and heat production of open vertical cracks in burst vibrothermography experiments, NDT and E Int. 102 (2019) 234–243.
[26] C. Cavallone, M. Colom, A. Mendioroz, A. Salazar, D. Palumbo, U. Galietti, Sizing the length of surface breaking cracks using vibrothermography, NDT and E Int. 112 (2020) 102250.
[27] L. Dong, B. Wang, H. Wang, M. Xiang, X. Chen, G. Ma, Y. Di, W. Guo, J. Kang, X. Zhou, Effects of crack surface roughness on crack heat generation characteristics of ultrasonic infrared thermography, Infrared Physics Technology 106 (2020) 103262.
[28] D. Di Maio, G. Voudouris, I. Sever, Investigation of fatigue damage growth and self-heating behaviour of cross-ply laminates using simulation-driven dynamic test, Int. J. Fatigue 155 (2022) 106617.
[29] Q. Wei, M. Han, J. Zhu, L. Zhuo, J. Huang, W. Li, W. Xie, Experimental and numerical investigation on detection fatigue crack in metallic plate by vibro-thermography, Infrared Physics Technology 126 (2022) 104347.
[30] J. Zhu, Z. Mao, D. Wu, J. Zhou, D. Jiao, W. Shi, W. Zhu, Z. Liu, Progress and trends in non-destructive testing for thermal barrier coatings based on infrared thermography: a review, J. Nondestr. Eval. 41 (3) (2022) 49.
[31] G. Zhou, Z.C. Ong, Z. Zhang, W. Yin, H. Chen, H. Ma, Y. Fu, Defect detection of carbon fiber deflectors based on laser infrared thermography and experimental modal analysis, Mech. Syst. Sig. Process. 221 (2024) 111763.
[32] P. Liu, C. Xu, Y. Zhang, L. Chen, Y. Han, R. Liu, Y. Qin, Detection and quantification of corrosion defects in CFRP-strengthened steel structures based on low-power vibrothermography, Nondestructive Testing and Evaluation (2024) 1–25.
[33] Z. Huang, J. Zhu, L. Zhuo, C. Li, C. Liu, W. Hao, W. Xie, Non-destructive evaluation of uneven coating thickness based on active long pulse thermography, NDT and E Int. 130 (2022) 102672.
[34] A. Wronkowicz, A. Katunin, D. Wachla, Enhancement of damage identification in composite structures with self-heating based vibrothermography, Optik 181 (2019) 545–554.
[35] F. Lahuerta, R. Nijssen, F. Van Der Meer, L. Sluys, Experimental–computational study towards heat generation in thick laminates under fatigue loading, Int. J. Fatigue 80 (2015) 121–127.
[36] J. Amraei, A. Katunin and M. Lipińska, Numerical simulation and experimental validation of self-heating of polymer-matrix composites during low-cycle fatigue loading. International Journal of Fatigue, 2024: p. 108510.
[37] A. Katunin, Criticality of the self-heating effect in polymers and polymer matrix composites during fatigue, and their application in non-destructive testing, Polymers 11 (1) (2018) 19.
[38] J. Amraei, A. Katunin, Recent advances in limiting fatigue damage accumulation induced by self-heating in polymer-matrix composites, Polymers 14 (24) (2022) 5384.
[39] F. Magi, D. Di Maio, I. Sever, Damage initiation and structural degradation through resonance vibration: application to composite laminates in fatigue, Composites Science Technology 132 (2016) 47–56.
[40] D. Di Maio, F. Magi, I. Sever, Damage monitoring of composite components under vibration fatigue using scanning laser Doppler vibrometer, Exp. Mech. 58 (2018) 499–514.
[41] J.S. Vaddi, S.D. Holland, M.R. Kessler, Absorptive viscoelastic coatings for full field vibration coverage measurement in vibrothermography, NDT and E Int. 82 (2016) 56–61.
[42] A. Katunin, A. Wronkowicz-Katunin, D. Wachla, Impact damage assessment in polymer matrix composites using self-heating based vibrothermography, Compos. Struct. 214 (2019) 214–226.
[43] S.M. Shepard, J.R. Lhota, B.A. Rubadeux, D. Wang, T. Ahmed, Reconstruction and enhancement of active thermographic image sequences, Opt. Eng. 42 (5) (2003) 1337–1342.
[44] G. Poelman, S. Hedayatrasa, W. Van Paepegem, M. Kersemans, Enhanced thermographic inspection of woven fabric composites by k-space filtering, Compos. B Eng. 252 (2023) 110508.
[45] O. Obeidat, Q. Yu, X. Han, Developing algorithms to improve defect extraction and suppressing undesired heat patterns in sonic IR images, Sensing Imaging 17 (2016) 1–15.
[46] U. Netzelmann, D. Müller, Modified pulse-phase thermography algorithms for improved contrast-to-noise ratio from pulse-excited thermographic sequences, NDT and E Int. 116 (2020) 102325.

[47] G. Poelman, S. Hedayatrasa, J. Segers, W. Van Paepegem, M. Kersemans, Multi-scale gapped smoothing algorithm for robust baseline-free damage detection in optical infrared thermography, NDT and E Int. 112 (2020) 102247.
[48] G. Poelman, S. Hedayatrasa, J. Segers, W. Van Paepegem, M. Kersemans, Adaptive spectral band integration in flash thermography: Enhanced defect detectability and quantification in composites, Compos. B Eng. 202 (2020) 108305.
[49] L. Cheng, M. Kersemans, Dual-IRT-GAN: A defect-aware deep adversarial network to perform super-resolution tasks in infrared thermographic inspection, Compos. B Eng. 247 (2022) 110309.
[50] K. Zheng, Y.-S. Chang, Y. Yao, Defect detection in CFRP structures using pulsed thermographic data enhanced by penalized least squares methods, Compos. B Eng. 79 (2015) 351–358.
[51] X. Chi, D. Di Maio, N.A. Lieven, Health monitoring of bolted joints using modal-based vibrothermography, SN Applied Sciences 2 (2020) 1–22.
[52] X. Chi, D. Di Maio, N.A. Lieven, Modal-based vibrothermography using feature extraction with application to composite materials, Struct. Health Monit. 19 (4) (2020) 967–986.
[53] H.D. Benítez, C. Ibarra-Castanedo, A. Bendada, X. Maldague, H. Loaiza, E. Caicedo, Definition of a new thermal contrast and pulse correction for defect quantification in pulsed thermography, Infrared Phys. Technol. 51 (3) (2008) 160–167.
[54] G. Poelman, S. Hedayatrasa, J. Segers, W. Van Paepegem and M. Kersemans. Application of flash thermography and advanced post-processing techniques for rapid NDT of CFRP aircraft component: a case study. in 11th Symposium on NDT in Aerospace. 2019.
[55] N. Rajic and DSTO-TR-1298, Principal Component Thermography, Defence Science and Technology Organisation Victoria (Australia) Aeronautical and Maritime Research Lab, 2002.
[56] N. Rajic, Principal component thermography for flaw contrast enhancement and flaw depth characterisation in composite structures, Compos. Struct. 58 (4) (2002) 521–528.
[57] J. Segers, S. Hedayatrasa, E. Verboven, G. Poelman, W. Van Paepegem and M. Kersemans, In-plane local defect resonances for efficient vibrothermography of impacted carbon fiber-reinforced polymers (CFRP). NDT & E International, 2019. 102: p. 218-225. [52] T. Reyno, C. Marsden and D. Wowk, Surface damage evaluation of honeycomb sandwich aircraft panels using 3D scanning technology. NDT & E International, 2018. 97: p. 11-19.
[58] A. Katunin, D. Wachla, Determination of fatigue limit of polymeric composites in fully reversed bending loading mode using self-heating effect, J. Compos. Mater. 53 (1) (2019) 83–91.
[59] H. Lopes, J.A. dos Santos, A. Katunin, Identification of material properties of a laminated plate from measurements of natural frequencies and modal rotations, Procedia Struct. Integrity 17 (2019) 971–978.
[60] S. Erfantalab, P. Sharma, G. Parish, A. Keating, Thermal analysis of surface micromachined porous silicon membranes using the 3ω method: Implications for thermal sensing, Appl. Therm. Eng. 222 (2023) 119965.
[61] M. Ye, K. Nagano, A.A. Serageldin, H. Sato, Field studies on the energy consumption and thermal comfort of a nZEB using radiant ceiling panel and open-loop groundwater heat pump system in a cold region, Journal of Building Engineering 67 (2023) 105999.
[62] T. Yuan, J. Fu, Y. Chen, Y. Lu, Y. Hou, G. Sun, D. Chen, Pulse-Voltage-Based method of thermal parameter extraction for thermopile infrared sensors, IEEE Sens. J. 23 (6) (2023) 5593–5600.

Declarations of co-authors

Andrzej Katunin, PhD, DSc, Eng., prof. SUT
Silesian University of Technology
Faculty of Mechanical Engineering
Department of Fundamentals of Machinery Design

Declaration

I hereby declare that my contribution percentages in the following publications were as follows:

[1] J. Amraei, and A. Katunin, *Recent Advances in limiting fatigue damage accumulation induced by self-heating in polymer–matrix composites*, Polymers, 2022, 14(24), 5384. Doi: 10.3390/polym14245384.-**30%**
CRediT author statement: Writing – review & editing, Writing – original draft, Methodology, Formal analysis, Data curation, Conceptualization.

[2] A. Premanand, T. Rogala, D. Wachla, J. Amraei, A. Katunin, B. Khatri, M. Rienks, F. Balle, *Fatigue strength estimation of a CF/PEKK composite through self-heating temperature analysis using cyclic bending tests at 20 kHz*, Composites Science and Technology, 2023, 243, 110218. Doi: 10.1016/j.compscitech.2023.110218.-**8%**
CRediT author statement: Conceptualization, Methodology, Formal analysis, Writing – original draft, Writing – review & editing, Project administration.

[3] J. Amraei, T. Rogala, A. Katunin, A. Premanand, G. Kokot, D. Wachla, W. Kuś, M. Bilewicz, B. Khatri, and F. Balle, *Thermomechanical fatigue behavior of CF/PEKK composite under low and ultrasonic frequencies*, Composites Part B: Engineering, 2024, 281,111539. Doi: 10.1016/j.compositesb.2024.111539.-**11%**
CRediT author statement: Writing – review & editing, Writing – original draft, Project administration, Methodology, Funding acquisition, Formal analysis, Conceptualization.

[4] J. Amraei, A. Katunin, and M. Lipińska, *Numerical simulation and experimental validation of self-heating of polymer-matrix composites during low-cycle fatigue loading*, International Journal of Fatigue, 2025, 188,108510. Doi: 10.1016/j.ijfatigue.2024.108510.-**20%**
CRediT author statement: Writing – review & editing, Writing – original draft, Methodology, Investigation, Conceptualization.

[5] J. Amraei, A. Katunin, D. Wachla, and K. Lis, *Damage assessment in composite plates using extended non-destructive self-heating based vibrothermography technique*, Measurement, 2025, 241,115670. Doi: 10.1016/j.measurement.2024.115670.-**25%**
CRediT author statement: Writing – review & editing, Writing – original draft, Software, Methodology, Formal analysis, Data curation, Conceptualization.

[6] P. N. B. Reis, A. Katunin, J. Amraei, *Critical analysis of the systems used to reduce self-heating in polymer composites subjected to very high cycle fatigue regimes*. Fatigue & Fracture of Engineering Materials & Structures, 2025, 48, 1371–1392. Doi: 10.1111/ffe.14561.-**15%**

[7] J. Amraei, and A. Katunin, *Thermomechanical fatigue life assessment of polymer-matrix composites via entropy-based damage evolution and stiffness degradation under different frequencies*, Submitted to Composites Part B: Engineering, 2025, 298, 12353. DOI: 10.1016/j.compositesb.2025.112353.-**20%**
CRediT author statement: Conceptualization, Methodology, Writing-review and editing.

[8] J. Amraei, T. Rogala, A. Katunin, I. Barszczewska-Rybarek, J. M. Parente, and P. N. B. Reis, *Synergistic effects of graphene nanoplatelets and carbon nanofibers on thermomechanical fatigue response of modified glass/epoxy composites*, Submitted to International Journal of Fatigue, Under Review. -**10%**

CRediT author statement: Conceptualization, Methodology, Formal analysis, Writing-original draft preparation, Writing-review and editing.

My specific contributions to the paper [1] additionally to those mentioned in the CRediT author statement consisted of:

- Mentoring, and formulation of overarching research goals and aims.

In particular, my primary contributions to the paper [2] consisted of:

- Ideas, and formulation of overarching research goals and aims,
- Leadership responsibility for the research activity.

In particular, my main contributions to the paper [3] including:

- Comparative formal analysis of fracture mechanisms in low and ultrasonic frequency fatigue results.
- Leadership responsibility for research activity planning including mentorship.

In particular, my main contributions to the paper [4] including:

- Mentoring for achieving the research goals,
- Sharing the data to validate the developed numerical model.
- Sharing the developed MATLAB routines of the algorithm for constructing master curves.

In particular, my main contributions to the paper [5] including:

- Development and adjustment of the MATLAB procedures for enhancing damage identification and quantification.

In particular, my main contributions to the paper [6] including:

- Adding specific points in the discussion of the paper.

In particular, my main contributions to the paper [7] including:

- Contributing to the review and editing of the manuscript,
- Contributing to answering the reviewers' comments.

In particular, my main contributions to the paper [8] including:

- Contributing to the introduction section of the manuscript,
- Contributing to the description and analysis of DSC results.

Furthermore, I declare that I have been informed about the use of the above publications in the doctoral dissertation of Jafar Amraei, MSc, Eng., entitled:

"Thermomechanical Fatigue Life Assessment of Polymer-Matrix Composites under Temperature Control and Different Loading Regimes"

.....

Andrzej Katunin

(podpis odręczny)

Dominik Wachla, Ph.D, Eng.
Silesian University of Technology
Faculty of Mechanical Engineering
Department of Fundamentals of Machinery Design

Declaration

I hereby declare that my contribution percentages in the following publications were as follows:

[1] A. Premanand, T. Rogala, D. Wachla, J. Amraei, A. Katunin, B. Khatri, M. Rienks, F. Balle, *Fatigue strength estimation of a CF/PEKK composite through self-heating temperature analysis using cyclic bending tests at 20 kHz*, Composites Science and Technology, 2023, 243, 110218. Doi: 10.1016/j.compscitech.2023.110218. – **10%**
CRediT author statement: Conceptualization, Methodology, Data curation, Formal analysis, Software, Writing – original draft.

[2] J. Amraei, T. Rogala, A. Katunin, A. Premanand, G. Kokot, D. Wachla, W. Kuś, M. Bilewicz, B. Khatri, and F. Balle, *Thermomechanical fatigue behavior of CF/PEKK composite under low and ultrasonic frequencies*, Composites Part B: Engineering, 2024, 281,111539. Doi: 10.1016/j.compositesb.2024.111539. – **8%**
CRediT author statement: Conceptualization, Writing – review & editing, Writing – original draft, Software, Formal analysis, Data curation.

[3] J. Amraei, A. Katunin, D. Wachla, and K. Lis, *Damage assessment in composite plates using extended non-destructive self-heating based vibrothermography technique*, Measurement, 2025, 241,115670. Doi: 10.1016/j.measurement.2024.115670. – **15%**
CRediT author statement: Writing – review & editing, Writing – original draft, Software, Methodology, Investigation, Conceptualization.

In particular, my primary contributions to the paper [1] consisted of:

- Evaluation of the variability of fitting parameters.

In particular, my main contributions to the paper [2] including:

- Estimating the critical self-heating temperature for low and ultrasonic fatigue testing scenarios.

In particular, my main contributions to the paper [3] including:

- Supporting in the preparation of the test setup,
- Supporting in performing the preliminary experiments and mentoring.

Furthermore, I declare that I have been informed about the use of the above publications in the doctoral dissertation of Jafar Amraei, MSc, Eng., entitled:

"Thermomechanical Fatigue Life Assessment of Polymer-Matrix Composites under Temperature Control and Different Loading Regimes"

Date & Signature .....

Dominik Wachla

/podpis odręczny/

Tomasz Rogala, Ph.D, Eng.
Silesian University of Technology
Faculty of Mechanical Engineering
Department of Fundamentals of Machinery Design

Declaration

I hereby declare that my contribution percentages in the following publications were as follows:

[1] A. Premanand, T. Rogala, D. Wachla, J. Amraei, A. Katunin, B. Khatri, M. Rienks, F. Balle, *Fatigue strength estimation of a CF/PEKK composite through self-heating temperature analysis using cyclic bending tests at 20 kHz*, Composites Science and Technology, 2023, 243, 110218. Doi: 10.1016/j.compscitech.2023.110218.-**18%**
CRediT author statement: Conceptualization, Methodology, Data curation, Formal analysis, Software, Writing – original draft, Writing – review & editing.

[2] J. Amraei, T. Rogala, A. Katunin, A. Premanand, G. Kokot, D. Wachla, W. Kuś, M. Bilewicz, B. Khatri, and F. Balle, *Thermomechanical fatigue behavior of CF/PEKK composite under low and ultrasonic frequencies*, Composites Part B: Engineering, 2024, 281,111539. Doi: 10.1016/j.compositesb.2024.111539.-**16%**
CRediT author statement: Conceptualization, Methodology, Experiments, Data curation, Formal analysis, Software, Writing – original draft preparation, Writing – review and editing.

[3] J. Amraei, T. Rogala, A. Katunin, I. Barszczewska-Rybarek, J. M. Parente, and P. N. B. Reis, *Synergistic effects of graphene nanoplatelets and carbon nanofibers on thermomechanical fatigue response of modified glass/epoxy composites*, Submitted to International Journal of Fatigue, Revised. -**16%**
CRediT author statement: Conceptualization, Methodology, Data curation, Formal analysis, Software, Writing-original draft preparation, Writing-review and editing.

In particular, my primary contributions to the paper [1] consisted of:

- Estimation of the fatigue strength using the thermographic approach (ΔT-σ),
- Extension of the fatigue strength estimation concept for variable pause duration and its validation.

In particular, my main contributions to the paper [2] including:

- Designing and performing the experiments,
- Estimation of the fatigue strength using the thermographic approach ($\Delta T - \sigma$) and *S-N* curves,
- Exploring the influence of mean load under different mean loads using the thermographic approach.

In particular, my main contributions to the paper [3] including:

- Drawing the schematic view of the customized laboratory test-rig,
- Adding the theory related to the determination of fatigue strength using the ΔT-σ approach,
- Estimation of fatigue strength using ΔT-σ approach based on MCR and MPD procedures,
- Determination of the uncertainties of the determined fatigue strength values derived from the thermography approaches.

Furthermore, I declare that I have been informed about the use of the above publications in the doctoral dissertation of Jafar Amraei, MSc, Eng., entitled:

"Thermomechanical Fatigue Life Assessment of Polymer-Matrix Composites under Temperature Control and Different Loading Regimes"

Date & Signature 20.02.2025

Tomasz Rogala
/podpis odręczny/

Magdalena Lipińska, PhD, DSc, Eng.
Lodz University of Technology
Faculty of Chemistry
Institute of Polymer and Dye Technology

Declaration

I hereby declare that my contribution percentage in the following publication was as follows:

[1] J. Amraei, A. Katunin, and M. Lipińska, *Numerical simulation and experimental validation of self-heating of polymer-matrix composites during low-cycle fatigue loading*, International Journal of Fatigue, 2025, 188,108510. Doi: 10.1016/j.ijfatigue.2024.108510.-**15%**

CRediT author statement: Writing – review & editing, Investigation.

In particular, my primary contribution to the paper [1] consisted of:

- Performing oscillatory shear rheometry experiments.

Furthermore, I declare that I have been informed about the use of the above publication in the doctoral dissertation of Jafar Amraei, MSc, Eng., entitled:

"Thermomechanical Fatigue Life Assessment of Polymer-Matrix Composites under Temperature Control and Different Loading Regimes"

20.02.2025, Lodz

Magdalena Lipińska

Wacław Kuś, PhD, DSc, Eng., prof. SUT
Silesian University of Technology
Faculty of Mechanical Engineering
Department of Computational Mechanics and Engineering

Declaration

I hereby declare that my contribution percentage in the following publication was as follows:

[1] J. Amraei, T. Rogala, A. Katunin, A. Premanand, G. Kokot, D. Wachla, W. Kuś, M. Bilewicz, B. Khatri, and F. Balle, *Thermomechanical fatigue behavior of CF/PEKK composite under low and ultrasonic frequencies*, Composites Part B: Engineering, 2024, 281,111539.
Doi: 10.1016/j.compositesb.2024.111539.**-6%**
CRediT author statement: Writing – review & editing, Investigation.

In particular, my primary contribution to the paper [1] consisted of:

- Performing the low-frequency fatigue testing.

Furthermore, I declare that I have been informed about the use of the above publication in the doctoral dissertation of Jafar Amraei, MSc, Eng., entitled:

"Thermomechanical Fatigue Life Assessment of Polymer-Matrix Composites under Temperature Control and Different Loading Regimes"

Signed by / Podpisano przez:
Wacław Michał Kuś
Politechnika Śląska
Date / Data: 2025-02-20 12:55

Date & Signature.....

Wacław Kuś

Grzegorz Kokot, PhD, DSc, Eng., prof. SUT
Silesian University of Technology
Faculty of Mechanical Engineering
Department of Computational Mechanics and Engineering

Declaration

I hereby declare that my contribution percentage in the following publication was as follows:

[1] J. Amraei, T. Rogala, A. Katunin, A. Premanand, G. Kokot, D. Wachla, W. Kuś, M. Bilewicz, B. Khatri, and F. Balle, *Thermomechanical fatigue behavior of CF/PEKK composite under low and ultrasonic frequencies*, Composites Part B: Engineering, 2024, 281,111539.
Doi: 10.1016/j.compositesb.2024.111539.-**8%**
CRediT author statement: Writing – review & editing, Investigation.

In particular, my primary contributions to the paper [1] consisted of:

- Preparation of the test rig for the low-frequency fatigue testing.
- Performing the low-frequency fatigue testing.

Furthermore, I declare that I have been informed about the use of the above publication in the doctoral dissertation of Jafar Amraei, MSc, Eng., entitled:

"Thermomechanical Fatigue Life Assessment of Polymer-Matrix Composites under Temperature Control and Different Loading Regimes"

Date & Signature .....

Grzegorz Kokot

/podpis odręczny nieczytelny/

Krzysztof Lis, Ph.D, Eng.
Silesian University of Technology
Faculty of Mechanical Engineering
Department of Machine Technology

Declaration

I hereby declare that my contribution percentage in the following publication was as follows:

[1] J. Amraei, A. Katunin, D. Wachla, and K. Lis, *Damage assessment in composite plates using extended non-destructive self-heating based vibrothermography technique*, Measurement, 2025, 241,115670. Doi: 10.1016/j.measurement.2024.115670.-**10%**
CRediT author statement: Writing – review & editing, Writing – original draft, Software, Investigation, Conceptualization.

In particular, my main contributions to the paper [1] including:

- Preparation of the fixture for performing the experiments,
- Introducing artificial damage on the tested composite specimens.

Furthermore, I declare that I have been informed about the use of the above publication in the doctoral dissertation of Jafar Amraei, MSc, Eng., entitled:

"Thermomechanical Fatigue Life Assessment of Polymer-Matrix Composites under Temperature Control and Different Loading Regimes"

Date & Signature .. ..

Krzysztof Lis

(podpis odręczny)

Marcin Bilewicz, Ph.D, Eng.
Silesian University of Technology
Faculty of Mechanical Engineering
Department of Engineering Materials and Biomaterials

Declaration

I hereby declare that my contribution percentage in the following publication was as follows:

[1] J. Amraei, T. Rogala, A. Katunin, A. Premanand, G. Kokot, D. Wachla, W. Kuś, M. Bilewicz, B. Khatri, and F. Balle, *Thermomechanical fatigue behavior of CF/PEKK composite under low and ultrasonic frequencies*, Composites Part B: Engineering, 2024, 281,111539.
Doi: 10.1016/j.compositesb.2024.111539.-**5%**
CRediT author statement: Writing – review & editing, Investigation.

In particular, my primary contribution to the paper [1] consisted of:

- Conducting the microscopy images for the CF/PEKK specimens in the low-cycle fatigue testing scenario.

Furthermore, I declare that I have been informed about the use of the above publication in the doctoral dissertation of Jafar Amraei, MSc, Eng., entitled:

"Thermomechanical Fatigue Life Assessment of Polymer-Matrix Composites under Temperature Control and Different Loading Regimes"

Date & Signature.....

Marcin Bilewicz

/podpis odręczny/

Izabela Barszczewska-Rybarek, PhD, DSc, Eng., prof. SUT
Silesian University of Technology
Faculty of Chemistry
Department of Physical Chemistry and Technology of Polymers

Declaration

I hereby declare that my contribution percentage in the following publication was as follows:

[1] J. Amraei, T. Rogala, A. Katunin, I. Barszczewska-Rybarek, J. M. Parente, and P. N. B. Reis, *Synergistic effects of graphene nanoplatelets and carbon nanofibers on thermomechanical fatigue response of modified glass/epoxy composites*, Submitted to International Journal of Fatigue, Revised. **-7%**
CRediT author statement: Investigation, Formal analysis, Writing-original draft preparation, Writing-review and editing.

In particular, my primary contributions to the paper [1] consisted of:

- Performing DSC tests,
- Contributing to the description and analysis of DSC results.

Furthermore, I declare that I have been informed about the use of the above publications in the doctoral dissertation of Jafar Amraei, MSc, Eng., entitled:

"Thermomechanical Fatigue Life Assessment of Polymer-Matrix Composites under Temperature Control and Different Loading Regimes"

Date & Signature .....

Izabela Barszczewska-Rybarek

/podpis odręczny/

Prof. Dr.-Ing. Frank Balle
Albert-Ludwigs-Universität Freiburg
Faculty of Engineering
Department for Sustainable Systems Engineering (INATECH)

Declaration

I hereby declare that my contribution percentages in the following publications were as follows:

[1] A. Premanand, T. Rogala, D. Wachla, J. Amraei, A. Katunin, B. Khatri, M. Rienks, F. Balle, *Fatigue strength estimation of a CF/PEKK composite through self-heating temperature analysis using cyclic bending tests at 20 kHz*, Composites Science and Technology, 2023, 243, 110218.
Doi: 10.1016/j.compscitech.2023.110218.-**8%**
CRediT author statement: Conceptualization, Methodology, Writing – review & editing, Project lead, Funding acquisition.

[2] J. Amraei, T. Rogala, A. Katunin, A. Premanand, G. Kokot, D. Wachla, W. Kuś, M. Bilewicz, B. Khatri, and F. Balle, *Thermomechanical fatigue behavior of CF/PEKK composite under low and ultrasonic frequencies*, Composites Part B: Engineering, 2024, 281,111539.
Doi: 10.1016/j.compositesb.2024.111539.-**5%**
CRediT author statement: Writing – review & editing, Project administration, Methodology, Funding acquisition, Conceptualization.

In particular, my primary contributions to the paper [1] consisted of:

- Ideas, and formulation of overarching research goals and aims,
- Materials and the experimental fatigue test setup,
- Design of experiments,
- Leadership responsibility for the research activity.

In particular, my main contributions to the paper [2] including:

- Management and coordination responsibility for the research activity for VHCF,
- Materials and the experimental fatigue test setup for the VHCF scenario,
- Leadership responsibility for research activity planning including mentorship.

Furthermore, I declare that I have been informed about the use of the above publications in the doctoral dissertation of Jafar Amraei, MSc, Eng., entitled:

"Thermomechanical Fatigue Life Assessment of Polymer-Matrix Composites under Temperature Control and Different Loading Regimes"

Freiburg, 20.02.2025 .....

Prof. Dr.-Ing. Frank Balle

/podpis odręczny/

M.Sc. Aravind Premanand
Albert-Ludwigs-Universität Freiburg
Faculty of Engineering
Department for Sustainable Systems Engineering (INATECH)

Declaration

I hereby declare that my contribution percentages in the following publications were as follows:

[1] A. Premanand, T. Rogala, D. Wachla, J. Amraei, A. Katunin, B. Khatri, M. Rienks, F. Balle, *Fatigue strength estimation of a CF/PEKK composite through self-heating temperature analysis using cyclic bending tests at 20 kHz*, Composites Science and Technology, 2023, 243, 110218. Doi: 10.1016/j.compscitech.2023.110218.-**30%**
CRediT author statement: Conceptualization, Methodology, Experiments, Data curation, Writing – original draft, Writing – review & editing.

[2] J. Amraei, T. Rogala, A. Katunin, A. Premanand, G. Kokot, D. Wachla, W. Kuś, M. Bilewicz, B. Khatri, and F. Balle, *Thermomechanical fatigue behavior of CF/PEKK composite under low and ultrasonic frequencies*, Composites Part B: Engineering, 2024, 281,111539. Doi: 10.1016/j.compositesb.2024.111539.-**11%**
CRediT author statement: Writing – original draft, Resources, Investigation, Formal analysis, Data curation, Conceptualization.

In particular, my primary contributions to the paper [1] consisted of:

- Design of experiments,
- Materials and the experimental fatigue test setup,
- Performing the monotonic and ultrasonic fatigue testing,
- Conducting microscopy images for the CF/PEKK specimens in the ultrasonic fatigue scenario,
- Experimental validation of fatigue strength in the VHCF regime.

In particular, my main contributions to the paper [2] including:

- Performing the ultrasonic fatigue testing,
- Conducting microscopy images for CF/PEKK specimens in the ultrasonic fatigue testing scenario.

Furthermore, I declare that I have been informed about the use of the above publications in the doctoral dissertation of Jafar Amraei, MSc, Eng., entitled:

"Thermomechanical Fatigue Life Assessment of Polymer-Matrix Composites under Temperature Control and Different Loading Regimes"

Date & Signature.....

Aravind Premanand
(podpis odręczny)

Dr.-Ing. Bilal Khatri
Albert-Ludwigs-Universität Freiburg
Faculty of Engineering
Department for Sustainable Systems Engineering (INATECH)

Declaration

I hereby declare that my contribution percentages in the following publications were as follows:

[1] A. Premanand, T. Rogala, D. Wachla, J. Amraei, A. Katunin, B. Khatri, M. Rienks, F. Balle, *Fatigue strength estimation of a CF/PEKK composite through self-heating temperature analysis using cyclic bending tests at 20 kHz*, Composites Science and Technology, 2023, 243, 110218. Doi: 10.1016/j.compscitech.2023.110218.-**8%**
CRediT author statement: Conceptualization, Writing – original draft, Writing – review & editing.

[2] J. Amraei, T. Rogala, A. Katunin, A. Premanand, G. Kokot, D. Wachla, W. Kuś, M. Bilewicz, B. Khatri, and F. Balle, *Thermomechanical fatigue behavior of CF/PEKK composite under low and ultrasonic frequencies*, Composites Part B: Engineering, 2024, 281,111539. Doi: 10.1016/j.compositesb.2024.111539.-**5%**
CRediT author statement: Conceptualization, Writing – review & editing.

In particular, my primary contributions to the paper [1] consisted of:

- Design of experiments,
- Ideas, and formulation of overarching research goals and aims,
- Specifically critical review, and revisions throughout both pre-publication and post-publication stages.

In particular, my main contributions to the paper [2] including:

- Specifically critical review, and revisions throughout both pre-publication and post-publication stages.

Furthermore, I declare that I have been informed about the use of the above publications in the doctoral dissertation of Jafar Amraei, MSc, Eng., entitled:

"Thermomechanical Fatigue Life Assessment of Polymer-Matrix Composites under Temperature Control and Different Loading Regimes"

Date & Signature .....

Bilal Khatri
(podpis odręczny)

Michael Rienks, Dipl.-Ing.
Albert-Ludwigs-Universität Freiburg
Faculty of Engineering
Department for Sustainable Systems Engineering (INATECH)

Declaration

I hereby declare that my contribution percentage in the following publication was as follows:

[1] A. Premanand, T. Rogala, D. Wachla, J. Amraei, A. Katunin, B. Khatri, M. Rienks, F. Balle, *Fatigue strength estimation of a CF/PEKK composite through self-heating temperature analysis using cyclic bending tests at 20 kHz*, Composites Science and Technology, 2023, 243, 110218. Doi: 10.1016/j.compscitech.2023.110218.-**8%**
CRediT author statement: Software, Implementation.

In particular, my primary contributions to the paper [1] consisted of:

- Supporting for the software and hardware and their implementation.

Furthermore, I declare that I have been informed about the use of the above publication in the doctoral dissertation of Jafar Amraei, MSc, Eng., entitled:

"Thermomechanical Fatigue Life Assessment of Polymer-Matrix Composites under Temperature Control and Different Loading Regimes"

Date & Signature .....

Michael Rienks
(podpis odręczny)

Paulo N.B. Reis, Assoc. Prof.
University of Coimbra
Faculty of Sciences and Technology
Department of Mechanical Engineering

Declaration

I hereby declare that my contribution percentages in the following publications were as follows:

[1] P. N. B. Reis, A. Katunin, J. Amraei, Critical analysis of the systems used to reduce self-heating in polymer composites subjected to very high cycle fatigue regimes. Fatigue & Fracture of Engineering Materials & Structures (2025). Doi: 10.1111/ffe.14561.-**70%**

[2] J. Amraei, T. Rogala, A. Katunin, I. Barszczewska-Rybarek, J. M. Parente, and P. N. B. Reis, *Synergistic effects of graphene nanoplatelets and carbon nanofibers on thermomechanical fatigue response of modified glass/epoxy composites*, Submitted to International Journal of Fatigue, Revised. -**25%**
CRediT author statement: Conceptualization, Methodology, Investigation, Formal analysis, Writing-original draft preparation, Writing-review and editing, Project administration, Funding acquisition.

In particular, my primary contributions to the paper [1] consisted of:

- Leadership responsibility for the research activity,
- Literature review and formal analysis of the systems used for limiting the self-heating in VHCF regime.

In particular, my primary contributions to the paper [2] consisted of:

- Producing of the unmodified, and modified GFRP specimens,
- Contributing to the design of experiments,
- Leadership responsibility for the research activity,
- Conducting SEM images for the PMC specimens to verify the degree of dispersion of the nanofillers,
- Microscopic morphological analysis on the fracture surfaces of the nano-reinforced GFRP specimens.

Furthermore, I declare that I have been informed about the use of the above publication in the doctoral dissertation of Jafar Amraei, MSc, Eng., entitled:

"Thermomechanical Fatigue Life Assessment of Polymer-Matrix Composites under Temperature Control and Different Loading Regimes"

Date & Signature Assinado por: **PAULO NOBRE BALBIS DOS REIS**
Num. de Identificação: 07731315
Data: 2025.02.20 18:18:50+00'00'

Paulo N.B. Reis

João M. Parente, MSc.
University of Beira Interior
Department of Electromechanical Engineering
Centre for Mechanical and Aerospace Science and Technologies (C-MAST)

Declaration

I hereby declare that my contribution percentage in the following publication was as follows:

[1] J. Amraei, T. Rogala, A. Katunin, I. Barszczewska-Rybarek, J. M. Parente, and P. N. B. Reis, *Synergistic effects of graphene nanoplatelets and carbon nanofibers on thermomechanical fatigue response of modified glass/epoxy composites*, Submitted to International Journal of Fatigue, Revised. -**7%**
CRediT author statement: Resources, Writing-review and editing.

In particular, my primary contributions to the paper [1] consisted of:

- Production of the unmodified, and modified GFRP specimens.

Furthermore, I declare that I have been informed about the use of the above publication in the doctoral dissertation of Jafar Amraei, MSc, Eng., entitled:

"Thermomechanical Fatigue Life Assessment of Polymer-Matrix Composites under Temperature Control and Different Loading Regimes"

Date & Signature

Assinado por: **João Miguel Nunes Parente**
Num. de Identificação: 14139047
Data: 2025.02.20 14:50:24+00'00'

CHAVE MÓVEL

João M. Parente